JUSTUS-LIEBIG-UNIVERSITÄT GIESSEN

Justus-Liebig-Universität Gießen

Fachbereich für Biologie und Chemie

Institut für Anorganische und Analytische Chemie

Multifunctional molecular materials for the interaction of magnetism and luminescence

Kumulativ-Dissertation zur Erlangung

des Doktorgrades der Naturwissenschaften

vorgelegt von

Heba Youssef

2023

Printed with the support of the German Academic Exchange Service

Selbstständigkeitserklärung

Ich erkläre hiermit, dass ich die vorgelegte Dissertation selbstständig und ohne unerlaubte fremde Hilfe und nur mit den Hilfen angefertigt, die ich in der Dissertation angegeben habe. Alle Textstellen, die wörtlich oder sinngemäß aus veröffentlichten Schriften entnommen sind, und alle Angaben, die auf mündlichen Auskünften beruhen, sind als solche kenntlich gemacht. Ich stimme einer eventuelle Überprüfung meiner Dissertation durch eine Antiplagiat-Software zu. Bei den von mir durchgeführten und in der Dissertation erwähnten Untersuchungen habe ich die Grundsätze guter wissenschaftlicher Praxis, wie sie in der „*Satzung der Justus-Liebig-Universität Gießen zur Sicherung guter wissenschaftlicher Praxis“* niedergelegt sind, eingehalten.

_____ _____

Ort, Datum Heba Youssef

Erstgutachter: Prof. Dr. Klaus Müller-Buschbaum

Zweitgutachter: Prof. Dr. Siegfried Schindler

Acknowledgements

I would like to express my gratitude to Prof. Dr. Klaus Müller-Buschbaum for giving me the opportunity to do my PhD under his supervision and for his outstanding, continuous support, and guidance.

Great thanks to Prof. Dr. Siegfried Schindler for the assessment of my doctoral thesis.

Many thanks to Prof. Dr. Bernd Smarsly and Prof. Dr. Richard Göttlich for accepting the request to join the assessment committee.

I gratefully acknowledge the Egyptian Ministry of Higher Education (MoHE) and the German Academic Exchange Service (DAAD) under the German Egyptian Research Long-term Scholarship (GERLS) Programme, 2017 (57311832), for a Ph.D. fellowship.

I also acknowledge the Justus-Liebig-University Giessen for awarding a dissertation completion grant in its 14th round of applications on the basis of JLU's Gender Equality Concept.

Additional thanks go to Prof. Dr. Ilya V. Taydakov (Lebedev Physical Institute of the Russian Academy of Sciences, Moscow, Russia) and his group for the synthesis of the ligands under study.

Many thanks to Prof. Dr. Florian Kraus and Dr. Clemens (Philipps University of Marburg, Marburg, Germany) for the magnetic measurements.

Special thanks to Dr. Jonathan Becker, who not only taught me crystallography but also provided support and help in many other areas. I would also like to thank Dr. Sven Zottnick, who taught me know-how at the beginning of my doctorate.

Thanks go to Carsten Paulmann and Heiko Schulz-Ritter for their assistance in using beamline P24 during the measurements at Deutsches Elektronen-Synchrotron DESY (Hamburg, Germany).

Many thanks to the current and former members of our scientific group, with whom I have had the privilege of collaborating. Further thanks go to Dr. Alexander E. Sedykh, Thomas Schäfer, and Marcel Seuffert for providing helpful comments and suggestions throughout the PhD period.

I would like to thank the students I had the privilege of mentoring during their advanced course: Maximilian Elfert and Leonardo Basso.

I would like to express my deep appreciation to my family, especially my husband, Dr. Ahmed Fetoh, and my lovely daughters, Malak and Mariam, for going through this long process with me. Without their endless love and support, it would not have been possible to complete my studies and do my PhD abroad. My husband has always had my back and this was no exception, so I thank him for always reminding me of the end goal and for the sacrifices he made to enable me to pursue my degree. I am very grateful to my large family in Egypt for believing in me and for their continued love and support.

I am incredibly grateful to all people, acquaintances included, who in one way or another led me to this step of my life.

For my father, Mohamed Metwally Youssef,

who supported me and encouraged me to pursue my dreams.

For my husband, Dr. Ahmed Fetoh,

without whom, this would have never been possible.

For Mariam and Malak,

who, despite their young age, have understood the demands of being a PhD student.

"Whoever takes a path upon which to obtain knowledge, Allah makes the path to Paradise easy for him."

"Knowledge can only be acquired through the process of learning."

Allah's messenger Mohammad (ﷺ)

Table of Contents

Abstract

The synthesis and characterization of new coordination polymers and complexes of the lanthanide series (Ln), besides heterobimetallic compounds of lanthanides and alkaline earth metals with the N-donor ligands 3-(2-pyridyl)pyrazole (2-PyPzH), 3-(3-pyridyl)pyrazole (3-PyPzH), and 3-(4-pyridyl)pyrazole (4-PyPzH) and the characterization of their photophysical and magnetic properties, have been achieved.

Chapter 1 provides an introduction to lanthanides and their photoluminescence and magnetic properties, as well as a literature survey of some N-donor ligands besides known coordination compounds of trivalent lanthanide elements with 2-PyPzH and its derivatives; no previous lanthanide-containing compounds with 3-PyPzH and 4-PyPzH have been reported in the literature. Research goals are stated in **Chapter 2**.

In **Chapter 3** and along the way to study the interaction between luminescence and magnetism within lanthanide-based coordination polymers (CPs), a synthesis of 76 CPs and complexes was achieved. Three series of 35 homoleptic 3D-, 2D-, and 1D-coordination polymers were prepared by redox reactions of elemental lanthanides with 2-PyPzH, 3-PyPzH, and 4-PyPzH. Three heteroleptic 2D-networks, including divalent europium, were also prepared as an example of another Ln oxidation state. Three heterobimetallic lanthanide/alkaline earth complexes and two alkaline earth complexes were synthesized by solvothermal synthesis of elemental lanthanide and/or alkaline earth metals (AE) with 2-PyPzH. The synthesis and structural characterization of 33 heteroleptic 3D- and 2D-coordination polymers and complexes, some of which are polymorphic, were achieved, along with salt-like complexes that differ in constitution and structural extension of lanthanide chlorides together with 2-PyPzH and 3-PyPzH.

Studying the photophysical properties of the synthesized CPs and complexes, one of the main goals, has revealed:

1. Unique pink through orange to bright red emitting Ce^{3+}-based 2D-networks, 3D-frameworks, and complexes are unusual cases of emission colors of Ce^{3+}, which marks an example of a strong reduction of the excited 5d states of Ce^{3+}.

2. The pyridylpyrazole/ates act as excellent photoluminescence sensitizers in trivalent lanthanide coordination compounds by increasing the intensity of the characteristic 4f–4f metal ion emission. The high luminescence efficiency is indicated by excellent to moderate quantum yields from 92 %, 76 % to 74 % for Tb^{3+} and up to 6 % for Eu^{3+} frameworks and complexes, for instance.

3. Tuning the luminescence chromaticity from green to yellow and red towards white light emission is achieved by co-doping the Gd-containing frameworks with Eu^{3+} and Tb^{3+}, as well as the co-doping of Eu^{3+} with Tb^{3+} and vice versa.

4. The study ligands do not only pass a strong antenna effect for the Ln^{3+} emitters in the visible region but also for the near-infrared (NIR) emitters. Uncommon NIR emission bands of Tm^{3+} and Ho^{3+} besides Pr^{3+}, Er^{3+}, and Nd^{3+} were detected.

Another goal was to characterize the magnetic properties using direct current (DC) measurements. The DC magnetic susceptibility studies show weak ferromagnetic interactions for Ho^{3+} and absence of interatomic interactions for Dy^{3+} and Er^{3+}, which limits the study of the interaction between the magnetic and photophysical properties.

Kurzzusammenfassung

Die Synthese und Charakterisierung neuer Koordinationspolymere und Komplexe der Lanthanidenreihe (Ln) mit heterobimetallischen Verbindungen von Lanthaniden und Erdalkalimetallen mit den N-Donor-Liganden 3-(2-Pyridyl)pyrazol (2-PyPzH), 3-(3-Pyridyl)pyrazol (3-PyPzH) und 3-(4-Pyridyl)pyrazol (4-PyPzH) sowie die Charakterisierung ihrer photophysikalischen und magnetischen Eigenschaften sind gelungen.

Kapitel 1 bietet eine Einführung in die Lanthanide und ihre Photolumineszenz- und magnetischen Eigenschaften sowie einen Literaturüberblick über einige N-Donor-Liganden neben den bekannten Koordinationsverbindungen von dreiwertigen Lanthaniden mit 2-PyPzH und seinen Derivaten; in der Literatur sind bisher keine lanthanidhaltigen Verbindungen mit 3-PyPzH und 4-PyPzH bekannt. Die Forschungsziele sind in **Kapitel 2** aufgeführt.

In **Kapitel 3** und auf dem Weg zur Untersuchung der Wechselwirkung zwischen Lumineszenz und Magnetismus in Koordinationspolymeren (CPs) auf Lanthanidenbasis wurde eine Synthese von 76 CPs und Komplexen erreicht. Drei Serien von 35 homoleptischen 3D-, 2D- und 1D-Koordinationspolymeren wurden durch Redoxreaktionen von elementaren Lanthaniden mit 2-PyPzH, 3-PyPzH und 4-PyPzH hergestellt. Drei heteroleptische 2D-Netze, einschließlich zweiwertigem Europium, wurden ebenfalls als Beispiel für eine andere Ln-Oxidationsstufe hergestellt. Drei heterobimetallische Lanthaniden/Erdalkalimetall-Komplexe und zwei Erdalkalimetall-Komplexe wurden durch solvothermalsynthese von elementaren Lanthaniden und/oder Erdalkalimetallen (AE) mit 2-PyPzH hergestellt. Die Synthese und strukturelle Charakterisierung von 33 heteroleptischen 3D- und 2D-Koordinationspolymeren und komplexen, von denen einige polymorph sind, sowie von salzähnlichen Komplexen, die sich in der Konstitution und strukturellen Ausdehnung von Lanthanidchloriden zusammen mit 2-PyPzH und 3-PyPzH unterscheiden, wurde erreicht.

Die Untersuchung der photophysikalischen Eigenschaften der synthetisierten CPs und Komplexe, eines der Hauptziele, hat gezeigt:

1. Einzigartige rosa zu orangefarbene bis leuchtend rote Ce^{3+}-basierte 2D-Netzwerke, 3D-Gerüste und Komplexe sind ungewöhnliche Fälle von Ce^{3+}-Emissionsfarben, die ein Beispiel für eine starke Reduzierung der angeregten 5d-Zustände von Ce^{3+} darstellen.

2. Die Pyridylpyrazol/ate wirken als ausgezeichnete Photolumineszenz-Sensibilisatoren in dreiwertigen Lanthanid-Koordinationsverbindungen, indem sie die Intensität der charakteristischen 4f–4f-Metallionenemission erhöhen. Die hohe Lumineszenzeffizienz zeigt sich in ausgezeichneten bis mäßigen Quantenausbeuten von 92 %, 76 % bis 74 % für Tb^{3+} und bis zu 6 % für Eu^{3+}-Gerüste und -Komplexe.

3. Die Abstimmung der Lumineszenzchromatizität von grün über gelb und rot bis hin zu weißer Lichtemission wird durch die Ko-dotierung der Gd-haltigen Gerüste mit Eu^{3+} und Tb^{3+} sowie durch die Ko-dotierung von Eu^{3+} mit Tb^{3+} und umgekehrt erreicht.

4. Die untersuchten Liganden haben nicht nur eine starke Antennenwirkung für die im sichtbaren Bereich emittierenden Ln^{3+}, sondern auch für die Nah-Infrarot (NIR)-

Emitter. Neben Pr^{3+}, Er^{3+} und Nd^{3+} wurden auch ungewöhnliche NIR-Emissionsbanden von Tm^{3+} und Ho^{3+} nachgewiesen.

Ein weiteres Ziel war die Charakterisierung der magnetischen Eigenschaften mit Hilfe von Gleichstrommessungen (DC). Die Untersuchungen der magnetischen Gleichstromsuszeptibilität zeigen schwache ferromagnetische Wechselwirkungen für Ho^{3+} und das Fehlen interatomarer Wechselwirkungen für Dy^{3+} und Er^{3+}, was die Untersuchung der Wechselwirkung zwischen den magnetischen und photophysikalischen Eigenschaften einschränkt.

1. Introduction

1.1. What is lanthanide?

Lanthanide or lanthanoid (Ln), is a series of 15 chemical elements from lanthanum (La) to lutetium (Lu) (atomic numbers 57–71). Although the IUPAC recommends using the name lanthanoid instead of lanthanide, as the suffix "-ide" is preferred for negative ions, whereas the suffix "-oid" implies similarity to one of the members of the enclosing family of elements,[1] lanthanide is the most commonly used nomenclature.[2-3] Lanthanides, along with the chemically similar elements scandium (Sc) and yttrium (Y) are often referred to as rare earths. "Rare" refers to the difficulty of separating out each of the individual lanthanide elements,[4] whereas "earth" refers to the fact that they naturally occur in their oxidized form in salts and minerals.[2] Group 3 elements (Sc, Y, and La) are in fact the first elements of their respective d-transition series (3d, 4d, and 5d). The remaining lanthanides (Ce–Lu) are not visible in the main frame of the periodic table of the elements and they are commonly listed separately at the bottom; their place has been and still is the subject of debate.

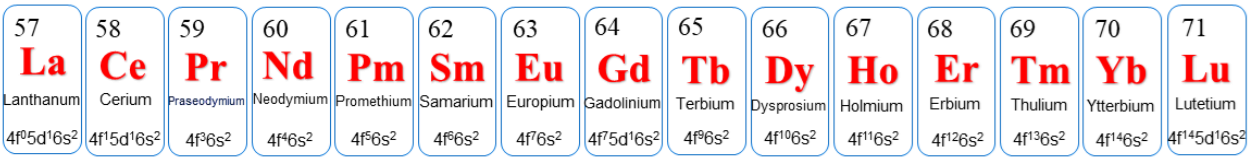

Figure 1.1. 4f-elements or lanthanides with the valence shell electronic configuration $[Xe]4f^{n,n-1}\,5d^{0,1}6S^2$.

The lanthanide chemistry started when J. Gadolin discovered a black mineral in 1794, known nowadays as gadolinite, and obtained yttria, an impure form of Y_2O_3. In 1803, Berzelius and Klaproth obtained ceria from cerite.[5] Mosander was the first to separate these earths into their oxides, from 1839 to 1843. However, the discovery of all 15 elements would not be complete until H. Moseley (1887–1915) analysed the X-ray spectra of the elements and gave meaning to the concept of atomic numbers.[6] Industrial applications had to wait for Carl Auer von Welsbach, who invented the incandescent mantle for gas lighting in 1891 and the mischmetal in 1903, a crucial component of flint stones and employed in a number of metallurgical processes.[3]

The most abundant lanthanide element in the earth's crust is clearly Ce (60–68 ppm), followed by Nd and La with abundances half that of Ce; Pr, Sm, Gd, and Dy have abundances in the range 5–10 ppm, while other elements are less abundant, with lutetium being the least abundant (<0.5 ppm).[2]

The trivalent state with the electronic configuration [Xe]4f^n, n = 0 for La^{3+} to n = 14 for Lu^{3+}, dominates the chemistry of lanthanides in solutions and solid states.[7] Additionally, the oxidation states +2 for Eu, Yb, and Sm and +4 for Ce, Tb, and Pr are accessible.[2] Ln^{3+} ions have large ionic radii and can therefore accommodate large coordination numbers from 6 to 12, making them very adaptable to many coordination environments. The ionic radius decreases gradually with increasing atomic number and thus increasing charge density, resulting in the so-called “lanthanide contraction”.[7]

1.2. Photoluminescence of trivalent lanthanides

The key aspect for understanding the chemistry, spectroscopic, and magnetic properties of lanthanide-based materials is the shielding of the valence 4f orbitals from the coordination environment by the filled 5s and 5p orbitals.[8] The energy level of a lanthanide ion is denoted by the term symbol $^{2S+1}r_J$, where S is the total spin quantum number, (2S + 1) the spin multiplicity, and J the total spin-orbit coupling quantum number, with values ranging from (L + S) to (L − S) where L is the total orbital angular quantum number, and r is denoted by the letters S,P,D,F,G,H, and I for L = 0, 1, 2, 3, 4, 5, and 6. The ground state of a specific Ln^{3+} ion can be determined using Hund's rules, in the sequence that follows: 1) the ground state has the largest spin multiplicity; 2) it has the largest orbital multiplicity; 3) it has the lowest value of J if the shell is less than half-filled or the highest value of J if the shell is more than half-filled. When a Ln^{3+} ion is introduced into a chemical environment, the (2J + 1)-degenerate J-levels are split into Stark sub-levels by ligand field effects.[9] For J-levels of odd-numbered electronic configurations, the degeneracy is not completely lifted, since all ligand field sublevels are at least doubly degenerate (Kramer’s doublets): the degeneracy can only be eliminated by applying a magnetic field, which explains the various lines observed in Ln^{3+} optical spectra.

<u>The electrical transitions involving lanthanide ions are of three different types:</u>

1) Sharp intraconfigurational 4f–4f transitions with electron rearrangement within the 4f^n subshell. Electric dipole transitions are forbidden by both Laporte’s and spin selection rules.[10] However, when the lanthanide ion is under the influence of a ligand field, noncentrosymmetric interactions allow electronic states of opposite parity to be mixed into the 4f wavefunctions, relaxing the selection rules, and the transition becomes partially-allowed; this is called the induced electric dipole (ED) transition.[9] The magnetic dipole (MD) transitions are allowed but very weak. Quadrupolar transitions are also parity-allowed, but they are much

weaker than MD transitions, so they are typically not detected. Hypersensitive (pseudo-quadrupolar) transitions are induced ED transitions that are extremely sensitive to the metal ion environment.

The f–f emission lines for the Ln^{3+} ions cover the entire spectrum, from the ultraviolet (Gd^{3+}) through the visible (Pr^{3+}, Sm^{3+}, Eu^{3+}, Tb^{3+}, Dy^{3+}, and Tm^{3+}) and near infrared (Pr^{3+}, Nd^{3+}, Ho^{3+}, Er^{3+}, and Yb^{3+}) spectral ranges.[11] Some ions are fluorescent ($\Delta S = 0$), others are phosphorescent ($\Delta S \neq 0$), and some are both. The 4f–4f emission lines are sharp because the electronic rearrangement following the promotion of an electron to a 4f orbital of higher energy does not significantly disrupt the binding pattern in the molecules since 4f orbitals do not participate much in this binding (the covalency of Ln^{3+}-ligand bonds is at most 5–7 %). Therefore, the internuclear distances remain almost the same in the excited state, which produces narrow bands and very small Stokes shifts when the ions are excited directly.

2) Not all the lanthanide ions give rise to f–f transitions, including obviously the f^0 and f^{14} species, La^{3+} and Lu^{3+}. Likewise, there are no f–f transitions for the f^1(Ce^{3+}) ion, as with only a single *L*-value, there is no upper 4f state. Ce^{3+} as well as Eu^{2+} give rise to parity-allowed, environment dependency and broad 4f→5d transitions. They enable tunable emission color, because the excited 5d energy levels are sensitive to the coordination environment, resulting in dependence of the coordination partners and the crystal field on the emission and its chromaticity.[12-15] Due to linkers and solvent molecules, most of the reported Ce^{3+} and Eu^{2+} coordination polymers (CPs) and complexes are non-emissive.[16] The most common examples of emissive Ce^{3+} compounds emit in the near ultraviolet and blue/green regions.[17-18] In addition, some doped materials exhibit green/yellow emission.[19-22] The most remarkable was the unusual yellow emitting Ce:YAG phosphors which have been extensively investigated in laser diode (LD) lighting because of their high quantum efficiency, thermal stability, and wide emission spectrum.[23-27] Recently, the red emission in solid state light emitting diodes (LEDs) was within the scope of Ce/Pr systems, such as $Lu_3Al_5O_{12}$:$Ce^{3+}Pr^{3+}$,[28-29] YAG:$Ce^{3+}Pr^{3+}$,[30-31] $Gd_3Ga_5O_{12}$:$Ce^{3+}Pr^3$,[32] $Y_3Al_5O_{12}$:Ce nanophosphor doped with Pr^{3+},[33] and the cerium-doped scandate.[34-35]

3) Broad allowed charge-transfer transitions in which an electron is transferred from the metal ion to the bonded ligands (MLCT) or vice versa (LMCT). MLCT

transitions are very rarely identified in Ln^{3+} spectra, with the exception of Ce^{3+}, which can be oxidized to Ce^{4+}. LMCT are commonly observed in Eu^{3+} and Yb^{3+}.

The lifetime of the excited state $\tau_{obs} = 1/k_{obs}$, k_{obs} is the rate constant (s^{-1}) of the depopulation of the excited state and the quantum yield Φ. The Φ is the ratio between the number of emitted photons divided by the number of absorbed photons. It is an important parameter characterizing the emission of light from the Ln^{3+} ion. The Φ differs from the intrinsic quantum yield ($\Phi_{\mathrm{Ln}}^{\mathrm{Ln}} = k^{rad}/k_{obs} = \tau_{obs}/\tau^{rad}$), which reflects the extent of non-radiative deactivation processes occurring in both the inner and outer coordination spheres of the metal ion. k^{rad} is the radiative rate constant and k_{obs} is the sum of the rates of the various radiative and non-radiative rate constants.[36] Furthermore, the internal quantum yields (IQY) of the Eu^{3+} centered emission can be calculated using the Wert's formula $\mathrm{IQY} = \tau_{obs}/\tau^{rad} = \tau_{obs} A_{MD,0} n^3 (I_{tot}/I_{MD})$, $A_{MD,0}$ = 14.65 S^{-1} for Eu^{3+}, which represents the constant spontaneous emission probability, I_{tot} represents the total area of the emission spectrum ($^5D_0 \rightarrow {}^7F_J$, J = 0–6), and $I_{MD,0}$ is the area of the $^5D_0 \rightarrow {}^7F_1$ transition.[37-38] The refractive index equals 1.5 according to the literature.[39] The lifetimes for the parity-allowed transitions are expected to be in nanoseconds, which are significantly shorter than those of the parity-forbidden transitions, where lifetimes approach micro- and milliseconds.

Ineffective luminescence is typically caused by direct excitation of 4f-excited levels. This aspect negatively influences both the intensities and the quantum yields associated with the processes. A well-known escaping route is the so-called antenna effect (or luminescence sensitization). This phenomenon can be modeled using Jablonsky's diagram (Figure 1.2).[40] Upon excitation in the UV region, the ligand is excited to higher singlet states (S_n) and can either radiatively decay to the ground state (fluorescence) or undergo a non-radiative intersystem crossing to a triplet state. The ligand in the long-lived triplet excited state (T_1) can either radiatively decay to the ground state (phosphorescence) or it can transfer its energy to the closely-lying lanthanide metal excited state (non-radiative energy transfer). To achieve an optimal luminescence quantum yield, the energy difference between the triplet excited state of the ligand and the excited state of the lanthanide should be around 2500–3500 cm^{-1} (Latva's rule).[41] A larger distance negatively affects the efficiency of the energy transfer, while a smaller distance allows partial back transfer from the metal to the ligand with subsequent radiative or non-radiative decay from the ligand excited state. The intrinsic nature of the energy transfer is often difficult to assess, as direct transfers from singlet states may

also be observed and charge transfer states (LMCT, MLCT, and intra-ligand charge transfer (ILCT)) can either positively or negatively perturb the mechanism. For lanthanides with charge-transfer states at low energies (e.g. Eu^{3+} and Sm^{3+}) or for complexes with low-lying ILCT states, an additional non-radiative quenching occurs through back energy transfer to the ligand. A direct electron exchange via a double electron exchange mechanism (Dexter) may occur when the antenna molecule is within the bonding distance to the lanthanide ion (30–50 pm). When the antenna molecule or complex is embedded as a guest in the framework of a lanthanide-based MOF, an electrostatic multipolar (Förster) transfer process with distances up to 1000 pm may be observed.[9]

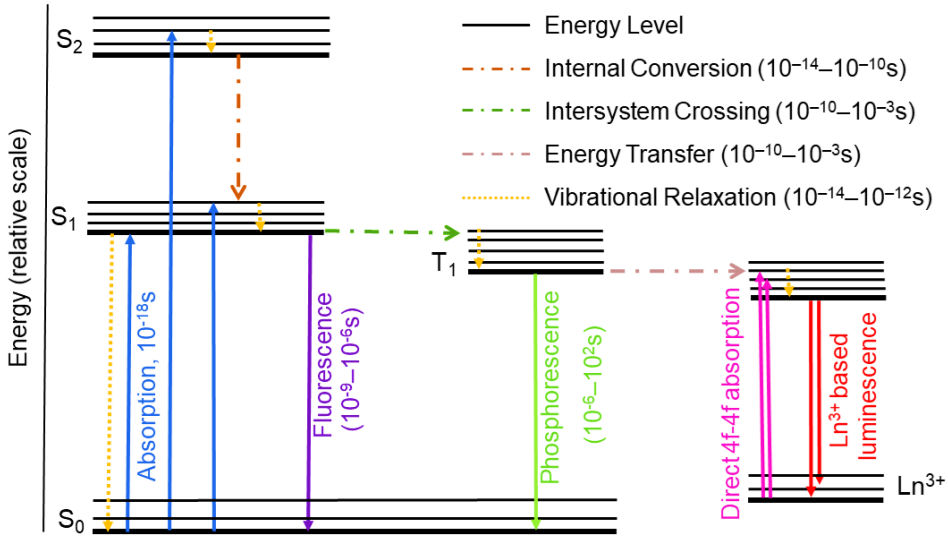

Figure 1.2. A simplified Jablonski diagram showing the possible radiative and non-radiative transitions. Back transfer processes are not drawn for the sake of clarity.

The synthesis and design of Ln-based compounds may also have a significant influence on their lifetimes and quantum yields. Vibrational quenching is one of the possibilities, which can be either direct or via phonons. It is related to the presence of high-energy O–H and N–H bond vibrations close to a luminescent metal center. When those vibrations originate from solvent molecules either within the porous structure or coordinated to the metal center, they can be eliminated by using solvent-free routes or post-synthetic treatment. Concentration quenching (or cross-relaxation) is another possibility, in which the excitation energy is transferred between nearby luminescent centers until a defect is reached or a non-radiative process takes place. As a result, energy is lost without any visible emissions. Reducing the concentration of luminous metal centers or separating them with extended ligands might improve the luminescent properties of CPs and metal organic frameworks (MOFs).[42]

1.3. Magnetism of trivalent lanthanides

With the discovery of the $[Tb(pc)_2]^-$ anion, where pc = dianion of phthalocyanine, lanthanide ions entered the field of molecular magnetism.[43-45] Molecular magnets are molecules that are able to retain their intrinsic magnetization for some time after the externally applied magnetic field has been removed. Magnetic hysteresis, magnetic remanence, and maxima in the out-of-phase magnetic susceptibility are all result of an efficient magnetization blocking property.[46] The comparatively high level of interest in molecular magnets was driven by the idea of storing information in an ultradense fashion, one bit per molecule (or atom), provided that the surface of a hard drive was covered with molecular magnets rather than traditional materials.

The lanthanide ions exhibit large spin-orbit couplings because of the smaller crystal field interactions, which results in a high magnetic anisotropy and a slow relaxation of the magnetization.[47] With the exception of La^{3+} and Lu^{3+} (diamagnetic), the Ln^{3+} ions all contain unpaired electrons and are paramagnetic. Their magnetic properties (with the exception of Sm^{3+} and Eu^{3+}) are completely determined by the ground state since the excited states are so well separated from the ground state (due to spin-orbit coupling) and thus thermally inaccessible. The characteristic magnetic moment for each Ln^{3+} leads to an interaction between this ion and an applied external magnetic field.[48] The magnetic moment of the Ln^{3+} ions is basically independent of the environment, similar to the photophysical properties. The magnetic moments in the second half of the series are larger than the moments in the first half because $J = L + S$ for a more than half-filled shell and $J = L - S$ for a less than half-filled shell. The following equation is used to calculate the effective magnetic moment for Ln^{3+}: $\mu_{eff} = g_J\sqrt{J(J+1)}$, $g_J = [J(J+1) + S(S+1) - L(L+1)]/2J(J+1)$.[2] The strength of the spin-orbit coupling means that the ground state is well separated from excited states, with the exception of Sm^{3+} and Eu^{3+} where contributions from low-lying paramagnetic excited states contribute to the magnetic moment. Thus, if the magnetic properties of the Eu^{3+} ion were solely determined by the $^7F_0$ ground state, its compounds would be diamagnetic, while contributions from thermally accessible levels such as $^7F_1$ and $^7F_2$ lead to the observed room-temperature magnetic moments in the region of 3.5 μB. In similarly, in the case of Sm^{3+}, the thermal population of the $^6H_{7/2}$ state leads to moments around 1.6 μB, rather than the value of 0.845 μB that would be expected if only the $^6H_{5/2}$ ground state were responsible.[6]

1.4. Coordination compounds of trivalent lanthanides with N-donor ligands including pyridylpyrazoles

The coordination polymers (CPs) and complexes of lanthanides with N-donor ligands have been the focus of research efforts in recent decades.[49-54] The ligands must be less sterically demanding in order to prevent the formation of small molecular complexes, which is essential for the formation of coordination polymers.[51] Especially multi-N aromatic heterocycles give Ln–N coordination polymers.[55-57] A lot of research focused mainly on solvent-free approaches for preparing Ln-based CPs, such as solid-state reaction routes where a solid reacts with a melt or a liquid under solvothermal conditions. These syntheses have made it possible to access a large number of different CPs and metal organic frameworks (MOFs) with a variety of N-heterocycles.[49, 58-59]

A lot of studies focused on the amines that, according to the following equation, can oxidize lanthanide metals to produce the appropriate amides and release hydrogen.[55]

$$\mathrm{Ln} + \mathrm{xHNR_2} \overset{\Delta T}{\rightarrow} \mathrm{Ln(NR_2)_x} + {}^{x}/_{2}\,\mathrm{H_2}$$

The solid-state reaction of the lanthanides with N-heterocycles and the elimination of typical solvents is particularly essential for the preparation of amides with small ring systems (Scheme 1.1) starting from 1N-heterocycles such as pyrrole[60-61] and carbazole[62-63] to 2-N ligands such as pyrazole[64-66] and imidazole[52-54] and to ring systems that contain 3-N atoms or more such as triazole,[49, 67-68] benzotriazole,[55-56] and triazolopyridine[57] compared to, for example, phthalocyanates,[69-70] as they are less suited for competition with coordinating solvent molecules due to their little sterical influence and can also not engage in multi-chelating.

The products obtained from the extreme conditions of melt reactions are unique and exhibit interesting features such as the formation of homoleptic compounds[51, 71-72] and coordination polymers,[63, 65-66] whereas for syntheses in solvents, ligand criteria such as multi-chelating[73-74] are necessary to obtain homoleptic compounds. For instance, the solvent-free melt reaction of Eu and Yb with the N-heterocycle 1,2,4-triazole, gave the first three-dimensional networks of the lanthanides with complete nitrogen coordination spheres.[49] Furthermore, this synthesis strategy was also a suitable approach to the chemistry of MOFs.[50] The avoidance of coordinated solvent molecules as well as the deprotonation of the N-H group of the ligands has raised the antenna efficiency of the ligands, which resulted in better photophysical properties.[67]

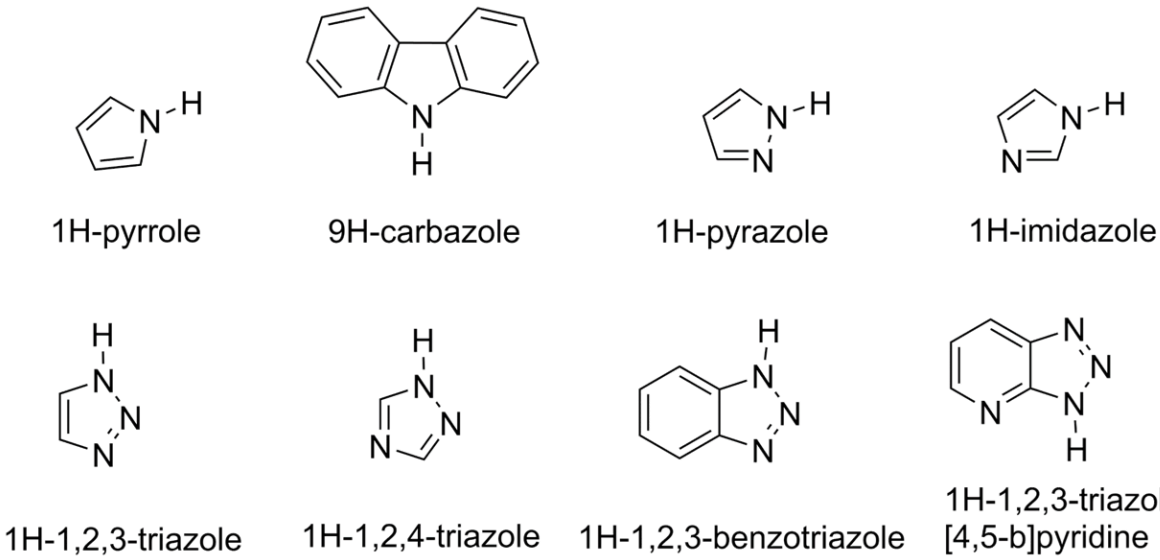

Scheme 1.1. Selected examples of N-heterocyclic amines from 1-N ligands to multi-N ligands.

The solid state reactions have expanded to include the reactions of anhydrous trivalent lanthanide chlorides and multiple N-donor ligands. The use of N-donor ligands (Scheme 1.2) has extended from one-ring aromatic ligands such as pyrimidine,[75] pyrazine[75] to two rings in 4,4´-bipyridine,[12, 76-79] 1,2-bis(4-pyridyl)ethane,[80-81] 1,2-Di(4-pyridyl)ethylene,[82-84] and chelating organic ligands such as 2,2´-bipyridine[85-86] to more bulky chelating ligands such as 1,10-phenanthroline,[87-88] and terpyridine including their multiple derivatives.[89-95] All the previously mentioned ligands has proven to be suitable to coordinate with trivalent lanthanides to form complexes and coordination polymers, depending on the coordination modes of the ligands and the reaction conditions. The pyrazine and pyrimidine, together with thiazole (thz) and lanthanide trichlorides, several complexes and coordination polymers were obtained that show efficient sensitization both, for Tb^{3+} in the visible and for Er^{3+} in the near-infrared (NIR) range. In the recent decades, we saw that bipyridyl ligands such as bipyridine or 1,2-bis(4-pyridyl)ethane can act as very efficient sensitizers for trivalent lanthanides.[77-78, 80, 96] For the 1,2-Di(4-pyridyl)ethylene, sensitization outside the beneficial energy gap could be observed for Ln^{3+}-NIR emitters such as Nd^{3+} or even Er^{3+}, if thz was included as co-ligand.[82] However, the respective pyridyl ligands could either effectively sensitize Ln emitters in the visible or in the NIR range. Terpyridine and its derivatives are known to enhance trivalent lanthanide luminescence.[89-92] Several coordination compounds with 4′-phenyl-2,2′:6′,2″-terpyridine (ptpy) were obtained at elevated temperatures as coordination polymers and as complexes at lower synthesis temperatures, covering the complete lanthanide series.[93] Recently, ptpy was engaged in a rapid “on the fly”-procedure which

was developed for a qualitative and semi-quantitative detection of trivalent ions used in recovery and urban mining processes.[97]

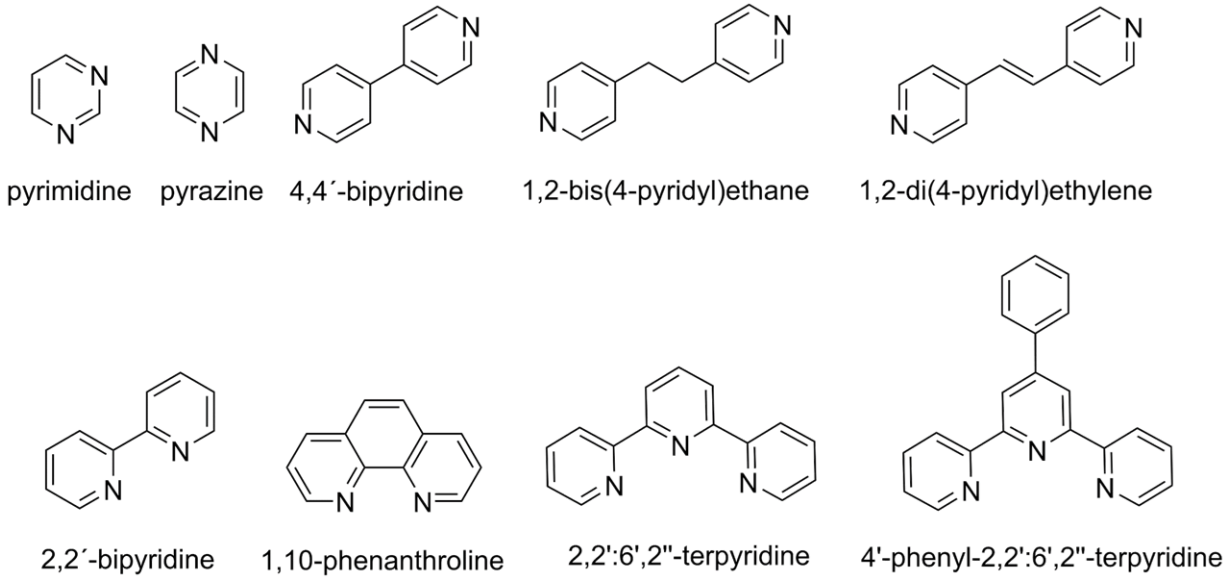

Scheme 1.2. Selected examples of N-heterocycles.

Pyridylpyrazole and its derivatives are a class of N-donor ligands that have been widely used in coordination chemistry because of their several coordination modes with transition metals, although few examples of reactions with lanthanides have been reported.[98-104] The general synthesis of the ligands is outlined in Scheme 1.3 and follows the usual pattern for the preparation of substituted pyridylpyrazole ligands.[105-107]

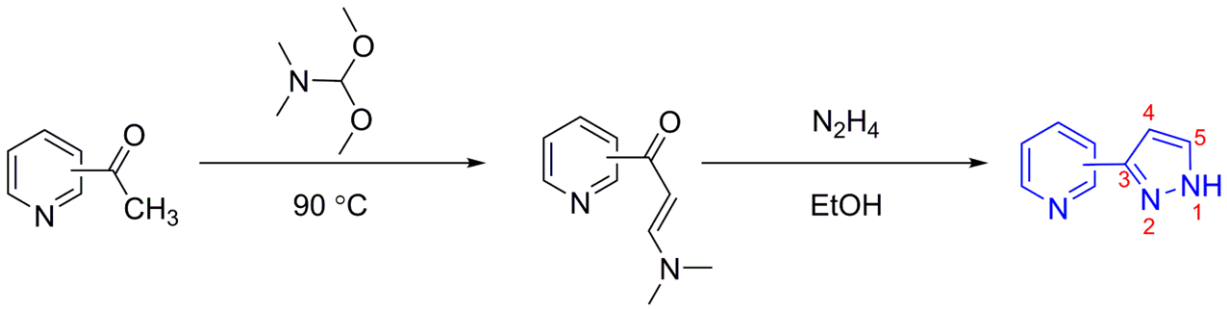

Scheme 1.3. General synthesis of pyridylpyrazol ligands from acetylpyridine and DMF-dimethyl acetal.

Various pyridylpyrazole-based ligands have shown good effectiveness for An^{3+}/Ln^{3+} separation, with the N-donor ligands showing better chemical and irradiation stability compared to the soft S-donor ligands.[108-109] For instance, 3-(2-pyridylpyrazole) (2-PyPzH) was used to study the complexation behavior with Ln^{3+} ions during the separation efficiency study of C8-2-PyPzH, with the C8 branched chain at position 5, obtaining two complexes $[Eu(2\text{-}PyPzH)_2(NO_3)_3]\cdot MeCN$ (**1**) and [Sm(2-

$PyPzH)_2(NO_3)_2(H_2O)(EtOH)][NO_3]\cdot MeCN$ (**2**) (Scheme 1.4).[108] The tetradentate 1,3-bis-[3-(2-pyridyl)pyrazol-1-yl]propane (Bippp) ligand, in which the two pyridylpyrazole groups are linked by an aliphatic bridge, has also been used as an extractant of Am^{3+} and Eu^{3+} to obtain $[Eu(Bippp)(NO_3)_2(H_2O)][NO_3]$ (**3**).[109] A further example is the formation of $[Ln(C5\text{-}BPP)(NO_3)_3(DMF)]$ (**4**), (Ln = Sm^{3+} and Eu^{3+}, C5-BPP = 2,6-bis(5-(2,2-dimethylpropyl)-1H-pyrazol-3-yl)pyridine).[110]

The poly(pyrazolyl)borate ligands have proven to be extremely popular among coordination chemists since their introduction in 1967[111] for a wide range of applications because of their ease of synthesis, ease of functionalization, and the steric protection that they afford to metal centers.[112-114] In the last two decades, other derivatives of these ligands have been prepared using substituents at the C^3-position of each pyrazolyl ring; these ligands have found wide application in both catalysis and modeling of metalloprotein active sites.[115-116] Tris[3-(2-pyridyl)pyrazolyl]-hydroborate (Tp^{Py}) was the first example of a podand-type ligand of the tris(pyrazolyl)borate family, prepared by attachment of additional coordinating groups (here, 2-pyridyl substituents).[117-127] Each arm of the ligand is thus an N,N-bidentate chelate. Efficient energy transfer from the ligand-based excited state to the lanthanide-based excited state has been proven, for example, for $[Ln(Tp^{Py})(NO_3)_2]$, Ln = Eu and Tb (**5**) (Scheme 1.4).[117] Although the main interest was in the structures of poly(pyrazolyl)borate ligands and the photophysics of their Eu^{3+} and Tb^{3+} complexes, NIR emitters such as Yb^{3+} and Nd^{3+} showed relatively strong luminescence, which could be a consequence of the lack of close oscillators suitable for quenching.[125, 128] Another example of a good NIR emitter would be $[Nd(Dp^{Py})_2(NO_3)]$ (**6**), (Dp^{Py} = dihydrobis-[3-(2-pyridyl)pyrazolyl]borate), whose coordination environment is shown in Scheme 1.4.[128] Good sensitization was observed along the lanthanide complexes with 3-(2-pyridyl)pyrazolyl arms.[117] 3-pyridyl and 4-pyridyl substituents at the C^3-position of the pyrazolyl group of bis-, tris-, and tetrakis(pyrazolyl)borate were reported with non-lanthanide metals in which the externally-directed 3- or 4-pyridyl groups cannot chelate to the central metal ion but instead are ‘exodentate’ and capable of binding additional metal centers.[129-130]

Among other N-donor-based pyridylpyrazole ligands, the ligand 2,6-bis(1H-pyrazol-3-yl)pyridine (L1) (Scheme1.4) plays an effective role in promoting lanthanide emission. The first example was published in 1997 and presented the synthesis and lifetime measurements of the trivalent terbium complex $[Tb(L)_3][PF_6]_3$.[122]

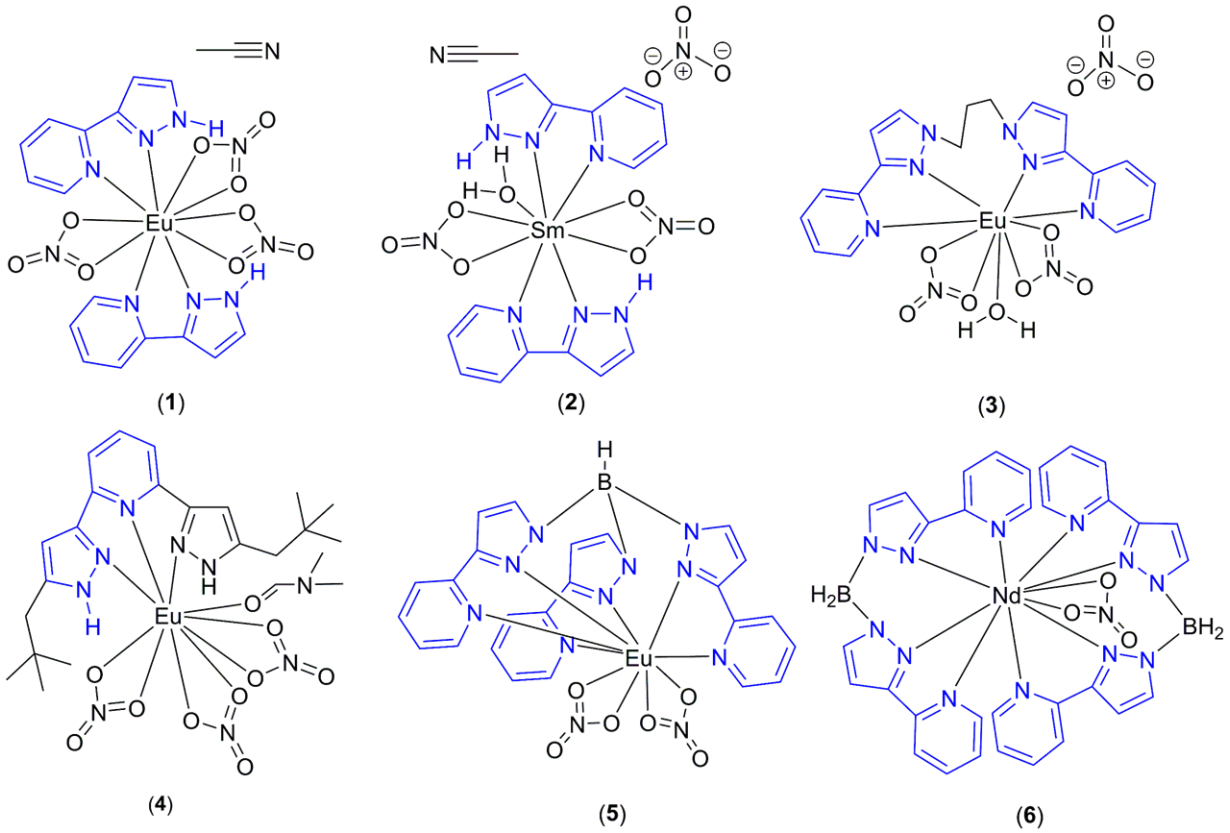

Scheme 1.4. Selected examples of functionalized 3-(2-pyridyl)pyrazole used in the coordination chemistry of trivalent rare earth elements.

This ligand was used again in 2012 to study the importance of coordination number and type in sensitizing the emission of Eu^{3+}. They have synthesized complexes with different metal/ligand ratios (1:1, 1:2, and 1:3) for Gd^{3+} and Eu^{3+}. The crystal structures of the europium complexes were determined and the photophysical properties were studied in solution and in the solid state at room and liquid-nitrogen temperatures. The antenna effect is most effective for Eu1:L3.[131] The complex $[Dy_4(L1)_3(CO_3)_6(H_2O)_3]DMSO{\cdot}18H_2O$ with a metal-CO_3^{2-} core obtained by fixation of atmospheric CO_2 was also synthesized. This complex shows slow magnetization reversal.[132] 3-(2-pyridyl)-1-pyrazolyl acetic acid (HL2) (Scheme 1.5) has been used to construct a large structural variety ranging from 1D to 2D network frameworks due to the combination between the nitrogen atoms of the pyridyl and pyrazolyl rings and the oxygen atoms of the carboxylate group. $[Eu_2(bta)_4(L2)_2]$, bta = 1-benzoyl-3,3,3-trifluoroacetonate, was the first Ln^{3+}-based complex with HL2 ligand. The photoluminescence data of the Eu^{3+}-based complex were consistent with the single-crystal X-ray structure, which revealed that both Eu^{3+} ions are in similar environments defined by the coordination sphere of seven oxygen atoms and two nitrogen atoms.[133] Later, $[Sm_2(L2)_2(H_2O)_{10}]Cl_4{\cdot}H_2O$ and $^1_\infty[Eu(L2)(C_2O_4)]$ were obtained by hydrothermal

reactions with the corresponding $LnCl_3 \cdot 6H_2O$. The luminescence properties of both products were investigated in the solid state at room temperature (RT) showing the ligand-centered fluorescence and the characteristic peaks of Eu^{3+}.[134]

The pyridylpyrazolyl-based complexes and coordination polymers with different coordination geometries around metal centers have shown intriguing magnetic properties,[135] which are mainly attributed to different coordination environments around metal centers. This was achieved through the combined influence of the asymmetric nature, semi-rigid backbone, and ability of the ligand to fulfill variable coordination modes, allowing the ligand to fine-tune its conformations by bending, stretching, or twisting the rings, depending on the coordination requirements.[136] Examples of these ligands would include one or two hard O-donors and three to five soft N-coordinating sites such as 4-(3-(pyridin-2-yl)-1H-pyrazol-5-yl)benzoic acid (L3), 3-(pyridin-2-yl)-N'-((pyridin- 2-yl) methylene)-1H-pyrazole-5-carbohydrazide (L4), and N′-(2-hydroxybenzylidene)-3-(pyridin-2-yl)-1H-pyrazole-5-carbohydrazideand (L5) (Scheme 1.5).[136-138] The resulting compounds exhibited some intriguing magnetic behavior with Ln-metal cores such as Dy^{3+} and Er^{3+} because of their doubly degenerate $\pm m_J$ levels, one of the requisites to observe a slow relaxation of the magnetization.[139-141]

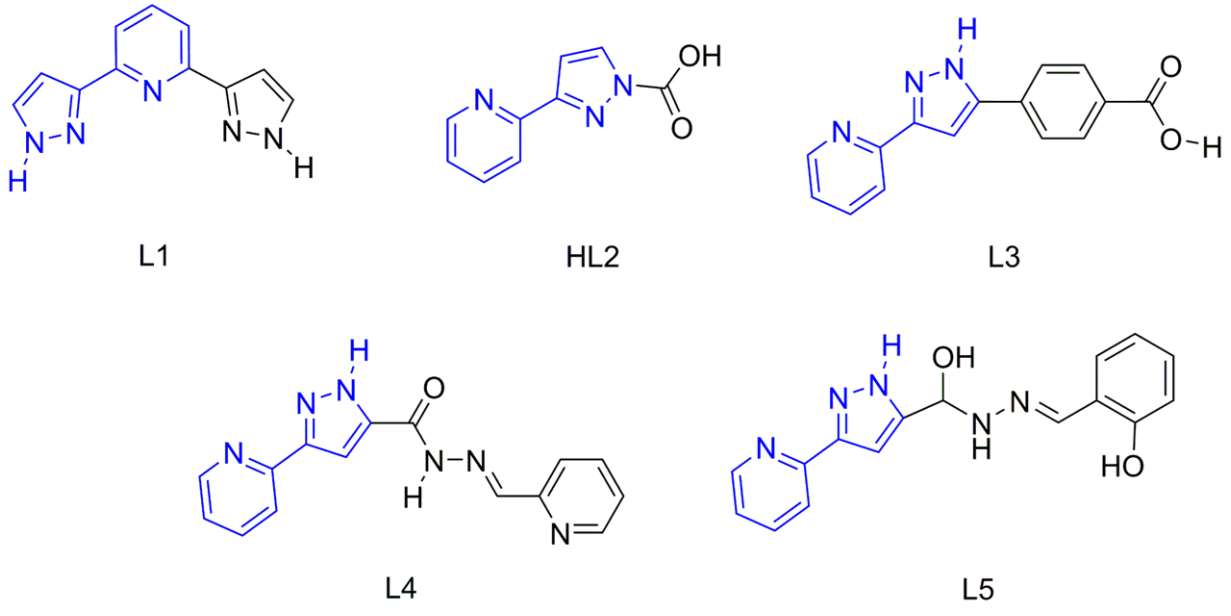

Scheme 1.5. Examples of pyridylpyrazolyl-based ligands used in the coordination chemistry of trivalent Ln elements.

In contrast to the 2-pyridyl substituent at the C^3-position of the pyrazolyl group (2-PyPzH), the 3-pyridyl and 4-pyridyl substituents (3-PyPzH and 4-PyPzH, respectively) and their derivatives had no lanthanide-containing compounds in the literature. 3-PyPzH

and 4-PyPzH were used to obtain Cu^{+} and Ag^{+} complexes that exhibit high-lying intersystem crossing that results in highly efficient phosphorescence.[142] The strong luminescence comes from ligand-centered T_1 states and the corresponding excimers. The design of pyridylpyrazole ligands was inspired by the highly emissive (QY up to ~81 %) planar mononuclear Pt^{2+} complexes with pyridyl/pyrizinyl pyrazole ligands, which also form excimers assisted by intermolecular metal−metal interactions in the solid-state packing.[143]

2. Research goals

The focus of the PhD project is to obtain fundamental knowledge on the options for combining magnetism and luminescence and study the possible interactions between the two properties. In order to achieve this main goal, it is essential to first synthesize multifunctional molecular materials based on complexes and coordination polymers of 4f-metal ions. The N-donor ligands 3-(2-pyridyl)pyrazole (2-PyPzH), 3-(3-pyridyl)pyrazole (3-PyPzH), and 3-(4-pyridyl)pyrazole (4-PyPzH) were chosen as starting materials for this project as they showed high-lying intersystem crossing resulting in highly efficient phosphorescence for their reactions with transition metals besides their chelating ability to the metal centers, as discussed in **Chapter 1**, which fits perfectly with the goals of the project. Another reason is the few reported coordination compounds and complexes of trivalent lanthanides with 2-PyPzH, whereas the photoluminescence properties of products are almost unexplored, and no lanthanide (Ln)-containing compounds with 3-PyPzH and 4-PyPzH have been known so far.

The first goal was the synthesis of new molecular materials using solid-state reaction routes, including melt synthesis and solvothermal reactions under inert conditions, to enhance the formation of a complete nitrogen coordination sphere as well as the formation of coordination polymers. The characterization of pyridylpyrazole reactivity with the elemental lanthanide series except promethium was the first step in the way to obtain new molecular materials. This step was successfully achieved as the selected ligands were shown to be able to react in a redox reaction with elemental lanthanides, yielding hydrogen. In addition, the synthesis probability of the reduced redox-sensitive divalent lanthanide ions, such as divalent europium, has been in focus as it can impart interesting photophysical and magnetic properties distinct from the trivalent ions, as discussed in **Chapter 1**.

Not forgetting that our main goal is to combine both magnetism and luminescence, the need to increase the distance between the Ln^{3+} ions is a requirement to achieve better magnetic results. Elemental alkaline earth (AE) was placed in a reaction with lanthanide metal to target the synthesis of bimetallic Ln/AE compounds. Although the coordination polymers and complexes based on a combination of lanthanides and alkaline earth metals (Ln/AE) still pose a synthetic challenge.

In a further extension of the study, Cl^- ligands have been added to the synthesis procedure using trivalent lanthanide chlorides to explore the influence of the heteroleptic environment on both the photoluminescence and the magnetic properties.

The second goal was to explore and compare the photophysical reactivity between the trivalent lanthanides and the ligands under study. In order to provide a better understanding of the photophysical properties observed for the Ln series, the absorption spectra were measured in addition to the emission and excitation spectra. The study revealed that pyridylpyrazole/ates are good sensitizers for Ln^{3+}, which is confirmed by an efficient antenna effect not only for the visible emitters but also for the near infrared (NIR) emitters. The resulted uncommon emission bands from the NIR-based coordination polymers (CPs) is attracting much interest in the application of optical amplification and biomedical applications.

A unique Ce^{3+}-based emission was detected during the characterization of the photophysical properties that differed from the expected blue/green Ce^{3} emission. An exception of pink through orange to bright red emission from undoped Ce^{3+}-based compounds was successfully achieved along five coordination polymers and complexes based on the three ligands; such a strong energetic reduction of the 5d excited states of Ce^{3+} was attractive. These unique Ce^{3+}-based phosphors can contribute to the understanding of the d-orbital splitting mechanism and its emission capability and offer a new perspective for solid-state lighting applications.

Tuning the luminescence chromaticity towards white light emission was achieved by co-doping the Gd-containing frameworks with Eu^{3+} and Tb^{3+} during the study. Therefore, the generation of white light by mixing different monochromatic light sources has been taken into focus as an attractive feature of light-emitting materials. The possibility of tuning the luminescence chromaticity by co-doping other homoleptic frameworks was also explored and verified for codoping the Tb-, Eu-, and Ce-containing frameworks with the respective counterions.

The third goal was to characterize the magnetic properties of Dy^{3+}-, Ho^{3+}-, and Er^{3+}-based homo- and heteroleptic coordination polymers in an attempt to understand the influence of magnetism on luminescence and vice versa. Direct current (DC) magnetic susceptibility measurements revealed mainly the magnetic isolation of the lanthanide centers, which limited the study of the interaction between the luminescence and magnetism properties. Along the PhD project, topological analysis to ensure a better understanding of the crystal structure and thermal analysis to investigate the thermal behavior and the stability of the synthesized CPs and complexes were in focus.

3. Results

3.1. Homoleptic and heteroleptic coordination polymers of trivalent lanthanides with 2-, 3-, and 4-pyridylpyrazolates as well as heterobimetallic lanthanide/alkaline earth complexes

3.1.1. Variable luminescence and chromaticity of homoleptic frameworks of the lanthanides together with pyridylpyrazolates

This article has been published in the

Chemistry−A European Journal

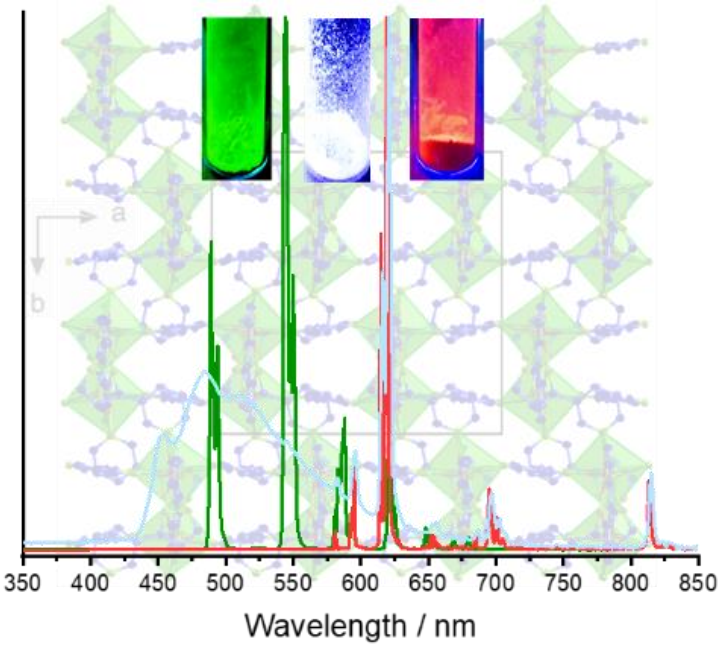

Heba Youssef, Alexander E. Sedykh, Jonathan Becker, Thomas Schäfer, Ilya V. Taydakov, Huanrong R. Li, and Klaus Müller-Buschbaum

Reprinted with permission from *Chem. Eur. J.* **2021**, *27*, 16634–16641.

DOI 10.1002/chem.202103068

Cover reprinted with permission from *Chem. Eur. J.* **2021**, 27, 16526-16526.

DOI 10.1002/chem.202103994


Chemistry
A European
Journal
Chemistry
Europe
European Chemical
Societies Publishing
Cover Feature:
K. Müller-Buschbaum et al.
Variable Luminescence and Chromaticity of Homoleptic Frameworks of the Lanthanides together with
Pyridylpyrazolates
67/2021
WILEY-VCH

Chemistry–A European Journal
Full Paper
doi.org/10.1002/chem.202103068
Chemistry Europe
European Chemical Societies Publishing

Variable Luminescence and Chromaticity of Homoleptic Frameworks of the Lanthanides together with Pyridylpyrazolates

Heba Youssef,[a, b] Alexander E. Sedykh,[a] Jonathan Becker,[a] Thomas Schäfer,[a] Ilya V. Taydakov,[c] Huanrong R. Li,[d] and Klaus Müller-Buschbaum*[a, e]

Abstract: Homoleptic, 3D coordination polymers of the formula $^{33}_{\infty}$[Ln(3-PyPz)$_3$] and $^{3}_{\infty}$[Ln(4-PyPz)$_3$], (3-PyPz)$^-$ = 3-(3-pyridyl)pyrazolate anion, (4-PyPz)$^-$ = 3-(4-pyridyl)pyrazolate anion, both $C_8H_6N_3^-$, Ln=Sm, Eu, Gd, Tb, Dy, were obtained as highly luminescent frameworks by reaction of the lanthanide metals (Ln) with the aromatic heterocyclic amine ligands 3-PyPzH and 4-PyPzH. The compounds form two isotypic series of 3D coordination polymers and exhibit fair thermal stability up to 360 °C. The luminescence properties of all ten compounds were determined in the solid state, with an antenna effect through ligand–metal energy transfer leading to high efficiency of the luminescence displayed by good quantum yields of up to 74%. The emission is mainly based on ion-specific lanthanide-dependent intra 4f–4f transitions for Tb^{3+}: green, Dy^{3+}: yellow, Sm^{3+}: orange-red, Eu^{3+}: red. For the Gd^{3+}-containing compounds, the yellow emission of ligand triplet-based phosphorescence is observed at room temperature and 77 K. Co doping of the Gd-containing frameworks with Eu^{3+} and Tb^{3+} allow further shifting of the chromaticity towards white light emission.

Introduction

During the past two decades, the hybrid nature of coordination polymers (CPs) and the related metal–organic frameworks (MOFs), composed of metal ions or clusters connected with organic linkers, has been the focus of many research efforts.[1] They give rise to properties derived from either one of the two components or the combination of both. The hybrid material can thereby generate cooperative properties, such as porosity,[2] magnetism,[3] photoluminescence (PL),[4] or nonlinear optical properties.[5]

Lanthanide-based hybrid compounds are important chromophores for lighting, displays, and lasers, giving characteristic narrow line emissions, whereas they have intrinsically low absorption coefficients as a result of the parity-forbidden 4f–4f transitions.[6] Consequently, an antenna such as an organic molecule promotes light harvesting by absorption of photon energy, usually in a broad UV range, and transfer it intramolecularly to the Ln^{3+} ion thereby enhance the efficiency of emission.[7] The direct coordination of a conjugated -electron system to the metal ions could act as a good sensitizer. However, the ion has to be shielded from vibronic quenchers, for instance, deactivating solvents such as water, as these allow quenching of the elevated state of the Ln^{3+}-ions due to vibronic deactivation.[8] Numerous efforts have been made to enlarge the absorption coefficients and thus obtain significantly more intense lanthanide ion emissions.[9] In addition, the generation of white light by mixing different monochromatic light sources is an attractive feature of light-emitting materials recently.[10]

The ligand 3-(3-pyridyl)pyrazole (3-PyPzH) was used mainly as a reactant in ligand synthesis, and some of those new derivative ligands were used later in coordination chemistry.[11] The ligand 3-(4-pyridyl)pyrazole (4-PyPzH) has been mainly applied in the synthesis of transition metal-based complexes and CPs. For instance, two Hofmann-like 2D coordination polymers with the general formula of $\{Fe^{2+}(Hppy)_2[M^{2+}(CN)_4]\cdot H_2O$, (M=Pd, Pt), are known. Both compounds show two-step spin-crossover behavior with hysteresis loops around 14–

[a] H. Youssef, A. E. Sedykh, Dr. J. Becker, T. Schäfer, Prof. Dr. K. Müller-Buschbaum
Institute of Inorganic and Analytical Chemistry
Justus-Liebig-University Giessen
Heinrich-Buff-Ring 17, 35392 Giessen (Germany)
E-mail: klaus.mueller-buschbaum@anorg.chemie.uni-giessen.de
[b] H. Youssef
Department of Chemistry
Faculty of Science, Mansoura University
El Gomhouria, Mansoura Qism 2, Dakahlia Governorate, 11432, Mansoura (Egypt)
[c] Prof. Dr. I. V. Taydakov
Lebedev Physical Institute of the Russian Academy of Sciences
Leninskiy pr-t, 53, 119991, Moscow (Russia)
[d] Prof. Dr. H. R. Li
Hebei University of Technology
Guanrong Dao 8, Hongqiao District, 300130, Tianjin (P. R. China)
[e] Prof. Dr. K. Müller-Buschbaum
Center of Materials Research (LAMA)
Justus-Liebig-University Giessen
Heinrich-Buff-Ring 16, 35392 Giessen (Germany)

Supporting information for this article is available on the WWW under https://doi.org/10.1002/chem.202103068

23 K.[12] This ligand was also used in the synthesis of a series of inorganic–organic hybrid materials based on polyoxometalates (POMs), $[M(HL)_2(H_2O)_2][Mo_6O_{20}]$ [M = Co, Ni, Cu, Zn], $[MnL_2(H_2O)_2][Mo_6O_{20}]$ and $(HL)_3PMo_{12}O_{40}$, with antiferromagnetic behavior.[13] 4-PyPzH was also used to prepare a Cu^{2+} containing discrete metal complex gelator able to gel dimethylformamide (DMF) at 0.51 wt%.[14] Both ligands were used to produce highly efficient phosphorescent Cu^{+} and Ag^{+} complexes.[15] To the best of our knowledge, no lanthanide-containing compounds with these ligands have been known.

Based on these results, we were prompted to construct novel lanthanide coordination polymers and succeeded in the synthesis of frameworks featuring either 3-(3-pyridyl)pyrazole or 3-(4-pyridyl)pyrazole (3-PyPzH or 4-PyPzH). Herein, we report the synthesis, characterization, luminescence, and thermal properties of the homoleptic and co-doped frameworks $^3_\infty$[Ln-(3-PyPz)$_3$] and $^3_\infty$[Ln(4-PyPz)$_3$].

Results and Discussion

Synthesis and structural analysis

The two series of ten coordination polymers $^3_\infty$[Ln(3-PyPz)$_3$] and $^3_\infty$[Ln(4-PyPz)$_3$] are formed in reactions of the elemental lanthanides with 3-(3-pyridyl)pyrazole (3-PyPzH) or 3-(4-pyridyl) pyrazole (4-PyPzH) (Scheme 1) in either pyridine or 1,2,4,5-tetramethyl-benzene (durene) with high yield (82–96%).

The homoleptic frameworks of the formula $^3_\infty$[Ln(3-PyPz)$_3$] (Ln = Sm, Eu, Gd, Tb, and Dy) (**1–5**, respectively) are isotypic and crystallize in the cubic space group $Pa\bar{3}$. The second isotypic coordination polymer series $^3_\infty$[Ln(4-PyPz)$_3$] (Ln = Sm, Eu, Gd, Tb, and Dy; **6–10**, respectively) is also formed of isotypic compounds that crystallize in the monoclinic crystal system in the space group $P2_1/n$. The $^3_\infty$[Ln(3-PyPz)$_3$] and $^3_\infty$[Ln(4-PyPz)$_3$] series constitute of three perspective pyridyl-pyrazolate anions per formula unit, resulting in the identical general chemical formula of $C_{24}H_{18}N_9Ln$. Each ligand acts as a tridentate ligand and forms a bridge between two neighboring trivalent lanthanide ions (Figures 1 and 2).[16] In sum, each Ln^{3+} ion coordinates to nine N atoms in a pseudo-octahedral fashion, in which the two nitrogen atoms of the pyrazolate anion are regarded as a single connection and therefore as one corner of the octahedron. The topology was determined for **4** and **9** as a representative example for the two isotypic series to ensure a better understanding of the crystal structure. It was determined

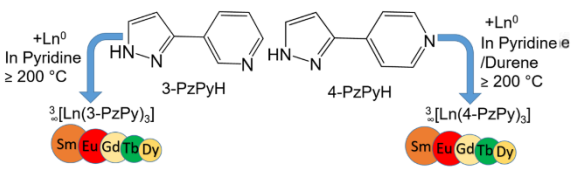

Scheme 1. Synthetic scheme for two novel series of 3D coordination polymers with 3-PyPzH (left) and 4-PyPzH (right) ligands.

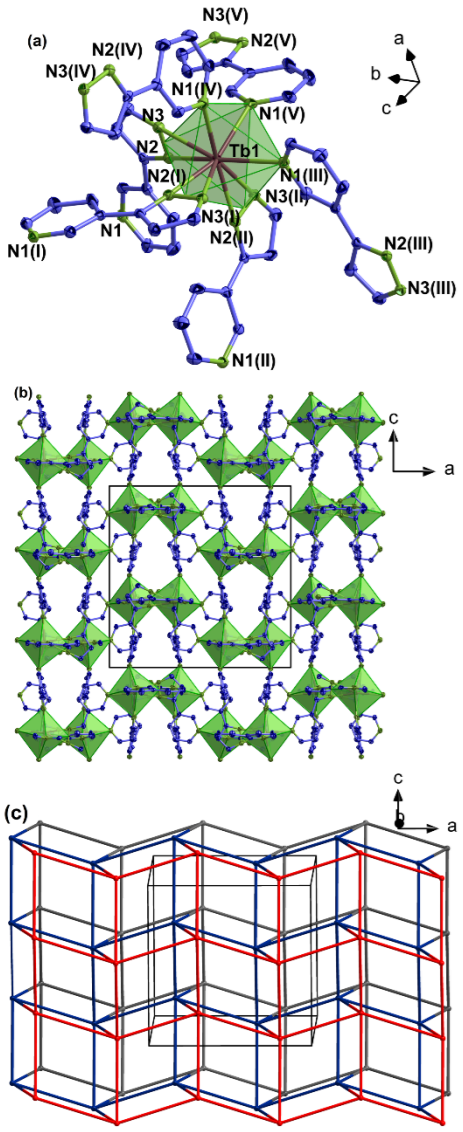

Figure 1. a) Extended coordination sphere of Ln^{3+} in $^3_\infty$[Tb(3-PyPzH)$_3$( ]**4**) representing the series of isotypic framework compounds (**1–5**). b) Crystal structure of **4** with a view along [010]. Hydrogen atoms are omitted for clarity. Tb^{3+} ions are shown in brown, nitrogen atoms in green, carbon atoms in blue, and the coordination polyhedra around Tb^{3+} are indicated in green with thermal ellipsoids depicted at the 50% probability level. c) Topological representation of **4** as a uninodal 6-c net with **pcu** topology. Symmetry operations: I = $-z+1,x+1/2,-y+3/2$, II = $y-1/2,-z+3/2,-x+1$, III = $x-1/2,y,-z+3/2$, IV = $y-1/2,z,-x+3/2$ V = $z-1/2,x,-y+3/2$.

in conformity with the Reticular Chemistry Structure Resource (RCSR) and the Wells terminology.[17] Both structures of **4** and **9** indicate that there is a 6-connected uninodal net with a Schläfli symbol of $4^{12}.6^3$ (**pcu**; 6/4/c1; sqc1) when assuming that the terbium centers act as nodes with threefold connectivity.

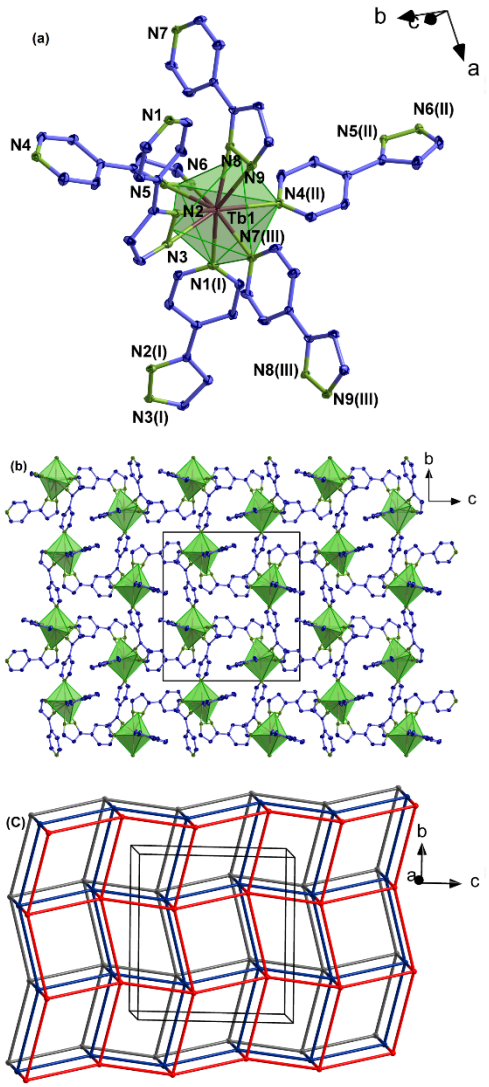

Figure 2. a) Extended coordination sphere of Ln^{3+} in $^{3}_{\infty}$[Tb(4-PyPzH)$_3$( )**9**) representing the series of isotypic framework compounds (**6**–**10**). b) Crystal structure of **9** with a view along [100]. Hydrogen atoms are omitted for clarity. Tb^{3+} ions are shown in brown, nitrogen atoms in green, carbon atoms in blue, and the coordination polyhedra around Tb^{3+} are indicated in green with thermal ellipsoids depicted at the 50% probability level. c) Topological representation of **9** as a uninodal 6-c net with **pcu** topology. Symmetry operations: I = $x+1/2,-y+1/2,z+1/2$, II = $-x+3/2,y-1/2,-z+3/2$, III = $x+1,y,z$.

Although the packing of nets in **4** and **9** differs, the connectivity of all nodes is the same, which leads to the same underlying network topology. This results in 3D framework structures, in which six ligands act as bridges between the adjacent lanthanide ions.

The average distances between the metal ions and the pyridine nitrogen atoms (Tables S3 and S4 in the Supporting Information; 258(2) pm) in **1**–**10** are longer than the Ln–N distances to the pyrazolate ring atoms (242(2) pm). This can be explained by the ionic character of the pyrazolate N sites compared to the neutral pyridyl donor.

For the frameworks **1**–**5**, comparison and analysis of the lattice parameters indicates that the volume of the unit cell and the Ln–N1 distances as well as an average value of the Ln–N2 and Ln–N3 distances have a decreasing trend for an increase of charge density from samarium to dysprosium. The same behavior is observed for the second series of frameworks **6**–**10**, the average of Ln–N1, Ln–N4, and Ln–N7 (pyridine ring) as well as the average value of Ln–N2, Ln–N3, Ln–N5, Ln–N6, Ln–N8, and Ln–N9 (pyrazolate rings) decreasing from Sm^{3+} to Dy^{3+}. Compound **4** cannot contribute to this, because the single-crystal X-ray measurement had to be performed at a different temperature of 200 K. At lower temperatures, the crystals cracked continuously.

Besides, the described phenomena are a direct consequence of lanthanide contraction.[18] For polymers, **6**–**10** partially occupied and heavily disordered pyridine solvent was found in voids in the crystal structure. For additional details on the crystal structure determinations of $^{3}_{\infty}$[Ln(3-PyPz)$_3$] and $^{3}_{\infty}$[Ln(4-PyPz)$_3$], see Tables S1 and S2; for selected interatomic distances and angles, see Tables S3, and S4, respectively.

All bulk products of the polymers (**1**–**10**) were proven to be phase pure bulk products by PXRD. The experimental diffraction patterns match well in terms of reflection positions and intensities with the diffraction patterns simulated from single-crystal data of compounds (**1**–**5**). No additional reflections of crystalline byproducts are observed, as shown in Figure 3 for **1** as a representative (for **2**–**5**, see also Figures S1–S4). To take the different measurement conditions of PXRD (298 K) and SCXRD (100 K) into account, additional Pawley-refinements for **6**–**10**, were carried out, confirming the phase purity of the respective series of coordination polymers. The resulting difference plots show no significant deviations as depicted in Figure 4 for **6** (see

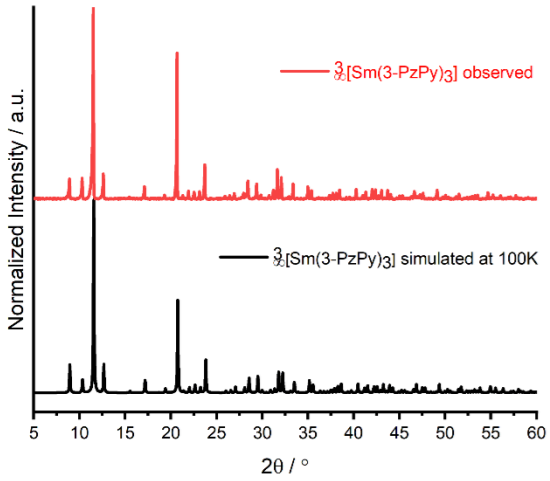

Figure 3. Comparison of the experimental X-ray powder diffraction pattern at 298 K (top) with a simulated pattern from single-crystal X-ray data of $^{3}_{\infty}$[Sm(3-PyPz)$_3$( )**1**) at 100 K (bottom).

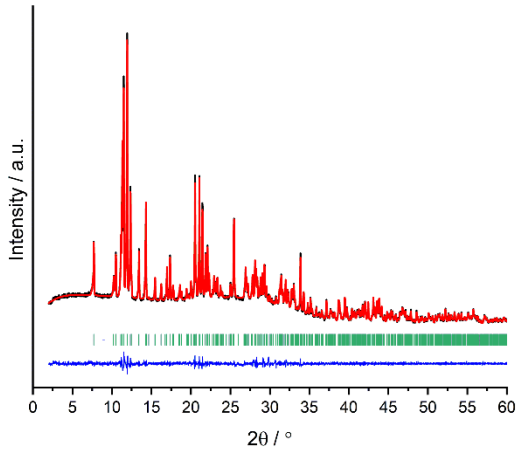

Figure 4. Pawley refinement results for PXRD of $^{3}_{\infty}$[Sm(4-PyPz)$_3$( ]**6**), showing the experimental data (black) together with the Pawley fit (red), the corresponding difference plot (blue) as well as *hkl* position markers (green).

also Figures S5–S8). The details of the Pawley-refinements are listed in the Supporting Information, Table S5.

Photophysical properties

The compounds of both series of homoleptic frameworks show photoluminescence properties for the range of investigated lanthanides. Excitation and emission spectra were recorded in the solid state at room temperature (RT = 298 K) and 77 K for the free ligands 3-PyPzH and 4-PyPzH,[14–15] as well as for the ten 3D coordination polymers $^{3}_{\infty}$[Ln(3-PyPz)$_3$] and $^{3}_{\infty}$[Ln(4-PyPz)$_3$], Ln = Sm, Eu, Tb, and Dy, and co-doped $^{3}_{\infty}$[Gd(3-PyPz)$_3$]:Eu^{3+},Tb^{3+} and $^{3}_{\infty}$[Gd(4-PyPz)$_3$]:Eu^{3-},Tb^{3+}.

The investigated compounds (Figures 5 and 6) show a broad excitation band dominant in the UV with maxima at 312–320 nm for **1**–**10** at 77 K, which refers to ligand-based excitation, 330 nm for 3-PyPzH, and 370 nm for 4-PyPzH.

At RT (Figures S9–S20), the excitation maxima appear for **4** at 312 nm, for **1**, **3**, **5**, **6**, **8**, **9**, and **10** at 319–326 nm, and for the free ligands at about 333 nm. Excluding compounds containing Gd^{3+} (**3** and **8**) and Eu^{3+} (**2** and **7**), at RT, direct and weak excitation of the spin forbidden (Laporte selection rule),[19] 4f–4f transitions are also observed at both temperatures for the highlighted frameworks.

For the Eu^{3+} containing compounds **2** and **7**, at RT, the spin-forbidden 4f–4f transitions are dominant in the excitation spectra, where the direct f-f excitation $^5D_2 \leftarrow {}^7F_0$ has the maximum intensity.

The synthesized compounds exhibit emission colors visible to the naked eye under the UV lamp which covers the primary RGB regions from blue (3-PyPzH, 4-PyPzH), green (Tb^{3+} in **4**, **9**, to yellow-white (co-dopped Gd^{3+} in **3**, **8**), through orange (Sm^{3+} in **1**, **6**) to red (Eu^{3+} in **2**, **7**). For 3-PyPzH and 4-PyPzH,

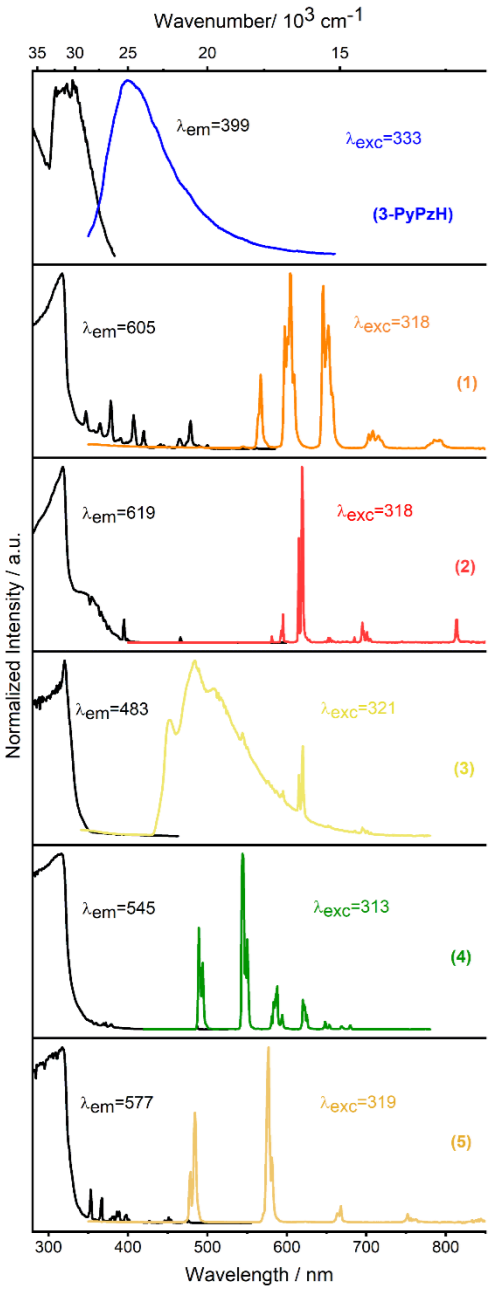

Figure 5. Normalized solid-state excitation (black) and emission (colored) spectra of $^{3}_{\infty}$[Ln(3-PyPz)$_3$], Ln = Sm, Eu, Gd, Tb, Dy (**1**–**5**) at 77 K. Wavelengths for which the spectra were recorded are reported in the legends.

the emission maxima appear in the range of 400 to 410 nm.[15] The emission profiles of Sm^{3} **1** and **6** display the characteristic transitions $^4G_{5/2} \rightarrow {}^6H_J$, $J = 5/2$–$13/2$ for Sm^{3+} with the $^4G_{5/2} \rightarrow {}^6H_{7/2}$

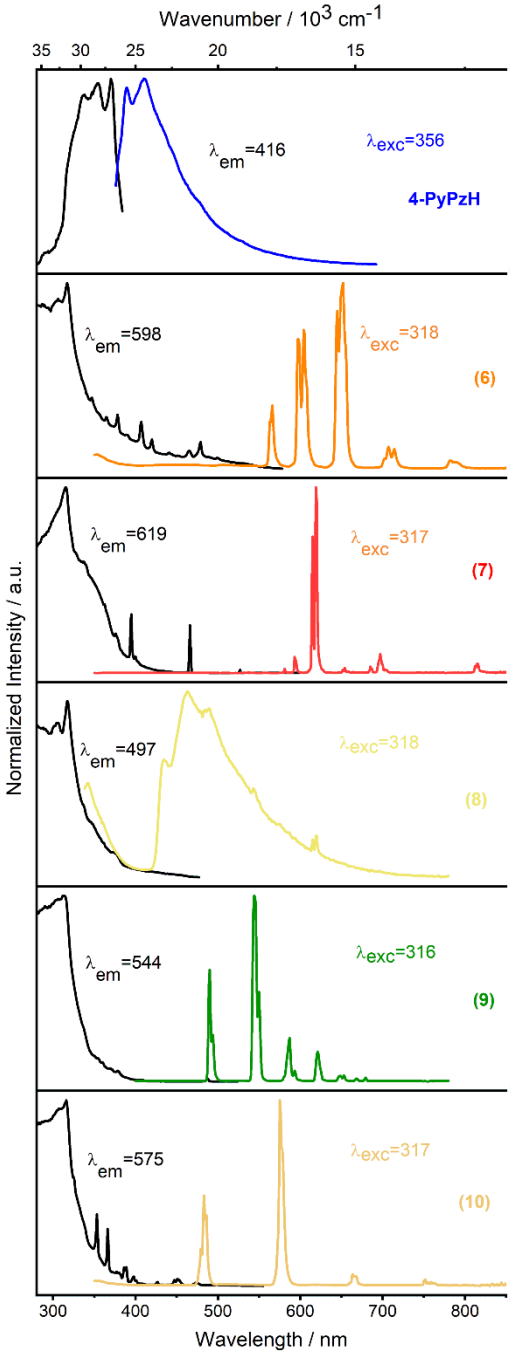

Figure 6. Normalized solid-state excitation (black) and emission (colored) spectra of $^{3}_{\infty}$[Ln(4-PyPz)$_3$], Ln = Sm, Eu, Gd, Tb, Dy (**6**–**10**) at 77 K. Wavelengths for which the spectra were recorded are reported in the legends.

transition at 605 nm dominating the spectrum for **1**, while the hypersensitive $^4G_{5/2}\rightarrow{}^6H_{9/2}$ transition at 652 nm dominating the spectrum for **6** at 77 K. At RT, the transition to $^6H_{9/2}$ is dominating for **1** and **6**. At both temperatures, the red luminescence of Eu^{3+} (**2** and **7**) is a result of transitions from its $^5D_0$ state to the ^7F_J, J=0–6, levels related to the typical red emission of Eu^{3+}. In the emission spectra of both compounds, the hypersensitive $^5D_0\rightarrow{}^7F_2$ transition has the maximum intensity at 619 nm. In addition, transitions from a higher-level $^5D_1\rightarrow{}^7F_1$ at 537 (**2**), 538 nm (**7**), and $^5D_1\rightarrow{}^7F_2$ at 555 nm are observed. The transition $^5D_0\rightarrow{}^7F_0$ is an indication that the Eu^{3-} ion occupies a site belonging to the C_{nv}, C_n, or C_s class of symmetry[20] (in this particular case C_3), to evade the selection rules described by the Judd-Ofelt theory.

The terbium containing coordination polymers **4** and **9** show the typical emission transitions between the excited $^5D_4$ state and the ^7F_J (J=6–0) levels of Tb^{3+}. The characteristic $^5D_4\rightarrow{}^7F_J$, J=3–6, transitions result in bright green photoluminescence color. The highest intensity is found for the transition $^5D_4\rightarrow{}^7F_5$ at 543 and 544 nm for **4** and **9**, respectively, as expected for a Tb^{3+}.[1c]

For $^{3}_{\infty}$[Dy(3-PyPz)$_3$( ]**5**) and $^{3}_{\infty}$[Dy(4-PyPz)$_3$( ]**10**), four emission lines are observed corresponding to the transition from the first excited $^4F_{9/2}$ state to the states $^6H_{15/2}$, $^6H_{13/2}$, $^6H_{11/2}$, and $^6H_{9/2}$. The highest intensity band at 575 nm is attributed to the $^4F_{9/2}\rightarrow{}^6H_{13/2}$ transition.

The heavy paramagnetic Gd^{III} ion in **3** and **8** enhances the inter-system crossing from the singlet to the triplet state of the pyrazolate anion.[21] Thus, it is feasible to obtain an evaluation of the T_1 energy level of both ligands by analyzing the emission spectra of $^{3}_{\infty}$[Gd(3-PyPz)$_3$] and $^{3}_{\infty}$[Gd(4-PyPz)$_3$], which is already visible at room temperature and more intense and better resolved at 77 K. The phosphorescent emission was also detected with a gating (cutting off the emission of the singlet state) to ensure a precise determination of the energetic positions of the T_1 level for the anions 3-$PyPz^-$ ($_{onset}$ = 430 nm, ~23 250 cm^{-1}; Figure S13) and 4-$PyPz^-$ ($_{onset}$ = 423 nm, ~23 640 cm^{-1}; Figure S18) at 77 K.[22] The emission spectra of the Gd^{3+} samples also show characteristic Eu^{3+} and Tb^{3+} 4f–4f transitions indicating a small Eu and Tb-impurity relevant for photoluminescence. The low concentration of Eu^{3+} and Tb^{3-} ions in the structure lowers the probability of cross-relaxation, thus enhancing its metal center-based luminescence. Besides, the ligands are themselves good sensitizers for Eu^{3+} and Tb^{3-}. The emission bands of $^{3}_{\infty}$[Gd(3-PyPz)$_3$]:Eu^{3-},Tb^{3+} (**3**) are observable at 544, 620 and 695 nm at 77 K and assigned to $^5D_4\rightarrow{}^7F_5$ transition of Tb^{3+}, $^5D_0\rightarrow{}^7F_2$ and $^5D_0\rightarrow{}^7F_4$ transitions of Eu^{3+}, respectively. Characteristic for Eu^{3-}, the band at 615 nm correlates with the transition $^5D_0\rightarrow{}^7F_6$. It is also observable at RT, where the $^5D_0\rightarrow{}^7F_2$ transition is dominating the spectrum for $_{ex}$ = 323 nm. At 77 K, the emission spectrum of $^{3}_{\infty}$[Gd(4-PyPz)$_3$]:Eu^{3+},Tb^{3+} (**8**) shows emission bands at 544 and 619 nm corresponding again to the $^5D_4\rightarrow{}^7F_5$ transition of Tb^{3+} and $^5D_0\rightarrow{}^7F_2$ transition of Eu^{3-}. At RT, the characteristic band for Tb^{3+} at 491 nm corresponding to the $^5D_4\rightarrow{}^7F_6$ transition appears, where the $^5D_4\rightarrow{}^7F_5$ transition is dominating the spectrum at $_{ex}$ = 321 nm. Besides, the transitions $^5D_0\rightarrow{}^7F_{3,4}$ of

Eu^{3+} at 654, and 699 nm are observable. For both cases, **3** and **8**, a deliberate co-doping of the Gd-containing frameworks with Tb^{3+} and Eu^{3+} can be established and used for chromaticity tuning. Mixing of the three emission colors results in a shift towards yellow, orange,[23] and even towards the white point with color coordinates of $x=0.30$ and $y=0.37$ for 0.5% Eu (**3b**) at 77 K. The possibility of tuning the luminescence chromaticity by co-doping of other homoleptic frameworks was also investigated and verified (Figures S24 and S25) for the co-doping of the Tb- and Eu-containing frameworks (**2** and **4**) with the respective counterions. The experiments were carried out for 5%Tb to 95% Eu and *vice versa* to produce $^3_\infty$[$Eu_{0.95}Tb_{0.05}$(3-PyPz)$_3$( ]**2a**), and $^3_\infty$[$Tb_{0.95}Eu_{0.05}$(3-PyPz)$_3$( ]**4a**), respectively. In both cases, the emission spectra of **2a** and **4a** are dominated by the main metal ion. In addition, a slight downshift metal-to-metal energy transfer (MMET) from excited 4f states of Tb^{3+} to Eu^{3+} is observed. The emission colors of $^3_\infty$[$Gd_{1-x-y}Eu_xTb_y$(3-PyPz)$_3$]:Eu^{3+},Tb^{3+} (**3a–3f**), $^3_\infty$[$Gd_{1-x-y}Eu_xTb_y$(4-PyPz)$_3$]:Eu^{3+},Tb^{3+} (**8a–8f**), $^3_\infty$[$Eu_{0.95}Tb_{0.05}$(3-PyPz)$_3$( ]**2a**) and $^3_\infty$[$Tb_{0.95}Eu_{0.05}$(3-PyPz)$_3$] (**4a**) are illustrated in CIE 1931 chromaticity diagrams (Figures 7 and S26), and the color coordinates are listed in Table S7. Excitation and emission spectra for the deliberate doping experiments are depicted in Figures S21–S25.

$$\phi_{calc} = \frac{\tau_{obs}}{\tau_0}$$

Neither a significant ligand-based fluorescence nor phosphorescence is being observed for the described coordination polymers except for Gd^{3+}. Thus 3-$PyPz^-$ and 4-$PyPz^-$ act as a suitable antenna for the sensitization of the lanthanide-based emission through absorption of light by the ligand by an $S_n \leftarrow S_0$ transition, ISC (intersystem crossing) from singlet (S) to triplet (T_1) levels of the ligands, followed by an energy transfer to the lanthanide ions, which then emit from their excited 4f states.

Lifetime measurements by determination of the overall process decay time were performed for all the compounds at room temperature and 77 K. In addition, quantum yields (QY) were determined if possible to further quantify the luminescence properties in the visible region supporting the discussion of transitions. The lifetimes were determined for Sm^{3+} (about 0.016 ms for **1** and **6**) and Dy^{3+} (0.016 for **6**, and 0.012 ms for **10**) as well as for Tb^{3+} (1.0874 ms for **4**, and 0.6273 ms for **9**; Table 1).

The PL of the coordination polymers decays monoexponentially on the timescale of a few milliseconds, thus indicating the presence of a single emissive species except for the co-doped Gd^{3+} frameworks. The lifetime for $^3_\infty$[Gd(3-PyPz)$_3$]:Eu^{3+},Tb^{3+} (**3**) and $^3_\infty$[Gd(4-PyPz)$_3$]:Eu^{3+},Tb^{3+} (**8**) at 77 K were fitted biexponentially, $_1=1.55$ ms, $_2=5.03$ ms for **3** and $_1=0.35$ ms, $_2=1.43$ ms for **8**, corroborating the observation of more than one PL process. The lifetime of the co-doped frameworks **3a–3f**, **8a–8f**, **2a**, and **4a** are varying from 0.516–0.750 ms at RT (Table S8). For most of the samples, the lifetime at 77 K rises slightly, as the thermal quenching of luminescence decreases.

The observed quantum yield (QY) for the Ln^{3+} emission through an antenna effect excitation (Table 1) is found to be highest for the Tb^{3+} compounds (**4** and **9**) with QY=74(1) and 23(1) %, respectively. This is a result of energy gaps in the optimal range (2500–3000 cm^{-1}) for **4** ($E=\sim2756$ cm^{-1}) and slightly above the optimal value for **9** ($E=\sim3141$ cm^{-1}), indicating an excellent antenna effect especially for **4**. The measured QY for Sm^{3+} is less than 1% and less than the calculated one ($_{calc}=6.15$%) which was determined using Equation (1), where $_{obs}$ (0.016 ms) is the measured radiative lifetime and $_o$ (3.25 ms) is the calculated average natural lifetime of Sm^{3+}.[24] Altogether, it is in the range of other known compounds containing Sm^{3+}.[22,24c,25] The quantum efficiencies for the Dy-containing frameworks **5** and **10** were determined as 1%, which is also in the range of other Dy^{3+} compounds.[26]

The internal quantum yields (IQY) of the Eu^{3+} centered emission were calculated using the following Wert's formula, see Equation (2).[27] $A_{MD,0}=14.65$ S^{-1} for Eu^{3+}, which represents the constant spontaneous emission probability, I_{tot} represents the total area of the emission spectrum ($^5D_0 \rightarrow {}^7F_J$, $J=0$–6), and

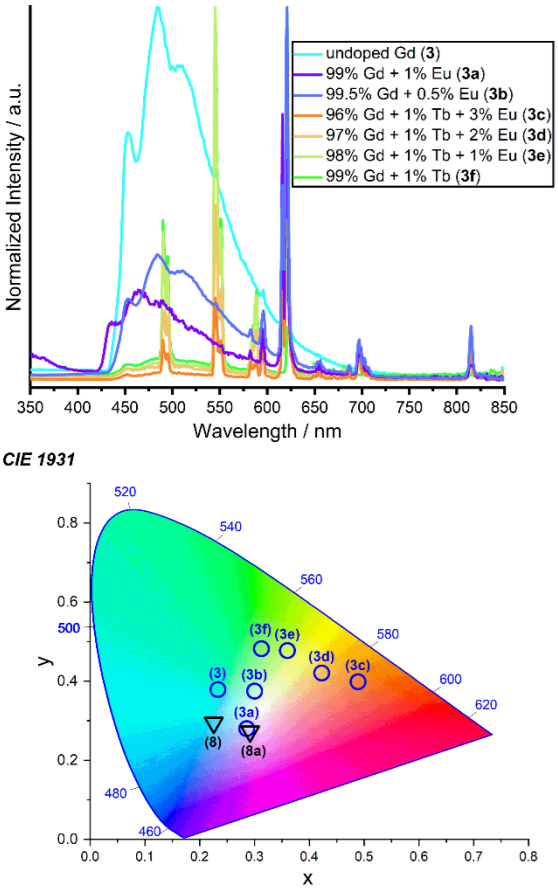

Figure 7. Normalized emission spectra of $^3_\infty$[$Gd_{1-x-y}Eu_xTb_y$(3-PyPz)$_3$]:Eu^{3+},Tb^{3+} (**3a–3f**) at 77 K (top), $_{ex}=323$ nm. Chromaticity coordinate diagram (CIE 1931) of the emission colors of the series $^3_\infty$[$Gd_{1-x-y}Eu_xTb_y$(3-PyPz)$_3$]:Eu^{3+},Tb^{3+} (**3**, **3a–3f**) and $^3_\infty$[$Gd_{1-x-y}Eu_xTb_y$(4-PyPz)$_3$]:Eu^{3+},Tb^{3+} (**8**, **8a**) at 77 K.

Table 1. Photophysical data of 3-PyPzH, 4-PyPzH, and **1**–**10** in the solid-state at room temperature and 77 K.

ID	[a] [ms]	ex/ em [nm][b]	[c] [ms]	ex/ em [nm][d]	[%][e]	ex/ em [nm][f]
3-PyPzH	3.4(1) ns	287/420	4.4(2) ns	287/420	n/a	n/a
4-PyPzH	6.07(9) ns	287/420	6.80(7) ns	287/420	n/a	n/a
1	0.01589(3)	324/605	0.02043(1)	318/605	0.46(1)	321/550–770
2	0.576(1)	466/619	0.754(2)	318/619	0.33(3)	363/570–715
3	0.5735(3)	323/545	3.29(6)	323/545	n/a	n/a
4	1.0874(8)	313/545	1.060(2)	314/545	74.3(2.2)	322/475–685
5	0.01573(5)	324/575	0.01587(7)	319/484	1.13(4)	321/460–675
6	0.01583(6)	327/646	0.01739(7)	318/598	0.40(1)	324/545–735
7	0.323(1)	466/619	0.498(1)	317/619	0.11(1)	330/570–715
8	0.56(1)	321/545	0.885(2)	314/545	n/a	n/a
9	0.6273(8)	323/544	0.6089(8)	316/544	23.2(3)	320/475–690
10	0.01207(2)	322/575	0.01270(3)	317/575	1.15(3)	321/460-675

[a] Emission lifetimes determined at 298 K. [b] Excitation and emission wavelengths for emission lifetime at 298 K. [c] Emission lifetime determined at 77 K. [d] Excitation and emission wavelengths for emission lifetime at 77 K. [e] Quantum yield. [f] Excitation wavelength and emission range of QY measurements.

$I_{MD,0}$ is the area of the $^5D_0 \rightarrow {}^7F_1$ transition. According to the literature,[28] the refractive index equals 1.5, $_{rad}$ = 1.187 and 0.988 ms, and $_{obs}$ = 0.576(1) and 0.016(6) for compounds **2** and **7**, respectively. The equation gives a moderate-high Internal QY (Eu^{3+}) of 48 and 33% for **2** and **7**, respectively.

$$IQY = \frac{\tau_{obs}}{\tau_{rad}} = \tau_{obs} A_{MD,0} n^3 \left(\frac{I_{tot}}{I_{MD}}\right) \quad (2)$$

Thermal analysis

Simultaneous DTA and TG investigations for $^3_\infty$[Tb(3-PyPz)$_3$( ]**4**, as well as DTA/TG, combined with mass spectrometry for $^3_\infty$[Tb(4-PyPz)$_3$( ]**9**), were carried out to investigate the thermal behavior of the two series of isotypic compounds. The DTA/TG investigations (Figures 8 and S27) reveal good temperature stability for both CPs. Except for the loss of pyridine incorporated in the pore system (signal 1) for **9** at 200 °C ($C_5H_5N^+$ *m/z* 79, and $C_5H_4N^+$ *m/z* 78), both compounds show rather similar behavior in the heat flow.[29] Decomposition occurs through two consecutive endothermic processes (signal 2 and 3) with onset temperatures of 360 °C and 385 °C for **4** and 370 °C and 405 °C for **9** resulting in overall mass loss of about 42% for both. The loss of pyridine at 200 °C with a corresponding mass loss of 10% in the TG-curve further confirms SCXRD data, where electron density was assigned to pyridine dispersed in the cavities of the porous 3D structure. Further confirmation for the decomposition process was the detection of a set of mass signals that can be assigned to fragments of the ligand ($C_7H_6N^-$ *m/z* 104, $C_5H_5N^+$ *m/z* 79, $C_5H_4N^+$ *m/z* 78).

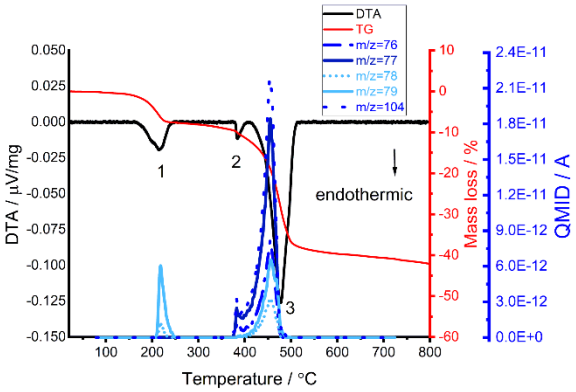

Figure 8. Simultaneous DTA/TG analysis together with mass spectrometry of $^{33}_\infty$[Tb(4-PyPz)$_3$( ]**9**) representing the series of isotypic frameworks **5**–**10**. Two consecutive thermal decomposition steps are numbered in the heat-flow plot. The investigation was performed under a constant flow of argon (50 mL·min^{-1}) with a heating from RT to 1000 °C at 5 K·min^{-1}.

Conclusion

Ten homoleptic and luminescent trivalent lanthanide-based 3D coordination polymers with 3-(3-pyridyl)pyrazolate and 4-(4-pyridyl)pyrazolate ligands were synthesized by anhydrous solvothermal reactions and characterized by SC and PXRD, elemental analysis, IR and photoluminescence spectroscopy, and thermal analysis. The investigated compounds form two series of 3D coordination frameworks that share the overall topology of a 6-connected uninodal net with a Schläfli symbol of $4^{12}.6^3$ with **pcu** topology. Both series of frameworks show photoluminescence with intra-4f emission of the Ln^{3+} ions being activated by antenna effects of the ligands leading to Ln^{3+} sensitization with quantum yields of up to QY = 74% for Tb^{3+}. Thereby, the specific trivalent Ln-ion-based emission ranges from green via yellow to red (from Tb via Dy and Sm to Eu). Tuning of the luminescence chromaticity is further possible by co-doping of the Gd-containing frameworks of both series with Eu^{3+} and Tb^{3+}, and allows for a chromaticity from green via yellow to red and tuning towards white-light emission.

Experimental Section

Synthesis and analytical data: The reactions of the different lanthanide metals with the aromatic N-heterocyclic 3-(3-pyridyl)

pyrazole (3-PyPzH) and 3-(4-pyridyl)pyrazole (4-PyPzH) is a redox reaction yielding hydrogen. For the two series of lanthanides ranging from Sm to Dy, the formation of trivalent compounds of the formula $^{3}_{\infty}$[Ln(3-PyPz)$_3$] and $^{3}_{\infty}$[Ln(4-PyPz)$_3$( ]**1**–**10**) is observed. Detailed description of the synthesis methods for all products **1**–**10** and the reagents can be found in the Supporting Information.

$$Ln + C_8H_7N_3 \rightarrow {}^{3}_{\infty}[Ln(C_8H_6N_3)_3] + {}^{3}/_{2}\,H_2$$

Deposition Numbers 2075974 (for **1**), 2075975 (for **2**), 2075976 (for **3**), 2075977 (for **4**), 2075978 (for **5**), 2075979 (for **6**), 2075980 (for **7**), 2075981 (for **8**), 2075982 (for **9**), and 2075983 (for **10**) contain the supplementary crystallographic data for this paper. These data are provided free of charge by the joint Cambridge Crystallographic Data Centre and Fachinformationszentrum Karlsruhe Access Structures service. Details on crystallographic data, comparison of simulated and recorded powder XRD patterns, detailed IR bands from ATR-MIR investigations, page size photoluminescence spectra with designated 4f–4f transitions for compounds **1**–**10** can be found in the Supporting Information.

Acknowledgements

The authors gratefully acknowledge the support of the Volkswagen Foundation within the project "Molecular materials–bridging magnetism and luminescence". H. Youssef gratefully acknowledges the Egyptian Ministry of Higher Education (MoHE) and the German Academic Exchange Service (DAAD) within the German Egyptian Research Long-term Scholarship (GERLS) Programme, 2017 (57311832) for a Ph.D. fellowship. I.V. Taydakov gratefully acknowledges the Russian Science Foundation (project no. 19-13-00272) for financial support. Open Access funding enabled and organized by Projekt DEAL.

Conflict of Interest

The authors declare no conflict of interest.

Keywords: coordination polymers · homoleptic · lanthanides · luminescence · N ligands

[1] a) M. F. Ashby, Y. J. M. Bréchet, *Acta Mater.* **2003**, *51*, 5801–5821; b) C. Janiak, J. K. Vieth, *New J. Chem.* **2010**, *34*, 2366–2388; c) K. Binnemans, *Chem. Rev.* **2009**, *109*, 4283–4374; d) H. Hiraga, H. Miyasaka, K. Nakata, T. Kajiwara, S. Takaishi, Y. Oshima, H. Nojiri, M. Yamashita, *Inorg. Chem.* **2007**, *46*, 9661–9671; e) X. Tan, Y.-Z. Du, Y.-X. Che, J.-M. Zheng, *Inorg. Chem. Commun.* **2013**, *36*, 63–67; f) B. Fernández, I. Oyarzabal, J. M. Seco, E. S. Sebastián, D. Fairen-Jiménez, S. Gómez-Ruiz, A. Salinas-Castillo, A. J. Calahorro, A. Rodríguez-Diéguez, *Polymer* **2016**, *8*, 39–49; g) S. R. Batten, B. Chen, J. J. Vittal, *ChemPlusChem* **2016**, *81*, 669–670; h) B. Y. Guan, A. Kushima, L. Yu, S. Li, J. Li, X. W. Lou, *Adv. Mater.* **2017**, *29*, 1605902–1605909; i) P. W. Zabierowski, O. Jeannin, T. Fix, J.-F. Guillemoles, L. J. Charbonnière, A. M. Nonat, *Inorg. Chem.* **2021**, *60*, 8304–8314; j) M. Kato, H. Ito, M. Hasegawa, K. Ishii, *Chem. Eur. J.* **2019**, *25*, 5105–5112.

[2] a) H. Furukawa, N. Ko, Y. B. Go, N. Aratani, S. B. Choi, E. Choi, A. Ö. Yazaydin, R. Q. Snurr, M. O'Keeffe, J. Kim, O. M. Yaghi, *Science* **2010**, *329*, 424–428; b) S. S. Mondal, A. Bhunia, A. G. Attallah, P. R. Matthes, A. Kelling, U. Schilde, K. Müller-Buschbaum, R. Krause-Rehberg, C. Janiak, H.-J. Holdt, *Chem. Eur. J.* **2016**, *22*, 6905–6913.

[3] a) J. Luzon, R. Sessoli, *Dalton Trans.* **2012**, *41*, 13556–13567; b) G. Cucinotta, M. Perfetti, J. Luzon, M. Etienne, P. E. Car, A. Caneschi, G. Calvez, K. Bernot, R. Sessoli, *Angew. Chem. Int. Ed.* **2012**, *51*, 1606–1610; *Angew. Chem.* **2012**, *124*, 1638–1642; c) S. Roy, A. Chakraborty, T. K. Maji, *Coord. Chem. Rev.* **2014**, *273*, 139–164.

[4] a) M. D. Allendorf, C. A. Bauer, R. K. Bhakta, R. J. T. Houk, *Chem. Soc. Rev.* **2009**, *38*, 1330–1352; b) J. Rocha, L. D. Carlos, F. A. A. Paz, D. Ananias, *Chem. Soc. Rev.* **2011**, *40*, 926–940; c) S. Sato, A. Ishii, C. Yamada, J. Kim, C. H. Song, A. Fujiwara, M. Takata, M. Hasegawa, *Polym. J.* **2015**, *47*, 195–200.

[5] a) Y. Cui, Y. Yue, G. Qian, B. Chen, *Chem. Rev.* **2012**, *112*, 1126–1162; b) J.-P. Zou, Q. Peng, Z. Wen, G.-S. Zeng, Q.-J. Xing, G.-C. Guo, *Cryst. Growth Des.* **2010**, *10*, 2613–2619; c) K. Mandel, T. Granath, T. Wehner, M. Rey, W. Stracke, N. Vogel, G. Sextl, K. Müller-Buschbaum, *ACS Nano* **2017**, *11*, 779–787.

[6] Q.-R. Wu, J.-J. Wang, H.-M. Hu, Y.-Q. Shangguan, F. Fu, M.-L. Yang, F.-X. Dong, G.-L. Xue, *Inorg. Chem. Commun.* **2011**, *14*, 484–488.

[7] a) M. Latva, H. Takalo, V.-M. Mukkala, C. Matachescu, J. C. Rodríguez-Ubis, J. Kankare, *J. Lumin.* **1997**, *75*, 149–169; b) L. Armelao, S. Quici, F. Barigelletti, G. Accorsi, G. Bottaro, M. Cavazzini, E. Tondello, *Coord. Chem. Rev.* **2010**, *254*, 487–505; c) A. Bellusci, G. Barberio, A. Crispini, M. Ghedini, M. La Deda, D. Pucci, *Inorg. Chem.* **2005**, *44*, 1818–1825.

[8] a) H. Zhang, R. Fan, W. Chen, X. Zheng, K. Li, P. Wang, Y. Yang, *J. Lumin.* **2013**, *143*, 611–618; b) T. Wehner, K. Mandel, M. Schneider, G. Sextl, K. Müller-Buschbaum, *ACS Appl. Mater. Interfaces* **2016**, *8*, 5445–5452.

[9] a) M. B. Coban, A. Amjad, M. Aygun, H. Kara, *Inorg. Chim. Acta* **2017**, *455*, 25–33; b) C. J. Höller, P. R. Matthes, M. Adlung, C. Wickleder, K. Müller-Buschbaum, *Eur. J. Inorg. Chem.* **2012**, *3*, 5479–5484.

[10] H. Zhang, X. Shan, L. Zhou, P. Lin, R. Li, E. Ma, X. Guo, S. Du, *J. Mater. Chem. C* **2013**, *1*, 888–891.

[11] a) H. Adams, S. R. Batten, G. M. Davies, M. B. Duriska, J. C. Jeffery, P. Jensen, J. Lu, G. R. Motson, S. J. Coles, M. B. Hursthouse, M. D. Ward, *Dalton Trans.* **2005**, 1910–1923; b) J.-C. Li, H.-X. Li, H.-Y. Li, W.-J. Gong, J.-P. Lang, *Cryst. Growth Des.* **2016**, *16*, 1617–1625.

[12] F. L. Liu, J. Tao, *Chem. Eur. J.* **2017**, *23*, 18252–18257.

[13] N. Li, B. Mu, X. Cao, R. Huang, *J. Solid State Chem.* **2014**, *217*, 180–186.

[14] W. J. Gee, S. R. Batten, *Chem. Commun.* **2012**, *48*, 4830–4832.

[15] L.-R. Xing, Z. Lu, M. Li, J. Zheng, D. Li, *J. Phys. Chem. Lett.* **2020**, *11*, 2067–2073.

[16] K. Müller-Buschbaum, Y. Mokaddem, *Chem. Commun.* **2006**, 2060–2062.

[17] a) M. O'Keeffe, M. A. Peskov, S. J. Ramsden, O. M. Yaghi, *Acc. Chem. Res.* **2008**, *41*, 1782–1789; b) A. F. Wells, *Three Dimensional Nets and Polyhedra*, Wiley, New York, **1977**.

[18] N. Du, X. Gao, J. Song, Z.-N. Wang, Y.-H. Xing, F.-Y. Bai, Z. Shi, *RSC Adv.* **2016**, *6*, 71012–71024.

[19] J. H. Van Vleck, *J. Phys. Chem.* **1937**, *41*, 67–80.

[20] K. Binnemans, C. Görller-Walrand, *J. Rare Earth* **1996**, *14*, 173–180.

[21] a) K. Binnemans, *Coord. Chem. Rev.* **2015**, *295*, 1–45; b) W. T. Carnall, P. R. Fields, K. Rajnak, *J. Chem. Phys.* **1968**, *49*, 4424–4442; c) A. E. Sedykh, D. G. Kurth, K. Müller-Buschbaum, *Eur. J. Inorg. Chem.* **2019**, *2019*, 4564–4571.

[22] A. E. Sedykh, D. G. Kurth, K. Müller-Buschbaum, *Z. Anorg. Allg. Chem.* **2021**, *647*, 359–364.

[23] P. R. Matthes, C. J. Höller, M. Mai, J. Heck, S. J. Sedlmaier, S. Schmiechen, C. Feldmann, W. Schnick, K. Müller-Buschbaum, *J. Mater. Chem.* **2012**, *22*, 10179–10187.

[24] a) A. P. Bassett, S. W. Magennis, P. B. Glover, D. J. Lewis, N. Spencer, S. Parsons, R. M. Williams, L. De Cola, Z. Pikramenou, *J. Am. Chem. Soc.* **2004**, *126*, 9413–9424; b) X. Y. Chen, M. P. Jensen, G. K. Liu, *J. Phys. Chem. B* **2005**, *109*, 13991–13999; c) J. M. Stanley, C. K. Chan, X. Yang, R. A. Jones, B. J. Holliday, *Polyhedron* **2010**, *29*, 2511–2515.

[25] H. Hakala, P. Liitti, J. Peuralahti, J. Karvinen, V.-M. Mukkala, J. Hovinen, *J. Lumin.* **2005**, *113*, 17–26.

[26] A. K. Mondal, S. Goswami, S. Konar, *Dalton Trans.* **2015**, *44*, 5086–5094.

[27] a) A. Aebischer, F. Gumy, J.-C. G. Bünzli, *Phys. Chem. Chem. Phys.* **2009**, *11*, 1346–1353; b) M. H. V. Werts, R. T. F. Jukes, J. W. Verhoeven, *Phys. Chem. Chem. Phys.* **2002**, *4*, 1542–1548.

[28] S. V. Eliseeva, J.-C. G. Bünzli, *Chem. Soc. Rev.* **2010**, *39*, 189–227.

[29] K. Müller-Buschbaum, C. C. Quitmann, *Inorg. Chem.* **2006**, *45*, 2678–2687.

Manuscript received: August 23, 2021
Accepted manuscript online: October 6, 2021
Version of record online: November 5, 2021

Chemistry–A European Journal

Supporting Information

Variable Luminescence and Chromaticity of Homoleptic Frameworks of the Lanthanides together with Pyridylpyrazolates

Heba Youssef, Alexander E. Sedykh, Jonathan Becker, Thomas Schäfer, Ilya V. Taydakov, Huanrong R. Li, and Klaus Müller-Buschbaum*

Table of Contents

Crystallographic Data

CCDC 2075974 (**1**), 2075975 (**2**), 2075976 (**3**), 2075977 (**4**), 2075978 (**5**), 2075979 (**6**), 2075980 (**7**), 2075981 (**8**), 2075982 (**9**), and 2075983 (**10**) contain the supplementary crystallographic data. These data are provided free of charge by the Cambridge Crystallographic Data Centre.

Table S1. Crystallographic data of $^3_\infty$[Ln(3-PyPz)$_3$] (**1-5**).

Compound	**$^3_\infty$[Sm(3-PyPz)$_3$]**	**$^3_\infty$[Eu(3-PyPz)$_3$]**	**$^3_\infty$[Gd(3-PyPz)$_3$]:Eu^{3+}, Tb^{3+}**	**$^3_\infty$[Tb(3-PyPz)$_3$]**	**$^3_\infty$[Dy(3-PyPz)$_3$]**
CCDC number	2075974	2075975	2075976	2075977	2075978
Empirical formula	$C_{24}H_{18}N_9Sm$	$C_{24}H_{18}N_9Eu$	$C_{24}H_{18}N_9Gd$	$C_{24}H_{18}N_9Tb$	$C_{24}H_{18}DyN_9$
M_r / g·mol^{-1}	582.82	584.43	589.72	591.39	594.97
T / K	100(2)	100(2)	100(2)	200(2)	100(2)
λ / pm	71.073, Mo-K$_\alpha$	71.073, Mo-K$_\alpha$	71.073, Mo-K$_\alpha$	71.073, Mo-K$_\alpha$	71.073, Mo-K$_\alpha$
Crystal system	Cubic	Cubic	Cubic	Cubic	Cubic
Space group	$Pa\bar{3}$	$Pa\bar{3}$	$Pa\bar{3}$	$Pa\bar{3}$	$Pa\bar{3}$
a, b, c / pm	1711.0(2)	1710.4(1)	1702.4(1)	1707.0(1)	1699.9(1)
α, β, γ / °	90	90	90	90	90
V / 10^6 pm^3	5009(2)	50034(2)	4934.3(4)	4973.6(3)	4912.6(4)
Z	8	8	8	8	8
ρ_{calc} / g·cm^{-3}	1.546	1.552	1.588	1.580	1.609
μ / mm^{-1}	2.374	2.536	2.718	2.873	3.072
F(000)	2296	2304	2312	2320	2328
Crystal size / mm^3	0.039 x 0.023 x 0.019	0.168 x 0.129 x 0.008	0.047 x 0.043 x 0.017	0.254 x 0.208 x 0.195	0.079 x 0.062 x 0.028
2θ_{min} / °	2.062	2.062	2.072	2.066	2.396
2θ_{max} / °	26.730	27.502	28.364	30.604	27.073
Reflections collected	46979	45916	57689	64936	17575
Independent reflections	1786	1936	2072	2566	1814
R(int)	0.1383	0.0591	0.3466	0.1016	0.1026
Completeness to theta = 25.242°	100.0 %	100.0 %	100.0 %	99.9 %	99.9 %
No. Of parameters	103	103	103	103	103

GOF	1.097	1.139	0.938	1.060	1.046
Final R indices [$I > 2\sigma(I)$]	R_1 = 0.0312, wR_2 = 0.0611	R_1 = 0.0216, wR_2 = 0.0457	R_1 = 0.0318, wR_2 = 0.0567	R_1 = 0.0297, wR_2 = 0.0527	R_1 = 0.0412, wR_2 = 0.0794
R indices (all data)	R_1 = 0.0535, wR_2 = 0.0688	R_1 = 0.0293, wR_2 = 0.0483	R_1 = 0.0727, wR_2 = 0.0644	R_1 = 0.0563, wR_2 = 0.0624	$R1$ = 0.0755, $wR2$ =0.0921
$\Delta\rho_{max}$, $\Delta\rho_{min}$ / e·10^{-6}·pm^{-3}	1.326, -0.662	0.388, -0.652	1.417, -0.510	0.510, -0.786	1.590, -1.101

Table S2. Crystallographic data of $^3_\infty$[Ln(4-PyPz)$_3$] (**6-10**).

Compound	**$^3_\infty$[Sm(4-PyPz)$_3$]**	**$^3_\infty$[Eu(4-PyPz)$_3$]**	**$^3_\infty$[Gd(4-PyPz)$_3$]:Eu^{3+},Tb^{3+}**	**$^3_\infty$[Tb(4-PyPz)$_3$]**	**$^3_\infty$[Dy(4-PyPz)$_3$]**
CCDC number	2075979	2075980	2075981	2075982	2075983
Empirical formula	$C_{24}H_{18}N_9Sm$	$C_{24}H_{18}N_9Eu$	$C_{24}H_{18}N_9Gd$	$C_{24}H_{18}N_9Tb$	$C_{24}H_{18}N_9Dy$
M_r / g·mol^{-1}	582.82	584.43	589.72	591.39	594.97
T / K	100(2)	100(2)	100(2)	100(2)	100(2)
λ / pm	71.073, Mo-K$_\alpha$	71.073 Mo-K$_\alpha$	71.073, Mo-K$_\alpha$	71.073, Mo-K$_\alpha$	71.073, Mo-K$_\alpha$
Crystal system	Monoclinic	Monoclinic	Monoclinic	Monoclinic	Monoclinic
Space group	$P2_1/n$	$P2_1/n$	$P2_1/n$	$P2_1/n$	$P2_1/n$
a / pm	923.5(1)	921.2(1)	919.5(2)	918.3(2)	916.8(1)
b / pm	1682.7(1)	1681.4(1)	1681.4(2)	1679.1(3)	1677.5(1)
c / pm	1582.0(1)	1577.9(1)	1578.3(2)	1576.6(3)	1572.6(1)
α / °	90	90	90	90	90
β / °	102.31(1)	102.30(1)	102.34(1)	102.33(1)	102.22(1)
γ / °	90	90	90	90	90
V / 10^6 pm^3	2401.8(2)	2387.8(2)	2383.7(6)	2375.0(6)	2363.6(2)
Z	4	4	4	4	4
ρ_{calc} / g·cm^{-3}	1.612	1.626	1.643	1.654	1.672
μ / mm^{-1}	2.475	2.657	2.813	3.009	3.192
F(000)	1148	1152	1156	1160	1164
Crystal size / mm3	0.037 x 0.035 x 0.018	0.059 x 0.036 x 0.021	0.029 x 0.022 x 0.017	0.253 x 0.226 x 0.151	0.084 x 0.076 x 0.053
2θ_{min} / °	1.789	1.792	2.368	2.645	1.797
2θ_{max} / °	27.538	26.370	27.875	30.032	26.021

Reflections collected	77055	47406	87613	32018	98317
Independent reflections	5521	4891	5685	6925	4664
R(int)	0.0632	0.1014	0.1333	0.1191	0.0668
Completeness to theta = 25.242°	100.0 %	100.0 %	100.0 %	99.9 %	100.0 %
No. Of parameters	307	307	307	308	307
GOF	1.045	1.056	1.086	1.024	1.084
Final *R* indices [$I > 2\sigma(I)$]	R_1 = 0.0209, wR_2 = 0.0418	R_1 = 0.0329, wR_2 = 0.0670	R_1 = 0.0343, wR_2 = 0.0727	R_1 = 0.0476, wR_2 = 0.0982	R_1 = 0.0182, wR_2 = 0.0370
R indices (all data)	R_1 = 0.0294, wR_2 = 0.0441	R_1 = 0.0510, wR_2 = 0.0739	R_1 = 0.0553, wR_2 = 0.0806	R_1 = 0.0778, wR_2 = 0.1100	R_1 = 0.0233, wR_2 = 0.0385
$\Delta\rho_{max}$, $\Delta\rho_{min}$ / e·10^{-6}·pm^{-3}	1.284, -0.477	1.785, -1.072	1.747, -0.878	1.894, -1.774	1.130, -0.600

Interatomic Distances and Angles

Table S3. Selected interatomic distances (pm) and angles (°) of $^3_\infty$[Ln(3-PyPz)$_3$] (**1-5**). Symmetry operations: I -z+1,x+1/2,-y+3/2 II y-1/2,-z+3/2,-x+1 III x-1/2,y,-z+3/2 IV y-1/2,z,-x+3/2 V z-1/2,x,-y+3/2.

Compound	$^3_\infty$[Sm(3-PyPz)$_3$]	$^3_\infty$[Eu(3-PyPz)$_3$]	$^3_\infty$[Gd(3-PyPz)$_3$]:Eu^{3+},Tb^{3+}	$^3_\infty$[Tb(3-PyPz)$_3$]	$^3_\infty$[Dy(3-PyPz)$_3$]
Ln-N2	241.2(3)	239.9(2)	238.5(4)	237.4(2)	236.0(4)
Ln-N3	245.9(3)	245.2(2)	243.6(4)	242.0(2)	241.0(4)
Ln-N1^{III}	262.0(3)	261.3(2)	258.6(4)	259.3(2)	256.5(4)
N2-Ln-N2^{I}	85.8(1)	85.6(1)	85.6(2)	85.8(1)	85.9(2)
N2-Ln-N3	32.7(1)	32.8(1)	33.1(2)	33.1(1)	33.2(2)
N2^{I}-Ln-N3	82.8(1)	82.7(1)	82.6(2)	83.1(1)	83.0(2)
N2^{II}-Ln-N3	117.9(1)	117.8(1)	118.1(1)	118.4(1)	118.5(2)
N3-Ln-N3^{II}	113.0(1)	113.0(1)	113.1(8)	113.5(1)	113.5(1)
N2-Ln-N1^{III}	161.3(1)	161.2(1)	161.3(1)	161.7(1)	161.6(2)
N2^{I}-Ln-N1^{III}	109.6(1)	109.8(1)	109.7(1)	109.3(1)	109.3(2)
N2^{II}-Ln-N1^{III}	84.8(1)	84.9(1)	84.9(2)	85.1(1)	84.9(2)
N3-Ln-N1^{III}	155.5(1)	155.4(1)	155.3(2)	154.8(1)	154.8(2)
N3^{II}-Ln-N1^{III}	80.6(1)	80.6(1)	80.7(2)	80.6(1)	80.6(2)

N3^{I}-Ln-N1^{III}	76.9(1)	77.0(1)	76.6(1)	76.2(1)	76.1(2)
N1^{III}-Ln-N1^{IV}	83.1(1)	83.0(1)	83.1(2)	83.0(1)	83.1(2)

Table S4. Selected interatomic distances (pm) and angles (°) of $^3_\infty$[Ln(4-PyPz)$_3$] (**6-10**). Symmetry operations: : I x+1/2,-y+1/2,z+1/2 II -x+3/2,y-1/2,-z+3/2 III x+1,y,z.

Compound	$^3_\infty$[Sm(4-PyPz)$_3$]	$^3_\infty$[Eu(4-PyPz)$_3$]	$^3_\infty$[Gd(4-PyPz)$_3$]:Eu^{3+},Tb^{3+}	$^3_\infty$[Tb(4-PyPz)$_3$]	$^3_\infty$[Dy(4-PyPz)$_3$]
Ln-N2	242.0(2)	240.8(4)	240.7(4)	238.8(4)	237.5(2)
Ln -N5	242.5(2)	241.0(4)	240.4(4)	239.1(4)	237.8(2)
Ln -N8	242.7(2)	241.4(4)	240.6(4)	239.1(4)	238.0(2)
Ln -N9	247.6(2)	246.2(4)	245.5(4)	244.4(4)	242.9(2)
Ln-N6	248.4(2)	247.6(4)	246.3(4)	245.6(5)	243.4(2)
Ln-N3	250.4(2)	248.6(4)	248.7(4)	246.8(4)	245.3(2)
Ln-N1^{I}	258.9(2)	257.7(4)	256.5(4)	256.3(4)	253.3(2)
Ln-N4^{II}	260.6(2)	258.8(4)	258.3(4)	255.8(4)	255.7(2)
Ln-N7^{III}	260.6(2)	258.8(3)	257.6(4)	256.7(5)	255.0(2)
N2-Ln-N5	86.2(1)	86.1(1)	86.1(1)	86.0(2)	85.8(1)
N2-Ln-N8	90.1(1)	90.1(1)	90.0(1)	90.1(2)	90.0(1)
N5-Ln-N8	84.5(1)	84.5(1)	84.6(1)	84.4(2)	84.6(1)
N2-Ln-N9	84.9(1)	85.1(1)	85.1(1)	85.0(2)	84.8(1)
N5-Ln-N9	115.8(1)	116.0(1)	116.0(1)	116.1(2)	116.4(1)
N8-Ln-N9	32.2(1)	32.4(1)	32.2(1)	32.7(2)	32.8(1)
N2-Ln-N6	118.3(1)	118.4(1)	118.4(1)	118.7(2)	118.7(1)
N5-Ln-N6	32.0(1)	32.3(1)	32.3(1)	32.7(2)	32.8(1)
N8-Ln-N6	85.2(1)	85.1(1)	85.3(1)	84.9(2)	84.9(1)
N9-Ln-N6	115.6(1)	115.7(1)	115.6(1)	115.6(2)	115.8(1)
N2-Ln-N3	32.0(1)	32.1(1)	32.2(1)	32.2(2)	32.7(1)
N5-Ln-N3	82.8(1)	82.6(1)	82.7(1)	82.8(2)	82.5(1)
N8-Ln-N3	121.2(1)	121.3(1)	121.3(1)	121.4(2)	121.7(1)
N9-Ln-N3	115.2(1)	115.3(1)	115.4(1)	115.2(2)	115.4(1)
N6-Ln-N3	109.8(1)	109.8(1)	109.9(1)	110.4(2)	110.3(1)
N2-Ln-N1^{I}	115.3(1)	115.4(1)	115.2(1)	115.0(2)	115.3(1)
N5-Ln-N1^{I}	87.6(1)	87.5(1)	87.4(1)	87.5(2)	87.1(1)
N8-Ln-N1^{I}	152.9(1)	152.7(1)	153.0(1)	153.0(2)	152.7(1)
N9-Ln-N1^{I}	150.8(1)	150.7(1)	150.9(1)	150.9(2)	151.0(1)
N6-Ln-N1^{I}	74.6(1)	74.5(1)	74.5(1)	74.6(2)	74.3(1)
N3-Ln-N1^{I}	83.3(1)	83.3(1)	83.0(1)	82.8(2)	82.7(1)
N2-Ln-N4^{II}	155.3(1)	80.8(1)	155.2(1)	155.3(2)	155.0(1)
N5-Ln-N4^{II}	115.2(1)	156.4(1)	115.3(1)	115.3(2)	115.6(1)
N8-Ln-N4^{II}	80.4(1)	114.8(1)	80.4(1)	80.4(2)	80.2(1)
N9-Ln-N4^{II}	74.9(1)	82.4(1)	74.6(1)	74.7(2)	74.5(1)
N6-Ln-N4^{II}	83.8(1)	153.4(1)	83.8(1)	83.4(2)	83.5(1)
N3-Ln-N4^{II}	154.4(1)	75.9(1)	154.3(1)	154.2(2)	154.1(1)

N1^{I}-Ln-N4^{II}	79.5(1)	80.6(1)	79.9(1)	80.0(2)	80.1(1)
N2-Ln-N7^{III}	80.8(1)	155.3(1)	80.8(1)	80.7(2)	80.7(1)
N5-Ln-N7^{III}	156.6(1)	115.3(1)	156.3(1)	156.0(2)	155.7(1)
N8-Ln-N7^{III}	114.7(1)	80.3(1)	115.0(1)	115.3(2)	115.3(1)
N9-Ln-N7^{III}	82.5(1)	74.6(1)	82.7(1)	82.7(2)	82.5(1)
N6-Ln-N7^{III}	153.4(1)	83.7(1)	153.2(1)	153.1(2)	153.0(1)
N3-Ln-N7^{III}	75.9(1)	154.5(1)	75.7(1)	75.3(2)	75.2(1)
N1^{I}-Ln-N7^{III}	80.5(1)	79.6(1)	80.5(1)	80.3(2)	80.6(1)
N4^{II}-Ln-N7^{III}	82.6(1)	82.7(1)	82.7(1)	82.9(2)	80.7(1)

Powder Diffraction

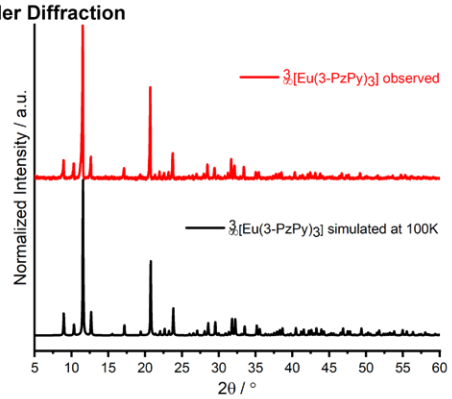

Figure S1. Comparison between the simulated diffraction pattern from the SCXRD data (black) and the observed X-ray powder diffraction pattern (red) of $^3_\infty$[Eu(3-PyPz)$_3$] (**2**).

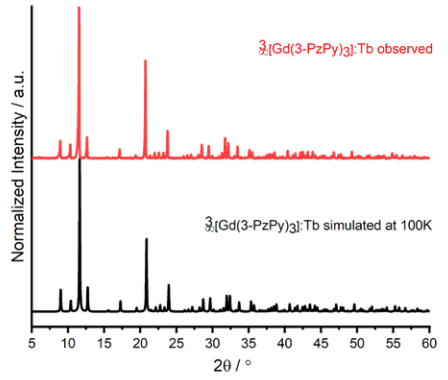

Figure S2. Comparison between the simulated diffraction pattern from the SCXRD data (Black) and the observed X-ray powder diffraction pattern (Red) of $^3_\infty$[Gd(3-PyPz)$_3$]:Eu^{3+},Tb^{3+} (**3**).

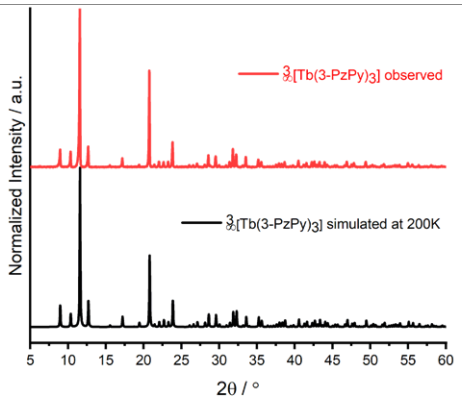

Figure S3. Comparison between the simulated diffraction pattern from the SCXRD data (Black) and the observed X-ray powder diffraction pattern (Red) of $^3_\infty$[Tb(3-PyPz)$_3$] (**4**).

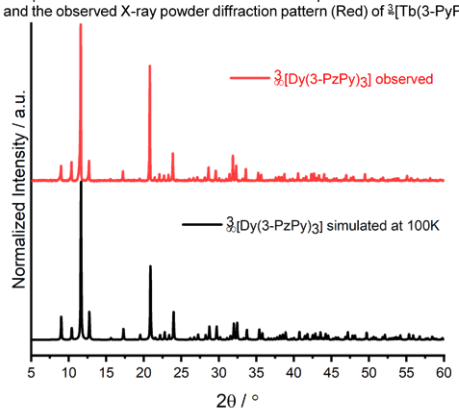

Figure S4. Comparison between the simulated diffraction pattern from the SCXRD data (Black) and the observed X-ray powder diffraction pattern (Red) of $^3_\infty$[Dy(3-PyPz)$_3$] (**5**).

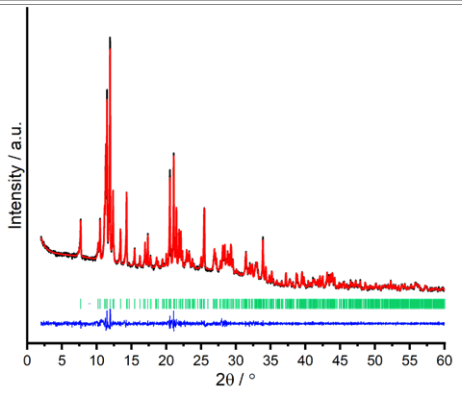

Figure S5. Pawley refinement of $^3_\infty$[Eu(4-PyPz)$_3$] (**7**), showing the experimental data (black) together with the Pawley fit (red), the corresponding difference plot (blue) as well as the hkl position markers (green).

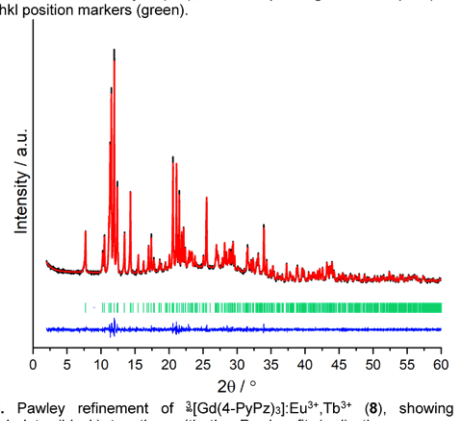

Figure S6. Pawley refinement of $^3_\infty$[Gd(4-PyPz)$_3$]:Eu^{3+},Tb^{3+} (**8**), showing the experimental data (black) together with the Pawley fit (red), the corresponding difference plot (blue) as well as the hkl position markers (green).

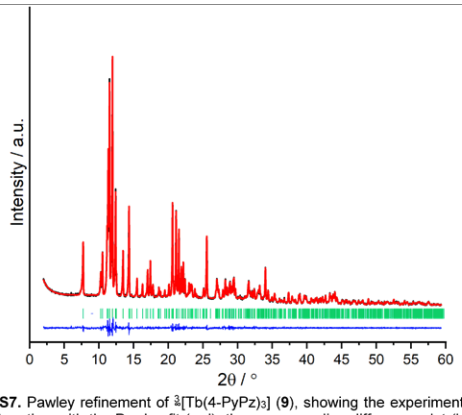

Figure S7. Pawley refinement of $^3_\infty$[Tb(4-PyPz)$_3$] (**9**), showing the experimental data (black) together with the Pawley fit (red), the corresponding difference plot (blue) as well as the hkl position markers (green).

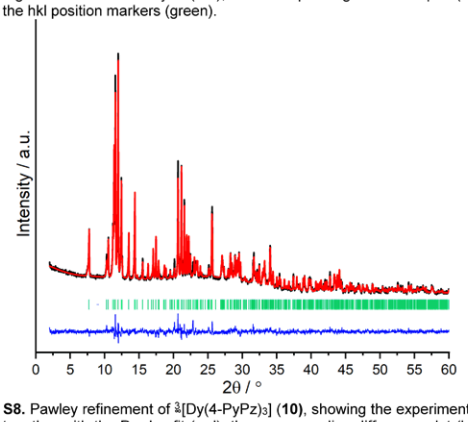

Figure S8. Pawley refinement of $^3_\infty$[Dy(4-PyPz)$_3$] (**10**), showing the experimental data (black) together with the Pawley fit (red), the corresponding difference plot (blue) as well as the hkl position markers (green).

Table S5. Pawley refinement details and results for $^3_\infty$[Ln(4-PyPz)$_3$] (**6-10**).

Compound	$^3_\infty$[Sm(4-PyPz)$_3$]	$^3_\infty$[Eu(4-PyPz)$_3$]	$^3_\infty$[Gd(4-PyPz)$_3$]:Eu^{3+},Tb^{3+}	$^3_\infty$[Tb(4-PyPz)$_3$]	$^3_\infty$[Dy(4-PyPz)$_3$]
R_{wp}	1.7401	1.9505	1.6597	1.9598	1.8547
GOF	0.9884	1.1330	1.0618	1.0540	1.0465
a / pm	922.3(1)	921.2(1)	919.3(1)	916.7(1)	916.0(1)
b / pm	1685.5(1)	1683.5(1)	1683.0(1)	1679.4(1)	1679.6(1)
c / pm	1601.6(1)	1599.8(1)	1597.9(1)	1595.3(1)	1592.8(1)
α / °	90	90	90	90	90
β / °	102.475(1)	102.455(2)	102.460(2)	102.476(1)	102.444(1)
γ / °	90	90	90	90	90
V / 10^6 pm^3	2430.8(1)	2422.7(2)	2413.9(1)	2398.0(1)	2392.9(1)

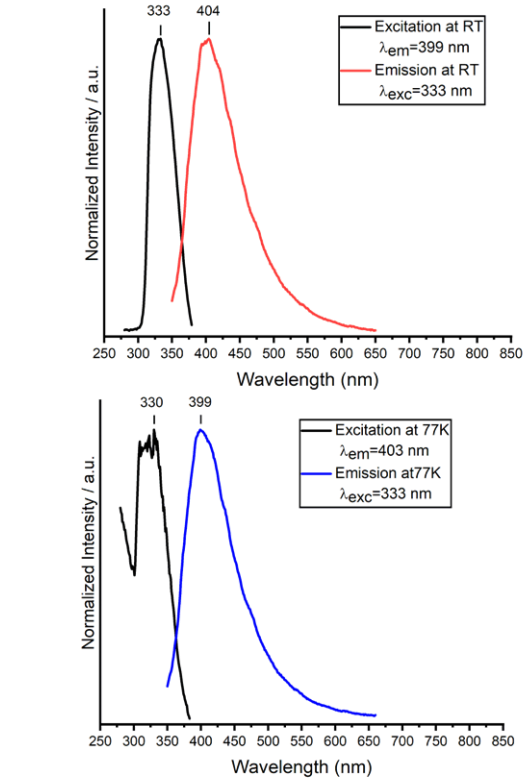

Figure S9. Normalized excitation and emission spectra of 3-PyPzH at room temperature (top) and 77K (bottom). Wavelengths at which the spectra were recorded are reported in the legends.

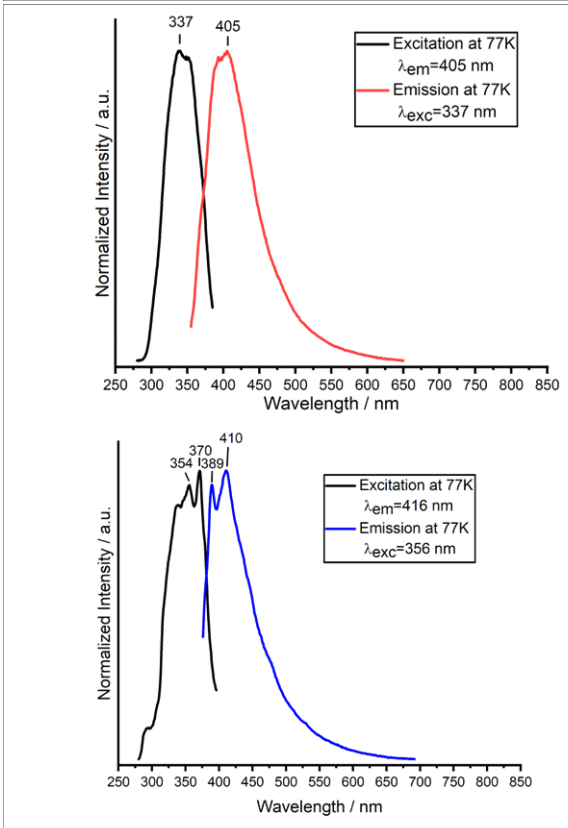

Figure S10. Normalized excitation and emission spectra of 4-PyPzH at room temperature (top) and 77K (bottom). Wavelengths at which the spectra were recorded are reported in the legends.

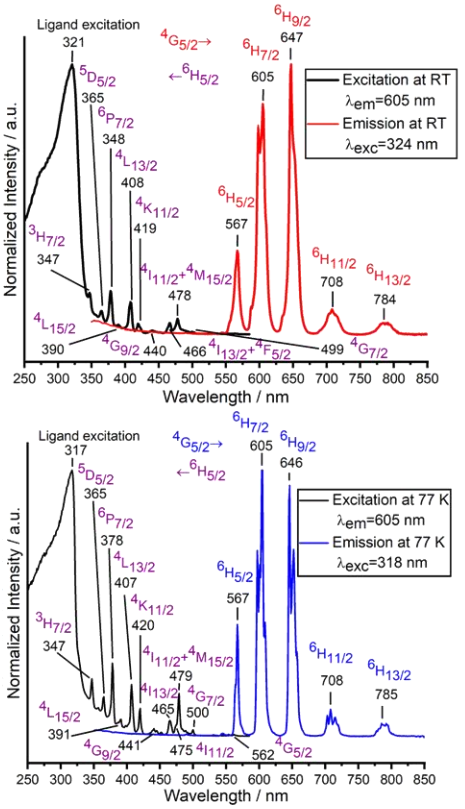

Figure S11. Normalized excitation and emission spectra of $^{3}_{\infty}$[Sm(3-PyPz)$_3$] (**1**) at room temperature (top) and 77K (bottom). Wavelengths at which the spectra were recorded are reported in the legends.

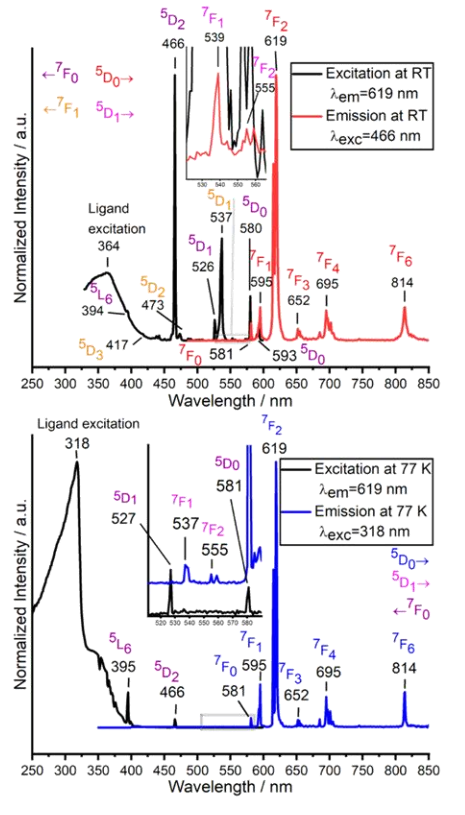

Figure S12. Normalized excitation and emission spectra of $^{3}_{\infty}$[Eu(3-PyPz)$_3$] (**2**) at room temperature (top) and 77K (bottom). Wavelengths at which the spectra were recorded are reported in the legends.

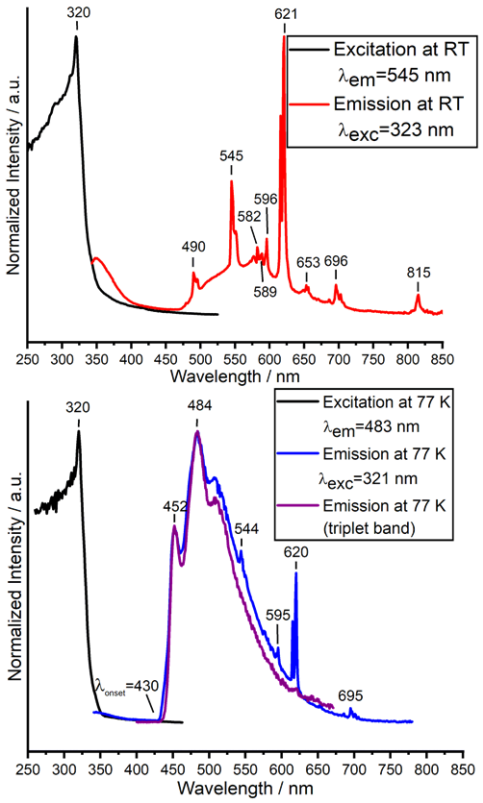

Figure S13. Normalized excitation and emission spectra of ∞[Gd(3-PyPz)$_3$]:Eu^{3+},Tb^{3+} (**3**) at room temperature (top) and 77K (bottom). Wavelengths at which the spectra were recorded are reported in the legends.

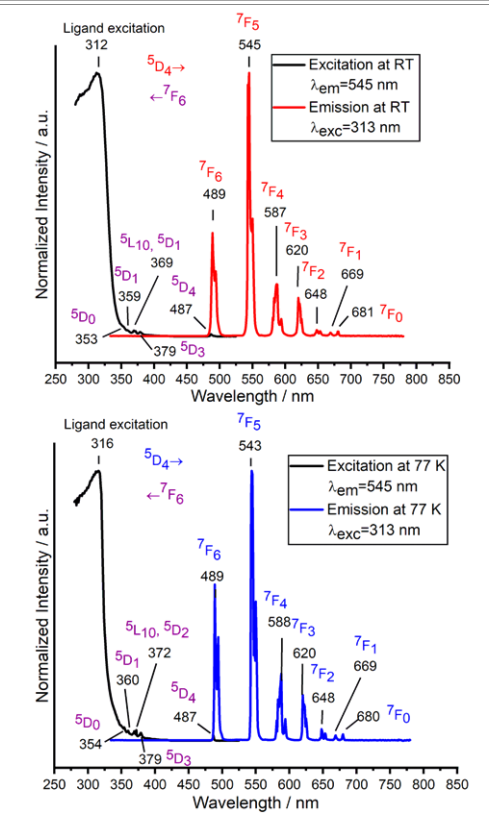

Figure S14. Normalized excitation and emission spectra of ∞[Tb(3-PyPz)$_3$] (**4**) at room temperature (top) and 77K (bottom). Wavelengths at which the spectra were recorded are reported in the legends.

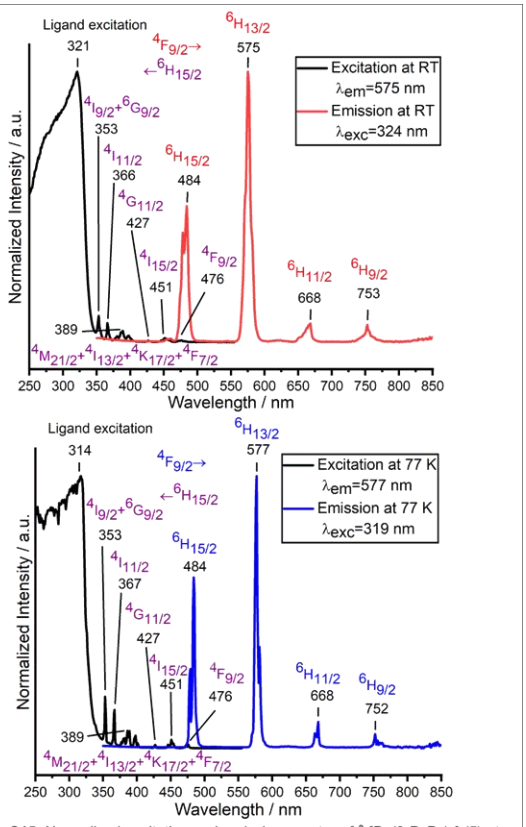

Figure S15. Normalized excitation and emission spectra of ∞[Dy(3-PyPz)$_3$] (**5**) at room temperature (top) and 77K (bottom). Wavelengths at which the spectra were recorded are reported in the legends.

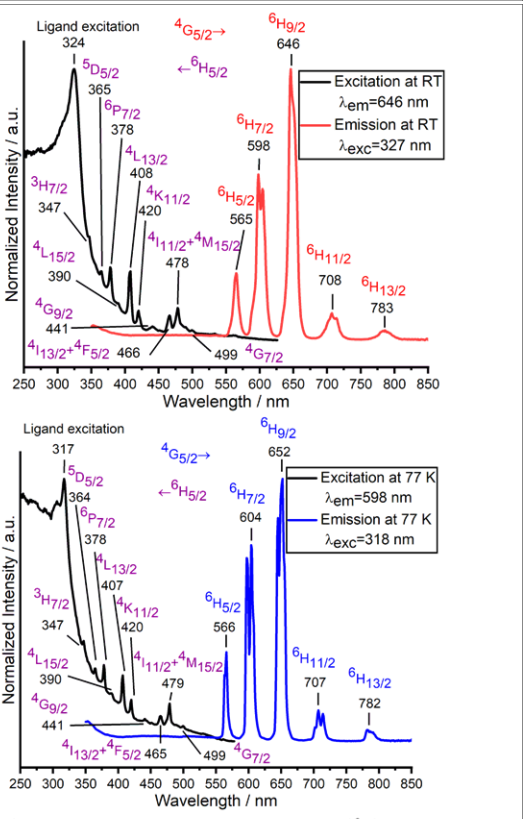

Figure S16. Normalized excitation and emission spectra of ∞[Sm(4-PyPz)$_3$] (**6**) at room temperature (top) and 77K (bottom). Wavelengths at which the spectra were recorded are reported in the legends.

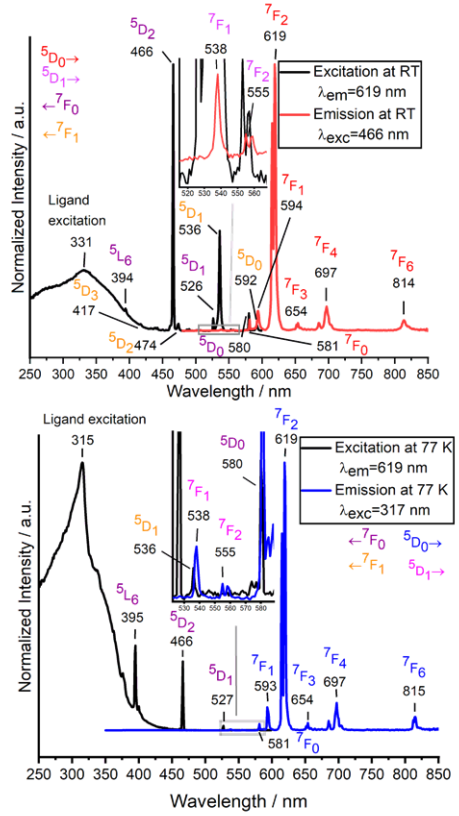

Figure S17. Normalized excitation and emission spectra of ∞[Eu(4-PyPz)$_3$] (**7**) at room temperature (top) and 77K (bottom). Wavelengths at which the spectra were recorded are reported in the legends.

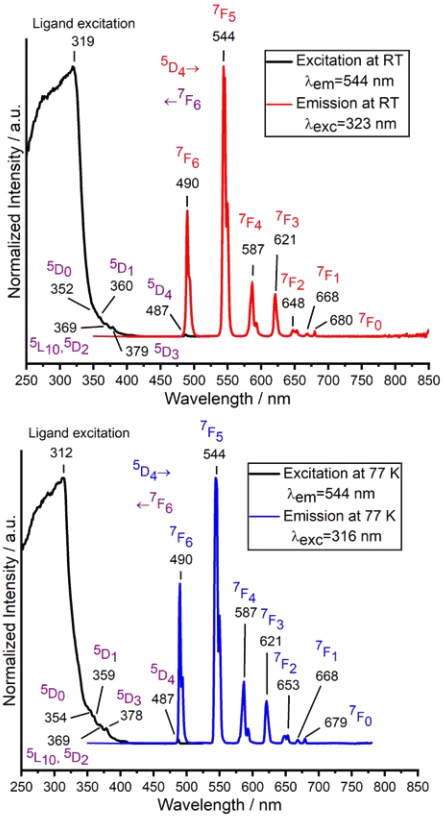

Figure S19. Normalized excitation and emission spectra of ∞[Tb(4-PyPz)$_3$] (**9**) at room temperature (top) and 77K (bottom). Wavelengths at which the spectra were recorded are reported in the legends.

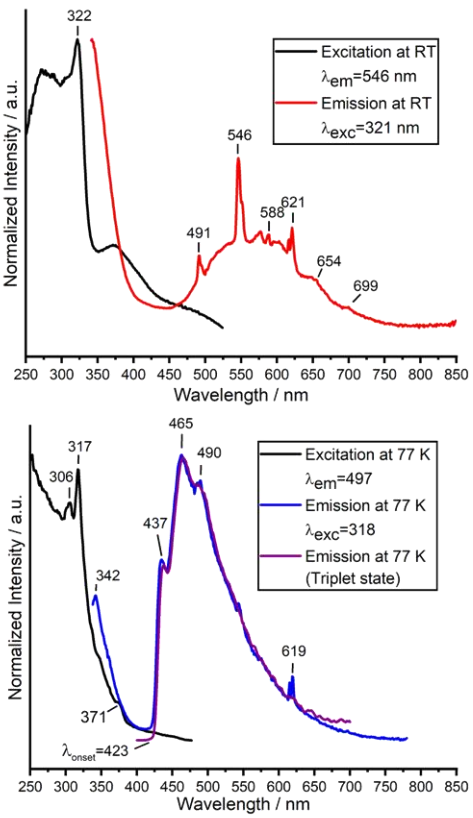

Figure S18. Normalized excitation and emission spectra of ∞[Gd(4-PyPz)$_3$]:Eu^{3+},Tb^{3+} (**8**) at room temperature (top) and 77K (bottom). Wavelengths at which the spectra were recorded are reported in the legends.

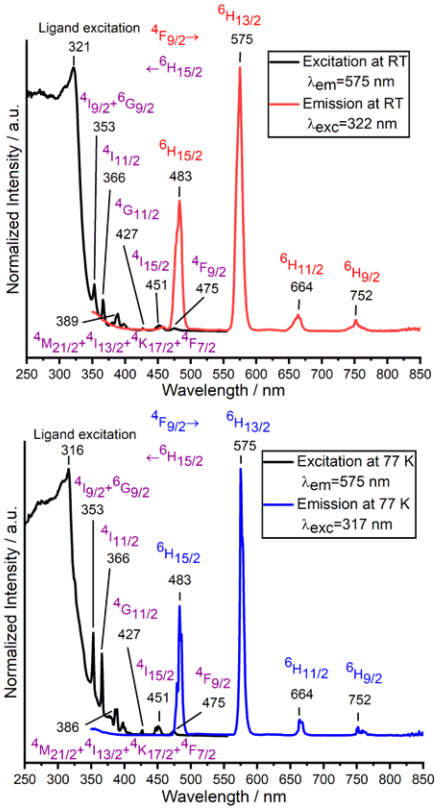

Figure S20. Normalized excitation and emission spectra of ∞[Dy(4-PyPz)$_3$] (**10**) at room temperature (top) and 77K (bottom). Wavelengths at which the spectra were recorded are reported in the legends.

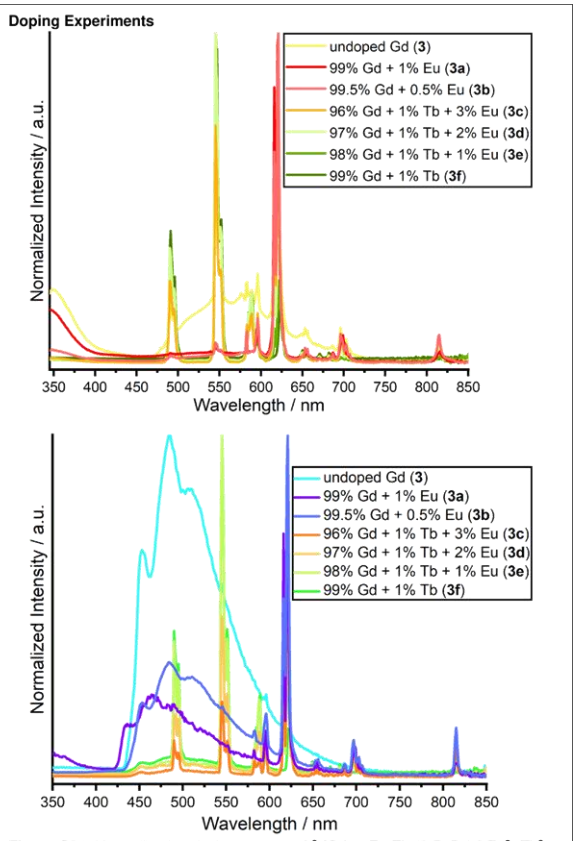

Figure S21. Normalized emission spectra of $^{3}_{\infty}[Gd_{1-x-y}Eu_xTb_y(3\text{-}PyPz)_3]:Eu^{3+},Tb^{3+}$ (**3a-3f**) at room temperature (top) and 77K (bottom), λ_{exc} = 323 nm.

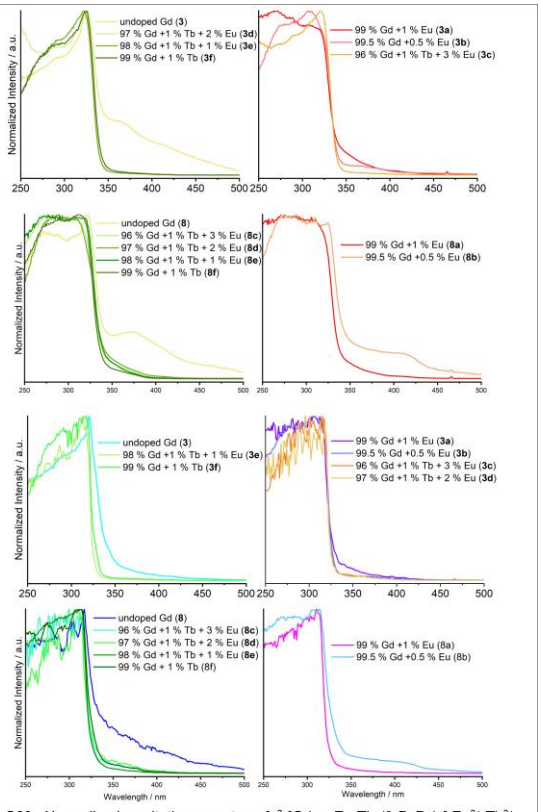

Figure S23. Normalized excitation spectra of $^{3}_{\infty}[Gd_{1-x-y}Eu_xTb_y(3\text{-}PyPz)_3]:Eu^{3+},Tb^{3+}$ (**3a-3f**) and $^{3}_{\infty}[Gd_{1-x-y}Eu_xTb_y(4\text{-}PyPz)_3]:Eu^{3+},Tb^{3+}$ (**8a-8f**) at room temperature (top) and 77K (bottom), λ_{em} = 545 nm (left) and 621 nm (right).

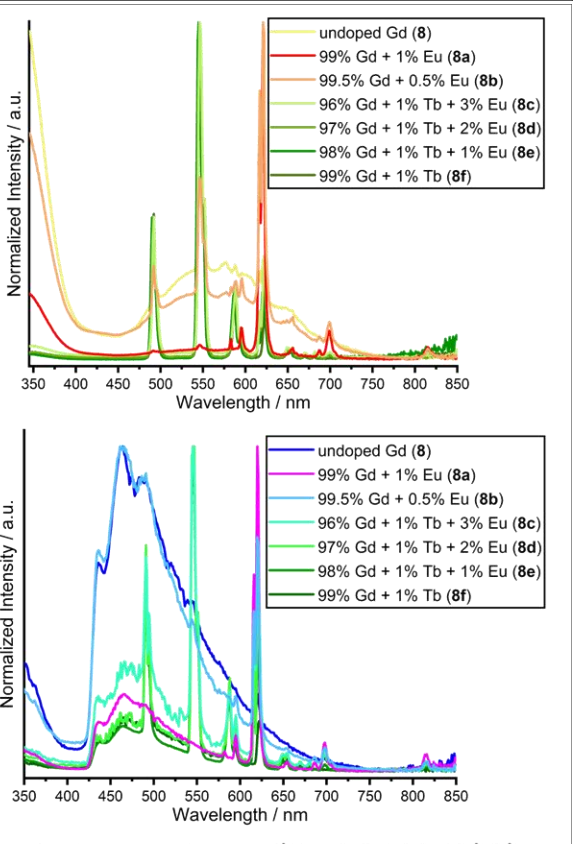

Figure S22. Normalized emission spectra of $^{3}_{\infty}[Gd_{1-x-y}Eu_xTb_y(4\text{-}PyPz)_3]:Eu^{3+},Tb^{3+}$ (**8a-8f**) at room temperature (top) and 77K (bottom), λ_{exc} = 321 nm.

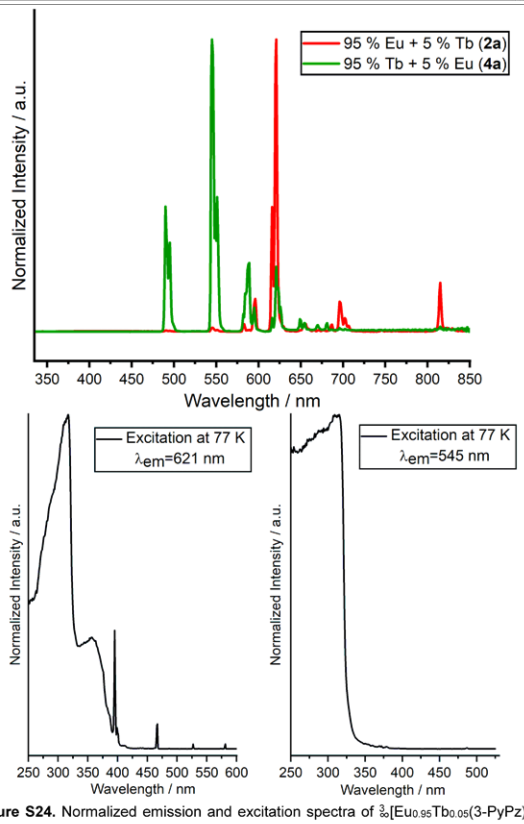

Figure S24. Normalized emission and excitation spectra of $^{3}_{\infty}[Eu_{0.95}Tb_{0.05}(3\text{-}PyPz)_3]$ (**2a**) (excitation spectrum, left, λ_{em} = 621 nm) (emission spectrum, red, top) and $^{3}_{\infty}[Tb_{0.95}Eu_{0.05}(3\text{-}PyPz)_3]$ (**4a**) (excitation spectrum, right, λ_{em} = 545 nm) (emission spectrum, green, top) at 77K. λ_{exc} = 317 nm.

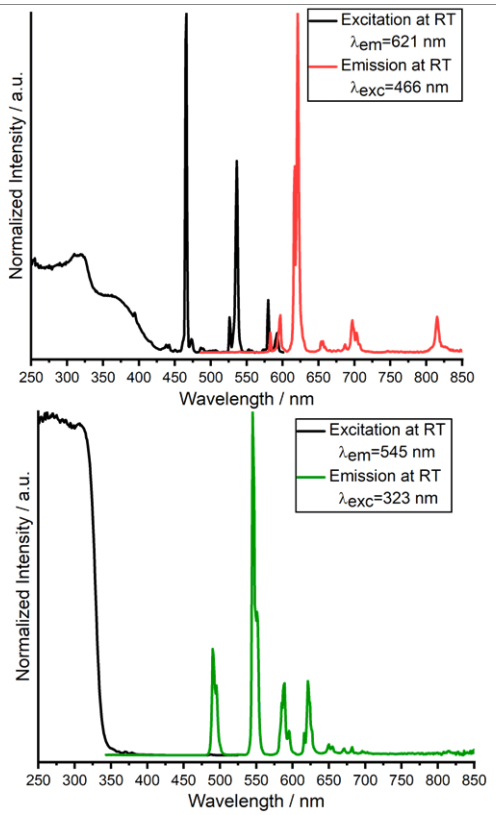

Figure S25. Normalized excitation and emission spectra of ∞[$Eu_{0.95}Tb_{0.05}$(3-PyPz)$_3$] (**2a**) (top) and ∞[$Tb_{0.95}Eu_{0.05}$(3-PyPz)$_3$] (**4a**) (bottom) at RT. Wavelengths at which the spectra were recorded are reported in the legends.

97 % Gd +1 % Tb + 2 % Eu	(**8d**)	0.29766	0.39469
98 % Gd +1 % Tb + 1 % Eu	(**8e**)	0.28393	0.40406
99 % Gd + 1 % Tb	(**8f**)	0.25872	0.40972
95 % Eu + 5 % Tb	(**2a**)	0.6519	0.32552
95 % Tb + 5 % Eu	(**4a**)	0.36027	0.56591

Table S8. Photophysical data of ∞[$Gd_{1-x-y}Eu_xTb_y$(3-PyPz)$_3$]:Eu^{3+},Tb^{3+} (**3a-3f**), ∞[$Gd_{1-x-y}Eu_xTb_y$(4-PyPz)$_3$]:Eu^{3+},Tb^{3+} (**8a - 8f**), ∞[$Eu_{0.95}Tb_{0.05}$(3-PyPz)$_3$] (**2a**) and ∞[$Tb_{0.95}Eu_{0.05}$(3-PyPz)$_3$] (**4a**) in the solid-state at room temperature and 77K.

compound	$\tau^{[a]}$/ms	$\lambda_{ex}/\lambda_{em}$ [nm][b]	$\tau^{[c]}$/ms	$\lambda_{ex}/\lambda_{em}$ [nm][d]
3a	0.516(2)	323/621	0.601(2)	323/621
3b	0.65(1)	323/621	0.880(4)	317/621
3c	0.72(1)	323/621	0.867(3)	317/621
3d	0.41(3)	323/545	0.808(2)	317/621
3e	0.416(8)	323/545	0.950(7)	323/545
3f	0.698(2)	323/545	1.014(3)	323/545
8a	0.661(3)	321/621	0.802(2)	314/621
8b	0.581(3)	321/621	0.73(2)	314/621
8c	0.658(4)	321/545	0.82(1)	314/545
8d	0.58(1)	321/545	0.81(1)	314/545
8e	0.721(2)	321/545	0.939(6)	314/545
8f	0.750(2)	321/545	0.887(5)	314/545
2a	0.518(5)	466/621	0.751(3)	317/621
4a	0.559(2)	323/545	0.751(4)	317/545

[a] Emission lifetimes determined at 298 K. [b] Excitation and emission wavelengths for emission lifetime at 298 K. [c] Emission lifetime determined at 77 K. [d] Excitation and emission wavelengths for emission lifetime at 77 K.

PL Chromaticity

CIE 1931

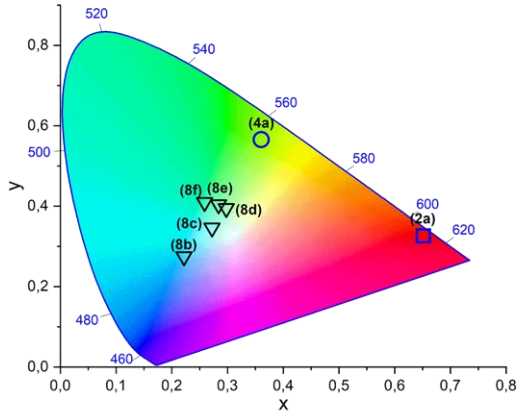

Figure S26. Chromaticity coordinate diagram (CIE 1931) of the emission colors of the series ∞[$Gd_{1-x-y}Eu_xTb_y$(4-PyPz)$_3$]:Eu^{3+},Tb^{3+} (**8b-8f**) (triangle, black), ∞[$Eu_{0.95}Tb_{0.05}$(3-PyPz)$_3$] (**2a**) (square, blue) and ∞[$Tb_{0.95}Eu_{0.05}$(3-PyPz)$_3$] (**4a**) (circles, blue) at 77K.

Table S7. Chromaticity coordinates (x,y) for **3**, **3a-3f, 8, 8a-8f, 2a** and **4a** at 77 K.

compound		CIE, x	CIE, y
∞[Gd(3-PyPz)$_3$]:Eu^{3+},Tb^{3+}	(**3**)	0.23306	0.37899
∞[$Gd_{1-x-y}Eu_xTb_y$(3-PyPz)$_3$]:Eu^{3+},Tb^{3+}			
99 % Gd +1 % Eu	(**3a**)	0.28554	0.28001
99.5 % Gd +0.5 % Eu	(**3b**)	0.30005	0.37495
96 % Gd +1 % Tb + 3 % Eu	(**3c**)	0.48876	0.39854
97 % Gd +1 % Tb + 2 % Eu	(**3d**)	0.42248	0.42079
98 % Gd +1 % Tb + 1 % Eu	(**3e**)	0.35993	0.47752
99 % Gd + 1 % Tb	(**3f**)	0.31242	0.48221
∞[Gd(4-PyPz)$_3$]:Eu^{3+},Tb^{3+}	(**8**)	0.22662	0.29516
∞[$Gd_{1-x-y}Eu_xTb_y$(4-PyPz)$_3$]:Eu^{3+},Tb^{3+}			
99 % Gd +1 % Eu	(**8a**)	0.29287	0.27322
99.5 % Gd +0.5 % Eu	(**8b**)	0.22179	0.2747
96 % Gd +1 % Tb + 3 % Eu	(**8c**)	0.27216	0.34616

Thermal Analysis

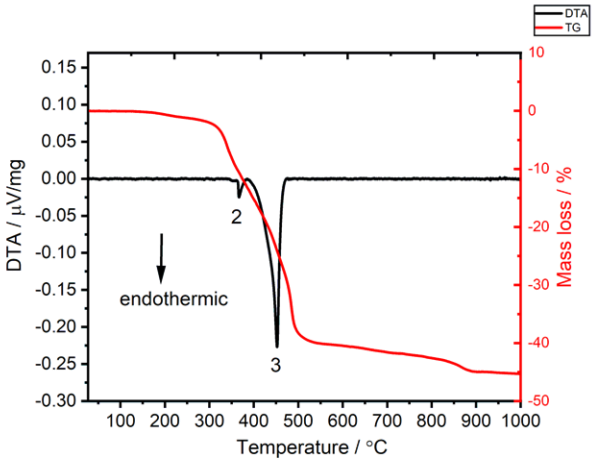

Figure S27. Simultaneous DTA-TG analysis of ∞[Tb(3-PyPz)$_3$] (**4**) representing the group of isostructural compounds (**1-5**). The measurement was performed in a constant argon flow of 50 ml·min^{-1} with a heating rate of 5 K·min^{-1} from room temperature to 1000 °C.

IR Spectroscopy

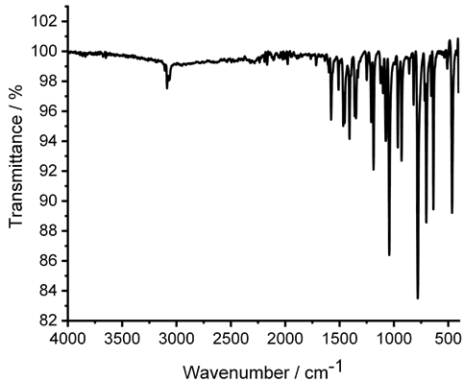

Figure S28. The infrared spectrum (ATR) of coordination polymer $^{3}_{\infty}$[Sm(3-PyPz)$_3$] (**1**).

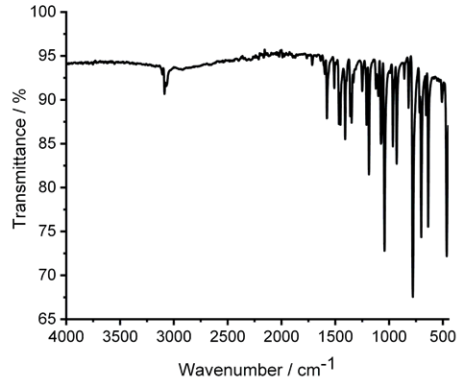

Figure S29. The infrared spectrum (ATR) of coordination polymer $^{3}_{\infty}$[Eu(3-PyPz)$_3$] (**2**).

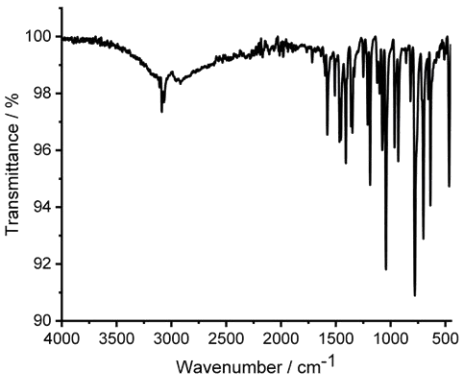

Figure S30. The infrared spectrum (ATR) of coordination polymer $^{3}_{\infty}$[Gd(3-PyPz)$_3$]:Eu^{3+},Tb^{3+} (**3**).

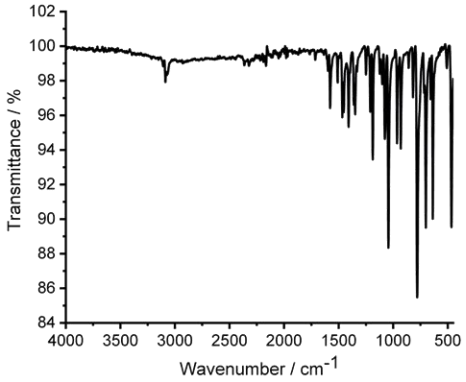

Figure S31. The infrared spectrum (ATR) of coordination polymer $^{3}_{\infty}$[Tb(3-PyPz)$_3$] (**4**).

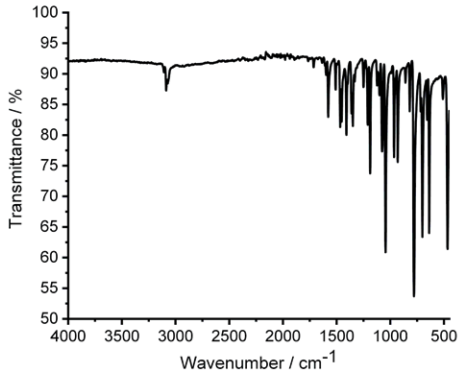

Figure S32. The infrared spectrum (ATR) of coordination polymer $^{3}_{\infty}$[Dy(3-PyPz)$_3$] (**5**).

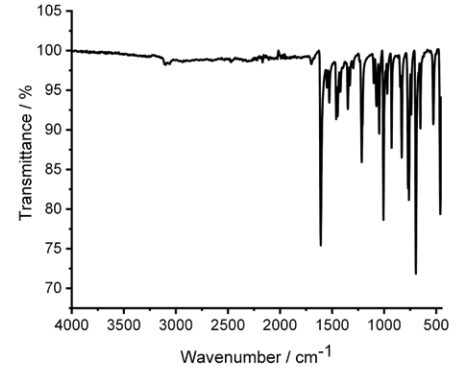

Figure S33. The infrared spectrum (ATR) of coordination polymer $^{3}_{\infty}$[Sm(4-PyPz)$_3$] (**6**).

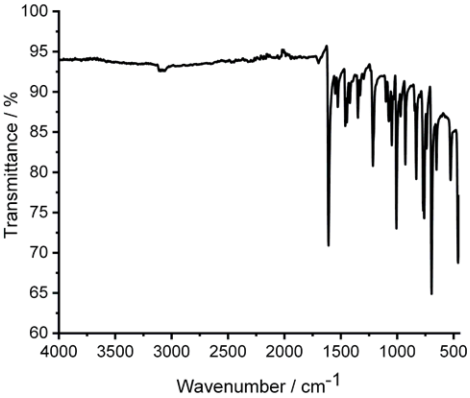

Figure S34. The infrared spectrum (ATR) of coordination polymer $^{3}_{\infty}$[Eu(4-PyPz)$_3$] (**7**).

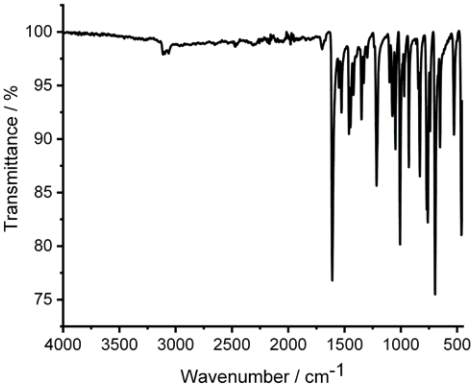

Figure S35. The infrared spectrum (ATR) of coordination polymer $^{3}_{\infty}$[Gd(4-PyPz)$_3$]:Eu^{3+},Tb^{3+} (**8**).

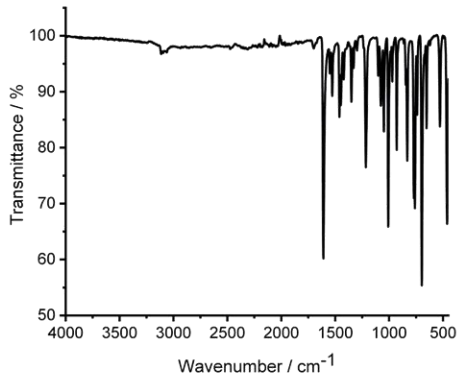

Figure S36. The infrared spectrum (ATR) of coordination polymer $^{3}_{\infty}$[Tb(4-PyPz)$_3$] (**9**).

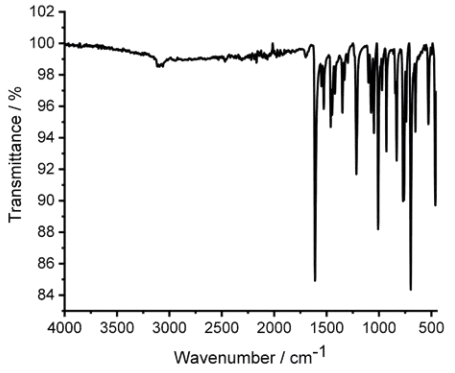

Figure S37. The infrared spectrum (ATR) of coordination polymer $^{3}_{\infty}$[Dy(4-PyPz)$_3$] (**10**).

Experimental Section

CHN Analysis: Carbon, hydrogen, and nitrogen elemental analyses were executed using a Thermo Scientific Flash EA – 1112. The polymers were placed in a tin crucible with no less than one mass equivalent to V_2O_5. Specimens were made ready and stored under inert conditions till the time of the measurements. Coordination polymers **6** - **10** were heated in advance under vacuum (p = 1.0×10^{-3} mbar) for further drying.

Single Crystal X-ray Diffraction (SCXRD): Single-crystal X-ray measurements of $^{3}_{\infty}$[Tb(3-PyPz)$_3$] (**4**), and $^{3}_{\infty}$[Tb(4-PyPz)$_3$] (**9**) were performed on a BRUKER AXS Smart Apex 1 diffractometer with graphite monochromator (Mo-Kα radiation; λ = 71.073 pm) and a Bruker CRYOFLEX low-temperature system. The Single-crystal X-ray determinations of the other 3D-coordination polymers were carried out on a BRUKER AXS D8 Venture diffractometer equipped with a dual IμS microfocus source, collimating Quazar multilayer mirror, a PHOTON100 detector, and an OXFORD CRYOSYSTEMS 700 low-temperature system. Data indexing for $^{3}_{\infty}$[Tb(3-PyPz)$_3$] (**4**) was done at 200 K conversely the data collection for all the other compounds mounted at 100 K as a result of the cracking behavior of the respective single-crystal upon cooling to 100 K. All structures were solved utilizing direct methods, refined with the least-square method using ShelXL[1] and expanded using Fourier techniques. All non-hydrogen atoms were refined anisotropically. Hydrogen atoms were assigned to idealized geometric positions and inserted in structure factors calculations. For polymers **6-10,** the SQUEEZE[2] algorithm in PLATON[3] was used to include a bulk solvent model in the refinement. Two voids per unit cell were identified with SQUEEZE. The average volume is found to be 132X10^6 pm^3 for each void. The equivalent of 6 electrons for (**6** and **7**), 3 for (**8**), 11 for (**9**), and 10 for (**10**) electrons per unit cell was also identified. Depictions of the crystal structures were generated using DIAMOND.[4] ToposPro program package was used to determine the Topology of the polymers.[5]

Powder X-ray Diffraction (PXRD): Specimens for powder diffraction were firstly ground in a mortar and filled into Lindemann glass capillaries with either 0.5 or 0.3 mm diameter under an inert gas atmosphere and then sealed. Diffraction data were collected on an STOE STADI P diffractometer with a focusing Ge(111) monochromator and a Dectris MYTHEN 1K strip detector in Debye-Scherrer geometry using CuKα radiation (λ =154.056 pm). Data collection was done using the STOE Powder Diffraction Software Package WinX^{POW} and Pawley fits on the data were performed using TOPAS Academic.[6] The peak shapes were described with the Thompson-Cox-Hastings pseudo-Voigt function, absorption was estimated by composition and the axial divergence was approximated using the simple axial model.

Vibrational Spectroscopy: MIR spectra were recorded from several milligrams of the compounds with an ALPHA FT-IR spectrometer from Bruker optics (ATR module) using OPUS software. Figures S26-S35 in the Supporting Information contain the IR spectra of the products.

Photoluminescence Spectroscopy: The excitation and emission spectra were recorded for ground solid samples after filling them in quartz glass tubes under argon. The measurements were performed at room temperature as well as 77 K (latter using the liquid nitrogen-filled assembly FL-1013 of HORIBA) with a HORIBA Jobin Yvon

Spex Fluorolog 3 spectrometer equipped with a 450 W Xe short-arc lamp (USHIO), double-grated excitation, and emission monochromators, and a photomultiplier tube (R928P) using the FluoroEssence™ software. Excitation and emission spectra were corrected for the spectral response of the monochromators and the detector using spectral corrections provided by the constructor. Besides, a photodiode reference detector was used to correct the excitation spectra for the spectral distribution of the lamp intensity. When required, the collection of the data was performed using an edge filter. Emission spectra with gating were recorded using a xenon flashlamp with a pulse repetition rate of 41 ms.

Photoluminescence quantum yields were determined with the above-mentioned HORIBA Jobin Yvon Spex Fluorolog 3 spectrometer equipped with a HORIBA Quanta–ϕ Integrating Sphere. For the measurements, solid samples were filled into Starna Micro Cell cuvettes 18-F/ST/C/Q/10 (fluorescence with ST/C closed-cap, material UV quartz glass Spectrosil Q, pathlength 10 mm, matched). Dry barium sulfate was used as reference material. Each sample was measured at least three times and the quantum yield values with standard deviation were evaluated afterward. Quanta–ϕ Integrating Sphere was checked with a standard (sodium salicylate as a powder, λ_{ex} = 340 nm, λ_{em} = 365-600 nm, measured QY = 52 %, in the literature: 53 %).[7]

Photoluminescence overall decay process times were determined using the above-mentioned HORIBA Jobin Yvon Spex Fluorolog 3 spectrometer equipped with a dual lamp housing (FL-1040A), a UV xenon flashlamp (Exelitas FX-1102), and a TCSPC (time-correlated single-photon counting) upgrade, or picosecond pulsed laser diode. Emission decays were recorded using DataStation software. Exponential tail fitting was used for the calculation of resulting intensity decay using Decay Analysis Software 6. The quality of the fit was confirmed by χ^2 values being below 1.2.

Thermal properties: were determined by simultaneous DTA/TG (NETZSCH STA 409-PC) coupled with a mass-spectrometer (NETZSCH QMS 403 Aëolos) in a constant argon flow of 50 ml·min^{-1} with a heating rate of 5 K/min from room temperature to 1000 °C for $^{3}_{\infty}$[Tb(3-PyPz)$_3$] (**4**), and $^{3}_{\infty}$[Tb(4-PyPz)$_3$] (**9**). DTA curve was baseline corrected after the measurement using Origin™ software.

Synthesis and Analytical Data

General Information: All syntheses with the participation of lanthanides were performed under argon or using vacuum line, gloveboxes (MBraun Labmaster SP, Innovative Technology PureLab), Schlenk tubes, and Duran® glass ampoules (outer ⌀ 10 mm, wall thickness 1.5 mm). Pyridine, dichloromethane, and cyclohexane were purified by distillation and dried by standard procedures or used from the solvent purification system SPS-800 by MBraun (Garching, Germany). Durene was purchased from J&K Scientific GMBH then was sublimed under dynamic vacuum (p = 1.0×10^{-3} mbar) for further drying and purification process. The bulk materials were characterized by powder X-ray diffraction (PXRD) as well as CHN analysis.

Starting Materials: 3-(3-pyridyl)pyrazole / 3-(1H-pyrazol-3-yl)pyridine (3-PyPzH) and 3-(4-pyridyl)pyrazole / 4-(1H-pyrazol-3-yl)pyridine (4-PyPzH) were synthesized as reported in the literature.[8] The lanthanide metals (gadolinium: 99.95 %, Smart

Element; rest: >99 %, Chempur) were purchased and used as received, as well as Hg (> 99.9 %, Alfa Aesar) used for activation.

Synthesis of (1*H*-pyrazol-3-yl)pyridines, the general method

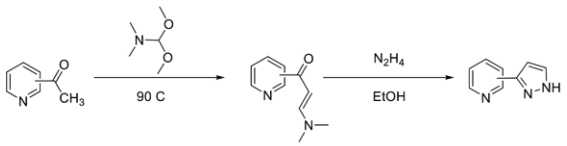

A mixture of acetylpyridine (15g, 124 mmol) and DMF-DMA (30mL, 26.9g, 225 mmol) was stirred at 90 °C on an oil bath. MeOH was removed via a short Vigreux column (10 cm) connected to a descending condenser. The reaction was stopped once the distillation of MeOH ceased (7-8 h) and the mixture was cooled to room temperature overnight. Afterward, 30 mL of hexane was added and the resulting suspension was stirred for 30 min and subsequently filtered. The obtained solid was washed with 2 portions of hexane (each of 40 mL) in case of the product from 2-acetylpyridine, or successively by 30 mL of hexane/Et$_2$O (50:50 by volume) mixture and 20 mL of Et$_2$O (for 3-pyridil isomer) or by 30 mL of a mixture of hexane/EtOAc (3:1 by volume) for 4-pyridil isomer. All solids were dried in air to a constant weight and were used without further purification. The products are darkening in the air at ambient temperature and should be used shortly after preparation or kept in a freezer at -18 °C.

(E/Z)-3-(dimethylamino)-1-(pyridin-3-yl)prop-2-en-1-one. Brown solid, Yield was 19.4 g (88%).

(E/Z)-3-(dimethylamino)-1-(pyridin-4-yl)prop-2-en-1-one. Brown crystals, Yield was 17.1 g (78%).

To a stirred warm (40°C) solution of 19.3 g (110 mmol) of the corresponding enaminoketone in 150 mL of 96% ethanol N_2H_4*H_2O (100 %, 8 mL, 160 mmol) was added in one portion and the resulted mixture was refluxed for 6 h with gentle stirring and then cooled to a room temperature. Further separation of (1H-pyrazol-3-yl)pyridines was varied for different isomers.

3-(1*H*-pyrazol-3-yl)pyridine / 3-(3-pyridyl)pyrazole (3-PyPzH)

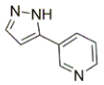

The cooled reaction mixture was evaporated to dryness under diminished pressure, the resulting solid was dissolved in 150 ml of CH_2Cl_2. The organic solution was washed with brine (30 mL), dried over $MgSO_4$, and evaporated to dryness. The resulted oil was dried at 45°C and 0.1 torr for 4 h until a solid crystalline mass was formed. The yield

was 14.2 g (89%). The compound is hygroscopic and deliquescing in the air. M.p. 54-55 °C (lit. 56-58°C).

^{1}H NMR (300 MHz, $CDCl_3$): δ = 10.39 (*br*, *s*, 1H), 9.08 (*m*, 1H), 8.61 (*dd*, *J* = 4.9 Hz, *J* =1.1 Hz, 1H), 8.12 (*d*, *J* = 7.7 Hz, 1H), 7.68 (*d*, *J* = 2.5 Hz, 1H), 7.34 (*m*, 1H), 6.70 (*d*, *J* = 2.4 Hz, 1H) ppm.

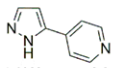

4-(1*H*-pyrazol-3-yl)pyridine / 3-(4-pyridyl)pyrazole (4-PyPzH)

The cooled reaction mixture was evaporated to dryness under diminished pressure. The resulting solid was dissolved in 500 mL of $CHCl_3$. The organic solution was washed by 20 mL of brine, dried over $MgSO_4$, and evaporated to dryness. The resulting solid was suspended in 20 mL of hexane, filtered and crystals were dried in air. The yield is 12.9 g (81%) of yellow solid. M.p. 155-157 °C (lit. 157-158°C).

^{1}H NMR (300 MHz, $CDCl_3$): δ = 11.5-11.0 (*br*, *s*, 1H), 8.65 (*dd*, *J* = 4.7 Hz, *J* = 1.7 Hz, 2H), 7.75 (*dd*, *J* = 4.6 Hz, *J* = 1.7 Hz, 2H), 7.70 (*d*, *J* = 2.5 Hz, 1H), 6.71 (*d*, *J* = 2.5 Hz, 1H) ppm.

Synthesis of $^3_\infty$[Sm(3-PyPz)$_3$] (1): Sm metal (0.09 mmol) and 3-PyPzH ($C_8H_7N_3$, 0.35 mmol) were mixed with pyridine (C_5H_5N, 0.3 mL). The reaction mixture was sealed in an evacuated Duran® glass ampule under reduced pressure (p = 1.0×10^{-3} mbar). Before applying a vacuum to the ampoule as well as for sealing of the ampoule, the solvent was frozen using liquid nitrogen. The ampoule was heated to 200 °C in 24 h and maintained at this temperature for 72 h. Afterward, the reaction mixture was cooled to room temperature for 48 h. Excess Sm metal was not observed, and the excess ligand was removed by sublimation in a temperature gradient from 80 °C to RT. Suitable cubic single-crystals were selected for a single-crystal X-ray diffraction (SCXRD) measurement. $C_{24}H_{18}N_9Sm$ (582.82 g·mol^{-1}): C 49.14 (calcd. 49.46); H 3.13 (3.11); N 21.32 (21.63) %. Yield: 43 mg (85 %). **FT-IR** (ATR): $\tilde{\nu}$ = 3087(w), 2167 (w), 1977 (w), 1597 (w), 1578 (m), 1509 (w), 1466 (m), 1453 (m), 1409 (m), 1361 (m), 1348 (m), 1250 (w), 1209 (m), 1187 (s), 1123 (w), 1100 (w), 1075 (m), 1042 (s), 964 (m), 930 (m), 859 (w), 819 (m), 780 (s), 717 (w), 702 (s), 657 (w), 637 (s), 509 (w), 465 (s) cm^{-1}.

Synthesis of $^3_\infty$[Eu(3-PyPz)$_3$] (2): The preparation was done as described for (**1**) but freshly-filed Eu metal (0.08 mmol) was added to 3-PyPzH ($C_8H_7N_3$, 0.31 mmol) together in 0.1 mL pyridine. The temperature of the ampoule was raised to 200 °C in 1 h and maintained at this temperature for 96 h. Then, the ampoule was cooled to room temperature for 72 h. Colorless crystals were obtained while the solution became red, which could be an indication of a complex formation where pyridine being coordinated. Excess Eu metal was not observed. Suitable cubic single-crystals were selected out for a SCXRD measurement. $C_{24}H_{18}N_9Eu$ (584.42 g·mol^{-1}): C 49.04 (calcd. 49.32); H 3.19 (3.10); N 21.30 (21.57) %. Yield: 43 mg (85 %). **FT-IR** (ATR): $\tilde{\nu}$ = 3087 (w), 1715 (w), 1598 (w), 1578 (w), 1509 (w), 1466 (w), 1453 (w), 1408 (w), 1361 (w),

1348 (w), 1249 (w), 1209 (w), 1187 (m), 1075 (m), 1043 (s), 965 (m), 930 (m), 779 (s), 717 (w), 702 (s), 657 (w), 637 (s), 509 (w), 465 (s) cm^{-1}.

Synthesis of $^3_\infty$[Eu$_{0.95}$Tb$_{0.05}$(3-PyPz)$_3$] (2a): a ratio of 5 % Tb was ground together with freshly filed Eu to gain the best homogeneity. The reaction was performed as described in **2** with further raising the heating temperature to 230 °C within 1 day.

Synthesis of $^3_\infty$[Gd(3-PyPz)$_3$]:Eu^{3+},Tb^{3+} (3): Same preparation as (**1**) but Gd metal (0.08 mmol) and 3-PyPzH ($C_8H_7N_3$, 0.29 mmol) in 0.3 mL pyridine were used. The mixture was heated to 220 °C in 2 h then to 230 °C in 30 h. This temperature was maintained for 48 h. Later, it was cooled to room temperature in 48 h. Suitable cubic single-crystals were selected for a SCXRD measurement. Unknown low amounts of Eu and Tb were detected by PL-spectroscopy, which was not added to the reaction but is a result of low impurities accompanied with the metal source. $C_{24}H_{18}N_9Gd$ (589.71 g·mol^{-1}): C 47.93 (calcd. 48.88); H 2.90 (3.08); N 20.69 (21.38) %. Yield: 48.7 mg (86 %). **FT-IR** (ATR): $\tilde{\nu}$ = 3087 (w), 2168 (w), 1980 (w), 1598 (w), 1578 (m), 1509 (w), 1466 (m), 1453 (m), 1409 (m), 1361 (m), 1349 (m), 1249 (w), 1210 (m), 1187 (s), 1123 (w), 1100 (w), 1076 (m), 1043 (s), 964 (m), 931 (m), 819 (w), 779 (s), 701 (s), 657 (w), 637 (s), 511 (w), 466 (s) cm^{-1}.

Synthesis of $^3_\infty$[Gd$_{1-x-y}$Eu$_x$Tb$_y$(3-PyPz)$_3$]:Eu^{3+},Tb^{3+} (3a-3f): Six ratios were synthesized with 1 % Eu (**3a**), 0.5 % Eu (**3b**), 1 % Tb with 3 % Eu (**3c**), 1 % Tb with 2 % Eu (**3d**), 1 % Tb with 1 % Eu (**3e**) and 1 % Tb (**3f**). The required amounts of the freshly filed metals (0.08 mmol) were mixed and ground in a mortar to acquire the best homogeneity. The reactions were carried out as described in **3** with the same heating conditions after adding 0.1 ml of pyridine.

Synthesis of $^3_\infty$[Tb(3-PyPz)$_3$] (4): The preparation was done as described for (**1**) but freshly-filed Tb metal (0.08 mmol), 3-PyPzH ($C_8H_7N_3$, 0.29 mmol), and catalytic amount of Hg (0.1 mmol) were mixed in 0.3 mL pyridine. The ampule was heated to 230 °C in 48 h and kept at this temperature for 96 h. The ampoule was allowed to cool down to room temperature in 72 h giving cubic single-crystals. $C_{24}H_{18}N_9Tb$ (591.401 g·mol^{-1}): C 49.04 (calcd. 48.74); H 3.19 (3.07); N 21.30 (21.32) %. Yield: 45.5 mg (91 %). **FT-IR** (ATR): $\tilde{\nu}$ = 3087 (w), 2166 (w), 1968 (w), 1598 (w), 1578 (m), 1509 (w), 1466 (m), 1453 (m), 1409 (m), 1361 (m), 1349 (m), 1249 (w), 1210 (m), 1187 (s), 1123 (w), 1101 (w), 1077 (m), 1044 (s), 965 (m), 931 (m), 819 (w), 780 (s), 701 (s), 657 (w), 637 (s), 509 (w), 467 (s) cm^{-1}.

Synthesis of $^3_\infty$[Tb$_{0.95}$Eu$_{0.05}$(3-PyPz)$_3$] (4a): a ratio of 5 % Eu was ground together with freshly filed Tb to earn the top homogeneity. The reaction was performed as described in **4** by adding 0.1 mL pyridine.

Synthesis of $^3_\infty$[Dy(3-PyPz)$_3$] (5): The preparation was performed similar to (**1**) but Dy metal (0.08 mmol), 3-PyPzH ($C_8H_7N_3$, 0.29 mmol) and Hg (0.1 mmol) were mixed in 0.3 mL pyridine. The heating program was similar to compound **4** giving colorless cubic crystals together with Hg. $C_{24}H_{18}N_9Dy$ (594.96 g·mol^{-1}): C 47.75 (calcd. 48.45); H 2.81 (3.05); N 20.54 (21.19) %. Yield: Dy, 47.6 (84%). **FT-IR** (ATR): $\tilde{\nu}$ = 3088 (w), 1714 (w), 1598 (w), 1578 (w), 1509 (w), 1466 (m), 1453 (m), 1409 (m), 1361 (w), 1349

(m), 1249 (w), 1210 (m), 1187 (m), 1076 (m), 1044 (s), 965 (m), 931 (m), 859 (w), 819 (w), 779 (s), 717 (w), 701 (s), 637 (s), 510 (w), 467 (s) cm^{-1}.

Synthesis of $^3_\infty$[Sm(4-PyPz)$_3$] (6): A mixture of Sm metal (0.11 mmol) and 4-PyPzH ($C_8H_7N_3$, 0.42 mmol), in 0.3 mL pyridine in the presence of a catalytic amount of Hg (0.1 mmol) were sealed in an evacuated DURAN glass ampule. Before applying a vacuum to the ampoule as well as for sealing the ampoule, the solvent was frozen using liquid nitrogen. The oven was heated to 180 °C in 24 h. Afterward, the temperature was raised to 230 °C in 48 h. The temperature was held for 96 h and then lowered to 25 °C in another 48 h. Except for an excess of the ligand and the activating Hg, the reaction was complete, resulting in highly reflective colorless crystals. The excess ligand was washed with a mixture of dichloromethane and cyclohexane (1:0.2 mL). $C_{24}H_{18}N_9Sm$ (582.82 g·mol^{-1}): C 49.06 (calcd. 49.46); H 3.16 (3.11) %N 21.34 (21.63) %. Yield: 64 mg (95 %). **FT-IR** (ATR): $\tilde{\nu}$ = 3098 (w), 1699 (w), 1609 (s), 1550 (w), 1527 (m), 1461 (m), 1447 (m), 1421 (w), 1349 (m), 1329 (w), 1216 (s), 1100 (w), 1075 (w), 1048 (m), 1007 (s), 970 (w), 929 (m), 846 (w), 832 (m), 771 (s), 762 (s), 740 (m), 696 (s), 652 (m), 528 (m), 461 (s) cm^{-1}.

Synthesis of$^3_\infty$[Eu(4-PyPz)$_3$] (7): The preparation was similar to compound **(6)** using freshly filed Eu metal (0.11 mmol) and 4-PyPzH ($C_8H_7N_3$, 0.42 mmol) in durene ($C_{10}H_{14}$, 0.74 mmol). The ampule was heated to 270 °C in 1 h then 290 °C in 20 h. The temperature was held for 24 h and then lowered to 25 °C in another 3 h. Colorless single crystal was separated. The durene was sublimed in a temperature gradient from 85 °C to RT under reduced pressure (p = 1×10^{-3} mbar). $C_{24}H_{18}N_9Eu$ (584.42 g·mol^{-1}): C 49.32 (calcd. 49.32); H 4.08 (3.10); N 22.50 (21.57) %. Yield: Eu, 40 mg (80 %). **FT-IR** (ATR): $\tilde{\nu}$ = 3096 (w), 1698 (w), 1609 (s), 1550 (w), 1527 (w), 1460 (m), 1447 (m), 1420 (w), 1349 (m), 1329 (w), 1216 (s), 1100 (w), 1075 (w), 1048 (m), 1008 (s), 970 (w), 928 (m), 832 (s), 771 (m), 761 (m), 740 (w), 696 (s), 652 (m), 527 (m), 461 (m) cm^{-1}.

Synthesis of $^3_\infty$[Gd(4-PyPz)$_3$]:Eu^{3+},Tb^{3+} (8): The preparation follows the same procedure as compound **(6)** but mixture of Gd metal (0.10 mmol) and 4-PyPzH ($C_8H_7N_3$, 0.37 mmol) in 0.3 mL and pyridine (C_5H_5N, 0.3 mL) was used. Highly reflective colorless single-crystal of the product was selected for a SCXRD measurement. Unknown low amounts of Eu and Tb were detected by PL-spectroscopy, which was not added to the reaction but is a result of low impurities accompanied with the metal source. $C_{24}H_{18}N_9Gd$ (589.71 g·mol^{-1}): C 47.98 (calcd. 48.88); H 3.00 (3.08); N 21.30 (21.38) %. Yield: Gd, 62 mg (82 %). **FT-IR** (ATR): $\tilde{\nu}$ = 3112 (w), 1980 (w), 1699 (w), 1610 (s), 1550 (w), 1527 (m), 1461 (m), 1448 (m), 1421 (w), 1349 (m), 1330 (w), 1298 (w), 1216 (s), 1101 (m), 1075 (w), 1049 (m), 1008 (s), 971 (w), 929 (s), 846 (w), 832 (s), 771 (s), 761 (s), 740 (m), 696 (s), 652 (m), 528 (m), 461 (s) cm^{-1}.

Synthesis of $^3_\infty$[Gd$_{1-x-y}$Eu$_x$Tb$_y$(4-PyPz)$_3$]:Eu^{3+},Tb^{3+} (8a-8f): By mixing and grinding Gd metal in a mortar with 1 % Eu (**8a**), 0.5 % Eu (**8b**), 1 % Tb with 3 % Eu (**8c**), 1 % Tb with 2 % Eu (**8d**), 1 % Tb with 1 % Eu (**8e**) and 1 % Tb (**8f**) to synthesize six co-doped samples differ in the Ln-content. 0.10 mmol of the mixture was taken in an Ampule where the reaction was carried out as described in **8** with the same heating conditions.

Synthesis of $^3_\infty$[Tb(4-PyPz)$_3$] (9): A freshly filed Tb metal (0.08 mmol) and 4-PyPzH ($C_8H_7N_3$, 0.29 mmol), in pyridine (C_5H_5N, 0.2 mL) together with a catalytic amount of Hg (0.1 mmol), were treated similar to compound **(6)**. The oven was heated to 200 °C in 72 h, held for 72 h and then lowered to 25 °C in another 72 h giving colorless single-crystals suitable for a SCXRD measurement. $C_{24}H_{18}N_9Tb$ (591.401 g·mol^{-1}): C 49.72 (calcd. 48.74); H 3.17 (3.07); N 21.88 (21.32) %. Yield: 42.5 mg (85 %). **FT-IR** (ATR): $\tilde{\nu}$ = 3114 (w), 2052 (w), 1699 (w), 1610 (s), 1550 (w), 1527 (m), 1461 (m), 1448 (m), 1421 (w), 1350 (m), 1330 (w), 1298 (w), 1216 (s), 1101 (w), 1076 (m), 1049 (m), 1008 (s), 971 (w), 930 (s), 846 (w), 832 (s), 771 (s), 761 (s), 740 (m), 697 (s), 653 (m), 529 (m), 462 (s) cm^{-1}.

Synthesis of $^3_\infty$[Dy(4-PyPz)$_3$] (10): The preparation is similar to compound **6**, but Dy metal (0.10 mmol) and 4-PyPzH ($C_8H_7N_3$, 0.38 mmol) were used giving colorless single-crystals. $C_{24}H_{18}N_9Dy$ (594.96 g·mol^{-1}): C 47.63 (calcd. 48.45); H 2.90 (3.05); N 20.69 (21.19) %. Yield: Dy, 60.4 mg (96%). **FT-IR** (ATR): $\tilde{\nu}$ = 3095 (w), 2169 (w), 1977 (w), 1699 (w), 1611 (s), 1550 (w), 1527 (m), 1461 (m), 1448 (m), 1421 (w), 1349 (m), 1329 (w), 1298 (w), 1216 (s), 1101 (w), 1076 (m), 1049 (m), 1008 (s), 971 (w), 930 (s), 845 (w), 832 (s), 771 (s), 761 (s), 740 (m), 697 (s), 653 (m), 529 (m), 462 (s) cm^{-1}.

References

[1] a) G. M. Sheldrick, *Acta Crystallogr., Sect. A: Found. Adv.* **2015**, *71*, 3-8; b) G. M. Sheldrick, *Acta Crystallogr., Sect. C: Struct. Chem.* **2015**, *71*, 3-8; c) G. M. Sheldrick, *Acta Crystallogr., Sect. A: Found. Crystallogr.* **2008**, *64*, 112-122.
[2] A. L. Spek, *Acta Crystallogr., Sect. C: Struct. Chem.* **2015**, *71*, 9-18.
[3] a) A. L. Spek, *Acta Crystallogr., Sect. D: Biol. Crystallogr.* **2009**, *65*, 148-155; b) A. L. Spek, *Inorg. Chim. Acta* **2018**, *470*, 232-237; c) A. L. Spek, *Acta Crystallogr. Sect. E: Crystallogr. Commun.* **2020**, *76*, 1-11; d) A. Spek, *J. Appl. Crystallogr.* **2003**, *36*, 7-11.
[4] W. T. Pennington, *J. Appl. Crystallogr.* **1999**, *32*, 1028-1029.
[5] V. A. Blatov, A. P. Shevchenko, D. M. Proserpio, *Cryst. Growth Des.* **2014**, *14*, 3576-3586.
[6] A. A. Coelho, *J. Appl. Crystallogr.* **2018**, *51*, 210-218.
[7] M. S. Wrighton, D. S. Ginley, D. L. Morse, *J. Phys. Chem.* **1974**, *78*, 2229-2233.
[8] a) M. R. Del Giudice, C. Mustazza, A. Borioni, F. Gatta, K. Tayebati, F. Amenta, P. Tucci, S. Pieretti, *Arch. Pharm. Pharm. Med. Chem.* **2003**, *336*, 143-154; b) V. J. Bauer, H. P. Dalalian, W. J. Fanshawe, S. Safir, E. Tocus, C. Boshart, *J. Med. Chem.* **1968**, *11*, 981-984.

3.1.2. Divalent europium, NIR and variable emission of trivalent Tm, Ho, Pr, Er, Nd, and Ce in 3D-frameworks and 2D-networks of Ln-pyridylpyrazolates

This article has been published in the

Journal Chemistry

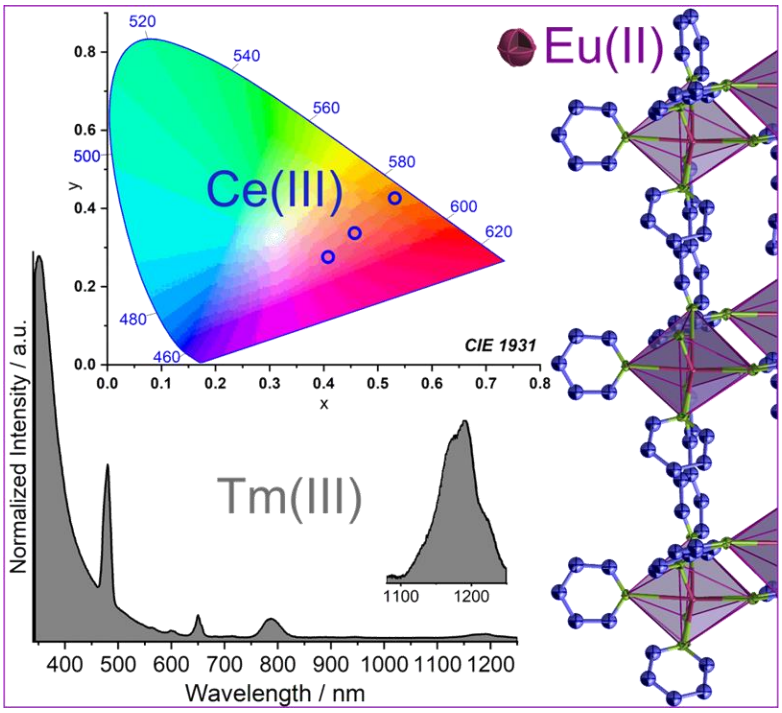

Heba Youssef, Jonathan Becker, Clemens Pietzonka, Ilya V. Taydakov, Florian Kraus, and Klaus Müller-Buschbaum

Reprinted with permission from *Chemistry* **2023**, *5*, 1006–1027.

DOI 10.3390/chemistry5020069

chemistry

MDPI

Article

Divalent Europium, NIR and Variable Emission of Trivalent Tm, Ho, Pr, Er, Nd, and Ce in 3D Frameworks and 2D Networks of Ln–Pyridylpyrazolates

Heba Youssef [1,2], Jonathan Becker [1], Clemens Pietzonka [3], Ilya V. Taydakov [4,5], Florian Kraus [3] and Klaus Müller-Buschbaum [1,6,*]

[1] Institute of Inorganic and Analytical Chemistry, Justus-Liebig-University Giessen, Heinrich-Buff-Ring 17, 35392 Giessen, Germany; heba.youssef@anorg.chemie.uni-giessen.de (H.Y.)
[2] Department of Chemistry, Faculty of Science, Mansoura University, El Gomhouria, Mansoura Qism 2, Dakahlia Governorate, Mansoura 11432, Egypt
[3] Fachbereich Chemie, Philipps-University Marburg, Hans-Meerwein-Straße, 35032 Marburg, Germany
[4] Lebedev Physical Institute of the Russian Academy of Sciences, Leninskiy pr-t, 53, 119991 Moscow, Russia
[5] Basic Department of Chemistry of Innovative Materials and Technologies, G.V. Plekhanov Russian University of Economics, Stremyanny Per. 36, 117997 Moscow, Russia
[6] Center of Materials Research (LAMA), Justus-Liebig-University Giessen, Heinrich-Buff-Ring 16, 35392 Giessen, Germany
* Correspondence: klaus.mueller-buschbaum@anorg.chemie.uni-giessen.de

Abstract: The redox reactions of various lanthanide metals with 3-(4-pyridyl)pyrazole (4-PyPzH) or 3-(3-pyridyl)pyrazole (3-PyPzH) ligands yield the 2D network $^{2}_{\infty}$[Eu(4-PyPz)$_2$(Py)$_2$] containing divalent europium, the 3D frameworks $^{3}_{\infty}$[Ln(4-PyPz)$_3$] and $^{3}_{\infty}$[Ln(3-PyPz)$_3$] for trivalent cerium, praseodymium, neodymium, holmium, erbium, and thulium as well as $^{3}_{\infty}$[La(4-PyPz)$_3$], and the 2D networks $^{2}_{\infty}$[Ln(4-PyPz)$_3$(Py)] for trivalent cerium and thulium and $^{2}_{\infty}$[Ln$_2$(4-PyPz)$_6$]·Py for trivalent ytterbium and lutetium. The 18 lanthanide coordination polymers were synthesized under solvothermal conditions in pyridine (Py), partly acting as a co-ligand for some networks. The compounds exhibit a variety of luminescence properties, including metal-centered 4f–4f/5d–4f emission in the visible and near-infrared spectral range, metal-to-ligand energy transfer, and ligand-centered fluorescence and phosphorescence. The anionic ligands 3-PyPz$^-$ and 4-PyPz$^-$ serve as suitable antennas for lanthanide-based luminescence in the visible and near-infrared range through effective sensitization followed by emission through intra–4f transitions of the trivalent thulium, holmium, praseodymium, erbium, and neodymium. $^{2}_{\infty}$[Ce(4-PyPz)$_3$(Py)], $^{3}_{\infty}$[Ce(4-PyPz)$_3$], and $^{3}_{\infty}$[Ce(3-PyPz)$_3$] exhibit strong degrees of reduction in the 5d excited states that differ in intensity compared to the ligand-based emission, resulting in a distinct emission ranging from pink to orange. The direct current magnetic studies show magnetic isolation of the lanthanide centers in the crystal lattice of $^{3}_{\infty}$[Ln(3-PyPz)$_3$], Ln = Dy, Ho, and Er.

Keywords: divalent europium; cerium; NIR emitter; N-donor ligand

Citation: Youssef, H.; Becker, J.; Pietzonka, C.; Taydakov, I.V.; Kraus, F.; Müller-Buschbaum, K. Divalent Europium, NIR and Variable Emission of Trivalent Tm, Ho, Pr, Er, Nd, and Ce in 3D Frameworks and 2D Networks of Ln–Pyridylpyrazolates. *Chemistry* **2023**, *5*, 1006–1027. https://doi.org/10.3390/chemistry5020069

Academic Editors: Christoph Janiak, Sascha Rohn and Georg Manolikakes

Received: 27 March 2023
Revised: 20 April 2023
Accepted: 26 April 2023
Published: 28 April 2023

1. Introduction

Divalent europium, the mildest reducing agent of the redox-sensitive divalent lanthanide ions, has been successfully used in a wide variety of material applications such as medical imaging [1,2], photochemistry [3,4], lanthanide-activated phosphors [5,6], and sensing [7,8]. Trivalent lanthanides are known for their luminescence properties, with f–f based emission covering the spectrum from the ultraviolet (UV) to the near-infrared (NIR) spectral region, characteristic for each metal ion [9,10]. Several ions of typical NIR emitters also have possible transitions in the visible range [11], but these are usually too weak to be readily observed, especially for Tm^{3+} and Ho^{3+} [12–16]. NIR emitters have played an

important role in many modern technologies such as organic light-emitting diodes (OLEDs) [17,18] and photovoltaics [19,20], which encouraged us to further study the photophysical properties of NIR emitters such as Tm, Ho, Nd, and Er [11,12,21,22].

In addition to the forbidden f–f transitions, 5d–4f transitions can also be detected among the trivalent and the divalent lanthanides such as Ce^{3+} and Eu^{2+}. The 5d–4f transitions have also been studied for decades on the luminescent mechanism and potential applications in various fields [23–25]. The emission occurs in the UV and/or in the blue spectral regions but can be shifted to a much longer wavelength depending on the environment of the Ln^{3+} ion [26,27]. Mostly, the 5d–4f transitions are absent due to thermal quenching by fast intersystem crossing from $4f^{n-1}5d^1$ to $4f^n$ configuration [4,28]. Pink-emitting cerium has rarely been detected in doped materials such as cerium-doped single-crystal aluminum nitride [29] and cerium–manganese-activated phosphor [30] and not for undoped systems. Furthermore, undoped red-emitting $^1_\infty$[Ce(2-PyPz)$_3$] and orange-emitting [Ce(2-PyPzH)$_3$Cl$_3$] (2-PyPzH = 3-(2-pyridyl)pyrazole) were just recently reported for orange emission [31,32]. These results inspired further investigations on the influence of changing the position of the nitrogen of the pyridyl ring in 3-(4-pyridyl)pyrazole (4-PyPzH) and 3-(3-pyridyl)pyrazole (3-PyPzH), which are presented in this work. The ligands 4-PyPzH and 3-PyPzH were used to synthesize homoleptic and highly luminescent trivalent lanthanide 3D coordination polymers with the formulas $^3_\infty$[Ln(3-PyPz)$_3$] and $^3_\infty$[Ln(4-PyPz)$_3$], Ln = Sm, Eu, Gd, Tb, Dy [33]. Neither 3-PyPzH nor 4-PyPzH as ligands have been explored for complexing divalent lanthanide ions. Following the reaction of europium metal with 4-PyPzH, a 2D network based on divalent europium was synthesized and presented in this work.

3-PyPzH was used to synthesize a wide variety of structures, from 3D and 2D networks to complexes of lanthanide trichlorides [14]. The weak ferromagnetic interaction for $^1_\infty$[Ho$_2$(3-PyPzH)$_3$Cl$_6$]·2MeCN encouraged us to study the magnetic properties of the presented Ln metal-based series.

2. Results and Discussion

Elemental lanthanides together with 3-(4-pyridyl)pyrazole (4-PyPzH) or 3-(3-pyridyl)pyrazole (3-PyPzH) in solvothermal synthesis-based reactions were used to obtain eighteen 3D frameworks and 2D networks (Scheme 1).

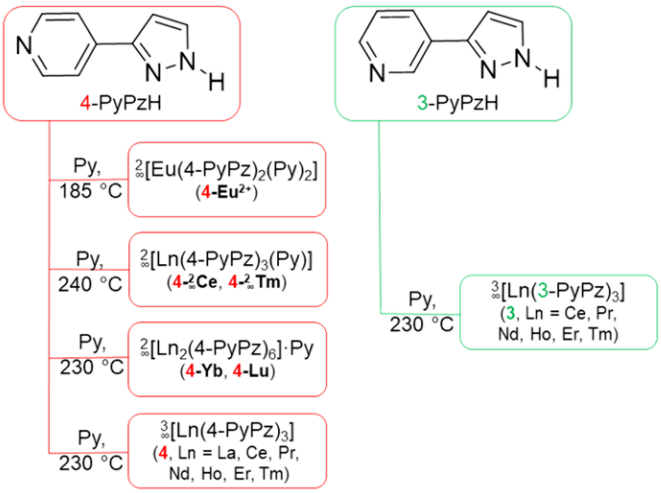

Scheme 1. Synthetic scheme for reactions of lanthanide metals with 4-PyPzH and 3-PyPzH to obtain 3D frameworks and 2D networks.

2.1. Structural Analysis

Structural diversity is observed along the series based on 4-PyPz$^-$, depending on the content of both 4-PyPz$^-$ and pyridine (Py) as linkers, all of which crystallize in the monoclinic crystal system and mostly with the space group $P2_1/n$. Exceptions are $^2_\infty$[Eu(4-PyPz)$_2$(Py)$_2$] (**4-Eu^{2+}**) and $^2_\infty$[Ln(4-PyPz)$_3$(Py)], Ln = Ce (**4-$^2_\infty$Ce**), Tm (**4-$^2_\infty$Tm**), which crystallize with the space groups $P2_1$ and *Cc*, respectively. The other 3-PyPz$^-$ based series $^3_\infty$[Ln(3-PyPz)$_3$], (**3**, Ln = Ce, Pr, Nd, Ho, Er, Tm) further crystallizes in the cubic crystal system with the space group $Pa\bar{3}$.

In $^2_\infty$[Eu(4-PyPz)$_2$(Py)$_2$] (**4-Eu^{2+}**), containing divalent europium, each Eu^{2+} ion coordinates to eight nitrogen atoms, six nitrogen atoms from four pyrazolate anions, and two nitrogen atoms from two pyridine molecules in a distorted pseudo-octahedral assembly (Figure 1), if the two nitrogen atoms of the pyrazolate anion are considered as one corner of the octahedron. The four pyrazolate anions act as bridges to the neighboring Eu^{2+} ions, forming a 2D coordination polymer. The Eu–N interatomic distances for divalent europium in $^2_\infty$[Eu(4-PyPz)$_2$(Py)$_2$] (**4-Eu^{2+}**) (254.9(4)–274.5(2) pm) are longer than those reported for the trivalent europium $^3_\infty$[Eu(4-PyPz)$_3$] (240.8–258.8 pm) [33], consistent with the difference in charge density and ionic radius [34]. Another comparison of the Eu–N of **4-Eu^{2+}** with the divalent europium complex [Eu(Ph$_2$pz)$_2$(Py)$_4$]·2Py (Ph$_2$pz = 3,5-diphenylpyrazolate, Eu–N = 253.8–274.1 pm) resulted in good agreement [35].

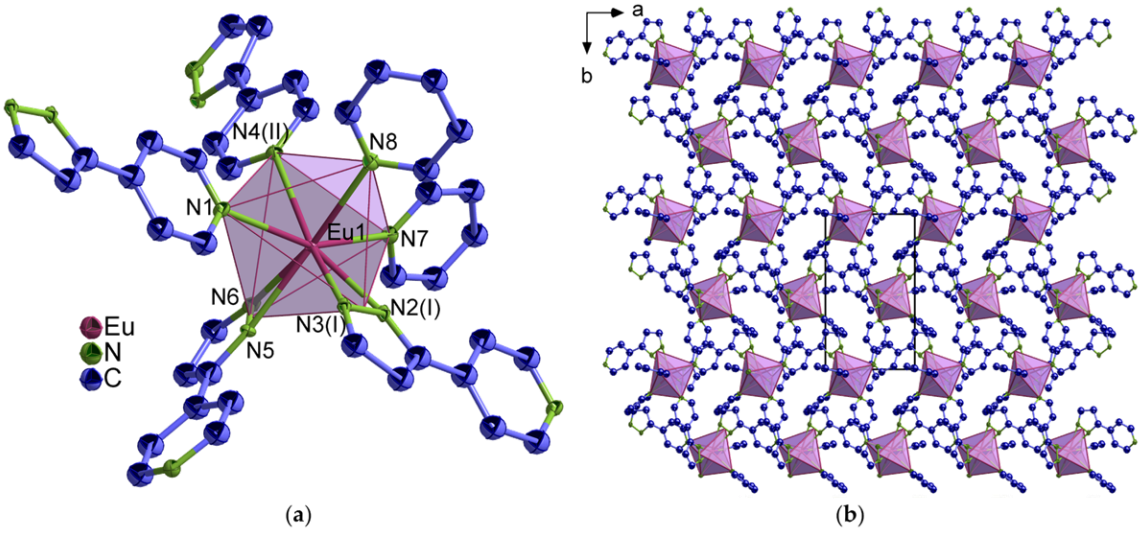

(**a**) (**b**)

Figure 1. (**a**) Extended coordination sphere of the Eu^{2+} ion in $^2_\infty$[Eu(4-PyPz)$_2$(Py)$_2$] (**4-Eu^{2+}**).; (**b**) crystal structure of **4-Eu^{2+}** with a view along [001]. The coordination polyhedra around Eu^{2+} are indicated in violet with thermal ellipsoids depicted at the 50% probability level. Symmetry operations: I x + 1, y, z II −x + 1, y + 1/2, −z. In all figures, the hydrogen atoms are omitted for clarity and the unit cell is depicted when required.

In $^2_\infty$[Ln(4-PyPz)$_3$(Py)], Ln = Ce^{3+} (**4-$^2_\infty$Ce**), Tm^{3+} (**4-$^2_\infty$Tm**), each Ln^{3+} ion coordinates to nine nitrogen atoms, eight nitrogen atoms from five pyrazolate anions, and a nitrogen atom from a pyridine molecule in a distorted pseudo-octahedral arrangement (Figure 2), if the two nitrogen atoms of the pyrazolate anion are viewed as one corner of the octahedron. The pyrazolate anions act as bridges to the neighboring Ln^{3+} ions, forming a 2D coordination polymer. Due to the lack of Tm^{3+}-nitrogen-based complexes and coordination polymers in the literature, only one example was comparable to **4-$^2_\infty$Tm**, [Tm(L^1)$_3$]$^{3+}$ (L^1 = 2,6-bis(5,6-dipropyl-1,2,4-triazin-3-yl)pyridine, Tm–N = 248.3–252.2 pm) [36], which is longer than **4-$^2_\infty$Tm** (Tm–N = 232.4–259.2 pm) due to the anionic character of the ligands, in the latter 4-PyPz$^-$.

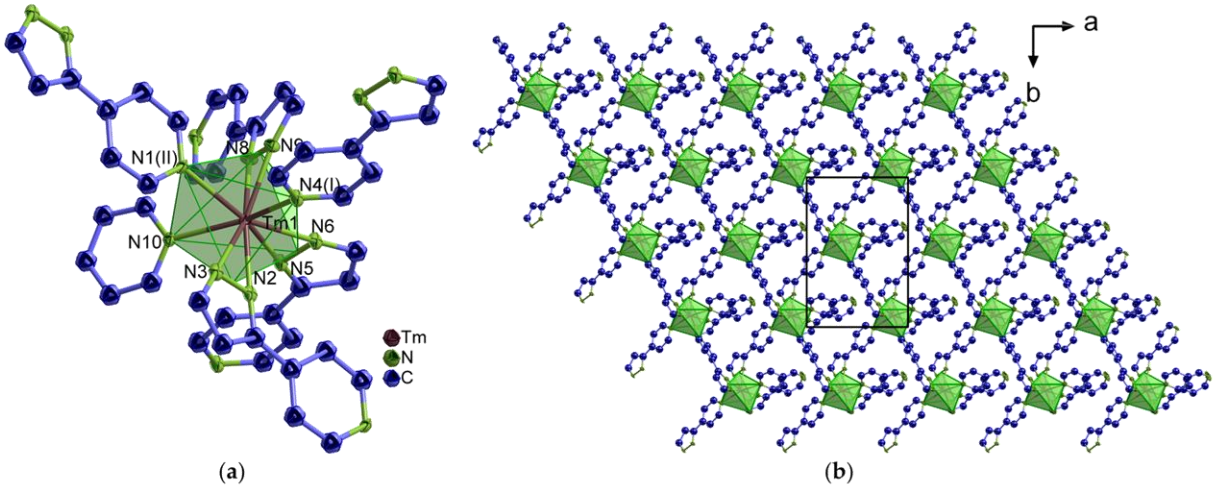

Figure 2. (**a**) Extended coordination sphere of Tm^{3+} in $^{2}_{\infty}$[Tm(4-PyPz)$_3$(Py)] (**4-$^{2}_{\infty}$Tm**).; (**b**) crystal structure of **4-$^{2}_{\infty}$Tm** with a view along [001]. The coordination polyhedra around Tm^{3+} are indicated in green with thermal ellipsoids depicted at the 50% probability level. Symmetry operations: I x − 1/2, y + 1/2, z II x + 1/2, y + 1/2, z.

The topology of the **4-Eu^{2+}** and **4-$^{2}_{\infty}$Tm** networks was determined according to the Reticular Chemistry Structure Resource (RCSR) and the Wells terminology [37,38] to result in an **sql** topology (Figure 3) with the Schläfli symbol $4^4{\cdot}6^2$ for both cases. This topology distinguishes from the rest of the series $^{3}_{\infty}$[Ln(4-PyPz)$_3$] (**4**, Ln = La, Ce, Pr, Nd, Ho, Er, Tm), which represent the **pcu** topology with the Schläfli symbol $4^{12}{\cdot}6^3$ [33]. The **pcu** topology was also found for the isotypic series $^{3}_{\infty}$[Ln(3-PyPz)$_3$] (**3**, Ln = Ce, Pr, Nd, Ho, Er, Tm).

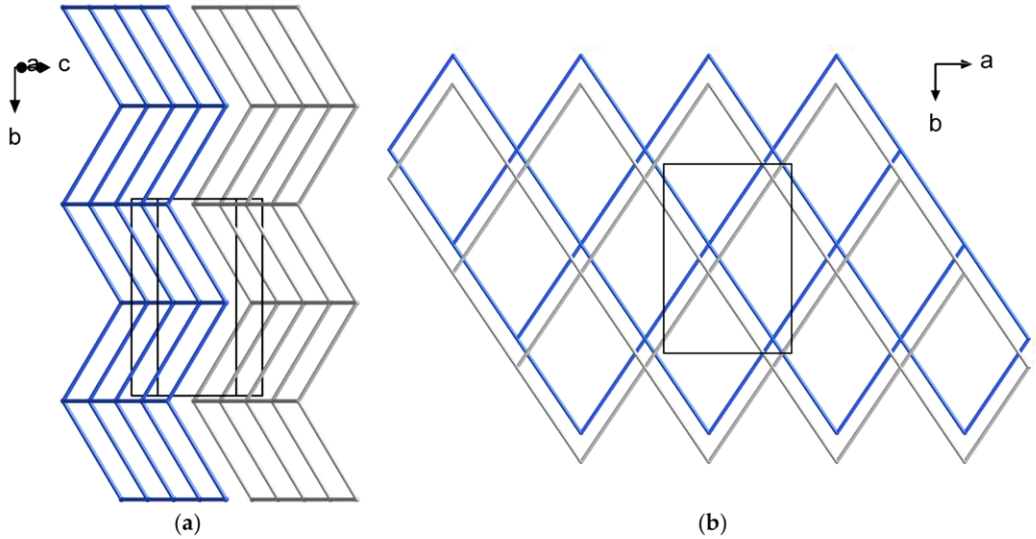

Figure 3. Topological representation of (**a**) $^{2}_{\infty}$[Eu(4-PyPz)$_2$(Py)$_2$] (**4-Eu^{2+}**).; (**b**) $^{2}_{\infty}$[Tm(4-PyPz)$_3$(Py)] (**4-$^{2}_{\infty}$Tm**) as a uninodal 4-c net with **sql** topology.

The crystal structure of $^{2}_{\infty}$[Ln$_2$(4-PyPz)$_6$]·Py, Ln = Yb (**4-Yb**), Lu (**4-Lu**) contains two lanthanide sites. One site coordinates to nine nitrogen atoms from six pyrazolate anions in a distorted pseudo-octahedron, while the other coordinates to eight nitrogen atoms from five pyrazolate anions in a distorted trigonal bipyramid (Figure 4), if the two

nitrogens of the pyrazolate anion are considered as a corner of the polyhedron. The two lanthanide sites are bridged through a pyrazolate anion, while each lanthanide site is simultaneously bridged through pyrazolate anions to adjacent identical sites to form a 2D layer extending along the bc plane. An anion coordinated to Ln1 does not act as a bridge through the nitrogen atom of its pyridine ring to another neighboring Ln ion (its position is pointed by arrows in Figure 4), making some ligands infinite and, thus, a correct topological analysis with the central atoms impossible.

The different coordination numbers are also reflected by the Yb–N distances, which range from 227.7(6)–247.9(6) pm for CN = 8 (Yb2) to 234.1(6)–257.5(5) pm for CN = 9 (Yb1). Comparison of the Yb–N distances with $[Yb(Ph_2pz)_3(Py)_2]\cdot 2(thf)$ (Ph_2pz = 3,5-diphenylpyrazolate, CN = 8, Yb–N = 225.7–244.3 pm) [39] and $[YbL_3]\cdot CH_3OH$ (HL = 2-(tetrazol-5-yl)-1,10-phenanthroline, CN = 9, Yb–N = 240.9–259.9) [40] shows good agreement for Yb–N. The Yb2–Npz (pz = pyrazolate nitrogen atom) is slightly shorter than the reported range, indicating the strength of the electrostatic interaction between the metal cation and the anionic pyrazolate ring.

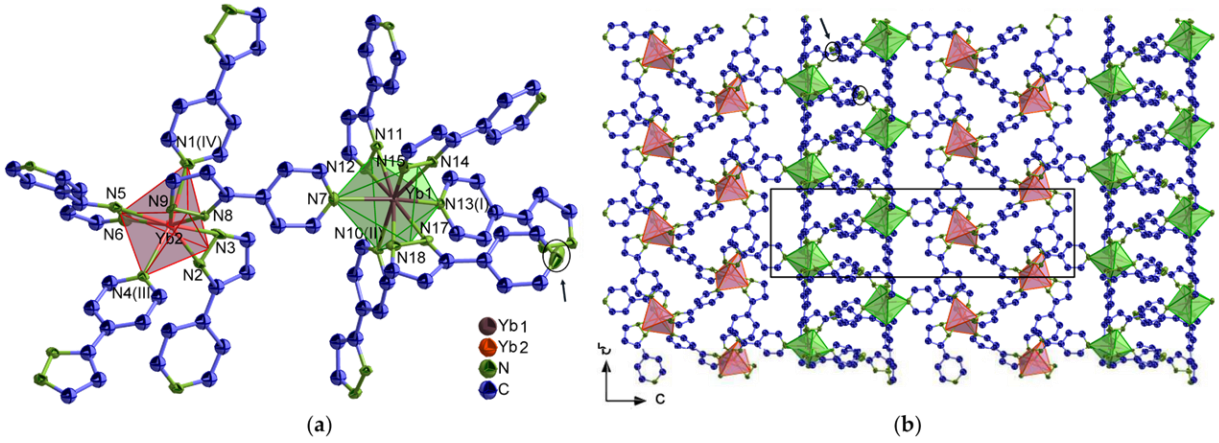

(**a**) (**b**)

Figure 4. (**a**) Extended coordination sphere of Yb^{3+} in $^{3}_{\infty}[Yb_2(4\text{-}PyPz)_6]$ (**4-Yb**).; (**b**) crystal structure of **4-Yb** with a view along [100]. The coordination polyhedra around Yb1 and Yb2 are indicated in green and red, respectively. The arrows point to the uncoordinated nitrogen atom. The solvent molecules are omitted for clarity. Symmetry operations: I −x + 1/2, y−1/2, −z + 1/2 II x, y−1, z III −x + 1/2,y − 1/2, − z + 3/2 IV x, y + 1,z.

The crystal structures of $^{3}_{\infty}[Ln(4\text{-}PyPz)_3]$ (**4**, Ln = La, Ce, Pr, Nd, Ho, Er, Tm) and $^{3}_{\infty}[Ln(3\text{-}PyPz)_3]$ (**3**, Ln = Ce, Pr, Nd, Ho, Er, Tm) are isotypic to the respective reported series of $^{3}_{\infty}[Ln(4\text{-}PyPz)_3]$ and $^{3}_{\infty}[Ln(3\text{-}PyPz)_3]$, Ln = Sm, Eu, Gd, Tb, Dy, respectively [33]. The extended coordination sphere of Ce^{3+} (CN = 9) in the two isotypic series $^{3}_{\infty}[Ln(4\text{-}PyPz)_3]$ and $^{3}_{\infty}[Ln(3\text{-}PyPz)_3]$ are shown in Figures S1 and S2. The volume of the unit cell and the average of Ln–N decrease with the increasing charge density along the two series $^{3}_{\infty}[Ln(4\text{-}PyPz)_3]$ and $^{3}_{\infty}[Ln(4\text{-}PyPz)_3]$ (Tables S10 and S11) as a direct consequence of the lanthanide contraction [41]. Tables with detailed crystallographic data and selected interatomic distances (pm) and angles (◦) of the studied compounds are given in the Supplementary Materials (Tables S1–S11).

The crystal structures were mostly determined by single-crystal X-ray diffraction (SCXRD), while the structures of $^{2}_{\infty}[Ce(4\text{-}PyPz)_3(Py)]$ (**4-$^{2}_{\infty}$Ce**) and $^{3}_{\infty}[Tm(4\text{-}PyPz)_3]$ (**4-Tm**) were characterized from microcrystalline products by powder X-ray diffraction (PXRD) and subsequent Pawley refinements (Figure 5a,b), confirming the isotypic character based on the SCXRD of $^{2}_{\infty}[Tm(4\text{-}PyPz)_3(Py)]$ (**4-$^{2}_{\infty}$Tm**) and $^{3}_{\infty}[Er(4\text{-}PyPz)_3]$ (**4-Er**), respectively.

All bulk products were investigated by PXRD. For $^{3}_{\infty}$[Ln(3-PyPz)$_3$] (**3**, Ln = Ce, Pr, Nd, Ho, Er), the experimental diffraction patterns agree with the diffraction patterns simulated from the single-crystal data with no observation of additional reflections indicating the absence of crystalline byproducts (Figure S3). To account for the different measurement conditions of PXRD (298 K) and SCXRD (100 K), Pawley refinements for $^{2}_{\infty}$[Eu(4-PyPz)$_2$(Py)$_2$] (**4-Eu^{2+}**) (Figure 5c), $^{3}_{\infty}$[Ce(4-PyPz)$_3$] (**4-Ce**) (Figure 5d), and $^{3}_{\infty}$[Ln(4-PyPz)$_3$] (**4**, Ln = La, Pr, Nd, Ho, Er) (Figures S4–S8) were carried out, confirming the phase purity of the respective series of coordination polymers. The resulting difference plots show no significant deviations, and the refinement results (R_{wp}, GOF) are shown in Table S12. Other crystalline phases were found in the PXRD of $^{2}_{\infty}$[Tm(4-PyPz)$_3$(Py)] (**4-$^{2}_{\infty}$Tm**) and $^{2}_{\infty}$[Ln$_2$(4-PyPzH)$_6$]·Py, Ln = Yb (**4-Yb**), Lu (**4-Lu**) (Figure S9). Isolation of $^{3}_{\infty}$[Tm(3-PyPz)$_3$] (**3-Tm**) as single crystals was also possible.

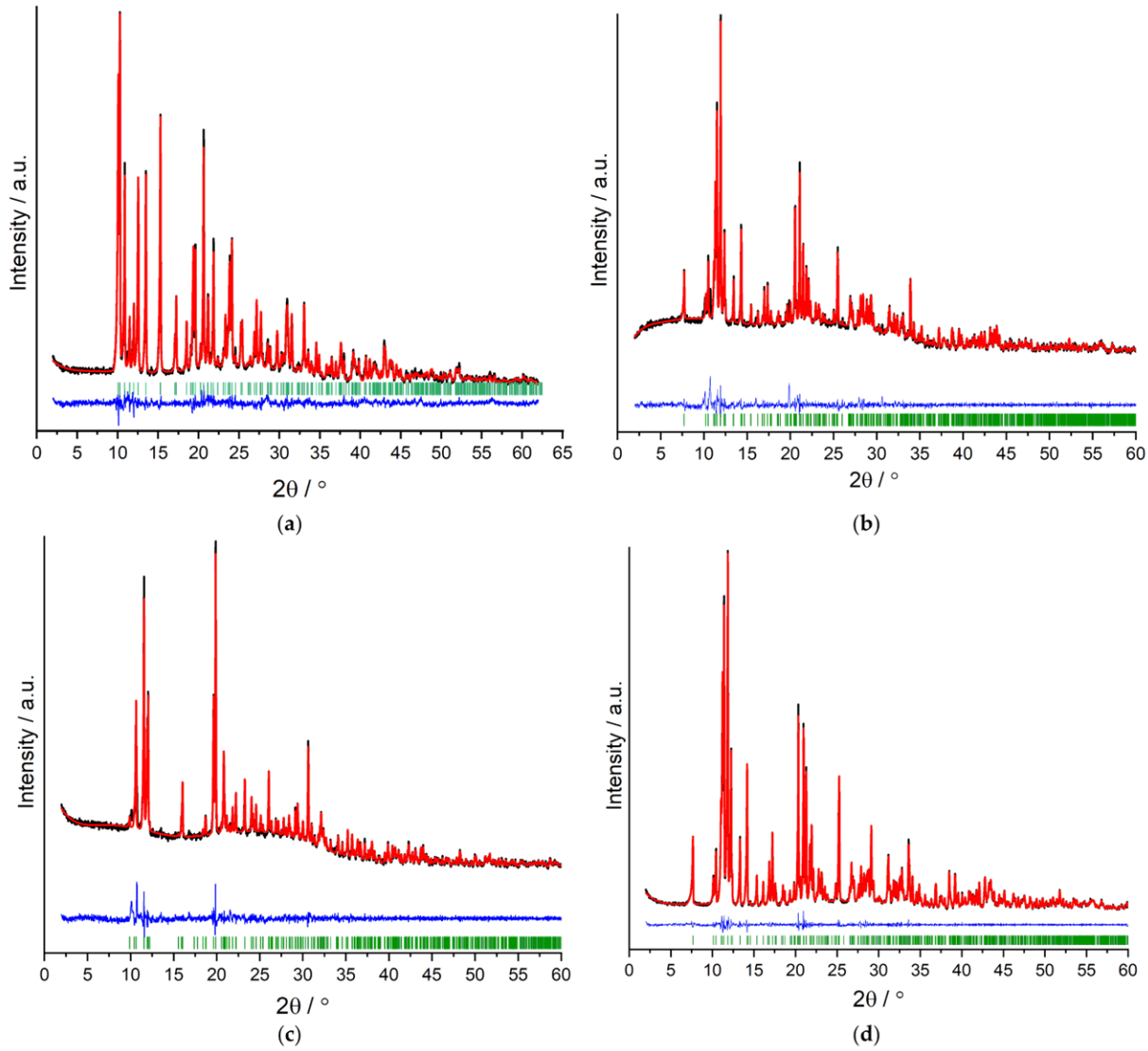

Figure 5. Pawley refinement results for PXRD of (**a**) $^{2}_{\infty}$[Ce(4-PyPz)$_3$(Py)] (**4-$^{2}_{\infty}$Ce**), (**b**) $^{3}_{\infty}$[Tm(4-PyPz)$_3$] (**4-Tm**), (**c**) $^{2}_{\infty}$[Eu(4-PyPz)$_2$(Py)$_2$] (**4-Eu^{2+}**), and (**d**) $^{3}_{\infty}$[Ce(4-PyPz)$_3$] (**4-Ce**), showing the experimental data (black) together with the Pawley fit (red), the corresponding difference plot (blue), as well as hkl position markers (green).

2.2. Photophysical Properties

2.2.1. UV–VIS–NIR Absorption Spectra

Electronic absorption spectra were recorded in the solid state at room temperature (RT) for 4-PyPzH, $^{2}_{\infty}$[Eu(4-PyPz)$_2$(Py)$_2$] (**4-Eu^{2+}**), $^{2}_{\infty}$[Ce(4-PyPz)$_3$(Py)] (**4-$^{2}_{\infty}$Ce**), $^{3}_{\infty}$[Ln(4-PyPz)$_3$] (**4**, Ln = Ce, Pr, Nd, Ho, Er, Tm), and $^{3}_{\infty}$[Ln(3-PyPz)$_3$] (**3**, Ln = Ce, Pr, Nd, Ho, Er) (Figure 6). The absorption spectra of the free ligand 3-PyPzH was shown for the solid state in a range from about 200–270 and 570–305 nm corresponding to the intra-ligand transitions π–π* and/or n–π* [14]. The free ligand 4-PyPzH shows a broad band from 200 to 280 nm corresponding to the intra-ligand transitions. In the investigated coordination polymers, the intense wide absorption band corresponding to either ligand appears in the UV region. For $^{2}_{\infty}$[Eu(4-PyPz)$_2$(Py)$_2$] (**4-Eu^{2+}**), a broad absorption shoulder from 356–640 nm is associated with a metal-to-ligand charge transfer (MLCT) transition from the Eu^{2+} 4f orbitals to the π* orbitals of the coordinated ligands. For $^{2}_{\infty}$[Ce(4-PyPz)$_3$(Py)] (**4-$^{2}_{\infty}$Ce**), $^{3}_{\infty}$[Ce(4-PyPz)$_3$] (**4-Ce**), and $^{3}_{\infty}$[Ce(3-PyPz)$_3$] (**3-Ce**), the formation of shoulders at a higher wavelength from 320–470 nm is observed due to the transition from 4f to 5d. These absorption shoulders are compatible with the shoulders observed for the orange and the red emitters [Ce(2-PyPzH)$_3$Cl$_3$] and $^{1}_{\infty}$[Ce(2-PyPz)$_3$] [31]. Moreover, sharp and weak to medium bands can be assigned to the respective f–f transitions in both the VIS and NIR regions for $^{3}_{\infty}$[Ln(4-PyPz)$_3$], Ln = Pr (**4-Pr**), Nd (**4-Nd**), Ho (**4-Ho**), Er (**4-Er**), Tm (**4-Tm**) and $^{3}_{\infty}$[Ln(3-PyPz)$_3$], Ln = Pr (**3-Pr**), Nd (**3-Nd**), Ho (**3-Ho**), Er (**3-Er**), as assigned in Table 1 [11,42–45].

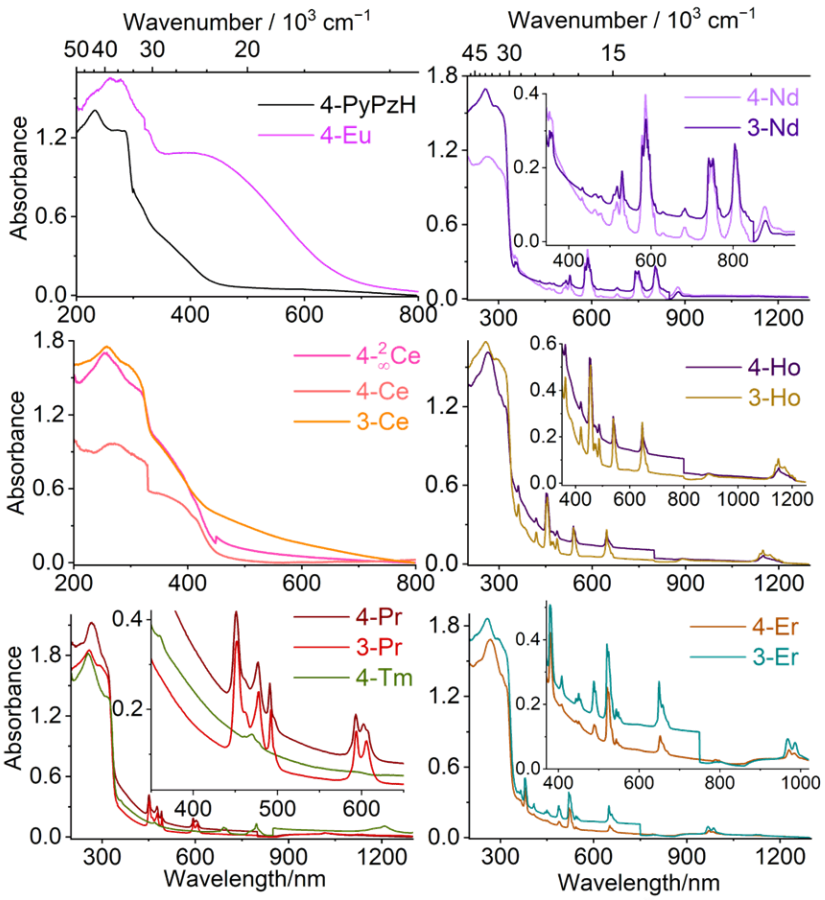

Figure 6. Solid-state absorption spectra of 4-PyPzH, $^{2}_{\infty}$[Eu(4-PyPz)$_2$(Py)$_2$] (**4-Eu^{2+}**), $^{2}_{\infty}$[Ce(4-PyPz)$_3$(Py)] (**4-$^{2}_{\infty}$Ce**), $^{3}_{\infty}$[Ln(4-PyPz)$_3$], (**4**, Ln = Ce, Pr, Nd, Ho, Er, Tm) and $^{3}_{\infty}$[Ln(3-PyPz)$_3$], (**3**, Ln = Ce, Pr, Nd, Ho, Er) in the solid state at room temperature.

Table 1. Absorption wavelengths of transitions of $^{3}_{\infty}$[Ln(4-PyPz)$_3$], (**4**, Ln = Pr, Nd, Ho, Er, Tm) and $^{3}_{\infty}$[Ln(3-PyPz)$_3$], (**3**, Ln = Pr, Nd, Ho, Er) in the solid state at room temperature.

ID		Intra–4f Absorption Transitions	λ_{max} (nm)
Ground State		**Excited States**	
4-Pr	$^3H_4\rightarrow$	$^3P_2$, $^3P_1$, $^3P_0$, $^1D_2$	451, 477, 491, 593 nm
3-Pr	$^3H_4\rightarrow$	$^3P_2$, $^3P_1$, $^3P_0$, $^1D_2$	451, 477, 492, 593 nm
4-Nd	$^4I_{9/2}\rightarrow$	$^4D_{3/2}$, $^2P_{1/2}$, $^2K_{15/2}$, $^2K_{13/2}$, $^4G_{5/2}$, $^4F_{9/2}$, $^4F_{7/2}$, $^4F_{5/2}$, $^4F_{3/2}$	353, 432, 478, 529, 586, 681, 746, 803, 878 nm
3-Nd	$^4I_{9/2}\rightarrow$	$^2I_{11/2}$, $^2P_{1/2}$, $^2K_{15/2}$, $^2K_{13/2}$, $^4G_{5/2}$, $^4F_{9/2}$, $^4F_{7/2}$, $^4F_{5/2}$, $^4F_{3/2}$	353, 433, 479, 529, 588, 682, 740, 804, 878 nm
4-Ho	$^5I_8\rightarrow$	(^{5}G, ^{3}H)$_5$, (^{5}G, ^{3}G)$_5$, $^5G_6$, $^5F_2$, $^5F_3$, ^{5}F4, $^5F_5$, $^5I_5$, $^5I_6$	362, 419, 452, 474, 486, 539, 646, 892, 1150 nm
3-Ho	$^5I_8\rightarrow$	(^{5}G, ^{3}H)$_5$, (^{5}G, ^{3}G)$_5$, $^5G_6$, $^5F_2$, $^5F_3$, $^5F_4$, $^5F_5$, $^5I_5$, $^5I_6$	362, 420, 455, 475, 486, 539, 646, 891, 1149 nm
4-Er	$^4I_{15/2}\rightarrow$	$^4G_{11/2}$, (^{2}G, 4F)$_{9/2}$, $^4F_{5/2}$, $^4F_{7/2}$, $^2H_{11/2}$, $^4S_{8/2}$, $^4F_{9/2}$, $^4I_{11/2}$	379, 408, 451, 488, 521, 543, 652, 971 nm
3-Er	$^4I_{15/2}\rightarrow$	$^4G_{11/2}$, (^{2}G, ^{4}F)$_{9/2}$, $^4F_{5/2}$, $^4F_{7/2}$, $^2H_{11/2}$, $^4S_{8/2}$, $^4F_{9/2}$, $^4I_{11/2}$	379, 408, 450, 487, 520, 543, 649, 968 nm
4-Tm	$^3H_6\rightarrow$	$^1D_2$, $^1G_4$, $^3F_3$, $^3H_4$, $^3H_5$	360, 470, 691, 796, 1209 nm

2.2.2. Emission and Excitation Spectra

The photoluminescence properties were recorded for all bulk products, $^{2}_{\infty}$[Eu(4-PyPz)$_2$(Py)$_2$] (**4-Eu^{2+}**), $^{2}_{\infty}$[Ce(4-PyPz)$_3$(Py)] (**4-$^{2}_{\infty}$Ce**), $^{3}_{\infty}$[Ln(4-PyPz)$_3$] (**4**, Ln = La, Ce, Pr, Nd, Ho, Er, Tm), and $^{3}_{\infty}$[Ln(3-PyPz)$_3$] (**3**, Ln = Ce, Pr, Nd, Ho, Er) in the solid state at RT and 77 K. The photoluminescence spectroscopy determinations for $^{2}_{\infty}$[Ce(4-PyPz)$_3$(Py)] (**4-$^{2}_{\infty}$Ce**), $^{3}_{\infty}$[Ce(4-PyPz)$_3$] (**4-Ce**), and $^{3}_{\infty}$[Ce(3-PyPz)$_3$] (**3-Ce**) (Figure 7) show interesting 5d−4f transitions with Ce^{3+}-centered light emission in the VIS range. Broad emission bands appear for **4-$^{2}_{\infty}$Ce**, **4-Ce**, and **3-Ce** from 520, 500, and 460 to 850 nm centered at 650, 650, and 641 nm, respectively, at RT, indicating large crystal field splitting and a large redshift for the emission wavelength reaches the red–orange visible region. The intensity of the ligand-based emission decreases from **4-$^{2}_{\infty}$Ce** through **4-Ce** to **3-Ce** which shifts the emission color from pink through orange pink to orange, the emission colors are represented in the CIE 1931 chromaticity diagram (Figure S24), and the color coordinates are listed in Table S13. In agreement with the absorption spectra, the excitation spectra show shoulders at higher wavelengths, which correlate with the lowest energy levels of the crystal field splitting bands of the 5d excited state of the Ce^{3+} ions.

The maximum excitation bands are at about 400 nm, corresponding to the respective coordinated pyrazolate anions. The lifetimes of **4-$^{2}_{\infty}$Ce** (1.08(2) ns)**, 4-Ce** (1.16(2) ns), and **3-Ce** (1.26(2) ns) are expected to be nanoseconds due to the parity allowed nature of the 5d−4f transition. These lifetimes are slightly shorter than the lifetimes of the reported red-emitting cerium $^{1}_{\infty}$[Ln(2-PyPz)$_3$] (2 ns, 2-PyPzH = 3-(2-pyridyl)pyrazole) [32] and orange-emitting cerium [Ce(2-PyPzH)$_3$Cl$_3$] (2.83 ns) [31].

The emission spectrum of $^{2}_{\infty}$[Eu(4-PyPz)$_2$(Py)$_2$] (**4-Eu^{2+}**) shows a ligand-based transition at 350 nm (Figure 7) along with some weak f−f transitions that can be assigned to a low content of trivalent Eu emission features. The ligand-based excitation band at around 335 nm for 4-PyPzH and 3-PyPzH [33] shows a hypochromic shift upon coordination to the investigated compounds to around 325 nm in **4-Pr**, **4-Nd**, **3-Nd**, **3-Ho**, **4-Er**, **3-Er**, and **4-Tm**. The blue shift for the ligand-based excitation band increases, reaching 318 nm for **3-Pr** and **4-Ho** and even below 300 nm for **4-Eu^{2+}**. For Pr^{3+}, Nd^{3+}, and Er^{3+}, additional direct f−f excitations from the ground states $^3H_4$, $^4I_{9/2}$, and $^4I_{15/2}$, respectively, were also observed. After coordination, the ligand-based emission band for both ligands at 405 nm shows a hypochromic shift to a value between 341 and 352 nm.

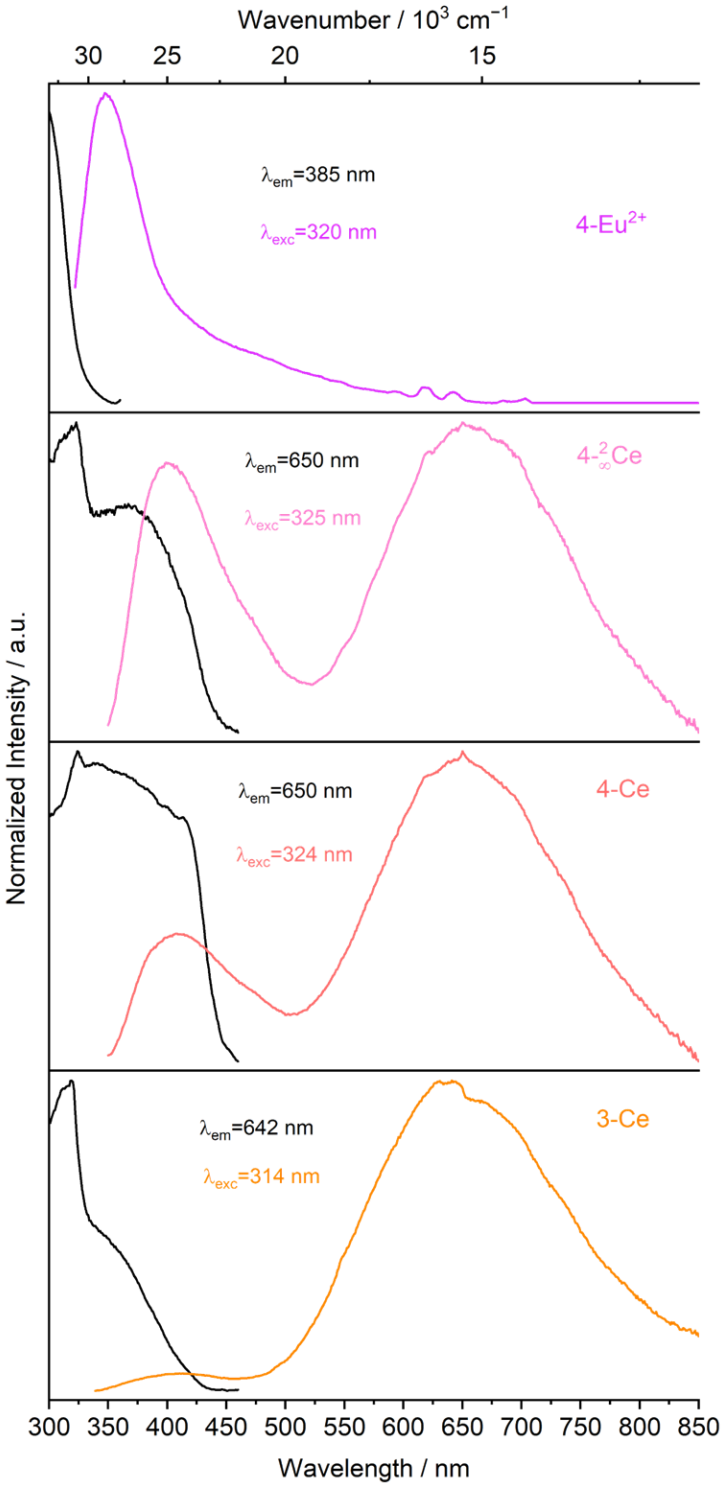

Figure 7. Normalized solid-state excitation (black) and emission (colored) spectra of $^{3}_{\infty}$[Eu(4-PyPz)$_2$(Py)$_2$] (**4-Eu^{2+}**), $^{2}_{\infty}$[Ce(4-PyPz)$_3$(Py)] (**4-$^{2}_{\infty}$Ce**), $^{3}_{\infty}$[Ce(4-PyPz)$_3$] (**4-Ce**), and $^{3}_{\infty}$[Ce(3-PyPz)$_3$] (**3-Ce**) at RT. Wavelengths for which the spectra were recorded are reported in the legends.

For ∞[La(4-PyPz)$_3$] (**4-La**), an additional resolved broad band with λ_{onset} = 423 nm (~23,640 cm^{-1}), corresponding to the triplet state of the pyrazolate anion, was observed in the emission spectrum (Figure S27) at 77 K, which agrees well with the previously reported value [33].

Although the excitation and emission spectra can provide a wealth of information, particularly about the coordination environment of the Ln^{3+} ions, it is uncommon to find the luminescence spectra for the Tm^{3+} and Ho^{3+}-based compounds. Nine-coordinated Tm^{3+} was only reported in three examples, and none of them investigated the photophysical properties, they mainly focused on the structural aspects [36,46,47]. In other cases, poor ligand-to-metal sensitization or back energy transfer occurs to allow only ligand-based luminescence, as in [Tm$_2$(C$_{15}$H$_{11}$N$_3$)$_2$(C$_7$H$_4$BrO$_2$)$_4$(C$_2$O$_4$)], (C$_{15}$H$_{11}$N$_3$ = 2,2′:6′2″-terpyridine and C$_7$H$_4$BrO$_2$ = *p*-bromobenzoic acid) [15], Tm(bfa)$_3$phen, (bfa = 4,4,4-trifluoro-1-phenyl-1,3-butanedione, phen = 1,10-phenanthroline) [12], and Tm(ppa)$_3$·2H$_2$O, (ppa = 3-phenyl-2,4-pentanedionate) [13], where a significant ligand emission dominates the spectrum in addition to a single spectral band for the Tm^{3+}. Even nonefficient ligand sensitization with only a ligand emission band in the emission spectra was shown for [(Tm-(TC)$_3$(H$_2$O)$_2$)·(HPy·TC)]$_n$, (TC = 2-thiophenecarboxylate and HPy = pyridinium cation) [16]. In contrast, very good ligand-to-metal sensitization is observed for ∞[Tm(4-PyPz)$_3$] (**4-Tm**) (Figure 8). The transitions ^{1}G$_4$→^{3}H$_6$, ^{3}F$_4$, ^{3}H$_5$, and ^{3}H$_4$ are readily observable at 480, 650, 787, and 1192 nm, respectively.

For ∞[Ho(4-PyPz)$_3$] (**4-Ho**) and ∞[Ho(3-PyPz)$_3$] (**3-Ho**), the ^{5}F$_5$→^{5}I$_8$ is observed at 648 nm in addition to the NIR transition ^{5}I$_6$→^{5}I$_8$ at 1155 nm. An additional NIR transition appears for **4-Ho** at 983, corresponding to the transition ^{5}F$_5$→^{5}I$_7$ and indicating more efficient ligand sensitization than in reported cases, such as [(Ho-(TC)$_3$(H$_2$O)$_2$)·(HPy·TC)]$_n$ with only ligand emission observable in the emission spectra [16]. The Ho^{3+}-based emission observed for both **3-Ho** and **4-Ho** is stronger than that of ∞[Ho$_2$(3-PyPzH)$_3$Cl$_6$]·2MeCN [14], which may be due to the absence of the vibrational energy of the chloride ligands.

For ∞[Pr(4-PyPz)$_3$] (**4-Pr**) and ∞[Pr(3-PyPz)$_3$] (**3-Pr**) (Figure 8), the highest intensity for the Pr^{3+}-based emission is found at 655 nm, corresponding to ^{3}P$_0$→^{3}F$_2$. NIR emission bands can also be observed at 738 and 1048 for **4-Pr** and at 736 and 1038 nm for **3-Pr**, corresponding to the transitions ^{3}P$_0$→^{3}F$_4$ and ^{1}D$_2$→^{3}F$_4$. Despite the ligand-based emission in **4-Pr** and **3-Pr** being more dominated than for the reported ∞[Pr(2-PyPz)$_3$] [32], the Pr^{3+}-based transitions are more characteristic than for other published cases, such as ∞[PrCl$_3$(ptpy)] and [PrCl$_3$(ptpy)(py)], ptpy = 4′-phenyl-2,2′:6′,2″-terpyridine) [48].

For ∞[Er(4-PyPz)$_3$] (**4-Er**) and ∞[Er(3-PyPz)$_3$] (**3-Er**), the NIR transition ^{4}I$_{13/2}$→^{4}I$_{15/2}$ is observed at about 1510 nm and the VIS transition at about 545 nm can also be observed for **4-Er** at RT and 77 K, while at 77 K for **3-Er**. Both **4-Er** and **3-Er** show Stark-level splitting in the emissive transitions in contrast, e.g., to the reported ∞[LnCl$_3$(bipy)(py)$_2$]·py, which shows no fine splitting [48].

For the NIR emitters ∞[Nd(4-PyPz)$_3$] (**4-Nd**) and ∞[Nd(3-PyPz)$_3$] (**3-Nd**), the transitions ^{4}F$_{3/2}$→^{4}I$_{J/2}$, (J = 9, 11, 13) are observed at about 915, 1065, and 1345 nm [11].

Generally, for the VIS–NIR and the NIR emitters, the emissive energy levels of the Ln^{3+}-based transitions are populated by an antenna effect between the pyridylpyrazolate-based ligands and the lanthanide ions, which leads to ligand-to-metal energy transfer, as observed for 2-PyPzH [32] and 4,4`-bipyridine (bipy) [49].

The ligands' fluorescence emission band has lifetimes of 6.07 ns for 4-PyPzH and 3.4 ns for 3-PyPzH [33] which are shortened by coordination with different Ln^{3+} (τ = 0.93–1.04; Table S14). The lifetime increases with decreasing the temperature to 77 K, especially for 4-Nd, which increases from 0.93(2) ns at RT to 3.04(9) ns at 77 K due to the decrease in thermal quenching. See the Supplementary Materials for half-page size absorption and photoluminescence spectra with designated 4f–4f transitions for the investigated compounds (Figures S10–S37).

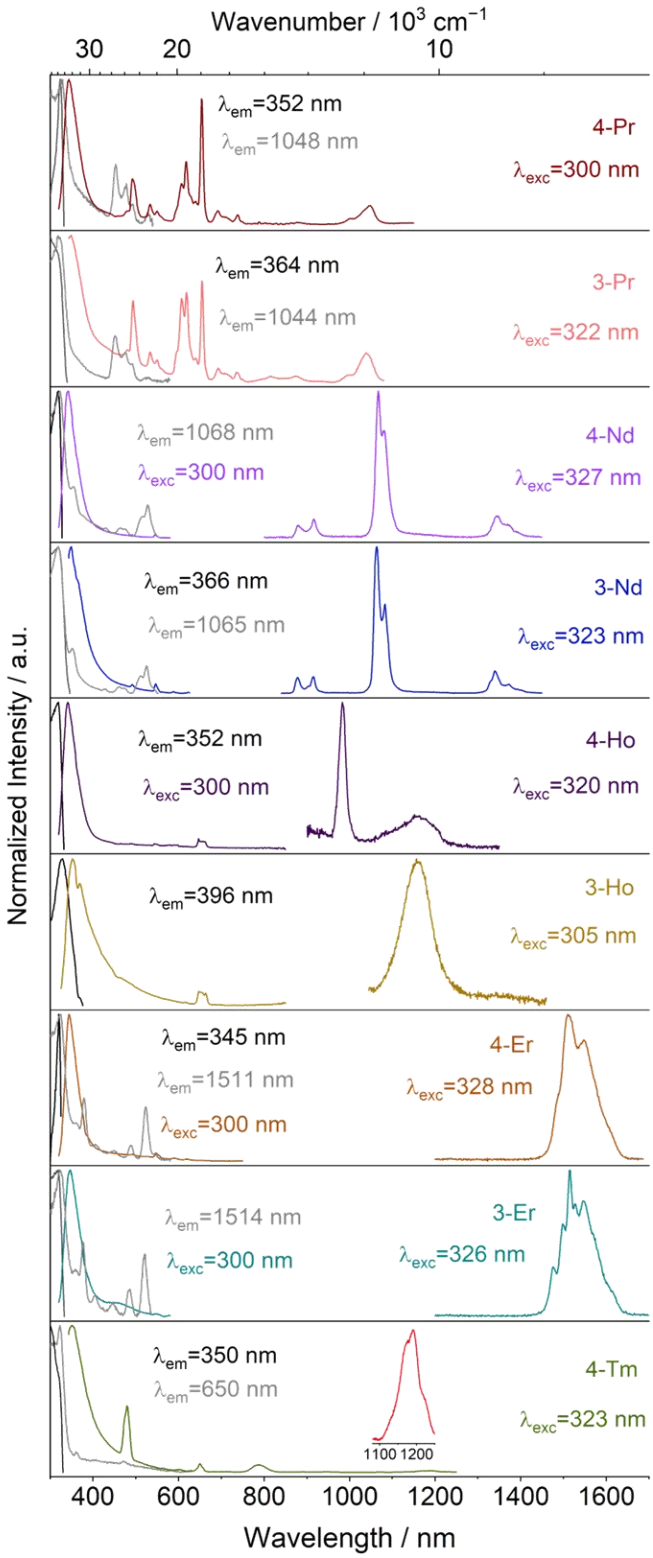

Figure 8. Normalized solid-state excitation (black) and emission spectra (colored) of ^{3}[Ln(4-PyPz)$_3$], (**4**, Ln = Pr, Nd, Ho, Er, Tm) and ^{3}[Ln(3-PyPz)$_3$], (**3**, Ln = Pr, Nd, Ho, Er) at RT. Wavelengths, for which the spectra were recorded, are reported in the legends.

2.2.3. Mechanism of Energy Transfer

To explain and understand the observed spectral results, a schematic diagram (Scheme 2) is shown, depicting the primary energy levels involved and the main energy transfer and relaxation pathways during the sensitization of lanthanide luminescence via the ligands. The ligands absorb energy and become excited from the singlet S_0 ground state to the singlet S_1 excited state by the absorption of visible light. The energy of the S_1 excited state is then transferred to the triplet-excited state (T) of the ligands through inter-system crossing (ISC). Competing processes include ligand fluorescence and nonradiative deactivation of the excited singlet state. Subsequently, the excitation energy is transferred to the excited 4f levels of the Ln^{3+} ions, resulting in the respective lanthanide ion emission to the respective 4f ground state [50]. According to Dexter's theory [51], the energy gap between the first excited energy level of the Ln^{3+} ions and the energy level of the triplet state of the respective ligand is important for an efficient energy transfer. If the energy gap is too large, the overlap between the ligand and the Ln^{3+} is reduced, and as a result, the energy transfer decreases sharply. On the other hand, if the energy gap is too small, energy transfer also occurs from the Ln^{3+} back to the resonance levels of the triplet states of the ligands, which also reduces the 4f-based emission.

In this study, the triplet-state energy levels of 4-$PyPz^-$ and 3-$PyPz^-$ were investigated by deduction from the phosphorescence spectra of the Gd-based coordination polymers and calculated to be 23,640 and 23,250 cm^{-1}, respectively [33]. This analogy is confirmed for 4-$PyPz^-$ through the spectra of **4-La**, as discussed before. The discussed 4f emission bands of the respective Ln-based CPs indicate that the triplet states of the ligands are suitable for a transfer of the absorbed light to the lanthanide ions via such an antenna effect. For instance, the energy difference (ΔE) between the ligand triplet state of 4-$PyPz^-$ (~23,640 cm^{-1}) and the energetic positions of Tm^{3+} ($^1G_4$ = ~21,300 cm^{-1}) results in an ΔE value in the optimal range. Pr^{3+} is slightly more complicated because it has two emission levels ($^3P_0$ and $^1D_2$). By considering the $^3P_0$ level as the main acceptor level with an energetic position of ~20,475 cm^{-1} [11], the ΔE values are calculated as 3165 and 2775 for **4-Pr** and **3-Pr**, respectively, both also being in the optimal range. For Ho^{3+}, the $^5F_4$, $^5S_2$, and $^5F_5$ levels are the main acceptor levels, and the emission from the $^5F_5$ and $^5I_6$ levels can partially be the result of a relaxation of the upper levels followed by transitions to the lower levels to give the eristic NIR emission of the Ho^{3+} ion [52].

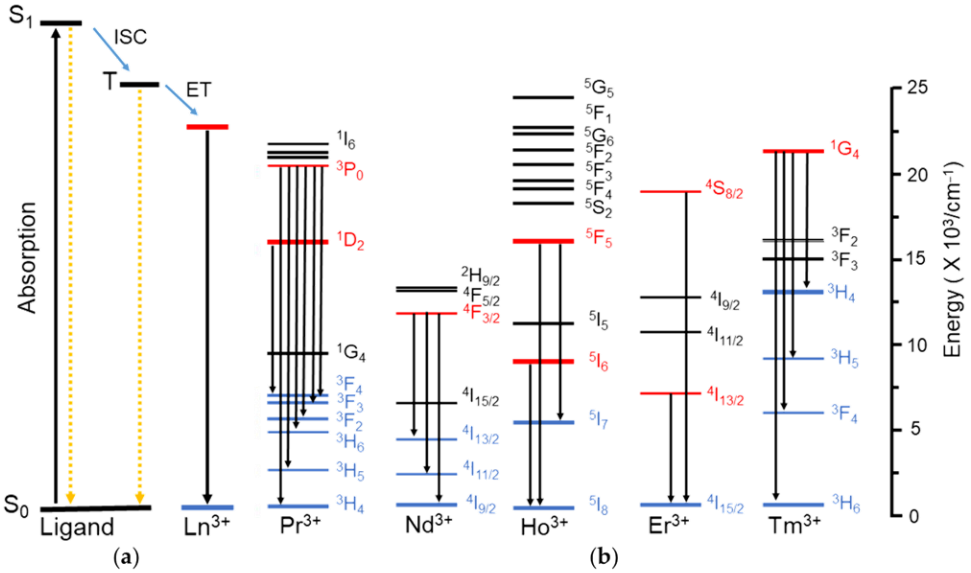

Scheme 2. (**a**) The Energy transfer mechanism; (**b**) energy level diagrams of Pr^{3+}, Nd^{3+}, Ho^{3+}, Er^{3+}, and Tm^{3+} ions.

2.3. Magnetic Properties

Direct current (DC) magnetic susceptibility measurements were performed for $^{3}_{\infty}$[Ln(3-PyPz)$_3$], Ln = Ho (**3-Ho**), Er (**3-Er**) in a temperature range of 3 to 300 K and a magnetic field of 1T. As a link to the reported isotypic series of $^{3}_{\infty}$[Ln(3-PyPz)$_3$], Ln = Sm, Eu, Gd, Tb, Dy [33], the DC magnetic susceptibility measurements of $^{3}_{\infty}$[Dy(3-PyPz)$_3$] (**3-Dy**) were also performed.

The temperature dependence of the product of χT for all samples can be observed in Figure 9. At room temperature, the $\chi_M T$ (χ_M = molar magnetic susceptibility) values are 15.03, 14.05, and 10.70 for **3-Dy**, **3-Ho**, and **3-Er**, respectively. These experimental data are in satisfactory agreement with the theoretical values for the corresponding noninteracting Dy^{3+} ($^6H_{15/2}$, S = 5/2, L = 5, g = 4/3, χT = 14.17 cm^3 K mol^{-1}), Ho^{3+} ($^5I_8$, S = 5/2, L = 6, g = 5/4. χT = 14.07 cm^3 K mol^{-1}), and Er^{3+} ($^4I_{15/2}$, S = 3/2, L = 6, g = 6/5, χT = 11.48 cm^3 K mol^{-1}) [53].

For **3-Dy**, **3-Ho**, and **3-Er**, a monotonic slow decrease in the $\chi_M T$ product was observed upon cooling, which could be related to thermal depopulation within the m_J levels of the ground $^6H_{15/2}$, $^5I_8$, and $^4I_{15/2}$ multiplet, respectively. In addition, the $\chi_M T$ vs T plot did not display abrupt changes, which suggests a lack of magnetic interactions down to 45, 75, and 80 K, with $\chi_M T$ reaching 3.01, 5.79, and 3.49 cm^3 K mol^{-1}, respectively, because of the efficient magnetic isolation of lanthanide centers in the crystal lattice.

The data were fitted for **3-Dy**, **3-Ho**, and **3-Er** in the given temperature range with an effective magnetic moment μ_{eff} of 10.651(2), 10.09(1), and 7.855(9) μB and a Weiss constant θ of −4.41(1), −5.77(7), and −5.72(8) K, as well as a temperature-independent paramagnetic susceptibility χ_0 of 4.03(3) × 10^{-3}, 6.18(2) × 10^{-3}, and 11.52(8) × 10^{-3} cm^3 mol^{-1}. The small, negative Weiss constants θ are the results of spin–orbit coupling as well as the crystal field effect [54,55].

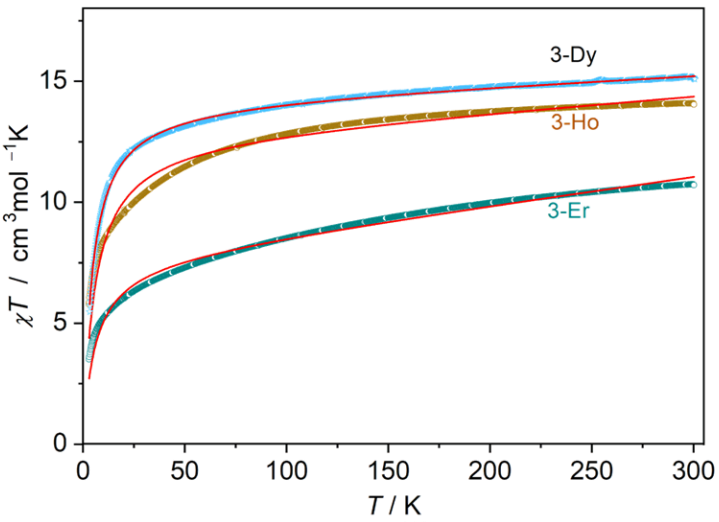

Figure 9. Variable temperature magnetic susceptibilities of $^{3}_{\infty}$[Ln(4-PyPz)$_3$], (**4**, Ln = Dy, Er), and $^{3}_{\infty}$[Ho(3-PyPz)$_3$] (**3-Ho**) in a temperature range from 3 to 300 K and a magnetic field of 1*T*.

3. Materials and Methods

3.1. General Procedures

3-(4-pyridyl)pyrazole (4-PyPzH) and 3-(3-pyridyl)pyrazole (3-PyPzH) were synthesized as reported in the literature [56,57]. Lanthanide metals (holmium: 99.9%, Chempur, Karlsruhe, Germany; rest: >99.99%, Smart Elements, Vienna, Austria) were purchased and used as received. Pyridine (Py), dichloromethane (DCM), and cyclohexane (Cy) were purified by distillation and dried by standard procedures. All syntheses involving lanthanide elements were performed under argon or using vacuum lines, gloveboxes (MBraun

Labmaster SP, Innovative Technology PureLab, Garching, Germany), Schlenk tubes, and Duran® glass ampoules (outer ⌀ 10 mm, wall thickness 1.5 mm). The solid reactants for the solvothermal reactions were mixed and sealed together with the solvent in an ampoule under reduced pressure ($p = 1.0 \times 10^{-3}$ mbar) after freezing the solvent with liquid nitrogen. Subsequently, the prepared ampoules were placed in heating furnaces based on Al_2O_3 tubes with Kanthal wire resistance heating and NiCr/Ni (Eurotherm 2416) temperature control elements, for which temperature programs and working steps according to the specific synthesis methods were used. After the solvents had been removed, the solid raw products were dried at RT in a dynamic vacuum ($p = 1.0 \times 10^{-3}$ mbar) before further steps. The bulk materials were characterized by PXRD and CHN analysis. The prepared 3D frameworks and 2D networks are air sensitive due to the known oxophilic behavior of the Ln-based CPs. It is expected that the CPs are insoluble in common organic solvents. We think the photostability tests are not significant in the possible applications of these synthesized CPs.

3.2. X-ray Crystallography

SCXRD determinations were performed on a Bruker AXS D8 Venture diffractometer (Karlsruhe, Germany) equipped with dual IμS microfocus sources, a collimating Quazar multilayer mirror, a Photon 100 detector, and an Oxford Cryosystems 700 low-temperature system (Mo–K_α radiation; λ = 71.073 pm). The structures were solved with direct methods and refined with the least squares method implemented in ShelX [58,59]. All nonhydrogen atoms were refined anisotropically. Hydrogen atoms were assigned to idealized geometric positions and included in structure factor calculations. Further, a ligand anion (4-PyPz$^-$) and the pyridine solvent in the asymmetric unit of **4-Yb** and **4-Lu** were found to be fully disordered and were refined with the help of restraints to achieve a proper structural model. For polymers **4-La**, **4-Ce**, **4-Pr**, **4-Nd**, **4-Ho**, and **4-Er**, the SQUEEZE [60] algorithm in PLATON [61–64] was used to include a bulk solvent model in the refinement. Two voids per unit cell were identified with SQUEEZE. The average volume was found to be 135×10^6 pm^3 for each void. The equivalent of 8 electrons for (**4-La**, **4-Ce**, **4-Pr**), 10 for (**4-Ho**), and 12 for (**4-Nd**) electrons per unit cell was also identified. ToposPro program package was used to determine the topology of the polymers [65]. Depictions of the crystal structures were created with Diamond [66]. The crystal structures have been deposited to the Cambridge Crystallographic Data Center (CCDC) as supplementary publication No. 2237763 (**4-Eu^{2+}**), 2237764 (**4-~~2~~Tm**), 2237765 (**4-Yb**), 2237766 (**4-Lu**), 2237767 (**4-La**), 2237768 (**4-Ce**), 2237769 (**4-Pr**), 2237770 (**4-Nd**), 2237771 (**4-Ho**), 2237772 (for **4-Er**), 2237773 (**3-Ce**), 2237774 (**3-Pr**), 2237775 (**3-Nd**), 2237776 (**3-Ho**), 2237777 (for **3-Er**), and 2237778 (**3-Tm**). Crystallographic data and selected interatomic distances are listed in Tables S1–S11 for the investigated compounds.

PXRD analyses of the investigated compounds were carried out on a Stoe Stadi P diffractometer (Darmstadt, Germany) with a focusing Ge(111) monochromator and a Dectris Mythen 1K strip detector in Debye–Scherrer geometry. All powder samples were ground in a mortar and filled into Lindemann glass capillaries with 0.3 mm diameter under an inert gas atmosphere. All samples were measured in transmission geometry with Cu–K_α radiation (λ = 154.056 pm). Data collection was performed using the Stoe Powder Diffraction Software Package WinXPOW V3.0.2.1 and Pawley fits on the data were performed using TOPAS Academic V7 [67]. The data are presented in Figures 5 and S3–S9 in addition to Table S12.

3.3. Spectroscopical Investigations

3.3.1. Absorption Spectra

The UV–Vis–NIR absorption spectra were measured on solid-state products using a standard Agilent Cary 5000 UV–VIS–NIR spectrophotometer (Agilent Technologies, Waldbronn, Germany) with a Praying Mantis accessory (Harrick Scientific Instruments,

New York, NY, USA), which had been mounted and aligned for use with the DRP-ASC ambient chamber. The source, detector, and grating changeovers were at the standard position of 350, 800, and 800 nm, respectively, for all studied compounds except **4-Ce**, **4-Nd, 4-Tm**, and **3-Nd**, the detector and grating changeovers were set to 850 nm, while 750 nm for **3-Er**. For **4-Eu²⁺**, **4-Ce**, **4-Ce**, **4-Nd**, **4-Tm**, **3-Ce**, and **3-Nd**, the source was set to 320, 450, 330, 340, 335, 320, and 340 nm, respectively. The reference spectrum was collected on PTFE and the reference and samples were packed in the ambient chamber within the glovebox under inert conditions.

3.3.2. Photoluminescence Spectroscopy

The excitation and emission spectra were recorded for ground solid samples after filling them in quartz glass tubes under argon. The measurements were performed at room temperature as well as 77 K (latter using the liquid nitrogen-filled assembly FL-1013 of HORIBA) with a HORIBA Jobin Yvon Spex Fluorolog 3 spectrometer (Horiba-Jobin Yvon, Oberursel, Germany) equipped with a 450 W Xe short-arc lamp (USHIO INC., Tokyo, Japan), double-grated excitation, and emission monochromators, and a photomultiplier tube (R928P) using the FluoroEssence™ software V3.9. Excitation and emission spectra were corrected for the spectral response of the monochromators and the detector using spectral corrections provided by the constructor. In addition, a photodiode reference detector was used to correct the excitation spectra for the spectral distribution of the lamp intensity. An R5509-73 detector was used to collect the data in the NIR region. When required, the collection of the data was performed using an edge filter (Newport 20CGA-345, 395, 495 for the visible region and Reichmann Optics RG 830 long pass for the NIR region). Emission spectra with gating were recorded using a xenon flashlamp with a pulse repetition rate of 41 ms.

Photoluminescence overall decay process times were determined using the above-mentioned HORIBA Jobin Yvon Spex Fluorolog 3 spectrometer equipped with a dual lamp housing (FL-1040A), a UV xenon flashlamp (Exelitas FX-1102), and a TCSPC (time-correlated single-photon counting) upgrade, or picosecond pulsed laser diode. Emission decays were recorded using DataStation software V2.7. Exponential tail fitting was used for the calculation of resulting intensity decay using Decay Analysis Software 6. The quality of the fit was confirmed by χ^2 values being below 1.2.

3.4. PPMS Magnetic Measurements

Magnetic data were obtained with the application of the VSM option of a Quantum Design physical property measurement system (ppms). The data were corrected with respect to the contribution of the polypropylen sample holder as well as the diamagnetic contribution of the sample through utilization of both experimental data and Pascal constants (increment method). The total magnetic susceptibility is comprised of different parts: the diamagnetic contribution $\chi_{Diam.}$, the Curie paramagnetic contribution χ_{CW}, and a temperature-independent paramagnetic contribution χ_0.

$$\chi_{tot.} = \chi_{Diam.} + \chi_{Param.} = \chi_{Diam.} + \chi_{CW} + \chi_0$$

The Curie paramagnetic part is the ratio of the Curie constant C and the modified temperature $(T - \theta)$. θ is the Weiss temperature

$$\chi_{CW} = \frac{C}{T - \theta}$$

The Curie constant is given by the formula:

$$C = \mu_0 \frac{N_A \mu_B^2 n_{eff}^2}{3k_B}$$

with μ_0 = magnetic constant, N_A = Avogadro number, μ_B = Bohr magneton, n_{eff} = effective magnetic moment, k_B = Boltzmann constant.

The molar Curie paramagnetic contribution of the susceptibility is:

$$\chi_{mol_{CW}} = \frac{N_A \mu_B^2 n_{eff}^2}{3k_B(T-\theta)}$$

Or:

$$\chi_{mol_{CW}} = 0.1250 \frac{n_{eff}^2}{T-\theta} \ / \ \mathrm{cm^3 mol^{-1}}$$

To calculate the molar paramagnetic contribution of the susceptibility, we used the equation:

$$\chi_{mol} = 0.1250 \frac{n_{eff}^2}{T-\theta} + \chi_0 \ / \ \mathrm{cm^3 mol^{-1}}$$

For the analysis of the data the OriginPro software V2021b (Academic) was used.

3.5. Synthesis

3.5.1. Synthesis of $^{2}_{\infty}$[Eu(4-PyPz)$_2$(Py)$_2$] (4-Eu^{2+})

Freshly filed Eu metal (108.6 µmol) and an excess of 4-PyPzH ($C_8H_7N_3$, 220 µmol) were mixed with Py (0.6 mL) and sealed in an evacuated ampoule. The ampoule was heated to 185 °C in 1 h and maintained at this temperature for 72 h. The reaction mixture was then cooled to room temperature within 4 h. The excess ligand was washed away using a mixture of DCM and Cy. Suitable single crystals were selected for a SCXRD measurement. $C_{26}H_{22}N_8Eu$ (598.47 g·mol^{-1}): C 51.59 (calcd. 52.18); H 3.04 (3.71); N 19.49 (18.72)%. Yield: 83%. FT-IR (ATR, Figure S39): $\tilde{\nu}$ = 3036 (w), 1065 (s), 1552 (w), 1522 (w), 1456 (w), 1439 (m), 1418 (w), 1404 (w), 1346 (w), 1293 (w), 1213 (m), 1187 (w), 1065 (w), 1044 (m), 999 (s), 963 (w), 951 (w), 925 (w), 871 (w), 830 (s), 761 (s), 690 (s), 659 (w), 614 (m), 532 (m), 451 (m) cm^{-1}.

3.5.2. Synthesis of $^{2}_{\infty}$[Ln(4-PyPz)$_3$(Py)] (4-$^{2}_{\infty}$Ce, 4-$^{2}_{\infty}$Tm)

The respective freshly filed Ln metal (81.4 µmol) and an excess of 4-PyPzH ($C_8H_7N_3$, 327.6 µmol) were mixed with Py and sealed in an evacuated ampoule. The ampoule was heated to 180 °C in 24 h then the temperature was raised to 240 °C within 48 h and maintained at this temperature for 72 h. The reaction mixture was then cooled to room temperature within 48 h. The excess ligand was washed away using a mixture of DCM and Cy. Suitable single crystals were selected for a SCXRD measurement. $C_{29}H_{23}N_{10}Ce$ (651.67 g·mol^{-1}): C 52.63 (calcd. 53.45); H 2.67 (3.06); N 22.16 (21.49)%. Yield: 83%. FT-IR (ATR, Figure S40): $\tilde{\nu}$ = 3085 (w), 1698 (w), 1606 (s), 1523 (w), 1459 (w), 1440 (m), 1418 (w), 1347 (w), 1330 (w), 1295 (w), 1212 (s), 1099 (w), 1066 (w), 1047 (m), 1003 (s), 992 (m), 968 (w), 929 (m), 857 (w), 830 (m), 773 (s), 741 (w), 692 (s), 652 (m), 622 (w), 572 (m), 457 (s) cm^{-1}.

3.5.3. Synthesis of $^{2}_{\infty}$[Ln$_2$(4-PyPz)$_6$]·Py (4-Yb, 4-Lu)

Freshly filed Yb (68.6 µmol) and an excess of 4-PyPzH ($C_8H_7N_3$, 275.6 µmol) were mixed with Py and sealed in an evacuated ampoule. The ampoule was heated to 180 °C in 24 h then the temperature was raised to 230 °C within 48 h and maintained at this temperature for 72 h. The reaction mixture was then cooled to room temperature within 48 h. Suitable single crystals were selected for a SCXRD measurement.

3.5.4. Synthesis of $^{3}_{\infty}$[Ln(4-PyPz)$_3$] (4, Ln = La, Ce, Pr, Nd, Ho, Er, Tm)

A mixture of the respective freshly filed Ln metal (91.1 µmol) and excess 4-PyPzH ($C_8H_7N_3$, 275.6 µmol), in 0.3 mL pyridine, was sealed in an evacuated ampoule. The temperature was raised to 230 °C in 48 h, held for 96 h, and then lowered to room temperature over a further 24 h. The excess ligand was washed away using a mixture of DCM and Cy. Colorless crystals were selected for SCXRD measurements.

$^{3}_{\infty}$[La(4-PyPz)$_3$] (**4-La**): $C_{24}H_{18}N_9La$ (571.38 g·mol^{-1}): C 49.53 (calcd. 50.45); H 2.89 (3.18); N 21.50 (22.06)%. Yield: 80%. FT-IR (ATR, Figure S41): $\tilde{\nu}$ = 3096 (w), 1698 (w), 1607 (s), 1550 (w), 1526 (w), 1460 (w), 1447 (m), 1420 (w), 1348 (w), 1329 (w), 1215 (m), 1099 (w), 1066

(w), 1046 (m), 1005 (s), 968 (w), 927 (m), 831 (m), 763 (s), 739 (w), 694 (s), 652 (m), 527 (m), 459 (s) cm^{-1}.

$^3_\infty$[Ce(4-PyPz)$_3$] (**4-Ce**): $C_{24}H_{18}N_9Ce$ (572.58 g·mol^{-1}): C 49.81 (calcd. 50.34); H 3.26 (3.17); N 21.73 (22.02)%. Yield: 85%. FT-IR (ATR, Figure S42): $\tilde{\nu}$ = 3101 (w), 1608 (s), 1526 (w), 1459 (w), 1447 (w), 1420 (w), 1348 (m), 1215 (m), 1066 (w), 1046 (m), 1006 (s), 969 (w), 927 (m), 831 (m), 763 (m), 739 (w), 695 (s), 652 (m), 527 (m), 460 (s) cm^{-1}.

$^3_\infty$[Pr(4-PyPz)$_3$] (**4-Pr**): $C_{24}H_{18}N_9Pr$ (573.37 g·mol^{-1}): C 49.39 (calcd. 50.27); H 3.07 (3.16); N 21.16 (21.99)%. Yield: 84%. FT-IR (ATR, Figure S43): $\tilde{\nu}$ = 3095 (w), 1607 (s), 1526 (w), 1460 (w), 1446 (w), 1420 (w), 1348 (w), 1328 (w), 1215 (m), 1099 (w), 1067 (w), 1046 (m), 1006 (s), 969 (w), 927 (m), 831 (m), 762 (s), 739 (w), 694 (s), 652 (m), 527 (m), 460 (s) cm^{-1}.

$^3_\infty$[Nd(4-PyPz)$_3$] (**4-Nd**): $C_{24}H_{18}N_9Nd$ (576.70 g·mol^{-1}): C 49.33 (calcd. 49.98); H 2.73 (3.15); N 21.11 (21.86)%. Yield: 83%. FT-IR (ATR, Figure S44): $\tilde{\nu}$ = 3093 (w), 1609 (s), 1526 (w), 1459 (w), 1447 (m), 1420 (w), 1348 (w), 1215 (m), 1074 (w), 1047 (m), 1007 (s), 969 (w), 928 (m), 831 (m), 771 (s), 763 (s), 740 (w), 696 (s), 652 (w), 527 (w), 461 (s) cm^{-1}.

$^3_\infty$[Ho(4-PyPz)$_3$] (**4-Ho**): $C_{24}H_{18}N_9Ho$ (597.39 g·mol^{-1}): C 47.44 (calcd. 48.25); H 2.75 (3.04); N 20.14 (21.10)%. Yield: 86%. FT-IR (ATR, Figure S45): $\tilde{\nu}$ = 3113 (w), 1697 (w), 1609 (s), 1549 (w), 1526 (w), 1460 (w), 1446 (w), 1419 (w), 1348 (w), 1328 (w), 1297 (w), 1214 (m), 1101 (w), 1075 (w), 1048 (m), 1007 (s), 970 (w), 929 (m), 845 (w), 831 (m), 770 (s), 760 (s), 739 (m), 696 (s), 652 (m), 528 (m), 461 (s) cm^{-1}.

$^3_\infty$[Er(4-PyPz)$_3$] (**4-Er**): $C_{24}H_{18}N_9Er$ (599.72 g·mol^{-1}): C 48.85 (calcd. 48.07); H 3.34 (3.03); N 20.69 (21.02)%. Yield: 89%. FT-IR (ATR, Figure S46): $\tilde{\nu}$ = 3062 (w), 1696 (w), 1609 (s), 1549 (w), 1526 (w), 1460 (w), 1446 (w), 1419 (w), 1348 (w), 1328 (w), 1214 (m), 1101 (w), 1076 (m), 1048 (m), 1008 (s), 971 (w), 929 (m), 831 (m), 770 (s), 759 (s), 739 (m), 697 (s), 652 (m), 528 (m), 461 (s) cm^{-1}.

$^3_\infty$[Tm(4-PyPz)$_3$] (**4-Tm**): $C_{24}H_{18}N_9Tm$ (601.39 g·mol^{-1}): C 48.90 (calcd. 47.93); H 3.11 (3.02); N 19.97 (20.96)%. Yield: 82%. FT-IR (ATR, Figure S47): $\tilde{\nu}$ = 3117 (w), 1697 (w), 1609 (s), 1550 (w), 1527 (m), 1460 (m), 1447 (m), 1419 (w), 1349 (m), 1329 (w), 1296 (w), 1214 (s), 1102 (w), 1077 (m), 1049 (m), 1008 (s), 971 (w), 930 (m), 845 (w), 830 (s), 770 (s), 759 (s), 740 (m), 696 (s), 652 (m), 528 (m), 461 (s) cm^{-1}.

3.5.5. Synthesis of $^3_\infty$[Ln(3-PyPz)$_3$] (3, Ln = Ce, Pr, Nd, Ho, Er)

A mixture of the respective freshly filed Ln metal (78.8 µmol) and an excess of 3-PyPzH ($C_8H_7N_3$, 240 µmol) together with 0.3 mL pyridine were sealed in an evacuated ampoule. The oven was heated to 180 °C in 24 h. Subsequently, the temperature was raised to 230 °C in 48 h. The temperature was held for 72 h and then lowered to room temperature over a further 48 h. Single crystals were selected for SCXRD measurements.

$^3_\infty$[Ce(3-PyPz)$_3$] (**3-Ce**): $C_{24}H_{18}N_9Ce$ (572.58 g·mol^{-1}): C 50.50 (calcd. 50.34); H 3.11 (3.17); N 21.16 (22.02)%. Yield: 83%. FT-IR (ATR, Figure S48): $\tilde{\nu}$ = 3085 (w), 1596 (w), 1576 (m), 1509 (w), 1464 (m), 1453 (m), 1407 (m), 1359 (w), 1346 (w), 1250 (w), 1206 (m), 1186 (m), 1122 (w), 1099 (w), 1072 (m), 1039 (s), 963 (m), 928 (m), 859 (w), 818 (m), 779 (s), 716 (w), 702 (s), 656 (w), 635 (s), 510 (w), 461 (s) cm^{-1}.

$^3_\infty$[Pr(3-PyPz)$_3$] (**3-Pr**): $C_{24}H_{18}N_9Pr$ (573.37 g·mol^{-1}): C 49.35 (calcd. 50.27); H 2.63 (3.16); N 22.89 (21.99)%. Yield: 81%. FT-IR (ATR, Figure S49): $\tilde{\nu}$ = 2897 (w), 1683 (m), 1596 (w), 1576 (w), 1508 (w), 1453 (m), 1407 (m), 1359 (w), 1345 (w), 1260 (w), 1249 (w), 1207 (m), 1186 (m), 1099 (w), 1074 (m), 1041 (s), 963 (m), 928 (m), 817 (w), 781 (s), 702 (s), 657 (w), 636 (s), 515 (w), 462 (s) cm^{-1}.

$^3_\infty$[Nd(3-PyPz)$_3$] (**3-Nd**): $C_{24}H_{18}N_9Nd$ (576.70 g·mol^{-1}): C 48.28 (calcd. 48.98); H 2.84 (3.15); N 21.39 (21.86)%. Yield: 80%. FT-IR (ATR, Figure S50): $\tilde{\nu}$ = 3085 (w), 1576 (m), 1509 (w), 1465 (m), 1452 (m), 1408 (m), 1360 (m), 1347 (m), 1330 (w), 1249 (w), 1207 (m), 1186 (s), 1122 (w), 1099 (w), 1072 (m), 1041 (s), 963 (m), 928 (s), 818 (m), 779 (s), 717 (w), 702 (s), 656 (m), 636 (s), 509 (w), 463 (s) cm^{-1}.

$^3_\infty$[Ho(3-PyPz)$_3$] (**3-Ho**): $C_{24}H_{18}N_9Ho$ (597.39 g·mol^{-1}): C 47.95 (calcd. 48.25); H 2.94 (3.04); N 20.16 (21.10)%. Yield: 86%. FT-IR (ATR, Figure S51): $\tilde{\nu}$ = 3086 (w), 1597 (w), 1577

(m), 1508 (w), 1465 (m), 1452 (m), 1408 (m), 1348 (m), 1248 (w), 1210 (m), 1187 (s), 1100 (w), 1075 (m), 1044 (s), 964 (m), 931 (m), 818 (m), 778 (s), 700 (s), 657 (m), 637 (s), 467 (s) cm^{-1}.

$^3_\infty$[Er(3-PyPz)$_3$] (**3-Er**): $C_{24}H_{18}N_9Er$ (599.72 g·mol^{-1}): C 48.86 (calcd. 48.07); H 2.69 (3.03); N 20.77 (21.02)%. Yield: 87%. FT-IR (ATR, Figure S52): $\tilde{\nu}$ = 3086 (w), 1577 (w), 1508 (w), 1465 (w), 1453 (w), 1408 (w), 1348 (w), 1248 (w), 1210 (w), 1187 (m), 1100 (w), 1077 (m), 1045 (s), 964 (m), 931 (m), 818 (w), 780 (s), 700 (m), 657 (w), 637 (m), 513 (w), 468 (s) cm^{-1}.

3.5.6. Single Crystal of $^3_\infty$[Tm(3-PyPz)$_3$] (3-Tm):

Freshly filed Tm (68.7 µmol) and excess of 4-PyPzH ($C_8H_7N_3$, 210.5 µmol) were mixed with Py and sealed in an evacuated ampoule. The ampoule was heated to 180 °C in 1 h then the temperature was raised to 240 °C within 48 h and maintained at this temperature for 168 h. The reaction mixture was then cooled to room temperature within 48 h. Suitable single crystals were selected for a SCXRD measurement.

4. Conclusions

Divalent europium in the 2D network $^2_\infty$[Eu(4-PyPz)$_2$(Py)$_2$] and the trivalent lanthanide containing 3D frameworks $^3_\infty$[Ln(4-PyPz)$_3$] and $^3_\infty$[Ln(3-PyPz)$_3$], Ln = Ce^{3+}, Pr^{3+}, Nd^{3+}, Ho^{3+}, Er^{3+}, Tm^{3+}, $^3_\infty$[La(4-PyPz)$_3$], as well as the 2D networks $^2_\infty$[Ln(4-PyPz)$_3$(Py)], Ln = Ce^{3+}, Tm^{3+} and $^2_\infty$[Ln$_2$(4-PyPz)$_6$]·Py, Ln = Yb^{3+}, Lu^{3+} were synthesized by redox reactions between the elemental lanthanide and the ligand 3-(4-pyridyl)pyrazole (4-PyPzH) or 3-(3-pyridyl)pyrazole (3-PyPzH). The 18 coordination polymers were synthesized in a solvothermal processes in pyridine, in which the latter can act as a co-ligand. Uncommon NIR emission for Tm^{3+} and Ho^{3+} was detected along with additional Pr^{3+}, Er^{3+}, and Nd^{3+} NIR emission benefited from a good ligand sensitizing effect. In addition, Ce^{3+}-based coordination polymers showed strong reductions in the 5d excited state, resulting in a distinctive pink to orange emission. Magnetic studies conducted with direct current (DC) showed magnetic isolation of the lanthanide centers in $^3_\infty$[Ln(3-PyPz)$_3$], Ln = Dy, Ho, Er. In summary, coordination polymers with pyridylpyrazolate ligands as N-donors can display a wide range of photoluminescent properties.

Supplementary Materials: The following supporting information can be downloaded at: https://www.mdpi.com/article/10.3390/chemistry5020069/s1, additional experimental details; Tables S1–S11: Crystallographic data and selected interatomic distances (pm) and angles (°) of $^2_\infty$[Eu(4-PyPz)$_2$(Py)$_2$] (**4-Eu^{2+}**), $^2_\infty$[Ln$_2$(4-PyPzH)$_6$]·Py, Ln = Yb (**4-Yb**) and Lu (**4-Lu**), $^2_\infty$[Tm(4-PyPz)$_3$(Py)] (**4-$^2_\infty$Tm**), $^3_\infty$[Ln(4-PyPz)$_3$], Ln = La (**4-La**), Ce (**4-Ce**), Pr (**4-Pr**), Nd (**4-Nd**), Ho (**4-Ho**), Er (**4-Er**), and $^3_\infty$[Ln(3-PyPz)$_3$], Ln = Ce (**3-Ce**), Pr (**3-Pr**), Nd (**3-Nd**), Ho (**3-Ho**), Er (**3-Er**), Tm (**3-Tm**); Figure S1: Extended coordination sphere of Ce^{3+} in $^3_\infty$[Ce(4-PyPz)$_3$] (**4-Ce**) representing the series of isotypic framework compounds (**4**, Ln = La, Ce, Pr, Nd, Ho, Er, Tm). The coordination polyhedra around Ce^{3+} is indicated in green and the thermal ellipsoids describe a 50% probability level of the atoms. Symmetry operations: I x + 1/2, −y + 1/2, z + 1/2 II −x + 3/2, y − 1/2, −z + 3/2 III x + 1, y, z; Figure S2: Extended coordination sphere of Ce^{3+} in $^3_\infty$[Ce(3-PyPz)$_3$] (**3-Ce**) representing the series of isotypic framework compounds (**3**, Ln = Ce, Pr, Nd, Ho, Er, Tm). The coordination polyhedra around Ce^{3+} is indicated in green and the thermal ellipsoids describe a 50% probability level of the atoms. Symmetry operations: I −z + 1, x + 1/2, −y + 3/2 II y − 1/2, −z + 3/2, −x + 1 III x − 1/2, y, −z + 3/2 IV y − 1/2, z, −x + 3/2 V z − 1/2, x, −y + 3/2; Figure S3: Comparison of the experimental X-ray powder diffraction pattern of $^3_\infty$[Ln(3-PyPz)$_3$] (**3**, Ln = Pr, Nd, Ho, Er, Tm) at RT with the simulated pattern from the single-crystal X-ray data of $^3_\infty$[Er(3-PyPz)$_3$] (**3-Er**) at 100 K; Figures S4–S8: Pawley refinement results for PXRD of $^3_\infty$[Ln(4-PyPz)$_3$], Ln = La (**4-La**), Pr (**4-Pr**), Nd (**4-Nd**), Ho (**4-Ho**), and Er (**4-Er**) showing the experimental data (black) together with the Pawley fit (red), the corresponding difference plot (blue), as well as hkl position markers (green); Table S12: Pawley refinement results for $^2_\infty$[Eu(4-PyPz)$_2$(Py)$_2$] (**4-Eu^{2+}**), $^2_\infty$[Ce(4-PyPz)$_3$(Py)] (**4-$^2_\infty$Ce**), and $^3_\infty$[Ln(4-PyPz)$_3$] (**4**, Ln = La, Pr, Nd, Ho, Er, Tm); Figure S9: Comparison of the experimental X-ray powder diffraction pattern of $^2_\infty$[Tm(4-PyPz)$_3$(Py)] (**4-$^2_\infty$Tm**), $^2_\infty$[Ln$_2$(4-PyPzH)$_6$]·Py, Ln = Yb (**4-Yb**) and Lu (**4-Lu**) at RT with the respective simulated pattern from single-crystal X-ray data at 100 K; Figures S10–S23: Absorption spectra of 4-PyPzH, $^2_\infty$[Eu(4-PyPz)$_2$(Py)$_2$] (**4-Eu^{2+}**), $^2_\infty$[Ce(4-PyPz)$_3$(Py)] (**4-$^2_\infty$Ce**), $^3_\infty$[Ln(4-PyPz)$_3$], (**4**, Ln = Ce, Pr, Nd, Ho, Er, Tm) and $^3_\infty$[Ln(3-PyPz)$_3$], (**3**, Ln = Ce, Pr, Nd, Ho, Er) in the solid state at room temperature; Figure

S24: Chromaticity coordinate diagram (CIE 1931) of the emission colors of $^{2}_{\infty}$[Ce(4-PyPz)$_3$(Py)] (**4-$^{2}_{\infty}$Ce**), $^{3}_{\infty}$[Ce(4-PyPz)$_3$] (**4-Ce**) and $^{3}_{\infty}$[Ce(3-PyPz)$_3$] (**3-Ce**); Table S13: Chromaticity coordinates (x,y) for $^{2}_{\infty}$[Ce(4-PyPz)$_3$(Py)] (**4-$^{2}_{\infty}$Ce**), $^{3}_{\infty}$[Ce(4-PyPz)$_3$] (**4-Ce**), and $^{3}_{\infty}$[Ce(3-PyPz)$_3$] (**3-Ce**); Figures S25–S38: Normalized excitation and emission spectra of $^{2}_{\infty}$[Eu(4-PyPz)$_2$(Py)$_2$] (**4-Eu^{2+}**), $^{2}_{\infty}$[Ce(4-PyPz)$_3$(Py)] (**4-$^{2}_{\infty}$Ce**), $^{3}_{\infty}$[Ln(4-PyPz)$_3$], (**4**, Ln = La, Ce, Pr, Nd, Ho, Er, Tm) and $^{3}_{\infty}$[Ln(3-PyPz)$_3$], (**3**, Ln = Ce, Pr, Nd, Ho, Er) at room temperature (top) and 77 K (bottom). Wavelengths at which the spectra were recorded are reported in the legends; Table S14: Photophysical data of $^{2}_{\infty}$[Eu(4-PyPz)$_2$(Py)$_2$] (**4-Eu^{2+}**), $^{2}_{\infty}$[Ce(4-PyPz)$_3$(Py)] (**4-$^{2}_{\infty}$Ce**), $^{3}_{\infty}$[Ln(4-PyPz)$_3$], (**4**, Ln = La, Ce, Pr, Nd, Ho, Er, Tm) and $^{3}_{\infty}$[Ln(3-PyPz)$_3$], (**3**, Ln = Ce, Pr, Nd, Ho, Er) in the solid state at room temperature and 77 K; Figures S39–S54: The infrared spectrum (ATR) of $^{2}_{\infty}$[Eu(4-PyPz)$_2$(Py)$_2$] (**4-Eu^{2+}**), $^{2}_{\infty}$[Ce(4-PyPz)$_3$(Py)] (**4-$^{2}_{\infty}$Ce**), $^{3}_{\infty}$[Ln(4-PyPz)$_3$], (**4**, Ln = La, Ce, Pr, Nd, Ho, Er, Tm), $^{3}_{\infty}$[Ln(3-PyPz)$_3$], (**3**, Ln = Ce, Pr, Nd, Ho, Er), 3-PyPzH, and 4-PyPzH.

Author Contributions: Conceptualization, K.M.-B. and H.Y.; methodology, H.Y.; software, H.Y. and J.B.; validation, H.Y.; formal analysis, H.Y. and C.P.; investigation, H.Y.; resources, I.V.T., F.K., and K.M.-B.; data curation, H.Y. and J.B.; writing—original draft preparation, H.Y.; writing—review and editing, H.Y., J.B., I.V.T., C.P., F.K. and K.M.-B.; visualization, H.Y.; supervision, K.M.-B.; project administration, K.M.-B. All authors have read and agreed to the published version of the manuscript.

Funding: This research was funded by the Deutsche Forschungsgemeinschaft DFG, grant No. MU-1562/7-2. H.Y. was awarded a PhD fellowship by the Egyptian Ministry of Higher Education (MoHE) and the German Academic Exchange Service (DAAD) within the German Egyptian Research Long-term Scholarship (GERLS) Program, 2017 (57311832), the funding agency is the German Academic Exchange Service Cairo. In the 14th round of applications, H.Y. was awarded a dissertation completion grant offered on the basis of JLU's Gender Equality Concept. The synthesis of the studied ligand was funded by the Russian Science Foundation (project No. 19–13–00272).

Data Availability Statement: CCDC 2237763 (**4-Eu^{2+}**), 2237764 (**4-$^{2}_{\infty}$Tm**), 2237765 (**4-Yb**), 2237766 (**4-Lu**), 2237767 (**4-La**), 2237768 (**4-Ce**), 2237769 (**4-Pr**), 2237770 (**4-Nd**), 2237771 (**4-Ho**), 2237772 (for **4-Er**), 2237773 (**3-Ce**), 2237774 (**3-Pr**), 2237775 (**3-Nd**), 2237776 (**3-Ho**), 2237777 (for **3-Er**), and 2237778 (**3-Tm**) contain the supplementary crystallographic data for this paper. These data can be obtained free of charge via http://www.ccdc.cam.ac.uk/conts/retrieving.html (or from the CCDC, 12 Union Road, Cambridge, CB2 1EZ, UK; Fax: +44 1223 336033; email: deposit@ccdc.cam.ac.uk).

Conflicts of Interest: The authors declare no conflict of interest.

References

1. Millward, J.M.; Ariza de Schellenberger, A.; Berndt, D.; Hanke-Vela, L.; Schellenberger, E.; Waiczies, S.; Taupitz, M.; Kobayashi, Y.; Wagner, S.; Infante-Duarte, C. Application of europium-doped very small iron oxide nanoparticles to visualize neuroinflammation with MRI and fluorescence microscopy. *Neuroscience* **2017**, *403*, 136–144. https://doi.org/10.1016/j.neuroscience.2017.12.014.
2. Lenora, C.U.; Carniato, F.; Shen, Y.; Latif, Z.; Haacke, E.M.; Martin, P.D.; Botta, M.; Allen, M.J. Structural features of europium(II)-containing cryptates that influence relaxivity. *Chem. Eur. J.* **2017**, *23*, 15404–15414. https://doi.org/10.1002/chem.201702158.
3. Acharjya, A.; Corbin, B.A.; Prasad, E.; Allen, M.J.; Maity, S. Solvation-controlled emission of divalent europium salts. *J. Photochem. Photobiol. A* **2022**, *429*, 113892–113899. https://doi.org/10.1016/j.jphotochem.2022.113892.
4. Dorenbos, P. Anomalous luminescence of Eu^{2+} and Yb^{2+} in inorganic compounds. *J. Phys. Condens. Matter* **2003**, *15*, 2645–2665. https://doi.org/10.1088/0953-8984/15/17/318.
5. Qin, X.; Liu, X.; Huang, W.; Bettinelli, M.; Liu, X. Lanthanide-activated phosphors based on 4f-5d optical transitions: Theoretical and experimental aspects. *Chem. Rev.* **2017**, *117*, 4488–4527. https://doi.org/10.1021/acs.chemrev.6b00691.
6. Zurawski, A.; Mai, M.; Baumann, D.; Feldmann, C.; Müller-Buschbaum, K. Homoleptic imidazolate frameworks $^{3}_{\infty}$[$Sr_{1-x}Eu_x$(Im)$_2$]—hybrid materials with efficient and tuneable luminescence. *Chem. Commun.* **2011**, *47*, 496–498. https://doi.org/10.1039/c0cc02093a.
7. Kajdas, C.; Furey, M.J.; Ritter, A.L.; Molina, G.J. Triboemission as a basic part of the boundary friction regime. *Lubr. Sci.* **2002**, *14*, 223–254. https://doi.org/10.1002/ls.3010140209.
8. Galimov, D.I.; Yakupova, S.M.; Vasilyuk, K.S.; Bulgakov, R.G. A novel gas assay for ultra-small amounts of molecular oxygen based on the chemiluminescence of divalent europium. *J. Photochem. Photobiol. A* **2021**, *418*, 113430–113437. https://doi.org/10.1016/j.jphotochem.2021.113430.
9. Eliseeva, S.V.; Bünzli, J.-C.G. Lanthanide luminescence for functional materials and bio-sciences. *Chem. Soc. Rev.* **2010**, *39*, 189–227. https://doi.org/10.1039/b905604c.

10. Bünzli, J.C.G.; Piguet, C. Taking advantage of luminescent lanthanide ions. *Chem. Soc. Rev.* **2005**, *34*, 1048–1077. https://doi.org/10.1039/b406082m.
11. Carnall, W.T.; Fields, P.R.; Rajnak, K. Electronic energy levels in the trivalent lanthanide aquo Ions. I. Pr^{3+}, Nd^{3+}, Pm^{3+}, Sm^{3+}, Dy^{3+}, Ho^{3+}, Er^{3+}, and Tm^{3+}. *J. Chem. Phys.* **1968**, *49*, 4424–4442. https://doi.org/10.1063/1.1669893.
12. Feng, J.; Zhang, H.-J.; Song, S.-Y.; Li, Z.-F.; Sun, L.-N.; Xing, Y.; Guo, X.-M. Syntheses, crystal structures, visible and near-IR luminescent properties of ternary lanthanide (Dy^{3+}, Tm^{3+}) complexes containing 4,4,4-trifluoro-1-phenyl-1,3-butanedione and 1,10-phenanthroline. *J. Lumin.* **2008**, *128*, 1957–1964. https://doi.org/10.1016/j.jlumin.2008.06.006.
13. Serra, O.A.; Nassar, E.J.; Calefi, P.S.; Rosa, I.L.V. Luminescence of a new Tm^{3+} β-diketonate compound. *J. Alloys Compd.* **1998**, *275–277*, 838–840. https://doi.org/10.1016/S0925-8388(98)00453-8.
14. Youssef, H.; Schäfer, T.; Becker, J.; Sedykh, A.E.; Basso, L.; Pietzonka, C.; Taydakov, I.V.; Kraus, F.; Müller-Buschbaum, K. 3D-Frameworks and 2D-networks of lanthanide coordination polymers with 3-pyridylpyrazole: Photophysical and magnetic properties. *Dalton Trans.* **2022**, *51*, 14673–14685. https://doi.org/10.1039/D2DT01999J.
15. Ridenour, J.A.; Carter, K.P.; Butcher, R.J.; Cahill, C.L. RE-*p*-halobenzoic acid–terpyridine complexes, Part II: Structural diversity, supramolecular assembly, and luminescence properties in a series of *p*-bromobenzoic acid rare-earth hybrid materials. *CrystEngComm* **2017**, *19*, 1172–1189. https://doi.org/10.1039/C6CE02355J.
16. Batrice, R.J.; Adcock, A.K.; Cantos, P.M.; Bertke, J.A.; Knope, K.E. Synthesis and characterization of an isomorphous lanthanide-thiophenemonocarboxylate series (Ln = La–Lu, except Pm) amenable to color tuning. *Cryst. Growth Des.* **2017**, *17*, 4603–4612. https://doi.org/10.1021/acs.cgd.7b00400.
17. Kawamura, Y.; Wada, Y.; Hasegawa, Y.; Iwamuro, M.; Kitamura, T.; Yanagida, S. Observation of neodymium electroluminescence. *Appl. Phys. Lett.* **1999**, *74*, 3245–3247. https://doi.org/10.1063/1.123357.
18. Curry, R.; Gillin, W.P. 1.54 μm electroluminescence from erbium (III) tris(8-hydroxyquinoline) (ErQ)-based organic light-emitting diodes. *Appl. Phys. Lett.* **1999**, *75*, 1380–1382. https://doi.org/10.1063/1.124700.
19. Mehrdel, B.; Nikbakht, A.; Aziz, A.A.; Jameel, M.S.; Dheyab, M.A.; Khaniabadi, P.M. Upconversion lanthanide nanomaterials: Basics introduction, synthesis approaches, mechanism and application in photodetector and photovoltaic devices. *Nanotechnology* **2021**, *33*, 082001. https://doi.org/10.1088/1361-6528/ac37e3.
20. Fischer, S.; Ivaturi, A.; Fröhlich, B.; Rüdiger, M.; Richter, A.; Krämer, K.W.; Richards, B.S.; Goldschmidt, J.C. Upconverter silicon solar cell devices for efficient utilization of sub-band-gap photons under concentrated solar radiation. *IEEE J. Photovolt.* **2013**, *4*, 183–189. https://doi.org/10.1109/JPHOTOV.2013.2282744.
21. Bünzli, J.-C.G.; Eliseeva, S.V. Basics of lanthanide photophysics. In *Springer Series on Fluorescence: Lanthanide Luminescence: Photophysical, Analytical and Biological Aspects*; Wolfbeis, O.S., Hof, M., Eds.; Springer: Berlin/Heidelberg, Germany, 2011; Volume 7, pp. 1–46.
22. Davies, G.M.; Aarons, R.J.; Motson, G.R.; Jeffery, J.C.; Adams, H.; Faulkner, S.; Ward, M.D. Structural and near-IR photophysical studies on ternary lanthanide complexes containing poly (pyrazolyl) borate and 1,3-diketonate ligands. *Dalton Trans.* **2004**, *4*, 1136–1144. https://doi.org/10.1039/B400992D.
23. Bao, S.; Liang, Y.; Wang, L.; Wang, L.; Xu, L.; Wang, Y.; Liang, X.; Xiang, W. Superhigh-luminance Ce:YAG phosphor in glass and phosphor-in-glass film for laser lighting. *ACS Sustain. Chem. Eng.* **2022**, *10*, 8105–8114. https://doi.org/10.1021/acssuschemeng.2c02657.
24. Li, J.; Wang, L.; Zhao, Z.; Sun, B.; Zhan, G.; Liu, H.; Bian, Z.; Liu, Z. Highly efficient and air-stable Eu(II)-containing azacryptates ready for organic light-emitting diodes. *Nat. Commun.* **2020**, *11*, 5218–5225. https://doi.org/10.1038/s41467-020-19027-x.
25. Meyer, L.V.; Schönfeld, F.; Zurawski, A.; Mai, M.; Feldmann, C.; Müller-Buschbaum, K. A blue luminescent MOF as a rapid turn-off/turn-on detector for H_2O, O_2 and CH_2Cl_2, MeCN: $^{3}_{\infty}$[Ce(Im)$_3$ImH]·ImH. *Dalton Trans.* **2015**, *44*, 4070–4079. https://doi.org/10.1039/c4dt03578j.
26. Matthes, P.R.; Müller-Buschbaum, K. Synthesis and characterization of the cerium(III) UV-emitting 2D-coordination polymer $^{2}_{\infty}$[Ce_2Cl_6(4,4′-bipyridine)$_4$]·py. *Z. Anorg. Allg. Chem.* **2014**, *640*, 2847–2851. https://doi.org/10.1002/zaac.201400375.
27. Zhao, Z.; Wang, L.; Zhan, G.; Liu, Z.; Bian, Z.; Huang, C. Efficient rare earth cerium(III) complex with nanosecond *d*−*f* emission for blue organic light-emitting diodes. *Natl. Sci. Rev.* **2021**, *8*, nwaa193. https://doi.org/10.1093/nsr/nwaa193.
28. Frey, S.T.; Horrocks Jr., W.D. Complexation, luminescence, and energy transfer of Ce^{3+} with a series of multidentate amino phosphonic acids in aqueous solution. *Inorg. Chem.* **1991**, *30*, 1073–1079. https://doi.org/10.1021/ic00005a036.
29. Wang, Q.; Wu, W.; Zhang, J.; Zhu, G.; Cong, R. Formation, photoluminescence and ferromagnetic characterization of Ce doped AlN hierarchical nanostructures. *J. Alloys Compd.* **2019**, *775*, 498–502. https://doi.org/10.1016/j.jallcom.2018.10.110.
30. Vadan, M.; Popovici, E.J.; Ungur, L.; Vasilescu, M.; Macarovici, D. Synthesis of luminescent strontium-magnesium orthophosphate activated with cerium and manganese. In Proceedings of the SIOEL'99: Sixth Symposium on Optoelectronics, Bucharest, Romania, 22–24 September 1999; pp. 111–116.
31. Youssef, H.; Sedykh, A.E.; Becker, J.; Taydakov, I.V.; Müller-Buschbaum, K. 3-(2-pyridyl)pyrazole based luminescent 1D-coordination polymers and polymorphic complexes of various lanthanide chlorides including orange-emitting cerium(III). *Inorganics* **2022**, *10*, 254–275. https://doi.org/10.3390/inorganics10120254.
32. Youssef, H.; Becker, J.; Sedykh, A.E.; Schäfer, T.; Taydakov, I.V.; Müller-Buschbaum, K. Red emitting cerium(III) and versatile luminescence chromaticity of 1D-coordination polymers and heterobimetallic Ln/AE pyridylpyrazolate complexes. *Z. Anorg. Allg. Chem.* **2022**, *648*, e202200295. https://doi.org/10.1002/zaac.202200295.

33. Youssef, H.; Sedykh, A.E.; Becker, J.; Schäfer, T.; Taydakov, I.V.; Li, H.R.; Müller-Buschbaum, K. Variable luminescence and chromaticity of homoleptic frameworks of the lanthanides together with pyridylpyrazolates. *Chem. Eur. J.* **2021**, *27*, 16634–16641. https://doi.org/10.1002/chem.202103068.
34. Shannon, R.D. Revised effective ionic radii and systematic studies of interatomic distances in halides and chalcogenides. *Acta Crystallogr. Sect. A Cryst. Phys. Diffr. Theor. Gen. Crystallogr.* **1976**, *32*, 751–767. https://doi.org/10.1107/S0567739476001551.
35. Guo, Z.; Blair, V.L.; Deacon, G.B.; Junk, P.C. Europium is different: Solvent and ligand effects on oxidation state outcomes and C-F activation in reactions between europium metal and pentafluorophenylsilver. *Chem. Eur. J.* **2022**, *28*, e202103865. https://doi.org/10.1002/chem.202103865.
36. Drew, M.G.B.; Guillaneux, D.; Hudson, M.J.; Iveson, P.B.; Russell, M.L.; Madic, C. Lanthanide(III) complexes of a highly efficient actinide(III) extracting agent—2,6-bis(5,6-dipropyl-1,2,4-triazin-3-yl)pyridine. *Inorg. Chem. Commun.* **2001**, *4*, 12–15. https://doi.org/10.1016/S1387-7003(00)00181-7.
37. O'Keeffe, M.; Peskov, M.A.; Ramsden, S.J.; Yaghi, O.M. The reticular chemistry structure resource (RCSR) database of, and symbols for, crystal nets. *Acc. Chem. Res.* **2008**, *41*, 1782–1789. https://doi.org/10.1021/ar800124u.
38. Wells, A.F. *Three-Dimensional Nets and Polyhedra*; Wiley-Interscience: New York, NY, USA, 1977.
39. Guo, Z.; Luu, J.; Blair, V.; Deacon, G.B.; Junk, P.C. Replacing mercury: Syntheses of lanthanoid pyrazolates from free lanthanoid metals, pentafluorophenylsilver, and pyrazoles, aided by a facile synthesis of polyfluoroarylsilver compounds. *Eur. J. Inorg. Chem.* **2019**, *2019*, 1018–1029. https://doi.org/10.1002/ejic.201801481.
40. Jiménez, J.R.; Díaz-Ortega, I.F.; Ruiz, E.; Aravena, D.; Pope, S.J.A.; Colacio, E.; Herrera, J.M. Lanthanide tetrazolate complexes combining single-molecule magnet and luminescence properties: The effect of the replacement of tetrazolate N_3 by β-diketonate ligands on the anisotropy energy barrier. *Chem. Eur. J.* **2016**, *22*, 14548–14559. https://doi.org/10.1002/chem.201601457.
41. Hughes, I.D.; Däne, M.; Ernst, A.; Hergert, W.; Lüders, M.; Poulter, J.; Staunton, J.B.; Svane, A.; Szotek, Z.; Temmerman, W.M. Lanthanide contraction and magnetism in the heavy rare earth elements. *Nature* **2007**, *446*, 650–653. https://doi.org/10.1038/nature05668.
42. Carnall, W.T.; Fields, P.R.; Rajnak, K. Electronic energy levels of the trivalent lanthanide aquo ions. IV. Eu^{3+}. *J. Chem. Phys.* **1968**, *49*, 4450–4455. https://doi.org/10.1063/1.1669896.
43. Carnall, W.T.; Fields, P.R.; Rajnak, K. Electronic energy levels of the trivalent lanthanide aquo ions. III. Tb^{3+}. *J. Chem. Phys.* **1968**, *49*, 4447–4449. https://doi.org/10.1063/1.1669895.
44. Seidel, C.; Lorbeer, C.; Cybińska, J.; Mudring, A.-V.; Ruschewitz, U. Lanthanide coordination polymers with tetrafluoroterephthalate as a bridging ligand: Thermal and optical properties. *Inorg. Chem.* **2012**, *51*, 4679–4688. https://doi.org/10.1021/ic202655d.
45. Huskowska, E.; Turowska-Tyrk, I.; Legendziewicz, J.; Riehl, J.P. The structure and spectroscopy of lanthanide(III) complexes with 2,2′-bipyridine-1,1′-dioxide in solution and in the solid state: Effects of ionic size and solvent on photophysics, ligand structure and coordination. *New J. Chem.* **2002**, *26*, 1461–1467. https://doi.org/10.1039/B201846M.
46. Fernández-Fernández, M.d.C.; Bastida, R.; Macías, A.; Pérez-Lourido, P.; Platas-Iglesias, C.; Valencia, L. Lanthanide(III) complexes with a tetrapyridine pendant-armed macrocyclic ligand: ^{1}H NMR structural determination in solution, X-ray diffraction, and density-functional theory calculations. *Inorg. Chem.* **2006**, *45*, 4484–4496. https://doi.org/10.1021/ic0603508.
47. Bochkarev, M.N.; Khoroshenkov, G.V.; Schumann, H.; Dechert, S. A novel bis(imino)amine ligand as a result of acetonitrile coupling with the diiodides of Dy(II) and Tm(II). *J. Am. Chem. Soc.* **2003**, *125*, 2894–2895. https://doi.org/10.1021/ja028311s.
48. Sedykh, A.E.; Kurth, D.G.; Müller-Buschbaum, K. Two series of lanthanide coordination polymers and complexes with 4′-phenylterpyridine and their luminescence properties. *Eur. J. Inorg. Chem.* **2019**, *2019*, 4564–4571. https://doi.org/10.1002/ejic.201900872.
49. Matthes, P.R.; Eyley, J.; Klein, J.H.; Kuzmanoski, A.; Lambert, C.; Feldmann, C.; Müller-Buschbaum, K. Photoluminescent one-dimensional coordination polymers from suitable pyridine antenna and $LnCl_3$ for visible and near-IR emission. *Eur. J. Inorg. Chem.* **2015**, *2015*, 826–836. https://doi.org/10.1002/ejic.201402973.
50. Bünzli, J.-C.G.; Comby, S.; Chauvin, A.-S.; Vandevyver, C.D.B. New Opportunities for Lanthanide Luminescence. *J. Rare Earths* **2007**, *25*, 257–274. https://doi.org/10.1016/S1002-0721(07)60420-7.
51. Dexter, D.L. A theory of sensitized luminescence in solids. *J. Chem. Phys.* **1953**, *21*, 836–850. https://doi.org/10.1063/1.1699044.
52. Dang, S.; Yu, J.; Wang, X.; Sun, L.; Deng, R.; Feng, J.; Fan, W.; Zhang, H. NIR-luminescence from ternary lanthanide [Ho^{III}, Pr^{III} and Tm^{III}] complexes with 1-(2-naphthyl)-4,4,4-trifluoro-1,3-butanedionate. *J. Lumin.* **2011**, *131*, 1857–1863. https://doi.org/10.1016/j.jlumin.2011.04.018.
53. Kahn, O. *Molecular Magnetism*; Wiley-VCH: Weinheim, Germany, 1993.
54. Pham, Y.H.; Trush, V.A.; Carneiro Neto, A.N.; Korabik, M.; Sokolnicki, J.; Weselski, M.; Malta, O.L.; Amirkhanov, V.M.; Gawryszewska, P. Lanthanide complexes with N-phosphorylated carboxamide as UV converters with excellent emission quantum yield and single-ion magnet behavior. *J. Mater. Chem. C* **2020**, *8*, 9993–10009. https://doi.org/10.1039/D0TC01445A.
55. Benelli, C.; Gatteschi, D. Magnetism of lanthanides in molecular materials with transition-metal ions and organic radicals. *Chem. Rev.* **2002**, *102*, 2369–2388. https://doi.org/10.1021/cr010303r.
56. Del Giudice, M.R.; Mustazza, C.; Borioni, A.; Gatta, F.; Tayebati, K.; Amenta, F.; Tucci, P.; Pieretti, S. Synthesis of 1-methyl-5-(pyrazol-3-and-5-yl- and 1,2,4-triazol-3- and 5-yl)-1,2,3,6-tetrahydropyridine derivatives and their evaluation as muscarinic receptor ligands. *Arch. Pharm. Pharm. Med. Chem.* **2003**, *336*, 143–154. https://doi.org/10.1002/ardp.200390013.

57. Bauer, V.J.; Dalalian, H.P.; Fanshawe, W.J.; Safir, S.R.; Tocus, E.C.; Boshart, C.R. 4-[3(5)-Pyrazolyl]pyridinium salts. A new class of hypoglycemic agents. *J. Med. Chem.* **1968**, *11*, 981–984. https://doi.org/10.1021/jm00311a015.
58. Sheldrick, G.M. SHELXT—Integrated space-group and crystal-structure determination. *Acta Crystallogr. Sect. A Found. Crystallogr.* **2015**, *71*, 3–8. https://doi.org/10.1107/S2053273314026370.
59. Sheldrick, G.M. Crystal structure refinement with SHELXL. *Acta Crystallogr. Sect. C Struct. Chem.* **2015**, *71*, 3–8. https://doi.org/10.1107/S2053229614024218.
60. Spek, A.L. PLATON SQUEEZE: A tool for the calculation of the disordered solvent contribution to the calculated structure factors. *Acta Crystallogr. Sect. C Struct. Chem.* **2015**, *71*, 9–18. https://doi.org/10.1107/S2053229614024929.
61. Spek, A.L. Structure validation in chemical crystallography. *Acta Crystallogr. Sect. D Biol. Crystallogr.* **2009**, *65*, 148–155. https://doi.org/10.1107/S090744490804362X.
62. Spek, A.L. What makes a crystal structure report valid? *Inorg. Chim. Acta* **2018**, *470*, 232–237. https://doi.org/10.1016/j.ica.2017.04.036.
63. Spek, A.L. CheckCIF validation ALERTS: What they mean and how to respond. *Acta Crystallogr. Sect. E Crystallogr. Commun.* **2020**, *76*, 1–11. https://doi.org/10.1107/S2056989019016244.
64. Spek, A.L. Single-crystal structure validation with the program PLATON. *J. Appl. Crystallogr.* **2003**, *36*, 7–13. https://doi.org/10.1107/S0021889802022112.
65. Blatov, V.A.; Shevchenko, A.P.; Proserpio, D.M. Applied topological analysis of crystal structures with the program package topospro. *Cryst. Growth Des.* **2014**, *14*, 3576–3586. https://doi.org/10.1021/cg500498k.
66. Pennington, W.T. DIAMOND—Visual crystal structure information system. *J. Appl. Crystallogr.* **1999**, *32*, 1028–1029. https://doi.org/10.1107/s0021889899011486.
67. Coelho, A.A. TOPAS and TOPAS-Academic: An optimization program integrating computer algebra and crystallographic objects written in C++. *J. Appl. Crystallogr.* **2018**, *51*, 210–218. https://doi.org/10.1107/S1600576718000183.

Table of Contents

Experimental section

Analytical Data

CHN Analysis: Carbon, hydrogen, and nitrogen elemental analyses were performed using a Thermo Scientific Flash EA – 1112. The polymers were placed in a tin crucible with no less than one mass equivalent to V_2O_5. The samples were prepared and stored under inert conditions until the time of measurements.

Vibrational Spectroscopy: ALPHA FT-IR spectrometer from Bruker optics (ATR module) using OPUS software was used to record MIR spectra from several milligrams of the compounds.

Crystallographic Data

CCDC 2237763 (**4-Eu²⁺**), 2237764 (**4-²∞Tm**), 2237765 (**4-Yb**), 2237766 (**4-Lu**), 2237767 (**4-La**), 2237768 (**4-Ce**), 2237769 (**4-Pr**), 2237770 (**4-Nd**), 2237771 (**4-Ho**), 2237772 (**4-Er**), 2237773 (**3-Ce**), 2237774 (**3-Pr**), 2237775 (**3-Nd**), 2237776 (**3-Ho**), 2237777 (**3-Er**), and 2237778 (**3-Tm**) contain the supplementary crystallographic data. These data are provided free of charge by the Cambridge Crystallographic Data Centre.

Table S1. Crystallographic data of $^{2}_{\infty}$[Eu(4-PyPz)$_2$(Py)$_2$] (**4-Eu²⁺**) and $^{2}_{\infty}$[Ln$_2$(4-PyPzH)$_6$]·Py, Ln = Yb (**4-Yb**) and Lu (**4-Lu**).

Compound	**$^{2}_{\infty}$[Eu(4-PyPz)$_2$(Py)$_2$]**	**$^{2}_{\infty}$[Yb$_2$(4-PyPzH)$_6$]·Py**	**$^{2}_{\infty}$[Lu$_2$(4-PyPzH)$_6$]·Py**
CCDC number	2237763	2237765	2237766
Empirical formula	$C_{26}H_{22}N_8Eu$	$C_{53}H_{41}N_{19}Yb_2$	$C_{53}H_{41}N_{19}Lu_2$
M_r / g·mol^{-1}	598.47	1290.13	1293.99
T / K	100(2)	100(2)	100(2)
λ / pm	71.073, Mo-K$_\alpha$	71.073, Mo-K$_\alpha$	71.073 Mo-K$_\alpha$
Crystal system	Monoclinic	Monoclinic	Monoclinic
Space group	$P2_1$	$P2_1/n$	$P2_1/n$
a / pm	944.4(1)	1701.5(2)	1702.1(2)
b / pm	1458.4(1)	910.7(1)	909.5(1)
c / pm	997.6(1)	3161.8(4)	3155.2(4)
α, γ / °	90	90	90
β / °	117.170(4)	97.289(5)	97.109(4)
V / 10^6 pm^3	1222.4(2)	4859(1)	4846.9(9)
Z	2	4	4
ρ_{calc} / g·cm^{-3}	1.626	1.763	1.773
μ / mm^{-1}	2.596	3.886	4.110
F(000)	594	2528	2536
Crystal size / mm^3	0.070 x 0.060 x 0.030	0.129 x 0.079 x 0.050	0.204 x 0.039 x 0.018
θ_{min} / °	2.295	2.157	2.163
θ_{max} / °	27.567	27.577	27.635
Reflections collected	44595	154420	164975
Independent reflections	5603	11219	11219
R(int)	0.0414	0.1890	0.1214
No. Of parameters	316	810	810
GOF	1.137	1.066	1.047
Final R indices [$I > 2\sigma(I)$]	R_1 = 0.0141, wR_2 = 0.0296	R_1 = 0.0515, wR_2 = 0.0849	R_1 = 0.0404, wR_2 = 0.0835

R indices (all data)	R_1 = 0.0159, wR_2 = 0.0302	R_1 = 0.1120, wR_2 = 0.1022	R_1 = 0.0734, wR_2 = 0.0962
$\Delta\rho_{max}$, $\Delta\rho_{min}$ / e·10^{-6}·pm^{-3}	0.734, –0.619	2.364, –1.425	2.721, –2.064

Table S2. Crystallographic data of $^{2}_{\infty}$[Tm(4-PyPz)$_3$(Py)] (**4-²∞Tm**).

Compound	**$^{2}_{\infty}$[Tm(4-PyPz)$_3$(Py)]**
CCDC number	2237764
Empirical formula	$C_{29}H_{23}N_{10}Tm$
M_r / g·mol^{-1}	680.50
T / K	100(2)
λ / pm	71.073, Mo-K$_\alpha$
Crystal system	Monoclinic
Space group	Cc
a / pm	1028.4(1)
b / pm	1507.8(1)
c / pm	1753.0(2)
α, γ / °	90
β / °	97.759(2)
V / 10^6 pm^3	2693.2(4)
Z	4
ρ_{calc} / g·cm^{-3}	1.678
μ / mm^{-1}	3.333
F(000)	1344
Crystal size / mm^3	0.055 x 0.023 x 0.020
θ_{min} / °	2.345
θ_{max} / °	27.160
Reflections collected	42246
Independent reflections	5807
R(int)	0.0860
Flack x	0.003(7)
No. Of parameters	361
GOF	1.039
Final R indices [$I > 2\sigma(I)$]	R_1 = 0.0286, wR_2 = 0.0472
R indices (all data)	R_1 = 0.0387, wR_2 = 0.0494
$\Delta\rho_{max}$, $\Delta\rho_{min}$ / e·10^{-6}·pm^{-3}	1.628, –0.744

Table S3. Crystallographic data of $^3_\infty$[Ln(4-PyPz)$_3$], Ln = La (**4-La**), Ce (**4-Ce**), Pr (**4-Pr**), and Nd (**4-Nd**).

Compound	$^3_\infty$[La(4-PyPz)$_3$]	$^3_\infty$[Ce(4-PyPz)$_3$]	$^3_\infty$[Pr(4-PyPz)$_3$]	$^3_\infty$[Nd(4-PyPz)$_3$]
CCDC number	2237767	2237768	2237769	2237770
Empirical formula	$C_{24}H_{18}N_9La$	$C_{24}H_{18}N_9Ce$	$C_{24}H_{18}N_9Pr$	$C_{24}H_{18}N_9Nd$
M_r / g·mol^{-1}	571.38	572.59	573.38	576.71
T / K	100(2)	100(2)	100(2)	100(2)
λ / pm	0.71073	0.71073	0.71073	0.71073
Crystal system	Monoclinic	Monoclinic	Monoclinic	Monoclinic
Space group	$P2_1/n$	$P2_1/n$	$P2_1/n$	$P2_1/n$
a / pm	934.0(2)	929.4(1)	927.9(2)	928.1(1)
b / pm	1693.2(3)	1689.7(1)	1687.5(2)	1689.6(2)
c / pm	1598.9(3)	1593.1(1)	1589.8(2)	1585.4(2)
α, γ / °	90	90	90	90
β / °	102.364(6)	102.384(2)	102.351(5)	102.289(4)
V / 10^6 pm^3	2469.9(7)	2443.6(2)	2431.5(6)	2429.1(4)
Z	4	4	4	4
ρ_{calc} / g·cm^{-3}	1.537	1.556	1.566	1.577
μ / mm^{-1}	1.759	1.893	2.034	2.168
F(000)	1128	1132	1136	1140
Crystal size / mm^3	0.026 x 0.013 x 0.010	0.042 x 0.021 x 0.017	0.055 x 0.022 x 0.015	0.789 x 0.147 x 0.075
θ_{min} / °	2.332	1.779	2.347	1.783
θ_{max} / °	26.501	27.103	27.533	27.485
Reflections collected	61095	85383	97993	61076
Independent reflections	5114	5395	5589	5565
R(int)	0.1635	0.1290	0.0941	0.0480
No. Of parameters	307	307	307	307
GOF	1.028	1.031	1.048	1.118
Final R indices [$I > 2\sigma(I)$]	R_1 = 0.0365, wR_2 = 0.0715	R_1 = 0.0290, wR_2 = 0.0530	R_1 = 0.0271, wR_2 = 0.0525	R_1 = 0.0225, wR_2 = 0.0509
R indices (all data)	R_1 = 0.0665, wR_2 = 0.0804	R_1 = 0.0491, wR_2 = 0.0585	R_1 = 0.0408, wR_2 = 0.0572	R_1 = 0.0276, wR_2 = 0.0528
$\Delta\rho_{max}$, $\Delta\rho_{min}$ / e·10^{-6}·pm^{-3}	1.611, –0.631	1.579, –0.661	1.651, –0.651	1.424, –0.898

Table S4. Crystallographic data of $^3_\infty$[Ln(4-PyPz)$_3$], Ln = Ho (**4-Ho**) and Er (**4-Er**).

Compound	$^3_\infty$[Ho(4-PyPz)$_3$]	$^3_\infty$[Er(4-PyPz)$_3$]
CCDC number	2237771	2237772
Empirical formula	$C_{24}H_{18}N_9Ho$	$C_{24}H_{18}N_9Er$
M_r / g·mol^{-1}	597.40	599.73
T / K	100(2)	100(2)
λ / pm	0.71073	0.71073
Crystal system	Monoclinic	Monoclinic
Space group	$P2_1/n$	$P2_1/n$
a / pm	915.9(2)	913.4(1)
b / pm	1674.0(2)	1673.0(2)
c / pm	1571.4(2)	1565.9(2)
α, γ / °	90	90
β / °	102.280(6)	102.156(5)
V / 10^6 pm^3	2354.2(6)	2339.3(3)
Z	4	4
ρ_{calc} / g·cm^{-3}	1.686	1.703
μ / mm^{-1}	3.392	3.619
F(000)	1168	1172
Crystal size / mm^3	0.114 x 0.070 x 0.034	0.116 x 0.073 x 0.043
θ_{min} / °	1.800	1.803
θ_{max} / °	27.557	27.377
Reflections collected	5422	5252
Independent reflections	5422	5252
No. Of parameters	308	308
GOF	1.111	1.053
Final R indices [$I > 2\sigma(I)$]	R_1 = 0.0296, wR_2 = 0.0603	R_1 = 0.0305, wR_2 = 0.0617
R indices (all data)	R_1 = 0.0398, wR_2 = 0.0641	R_1 = 0.0443, wR_2 = 0.0659
$\Delta\rho_{max}$, $\Delta\rho_{min}$ / e·10^{-6}·pm^{-3}	2.670, –1.636	2.145, –1.695

Table S5. Crystallographic data of $^3_\infty$[Ln(3-PyPz)$_3$], Ln = Ce (**3-Ce**), Pr (**3-Pr**), Nd (**3-Nd**), and Ho (**3-Ho**).

Compound	$^3_\infty$[Ce(3-PyPz)$_3$]	$^3_\infty$[Pr(3-PyPz)$_3$]	$^3_\infty$[Nd(3-PyPz)$_3$]	$^3_\infty$[Ho(3-PyPz)$_3$]
CCDC number	2237773	2237774	2237775	2237776
Empirical formula	$C_{24}H_{18}N_9Ce$	$C_{24}H_{18}N_9Pr$	$C_{24}H_{18}N_9Nd$	$C_{24}H_{18}N_9Ho$
M_r / g·mol^{-1}	572.59	573.38	576.71	597.40
T / K	100(2)	100(2)	100(2)	100(2)
λ / pm	0.71073	0.71073	0.71073	0.71073
Crystal system	Cubic	Cubic	Cubic	Cubic
Space group	$Pa\bar{3}$	$Pa\bar{3}$	$Pa\bar{3}$	$Pa\bar{3}$
a, b, c / pm	1724.8(1)	1720.9(1)	1717.9(1)	1698.8(1)
α, β, γ / °	90	90	90	90
V / 10^6 pm^3	5131.2(7)	5096.1(4)	5069.8(3)	4902.3(4)
Z	8	8	8	8
ρ_{calc} / g·cm^{-3}	1.482	1.495	1.511	1.619
μ / mm^{-1}	1.803	1.941	2.077	3.258
F(000)	2264	2272	2280	2336
Crystal size / mm^3	0.105 x 0.094 x 0.075	0.086 x 0.052 x 0.043	0.059 x 0.041 x 0.018	0.138 x 0.094 x 0.065
θ_{min} / °	2.045	2.050	2.053	2.076
θ_{max} / °	27.074	26.718	27.522	27.524
Reflections collected	37796	48365	86496	97322
Independent reflections	1889	1815	1955	1888
R(int)	0.1778	0.0775	0.0990	0.0644
No. Of parameters	103	103	103	103
GOF	1.065	1.096	1.100	1.066
Final R indices [$I > 2\sigma(I)$]	R_1 = 0.0399, wR_2 = 0.0669	R_1 = 0.0248, wR_2 = 0.0493	R_1 = 0.0266, wR_2 = 0.0506	R_1 = 0.0221, wR_2 = 0.0487
R indices (all data)	R_1 = 0.0808, wR_2 = 0.0784	R_1 = 0.0382, wR_2 = 0.0535	R_1 = 0.0427, wR_2 = 0.0555	R_1 = 0.0297, wR_2 = 0.0517
$\Delta\rho_{max}$, $\Delta\rho_{min}$ / e·10^{-6}·pm^{-3}	1.325, –0.530	0.674, –0.567	0.843, –0.546	0.799, –0.641

Table S6. Crystallographic data of $^3_\infty$[Ln(3-PyPz)$_3$], Ln = Er (**3-Er**) and Tm (**3-Tm**).

Compound	$^3_\infty$[Er(3-PyPz)$_3$]	$^3_\infty$[Tm(3-PyPz)$_3$]
CCDC number	2237777	2237778
Empirical formula	$C_{24}H_{18}N_9Er$	$C_{24}H_{18}N_9Tm$
M_r / g·mol^{-1}	599.73	601.40
T / K	100(2)	100(2)
λ / pm	0.71073	0.71073
Crystal system	Cubic	Cubic
Space group	$Pa\bar{3}$	$Pa\bar{3}$
a, b, c / pm	1695.5(1)	1695.2(4)
α, β, γ / °	90	90
V / 10^6 pm^3	4874.2(3)	4872(3)
Z	8	8
ρ_{calc} / g·cm^{-3}	1.635	1.640
μ / mm^{-1}	3.474	3.672
F(000)	2344	2352
Crystal size / mm^3	0.093 x 0.089 x 0.074	0.051 x 0.027 x 0.012
θ_{min} / °	2.080	2.081
θ_{max} / °	27.520	25.701
Reflections collected	30024	39425
Independent reflections	1883	1558
R(int)	0.0670	0.1755
No. Of parameters	103	103
GOF	1.098	1.070
Final R indices [$I > 2\sigma(I)$]	R_1 = 0.0247, wR_2 = 0.0481	R_1 = 0.0386, wR_2 = 0.0718
R indices (all data)	R_1 = 0.0382, wR_2 = 0.0521	R_1 = 0.0715, wR_2 = 0.0824
$\Delta\rho_{max}$, $\Delta\rho_{min}$ / e·10^{-6}·pm^{-3}	1.160, –0.601	1.580, –0.905

Interatomic Distances and Angles

Table S7. Selected interatomic distances (pm) and angles (°) of $^{2}_{\infty}$[Eu(4-PyPz)$_2$(Py)$_2$] (**4-Eu^{2+}**). Symmetry operations: I x+1,y,z II –x+1,y+1/2,–z.

Atoms	$^{2}_{\infty}$[Eu(4-PyPz)$_2$(Py)$_2$]	Atoms	$^{2}_{\infty}$[Eu(4-PyPz)$_2$(Py)$_2$]
Eu1-N1	270.0(2)	N3^{I}-Eu1-N4^{II}	157.2(1)
Eu1-N2^{I}	256.8(4)	N3^{I}-Eu1-N6	114.8(1)
Eu1-N3^{I}	264.1(2)	N3^{I}-Eu1-N7	116.0(1)
Eu1-N4^{II}	272.8(2)	N3^{I}-Eu1-N8	82.1(1)
Eu1-N5	254.9(4)	N4^{II}-Eu1-N8	79.8(1)
Eu1-N6	268.0(4)	N5-Eu1-N1	85.4(1)
Eu1-N7	272.3(4)	N5-Eu1-N2^{I}	90.4(1)
Eu1-N8	274.5(2)	N5-Eu1-N3^{I}	86.6(1)
N1-Eu1-N4^{II}	76.9(1)	N5-Eu1-N4^{II}	108.6(1)
N1-Eu1-N7	153.1(1)	N5-Eu1-N6	30.2(1)
N1-Eu1-N8	85.0(1)	N5-Eu1-N7	107.1(1)
N2^{I}-Eu1-N1	118.2(1)	N5-Eu1-N8	165.4(1)
N2^{I}-Eu1-N3^{I}	30.3(1)	N6-Eu1-N1	97.0(1)
N2^{I}-Eu1-N4^{II}	157.3(1)	N6-Eu1-N4^{II}	84.3(1)
N2^{I}-Eu1-N6	108.9(2)	N6-Eu1-N7	84.4(1)
N2^{I}-Eu1-N7	86.2(1)	N6-Eu1-N8	163.1(1)
N2^{I}-Eu1-N8	84.5(2)	N7-Eu1-N4^{II}	76.5(1)
N3^{I}-Eu1-N1	87.9(1)	N7-Eu1-N8	86.3(1)

Table S8. Selected interatomic distances (pm) and angles (°) of $^{2}_{\infty}$[Ln$_2$(4-PyPzH)$_6$]·Py, Ln = Yb(**4-Yb**), Lu (**4-Lu**). Symmetry operations: I –x+1/2,y–1/2,–z+1/2 II x,y–1,z III –x+1/2,y–1/2,–z+3/2 IV x,y+1,z

Atoms	$^{2}_{\infty}$[Yb(4-PyPzH)$_6$]·Py	$^{2}_{\infty}$[Lu(4-PyPzH)$_6$]·Py	Atoms	$^{2}_{\infty}$[Yb(4-PyPzH)$_6$]·Py	$^{2}_{\infty}$[Lu(4-PyPzH)$_6$]·Py
Ln1-N7	245(2)	245(1)	N17-Ln1-N10^{II}	83.9(2)	84.2(2)
Ln1-N10^{II}	257.5(5)	256.7(4)	N17-Ln1-N12	160.4(2)	159.8(2)
Ln1-N11	234.1(6)	234.0(4)	N17-Ln1-N13^{I}	84.4(2)	84.3(2)
Ln1-N12	242.0(5)	240.2(5)	N17-Ln1-N14	80.3(2)	79.9(2)
Ln1-N13^{I}	247.5(5)	245.2(4)	N17-Ln1-N15	80.9(2)	80.4(2)
Ln1-N14	239.9(6)	239.2(4)	N18-Ln1-N7	78.5(4)	78.2(3)
Ln1-N15	238.2(6)	236.6(4)	N18-Ln1-N10^{II}	76.7(2)	76.5(2)
Ln1-N17	235.8(6)	235.1(4)	N18-Ln1-N12	148.0(2)	146.9(2)
Ln1-N18	234.1(6)	234.6(5)	N18-Ln1-N13^{I}	112.4(2)	113(2)
Ln2-N1^{IV}	247.9(6)	244.5(4)	N18-Ln1-N14	98.8(2)	99.2(2)
Ln2-N2	232.3(6)	232.6(4)	N18-Ln1-N15	82.1(2)	82.1(2)
Ln2-N3	231.0(6)	231.5(5)	N18-Ln1-N17	32.9(2)	33.9(2)

Ln2-N4^{III}	245.4(5)	243.5(4)	N2-Ln2-N1^{IV}	115.9(2)	116.5(2)
Ln2-N5	227.7(6)	228.0(4)	N2-Ln2-N4^{III}	85.3(2)	85.1(2)
Ln2-N6	231.2(6)	231.9(5)	N2-Ln2-N8	108.4(5)	109.4(3)
Ln2-N8	237(2)	236(1)	N2-Ln2-N9	137.6(3)	139.4(5)
Ln2-N9	241(2)	243(1)	N3-Ln2-N1^{IV}	83.1(2)	83.7(2)
N7-Ln1-N10^{II}	87.0(3)	86.7(3)	N3-Ln2-N2	34.3(2)	34.2(2)
N7-Ln1-N13^{I}	154.0(3)	153.5(2)	N3-Ln2-N4^{III}	116.8(2)	116.5(2)
N11-Ln1-N7	81.5(4)	80.9(3)	N3-Ln2-N6	105.0(2)	104.2(2)
N11-Ln1-N10^{II}	112.1(2)	112.4(2)	N3-Ln2-N8	92.8(5)	93.9(3)
N11-Ln1-N12	32.3(2)	33.4(2)	N3-Ln2-N9	125.7(4)	126.9(4)
N11-Ln1-N13^{I}	89.9(2)	90.2(2)	N4^{III}-Ln2-N1^{IV}	158.5(2)	158.0(2)
N11-Ln1-N14	81.1(2)	80.9(2)	N5-Ln2-N1^{IV}	86.8(2)	86.5(2)
N11-Ln1-N15	86.2(2)	86.0(2)	N5-Ln2-N2	125.8(2)	125.5(2)
N11-Ln1-N17	160.8(2)	160.3(2)	N5-Ln2-N3	138.1(2)	137.4(2)
N11-Ln1-N18	157.7(2)	156.8(2)	N5-Ln2-N4^{III}	83.1(2)	83.7(2)
N12-Ln1-N7	79.0(4)	78.5(3)	N5-Ln2-N6	34.8(2)	34.8(2)
N12-Ln1-N10^{II}	79.8(2)	79(2)	N5-Ln2-N8	124.7(4)	124.1(3)
N12-Ln1-N13^{I}	80.7(2)	80.5(2)	N5-Ln2-N9	92.2(4)	91.1(4)
N13^{I}-Ln1-N10^{II}	73.5(2)	73.7(2)	N6-Ln2-N1^{IV}	92.6(2)	92.2(2)
N14-Ln1-N7	115.8(3)	116.0(3)	N6-Ln2-N2	92.7(2)	92.5(2)
N14-Ln1-N10^{II}	155.7(2)	155.9(2)	N6-Ln2-N4^{III}	89.9(2)	90.9(2)
N14-Ln1-N12	111.3(2)	112.0(2)	N6-Ln2-N8	158.9(5)	158.1(4)
N14-Ln1-N13^{I}	86.7(2)	86.7(2)	N6-Ln2-N9	127.0(3)	125.9(4)
N15-Ln1-N7	84.1(3)	84.8(2)	N8-Ln2-N1^{IV}	78.1(5)	77.4(4)
N15-Ln1-N10^{II}	158.3(2)	158.2(2)	N8-Ln2-N4^{III}	92.1(5)	91.9(4)
N15-Ln1-N12	117.7(2)	118.7(2)	N8-Ln2-N9	33.2(4)	33.5(3)
N15-Ln1-N13^{I}	119.9(2)	119.7(2)	N9-Ln2-N1^{IV}	80.3(3)	78.5(5)
N15-Ln1-N14	33.5(2)	33.2(2)	N9-Ln2-N4^{III}	81.1(3)	82.0(5)
N17-Ln1-N7	111.0(4)	111.7(3)			

Table S9. Selected interatomic distances (pm) and angles (°) of $^{2}_{\infty}$[Tm(4-PyPz)$_3$(Py)] (**4-$^{2}_{\infty}$Tm**). Symmetry operations: I x–1/2,y+1/2,z II x+1/2,y+1/2,z.

Atoms	$^{2}_{\infty}$[Tm(4-PyPz)$_3$(Py)]	Atoms	$^{2}_{\infty}$[Tm(4-PyPz)$_3$(Py)]
Tm1-N1^{II}	259.2(5)	N5-Tm1-N4^{I}	117.2(2)
Tm1-N2	234.5(5)	N5-Tm1-N10	85.3(2)
Tm1-N3	241.4(5)	N6-Tm1-N1^{II}	158.9(2)
Tm1-N4^{I}	246.5(5)	N6-Tm1-N3	117.6(2)
Tm1-N5	239.5(5)	N6-Tm1-N4^{I}	85.3(2)
Tm1-N6	234.9(5)	N6-Tm1-N5	33.5(2)
Tm1-N8	239.2(6)	N6-Tm1-N8	80.5(2)
Tm1-N9	232.4(6)	N6-Tm1-N10	118.4(2)

Tm1-N10	250.5(6)	N8-Tm1-N1^{II}	82.9(2)
N2-Tm1-N1^{II}	113.3(2)	N8-Tm1-N3	161.2(2)
N2-Tm1-N3	32.8(2)	N8-Tm1-N4^{I}	108.3(2)
N2-Tm1-N4^{I}	82.4(2)	N8-Tm1-N5	80.8(2)
N2-Tm1-N5	80.8(2)	N8-Tm1-N10	84.2(2)
N2-Tm1-N6	85.4(2)	N9-Tm1-N1^{II}	77.6(2)
N2-Tm1-N8	161.4(2)	N9-Tm1-N2	155.4(2)
N2-Tm1-N10	91.9(2)	N9-Tm1-N3	147.8(2)
N3-Tm1-N1^{II}	80.5(2)	N9-Tm1-N4^{I}	75.9(2)
N3-Tm1-N4^{I}	79.9(2)	N9-Tm1-N5	98.9(2)
N3-Tm1-N10	82.4(2)	N9-Tm1-N6	81.4(2)
N4^{I}-Tm1-N1^{II}	87.6(2)	N9-Tm1-N8	32.7(2)
N4^{I}-Tm1-N10	155.3(2)	N9-Tm1-N10	112.6(2)
N5-Tm1-N1^{II}	153.6(2)	N10-Tm1-N1^{II}	72.5(2)
N5-Tm1-N3	111.0(2)		

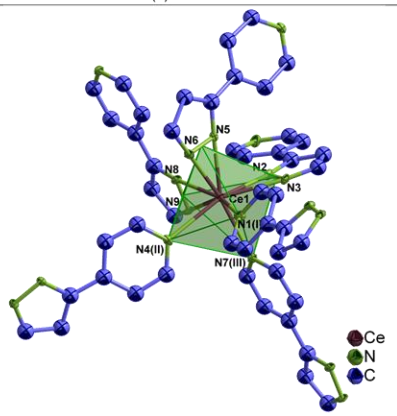

Figure S1. Extended coordination sphere of Ce^{3+} in $^{3}_{\infty}$[Ce(4-PyPz)$_3$] (**4-Ce**) representing the series of isotypic framework compounds (**4**, Ln = La, Ce, Pr, Nd, Ho, Er, Tm). The coordination polyhedra around Ce^{3+} is indicated in green and the thermal ellipsoids describe a 50 % probability level of the atoms. Symmetry operations: I x+1/2,–y+1/2,z+1/2 II –x+3/2,y–1/2,–z+3/2 III x+1,y,z

Table S10. Selected interatomic distances (pm) and angles (°) of $^{3}_{\infty}$[Ln(4-PyPz)$_3$] (**4**, Ln = La, Ce, Pr, Nd, Ho, Er). Symmetry operations: I x+1/2,–y+1/2,z+1/2 II –x+3/2,y–1/2,–z+3/2 III x+1,y,z

Atoms	$^{3}_{\infty}$[La(4-PzPy)$_3$]	$^{3}_{\infty}$[Ce(4-PzPy)$_3$]	$^{3}_{\infty}$[Pr(4-PzPy)$_3$]	$^{3}_{\infty}$[Nd(4-PzPy)$_3$]	$^{3}_{\infty}$[Ho(4-PzPy)$_3$]	$^{3}_{\infty}$[Er(4-PzPy)$_3$]
Ln1-N2	251.0(3)	248.2(3)	246.3(2)	244.8(2)	236.0(4)	235.2(3)
Ln1-N5	251.3(3)	247.5(3)	246.1(2)	245.0(2)	236.1(3)	235.3(3)
Ln1-N8	251.2(3)	248.1(3)	246.4(2)	245.5(2)	236.9(4)	235.9(4)
Ln1-N9	256.2(3)	254.0(3)	251.8(2)	250.3(2)	241.4(4)	240.6(3)
Ln1-N6	256.8(3)	254.3(3)	252.3(2)	251.2(2)	242.8(4)	241.4(3)
Ln1-N3	259.3(3)	256.7(3)	254.2(2)	252.9(2)	243.8(4)	242.9(3)
Ln1-N1^{I}	267.7(4)	264.9(3)	263.3(2)	262.1(2)	253.3(3)	251.8(3)
Ln1-N4^{II}	269.5(3)	266.8(2)	264.9(2)	264.1(2)	254.5(3)	253.0(3)
Ln1-N7^{III}	269.9(3)	267.1(3)	265.4(2)	264.2(2)	254.2(3)	252.8(3)
N2-Ln1-N5	86.5(1)	86.4(1)	86.3(1)	86.2(1)	86.0(2)	85.6(2)
N2-Ln1-N8	90.5(1)	90.1(1)	90.2(1)	90.3(1)	89.9(2)	89.9(2)
N5-Ln1-N8	84.5(1)	84.4(1)	84.4(1)	84.4(1)	84.5(2)	84.6(2)
N2-Ln1-N9	85.2(1)	85.2(1)	85.1(1)	85.2(1)	84.7(2)	84.8(2)
N5-Ln1-N9	114.7(1)	115(1)	115.3(1)	115.4(1)	116.6(2)	116.6(2)
N8-Ln1-N9	31.1(1)	31.4(1)	31.8(1)	31.9(1)	33.1(2)	33.0(1)
N2-Ln1-N6	117.6(1)	117.8(1)	118.0(1)	118.1(1)	118.8(2)	118.7(2)
N5-Ln1-N6	31.1(1)	31.4(1)	31.7(1)	31.9(1)	32.8(2)	33.1(1)
N8-Ln1-N6	85.7(1)	85.5(1)	85.4(1)	85.2(1)	84.7(2)	84.7(2)
N9-Ln1-N6	115.2(1)	115.2(1)	115.5(1)	115.4(1)	115.9(2)	115.7(2)
N2-Ln1-N3	31.1(1)	31.2(1)	31.4(1)	31.7(1)	32.8(1)	32.9(1)
N5-Ln1-N3	82.7(1)	82.7(1)	82.8(1)	82.7(1)	82.6(2)	82.4(1)
N8-Ln1-N3	120.5(1)	120.4(1)	120.7(1)	121.0(1)	121.8(2)	121.9(2)
N9-Ln1-N3	114.9(1)	115(1)	115.0(1)	115.1(1)	115.5(2)	115.6(2)
N6-Ln1-N3	108.9(1)	109.2(1)	109.4(1)	109.6(1)	110.4(2)	110.4(1)
N2-Ln1-N1^{I}	115.1(1)	115(1)	115.2(1)	115.2(1)	115.5(2)	115.4(2)
N5-Ln1-N1^{I}	88.8(1)	88.3(1)	88.3(1)	88.2(1)	87.2(2)	87.0(1)
N8-Ln1-N1^{I}	153.1(1)	153.4(1)	153.0(1)	152.9(1)	152.6(2)	152.6(2)
N9-Ln1-N1^{I}	150.6(1)	150.9(1)	150.6(1)	150.6(1)	150.6(2)	151.0(1)
N6-Ln1-N1^{I}	75.5(1)	75.2(1)	75.0(1)	75.0(1)	74.4(2)	74.2(2)
N3-Ln1-N1^{I}	84.1(1)	83.8(1)	83.9(1)	83.6(1)	82.7(2)	82.5(1)
N2-Ln1-N4^{II}	156.1(1)	156.2(1)	155.6(1)	155.5(1)	154.9(2)	155.1(1)
N5-Ln1-N4^{II}	114.4(1)	114.3(1)	114.8(1)	115.2(1)	115.5(1)	115.8(1)
N8-Ln1-N4^{II}	80.7(1)	80.7(1)	80.5(1)	80.6(1)	80.2(2)	80.2(2)
N9-Ln1-N4^{II}	75.7(1)	75.5(1)	75.1(1)	75.1(1)	74.4(2)	74.4(1)
N6-Ln1-N4^{II}	84.1(1)	83.6(1)	83.9(1)	84.0(1)	83.4(2)	83.3(1)
N3-Ln1-N4^{II}	155.1(1)	155.2(1)	154.9(1)	154.4(1)	154.0(1)	153.9(1)
N1^{I}-Ln1-N4^{II}	78.6(1)	79.0(1)	79.1(1)	79.0(1)	80.0(2)	80.2(1)
N2-Ln1-N7^{III}	81.2(1)	81.1(1)	80.9(1)	80.9(1)	80.6(2)	80.8(1)

N5-Ln1-N7^{III}	158(1)	158(1)	157.5(1)	157.0(1)	155.6(1)	155.4(2)
N8-Ln1-N7^{III}	113.6(1)	113.5(1)	113.9(1)	114.5(1)	115.7(2)	115.6(2)
N9-Ln1-N7^{III}	82.5(1)	82.1(1)	82.1(1)	82.6(1)	82.5(2)	82.6(2)
N6-Ln1-N7^{III}	153.9(1)	154.1(1)	153.8(1)	153.5(1)	153.0(2)	153.0(2)
N3-Ln1-N7^{III}	77.3(1)	77.2(1)	76.7(1)	76.3(1)	75.0(1)	75.0(1)
N1^{I}-Ln1-N7^{III}	80.2(1)	80.8(1)	80.6(1)	80.2(1)	80.3(2)	80.6(2)
N4^{II}-Ln1-N7^{III}	82.2(1)	82.5(1)	82.3(1)	82.3(1)	83.0(1)	83.0(1)

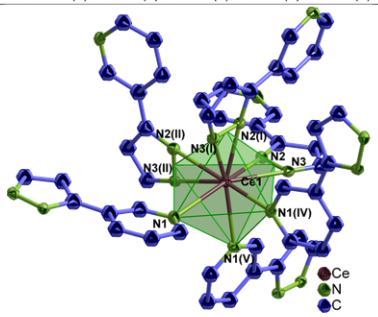

Figure S2. Extended coordination sphere of Ce^{3+} in $^{3}_{\infty}$[Ce(3-PyPz)$_3$] (**3-Ce**) representing the series of isotypic framework compounds (**3**, Ln = Ce, Pr, Nd, Ho, Er, Tm). The coordination polyhedra around Ce^{3+} is indicated in green and the thermal ellipsoids describe a 50 % probability level of the atoms. Symmetry operations: I −z+1,x+1/2,−y+3/2 II y−1/2,−z+3/2, −x+1 III x−1/2,y,−z+3/2 IV y−1/2,z,−x+3/2 V z−1/2,x,−y+3/2.

Table S11. Selected interatomic distances (pm) and angles (°) of $^{3}_{\infty}$[Ln(3-PyPz)$_3$], (**3**, Ln = Ce, Pr, Nd, Ho, Er,Tm). Symmetry operations: I −z+1,x+1/2,−y+3/2 II y−1/2,−z+3/2,−x+1 III x−1/2,y,−z+3/2 IV y−1/2,z,−x+3/2 V z−1/2,x,−y+3/2.

Atoms	**$^{3}_{\infty}$[Ce(3-PyPz)$_3$]**	**$^{3}_{\infty}$[Pr(3-PyPz)$_3$]**	**$^{3}_{\infty}$[Nd(3-PyPz)$_3$]**	**$^{3}_{\infty}$[Ho(3-PyPz)$_3$]**	**$^{3}_{\infty}$[Er(3-PyPz)$_3$]**	**$^{3}_{\infty}$[Tm(3-PyPz)$_3$]**
Ln1-N2	246.6(3)	245.0(2)	243.5(2)	235.2(2)	234.2(2)	233.6(5)
Ln1-N3	252.7(3)	250.3(2)	249.0(2)	239.8(2)	238.6(2)	238.3(5)
Ln1-N1^{III}	268.7(3)	267.1(2)	265.4(2)	256.0(2)	255.0(2)	254.2(5)
N2-Ln1-N2^{I}	85.6(1)	85.5(1)	85.6(1)	85.8(1)	85.8(1)	86.0(2)
N2-Ln1-N3	31.9(1)	32.1(1)	32.3(1)	33.3(1)	33.5(1)	33.4(2)
N2^{I}-Ln1-N3	82.6(1)	82.6(1)	82.8(1)	83.0(1)	82.9(1)	83.0(2)
N2^{II}-Ln1-N3	116.9(1)	117.0(1)	117.3(1)	118.6(1)	118.7(1)	118.8(2)
N3-Ln1-N3^{II}	112.3(1)	112.5(1)	112.7(1)	113.5(1)	113.7(1)	113.6(1)

N2-Ln1-N1^{III}	161.3(1)	161.2(1)	161.4(1)	161.6(1)	161.6(1)	161.9(2)
N2^{I}-Ln1-N1^{III}	109.7(1)	109.9(1)	109.7(1)	109.4(1)	109.4(1)	109.0(2)
N2^{II}-Ln1-N1^{III}	84.9(1)	85.1(1)	85.1(1)	85.0(1)	85.0(1)	85.0(2)
N3-Ln1-N1^{III}	156.4(1)	156.0(1)	155.7(1)	154.7(1)	154.6(1)	154.7(2)
N3^{II}-Ln1-N1^{III}	80.8(1)	80.8(1)	80.8(1)	80.6(1)	80.6(1)	80.8(2)
N3^{I}-Ln1-N1^{III}	77.7(1)	77.8(1)	77.4(1)	76.0(1)	75.9(1)	75.6(2)
N1^{III}-Ln1-N1^{IV}	83.2(1)	82.9(1)	82.8(1)	83.0(1)	83.0(1)	83.1(2)

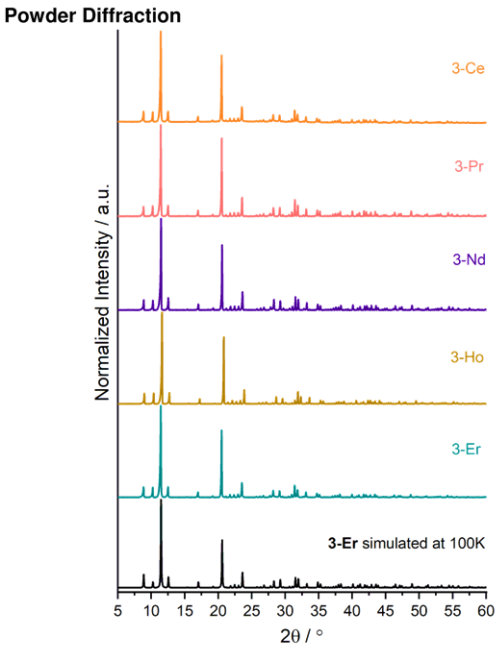

Figure S3. Comparison of the experimental X-ray powder diffraction pattern of $^{3}_{\infty}$[Ln(3-PyPz)$_3$] (**3**, Ln = Pr, Nd, Ho, Er, Tm) at RT with the simulated pattern from the single-crystal X-ray data of $^{3}_{\infty}$[Er(3-PyPz)$_3$] (**3-Er**) at 100 K.

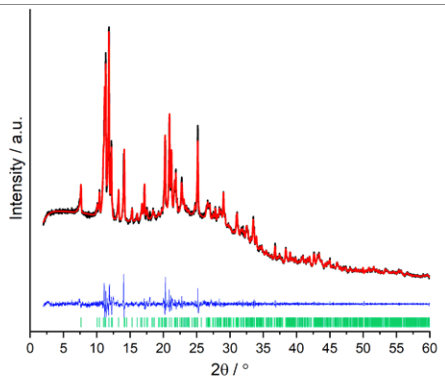

Figure S4. Pawley refinement results for PXRD of $^{3}_{\infty}$[La(4-PyPz)$_3$] (**4-La**), showing the experimental data (black) together with the Pawley fit (red), the corresponding difference plot (blue) as well as hkl position markers (green).

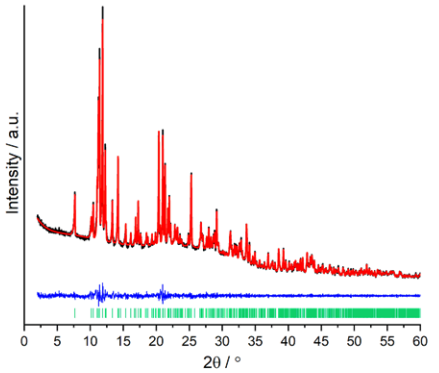

Figure S5. Pawley refinement results for PXRD of $^{3}_{\infty}$[Pr(4-PyPz)$_3$] (**4-Pr**), showing the experimental data (black) together with the Pawley fit (red), the corresponding difference plot (blue) as well as hkl position markers (green).

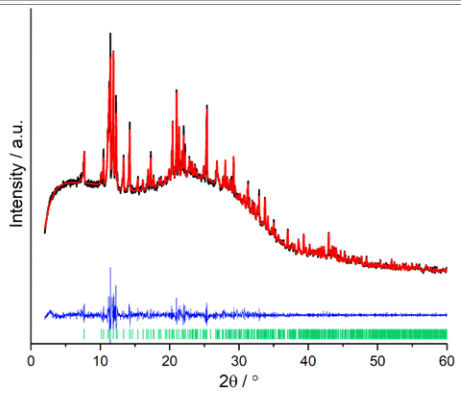

Figure S6. Pawley refinement results for PXRD of $^{3}_{\infty}$[Nd(4-PyPz)$_3$] (**4-Nd**), showing the experimental data (black) together with the Pawley fit (red), the corresponding difference plot (blue) as well as hkl position markers (green).

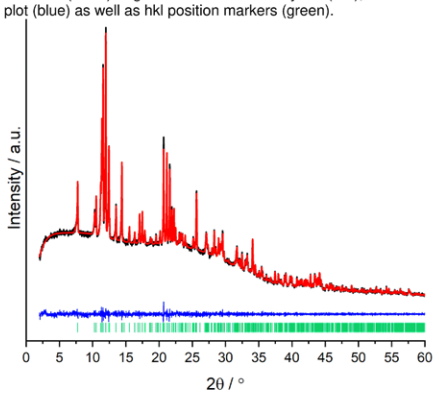

Figure S7. Pawley refinement results for PXRD of $^{3}_{\infty}$[Ho(4-PyPz)$_3$] (**4-Ho**), showing the experimental data (black) together with the Pawley fit (red), the corresponding difference plot (blue) as well as hkl position markers (green).

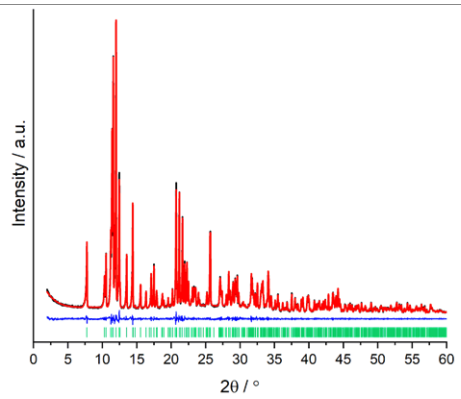

Figure S8. Pawley refinement results for PXRD of $^{3}_{\infty}$[Er(4-PyPz)$_3$] (**4-Er**), showing the experimental data (black) together with the Pawley fit (red), the corresponding difference plot (blue) as well as hkl position markers (green).

Table S12. Pawley refinement results for $^{2}_{\infty}$[Eu(4-PyPz)$_2$(Py)$_2$] (**4-Eu^{2+}**), $^{2}_{\infty}$[Ce(4-PyPz)$_3$(Py)] (**4-$^{2}_{\infty}$Ce**), and $^{3}_{\infty}$[Ln(4-PyPz)$_3$] (**4**, Ln = La, Pr, Nd, Ho, Er, Tm).

Compound	**$^{2}_{\infty}$[Eu(4-PyPz)$_2$(Py)$_2$]**	**$^{2}_{\infty}$[Ce(4-PyPz)$_3$(Py)]**	**$^{3}_{\infty}$[La(4-PyPz)$_3$]**	**$^{3}_{\infty}$[Pr(4-PyPz)$_3$]**
R_{wp}	2.7359	4.3334	2.3996	2.4706
GOF	1.3696	1.0395	1.6364	1.0812
Compound	**$^{3}_{\infty}$[Nd(4-PyPz)$_3$]**	**$^{3}_{\infty}$[Ho(4-PyPz)$_3$]**	**$^{3}_{\infty}$[Er(4-PyPz)$_3$]**	**$^{3}_{\infty}$[Tm(4-PyPz)$_3$]**
R_{wp}	2.1610	2.0778	3.7015	2.8265
GOF	1.7183	1.0298	1.2168	1.5827

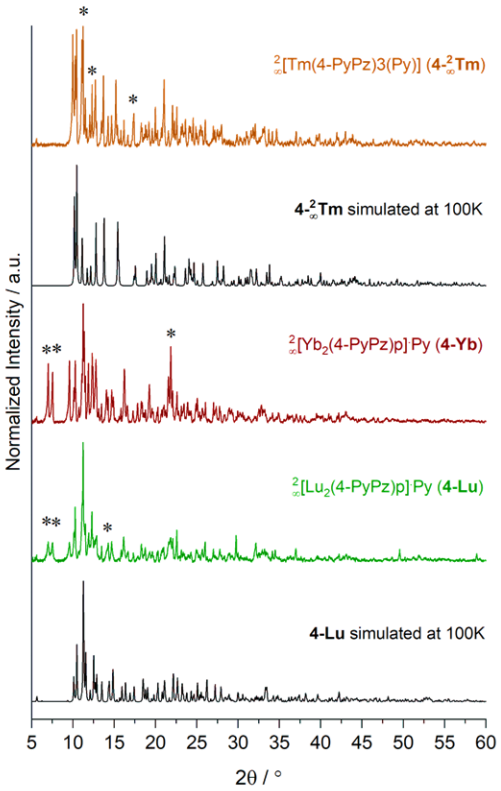

Figure S9. Comparison of the experimental X-ray powder diffraction pattern of $^{2}_{\infty}$[Tm(4-PyPz)$_3$(Py)] (**4-$^{2}_{\infty}$Tm**), $^{2}_{\infty}$[Ln$_2$(4-PyPzH)$_6$]·Py, Ln =Yb (**4-Yb**) and Lu (**4-Lu**) at RT with the respective simulated pattern from single-crystal X-ray data at 100 K.

Photophysical Properties

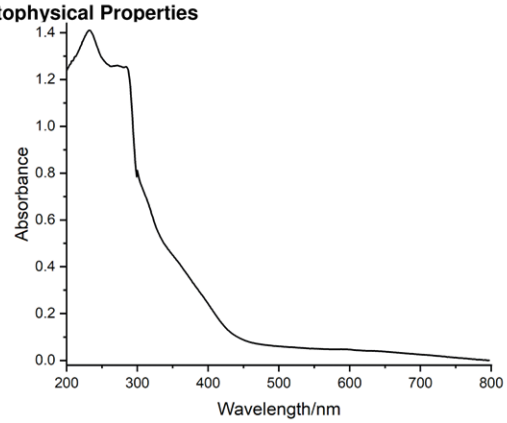

Figure S10. Absorption spectra of **4-PyPzH** in the solid state at room temperature.

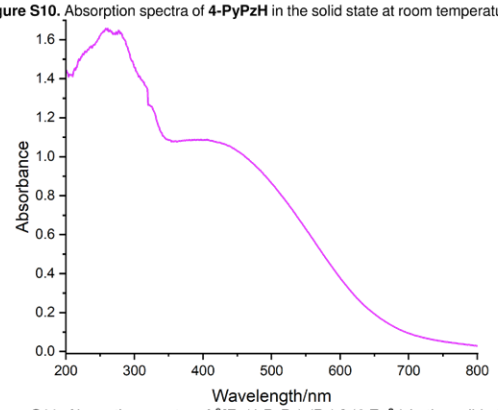

Figure S11. Absorption spectra of $^{2}_{\infty}$[Eu(4-PyPz)$_2$(Py)$_2$] (**4-Eu^{2+}**) in the solid state at room temperature.

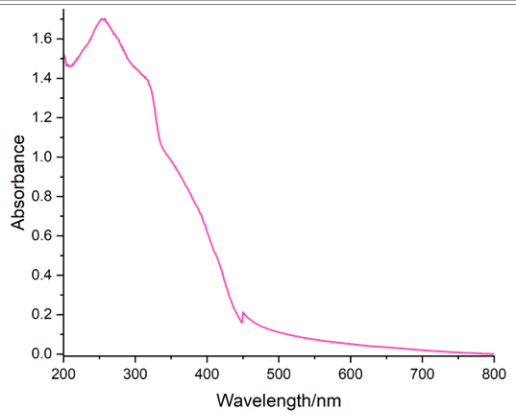

Figure S12. Absorption spectra of $^{2}_{\infty}$[Ce(4-PyPz)$_3$(Py)] (**4-$^{2}_{\infty}$Ce**) in the solid state at room temperature.

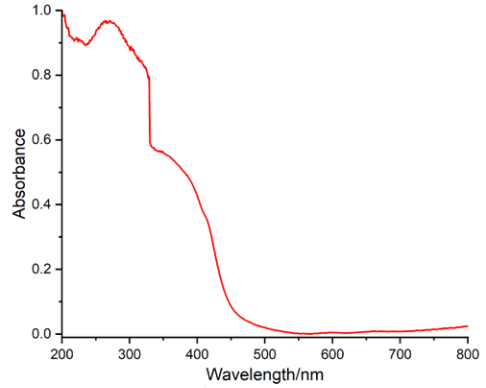

Figure S13. Absorption spectra of $^{3}_{\infty}$[Ce(4-PyPz)$_3$] (**4-Ce**) in the solid state at room temperature.

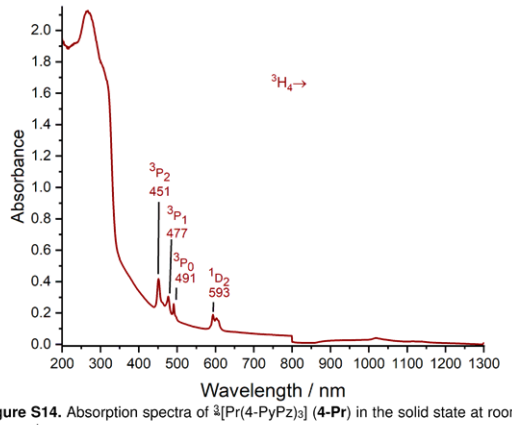

Figure S14. Absorption spectra of ^{3}[Pr(4-PyPz)$_3$] (**4-Pr**) in the solid state at room temperature.

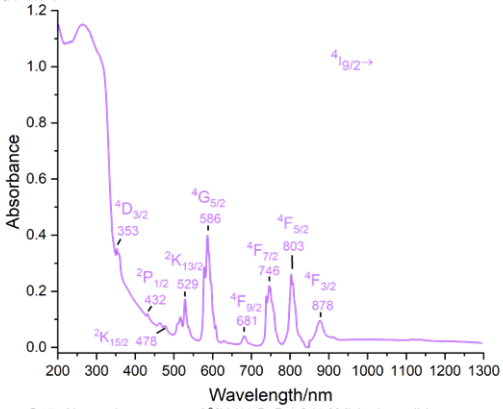

Figure S15. Absorption spectra of ^{3}[Nd(4-PyPz)$_3$] (**4-Nd**) in the solid state at room temperature.

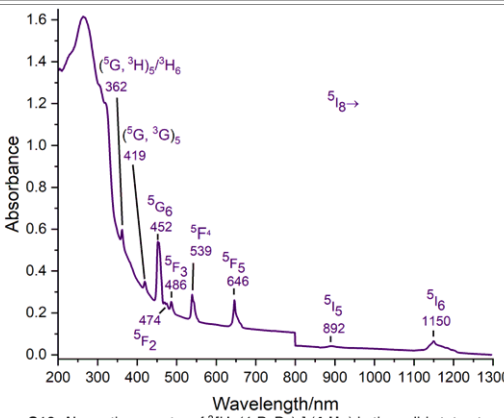

Figure S16. Absorption spectra of ^{3}[Ho(4-PyPz)$_3$] (**4-Ho**) in the solid state at room temperature.

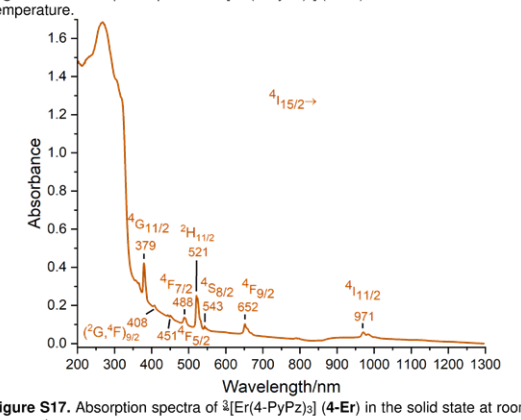

Figure S17. Absorption spectra of ^{3}[Er(4-PyPz)$_3$] (**4-Er**) in the solid state at room temperature.

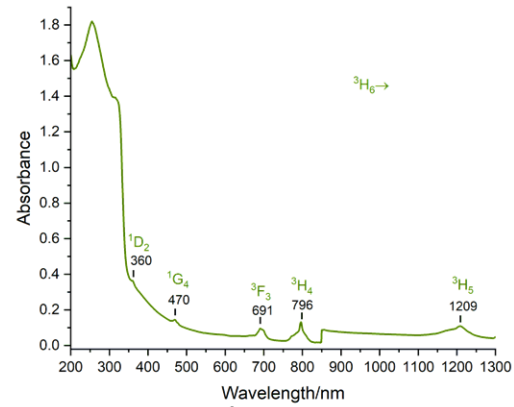

Figure S18. Absorption spectra of ^{3}[Tm(4-PyPz)$_3$] (**4-Tm**) in the solid state at room temperature.

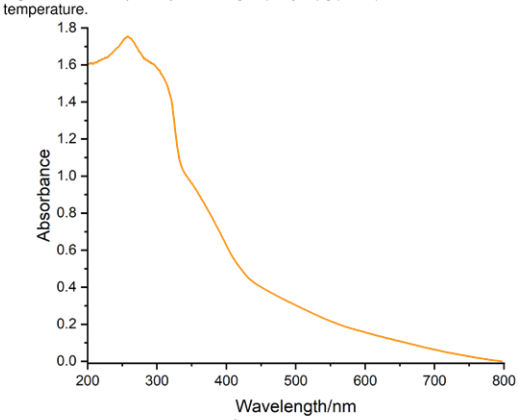

Figure S19. Absorption spectra of ^{3}[Ce(3-PyPz)$_3$] (**3-Ce**) in the solid state at room temperature.

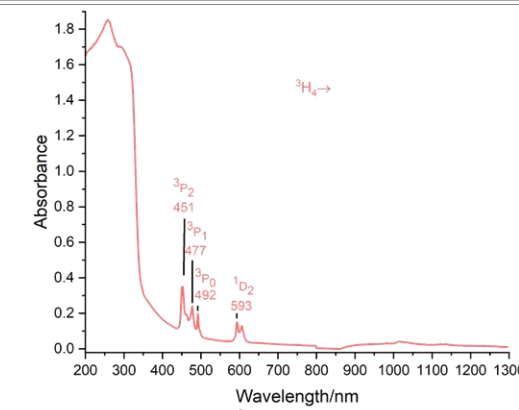

Figure S20. Absorption spectra of ^{3}[Pr(3-PyPz)$_3$] (**3-Pr**) in the solid state at room temperature.

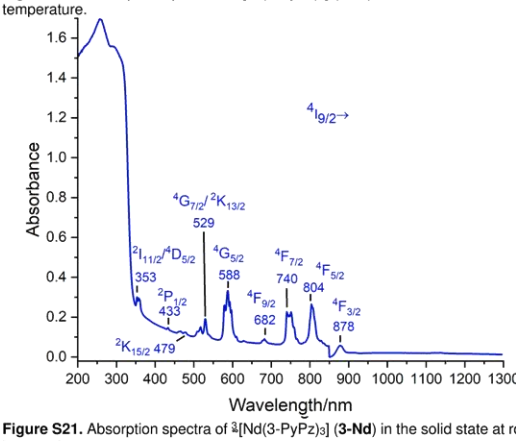

Figure S21. Absorption spectra of ^{3}[Nd(3-PyPz)$_3$] (**3-Nd**) in the solid state at room temperature.

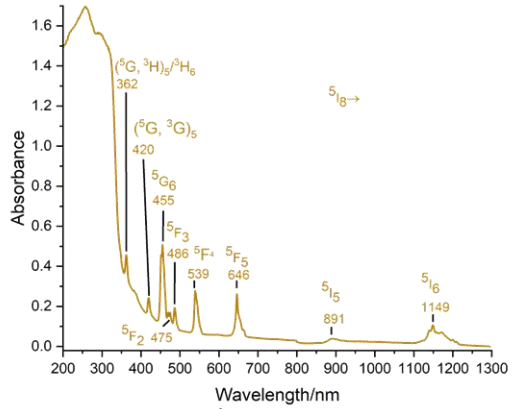

Figure S22. Absorption spectra of §[Ho(3-PyPz)$_3$] (**3-Ho**) in the solid state at room temperature.

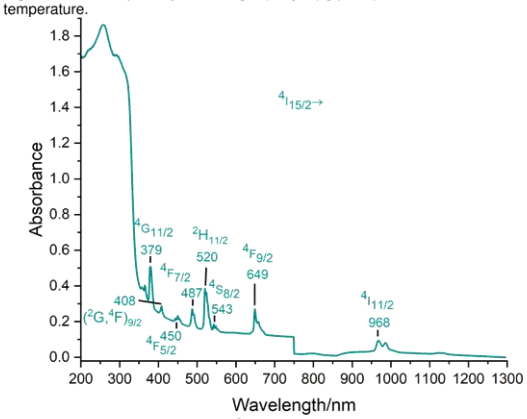

Figure S23. Absorption spectra of §[Er(3-PyPz)$_3$] (**3-Er**) in the solid state at room temperature.

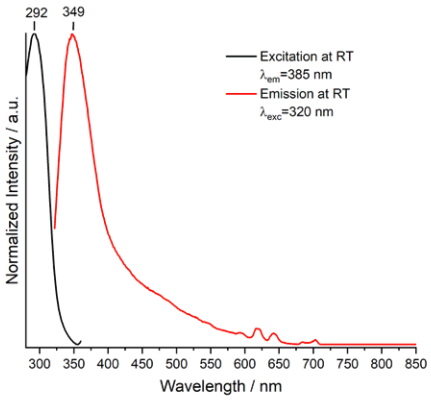

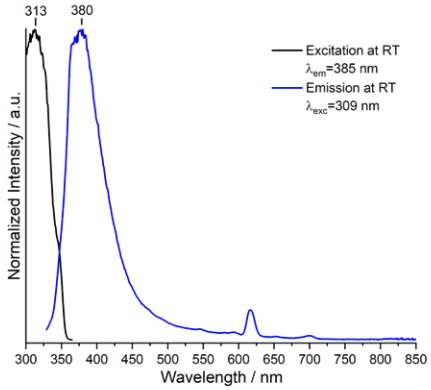

Figure S25. Normalized excitation and normalized emission spectra of §[Eu(4-PyPz)$_2$(Py)$_2$] (**4-Eu^{2+}**) at room temperature (top) and 77K (bottom). Wavelengths at which the spectra were recorded are reported in the legends.

CIE 1931

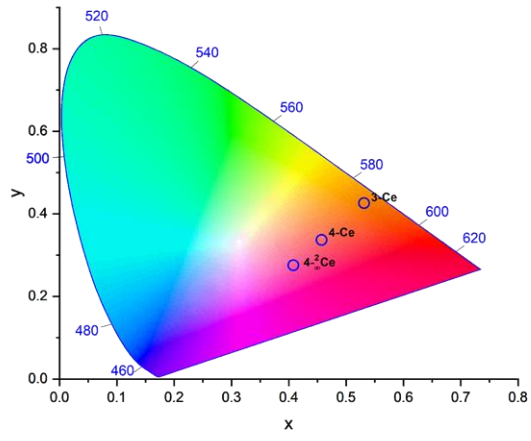

Figure S24. Chromaticity coordinate diagram (CIE 1931) of the emission colors of §[Ce(4-PyPz)$_3$(Py)] (**4-§Ce**), §[Ce(4-PyPz)$_3$] (**4-Ce**) and §[Ce(3-PyPz)$_3$] (**3-Ce**).

Table S13. Chromaticity coordinates (x,y) for §[Ce(4-PyPz)$_3$(Py)] (**4-§Ce**), §[Ce(4-PyPz)$_3$] (**4-Ce**), and §[Ce(3-PyPz)$_3$] (**3-Ce**).

compound		CIE, x	CIE, y
§[Ce(4-PyPz)$_3$(Py)]	**4-§Ce**	0.40748	0.27594
§[Ce(4-PyPz)$_3$]	**4-Ce**	0.45714	0.33718
§[Ce(3-PyPz)$_3$]	**3-Ce**	0.53121	0.42624

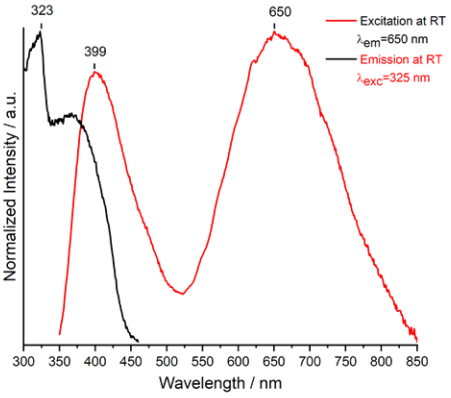

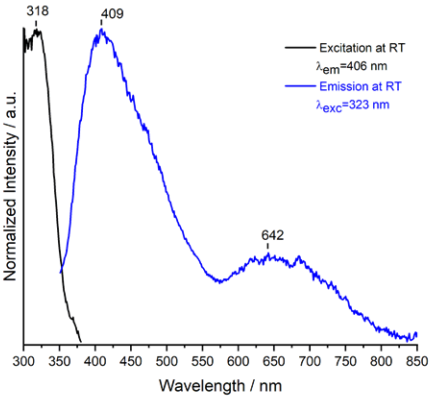

Figure S26. Normalized excitation and normalized emission spectra of §[Ce(4-PyPz)$_3$(Py)] (**4-§Ce**) at room temperature (top) and 77K (bottom). Wavelengths at which the spectra were recorded are reported in the legends.

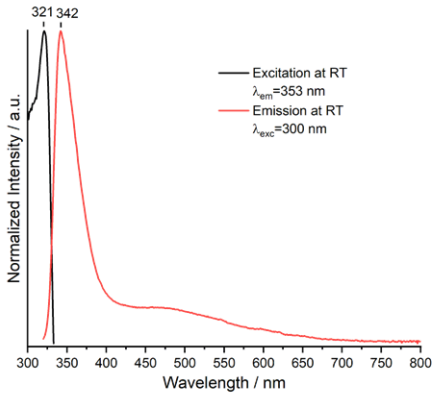

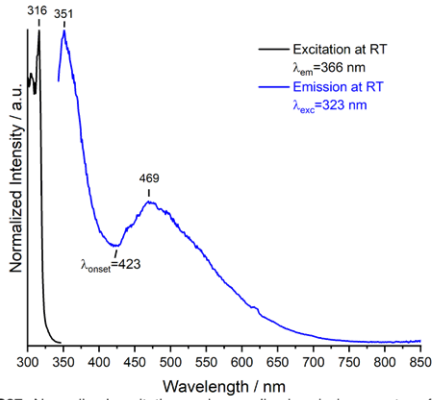

Figure S27. Normalized excitation and normalized emission spectra of [La(4-PyPz)3] (**4-La**) at room temperature (top) and 77K (bottom). Wavelengths at which the spectra were recorded are reported in the legends.

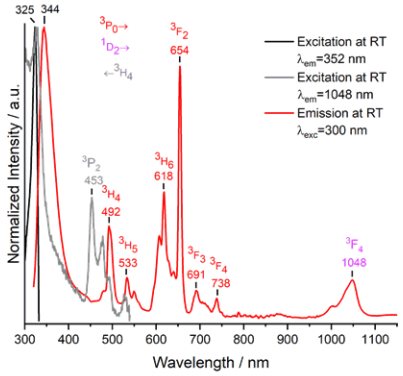

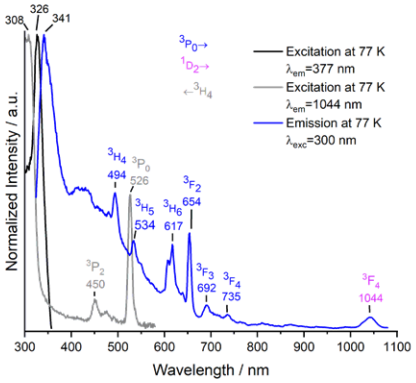

Figure S29. Normalized excitation and normalized emission spectra of [Pr(4-PyPz)3] (**4-Pr**) at room temperature (top) and 77K (bottom). Visible and NIR range emission spectra were brought to the same intensity at 738 (at RT) and 735 (at 77 K) nm. Wavelengths at which the spectra were recorded are reported in the legends.

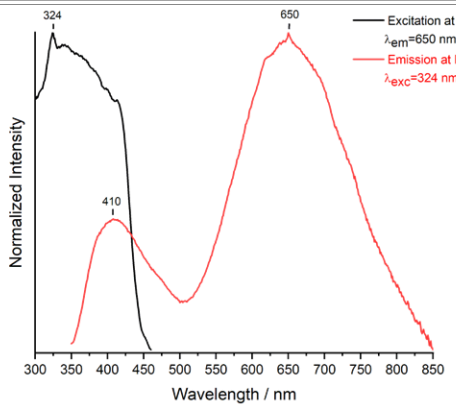

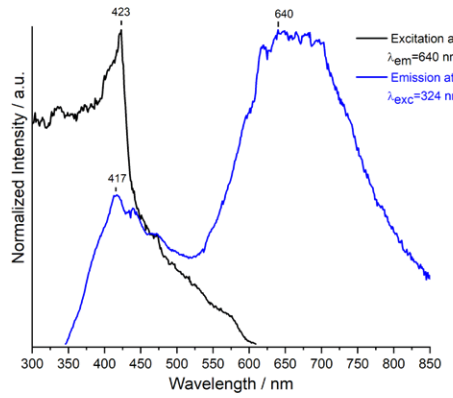

Figure S28. Normalized excitation and normalized emission spectra of [Ce(4-PyPz)3] (**4-Ce**) at room temperature (top) and 77K (bottom). Wavelengths at which the spectra were recorded are reported in the legends.

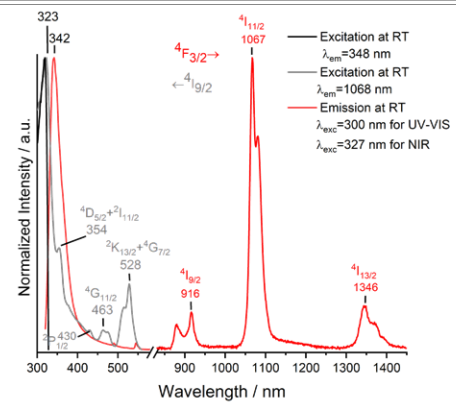

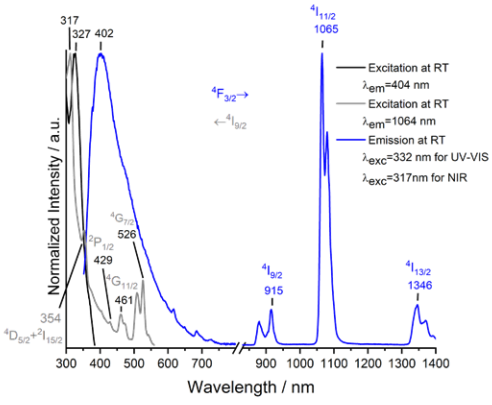

Figure S30. Normalized excitation and normalized emission spectra of [Nd(4-PyPz)3] (**4-Nd**) at room temperature (top) and 77K (bottom). Wavelengths at which the spectra were recorded are reported in the legends.

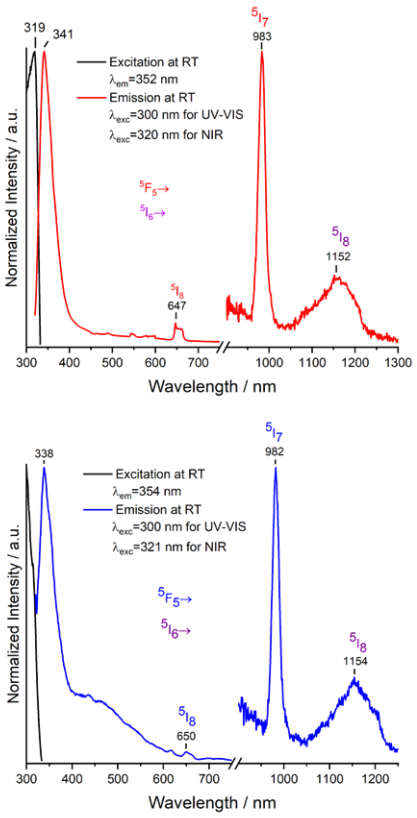

Figure S31. Normalized excitation and normalized emission spectra of ^{3}[Ho(4-PyPz)$_3$] (**4-Ho**) at room temperature (top) and 77K (bottom). Wavelengths at which the spectra were recorded are reported in the legends.

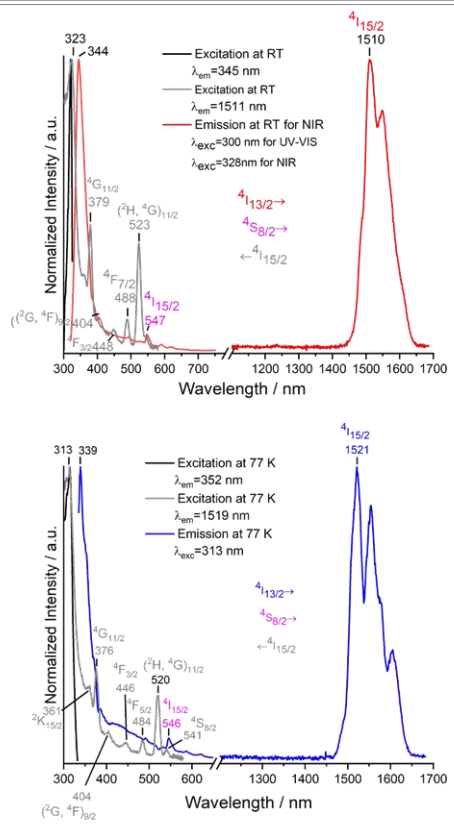

Figure S32. Normalized excitation and normalized emission spectra of ^{3}[Er(4-PyPz)$_3$] (**4-Er**) at room temperature (top) and 77K (bottom). Wavelengths at which the spectra were recorded are reported in the legends.

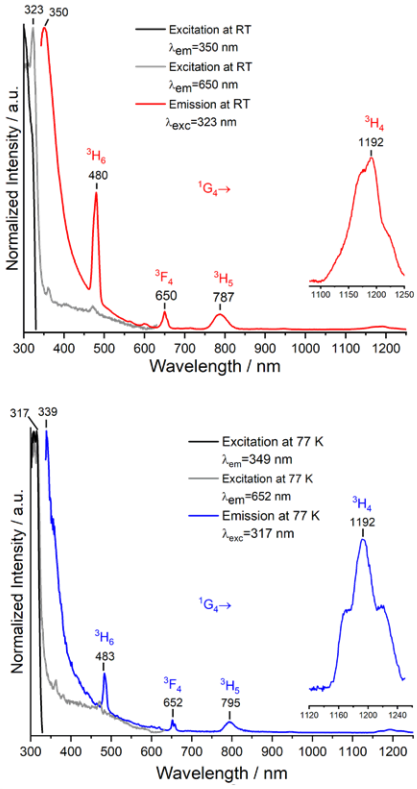

Figure S33. Normalized excitation and normalized emission spectra of ^{3}[Tm(4-PyPz)$_3$] (**4-Tm**) at room temperature (top) and 77K (bottom). Visible and NIR range emission spectra were brought to the same intensity at 650 (at RT) and 652 (at 77 K) nm. Wavelengths at which the spectra were recorded are reported in the legends.

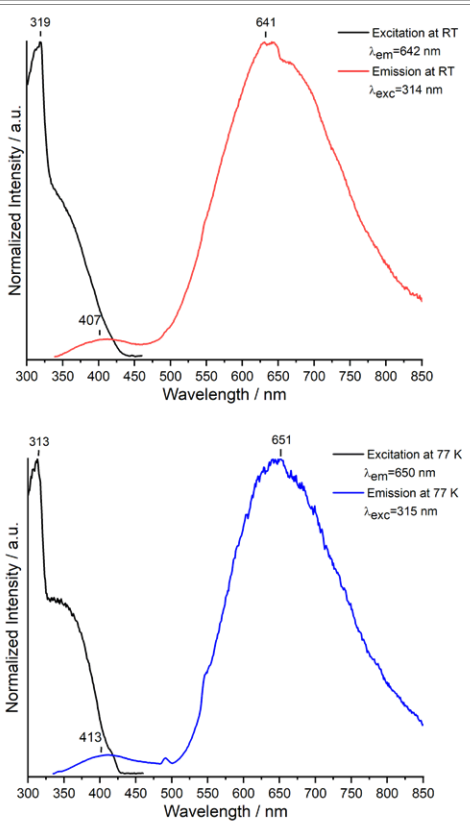

Figure S34. Normalized excitation and normalized emission spectra of ^{3}[Ce(3-PyPz)$_3$] (**3-Ce**) at room temperature (top) and 77K (bottom). Wavelengths at which the spectra were recorded are reported in the legends.

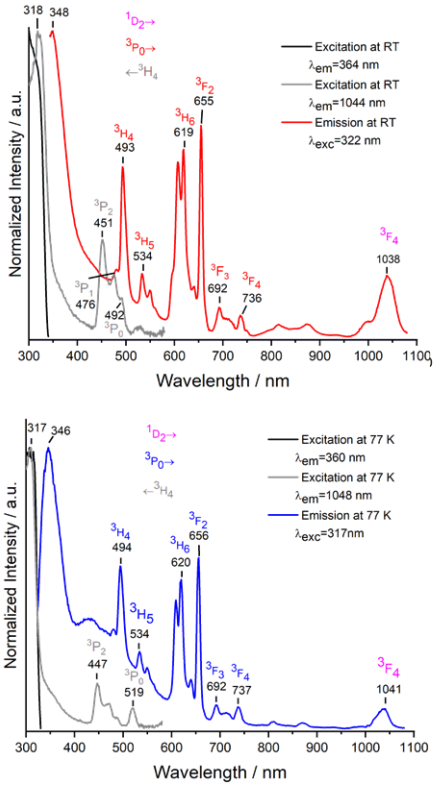

Figure S35. Normalized excitation and normalized emission spectra of [Pr(3-PyPz)$_3$] (**3-Pr**) at room temperature (top) and 77K (bottom). Visible and NIR range emission spectra were brought to the same intensity at 736 (at RT) and 737 (at 77 K) nm. Wavelengths at which the spectra were recorded are reported in the legends.

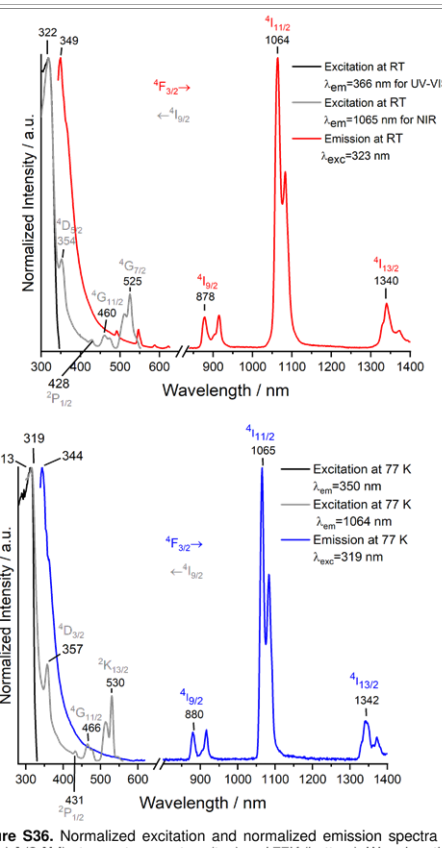

Figure S36. Normalized excitation and normalized emission spectra of [Nd(3-PyPz)$_3$] (**3-Nd**) at room temperature (top) and 77K (bottom). Wavelengths at which the spectra were recorded are reported in the legends.

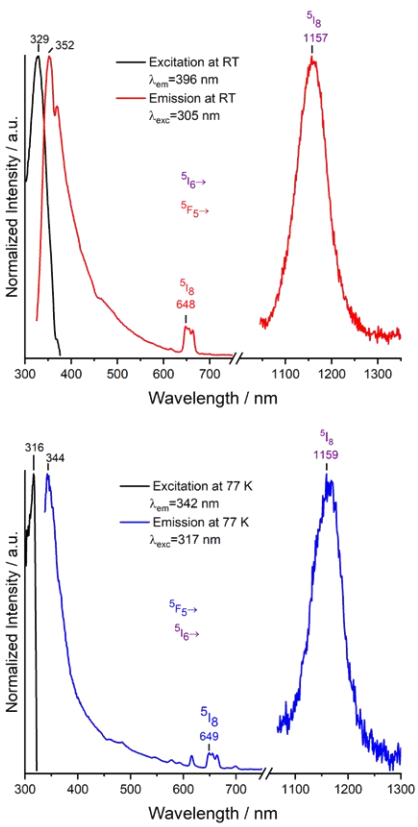

Figure S37. Normalized excitation and normalized emission spectra of [Ho(3-PyPz)$_3$] (**3-Ho**) at room temperature (top) and 77K (bottom). Wavelengths at which the spectra were recorded are reported in the legends.

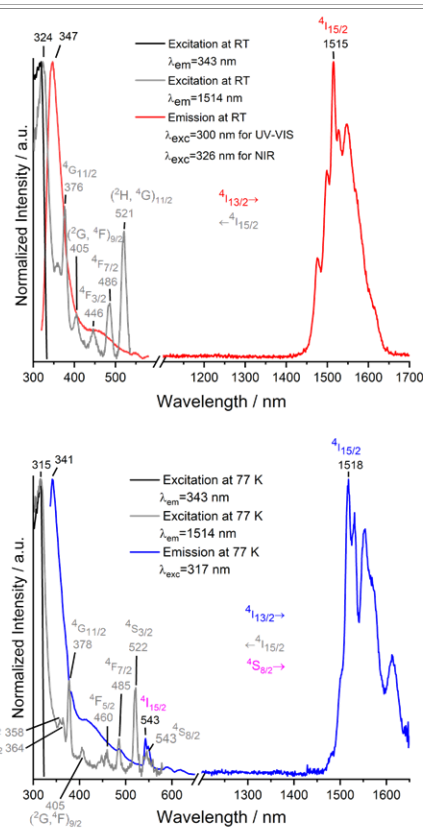

Figure S38. Normalized excitation and normalized emission spectra of [Er(3-PyPz)$_3$] (**3-Er**) at room temperature (top) and 77K (bottom). Wavelengths at which the spectra were recorded are reported in the legends.

Table S14. Photophysical data of $^{2}_{\infty}$[Eu(4-PyPz)$_2$(Py)$_2$] (**4-Eu^{2+}**), $^{2}_{\infty}$[Ce(4-PyPz)$_3$(Py)] (**4-$^{2}_{\infty}$Ce**), $^{3}_{\infty}$[Ln(4-PyPz)$_3$], (**4**, Ln = La, Ce, Pr, Nd, Ho, Er, Tm) and $^{3}_{\infty}$[Ln(3-PyPz)$_3$], (**3**, Ln = Ce, Pr, Nd, Ho, Er) in the solid state at room temperature and 77 K.

ID	$\tau_{(RT)}$[a]	$\lambda_{ex}/\lambda_{em}$ [nm][b]	$\tau_{(77\ K)}$[c]	$\lambda_{ex}/\lambda_{em}$ [nm][d]
4-Eu^{2+}	1.34(3) ns	287/385	2.18(5) ns	287/377
4-$^{2}_{\infty}$Ce	1.08(2) ns	287/650	1.18(3) ns	287/643
4-Ce	1.16(2) ns	287/650	1.06(5) ns	287/640
3-Ce	1.26(2) ns	287/641	1.20(3) ns	287/650
4-La	1.079(5) ns	287/342	1.738(9) ns	351/287
			<2 µs	316/469
4-Pr	0.96(2) ns	287/344	1.23(5) ns	287/341
3-Pr	0.99(2) ns	287/348	1.20(2) ns	287/346
4-Nd	0.93(2) ns	287/342	3.04(9) ns	287/402
3-Nd	0.99(2) ns	287/349	1.30(2) ns	287/344
4-Ho	0.97(2) ns	287/341	1.34(4) ns	287/338
3-Ho	1.00(2) ns	287/352	1.19(2) ns	287/344
4-Er	0.98(1) ns	287/344	1.16(5) ns	287/339
3-Er	1.02(1) ns	287/347	1.19(4) ns	287/341
4-Tm	1.04(1) ns	287/350	1.15(3) ns	287/349

[a] Emission lifetime determined at RT. [b] Excitation and emission wavelengths for emission lifetime at RT. [c] Emission lifetime determined at 77 K. [d] Excitation and emission wavelengths for emission lifetime at 77 K.

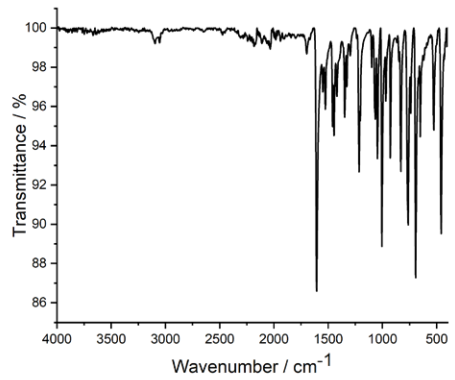

Figure S41. The infrared spectrum (ATR) of coordination polymer of $^{3}_{\infty}$[La(4-PyPz)$_3$] (**4-La**).

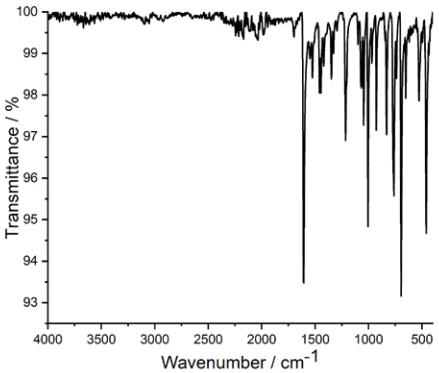

Figure S42. The infrared spectrum (ATR) of coordination polymer of $^{3}_{\infty}$[Ce(4-PyPz)$_3$] (**4-Ce**).

IR Spectroscopy

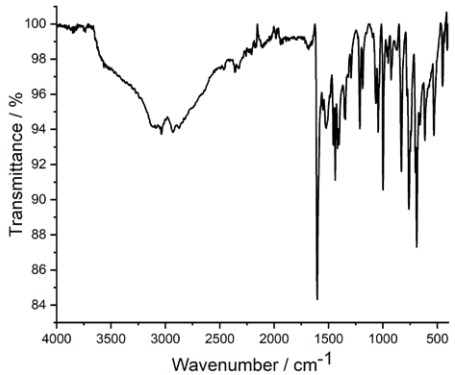

Figure S39. The infrared spectrum (ATR) of coordination polymer $^{2}_{\infty}$[Eu(4-PyPz)$_3$(Py)$_2$] (**4-Eu^{2+}**).

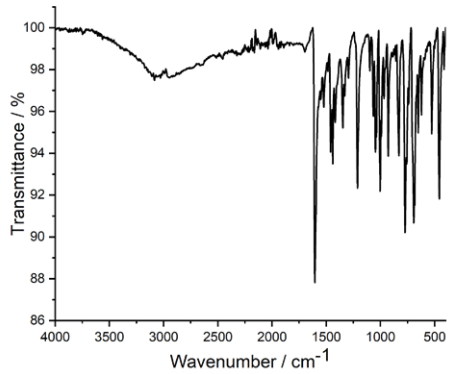

Figure S40. The infrared spectrum (ATR) of coordination polymer $^{2}_{\infty}$[Ce(4-PyPz)$_3$(Py)] (**4-$^{2}_{\infty}$Ce**).

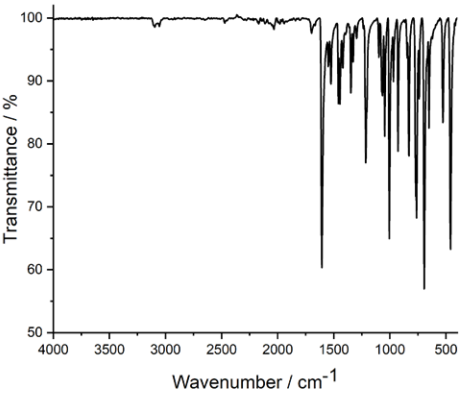

Figure S43. The infrared spectrum (ATR) of coordination polymer of $^{3}_{\infty}$[Pr(4-PyPz)$_3$] (**4-Pr**).

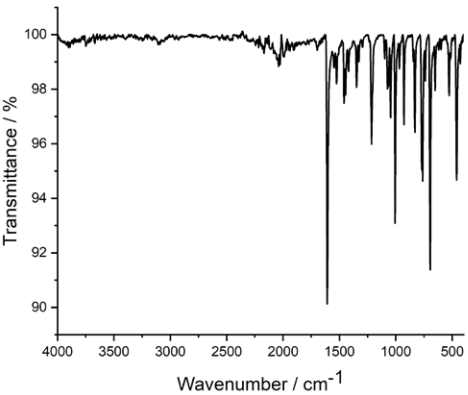

Figure S44. The infrared spectrum (ATR) of coordination polymer of $^{3}_{\infty}$[Nd(4-PyPz)$_3$] (**4-Nd**).

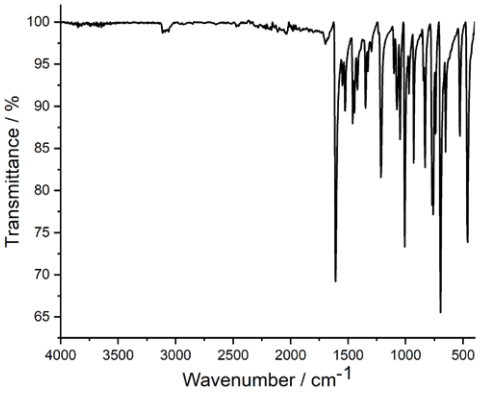

Figure S45. The infrared spectrum (ATR) of coordination polymer of $^{3}_{\infty}$[Ho(4-PyPz)$_3$] (**4-Ho**).

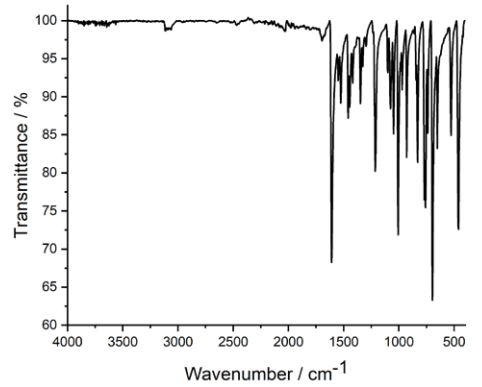

Figure S46. The infrared spectrum (ATR) of coordination polymer of $^{3}_{\infty}$[Er(4-PyPz)$_3$] (**4-Er**).

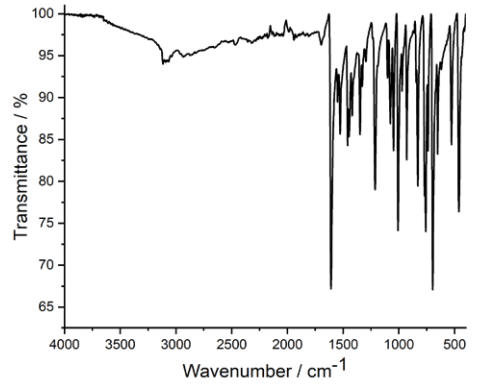

Figure S47. The infrared spectrum (ATR) of coordination polymer $^{3}_{\infty}$[Tm(4-PyPz)$_3$] (**4-Tm**).

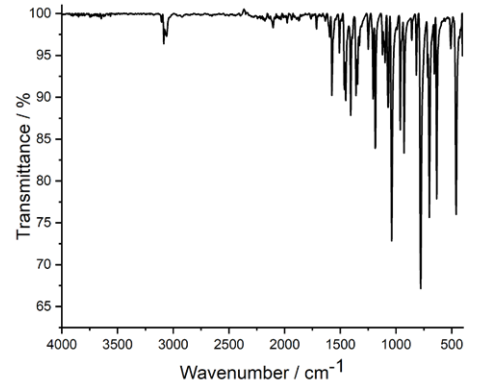

Figure S48. The infrared spectrum (ATR) of coordination polymer of $^{3}_{\infty}$[Ce(3-PyPz)$_3$] (**3-Ce**)

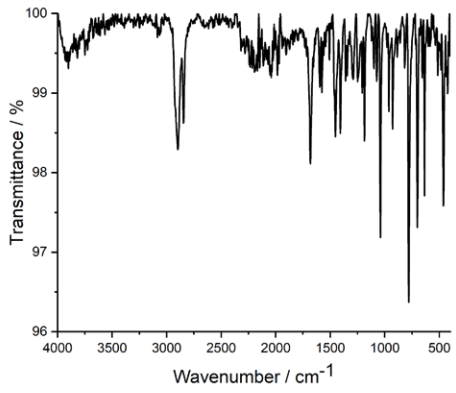

Figure S49. The infrared spectrum (ATR) of coordination polymer of $^{3}_{\infty}$[Pr(3-PyPz)$_3$] (**3-Pr**).

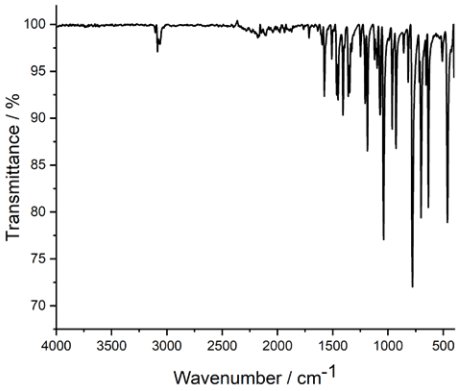

Figure S50. The infrared spectrum (ATR) of coordination polymer of $^{3}_{\infty}$[Nd(3-PyPz)$_3$] (**3-Nd**).

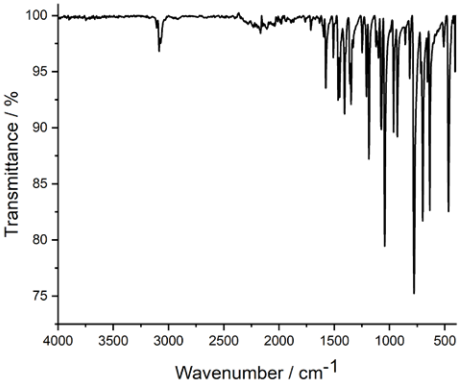

Figure S51. The infrared spectrum (ATR) of coordination polymer of $^{3}_{\infty}$[Ho(3-PyPz)$_3$] (**3-Ho**).

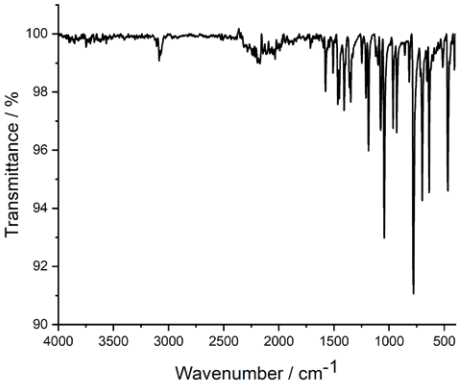

Figure S52. The infrared spectrum (ATR) of coordination polymer of $^{3}_{\infty}$[Er(3-PyPz)$_3$] (**3-Er**).

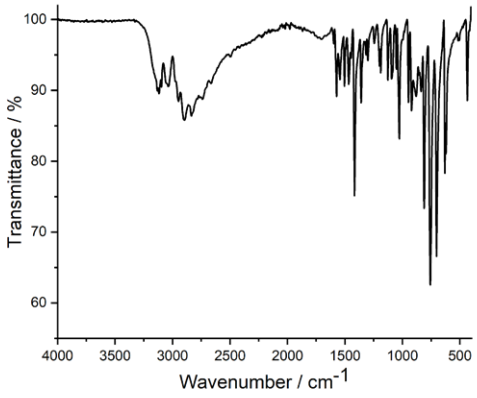

Figure S53. The infrared spectrum (ATR) of 3-PyPzH.

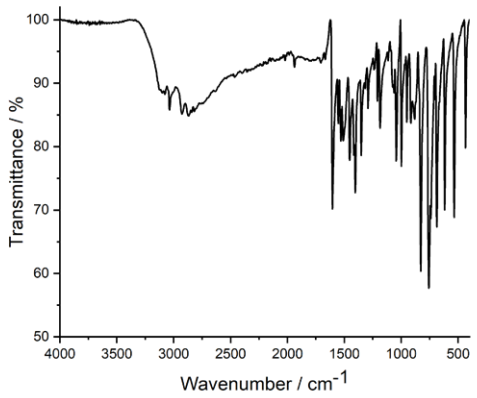

Figure S54. The infrared spectrum (ATR) of 4-PyPzH.

S49

3.1.3. Red emitting cerium(III) and versatile luminescence chromaticity of 1D-coordination polymers and heterobimetallic Ln/AE pyridylpyrazolate complexes

This article has been published in the

Zeitschrift für Anorganische und Allgemeine Chemie

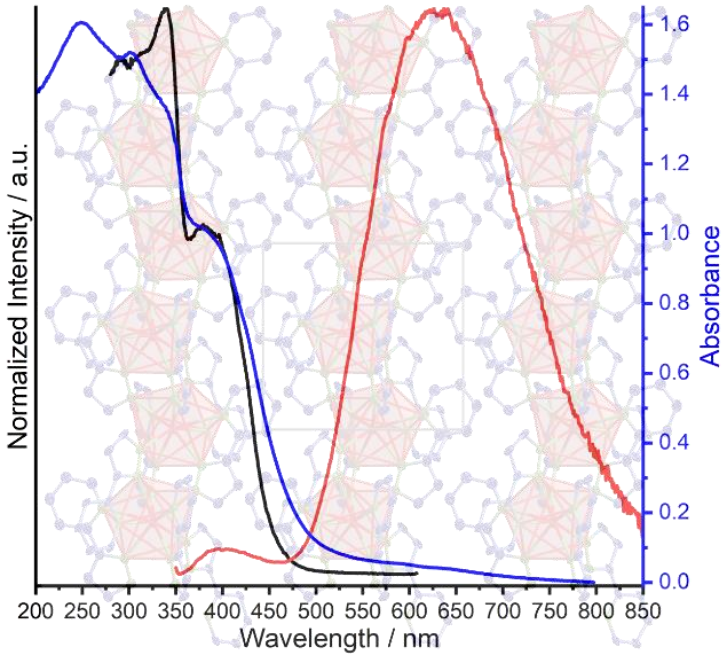

Heba Youssef, Jonathan Becker, Alexander E. Sedykh, Thomas Schäfer, Ilya V. Taydakov, and Klaus Müller-Buschbaum

Reprinted with permission from *Z. Anorg. Allg. Chem.* **2021**, 647, 359–364

DOI 10.1002/zaac.202200295

Journal of Inorganic and General Chemistry
ZAAC
Zeitschrift für anorganische und allgemeine Chemie
www.zaac.wiley-vch.de
RESEARCH ARTICLE

DOI: 10.1002/zaac.202200295

Red Emitting Cerium(III) and Versatile Luminescence Chromaticity of 1D-Coordination Polymers and Heterobimetallic Ln/AE Pyridylpyrazolate Complexes

Heba Youssef,[a, b] Jonathan Becker,[a] Alexander E. Sedykh,[a] Thomas Schäfer,[a] Ilya V. Taydakov,[c] and Klaus Müller-Buschbaum*[a, d]

Dedicated to the late Professor Rudolf Hoppe on the occasion of his 100th birthday

Ten homoleptic lanthanide containing 1D-coordination polymers, three heterobimetallic lanthanide/alkaline earth complexes as well as two alkaline earth complexes of the formula $^1_\infty$[Ln(2-PyPz)$_3$], [Tb$_2$AE(2-PyPz)$_8$], and [AE(2-PyPz)$_2$(2-PyPzH)$_2$], Ln=La–Nd, Sm–Ho, AE=Ca, Sr, Ba were obtained by reactions of the lanthanide (Ln) and/or the alkaline earth metals (AE) with the ligand 3-(2-pyridyl)pyrazole. Organic melt based and/or solvothermal synthesis results in a redox reaction. The investigated compounds exhibit fair thermal stability up to 400 °C. The Ce^{3+} compound exhibits a bright and red 5d-based broad band emission with a maximum at around 640 nm under UV excitation marking an example of a strong reduction of the exited 5d states of Ce(III). The co-doping of the Gd-containing coordination polymers with Eu^{3+} and Tb^{3+} allows for a shift in the chromaticity from the ion specific 4f-based emission colors close to white light emission and thus for a versatile tuning of the chromaticity. The co-doping of Eu^{3+} with Tb^{3+} and *vice versa* shows metal-to-metal energy transfer (MMET) between 4f-levels of Tb^{3+} and Eu^{3+}, which influences the tuning of the emission colour.

Introduction

High intensity, low electricity consumption, and long lifetime are the advantages of solid state lighting (SSL) which is expected to replace incandescent lamps.[1] The Ce^{3+}-doped yellow- emitting phosphor ceramic $Y_3Al_5O_{12}$ can be effectively excited by a blue-emitting laser and used in higher-power white light applications due to its high luminescent efficiency and thermal stability.[2] Also, Ce^{3+} containing coordination polymers and complexes have short excited-state lifetimes (< 100 ns)[3] ascribed to the beneficial character of the spin- and parity-allowed d-f transitions.[4] Ce^{3+} allows for a tunable emission color, because the excited 5d energy levels are sensitive to the coordination environment, resulting in dependence of the coordination partners and the crystal field on the emission and its chromaticity.[5] The cost of cerium is rather low due to its abundance on Earth (higher than copper) and a less complicated isolation process from other lanthanide elements.[4b,6] Most reported Ce^{3+} complexes are non-emissive due to luminescence quenching by linkers and solvent molecules.[7] The emissive Ce^{3+} examples in the literature are mainly near UV and blue emitters[8] beside some doped materials exhibiting green/yellow[9] or even the unusual yellow emission.[10] Recently, the red emission in solid state LEDs was within the scope of Ce/Pr systems, such as $Lu_3Al_5O_{12}$:$Ce^{3+}Pr^{3+}$,[11] YAG:$Ce^{3+}Pr^{3+}$,[12] $Gd_3Ga_5O_{12}$:$Ce^{3+}Pr^{3}$,[13] $Y_3Al_5O_{12}$:Ce nanophosphor doped with Pr^{3+},[14] and the cerium-doped scandate.[15] We now present an undoped Ce^{3+} red phosphor, which indicates the value of investigating new N-donor based ligands and coordination compounds to achieve a high variety of photoluminescence of the lanthanides.

Heterobimetallic terbium/alkaline earth (Tb/AE) compounds reported in the literature contain either oxygen donors or multifunctional donors,[16] such as [Tb$_2$Ca(OQ)8]·nHOQ (OQ = 8-quinolate).[17] Fewer examples are known for the bimetallic system Tb/Sr, e.g. [Tb$_2$Sr$_3$(pda)$_6$(H$_2$O)$_{18}$]·13H$_2$O.[18]

Previously, the ligand 3-(2-pyridyl)pyrazole (2-PyPzH) was mainly used in the synthesis of transition-metal complexes and CPs, either as the main reacting ligand[19] or as a co-ligand,[20] such as the formation of 2D open-channel cadmium(II) frame-

[a] H. Youssef, Dr. J. Becker, A. E. Sedykh, T. Schäfer, Prof. Dr. K. Müller-Buschbaum
Institute of Inorganic and Analytical Chemistry
Justus-Liebig-University Giessen
Heinrich-Buff-Ring 17, 35392 Giessen, Germany
E-mail: klaus.mueller-buschbaum@anorg.chemie.uni-giessen.de
[b] H. Youssef
Department of Chemistry
Faculty of Science, Mansoura University
El Gomhouria, Mansoura Qism 2, 11432, Mansoura Dakahlia Governorate, (Egypt)
[c] Prof. Dr. I. V. Taydakov
Lebedev Physical Institute of the Russian Academy of Sciences
Leninskiy pr-t, 53, 119991, Moscow, Russia
[d] Prof. Dr. K. Müller-Buschbaum
Center of Materials Research (LAMA)
Justus-Liebig-University Giessen
Heinrich-Buff-Ring 16, 35392 Giessen, Germany

Supporting information for this article is available on the WWW under https://doi.org/10.1002/zaac.202200295

works using the mixed ligands terephthalic acid and 2-PyPzH.[21] The tridentate ligand was previously reacted with Ln-$(NO_3)_3.6H_2O$, Ln=Eu^{3+}, Sm^{3+} using ethanol as solvent to obtain complexes, for a selective extraction of actinides over [Eu-$(PyPzH)_2(NO_3)_3$].[22] To the best of our knowledge, the ligand 2-PyPzH has not yet been used in reactions with a heterobimetallic AE/Ln system, nor monometallic AE. Instead, 2-PyPzH was used as a starting material in a large number of ligand syntheses. Some of these derivatized ligands were later used in coordination chemistry with transition metals[23] and lanthanides.[24] as well as a few examples with AE metals.[25] Related ligands, such as 3-(3-pyridyl)pyrazole (3-PyPzH), and 3-(4-pyridyl)pyrazole (4-PyPzH), have been used to obtain Cu^{+} and Ag^{+} complexes, indicating a high-lying intersystem crossing that can lead to efficient phosphorescence.[26] Besides, homoleptic and highly luminescent trivalent lanthanide 3D coordination polymers with the formulas $^{3}_{\infty}$[Ln(3-PyPz)$_3$], and $^{3}_{\infty}$[Ln(4-PyPz)$_3$], Ln=Sm, Eu, Gd, Tb, Dy were recently investigated in our group.[27] Based on these results, we successfully attempted to synthesize new luminescent coordination polymers along the lanthanide series, homoleptic, heterobimetallic rare earth/alkaline earth compounds.

Results and Discussion

Synthesis and Structural Analysis

Either organic melt or solvothermal synthesis-based reactions of 3-(2-pyridyl)pyrazole (2-PyPzH) (Scheme 1) with elemental lanthanides were used to obtain a series of ten coordination polymers $^{1}_{\infty}$[Ln(2-PyPz)$_3$], Ln=La (**1**), Ce (**2**), Pr (**3**), Nd (**4**), Sm (**5**), Eu (**6**), Gd (**7**), Tb (**8**), Dy (**9**), and Ho (**10**). Solvothermal reactions of 2-PyPzH with a mixture of elemental Tb and AE yielded three complexes [Tb_2AE(2-PyPz)$_8$], AE=Ca (**11**), Sr (**12**), and Ba (**13**), while the reaction with elemental alkaline earth metal obtained two complexes [AE(2-PyPz)$_2$(2-PyPzH)$_2$], AE=Ca (**14**), and Sr (**15**).

All synthesized compounds crystallize in the monoclinic crystal system, $^{1}_{\infty}$[Ln(2-PyPz)$_3$], Ln=La–Ho (**1–10**) in $P2_1$, [Tb_2AE-(2-PyPz)$_8$], AE=Sr (**12**), Ba (**13**) and [Sr(2-PyPz)$_2$(2-PyPzH)$_2$] (**15**) in $P2_1/n$, and [Ca(2-PyPz)$_2$(2-PyPzH)$_2$] (**14**) in $C2/c$, except for [Tb_2Ca(2-PyPz)$_8$] (**11**), which crystallizes in the triclinic crystal system with space group $P\bar{1}$. In $^{1}_{\infty}$[Ln2-PyPz)$_3$] (**1–10**), each Ln^{3+} ion coordinates to nine nitrogen atoms in a distorted tricapped trigonal fashion, two nitrogen atoms of the pyrazolate anion acting as a bridge between two neighboring trivalent lanthanide ions, resulting in an altogether one-dimensional coordination polymer (Figure 1a, 1b). The coordination environment of Tb^{3+} decreases to eight when AE^{2+} is added to the heterobimetallic system [Tb_2AE(2-PyPz)$_8$] (**11–13**) forming a distorted bi-capped trigonal prism (Figure 1c, 1d). The higher tendency of Ln^{3+} to form high coordination numbers drives Tb^{3+} to allocate a position, in which it can coordinate with two nitrogen atoms of both, the pyridyl ring and the pyrazolate ring of each tridentate ligand, so that each rare earth ion binds to three chelating bridging ligands and a terminal pyridylpyrazolate anion. These ligands bridge through the pyrazolate ring to the central hexacoordinated alkaline earth atom in a distorted tetragonal bipyramidal environment. The absence of Ln^{3+} in the [AE(2-PyPz)$_2$(2-PyPzH)$_2$] complexes allows the AE^{2+} ions to occupy a central position to coordinate with eight nitrogen atoms leading to a higher coordination number of AE compared to the bimetallic complexes, and each ligand acts as a bidentate chelating Lewis base (Figure 1e, 1f). Electroneutrality is settled by two protons bridging two pyrazolate moieties with two neutral ligands. The backbones of the two pyridylpyrazolate units are perpendicular to each other, resulting in a triangular dodecahedron as coordination polyhedron. The larger ionic radius of eight-coordinate AE^{2+} in the monometallic complexes [AE(2-PyPz)$_2$(2-PyPzH)$_2$], AE=Ca (**14**), and Ba (**15**) leads to a general elongation of the Ca–N(pz) distance, N(pz) being the pyrazolate nitrogen atom, compared to the heterobimetallic complexes [Tb_2AE(2-PyPz)$_8$], AE=Ca (**11**), and Sr (**12**), in which AE^{2+} is six-coordinate. The average Ca–N(pz) distance in **11**, and **12** is 253 pm, while in **14**, and **15**, it is 258 pm. This corresponds well with the change in the ionic radius of AE^{2+} as does the increase in the AE–N distances from an average of 244 in **11** to 280 pm in **13** for the AE^{2+} ions Ca^{2+} and Sr^{2+}. Similar trinuclear complexes with homoleptic nitrogen donor Lewis base could not be found in the literature, so we compare the average of Ca–N(pz) (244 pm, **11**), and Sr–N(pz) (262 pm, **12**) with a mononuclear system, such as AE bis[κ^3N–tris(3,4,5-trimethylpyrazolyl)methanide] (Ca–N 244.1, Sr–N 258.3 pm),[28] revealing good agreement. For **15**, the average of Sr–N(py) (273 pm), N(py) being the pyridyl nitrogen atom are larger than the corresponding average of the Sr–N of the pyrazolate rings (Sr–N(pz) 264 pm) as a result of larger electrostatic attraction. In addition, the Sr1–N(py) distances (274.0(2) pm), and Sr2–N(py) (271.4(3) pm) of the deprotonated ligands are shorter than to the pyridyl groups of the neutral ligands (271.7(2), and 272.6(2) pm). Good agreement of the Sr–N distances is observed between **15** (263.2(2)–277.9(3) pm) and the strontium complex bis[3-(1-naphthyl)-5-(2-pyridyl)-2H-pyrazole]strontium bis[3-(1-naphthyl)-5-(2-pyridyl)pyrazolate] (263.8–276.3 pm) with slightly smaller values for the anionic pyrazolate anions.[25b] The interatomic distances of the pyridylpyrazolate anions and the neutral pyridylpyrazole molecules are similar (Table S5), indicating aromatic character in all eight pyridylpyrazolate units, supporting the highly acidic character

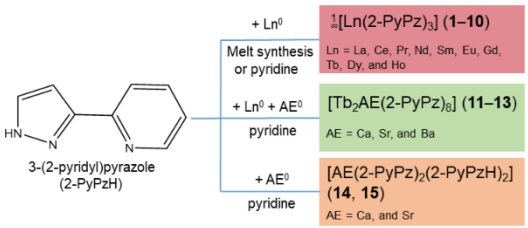

Scheme 1. Synthetic scheme for reactions with 2-PyPzH to obtain the presented 15 compounds: 1D-coordination polymers (top), bimetallic complexes (center), and alkaline earth-based complexes (bottom).

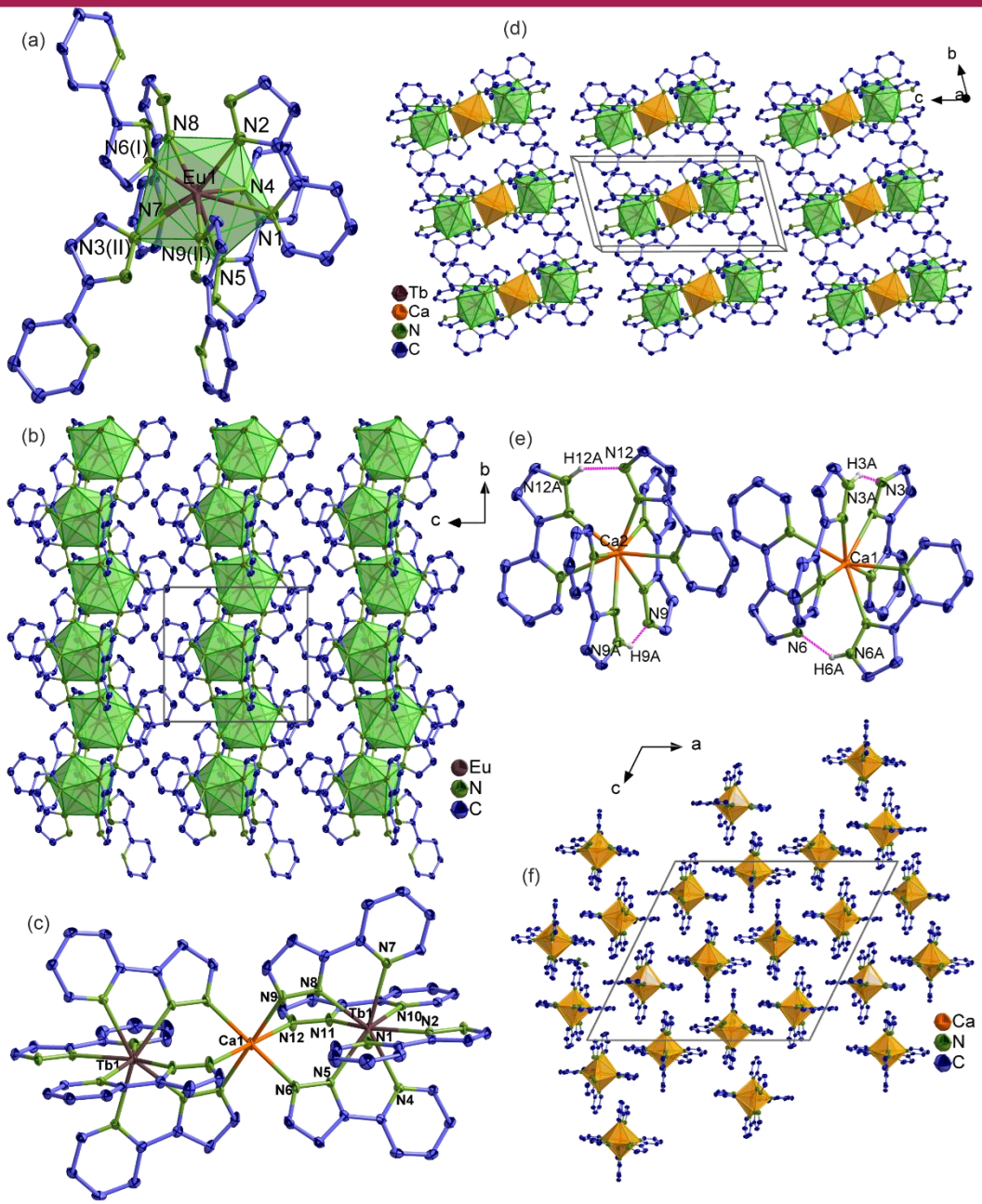

Figure 1. (a) Extended coordination sphere of Eu^{3+} in $^{1}_{\infty}[Eu(2\text{-}PyPzH)_3]$ (**6**), representing the series of isotypic one-dimensional coordination polymers (**1**–**10**). (b) Exemplary crystal structure of **6** with a view along [100]. (c), (d) Excerpts of the crystal structure and view of the unit cell of $[Tb_2Ca(2\text{-}PyPz)_8]$ (**11**). (e), (f) Excerpts of the crystal structure and unit cell of $[Ca(2\text{-}PyPz)_2(2\text{-}PyPzH)_2]$ (**14**) with a view along [010]. N···H···N hydrogen bridges are indicated by dashed lines, the polyhedra around Ln^{3+}, and Ca^{2+} are indicated in green, and orange, respectively. Hydrogen atoms are omitted for clarity, and the thermal ellipsoids are depicted at a 50% probability level for all structures. Symmetry operations: I = −x+2, y+1/2, −z+1 II = −x+2, y−1/2, −z+1.

of the bridging hydrogen atoms. No delocalization of the negative charge of the pyrazolate moieties to the outer aromatic rings is obvious from interatomic distances.

All bulk products (**1–15**) were invistigated by PXRD (Figure 2, S4, S5). The experimental diffraction patterns agree with the diffraction patterns simulated from single-crystal data for all investigated compounds, taking into account the possibility of the first two reflections in $^{1}_{\infty}$[Eu(2-PyPzH)$_3$] (**1–10**) to merge and appear as one reflection (Figure S3). Since the lengths of the *a*-axis (1114.7 pm) and the *c*-axis (1130.1 pm) are close, the spacing of the lattice planes d_{hkl} for [001] and [100], representing the first ($2\theta = 8.786°$) and the second reflection ($2\theta = 8.907°$), respectively, is low. With less than 14 pm between the two lattice planes, the expansion of the volume of the unit cell and the lattice parameters due to the increase in the ionic radii from Ho^{3+} to La^{3+}, and contractions of the angles, one merged broader reflection can be expected to be observed instead of the previously discussed two reflections.

Photophysical Properties

UV-Vis-NIR absorption spectra

Electronic absorption spectra as well as excitation and emission spectra were recorded in the solid state to allow photophysical interpretations of the products $^{1}_{\infty}$[Ln(2-PyPz)$_3$], Ln=La (**1**), Ce (**2**), Pr (**3**), Nd (**4**), Sm (**5**), Eu (**6**), Tb (**8**), Dy (**9**), Ho (**10**), and [Tb$_2$AE(2-PyPz)$_8$] (**11–13**) at room temperature (Figure 3). Absorption spectra localized to the ligand moieties of the Ln^{3+}-based compounds have been reported in the literature and were mostly studied in solution,[29] whereas fewer examples of lanthanide nitrate-based compounds have been reported for the solid state for a wavelength range not exceeding 1000 nm.[30] The absorption spectrum for 2-PyPZH was shown in the literature for the solid state and in acetonitrile solution (7.8×10^{-5} mol L^{-1}) where two characteristic K-band (*ca.* 210 ~ 265 nm; 47619 ~ 37736 cm^{-1}) and B-band (285 ~ 350 nm; 35088 ~ 28571 cm^{-1}) regions corresponding to the π–π^* transitions were observed.[20i,31] In the products presented here, an intense wide absorption band of the ligand in the UV region due to coordination appears for every sample, as shown in Figure 3. In addition, sharp and weak to medium bands can be assigned to the respective f–f transitions in both VIS and NIR regions for $^{1}_{\infty}$[Ln(2-PyPz)$_3$], Ln=Pr^{3+} (**3**), Nd^{3+} (**4**), Sm^{3+} (**5**), Dy^{3+} (**9**), and Ho^{3+} (**10**) ions, as assigned in Table 1.[30d,32] For $^{1}_{\infty}$[Ce(2-PyPz)$_3$] (**2**), formation of a shoulder at a higher wavelength is observed due to transition from 4f to 5d. The addition of alkaline earth ions to Tb^{3+} led to the formation of a new broad absorption band starting at 515 nm (19417 cm^{-1}) in [Tb$_2$Ca(2-PyPz)$_8$] (**11**) and 470 nm (21277 cm^{-1}) in [Tb$_2$Sr(2-PyPz)$_8$] (**12**) with maxima at 583 and 532 nm (17153 and 18797 cm^{-1}), respectively, and at 480 nm (20833 cm^{-1}) for [Tb$_2$Ba(2-PyPz)$_8$] (**13**) being less distinguishable between two maxima.

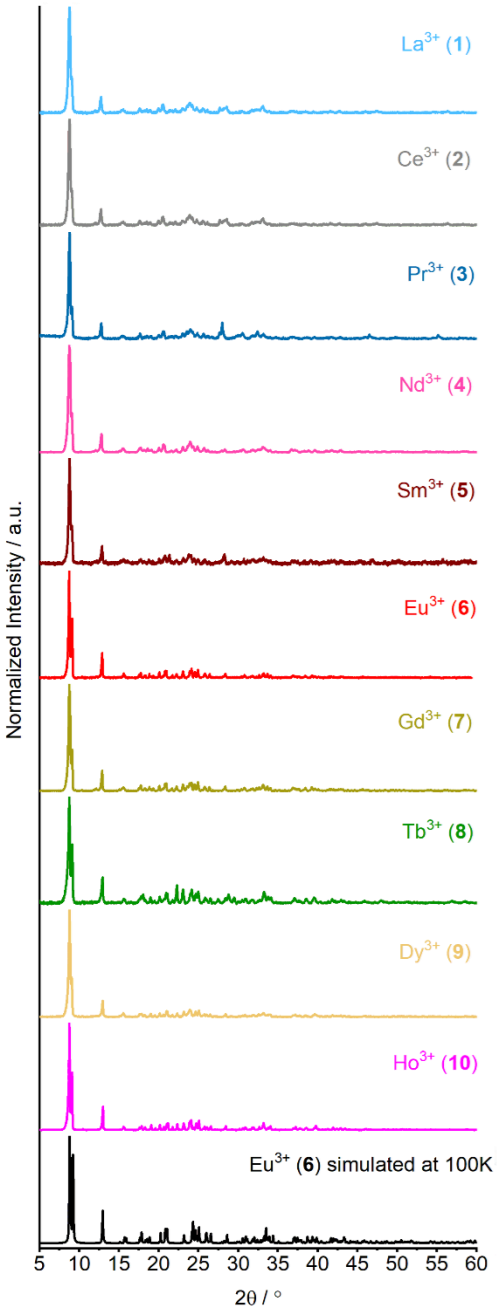

Figure 2. Comparison of the experimental X-ray powder diffraction patterns of $^{1}_{\infty}$[Ln(2-PyPz)$_3$], Ln=La (**1**), Ce (**2**), Pr (**3**), Nd (**4**), Sm (**5**), Eu (**6**), Gd (**7**), Tb (**8**), Dy (**9**), Ho (**10**) at 298 K with the respective simulated pattern from single-crystal X-ray data at 100 K.

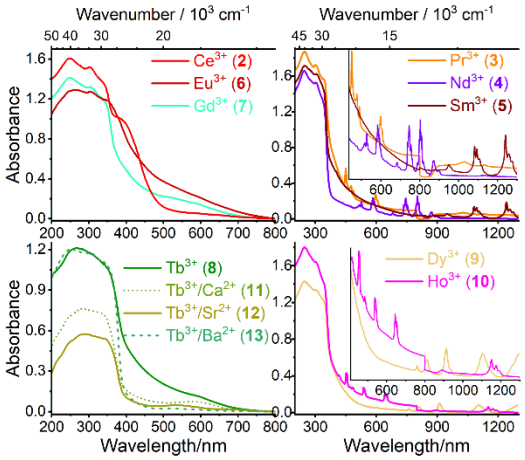

Figure 3. Solid state absorption spectra of $^{1}_{\infty}$[Ln(2-PyPz)$_3$], Ln=Ce^{3+} (**2**), Pr^{3+} (**3**), Nd^{3+} (**4**), Sm^{3+} (**5**), Eu^{3+} (**6**), Gd^{3+} (**7**), Tb^{3+} (**8**), Dy^{3+} (**9**), Ho^{3+} (**10**) and [Tb$_2$AE(2-PyPz)$_8$], AE=Ca (**11**), Sr (**12**), and Ba (**13**) in the solid state at room temperature.

Emission and excitation spectra

The one-dimensional coordination polymer $^{1}_{\infty}$[Ce(2-PyPz)$_3$] (**2**) shows interesting photoluminescence properties with Ce^{3+}-centered emission in the VIS range of red color, which can already be seen with the naked eye under the UV lamp. Photoluminescence spectroscopy determinations of **2** (Figure 4) reveal broadband emission from 500 to exceed 850 nm being centered at 640 and 620 nm (15625 and 16129 cm^{-1}) for 77 K and RT, respectively, and indicating large crystal field splitting and a large redshift for the emission wavelength of Ce^{3+}. The excitation spectrum exhibits a shoulder at 392 nm (25510 cm^{-1}) at 77 K, and 379 nm (26385 cm^{-1}) at RT, which correspond to the lowest energy levels of the crystal field splitting bands of the 5d excited state of the Ce^{3+} ion. The maximum excitation band at 335 nm (29851 cm^{-1}) is correlated with the coordinated 2-PyPzH ligand. The lifetime of **2** is only 2 ns as a result of the parity allowed nature of the 5d–4f transition. Actually, red-emitting cerium in **2** has a shorter lifetime than the reported yellow, blue, and green Ce^{3+} emitters, being on the order of tens of nanoseconds.[3a,b,8b] For instance, the mixed ligand series of the luminescent Ce^{3+} complex with the general one formula [(Me$_3$Si)$_2$NC–(NiPr)$_2$]$_x$Ce[N(SiMe$_3$)$_2$]$_{3-x}$ (x=0, **1-N**; x=1, **2-N**; x=2, **3-N**; x=3, **4**) that exhibit yellow (**1-N**), lime-green (**2-N**), green (**3-N**), and blue light (**4**) emission with lifetimes of 24, 65, 117, and 83 ns, respectively.[5d] In contrast, distinct longer lifetimes are observed for the parity-forbidden 4f–4f transitions, which reach the microsecond scale for Sm^{3+}, Eu^{3+}, Tb^{3+}, and Dy^{3+} (Table 2). A considerable antenna effect is expected for both Eu^{3+} (**6**), and Tb^{3+} (**8**), with the ligand being mainly responsible for the excitation. For Pr^{3+} (**3**), Nd^{3+} (**4**), Sm^{3+} (**5**), and Dy^{3+} (**9**), additional weak direct 4f–4f-excitation is indicated by a series of low intensities of ion-specific sharp lines (Figures 4, 5). As a result of the energy differences (ΔE) between the ligand triplet state (~ 22831 cm^{-1}) and the energy positions of Eu^{3+} (^{5}D$_0$=20100 cm^{-1}), and Tb^{3+} (^{5}D$_4$=20500 cm^{-1})[32a,c] considering the Latva rule, ΔE is 2731, and 2331, respectively. Thereby, the ΔE value is in the optimal range (2500–3000 cm^{-1}) in Eu^{3+} and still close enough for Tb^{3+}. Thus, it is expected that the Eu^{3+}, Tb^{3+} based compounds would have the highest lifetime and quantum yield among the series. This conclusion is supported by the observation of long lifetimes for Eu^{3+} (**6**) emissive state (870 μs), and Tb^{3+} (**8**) (280 μs) in comparison to Sm^{3+} (**5**) (8.28 μs), and Dy^{3+} (**9**) (4.14 μs).

In addition, the observed quantum yield (QY) is found to be highest for the Eu^{3+}, and Tb^{3+} coordination polymers **6**, and **8**, although it is altogether limited, with QY=5.8(4), and 6.3(5)%, respectively. Notably, the triplet state of the ligand was revealed by the emission of the Gd^{3+} containing compound, a phosphorescence band with onset at λ_{onset}=438 nm (22831 cm^{-1}) being intense and better resolved at 77 K. The phosphorescent emission was also detected with a gating (cutting off the emission of the singlet state, Figure S13). The photophysical properties of the obtained products with Sm^{3+} (**5**), Eu^{3+} (**6**), Tb^{3+} (**8**), and Dy^{3+} (**9**) are comparable to homoleptic frameworks with 3-(3-pyridyl)pyrazolate (3-PyPz$^-$), and 3-(4-pyridyl)pyrazole (4-PyPz$^-$). The longer lifetime observed for Eu^{3+} (870 μs) and the shorter lifetime for Tb^{3+} (**8**) (280 μs) in comparison to those reported for the $^{3}_{\infty}$[Ln(3-PyPz)$_3$], (Ln=Eu (576 μs), and Tb (1087.4 μs), and $^{3}_{\infty}$[Ln(4-PyPz)$_3$] (Ln=Eu (323 μs), Tb (627.3 μs)[27] is related to the position of the triplet state for 3-PyPz$^-$ (λ_{onset}=430 nm, ~23250 cm^{-1}) and 4-PyPz$^-$ (λ_{onset}=423 nm, ~23640 cm^{-1}). This leads to a better energy transfer to Tb^{3+} and less for Eu^{3+} excited 4f states. The lifetimes for Sm^{3+} (**5**), and Dy^{3+} (**9**) are shorter than for $^{3}_{\infty}$[Ln(3-PyPz)$_3$], (Ln=Sm (15.9 μs), and Dy (15.7 μs), and $^{3}_{\infty}$[Ln(4-PyPz)$_3$] (Ln=Sm (15.8 μs), Dy (12.1 μs). However, the lifetimes for Sm^{3+} (**5**), Tb^{3+} (**8**), and Dy^{3+} (**9**) are still higher than several examples in the literature.[33] The internal quantum yield (IQY) of the Eu^{3+} centered emission was calculated using Wert's formula with

Table 1. Absorption wavelengths of transitions of $^{1}_{\infty}$[Ln(2-PyPz)$_3$], Ln=Pr, Nd, Sm, Dy, and Ho in the solid state at room temperature.

Intra-4f absorption transitions			
	Ground state	Excited states	
Pr^{3+} (**3**)	^{3}H$_4$→	^{3}P$_2$, ^{3}P$_1$, ^{3}P0, ^{1}D$_2$	450, 476, 489, 597 nm
Nd^{3+} (**4**)	^{4}I$_{9/2}$→	^{4}G$_{7/2}$, ^{4}G$_{5/2}$, ^{4}F$_{9/2}$, ^{4}F$_{7/2}$, ^{4}F$_{5/2}$, ^{4}F$_{3/2}$	527, 583, 683, 745, 802, 871 nm
Sm^{3+} (**5**)	^{6}H$_{5/2}$→	^{6}F$_{11/2}$, ^{6}F$_{9/2}$, ^{6}F$_{7/2}$	949, 1081, 1240 nm
Dy^{3+} (**9**)	^{6}H$_{15/2}$→	^{6}F$_{3/2}$, ^{6}F$_{5/2}$, ^{6}F$_{7/2}$, ^{6}F$_{9/2}$	760, 810, 913, 1104 nm
Ho^{3+} (**10**)	^{5}I$_8$→	(^{5}G, ^{3}G)$_5$, ^{5}G$_6$, ^{5}F$_3$, ^{5}F$_4$, ^{5}F$_5$, ^{5}I$_6$	417, 452, 484, 538, 644, 1151 nm

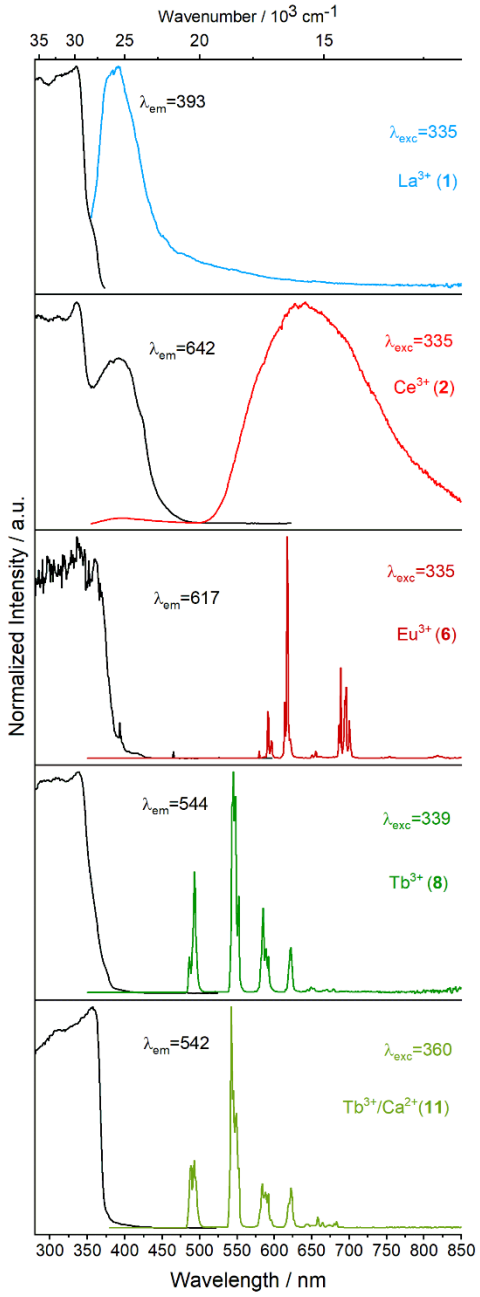

Figure 4. Normalized solid state excitation (black) and emission (colored) spectra of $^{1}_{\infty}$[Ln(2-PyPz)$_3$], Ln=La (**1**), Ce (**2**), Eu (**6**), and Tb (**8**) as well as [Tb$_2$Ca(2-PyPz)$_8$] (**11**) at 77 K. Wavelengths for which the spectra were recorded are reported in the legends.

refractive index equals 1.5.[34] The equation gives a moderate-high Internal QY of 37.2 % which is in the middle of $^{3}_{\infty}$[Eu(3-PyPz)$_3$] and $^{3}_{\infty}$[Eu(4-PyPz)$_3$] 48 and 33%, respectively.

The excitation spectra for 2-PyPzH at RT and 77 K show broadband in the UV region with maxima at 364 nm (27472 cm^{-1}) corresponding to the $S_n \leftarrow S_0$ transitions.[19c,20g,i] This ligand-based excitation band shows a hypochromic shift upon coordination to the investigated compounds (**1**–**11**). The emission maxima of the ligand are observed in the range of 400 to 410 nm (25000 to 24390 cm^{-1}), as reported.[19c,20g,i] This fluorescence band has a lifetime of 1.47(7) ns, which is shorter than the related ligands 3-PyPzH (3.4 ns), and 4-PyPzH (6.07 ns).[27]

For $^{1}_{\infty}$[Eu(2-PyPz)$_3$] (**6**) and $^{1}_{\infty}$[Tb(2-PyPz)$_3$] (**8**) (Figure 4), the highest intensity is found for the transitions $^5D_0 \rightarrow {}^7F_2$ at 517 nm (19342 cm^{-1}), and $^5D_4 \rightarrow {}^7F_5$ at 545 nm (18349 cm^{-1}), respectively, as expected for Eu^{3+} and Tb^{3+}.[35] For **6**, the transition $^5D_0 \rightarrow {}^7F_0$ indicates that the Eu^{3-} ion occupies a site of the C_{nv}, C_n, or C_s symmetry class (in this particular case C_3), to evade the selection rules of the Judd-Ofelt theory.[35a]

The emission spectra of [Tb$_2$AE(2-PyPz)$_8$] (**11**–**13**) display rather sharp lines, which can be identified with f–f transitions regarding Tb^{3+} between the $^5D_4$ excited state and the $^7F_{6-0}$ levels. Ligand emission is also observable at RT for [Tb$_2$Ca(2-PyPz)$_8$] (**11**), and [Tb$_2$Sr(2-PyPz)$_8$] (**12**), exhibiting a hypsochromic shift caused by a decrease in the π-electron density of the pyridylpyrazolate anions by the double linkage to two metal ions. For $^{1}_{\infty}$[Pr(2-PyPz)$_3$] (**3**), $^{1}_{\infty}$[Sm(2-PyPz)$_3$] (**5**), and $^{1}_{\infty}$[Dy(2-PyPz)$_3$] (**9**) (Figure 5), the highest intensity is found at 617 (16207 cm^{-1}, for Pr^{3+}, corresponding to $^3P_0 \rightarrow {}^3H_6$), 598 (16722 cm^{-1}, for Sm^{3+}, corresponding to $^4G_{5/2} \rightarrow {}^6H_{7/2}$), and 572 nm (17482 cm^{-1}, for Dy^{3+}, corresponding to $^4F_{9/2} \rightarrow {}^6H_{13/2}$), respectively. NIR emission bands can also be observed for **3** at 1045 nm (9569 cm^{-1}) corresponding to $^1D_2 \rightarrow {}^3F_4$ transition of Pr^{3+}, for **5** at 782, 898, 945, 1025, and 1172 nm (12788, 11136, 10582, 9756, and 8532 cm^{-1}) corresponding to the $^4G_{5/2} \rightarrow {}^6H_{13/2}$ and $^4G_{5/2} \rightarrow {}^6F_{J/2}$, J = 3–9 transitions of Sm^{3+} and for **9** at 750, 849, 948, 1008, 1170, and 1288 nm (13333, 11779, 10548, 9921, 8547, and 7764 cm^{-1}) corresponding to the transitions $^4F_{9/2} \rightarrow {}^6H_{J/2}$, (J = 9, 7, 5), and $^6F_{J/2}$, (J = 7, 5, 3) of Dy^{3+}, respectively. NIR emission bands can also be observed for Nd^{3-} (**4**), and Ho^{3+} (**10**) at 900, 1063, and 1370 nm (11111, 9407, and 7299 cm^{-1}) corresponding to $^4F_{3/2} \rightarrow {}^4I_{J/2}$, (J = 9, 11, 13) transitions of Nd^{3+} ions and for **10** at 985, 1186 nm (10152, 8432 cm^{-1}) corresponding to $^5F_5 \rightarrow {}^5I_7$ and $^5I_6 \rightarrow {}^5I_8$ transitions beside the VIS transition at 656 nm (15244 cm^{-1}) corresponding to $^5F_5 \rightarrow {}^5I_8$ of Ho^{3+}, respectively.

Tuning of the luminescence chromaticity is further possible by co-doping of several of the products with Tb^{3+} and/or Eu^{3+}, including the Ce-based emitter. Deliberate co-doping of the Ce-containing coordination polymer with 0.5% Tb^{3+} already shifts the emission color towards a higher energy region, this shift continues with the statistic replacement of Ce^{3+} by 5% Tb^{3+} (Figure S21). The Ce emission in the co-doped samples is partly quenched and an enhancement of the Tb emission observed.

This can be attributed to the fact that Ce^{3-} is a sensitizer due to its allowed f–d transitions and its broad emission band

Table 2. Photophysical data of 2-PyPzH, $^{1}_{\infty}$[Ln(2-PyPz)$_3$] (**1**–**10**) and [Tb$_2$AE(2-PyPz)$_3$] (**11**–**13**) in the solid state at room temperature and 77 K.

ID	τ(RT)[a]	λex/λem [nm][b]	τ(77 K)[c]	λex/λem [nm][d]	Φ [%][e]	λex/λem [nm][f]
2-PyPzH	1.47(7) ns	287/407	2.7(1) ns	287/410	n/a	n/a
La^{3+}	1.51(2) ns	368/393	1.69(1) ns	368/393	n/a	n/a
Ce^{3+}	2.03(4) ns	287/628	1.30(3) ns	287/642	0.3(1)	310/475–800
Pr^{3+}	1.03(2) ns	287/372	1.30(3) ns	287/373	n/a	n/a
Nd^{3+}	0.97(4) ns	287/375	0.98(4) ns	287/373	n/a	n/a
Sm^{3+}	8.28(2) µs	346/598	7.75(5) µs	340/598	0.3(1)	345/550–730
Eu^{3+}	870(2) µs	341/617	1179(2) µs	335/617	5.8(4)	345/575–715
Gd^{3+}	9.9(2) µs	428/536	656(12) µs	344/482	0.3(1)	330/475–750
	0.93(3) ns	287/381	1.08(2) ns	287/388	< 0.1	330/345–460
Tb^{3+}	280(1) µs	347/545	806(2) µs	339/545	6.3(5)	340/475–690
Dy^{3+}	4.14(4) µs	348/573	6.45(5) µs	342/572	0.4(1)	345/460–770
Ho^{3+}	1.08(1) ns	287/382	1.01(4) ns	287/393	n/a	n/a
Tb/Ca	795(4) µs	313/545	1019(7) µs	360/542	1.87(6)	355/475–690
Tb/Sr	37.3(3) µs	356/545	1226(3) µs	363/545	n/a	n/a
Tb/Ba	49.8(3) µs	363/545	1048(5) µs	362/545	2.0(1)	355/475–690

[a] Emission lifetime determined at 298 K. [b] Excitation and emission wavelengths for emission lifetime at 298 K. [c] Emission lifetime determined at 77 K. [d] Excitation and emission wavelengths for emission lifetime at 77 K. [e] Quantum yield. [f] Excitation wavelength and emission range of QY measurements.

that can overlap with an acceptor absorption band of Tb^{3+}, resulting in energy transfer from Ce^{3+} to Tb^{3+}.[36] The Gd^{3+} sample (**7**) shows beside the triplet state of 2-PyPz , characteristic Eu^{3+} and Tb^{3+} 4f–4f transitions indicating a small Eu and Tb-impurity relevant for photoluminescence. The low concentration of Eu^{3+} and Tb^{3+} ions in the structure reduced the probability of cross-relaxation, thus enhancing its metal center-based luminescence. In addition, the ligand is a good sensitizer for Eu^{3+} and Tb^{3+}. A deliberate co-doping of the Gd-containing coordination polymer with Eu^{3+} and Tb^{3+} allows a tuning towards white-light emission. Mixing the three emission colors results in a shift towards yellow, orange, and even the white point with color coordinates x = 0.29 and y = 0.36 for 0.2 % Eu (**7a**) at 77 K.[37] The statistic replacement of Eu^{3+} with 5–25 % Tb^{3+} was not sufficient to observe the characteristic emission bands of Tb^{3+} indicating a metal-to-metal energy transfer (MMET) from Tb to Eu. Even for the equal percentage (50 % Eu + 50 % Tb), the characteristic Tb^{3+} emission bands are just observable, but with much lower intensity than the transitions of Eu^{3+}. The intensity of the Tb^{3+} transitions increases for 95 % Tb, but still does not dominate the spectra, confirming an MMET from 4f-excited states of Tb^{3+} to 4f-excited states of Eu^{3+}. The emission colors of $^{1}_{\infty}$[$Ce_{1-x}Tb_x$(2-PyPz)$_3$] (**2a**, **2b**; x = 0.005, 0.05), $^{1}_{\infty}$[$Tb_{0.90}Ce_{0.1}$(2-PyPz)$_3$] (**8a**), $^{1}_{\infty}$[$Gd_{1-x-y}Eu_xTb_y$(2-PyPz)$_3$]:Eu^{3+},Tb^{3+} (**7a**–**7f**; x = 0.002 – y = 0.01), $^{1}_{\infty}$[$Eu_{1-x}Tb_x$(2-PyPz)$_3$] (**6a**–**6c**; x = 0.05–0.50), $^{1}_{\infty}$[$Tb_{0.95}Eu_{0.05}$(2-PyPz)$_3$] (**8b**) are represented in CIE 1931 chromaticity diagrams in the SI (Figure S27), and the color coordinates are listed in Table S6. Excitation and emission spectra for the deliberate doping experiments are shown in Figures S21–S26.

Thermal analysis

Simultaneous DTA and TG investigations combined with mass spectrometry for $^{1}_{\infty}$[Eu(2-PyPz)$_3$] (**6**) and [Tb$_2$Ca(2-PyPz)$_3$] (**11**) as representatives were carried out to investigate the thermal behavior of both the Ln series and the Ln/AE series. The DTA/TG investigations for **6** and **11** (Figure 6) show endothermic signals with an onset temperature of about 400 °C and a mass loss of 49.8 % (**6**), and 38.2 % (**11**) coinciding with two (**6**) and four (**11**) equivalents of 2-PyPzH (theoretical mass loss of 49.7 (**6**), 38.4 % (**11**)). Further confirmation of the decomposition process was the detection of a set of mass signals that can be assigned to fragments of the ligand ($C_7H_6N^+$ m/z = 104, $C_5H_5N^+$ m/z = 79, $C_5H_4N^+$ m/z = 78, $C_2HN_2^+$ m/z = 53, $C_2N_2^+$ m/z = 52, $C_2NH_3^+$ m/z = 41, $C_2H_3^+$ m/z = 27, $C_2H_2^+$ m/z = 26, CH_3^+ m/z = 15). An additional exothermic signal was observed at about 900 °C in **6** indicating further decomposition or unknown phase formation with the remaining constituents (that is, the metal ions and one equivalent of 2-PyPzH).

Conclusion

A novel Ce^{3+}-based broad-band red-emitting material was synthesized from the metal together with the ligand 3-(2-pyridyl)pyrazole (2-PyPzH). $^{1}_{\infty}$[Ce(2-PyPz)$_3$] represents the exception of an undoped Ce^{3+} phosphor material to show intense red emission based on 5d–4f transitions.

Along the lanthanide series, nine other homoleptic lanthanide-based 1D-coordination polymers of composition $^{1}_{\infty}$[Ln(2-PyPz)$_3$] have been synthesized and characterized, all being luminescent. Heterobimetallic complexes of the lanthanides together with alkaline earth metals of the formula [Tb$_2$AE(2-PyPz)$_3$], and two mononuclear complexes [AE(2-PyPz)$_2$(2-

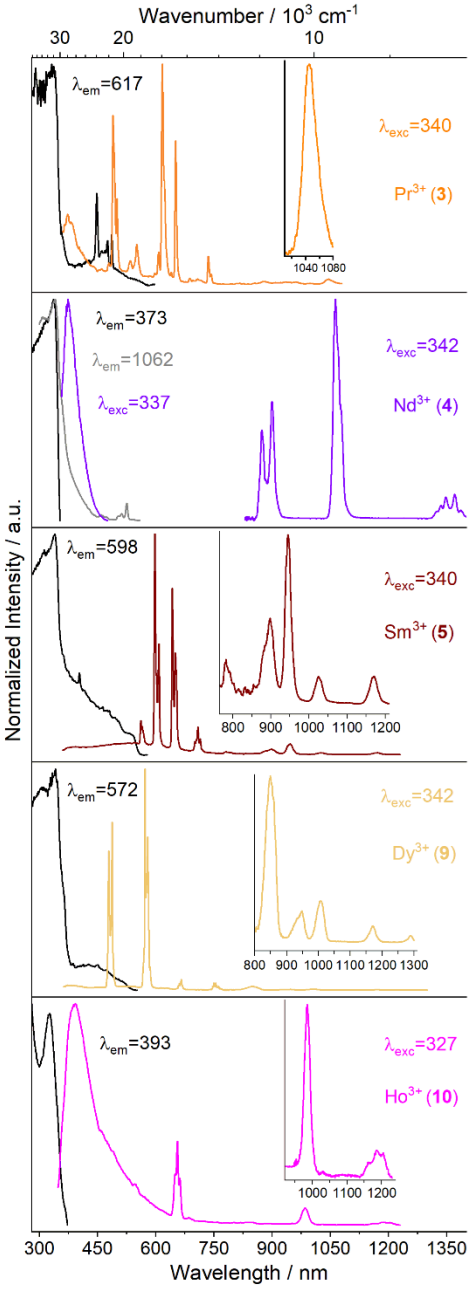

Figure 5. Normalized solid state excitation (black) and emission spectra (colored) of $^{1}_{\infty}$[Ln(2-PyPz)$_3$], Ln=Pr (**3**), Nd (**4**), Sm (**5**), Dy (**9**), and Ho (**10**) at 77 K. Wavelengths, for which the spectra were recorded, are reported in the legends.

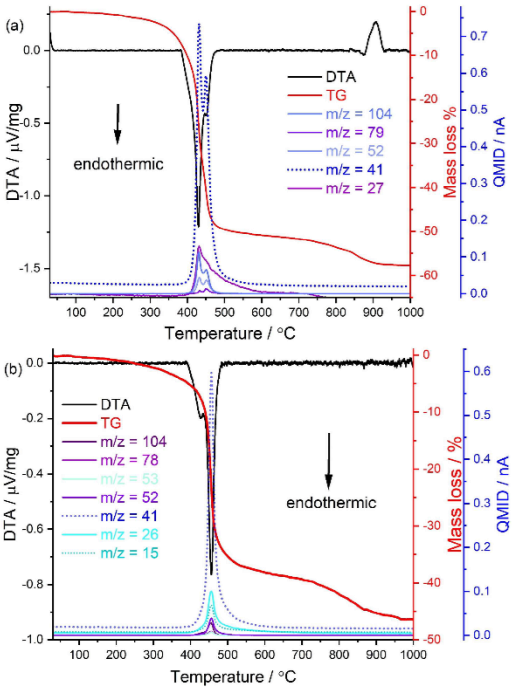

Figure 6. Simultaneous DTA/TG analysis together with mass spectrometry of $^{1}_{\infty}$[Eu(2-PyPz)$_3$] (**6**) representing the series of isotypic compounds (**1**–**10**) (a) and [Tb$_2$Ca(2-PyPz)$_3$] (**11**) (b). The investigation was performed in a constant flow of argon of 50 ml·min^{-1} with a heating rate of 5 K·min^{-1} from room temperature to 1000 °C.

PyPzH)$_2$] have also been obtained. The Ln^{3+} ions exhibit a change in coordination number from nine to eight and the AE^{2+} ions from six to eight upon the change between monometallic and bimetallic products. SC and PXRD, elemental analysis, IR as well as photoluminescence spectroscopy, and thermal analysis led to characterization of the new compounds. The luminescence of the other products is dominated by ion specific Ln-based 4f–4f transitions from this VIS to the NIR range benefitting from a strong sensitizing effect of the ligand. Tuning of the luminescence chromaticity is further possible by co-doping several of the products including the Ce-based emitter with Tb^{3+} and/or Eu^{3+}. The co-doping of the Gd-containing coordination polymer with Eu^{3+} and Tb^{3+} allows tuning towards white-light emission. Altogether, this shows the high potential of coordination polymers together with pyridylpyrazolate ligands as N-donors for versatile photoluminescence properties.

Experimental Section

Synthesis and Analytical Data

Reactions of the different lanthanide and/or alkaline earth metals with the aromatic N-heterocyclic ligand 3-(2-pyridyl)pyrazole (2-PyPzH) proceed by a redox reaction yielding hydrogen:

$$RE + 3\ C_8H_7N_3 \longrightarrow {}^1_\infty[RE(C_8H_6N_3)_3] + 3/2\ H_2$$

$$2RE + AE + 8\ C_8H_7N_3 \longrightarrow [RE_2AE(C_8H_6N_3)_8] + 4H_2$$

$$AE + 4\ C_8H_7N_3 \longrightarrow [AE(C_8H_6N_3)_2(C_8H_7N_3)_2] + H_2$$

Deposition Numbers 2204784 (for **6**), 2204790 (for **11**), 2204792 (for **12**), 2204788 (for **13**), 2204791 (for **14**), 2204789 (for **15**), contain the supplementary crystallographic data for this paper. These data are provided free of charge by the joint Cambridge Crystallographic Data Centre and Fachinformationszentrum Karlsruhe.

General Information: All syntheses involving lanthanide and alkaline earth elements were performed under argon or using vacuum lines, gloveboxes (MBraun Labmaster SP, Innovative Technology PureLab), Schlenk tubes, and Duran® glass ampoules (outer Ø 10 mm, wall thickness 1.5 mm). Pyridine and dichloromethane were purified by distillation and dried by standard procedures or used from the solvent purification system SPS-800 by MBraun (Garching, Germany). The bulk materials were characterized by both powder X-ray diffraction (PXRD) as well as CHN analysis.

Starting Materials: 3-(2-pyridyl)pyrazole (2-PyPzH) was synthesized as reported in the literature.[38] The method is described in detail in the Supporting Information. Lanthanide metals (gadolinium: 99.95%, Smart Element; rest: >99%, Chempur) were purchased and used as received.

Melt synthesis of $^1_\infty$[Ln(2-PyPz)$_3$], Ln = La, Ce, Pr, Nd, Sm, Eu, Gd, Tb, Dy, Ho (1–10): the freshly-filed respective rare earth metal (87.1 µmol) and a slight excess of 2-PyPzH ($C_8H_7N_3$, 275.5 µmol) were sealed under reduced pressure ($p = 1.0 \times 10^{-3}$ mbar) in an evacuated Duran® glass ampoule. The ampoule was heated to 200 °C within 48 h and maintained at this temperature for 120 h. The reaction mixture was then cooled to room temperature within 24 h. Excess Ln metal was not observed in any case and the excess ligand was washed away using dichloromethane (DCM).

Solvothermal synthesis of $^1_\infty$[Ln(2-PyPz)$_3$], Ln = La, Ce, Pr, Nd, Sm, Eu, Gd, Tb, Dy, Ho (1–10): prepared as described for melt synthesis with addition of 0.3 m of pyridine before freezing with liquid nitrogen and sealing the ampoule. The temperature of the ampoule was raised to 240 °C within 72 h and maintained at this temperature for 96 h. The ampoule was then cooled to room temperature within 72 h. In $^1_\infty$[Eu(2-PyPz)$_3$] (**6**), colorless block crystals were obtained and selected for SCXRD measurement.

$^1_\infty$**[La(2-PyPz)$_3$]**: $C_{24}H_{18}N_9La$ (571.36 g·mol^{-1}): C 49.51 (calcd. 50.45); H 3.30 (3.18); N 21.44 (22.06)%. Yield: 40 mg (80%). **FT-IR** (ATR): $\tilde{\nu}$ = 3070 (w), 1597 (m), 1565 (w), 1523 (w), 1454 (w), 1425 (m), 1342 (m), 1273 (w), 1152 (m), 1104 (w), 1083 (s), 1060 (w), 1003 (w), 969 (m), 935 (w), 852 (w), 788 (w), 755 (s), 709 (m), 656 (m), 631 (m), 511 (w), 467 (m) cm^{-1}.

$^1_\infty$**[Ce(2-PyPz)$_3$]**: $C_{24}H_{18}N_9Ce$ (572.58 g·mol^{-1}): C 49.81 (calcd. 50.34); H 3.26 (3.17); N 21.37 (22.02)%. Yield: 42 mg (84%). **FT-IR** (ATR): $\tilde{\nu}$ = 3065 (w), 1712 (w), 1596 (s), 1565 (m), 1524 (m), 1453 (m), 1425 (s), 1342 (m), 1273 (w), 1152 (m), 1127 (w), 1104 (w), 1083 (s), 1061 (m), 1003 (w), 969 (m), 935 (m), 788 (w), 755 (s), 709 (m), 656 (m), 630 (m), 513 (w), 468 (w) cm^{-1}.

$^1_\infty$**[Pr(2-PyPz)$_3$]**: $C_{24}H_{18}N_9Pr$ (573.37 g·mol^{-1}): C 49.39 (calcd. 50.27); H 3.07 (3.16); N 21.16 (21.99)%. Yield: 43 mg (85%). **FT-IR** (ATR): $\tilde{\nu}$ = 3088 (w), 1714 (w), 1597 (s), 1566 (m), 1525 (m), 1454 (m), 1425 (m), 1343 (m), 1273 (w), 1152 (m), 1104 (w), 1083 (s), 1061 (m), 1008 (w), 970 (m), 935 (m), 861 (w), 788 (w), 755 (s), 710 (m), 657 (m), 631 (m), 512 (w), 470 (m), 435 (m) cm^{-1}.

$^1_\infty$**[Nd(2-PyPz)$_3$]**: $C_{24}H_{18}N_9Nd$ (576.70 g·mol^{-1}): C 48.95 (calcd. 49.98); H 3.12 (3.15); N 20.98 (21.86)%. Yield: 41 mg (81%). **FT-IR** (ATR): $\tilde{\nu}$ = 3063 (w), 1713 (w), 1596 (m), 1565 (m), 1524 (m), 1454 (m), 1425 (m), 1343 (m), 1273 (w), 1151 (m), 1128 (w), 1104 (w), 1082 (s), 1061 (m), 1002 (w), 968 (m), 935 (m), 859 (w), 788 (w), 754 (s), 709 (m), 656 (m), 630 (m), 512 (w), 469 (m) cm^{-1}.

$^1_\infty$**[Sm(2-PyPz)$_3$]**: $C_{24}H_{18}N_9Sm$ (582.82 g·mol^{-1}): C 48.94 (calcd. 49.46); H 2.81 (3.11); N 21.52 (21.63)%. Yield: 48 mg (94%). **FT-IR** (ATR): $\tilde{\nu}$ = 3102 (w), 1714 (w), 1596 (m), 1566 (m), 1526 (m), 1454 (w), 1426 (m), 1344 (m), 1273 (w), 1152 (m), 1104 (w), 1082 (m), 1062 (w), 1002 (w), 970 (m), 935 (m), 859 (w), 788 (w), 754 (s), 710 (m), 657 (m), 630 (m), 513 (m), 472 (m) cm^{-1}.

$^1_\infty$**[Eu(2-PyPz)$_3$]**: $C_{24}H_{18}N_9Eu$ (584.42 g·mol^{-1}): C 48.80 (calcd. 49.32); H 3.05 (3.10); N 20.49 (21.57)%. Yield: 41 mg (82%). **FT-IR** (ATR): $\tilde{\nu}$ = 3075 (w), 1721 (w), 1598 (s), 1567 (m), 1527 (m), 1455 (m), 1427 (m), 1346 (m), 1274 (w), 1153 (m), 1129 (w), 1105 (m), 1084 (s), 1063 (m), 1009 (w), 972 (m), 936 (m), 862 (w), 789 (w), 757 (s), 711 (m), 659 (s), 631 (m), 516 (w), 473 (m) cm^{-1}.

$^1_\infty$**[Gd(2-PyPz)$_3$]**: $C_{24}H_{18}N_9Gd$ (589.71 g·mol^{-1}): C 49.74 (calcd. 48.88); H 2.32 (3.08); N 20.34 (21.38)%. Yield: 45 mg (88%). **FT-IR** (ATR): $\tilde{\nu}$ = 3067 (w), 1720 (w), 1597 (s), 1566 (m), 1527 (m), 1454 (m), 1426 (m), 1345 (m), 1273 (w), 1152 (m), 1104 (w), 1082 (s), 1062 (m), 967 (m), 935 (m), 861 (w), 788 (w), 754 (s), 710 (m), 658 (m), 629 (m), 514 (w), 473 (m) cm^{-1}.

$^1_\infty$**[Tb(2-PyPz)$_3$]**: $C_{24}H_{18}N_9Tb$ (591.38 g·mol^{-1}): C 49.36 (calcd. 48.74); H 2.67 (3.07); N 22.1 (21.32)%. Yield: 43 mg (83%). **FT-IR** (ATR): $\tilde{\nu}$ = 3065 (w), 1723 (w), 1597 (s), 1567 (m), 1528 (m), 1455 (w), 1426 (m), 1346 (m), 1274 (w), 1152 (m), 1104 (w), 1082 (s), 1062 (w), 1010 (w), 968 (m), 935 (m), 863 (w), 788 (w), 755 (s), 710 (m), 658 (m), 629 (m), 513 (w), 473 (m) cm^{-1}.

$^1_\infty$**[Dy(2-PyPz)$_3$]**: $C_{24}H_{18}N_9Dy$ (594.96 g·mol^{-1}): C 48.75 (calcd. 48.45); H 3.32 (3.05); N 20.77 (21.19)%. Yield: 44 mg (85%). **FT-IR** (ATR): $\tilde{\nu}$ = 3098 (w), 1722 (m), 1597 (m), 1566 (w), 1528 (w), 1454 (w), 1426 (m), 1346 (m), 1274 (w), 1151 (w), 1104 (w), 1081 (m), 1062 (w), 1010 (w), 967 (m), 935 (w), 864 (w), 788 (w), 754 (s), 710 (m), 658 (m), 629 (w), 514 (w), 474 (m cm^{-1}.

$^1_\infty$**[Ho(2-PyPz)$_3$]**: $C_{24}H_{18}N_9Ho$ (597.39 g·mol^{-1}): C 49.14 (calcd. 48.25); H 3.84 (3.04); N 20.69 (21.10)%. Yield: 40 mg (77%). **FT-IR** (ATR): $\tilde{\nu}$ = 2988 (w), 1728 (w), 1599 (s), 1567 (m), 1530 (m), 1455 (m), 1428 (s), 1348 (m), 1274 (w), 1152 (w), 1082 (s), 1063 (m), 1010 (w), 986 (m), 936 (w), 867 (w), 789 (w), 757 (s), 711 (m), 660 (m), 631 (w), 515 (w), 478 (m), 430 (m) cm^{-1}.

Synthesis of $^1_\infty$[Ce$_{1-x}$Tb$_x$(2-PyPz)$_3$] (2a, 2b), $^1_\infty$**[Tb$_{0.90}$Ce$_{0.1}$(2-PyPz)$_3$] (8a)**: By mixing and grinding Ce metal in a mortar with 0.5% Tb (**2a**), 5% Tb (**2b**) and the other way around with 10% Ce (**8a**) for the synthesis of three co-doped samples differing in Ln content. 87.1 µmol of the mixture was placed in an ampoule, where the reaction was carried out under the same heating conditions as described above.

Synthesis of $^1_\infty$[Gd$_{1-x-y}$Eu$_x$Tb$_y$(2-PyPz)$_3$]:Eu^{3+},Tb^{3+} (7a–7f): Six ratios were synthesized with 0.2% Eu (**7a**), 0.3% Eu (**7b**), 0.5% Eu (**7c**), 1% Eu (**7d**), 1% Eu with 1% Tb (**7e**), and 1% Tb (**7f**). The required amounts of the freshly filed metals (87.1 µmol) were mixed and ground in a mortar to acquire the best homogeneity. Reactions

were carried out under the same heating conditions as previously described.

Synthesis of $^{1}_{\infty}[Eu_{1-x}Tb_x(2\text{-}PyPz)_3]$ (6a–6c), $^{1}_{\infty}[Tb_{0.95}Eu_{0.05}(2\text{-}PyPz)_3]$ (8b): a ratio of 5% (**6a**), 25% (**6b**), 50% (**6c**), 95% (**8b**) Tb was ground together with freshly filed Eu to achieve the best homogeneity. The reaction was carried out as previously described.

Synthesis of $[Tb_2Ca(2\text{-}PyPz)_8]$ (11): Tb metal filing (66.1 µmol), calcium metal (33.2 µmol) and 2-PyPzH ($C_8H_7N_3$, 265.6 µmol) in the presence of 0.2 ml of pyridine were sealed in an evacuated ampoule. Before applying a vacuum to the ampoule as well as for sealing the ampoule, the solvent was frozen using liquid nitrogen. The reaction mixture was heated to 180 °C in 24 h, the temperature was raised again to 200 °C in 48 h and maintained at this temperature for 72 h. The ampoule was cooled to room temperature over a further 72 h. Plate crystals were selected for the SCXRD measurement. $C_{64}H_{48}N_{24}CaTb_2$ (1511.15 g·mol^{-1}): C 49.50 (calcd. 50.87); H 3.09 (3.20); N 21.61 (22.25)%. Yield: 53 mg (78%). **FT-IR** (ATR): $\tilde{\nu}$ = 3080 (w), 1716 (w), 1601 (s), 1564 (m), 1531 (m), 1458 (m), 1423 (m), 1342 (m), 1278 (m), 1156 (m), 1126 (w), 1106 (m), 1088 (s), 1057 (m), 1005 (m), 971 (m), 939 (w), 861 (w), 790 (w), 754 (s), 710 (w), 702 (w), 653 (m), 635 (m), 509 (w), 470 (m) cm^{-1}.

Synthesis of $[Tb_2AE(2\text{-}PyPz)_8]$, AE = Sr (12), Ba (13): A mixture of freshly-filed Tb (62.2 µmol), pieces of the respective AE metal (31.0 µmol), and 2-PyPzH ($C_8H_7N_3$, 248 µmol), in 0.6 ml pyridine was sealed in an evacuated DURAN glass ampoule. Before applying a vacuum to the ampoule as well as for sealing the ampoule, the solvent was frozen with liquid nitrogen. The oven was heated to 180 °C in 1 h. Subsequently, the temperature was raised to 205 °C in 24 h. The temperature was held for 96 h and then lowered to room temperature over a further 24 h. Colorless crystals were selected for SCXRD measurements.

$[Tb_2Sr(2\text{-}PyPz)_8]$: $C_{64}H_{48}N_{24}SrTb_2$ (1558.70 g·mol^{-1}): C 49.04 (calcd. 49.32); H 3.18 (3.10); N 20.68 (21.57)%. Yield: 44 mg (75%). **FT-IR** (ATR): $\tilde{\nu}$ = 3076 (w), 1715 (w), 1599 (s), 1563 (m), 1529 (m), 1454 (m), 1424 (m), 1349 (w), 1333 (m), 1276 (m), 1151 (w), 1108 (w), 1087 (m), 1074 (w), 1052 (w), 1005 (w), 969 (w), 939 (w), 878 (w), 788 (w), 757 (s), 710 (m), 653 (m), 634 (m), 510 (m), 468 (w) cm^{-1}.

$[Tb_2Ba(2\text{-}PyPz)_8]$: $C_{64}H_{48}N_{24}BaTb_2$ (1608.40 g·mol^{-1}): C 46.66 (calcd. 47.79); H 3.19 (3.01); N 20.05 (20.90)%. Yield: 35 mg (79%). **FT-IR** (ATR): $\tilde{\nu}$ = 3075 (w), 1712 (w), 1599 (m), 1563 (w), 1529 (m), 1453 (m), 1421 (w), 1347 (w), 1333 (w), 1275 (w), 1152 (w), 1124 (w), 1106 (w), 1087 (m), 1071 (w), 1052 (w), 1005 (w), 968 (w), 937 (w), 927 (w), 878 (w), 860 (w), 788 (w), 758 (s), 710 (w), 700 (w), 652 (w), 633 (m), 510 (w), 468 (w) cm^{-1}.

Synthesis of $[AE(2\text{-}PyPz)_2(2\text{-}PyPzH)_2]$, AE = Ca (14), Sr (15): Pieces of the respective AE metal or even $CaCl_2$ (68.8 µmol) and a slight excess of 2-PyPzH ($C_8H_7N_3$, 289.3 µmol) together with 0.3 ml pyridine were sealed in an evacuated ampoule. Before applying a vacuum to the ampoule as well as for sealing the ampoule, the solvent was frozen with liquid nitrogen. The ampoule was heated to 180 °C in 24 h and then 200 °C in 48 h. The temperature was held for 72 h and then lowered to 25 °C in another 24 h. Colorless single crystals were separated. The excess ligand was washed using DCM.

$[Ca(2\text{-}PyPz)_2(2\text{-}PyPzH)_2]$: $C_{32}H_{26}N_{12}Ca$ (618.71 g·mol^{-1}): C 61.32 (calcd. 62.21); H 4.01 (4.24); N 26.50 (27.17)%. Yield: 35 mg (82%). **FT-IR** (ATR): $\tilde{\nu}$ = 3084 (w), 1698 (s), 1567 (m), 1515 (m), 1446 (w), 1428 (m), 1357 (w), 1341 (w), 1307 (w), 1281 (w), 1244 (w), 1223 (m), 1195 (w), 1156 (m), 1081 (m), 1052 (m), 1001 (m), 961 (m), 855 (w), 793 (w), 754 (s), 701 (m), 651 (w), 630 (m), 512 (w), 466 (m), 436 (m) cm^{-1}.

$[Sr(2\text{-}PyPz)_2(2\text{-}PyPzH)_2]$: $C_{32}H_{26}N_{12}Sr$ (666.25 g·mol^{-1}): C 56.66 (calcd. 57.69); H 4.68 (3.93); N 24.50 (25.23)%. Yield: 38 mg (83%). **FT-IR** (ATR): $\tilde{\nu}$ = 3091 (w), 1596 (s), 1565 (w), 1512 (m), 1445 (w), 1428 (m), 1339 (w), 1307 (w), 1278 (w), 1222 (w), 1154 (m), 1083 (m), 1050 (m), 1000 (w), 961 (m), 793 (w), 757 (s), 708 (m), 630 (m), 513 (w), 501 (w), 463 (w), 442 (w) cm^{-1}.

Acknowledgments

The authors acknowledge DESY (Hamburg, Germany), a member of the Helmholtz Association HGF, for providing experimental facilities. Parts of this research were carried out at PETRA III, and we thank Carsten Paulmann and Heiko Schulz-Ritter for assistance in using beamline P24, beamtime allocated for proposal I-20180762. In addition, we gratefully acknowledge the support of the Volkswagen Foundation within the project "Molecular materials – bridging magnetism and luminescence". H. Youssef gratefully acknowledges the Egyptian Ministry of Higher Education (MoHE) and the German Academic Exchange Service (DAAD) under the German Egyptian Research Long-term Scholarship (GERLS) Programme, 2017 (57311832) for a Ph.D. fellowship. I. V. Taydakov gratefully acknowledges the Russian Science Foundation (project N° 19-13-00272) for financial support. Open Access funding enabled and organized by Projekt DEAL.

Conflict of Interest

The authors declare no conflict of interest.

Data Availability Statement

The data that support the findings of this study are available in the supplementary material of this article.

Keywords: Cerium · Alkaline earth metals · Luminescence · Heterobimetallic · melt synthesis

[1] a) Y. Yuan, D. Wang, B. Zhou, S. Feng, M. Sun, S. Zhang, W. Gao, Y. Bi, H. Qin, *Opt. Mater. Express* **2018**, *8*, 2760–2767; b) G. Fasol, *Science* **1997**, *275*, 941–942; c) Y. Wang, L. Wang, S. Bao, L. Xu, J. Zhang, Y. Liang, L. Wang, X. Liang, W. Xiang, *J. Alloys Compd.* **2022**, *921*, 166083.
[2] a) Q.-Q. Zhu, Y. Meng, H. Zhang, S. Li, L. Wang, R.-J. Xie, *ACS Appl. Electron. Mater.* **2020**, *2*, 2644–2650; b) S. Bao, Y. Liang, L. Wang, L. Wang, L. Xu, Y. Wang, X. Liang, W. Xiang, *ACS Sustainable Chem. Eng.* **2022**, *10*, 8105–8114; c) T. Long, Z. Wang, Y. Fan, H. Lin, H. Sun, C. Zou, D. Zhang, S. Zhuang, *Ceram. Int.* **2022**, *48*, 16391–16396.
[3] a) H. Yin, P. J. Carroll, J. M. Anna, E. J. Schelter, *J. Am. Chem. Soc.* **2015**, *137*, 9234–9237; b) Y. Qiao, D.-C. Sergentu, H. Yin, A. V. Zabula, T. Cheisson, A. McSkimming, B. C. Manor, P. J. Carroll, J. M. Anna, J. Autschbach, E. J. Schelter, *J. Am. Chem. Soc.* **2018**, *140*, 4588–4595; c) P. Lindqvist-Reis, F. Réal, R. Janicki, V. Vallet, *Inorg. Chem.* **2018**, *57*, 10111–10121.
[4] a) L. Wang, Z. Zhao, G. Zhan, H. Fang, H. Yang, T. Huang, Y. Zhang, N. Jiang, L. Duan, Z. Liu, Z. Bian, Z. Lu, C. Huang, *Light-*

Sci. Appl. **2020**, *9*, 1–9; b) Z. Zhao, L. Wang, G. Zhan, Z. Liu, Z. Bian, C. Huang, *Natl. Sci. Rev.* **2021**, *8*, nwaa193.
[5] a) L. V. Meyer, F. Schönfeld, A. Zurawski, M. Mai, C. Feldmann, K. Müller-Buschbaum, *Dalton Trans.* **2015**, *44*, 4070–4079; b) X. Qin, X. Liu, W. Huang, M. Bettinelli, X. Liu, *Chem. Rev.* **2017**, *117*, 4488–4527; c) P. R. Matthes, K. Müller-Buschbaum, *Z. Anorg. Allg. Chem.* **2014**, *640*, 2847–2851; d) H. Yin, P. J. Carroll, B. C. Manor, J. M. Anna, E. J. Schelter, *J. Am. Chem. Soc.* **2016**, *138*, 5984–5993.
[6] O. S. Wenger, *J. Am. Chem. Soc.* **2018**, *140*, 13522–13533.
[7] S. T. Frey, W. D. Horrocks Jr., *Inorg. Chem.* **1991**, *30*, 1073–1079.
[8] a) G. Blasse, B. C. Grabmaier, in *A general introduction to luminescent materials*, Springer Berlin, **1994**, pp. 1–9; b) P. Fang, L. Wang, G. Zhan, W. Yan, P. Huo, A. Ying, Y. Zhang, Z. Zhao, G. Yu, Y. Huang, S. Gong, L. Duan, Z. Liu, Z. Bian, C. Huang, *ACS Appl. Mater. Interfaces* **2021**, *13*, 45686–45695.
[9] a) N. Kodama, Y. Tanii, M. Yamaga, *J. Lumin.* **2000**, *87*, 1076–1078; b) G. C. Kim, H. L. Park, S. I. Yun, B. G. Moon, *J. Mater. Sci. Lett.* **1986**, *5*, 359–360; c) J. W. H. Van Krevel, H. T. Hintzen, R. Metselaar, A. Meijerink, *J. Alloys Compd.* **1998**, *268*, 272–277; d) G. Gauthier, S. Jobic, M. Evain, H.-J. Koo, M.-H. Whangbo, C. Fouassier, R. Brec, *Chem. Mater.* **2003**, *15*, 828–837.
[10] G. Blasse, A. Bril, *Appl. Phys. Lett.* **1967**, *11*, 53–55.
[11] a) D. Wu, Z. Hao, X. Zhang, G.-H. Pan, Y. Luo, L. Zhang, H. Zhao, J. Zhang, *J. Lumin.* **2017**, *186*, 170–174; b) J. M. Ogiegło, A. Zych, T. Jüstel, A. Meijerink, C. R. Ronda, *Opt. Mater.* **2013**, *35*, 322–331.
[12] a) D. A. I. Peng, J. I. Cheng, S. H. E. N. Liming, Q. I. A. N. Qi, G. U. O. Guobiao, X. Zhang, B. A. O. Ningzhong, *J. Rare Earth* **2017**, *35*, 341–346; b) P. Zeng, X. Wei, S. Zhou, M. Yin, Y. Chen, *J. Appl. Phys.* **2016**, *120*, 093104.
[13] R. M. Kowalski, J. Komar, P. Solarz, *J. Alloys Compd.* **2020**, *848*, 156228.
[14] S. Chawla, T. Roy, K. Majumder, A. Yadav, *J. Exp. Nanosci.* **2014**, *9*, 776–784.
[15] a) T. Hasegawa, S. W. Kim, T. Ueda, T. Ishigaki, K. Uematsu, H. Takaba, K. Toda, M. Sato, *J. Mater. Chem. C* **2017**, *5*, 9472–9478; b) Y. Wang, J. Ding, Z. Zhao, Y. Wang, *Inorg. Chem.* **2018**, *57*, 14542–14553.
[16] a) Y. Chen, L. Li, Q. Zhang, S. Liu, Z. Tian, Z. Ju, *J. Solid State Chem.* **2020**, *281*, 121053; b) E. Bartolomé, A. Arauzo, J. Luzón, S. Melnic, S. Shova, D. Prodius, J. Bartolomé, A. Amann, M. Nallaiyan, S. Spagna, *Dalton Trans.* **2019**, *48*, 5022–5034; c) B. D. Chandler, D. T. Cramb, G. K. H. Shimizu, *J. Am. Chem. Soc.* **2006**, *128*, 10403–10412.
[17] G. B. Deacon, P. C. Junk, S. G. Leary, A. Urbatsch, *Z. Anorg. Allg. Chem.* **2012**, *638*, 2001–2007.
[18] Y. Chen, Q. Gao, D. Gao, D. Wang, Y. Li, W. Liu, W. Li, *J. Coord. Chem.* **2013**, *66*, 3829–3838.
[19] a) K. Singh, J. R. Long, P. Stavropoulos, *J. Am. Chem. Soc.* **1997**, *119*, 2942–2943; b) A. C. Coelho, M. Nolasco, S. S. Balula, M. M. Antunes, C. C. L. Pereira, F. A. Almeida Paz, A. A. Valente, M. Pillinger, P. Ribeiro-Claro, J. Klinowski, I. S. Gonçalves, *Inorg. Chem.* **2011**, *50*, 525–538; c) T. L. Hu, J. R. Li, C. S. Liu, X. S. Shi, J. N. Zhou, X. H. Bu, J. Ribas, *Inorg. Chem.* **2006**, *45*, 162–173; d) P. L. Jones, J. C. Jeffery, J. A. McCleverty, M. D. Ward, *Polyhedron* **1997**, *16*, 1567–1571; e) S. Sethi, S. Jena, P. K. Das, N. Behera, *J. Mol. Struct.* **2019**, *1193*, 495–521.
[20] a) R. Q. Zou, X. H. Bu, M. Du, Y. X. Sui, *J. Mol. Struct.* **2004**, *707*, 11–15; b) Y. Zhang, D. Zhao, Z. Liu, J. Yang, X. Niu, L. Fan, T. Hu, *J. Solid State Chem.* **2020**, *282*, 121086; c) D. Ma, L. Duan, Y. Wei, Y. Qiu, *Chem. Eur. J.* **2014**, *20*, 15903–15912; d) J. Abbenseth, M. Diefenbach, A. Hinz, L. Alig, C. Würtele, J. M. Goicoechea, M. C. Holthausen, S. Schneider, *Angew. Chem. Int. Ed.* **2019**, *58*, 10966–10970; *Angew. Chem.* **2019**, *131*, 11082–11086; e) L. Fan, F. Wang, D. Zhao, X. Sun, H. Chen, H. Wang, X. Zhang, *Spectrochim. Acta Part A* **2020**, *239*, 118467; f) L. He, L. Duan, J. Qiao, D. Zhang, L. Wang, Y. Qiu, *Chem. Commun.* **2011**, *47*, 6467–6469; g) C.-S. Liu, J.-J. Wang, Z. Chang, L.-F. Yan, X.-H. Bu, *CrystEngComm* **2010**, *12*, 1833–1841; h) T.-L. Hu, R.-Q. Zou, J.-R. Li, X.-H. Bu, *Dalton Trans.* **2008**, *10*, 1302–1311; i) J.-J. Wang, C.-S. Liu, T.-L. Hu, Z. Chang, C.-Y. Li, L.-F. Yan, P.-Q. Chen, X.-H. Bu, Q. Wu, L.-J. Zhao, Z. Wang, X.-Z. Zhang, *CrystEngComm* **2008**, *10*, 681–692.
[21] R. Q. Zou, X. H. Bu, R. H. Zhang, *Inorg. Chem.* **2004**, *43*, 5382–5386.
[22] D. Su, Y. Liu, S. Li, S. Ding, Y. Jin, Z. Wang, X. Hu, L. Zhang, *Eur. J. Inorg. Chem.* **2017**, *2017*, 651–658.
[23] a) T. J. Sherbow, J. C. Fettinger, L. A. Berben, *Inorg. Chem.* **2017**, *56*, 8651–8660; b) C. M. Pask, S. Greatorex, R. Kulmaczewski, A. Baldansuren, E. J. McInnes, F. Bamiduro, M. Yamada, N. Yoshinari, T. Konno, M. A. Halcrow, *Chem. Eur. J.* **2020**, *26*, 4833–4841; c) Y. Pankratova, D. Aleshin, I. Nikovskiy, V. Novikov, Y. Nelyubina, *Inorg. Chem.* **2020**, *59*, 7700–7709; d) N. S. Labrum, M. Pink, C.-H. Chen, K. G. Caulton, *Eur. J. Inorg. Chem.* **2019**, *2019*, 1932–1940; e) E. Coronado, J. R. G. Mascarós, M. C. Giménez-López, M. Almeida, J. C. Waerenborgh, *Polyhedron* **2007**, *26*, 1838–1844.
[24] a) N. Du, X. Gao, J. Song, Z.-N. Wang, Y.-H. Xing, F.-Y. Bai, Z. Shi, *RSC Adv.* **2016**, *6*, 71012–71024; b) M. H. W. Lam, D. Y. K. Lee, S. S. M. Chiu, K. W. Man, W. T. Wong, *Eur. J. Inorg. Chem.* **2000**, *2000*, 1483–1488; c) L. Norel, L. E. Darago, B. Le Guennic, K. Chakarawet, M. I. Gonzalez, J. H. Olshansky, S. Rigaut, J. R. Long, *Angew. Chem. Int. Ed.* **2018**, *57*, 1933–1938; *Angew. Chem.* **2018**, *130*, 1951–1956; d) G. M. Davies, H. Adams, S. J. A. Pope, S. Faulkner, M. D. Ward, *Photochem. Photobiol. Sci.* **2005**, *4*, 829–834; e) Y.-W. Yip, H. Wen, W.-T. Wong, P. A. Tanner, K.-L. Wong, *Inorg. Chem.* **2012**, *51*, 7013–7015.
[25] a) E. Psillakis, J. C. Jeffery, J. A. McCleverty, M. D. Ward, *J. Chem. Soc. Dalton Trans.* **1997**, *9*, 1645–1651; b) B. Schowtka, H. Görls, M. Westerhausen, *Z. Anorg. Allg. Chem.* **2015**, *641*, 650–654; c) T. Kloubert, C. Müller, S. Krieck, T. Schlotthauer, H. Görls, M. Westerhausen, *Eur. J. Inorg. Chem.* **2012**, *2012*, 5991–6001.
[26] L.-R. Xing, Z. Lu, M. Li, J. Zheng, D. Li, *J. Phys. Chem. Lett.* **2020**, *11*, 2067–2073.
[27] H. Youssef, A. E. Sedykh, J. Becker, T. Schäfer, I. V. Taydakov, H. R. Li, K. Müller-Buschbaum, *Chem. Eur. J.* **2021**, *27*, 16634–16641.
[28] C. Müller, A. Koch, H. Görls, S. Krieck, M. Westerhausen, *Inorg. Chem.* **2015**, *54*, 635–645.
[29] a) D. J. Lewis, F. Moretta, A. T. Holloway, Z. Pikramenou, *Dalton Trans.* **2012**, *41*, 13138–13146; b) M. Mahato, P. P. Jana, K. Harms, H. P. Nayek, *RSC Adv.* **2015**, *5*, 62167–62172; c) C. Y. Chow, S. V. Eliseeva, E. R. Trivedi, T. N. Nguyen, J. W. Kampf, S. Petoud, V. L. Pecoraro, *J. Am. Chem. Soc.* **2016**, *138*, 5100–5109.
[30] a) P. R. Sathees Chandran, U. S. Soumya Mol, R. Drisya, M. R. Sudarsanakumar, M. R. Prathapachandra Kurup, *J. Mol. Struct.* **2017**, *1137*, 396–402; b) X. Zhou, H. Wang, S. Jiang, G. Xiang, X. Tang, X. Luo, L. Li, X. Zhou, *Inorg. Chem.* **2019**, *58*, 3780–3788; c) M. Hasegawa, H. Ohtsu, D. Kodama, T. Kasai, S. Sakurai, A. Ishii, K. Suzuki, *New J. Chem.* **2014**, *38*, 1225–1234; d) C. Seidel, C. Lorbeer, J. Cybińska, A.-V. Mudring, U. Ruschewitz, *Inorg. Chem.* **2012**, *51*, 4679–4688.
[31] C. S. Liu, X. S. Shi, J. R. Li, J. J. Wang, X. H. Bu, *Cryst. Growth Des.* **2006**, *6*, 656–663.
[32] a) W. T. Carnall, P. R. Fields, K. Rajnak, *J. Chem. Phys.* **1968**, *49*, 4424–4442; b) W. T. Carnall, P. R. Fields, K. Rajnak, *J. Chem. Phys.* **1968**, *49*, 4450–4455; c) W. T. Carnall, P. R. Fields, K. Rajnak, *J. Chem. Phys.* **1968**, *49*, 4447–4449; d) E. Huskowska, I. Turowska-Tyrk, J. Legendziewicz, J. P. Riehl, *New J. Chem.* **2002**, *26*, 1461–1467.

[33] a) P. Wang, R.-Q. Fan, Y.-L. Yang, X.-R. Liu, P. Xiao, X.-Y. Li, W. Hasi, W.-W. Cao, *CrystEngComm* **2013**, *15*, 4489–4506; b) P. Wang, R.-Q. Fan, X.-R. Liu, L.-Y. Wang, Y.-L. Yang, W.-W. Cao, B. Yang, W. Hasi, Q. Su, Y. Mu, *CrystEngComm* **2013**, *15*, 1931–1949; c) A. E. Sedykh, D. G. Kurth, K. Müller-Buschbaum, *Eur. J. Inorg. Chem.* **2019**, *2019*, 4564–4571.
[34] a) M. H. V. Werts, R. T. F. Jukes, J. W. Verhoeven, *Phys. Chem. Chem. Phys.* **2002**, *4*, 1542–1548; b) A. Aebischer, F. Gumy, J.-C. G. Bünzli, *Phys. Chem. Chem. Phys.* **2009**, *11*, 1346–1353.
[35] a) K. Binnemans, *Coord. Chem. Rev.* **2015**, *295*, 1–45; b) K. Binnemans, *Chem. Rev.* **2009**, *109*, 4283–4374.
[36] H. A. A. Seed Ahmed, O. M. Ntwaeaborwa, R. E. Kroon, *Curr. Appl. Phys.* **2013**, *13*, 1264–1268.
[37] P. R. Matthes, C. J. Höller, M. Mai, J. Heck, S. J. Sedlmaier, S. Schmiechen, C. Feldmann, W. Schnick, K. Müller-Buschbaum, *J. Mater. Chem.* **2012**, *22*, 10179–10187.
[38] a) A. J. Amoroso, A. M. C. Thompson, J. C. Jeffery, P. L. Jones, J. A. McCleverty, M. D. Ward, *J. Chem. Soc. Chem. Commun.* **1994**, *24*, 2751–2752; b) J. Salinas Uber, Y. Vogels, D. van den Helder, I. Mutikainen, U. Turpeinen, W. T. Fu, O. Roubeau, P. Gamez, J. Reedijk, *Eur. J. Inorg. Chem.* **2007**, *26*, 4197–4206

Manuscript received: September 7, 2022
Revised manuscript received: November 3, 2022
Accepted manuscript online: November 22, 2022

Zeitschrift für anorganische und allgemeine Chemie

Supporting Information

Red Emitting Cerium(III) and Versatile Luminescence Chromaticity of 1D-Coordination Polymers and Heterobimetallic Ln/AE Pyridylpyrazolate Complexes

Heba Youssef, Jonathan Becker, Alexander E. Sedykh, Thomas Schäfer, Ilya V. Taydakov, and Klaus Müller-Buschbaum*

Table of Contents

Experimental section

Analytical Data

CHN Analysis: Carbon, hydrogen, and nitrogen elemental analyses were executed using a Thermo Scientific Flash EA – 1112. The polymers were placed in a tin crucible with no less than one mass equivalent to V_2O_5. Specimens were prepared and stored under inert conditions till the time of the measurements.

Single Crystal X-ray Diffraction (SCXRD): Single-crystal X-ray measurements of $^1_\infty$[Eu(2-PyPz)$_3$] (**6**) were performed on PETRA III/DESY using beamline P24. While [Tb$_2$Ln(2-PyPz)$_8$], Ln = Ca (**11**), Sr (**12**), Ba (**13**) as well as [Ln(2-PyPz)$_2$(2-PyPzH)$_2$], Ln = Ca (**14**), Sr (**15**) measurements were performed on a BRUKER AXS Smart Apex 1 diffractometer with graphite monochromator (Mo-Kα radiation; λ = 71.073 pm) and a Bruker CRYOFLEX low-temperature system. Data indexing for [Tb$_2$Ba(2-PyPz)$_8$] (**13**) was done at 150 K conversely the data collection for all the other compounds mounted at 100 K as a result of the cracking behavior of the respective single-crystal upon cooling to 100 K. All structures were solved utilizing direct methods, refined with the least-square method using ShelXL[1] and expanded using Fourier techniques. All non-hydrogen atoms were refined anisotropically. Hydrogen atoms were assigned to idealized geometric positions and inserted in structure factors calculations. Depictions of the crystal structures were generated using DIAMOND.[2]

Powder X-ray Diffraction (PXRD): Specimens for powder diffraction were firstly ground in a mortar and filled into Lindemann glass capillaries with either 0.5 or 0.3 mm diameter under an inert gas atmosphere and then sealed. Diffraction data were collected on an STOE STADI P diffractometer with a focusing Ge(111) monochromator and a Dectris MYTHEN 1K strip detector in Debye-Scherrer geometry using CuKα radiation (λ = 154.056 pm). Data collection was done using the STOE Powder Diffraction Software Package WinX^{POW}.

Vibrational Spectroscopy: MIR spectra were recorded from several milligrams of the compounds with an ALPHA FT-IR spectrometer from Bruker optics (ATR module) using OPUS software.

Absorption Spectra: The UV-Vis-NIR absorption spectra were measured on solid–state products using a standard Agilent Cary 5000 UV-VIS-NIR spectrophotometer with a Praying Mantis accessory, which had been mounted and aligned for use with the DRP-ASC ambient chamber. The source, detector, and grating changeovers were at the standard position of 350, 800, and 800 nm, respectively, for all studied compounds except $^1_\infty$[Nd(2-PyPz)$_3$] (**4**) and $^1_\infty$[Dy(2-PyPz)$_3$] (**9**), the detector and grating changeovers were set to 850 and 780 nm, respectively. For 2-PyPzH and $^1_\infty$[Eu(2-PyPz)$_3$] (**6**), the source has been set to 310 and 380, respectively, while $^1_\infty$[Ln(2-PyPz)$_3$], Gd (**7**), Tb (**8**), and Dy (**9**), the source has been set to 370. The reference spectrum was collected on PTFE and the reference and samples were packed in the ambient chamber within the glovebox under inert conditions.

Photoluminescence Spectroscopy: The excitation and emission spectra were recorded for ground solid samples after filling them in quartz glass tubes under argon. The measurements were performed at room temperature as well as 77 K (latter using

the liquid nitrogen-filled assembly FL-1013 of HORIBA) with a HORIBA Jobin Yvon Spex Fluorolog 3 spectrometer equipped with a 450 W Xe short-arc lamp (USHIO), double-grated excitation, and emission monochromators, and a photomultiplier tube (R928P) using the FluoroEssence™ software. Excitation and emission spectra were corrected for the spectral response of the monochromators and the detector using spectral corrections provided by the constructor. Besides, a photodiode reference detector was used to correct the excitation spectra for the spectral distribution of the lamp intensity. A R5509-73 detector was used to collect the data in the NIR region. When required, the collection of the data was performed using an edge filter (Newport 20CGA-345, 395, 495 for the visible region and Reichmann Optics RG 830 long pass for the NIR region). Emission spectra with gating were recorded using a xenon flashlamp with a pulse repetition rate of 41 ms.

Photoluminescence overall decay process times were determined using the above-mentioned HORIBA Jobin Yvon Spex Fluorolog 3 spectrometer equipped with a dual lamp housing (FL-1040A), a UV xenon flashlamp (Exelitas FX-1102), and a TCSPC (time-correlated single-photon counting) upgrade, or picosecond pulsed laser diode. Emission decays were recorded using DataStation software. Exponential tail fitting was used for the calculation of resulting intensity decay using Decay Analysis Software 6. The quality of the fit was confirmed by χ^2 values being below 1.2.

Photoluminescence quantum yields were determined with a second similar instrument HORIBA Jobin Yvon Spex Fluorolog 3 spectrometer equipped with a HORIBA Quanta-φ Integrating Sphere. For the measurements, solid samples were filled into Starna Micro Cell cuvettes 18-F/ST/C/Q/10 (fluorescence with ST/C closed-cap, material UV quartz glass Spectrosil Q, pathlength 10 mm, matched). Magnesium oxide was used as reference material. Each sample was measured at least three times and the quantum yield values with standard deviation were evaluated afterward. Quanta-φ Integrating Sphere was checked with a standard (sodium salicylate as a powder, λ_{ex} = 340 nm, λ_{em} = 365–600 nm, measured QY = 52 %, in the literature: 53 %).[3]

Thermal properties: were determined by simultaneous DTA/TG (NETZSCH STA 409-PC) coupled with a mass-spectrometer (NETZSCH QMS 403 Aëolos) in a constant argon flow of 50 ml·min^{-1} with a heating rate of 5 K/min from room temperature to 1000 °C for $^1_\infty$[Eu(2-PyPz)$_3$] (**6**), and [Tb$_2$Ca(2-PyPz)$_8$] (**11**). DTA curve was baseline corrected after the measurement using Origin™ software.

[1] a) G. M. Sheldrick, *Acta Crystallogr., Sect. A: Found. Adv.* **2015**, *71*, 3-8; b) G. M. Sheldrick, *Acta Crystallogr., Sect. C: Struct. Chem.* **2015**, *71*, 3-8; c) G. M. Sheldrick, *Acta Crystallogr., Sect. A: Found. Crystallogr.* **2008**, *64*, 112-122.
[2] W. T. Pennington, *J. Appl. Crystallogr.* **1999**, *32*, 1028-1029.
[3] M. S. Wrighton, D. S. Ginley and D. L. Morse, *J. Phys. Chem.* **1974**, *78*, 2229-2233.

Crystallographic Data

CCDC 2204784 (**6**), 2204790 (**11**), 2204792 (**12**), 2204788 (**13**), 2204791 (**14**), 2204789 (**15**) contain the supplementary crystallographic data. These data are provided free of charge by the Cambridge Crystallographic Data Centre.

Table S1. Crystallographic data of $^1_\infty$[Eu(2-PyPz)$_3$] (**6**), [Tb$_2$Ca(2-PyPz)$_8$] (**11**), [Tb$_2$Sr(2-PyPz)$_8$] (**12**), [Tb$_2$Ba(2-PyPz)$_8$] (**13**).

Compound	$^1_\infty$[Eu(2-PyPz)$_3$]	[Tb$_2$Ca(2-PyPz)$_8$]	[Tb$_2$Sr(2-PyPz)$_8$]	[Tb$_2$Ba(2-PyPz)$_8$]
CCDC number	2204784	2204790	2204792	2204788
Empirical formula	$C_{24}H_{18}N_9Eu$	$C_{64}H_{48}N_{24}CaTb_2$	$C_{64}H_{48}N_{24}SrTb_2$	$C_{64}H_{48}N_{24}BaTb_2$
M_r / g·mol^{-1}	584.43	1511.18	1558.72	1608.44
T / K	100(2)	100(2)	100(2)	150(2)
λ / pm	56.076, synchrotron	71.073, Mo-K$_\alpha$	71.073, Mo-K$_\alpha$	71.073, Mo-K$_\alpha$
Crystal system	Monoclinic	Triclinic	Monoclinic	Monoclinic
Space group	$P2_1$	$P\bar{1}$	$P2_1/n$	$P2_1/n$
a / pm	1114.7 (2)	909.37(4)	1211.5(2)	1209.75(5)
b / pm	940.0(2)	926.33(5)	1758.4(2)	1777.40(6)
c / pm	1130.1(2)	1839.05(9)	1417.0(2)	1425.83(5)
α / °	90	75.563(2)	90	90
β / °	117.14(3)	85.271(2)	99.368(4)	99.950(1)
γ / °	90	88.516(2)	90	90
V / 10^6 pm^3	1053.8(4)	1495.1(2)	2978.4(6)	3019.7(2)
Z	2	1	2	2
ρ_{calc} / g·cm^{-3}	1.842	1.678	1.738	1.769
μ / mm^{-1}	3.011	2.497	3.306	3.026
F(000)	576	750	1536	1572
Crystal size / mm^3	0.050 x 0.040 x 0.040	0.157 x 0.043 x 0.015	0.158 x 0.153 x 0.036	0.145 x 0.080 x 0.012
θ_{min} / °	2.025	2.247	1.861	2.058
θ_{max} / °	25.675	29.130	27.562	27.525
Reflections collected	9307	244960	47360	67628
Independent reflections	3858	8053	6855	6940
R(int)	0.0807	0.0557	0.0554	0.0467
No. Of parameters	564	412	412	412
GOF	1.101	1.094	1.156	1.072
Final R indices [$I > 2\sigma$(I)]	R_1 = 0.0520, wR_2 = 0.1236	R_1 = 0.0185, wR_2 = 0.0402	R_1 = 0.0339, wR_2 = 0.0890	R_1 = 0.0242, wR_2 = 0.0523
R indices (all data)	R_1 = 0.0673, wR_2 = 0.1318	R_1 = 0.0229, wR_2 = 0.0416	R_1 = 0.0445, wR_2 = 0.0989	R_1 = 0.0320, wR_2 = 0.0554
$\Delta\rho_{max}$, $\Delta\rho_{min}$ / e·10^{-6}·pm^{-3}	1.639, -1.431	1.948, -0.617	2.061, -1.480	1.148, -0.803

Table S2. Crystallographic data of [Ca(2-PyPz)$_2$(2-PyPzH)$_2$] (**14**), [Sr(2-PyPz)$_2$(2-PyPzH)$_2$] (**15**).

Compound	[Ca(2-PyPz)$_2$(2-PyPzH)$_2$]	[Sr(2-PyPz)$_2$(2-PyPzH)$_2$]
CCDC number	2204791	2204789
Empirical formula	$C_{32}H_{26}N_{12}Ca$	$C_{32}H_{26}N_{12}Sr$
M_r / g·mol^{-1}	618.73	666.27
T / K	100(2)	100(2)
λ / pm	71.073, Mo-K$_\alpha$	71.073 Mo-K$_\alpha$
Crystal system	Monoclinic	Monoclinic
Space group	$C2/c$	$P2_1/n$
a / pm	2910.0(3)	1855.5(2)
b / pm	1718.0(2)	1716.2(2)
c / pm	2611.1(3)	1908.2(2)
α / °	90	90
β / °	116.283(4)	90.595(3)
γ / °	90	90
V / 10^6 pm^3	11705(2)	6076.2(8)
Z	16	8
ρ_{calc} / g·cm^{-3}	1.404	1.457
μ / mm^{-1}	0.261	1.819
F(000)	5152	2720
Crystal size / mm3	0.250 x 0.131 x 0.084	0.280 x 0.241 x 0.099
θ_{min} / °	1.959	1.523
θ_{max} / °	27.101	27.156
Reflections collected	143045	91261
Independent reflections	12904	13457
R(int)	0.0720	0.0661
No. Of parameters	812	811
GOF	1.015	1.027
Final R indices [$I > 2\sigma$(I)]	R_1 = 0.0397, wR_2 = 0.0865	R_1 = 0.0456, wR_2 = 0.0966
R indices (all data)	R_1 = 0.0629, wR_2 = 0.0968	R_1 = 0.0770, wR_2 = 0.1104
$\Delta\rho_{max}$, $\Delta\rho_{min}$ / e·10^{-6}·pm^{-3}	0.623, -0.632	0.852, -0.645

Interatomic Distances and Angles

Table S3. Selected interatomic distances (pm) and angles (°) of $^1_\infty$[Eu(2-PyPz)$_3$] (**1**). Symmetry operations: I -x+2,y+1/2,-z+1 II -x+2,y-1/2,-z+1.

Atoms	$^1_\infty$[Eu(2-PyPz)$_3$]	Atoms	$^1_\infty$[Eu(2-PyPz)$_3$]
Eu1-N1	275(2)	N4-Eu1-N3^{II}	123.6(9)
Eu1-N2	250(2)	N4-Eu1-N5	64.8(7)
Eu1-N3^{II}	261(2)	N4-Eu1-N9^{II}	127(1)
Eu1-N4	258(2)	N6^{I}-Eu1-N9^{II}	74(1)
Eu1-N5	262(2)	N6^{I}-Eu1-N3^{II}	75.3(9)
Eu1-N6^{I}	258(2)	N6^{I}-Eu1-N4	153.0(8)
Eu1-N7	273(5)	N6^{I}-Eu1-N5	142.1(8)
Eu1-N8	249(2)	N8-Eu1-N2	79.7(9)
Eu1-N9^{II}	260(2)	N8-Eu1-N3^{II}	99.0(9)
N2-Eu1-N3^{II}	155(2)	N8-Eu1-N4	78.3(9)
N2-Eu1-N4	80.8(9)	N8-Eu1-N5	126.2(8)
N2-Eu1-N5	127.3(8)	N8-Eu1-N6^{I}	80(1)
N2-Eu1-N6^{I}	80.0(9)	N8-Eu1-N9^{II}	153.9(9)
N2-Eu1-N9^{II}	98.3(9)	N9^{II}-Eu1-N3^{II}	72(1)
N3^{II}-Eu1-N5	73.6(8)	N9^{II}-Eu1-N5	76(1)

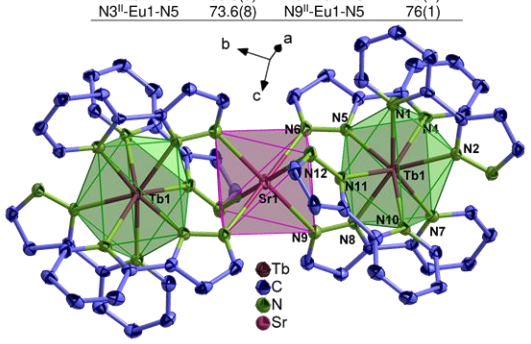

Figure S1: Excerpt of the crystal structure of [Tb$_2$Sr(2-PyPz)$_8$] (**12**). The polyhedral around Tb^{3+} and Ca^{2+} are indicated in green, and violet, respectively. The hydrogen atoms are omitted for clarity and the thermal ellipsoids are depicted at a 50% probability level for all structures. The central alkaline-earth atom in **11–13** is positioned on an inversion center and possesses two rare-earth atoms which are symmetry-related around the central alkaline-earth atom making the asymmetric unit consisting of a single Tb^{3+} and single AE^{2+} ion.

Table S4. Selected interatomic distances (pm) and angles (°) of [Tb$_2$Ca(2-PyPz)$_8$] (**11**), [Tb$_2$Sr(2-PyPz)$_8$] (**12**), [Tb$_2$Ba(2-PyPz)$_8$] (**13**). Symmetry operations: I -x+1,-y+1,-z+1.

Atoms	[Tb$_2$Ca(2-PyPz)$_8$]	[Tb$_2$Sr(2-PyPz)$_8$]	[Tb$_2$Ba(2-PyPz)$_8$]
Tb-N1	252.2(2)	254.5(3)	254.7(2)
Tb-N2	247.9(2)	243.1(3)	242.3(2)
Tb-N4	261.3(2)	260.2(3)	255.1(2)
Tb-N5	244.9(2)	243.4(3)	246.8(2)
Tb-N7	259.6(2)	261.9(3)	262.6(2)
Tb-N8	248.4(2)	245.0(3)	246.7(2)
Tb-N10	261.7(2)	255.1(3)	261.5(2)
Tb-N11	243(2)	245.6(3)	242.8(2)
AE-N6	242.7(2)	262.0(3)	285.0(3)
AE-N9	242.5(2)	258.5(3)	273.6(3)
AE-N12	246.6(2)	266.7(4)	280.0(3)
N1-Tb-N4	98.1(1)	72.9(1)	113.8(1)
N1-Tb-N7	85.8(1)	145.8(1)	144.6(1)
N1-Tb-N10	152.1(1)	112.5(1)	72.3(1)
N2-Tb-N1	65.7(1)	66.4(1)	66.6(1)
N2-Tb-N4	72.2(1)	74.8(1)	78.2(1)
N2-Tb-N7	73.0(1)	87.0(1)	86.5(1)
N2-Tb-N8	124.2(1)	143.8(1)	142.7(1)
N2-Tb-N10	87.1(1)	77.4(1)	75.0(1)
N4-Tb-N10	78.4(1)	146.2(1)	147.0(1)
N5-Tb-N1	76.7(1)	77.4(1)	75.4(1)
N5-Tb-N2	116.8(1)	132.5(1)	109.4(1)
N5-Tb-N4	64.9(1)	65.6(1)	66.0(1)
N5-Tb-N7	152.6(1)	109.7(1)	137.8(1)
N5-Tb-N8	90.6(1)	80.7(1)	82.0(1)
N5-Tb-N10	124.2(1)	147.5(1)	142.1(1)
N7-Tb-N4	139.5(1)	79.8(1)	80.4(1)
N7-Tb-N10	79.9(1)	80.1(1)	79.0(1)
N8-Tb-N1	76.3(1)	147.7(1)	149.0(1)
N8-Tb-N4	155.4(1)	118.4(1)	74.4(1)
N8-Tb-N7	64.7(1)	64.7(1)	64.4(1)
N8-Tb-N10	117.6(1)	75.8(1)	118.1(1)
N11-Tb-N1	142.6(1)	76.5(1)	77.5(1)
N11-Tb-N2	151.6(1)	111.2(1)	133.0(1)
N11-Tb-N4	96.2(1)	142.9(1)	146.5(1)
N11-Tb-N5	78.5(1)	87.8(1)	88.5(1)
N11-Tb-N7	104.9(1)	135.7(1)	109.3(1)
N11-Tb-N8	76.5(1)	79.2(1)	81.0(1)
N11-Tb-N10	64.9(1)	66.2(1)	65.7(1)
N6-AE-N6^{I}	180.0	180.0	180.0
N9-AE-N6^{I}	92.4(1)	94.9(1)	83.9(1)
N9-AE-N6	87.6(1)	85.1(1)	96.1(1)
N9-AE-N9^{I}	180.0	180.0	180.0
N9-AE-N12^{I}	97.5(1)	82.1(1)	99.1(1)

N9-AE-N12	82.6(1)	97.9(1)	80.9(1)
N12-AE-N6	91.5(1)	80.6(1)	76.4(1)
N12^{I}-AE-N6	88.5(1)	99.4(1)	103.6(1)
N12-AE-N12^{I}	180.0(1)	180.0	103.6(1)

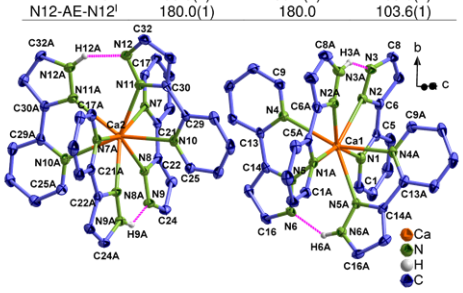

Figure S2: Excerpt of the crystal structure of [Ca(2-PyPz)$_2$(2-PyPzH)$_2$] (**14**). The ligands numbered with (A) letters are the neutral ligands while the others are deprotonated ligands. The N···H···N hydrogen bridges are indicated by dashed lines, the hydrogen atoms are omitted for clarity. The thermal ellipsoids are depicted at a 50 % probability level. The asymmetric unit of the mononuclear complexes **14**, **15** contains two crystallographically independent molecules that differ insignificantly in their geometrical parameters.

Table S5. Selected interatomic distances (pm) and angles (◦) of [Ca(2-PyPz)$_2$(2-PyPzH)$_2$] (**14**), and [Sr(2-PyPz)$_2$(2-PyPzH)$_2$] (**15**).

Atoms	[Ca(2-PyPz)$_2$(2-PyPzH)$_2$]	[Sr(2-PyPz)$_2$(2-PyPzH)$_2$]	Atoms	[Ca(2-PyPz)$_2$(2-PyPzH)$_2$]	[Sr(2-PyPz)$_2$(2-PyPzH)$_2$]
AE1-N1	255.2(2)	277.9(3)	N9-C24	135.4(2)	134.3(4)
AE1-N2	253.1(2)	264.1(3)	N12-C32	134.6(2)	134.2(7)
AE1-N4	268.1(2)	270.1(2)	N3A-C8A	134.3(3)	133.9(4)
AE1-N5	253.0(2)	263.2(2)	N6A-C16A	133.8(2)	134.1(4)
AE2-N7	260.3(2)	269.5(3)	N9A-C24A	133.6(2)	134.5(4)
AE2-N8	255.5(2)	263.4(3)	N12A-C32A	134.2(2)	137.0(7)
AE2-N10	253.8(2)	273.3(3)	N1A-AE1-N4	93.9(1)	84.2(1)
AE2-N11	254.5(2)	266.1(3)	N1A-AE1-N4A	87.7(1)	87.0(1)
AE1-N1A	261.7(2)	267.5(3)	N1A-AE1-N1	153.6(1)	160.4(1)
AE1-N2A	252.0(2)	265.3(3)	N4-AE1-N1	99.0(1)	90.1(1)
AE1-N4A	256.5(2)	275.9(2)	N4A-AE1-N1	89.3(1)	103.9(1)
AE1-N5A	253.8(2)	264.1(3)	N2-AE1-N4	81.3(1)	85.1(1)
AE2-N7A	258.1(2)	275.5(2)	N2A-AE1-N4	79.5(1)	80.4(1)
AE2-N8A	251.4(2)	266.2(2)	N2-AE1-N4A	82.5(1)	89.1(1)
AE2-N10A	261.00(2)	269.7(3)	N2A-AE1-N4A	80.5(1)	79.3(1)
AE2-N11A	253.9(2)	264.7(3)	N2-AE1-N1	65.5(1)	60.0(1)
N3A-H3A...N3	268.1(2)	266.9(4)	N2A-AE1-N1	141.7(1)	134.4(1)

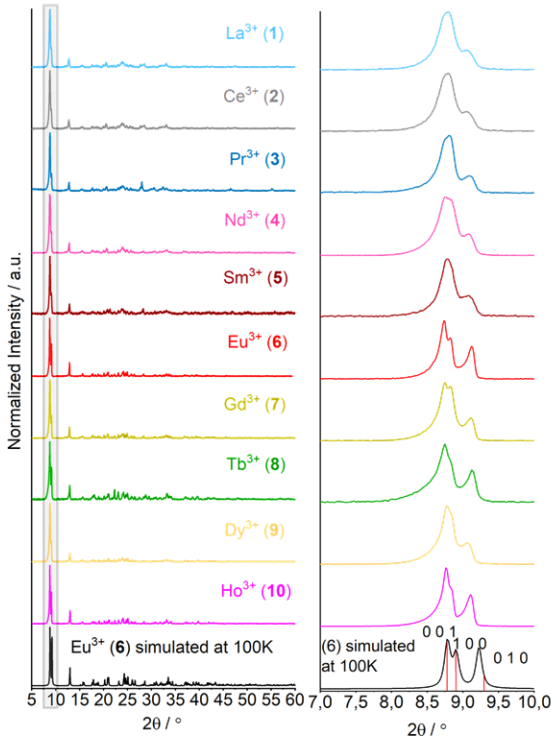

Figure S3. (Left) Comparison between the simulated diffraction pattern from the SCXRD data of $^{1}_{\infty}$[Eu(2-PyPz)$_3$] (**6**) (black) and the observed X-ray powder diffraction pattern of $^{1}_{\infty}$[Ln(2-PyPz)$_3$], Ln = La, Ce, Pr, Nd, Sm, Eu, Gd, Tb, Dy, and Ho (**1-10**). (Right) Zoom in for the grey highlighted part on the left side showing excerpts of the simulated powder diffractograms of $^{1}_{\infty}$[Eu(2-PyPz)$_3$] (**6**) at 100 K (black) with the respective hkl positions (red) in the region 7°<2θ<10° illustrating the cause of the reflection overlapping in the obtained powder diffractogram of $^{1}_{\infty}$[Ln(2-PyPz)$_3$] (**1-10**).

N6A-H6A...N6	262.2(2)	267.7(4)	N4-AE1-N4A	156.7(1)	159.6(1)
N9A-H9A...N9	265.6(2)	266.8(4)	N5-AE1-N5A	75.6(1)	74.8(1)
N12A-H12A...N12	269.1(2)	265.1(7)	N5-AE1-N2	127.1(1)	127.1(1)
N1-C1	133.6(2)	134.1(4)	N5A-AE1-N2	130.7(1)	126.9(1)
N4-C9	133.9(2)	134.5(4)	N5-AE1-N2A	127.0(1)	131.4(1)
N7-C17	133.6(2)	133.4(5)	N5A-AE1-N2A	128.5(1)	131.1(1)
N10-C25	134.3(2)	131.3(6)	N2-AE1-N2A	76.5(1)	74.7(1)
N1A-C1A	133.6(2)	133.7(4)	N5-AE1-N1A	83.1(1)	82.2(1)
N4A-C9A	133.9(2)	134.4(4)	N5A-AE1-N1A	77.5(1)	86.7(1)
N7A-C17A	134.3(2)	134.0(4)	N2-AE1-N1A	139.7(1)	137.7(1)
N10A-C25A	133.9(2)	135.6(5)	N2A-AE1-N1A	63.3(1)	63.1(1)
N1-C5	135.1(2)	135.0(4)	N5-AE1-N4	62.4(1)	62.2(1)
N4-C13	134.9(2)	135.0(4)	N5A-AE1-N4	137.9(1)	136.8(1)
N7-C21	135.3(2)	135.2(5)	N5-AE1-N4A	140.7(1)	134.6(1)
N10-C29	135.0(2)	138.4(5)	N5A-AE1-N4A	65.1(1)	60.6(1)
N1A-C5A	135.0(2)	134.7(4)	N5-AE1-N1	82.7(1)	78.5(1)
N4A-C13A	135.0(2)	134.9(4)	N5A-AE1-N1	77.5(1)	84.7(1)
N7A-C21A	135.2(2)	134.9(4)	N7-AE2-N10A	101.4(1)	90.2(1)
N10A-C29A	134.8(2)	132.6(5)	N7-AE2-N10	91.8(1)	82.6(1)
C5-C6	145.8(3)	147.0(5)	N7-AE2-N7A	154.8(1)	129.3(1)
C13-C14	146.2(2)	146.5(4)	N8-AE2-N11	130.2(1)	129.8(1)
C21-C22	146.3(2)	146.0(5)	N8-AE2-N11A	126.8(1)	74.3(1)
C29-C30	146.3(2)	144.9(7)	N8-AE2-N8A	75.4(1)	129.6(1)
C5A-C6A	146.4(3)	146.8(4)	N8A-AE2-N11	131.0(1)	63.0(1)
C13A-C14A	146.2(3)	146.0(4)	N8-AE2-N7	63.3(1)	137.3(1)
C21A-C22A	146.4(3)	146.6(4)	N8A-AE2-N7	138.4(1)	80.6(1)
C29A-C30A	146.6(3)	142.0(7)	N8-AE2-N10A	81.6(1)	84.6(1)
N2-C6	135.0(2)	134.3(4)	N8A-AE2-N10A	76.4(1)	79.7(1)
N5-C14	133.9(2)	134.7(4)	N8-AE2-N10	85.3(1)	88.3(1)
N8-C22	134.3(2)	134.8(4)	N8A-AE2-N10	79.5(1)	60.1(1)
N11-C30	135.0(2)	131.5(6)	N8A-AE2-N7A	65.5(1)	133.9(1)
N2A-C6A	133.6(2)	134.6(4)	N8-AE2-N7A	140.7(1)	160.2(1)
N5A-C14A	134.5(2)	134.6(4)	N10A-AE2-N10	154.7(1)	88.4(1)
N8A-C22A	134.6(2)	134.4(4)	N10A-AE2-N7A	92.0(1)	104.0(1)
N11A-C30A	134.2(2)	138.8(6)	N10-AE2-N7A	84.6(1)	128.5(1)
N2-N3	136.8(2)	135.8(4)	N11A-AE2-N8A	125.0(1)	74.8(2)
N5-N6	135.6(2)	136.0(3)	N11A-AE2-N11	76.8(1)	83.9(1)
N8-N9	135.9(2)	136.2(4)	N11A-AE2-N7	86.3(1)	80.6(1)
N11-N12	136.8(2)	138.1(5)	N11-AE2-N7	77.9(1)	61.8(1)
N2A-N3A	134.4(2)	136.4(4)	N11A-AE2-N10A	61.9(1)	136.3(1)
N5A-N6A	135.8(2)	134.8(4)	N11-AE2-N10A	138.5(1)	134.9(1)
N8A-N9A	135.6(2)	134.8(4)	N11A-AE2-N10	141.4(1)	60.7(1)
N11A-N12A	134.6(2)	133.4(5)	N11-AE2-N10	65.2(1)	79.9(1)
N3-C8	134.8(2)	134.2(4)	N11A-AE2-N7A	81.2(1)	88.3(1)
N6-C16	134.8(2)	134.5(4)	N11-AE2-N7A	78.0(1)	162.3(1)

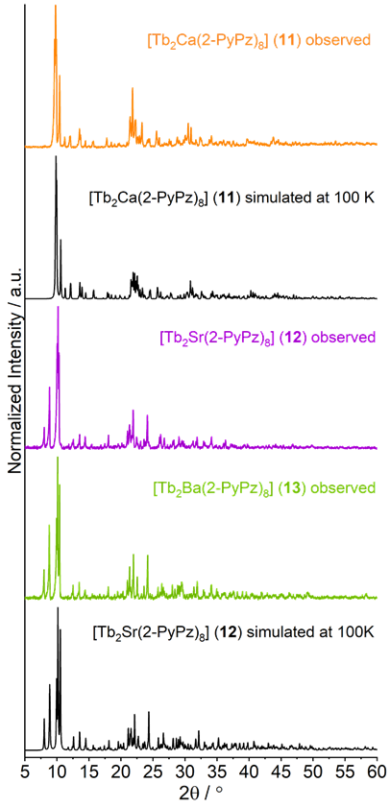

Figure S4. Comparison of the experimental X-ray powder diffraction pattern of [Tb$_2$AE(2-PyPz)$_8$], AE = Ca (**11**), Sr (**12**), Ba (**13**) at 298 K with the respective simulated pattern from single-crystal X-ray data at 100 K.

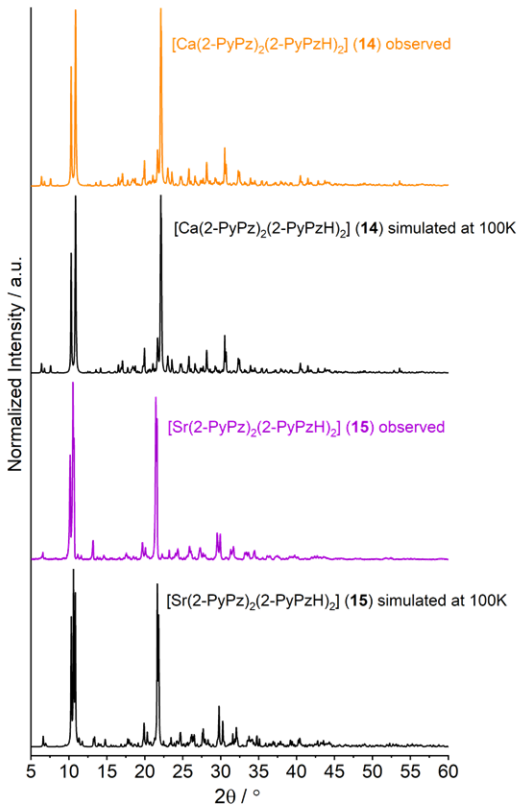

Figure S5. Comparison of the experimental X-ray powder diffraction pattern of [AE(2-PyPz)$_2$(2-PyPzH)$_2$], AE = Ca (**14**), Sr (**15**) at 298 K with the respective simulated pattern from single-crystal X-ray data at 100 K.

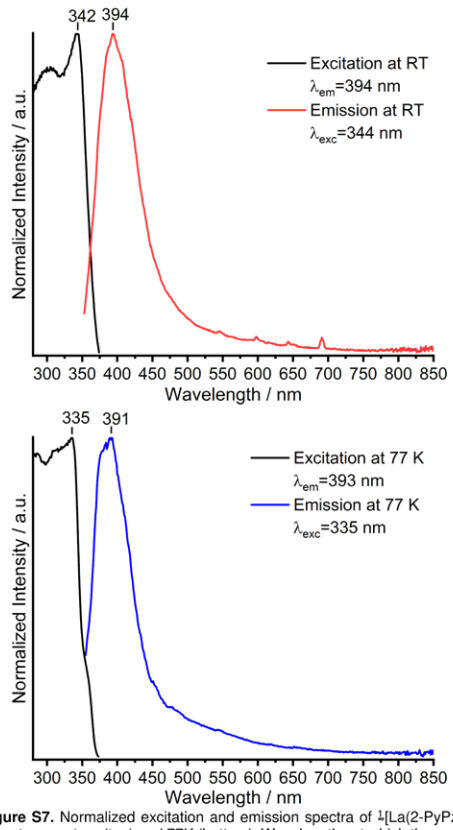

Figure S7. Normalized excitation and emission spectra of ¹∞[La(2-PyPz)$_3$] (**1**) at room temperature (top) and 77K (bottom). Wavelengths at which the spectra were recorded are reported in the legends.

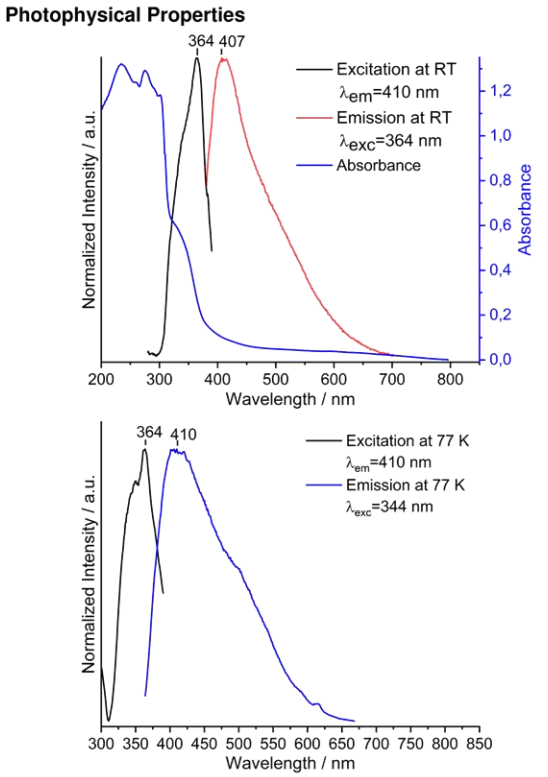

Figure S6. Absorption, normalized excitation and normalized emission spectra of 2-PyPzH at room temperature (top). Normalized excitation and emission spectra of 2-PyPzH at 77K (bottom). Wavelengths at which the spectra were recorded are reported in the legends.

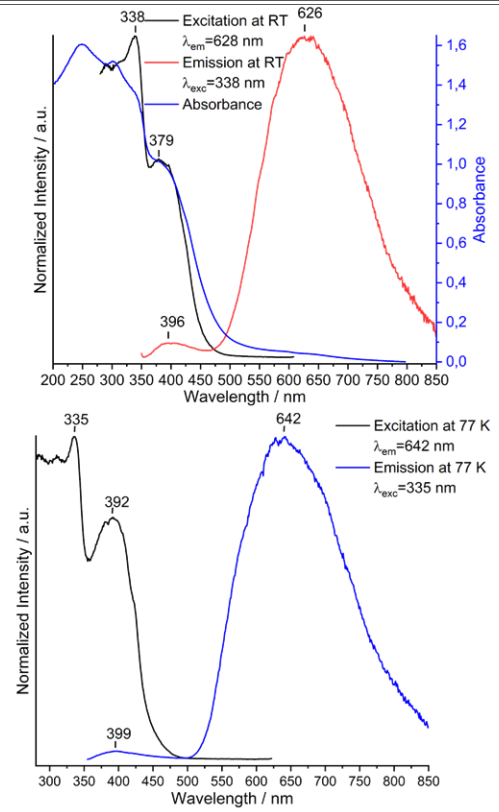

Figure S8. Absorption, normalized excitation and normalized emission spectra of ¹∞[Ce(2-PyPz)$_3$] (**2**) at room temperature (top). Normalized excitation and emission spectra of **2** at 77K (bottom). Wavelengths at which the spectra were recorded are reported in the legends.

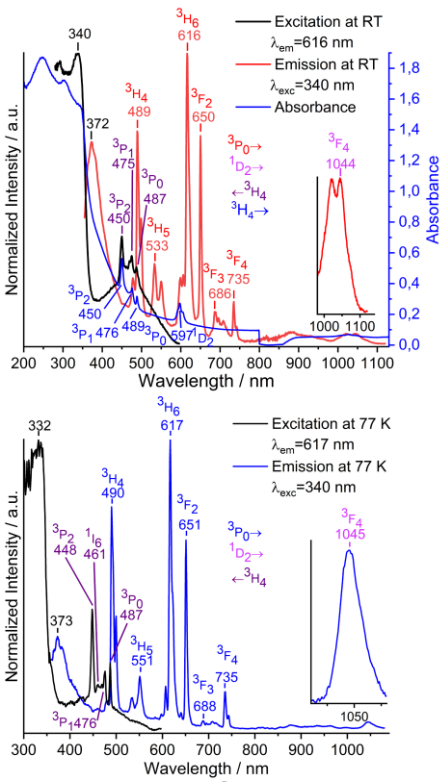

Figure S9. Absorption, normalized excitation and normalized emission spectra of ⊥[Pr(2-PyPz)$_3$] (**3**) at room temperature (top). Normalized excitation and emission spectra of **3** at 77K (bottom). Visible and NIR range emission spectra were brought to the same intensity at 650 (at RT) and 651 (at 77 K) nm. Wavelengths at which the spectra were recorded are reported in the legends.

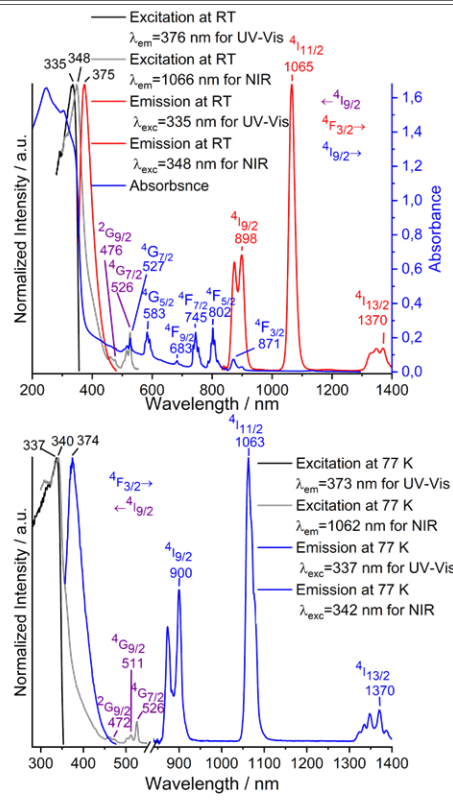

Figure S10. Absorption, normalized excitation and normalized emission spectra of ⊥[Nd(2-PyPz)$_3$] (**4**) at room temperature (top). Normalized excitation and emission spectra of **4** at 77K (bottom). Wavelengths at which the spectra were recorded are reported in the legends.

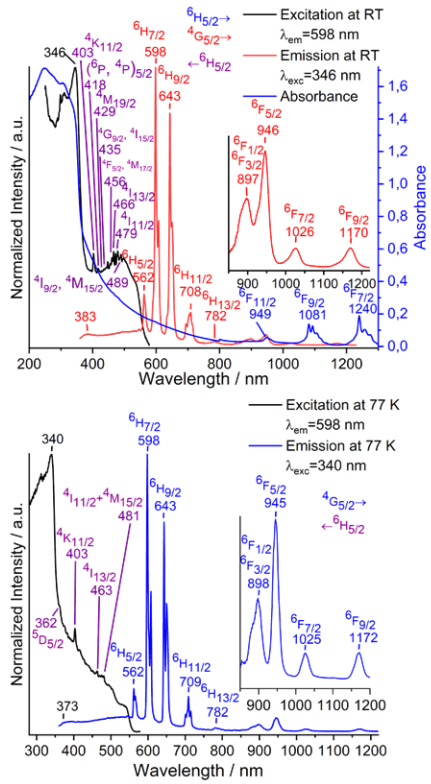

Figure S11. Absorption, normalized excitation and normalized emission spectra of ⊥[Sm(2-PyPz)$_3$] (**5**) at room temperature (top). Normalized excitation and emission spectra of **5** at 77K (bottom). Visible and NIR range emission spectra were brought to the same intensity at 708 (at RT) and 709 (at 77 K) nm. Wavelengths at which the spectra were recorded are reported in the legends.

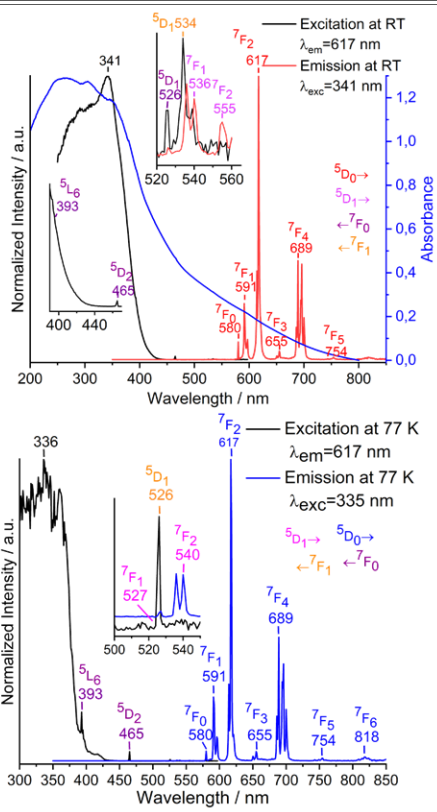

Figure S12. Absorption, normalized excitation and normalized emission spectra of ⊥[Eu(2-PyPz)$_3$] (**6**) at room temperature (top). Normalized excitation and emission spectra of **6** at 77K (bottom). Wavelengths at which the spectra were recorded are reported in the legends.

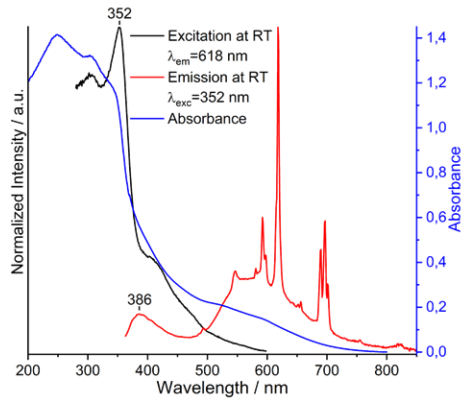

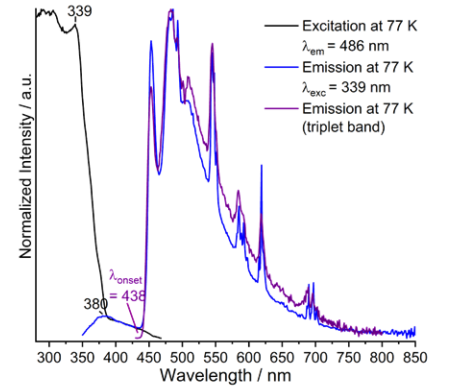

Figure S13. Absorption, normalized excitation and normalized emission spectra of ↓[Gd(2-PyPz)$_3$]:Eu^{3+},Tb^{3+} (**7**) at room temperature (top). Normalized excitation and emission spectra of **7** at 77K (bottom). Wavelengths at which the spectra were recorded are reported in the legends.

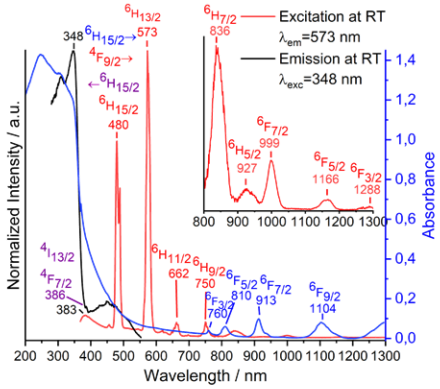

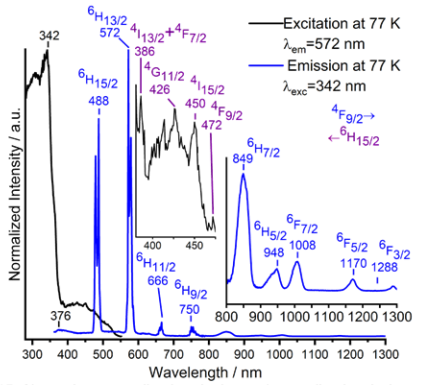

Figure S15. Absorption, normalized excitation and normalized emission spectra of ↓[Dy(2-PyPz)$_3$] (**9**) at room temperature (top). Normalized excitation and emission spectra of **9** at 77K (bottom). Visible and NIR range emission spectra were brought to the same intensity at 750 nm. Wavelengths at which the spectra were recorded are reported in the legends.

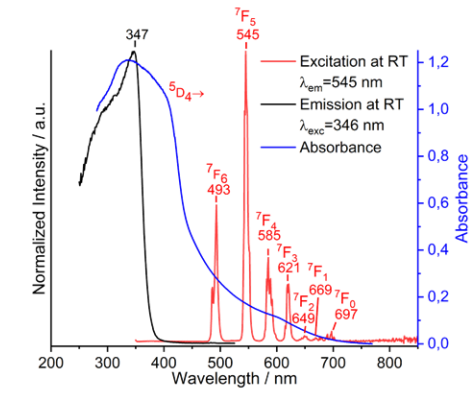

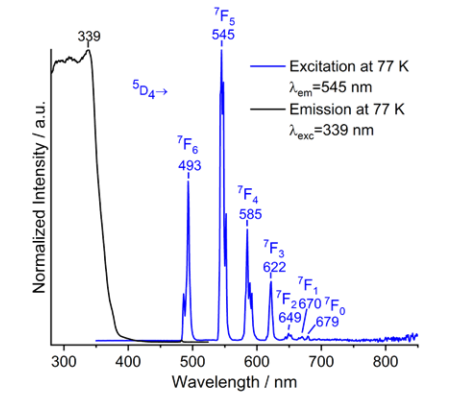

Figure S14. Absorption, normalized excitation and normalized emission spectra of ↓[Tb(2-PyPz)$_3$] (**8**) at room temperature (top). Normalized excitation and emission spectra of **8** at 77K (bottom). Wavelengths at which the spectra were recorded are reported in the legends.

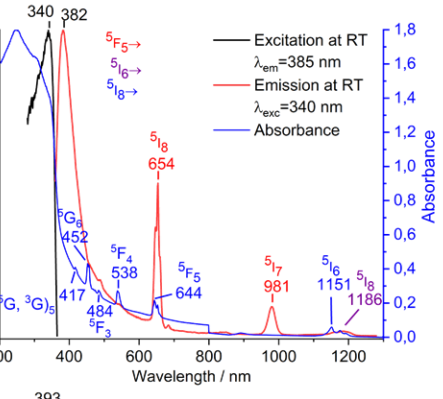

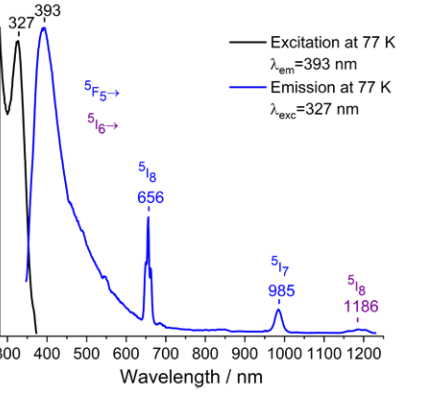

Figure S16. Absorption, normalized excitation and normalized emission spectra of ↓[Ho(2-PyPz)$_3$] (**10**) at room temperature (top). Normalized excitation and emission spectra of **10** at 77K (bottom). Visible and NIR range emission spectra were brought to the same intensity at 654 (at RT) and 656 (at 77 K) nm. Wavelengths at which the spectra were recorded are reported in the legends.

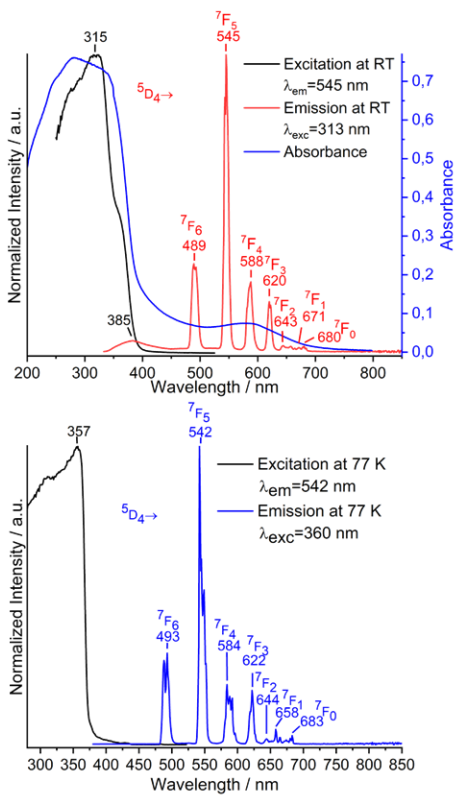

Figure S17. Absorption, normalized excitation and normalized emission spectra of $[Tb_2Ca(2\text{-}PyPz)_8]$ (**11**) at room temperature (top). Normalized excitation and emission spectra of **11** at 77K (bottom). Wavelengths at which the spectra were recorded are reported in the legends.

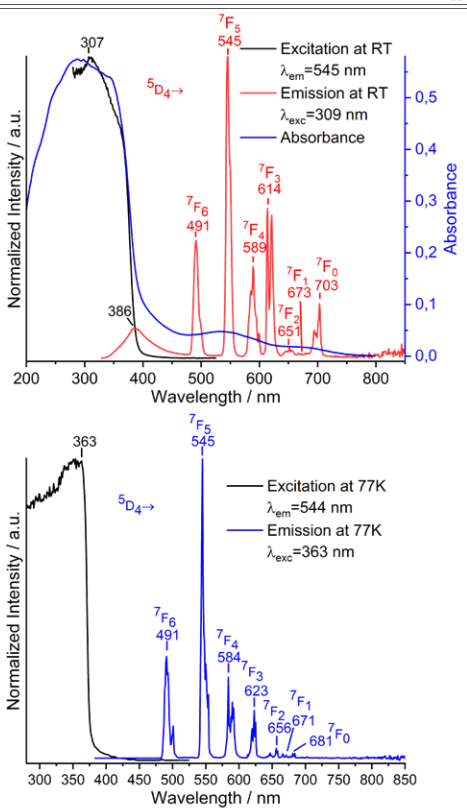

Figure S18. Absorption, normalized excitation and normalized emission spectra of $[Tb_2Sr(2\text{-}PyPz)_8]$ (**12**) at room temperature (top). Normalized excitation and emission spectra of **12** at 77K (bottom). Wavelengths at which the spectra were recorded are reported in the legends.

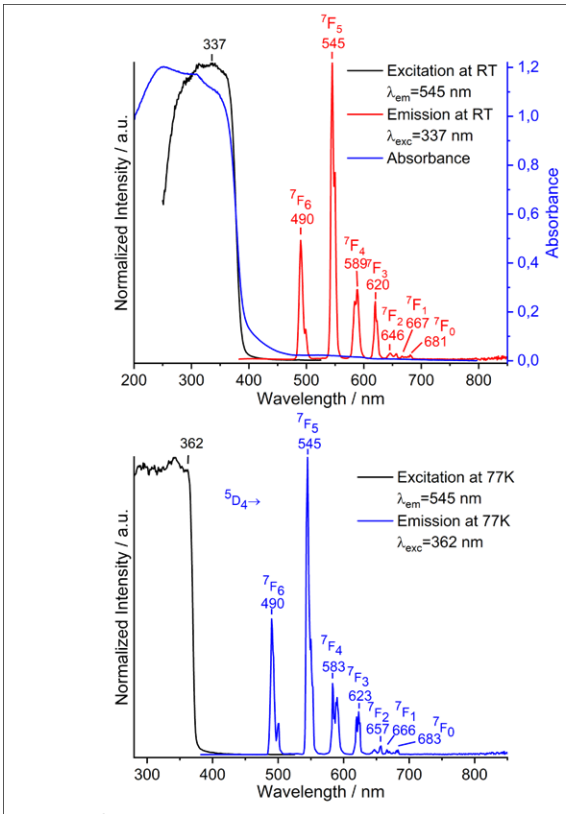

Figure S19. Absorption, normalized excitation and normalized emission spectra of $[Tb_2Ba(2\text{-}PyPz)_8]$ (**13**) at room temperature (top). Normalized excitation and emission spectra of **13** at 77K (bottom). Wavelengths at which the spectra were recorded are reported in the legends.

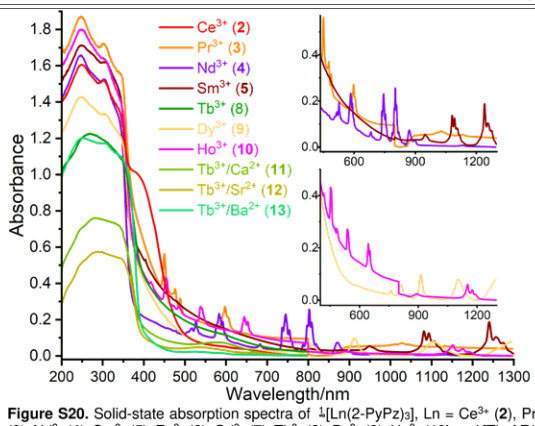

Figure S20. Solid-state absorption spectra of $^1[Ln(2\text{-}PyPz)_3]$, Ln = Ce^{3+} (**2**), Pr^{3+} (**3**), Nd^{3+} (**4**), Sm^{3+} (**5**), Eu^{3+} (**6**), Gd^{3+} (**7**), Tb^{3+} (**8**), Dy^{3+} (**9**), Ho^{3+} (**10**) and $[Tb_2AE(2\text{-}PyPz)_8]$, AE = Ca (**11**), Sr (**12**), and Ba (**13**) in the solid state at room temperature.

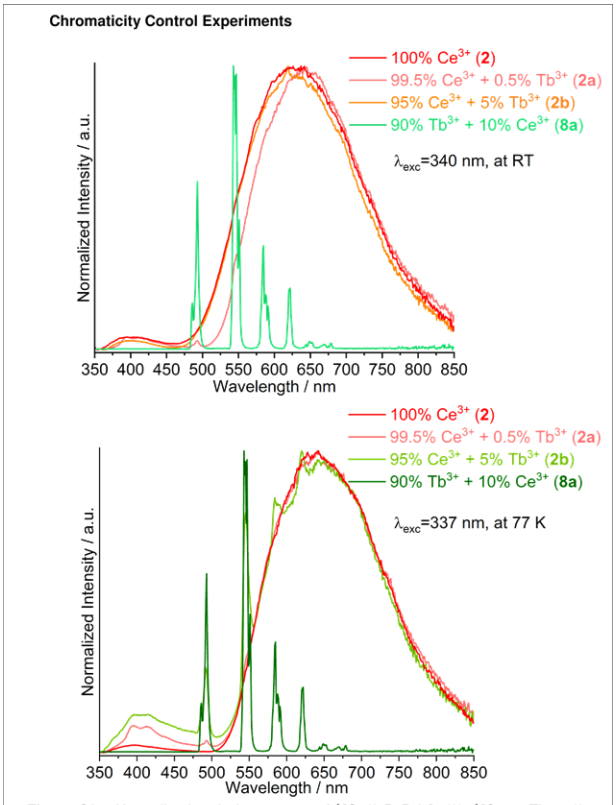

Figure S21. Normalized emission spectra of [Ce(2-PyPz)3] (**2**), [Ce0.995Tb0.005(2-PyPz)3] (**2a**), [Ce0.95Tb0.05(2-PyPz)3] (**2b**), [Tb0.90Ce0.1(2-PyPz)3] (**8a**) at room temperature (top) and 77K (bottom). Wavelengths at which the spectra were recorded are reported in the legends.

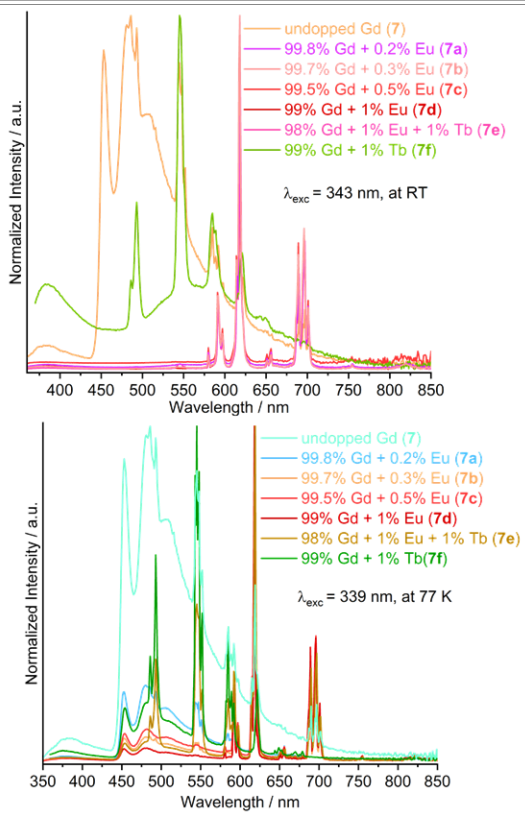

Figure S22. Normalized emission spectra of [Gd(2-PyPz)3]:Eu3+,Tb3+ (**7**), and [Gd1-x-yEuxTby(2-PyPz)3]:Eu3+,Tb3+ (**7a-7f**) at room temperature (top) and 77K (bottom). Wavelengths at which the emission spectra were recorded are reported in the legends.

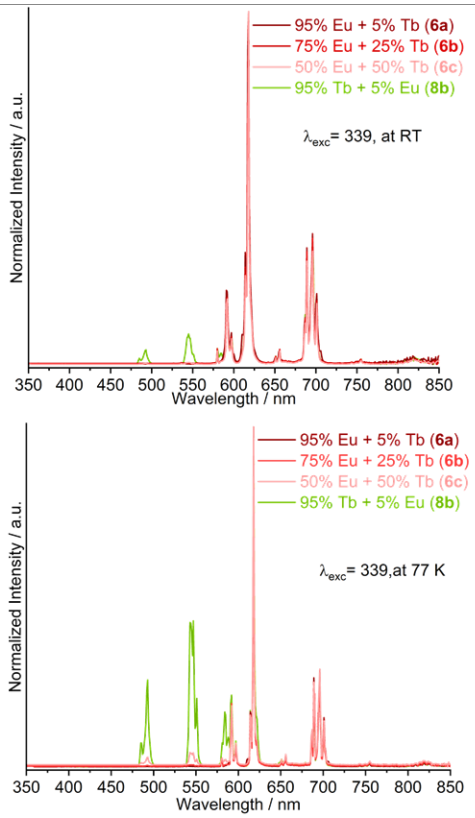

Figure S23. Normalized emission spectra of [Eu1-xTbx(2-PyPz)3] (**6a-6c**), and [Tb0.95Tb0.05(2-PyPz)3] (**8b**) at room temperature (top) and 77K (bottom). Wavelengths at which the emission spectra were recorded are reported in the legends.

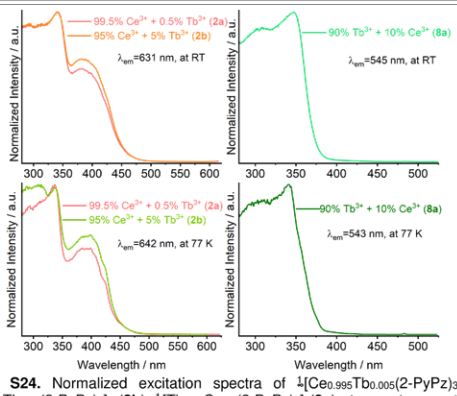

Figure S24. Normalized excitation spectra of [Ce0.995Tb0.005(2-PyPz)3] (**2a**), [Ce0.95Tb0.05(2-PyPz)3] (**2b**), [Tb0.90Ce0.1(2-PyPz)3] (**8a**) at room temperature (top) and 77K (bottom). Wavelengths at which the spectra were recorded are reported in the legends.

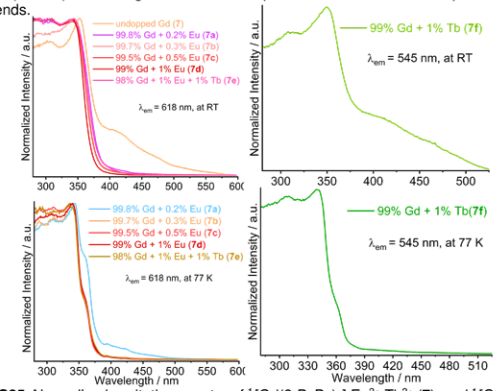

Figure S25. Normalized excitation spectra of [Gd(2-PyPz)3]:Eu3+,Tb3+ (**7**), and [Gd1-x-yEuxTby(2-PyPz)3]:Eu3+,Tb3+ (**7a-7f**), at room temperature (top) and 77K (bottom). Wavelengths at which the excitation spectra were recorded are reported in the legends.

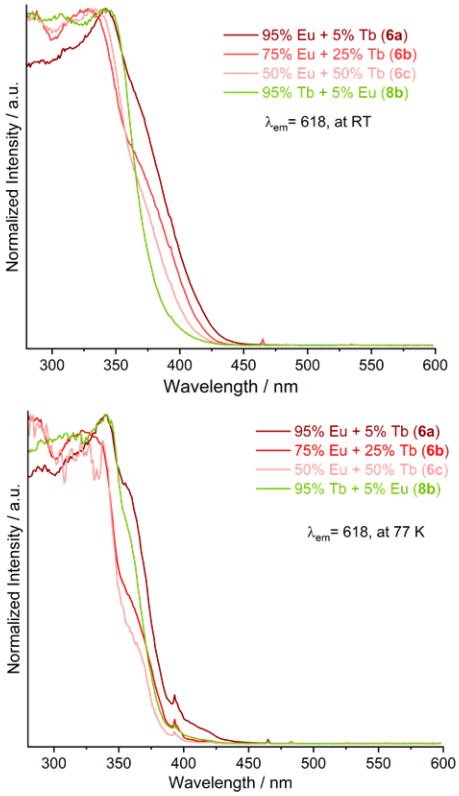

Figure S26. Normalized excitation of $^1_\infty$[Eu$_{1-x}$Tb$_x$(2-PyPz)$_3$] (**6a-6c**), and $^1_\infty$[Tb$_{0.95}$Tb$_{0.05}$(2-PyPz)$_3$] (**8b**) at room temperature (top) and 77K (bottom). Wavelengths at which the excitation spectra were recorded are reported in the legends.

Table S7. Photophysical data of $^1_\infty$[Ce$_{1-x}$Tb$_x$(2-PyPz)$_3$] (**2a, 2b**), $^1_\infty$[Tb$_{0.90}$Ce$_{0.1}$(2-PyPz)$_3$] (**8a**), $^1_\infty$[Gd$_{1-x-y}$Eu$_x$Tb$_y$(2-PyPz)$_3$]:Eu^{3+},Tb^{3+} (**7a-7f**), $^1_\infty$[Eu$_{1-x}$Tb$_x$(2-PyPz)$_3$] (**6a – 6c**), $^1_\infty$[Tb$_{0.95}$Eu$_{0.05}$(2-PyPz)$_3$] (**8b**) in the solid-state at room temperature and 77K.

compound	τ[a]	$\lambda_{ex}/\lambda_{em}$ [nm][b]	τ[c]	$\lambda_{ex}/\lambda_{em}$ [nm][d]	Φ [%][e]	$\lambda_{ex}/\lambda_{em}$ [nm][f]
$^1_\infty$[Ce$_{0.995}$Tb$_{0.005}$(2-PyPz)$_3$] (**2a**)	2.18(4) ns	287/631	2.0(6) ns	337/642	n/a	n/a
$^1_\infty$[Ce$_{0.95}$Tb$_{0.05}$(2-PyPz)$_3$] (**2b**)	2.29(3) ns	287/631	3.18(6) ns	337/620	n/a	n/a
$^1_\infty$[Tb$_{0.90}$Ce$_{0.1}$(2-PyPz)$_3$] (**8a**)	106.8(6) µs	347/545	571(6) µs	342/543	n/a	n/a
$^1_\infty$[Gd$_{0.998}$Eu$_{0.002}$(2-PyPz)$_3$]:Eu^{3+},Tb^{3+} (**7a**)	986(10) µs	343/618	1045(6) µs	344/618	n/a	n/a
$^1_\infty$[Gd$_{0.997}$Eu$_{0.003}$(2-PyPz)$_3$]:Eu^{3+},Tb^{3+} (**7b**)	939(5) µs	339/618	951(5) µs	339/618	n/a	n/a
$^1_\infty$[Gd$_{0.995}$Eu$_{0.005}$(2-PyPz)$_3$]:Eu^{3+},Tb^{3+} (**7c**)	918(7) µs	343/618	1027(18) µs	337/618	n/a	n/a
$^1_\infty$[Gd$_{0.99}$Eu$_{0.01}$(2-PyPz)$_3$]:Eu^{3+},Tb^{3+} (**7d**)	731(8) µs	340/618	810(6) µs	340/618	n/a	n/a
$^1_\infty$[Gd$_{0.98}$Eu$_{0.01}$Tb$_{0.01}$(2-PyPz)$_3$]:Eu^{3+},Tb^{3+} (**7e**)	990(3) µs	344/618	988(5) µs	335/619	n/a	n/a
$^1_\infty$[Gd$_{0.99}$Tb$_{0.01}$(2-PyPz)$_3$]:Eu^{3+},Tb^{3+} (**7f**)	31.9(3) µs	350/545	629(9) µs	339/545	n/a	n/a
$^1_\infty$[Eu$_{0.95}$Tb$_{0.05}$(2-PyPz)$_3$] (**6a**)	582(6) µs	342/618	878(7) µs	340/618	n/a	n/a
$^1_\infty$[Eu$_{0.75}$Tb$_{0.25}$(2-PyPz)$_3$] (**6b**)	748(6) µs	328/618	1004(7) µs	324/618	4.9(5)	330 / 575-715
$^1_\infty$[Eu$_{0.50}$Tb$_{0.50}$(2-PyPz)$_3$] (**6c**)	980(6) µs	334/618	1158(5) µs	338/618	5.1(4)	330 / 575-715
$^1_\infty$[Tb$_{0.95}$Eu$_{0.05}$(2-PyPz)$_3$] (**8b**)	967(5) µs	343/618	1224(7) µs	339/618	n/a	n/a

[a] Emission lifetimes determined at 298 K. [b] Excitation and emission wavelengths for emission lifetime at 298 K. [c] Emission lifetime determined at 77 K. [d] Excitation and emission wavelengths for emission lifetime at 77 K. [e] Quantum yield. [f] Excitation wavelength and emission range of QY measurements.

CIE 1931

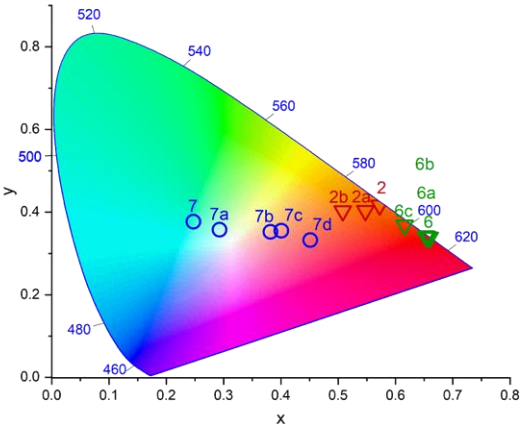

Figure S27. Chromaticity coordinate diagram (CIE 1931) of the emission colors of $^1_\infty$[Ce(2-PyPz)$_3$] (**2**), $^1_\infty$[Ce$_{1-x}$Tb$_x$(2-PyPz)$_3$] (**2a, 2b**), $^1_\infty$[Gd(2-PyPz)$_3$]:Eu^{3+},Tb^{3+} (**7**) $^1_\infty$[Gd$_{1-x-y}$Eu$_x$Tb$_y$(2-PyPz)$_3$]:Eu^{3+},Tb^{3+} (**7a–7d**), $^1_\infty$[Eu(2-PyPz)$_3$] (**6**), and $^1_\infty$[Eu$_{1-x}$Tb$_x$(2-PyPz)$_3$] (**6a–6c**).

Table S6. Chromaticity coordinates (x,y) for **2**, **2a**, **2b**, **8a**, **8**, **7**, **7a-7f**, **6**, **6a-6c**, **8b** at 77 K.

compound		CIE, x	CIE, y
$^1_\infty$[Ce(2-PyPz)$_3$]	(**2**)	0.57229	0.41665
99.5% Ce +0.5% Tb	(**2a**)	0.54739	0.40324
95% Ce +5% Tb	(**2b**)	0.5079	0.40274
$^1_\infty$[Gd(2-PyPz)$_3$]:Eu^{3+},Tb^{3+}	(**7**)	0.24674	0.37754
$^1_\infty$[Gd$_{1-x-y}$Eu$_x$Tb$_y$(2-PyPz)$_3$]:Eu^{3+},Tb^{3+}			
99.8% Gd +0.2% Eu	(**7a**)	0.29239	0.35807
99.7% Gd +0.3% Eu	(**7b**)	0.3812	0.35275
99.5% Gd +0.5% Eu	(**7c**)	0.40021	0.35565
99% Gd +1% Eu	(**7d**)	0.45066	0.33305
$^1_\infty$[Eu(2-PyPz)$_3$]	(**6**)	0.65959	0.33973
95% Eu + 5% Tb	(**6a**)	0.65565	0.34132
75% Eu + 25% Tb	(**6b**)	0.65293	0.34296
50% Eu + 50% Tb	(**6c**)	0.61586	0.36941

IR Spectroscopy

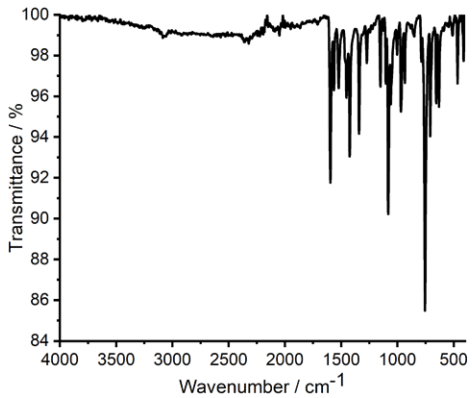

Figure S28. Infrared spectrum (ATR) of coordination polymer $^1_\infty$[La(2-PyPz)$_3$] (**1**).

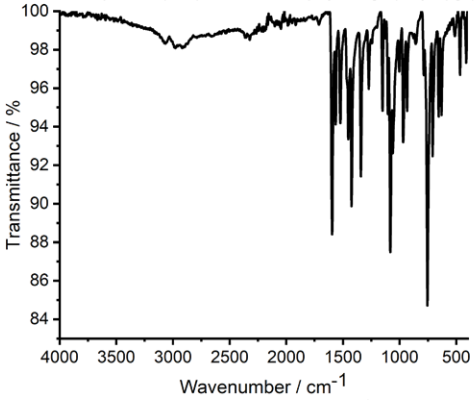

Figure S29. Infrared spectrum (ATR) of coordination polymer $^1_\infty$[Ce(2-PyPz)$_3$] (**2**).

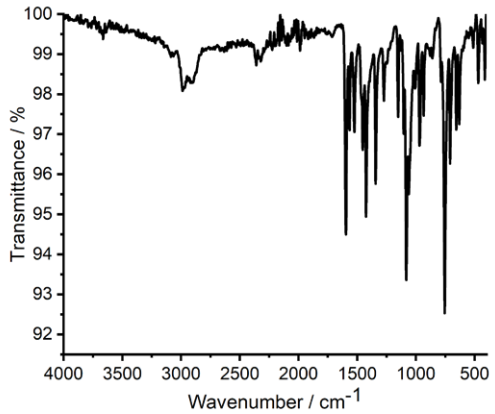

Figure S30. Infrared spectrum (ATR) of coordination polymer $^1_\infty$[Pr(2-PyPz)$_3$] (**3**).

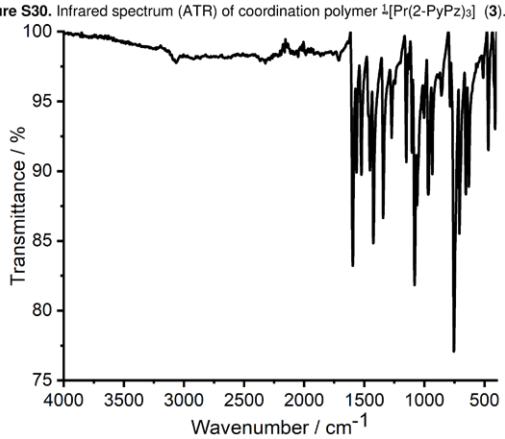

Figure S31. Infrared spectrum (ATR) of coordination polymer $^1_\infty$[Nd(2-PyPz)$_3$] (**4**).

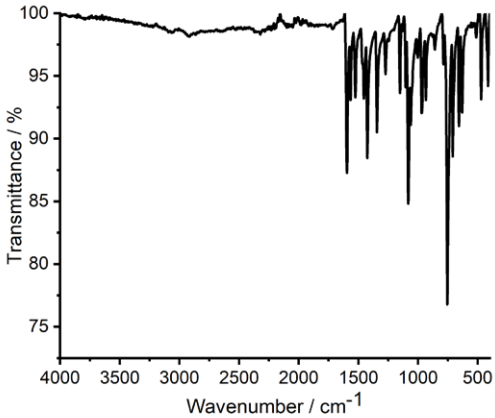

Figure S32. Infrared spectrum (ATR) of coordination polymer $^1_\infty$[Sm(2-PyPz)$_3$] (**5**).

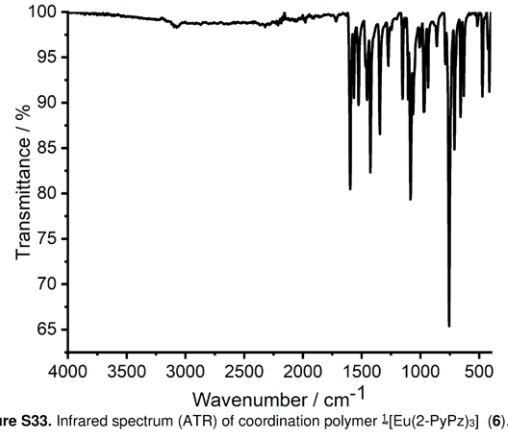

Figure S33. Infrared spectrum (ATR) of coordination polymer $^1_\infty$[Eu(2-PyPz)$_3$] (**6**).

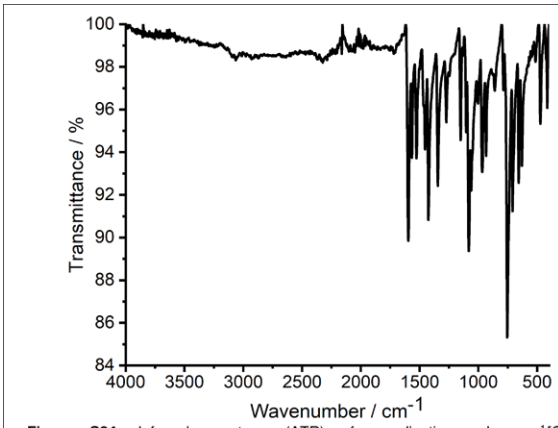

Figure S34. Infrared spectrum (ATR) of coordination polymer $^1_\infty$[Gd(2-PyPz)$_3$]:Eu^{3+},Tb^{3+} (**7**).

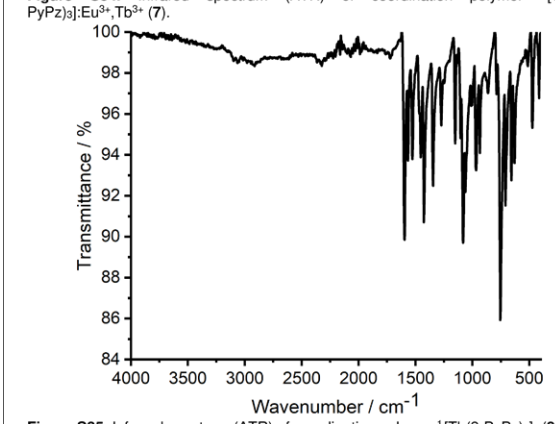

Figure S35. Infrared spectrum (ATR) of coordination polymer $^1_\infty$[Tb(2-PyPz)$_3$] (**8**).

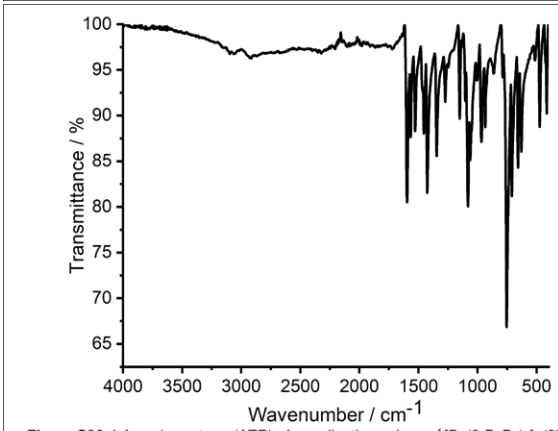

Figure S36. Infrared spectrum (ATR) of coordination polymer $^1_\infty$[Dy(2-PyPz)$_3$] (**9**).

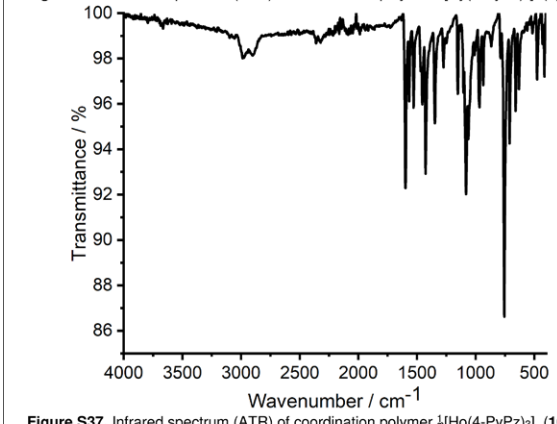

Figure S37. Infrared spectrum (ATR) of coordination polymer $^1_\infty$[Ho(4-PyPz)$_3$] (**10**).

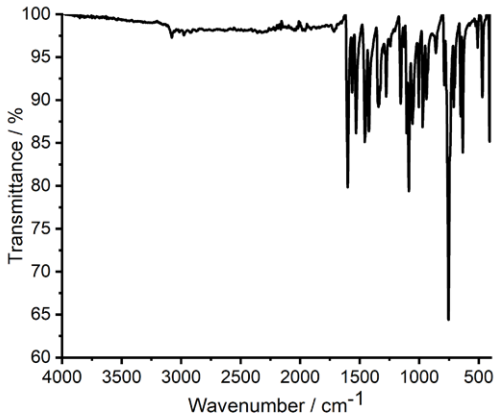

Figure S38. Infrared spectrum (ATR) of $[Tb_2Ca(2\text{-}PyPz)_8]$ (**11**).

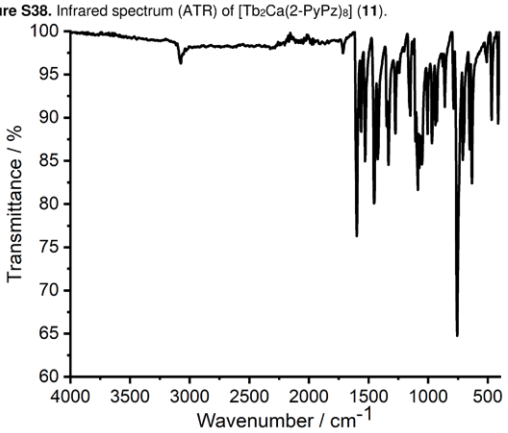

Figure S39. Infrared spectrum (ATR) of $[Tb_2Sr(2\text{-}PyPz)_8]$ (**12**).

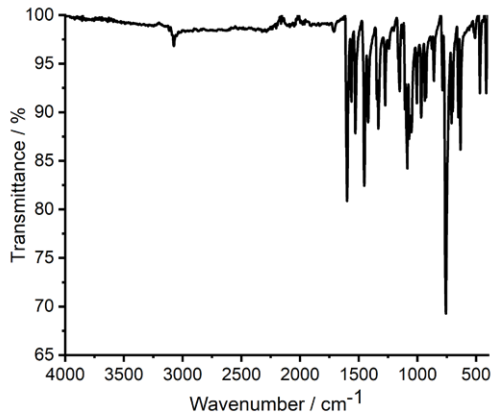

Figure S40. Infrared spectrum (ATR) of $[Tb_2Ba(2\text{-}PyPz)_8]$ (**13**).

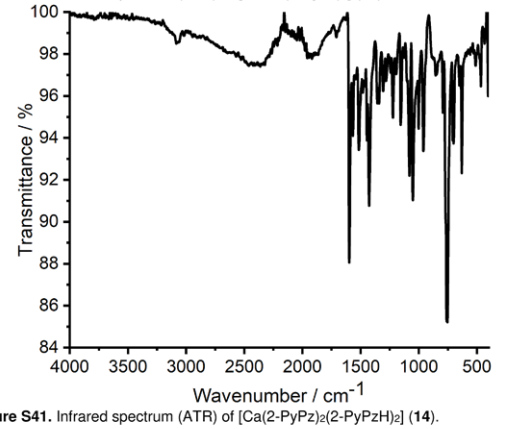

Figure S41. Infrared spectrum (ATR) of $[Ca(2\text{-}PyPz)_2(2\text{-}PyPzH)_2]$ (**14**).

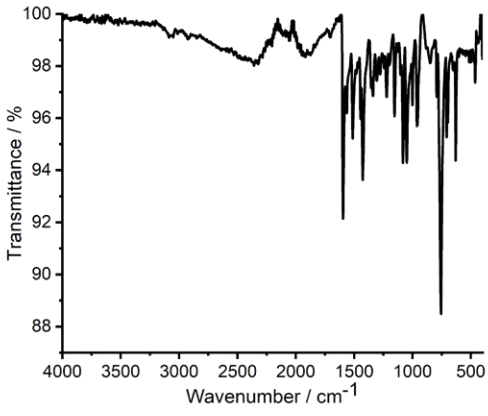

Figure S42. Infrared spectrum (ATR) of $[Sr(2\text{-}PyPz)_2(2\text{-}PyPzH)_2]$ (**15**).

3.2. Heteroleptic lanthanide coordination polymers and complexes of anhydrous trivalent lanthanide chlorides with 2- and 3-pyridylpyrazoles

3.2.1. 3D-Frameworks and 2D-networks of lanthanide coordination polymers with 3-pyridylpyrazole: photophysical and magnetic properties

This article has been published in the

Journal Dalton Transaction

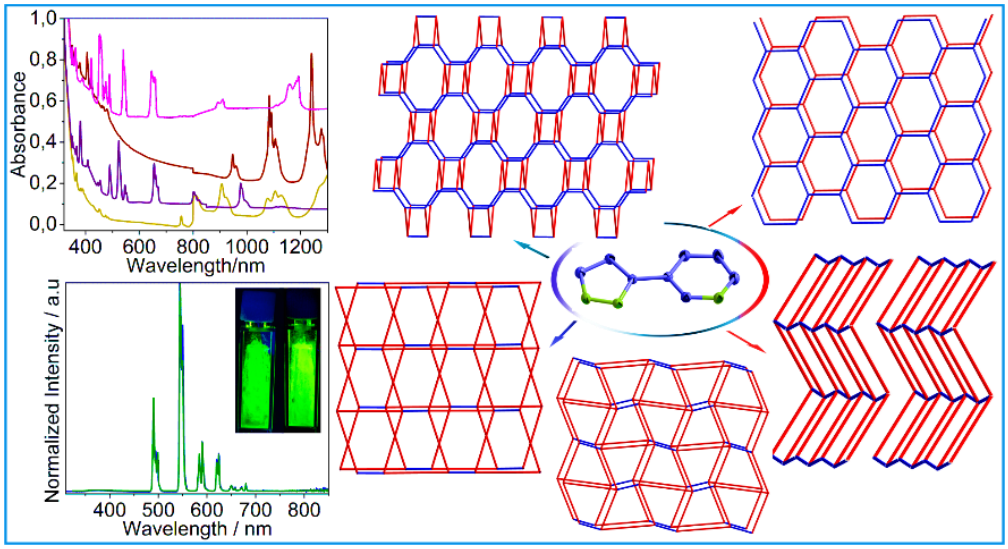

Heba Youssef, Thomas Schäfer, Jonathan Becker, Alexander E. Sedykh, Leonardo Basso, Clemens Pietzonka, Ilya V. Taydakov, Florian Kraus, and Klaus Müller-Buschbaum

Reprinted with permission from *Dalton Trans.* **2022**, *51*, 14673–14685.

DOI 10.1039/D2DT01999J

Dalton Transactions

ROYAL SOCIETY OF CHEMISTRY

PAPER

View Article Online
View Journal | View Issue

Cite this: *Dalton Trans.*, 2022, **51**, 14673

3D-Frameworks and 2D-networks of lanthanide coordination polymers with 3-pyridylpyrazole: photophysical and magnetic properties†

Heba Youssef,[a,b] Thomas Schäfer,[a] Jonathan Becker,[a] Alexander E. Sedykh,[a] Leonardo Basso,[a] Clemens Pietzonka,[c] Ilya V. Taydakov,[d] Florian Kraus[c] and Klaus Müller-Buschbaum *[a,e]

A series of 15 lanthanide-containing coordination polymers, both 3D- and 2D-networks, as well as complexes of Ln-trichlorides with 3-(3-pyridyl)pyrazole (3-PyPzH), were synthesized. A large structural diversity is observed depending on the ligand content: $^{3}_{\infty}$[Ln(3-PyPzH)Cl_3], Ln = Eu and Gd, of **sra** topology, $^{2}_{\infty}$[Sm(3-PyPzH)Cl_3], $^{2}_{\infty}$[Ln_2(3-PyPzH)$_3Cl_6$]·2solv, Ln = Eu^{3+}, Tb^{3+}, Dy^{3+}, Ho^{3+} and Er^{3+}, solv = Tol and MeCN, of **sql** topology and $^{2}_{\infty}$[Ln(3-PyPzH$_2$)Cl_4], Ln = La and Nd, of **hcb** topology with salt like complexes of the formula [(3-PyPzH$_2$)][Ln(3-PyPzH)$_2Cl_4$], Ln = Eu, Tb, Dy and Ho. The products were characterized by single-crystal and powder X-ray diffraction, high-temperature X-ray diffraction, differential thermal analysis and thermogravimetry (DTA/TG) combined with mass spectrometry, differential scanning calorimetry (DSC), IR-spectroscopy, UV–visible spectrophotometry, photoluminescence spectroscopy, and magnetic susceptibility. Absorption spectroscopy shows ion-specific 4f–4f transitions that can be assigned to Sm^{3+}, Eu^{3+}, Dy^{3+}, Ho^{3+} and Er^{3+} in a wide range from the UV-VIS to NIR region. An excellent antenna effect through ligand–metal energy transfer was observed in $^{2}_{\infty}$[Tb_2(3-PyPzH)$_3Cl_6$]·2solv, leading to high efficiency of the luminescence indicated by a quantum yield up to 76%. Direct current magnetic susceptibility studies reveal the absence of interatomic interaction for Dy^{3+} and Er^{3+} and weak ferromagnetic interaction for Ho^{3+}. Thermal analysis shows good stability up to 365 °C for $^{2}_{\infty}$[Ho_2(3-PyPzH)$_3Cl_6$]·2MeCN.

Received 23rd June 2022,
Accepted 1st September 2022

DOI: 10.1039/d2dt01999j

rsc.li/dalton

Introduction

Due to their versatile properties, lanthanide-based coordination polymers (CPs) and metal–organic frameworks (MOFs) have attracted great attention in a number of fields, including optoelectronics[1] and molecular magnetism.[2] A fundamental base of the electronic states of the lanthanides stems from the deep shielding of the 4f orbitals by the fully occupied 5s and 5p orbitals,[3] leading to an energy independence of the luminescence-based transitions from the chemical surrounding because of the intra-configurational nature of the $4f^n$–$4f^n$ electronic transitions.[4] Interest in the magnetic properties arises from the possibility of forming single-molecule magnets (SMMs).[2b,5] A combination of both properties for the development of magneto-luminescent materials is of interest because of their potential applications as sensors.[5d,6] The magnetic properties of trivalent lanthanide ions (Ln^{3+}) result from a high magnetic moment and intrinsic magnetic anisotropy,[5b] which is necessary for a strong magnetic behavior.[2,7] The luminescence properties of Ln^{3+} ions arise from the optical 4f–4f orbital transitions resulting in ion-specific emission spectra in the visible and the near-infrared spectral range.[8] An adjacent, strongly absorbing chromophore such as an organic molecule can be used to enhance the efficiency of luminescence from the lanthanides (the so-called "antenna effect").[8a,9] This is advantageous because Ln^{3+} ions are poor at absorbing light directly, because of the low extinction coefficients of the Laporte forbidden 4f–4f transitions.[10] In contrast, the absorption spectra, covering part of the photophysical pro-

[a]*Institute of Inorganic and Analytical Chemistry, Justus-Liebig-University Giessen, Heinrich-Buff-Ring 17, 35392 Giessen, Germany. E-mail: Klaus.Müller-Buschbaum@anorg.chemie.uni-giessen.de*
[b]*Department of Chemistry, Faculty of Science, Mansoura University, El Gomhouria, Mansoura Qism 2, Dakahlia Governorate, 11432 Mansoura, Egypt*
[c]*Fachbereich Chemie, Philipps-Universitaet Marburg, Hans-Meerwein-Straße, 35032 Marburg, Germany*
[d]*Lebedev Physical Institute of the Russian Academy of Sciences, Leninskiy pr-t, 53, 119991 Moscow, Russia*
[e]*Center for Materials Research (LAMA), Justus-Liebig-University Giessen, Heinrich-Buff-Ring 16, 35392 Giessen, Germany. E-mail: kmbac@uni-giessen.de*

†Electronic supplementary information (ESI) available: 47 figures and 11 tables showing the crystallographic data, powder X-ray-diffraction, absorption spectra, luminescence spectra, thermal properties, and IR-spectroscopy as well as instrumentation details. CCDC 2159935–2159947. For ESI and crystallographic data in CIF or other electronic format see DOI: https://doi.org/10.1039/d2dt01999j

perties of Ln^{3+}, did not generate the same interest until recently, despite having the potential to display the uptake of light.[11] Measurements of the absorption spectra are essential, especially when the sample does not obey the Kasha rule[12] and the Vavilov rule.[13]

The ligand 3-(3-pyridyl)pyrazole (3-PyPzH) was chosen for this work. Besides its use in ligand synthesis,[14] green chemistry,[15] and medicinal chemistry,[16] it has also been used to obtain Cu^{+} and Ag^{+} complexes that exhibit high-lying intersystem crossing that results in phosphorescence of high efficiency.[17] Recently, homoleptic and highly luminescent trivalent lanthanide 3D coordination polymers were reported, such as $^{3}_{\infty}[Ln(3\text{-PyPz})_3]$, Ln = Sm, Eu, Gd, Tb and Dy with 3-(3-pyridyl)pyrazolate as the ligand.[18] The series of frameworks shows photoluminescence with intra-4f emission of the Ln^{3+} ions activated by the antenna effect of the ligand, resulting in Ln^{3+} sensitization. Based on this work, we investigated the influence of chlorido ligands on the coordination of Ln^{3+}, the resulting structural aggregation and topological behavior, the stability, and the influence of the neutrally coordinated ligand on the photophysical properties and the magnetic properties of the respective Ln^{3+}-based coordination polymers.

Results and discussion

Synthesis and structural analysis

Fifteen coordination polymers and complexes were synthesized from anhydrous lanthanide trichlorides and 3-(3-pyridyl)pyrazole (3-PyPzH) through a solvothermal reaction route in either anhydrous acetonitrile, toluene, or chlorobenzene. Nine coordination polymers $^{2}_{\infty}[Sm(3\text{-PyPzH})Cl_3]$ (**1**), $^{3}_{\infty}[Ln(3\text{-PyPzH})Cl_3]$, Ln = Eu^{3+} and Gd^{3+} (**2**, **3**), $^{2}_{\infty}[Tb_2(3\text{-PyPzH})_3Cl_6]\cdot 2Tol$ (**4**), and $^{2}_{\infty}[Ln_2(3\text{-PyPzH})_3Cl_6]\cdot 2MeCN$, Ln = Eu^{3+}, Tb^{3+}, Dy^{3+}, Ho^{3+} and Er^{3+} (**5–9**) were obtained as bulk products. The crystal structures of $^{2}_{\infty}[Sm(3\text{-PyPzH})Cl_3]$ (**1**), $^{3}_{\infty}[Ln(3\text{-PyPzH})Cl_3]$, Ln = Eu and Gd (**2**, **3**), $^{2}_{\infty}[Tb_2(3\text{-PyPzH})_3Cl_6]\cdot 2Tol$ (**4**), and $^{2}_{\infty}[Ln_2(3\text{-PyPzH})_3Cl_6]\cdot 2MeCN$, Ln = Eu^{3+}, Ho^{3+} and Er^{3+} (**5**, **8**, **9**) were determined by single-crystal X-ray diffraction, while the structures of $^{2}_{\infty}[Ln_2(3\text{-PyPzH})_3Cl_6]\cdot 2MeCN$, Ln = Tb^{3+} and Dy^{3+} (**6**, **7**) were identified from microcrystalline products by powder X-ray diffraction (PXRD) and subsequent Rietveld refinements based on the single-crystal X-ray data of $^{2}_{\infty}[Ho_2(3\text{-PyPzH})_3Cl_6]\cdot 2MeCN$ (**8**), confirming the isotypic character of **5–9** (Fig. S7 and S8†).

Single-crystal X-ray diffraction studies reveal that $^{2}_{\infty}[Sm(3\text{-PyPzH})Cl_3]$ (**1**) crystallizes in the orthorhombic crystal system with the centrosymmetric space group *Pbcm* (57). The Sm^{3+} ion exhibits an eight-fold coordinated environment of N atoms forming a distorted bi-capped trigonal prism with C_{2v} symmetry (Fig. 1). The Sm^{3+} coordination sphere consists of two nitrogen atoms from two different 3-PyPzH ligands and six Cl^{-} ligands. The 3-PyPzH molecule acts as a bridge between two adjacent Sm^{3+} ions to form a 1D zigzag building unit (Fig. 1a). A secondary building unit (SBU) is formed by a 1D inorganic zigzag chain, in which three chloride ions act as a bridge between two adjacent Sm^{3+} ions (Fig. 1b). The combination of two zigzag 1D chains creates a two-dimensional network. The topology of the network was determined in accordance with the Reticular Chemistry Structure Resource (RCSR) and the Wells terminology.[19] $^{2}_{\infty}[Sm(3\text{-PyPzH})Cl_3]$ (**1**) has an **sql** topology[20] with the Schläfli symbol $4^4\cdot 6^2$. The Ln–N and Ln–Cl distances agree with the expected values for the trivalent state of halides.[21] A comparison of the interatomic distances of **1** (Sm–N 257.0(2)–264.0(3) and Sm–Cl 275.05(6)–282.80(6) pm) with $^{2}_{\infty}[Sm_3Cl_9(bipy)_3]$ (bipy = 4,4′-bipyridine)[22] resulted in good agreement for Sm–Cl. The Sm–N bond is slightly longer than that in the previous example but still in the range of Sm–N in $[Sm_2Cl_6(\mu\text{-}4,4'\text{-bipy})(py)_6]$ (py = pyridine).[23]

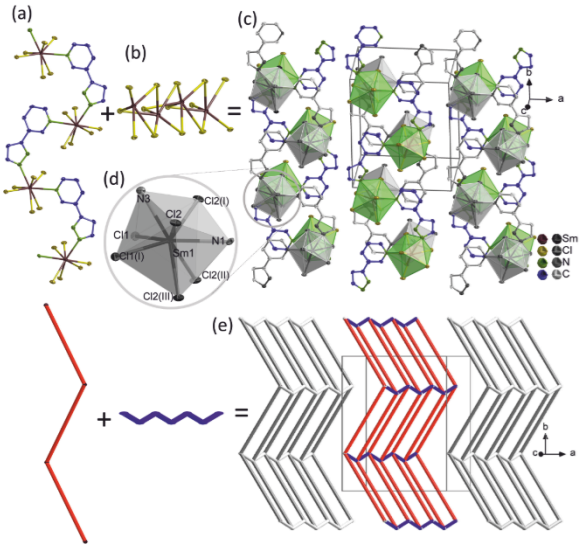

Fig. 1 (a) 1D building unit in $^{2}_{\infty}[Sm(3\text{-PyPzH})Cl_3]$ (**1**), in which the ligands act as a bridge between two adjacent Sm^{3+} ions to form a zigzag chain. (b) A SBU of inorganic zigzag 1D chain constructed from three chloride ions bridging two adjacent Ln^{3+}. (c) Crystal structure of **1** where the 2D sheets are built up by the combination of both Ln–Cl chains and the 3-PyPzH molecular chain, whereas the second layer is shown in grayish colors. (d) A distorted bi-capped trigonal prismatic coordination sphere of the Sm^{3+} ion. (e) Topological representation of **1** as a uninodal 4-c net with **sql** topology. Symmetry operations: I *x*, *y*, *−z* + 1/2 II *x*, *−y* + 1/2, *z* − 1/2 III *x*, *−y* + 1/2, *−z* + 1. In all figures, the hydrogen atoms are omitted for clarity and the coordination polyhedra around Ln^{3+} are indicated in green with thermal ellipsoids depicted at a 50% probability level.

$^{3}_{\infty}[Ln(3\text{-PyPzH})Cl_3]$, Ln = Eu and Gd (**2**, **3**) crystallize in the orthorhombic crystal system with the primitive centrosymmetric space group *Pcca* (54). Each Ln^{3+} ion is hepta-coordinated to five chloride anions, one of which is terminal, and two N atoms from two (3-PyPzH) ligands in a distorted pentagonal bipyramidal geometry (Fig. 2). The neighboring Ln^{3+} ions are linked by a chlorine bridge forming a 1D inorganic wavelike $[Ln(Cl)_2]_n$ chain as a building unit (Fig. 2a).

The 1D infinite chains are interconnected by pyridylpyrazole bridges, creating a 3D coordination polymer. A wavelike 4-c uninodal net of **sra** topology[24] with the Schläfli symbol

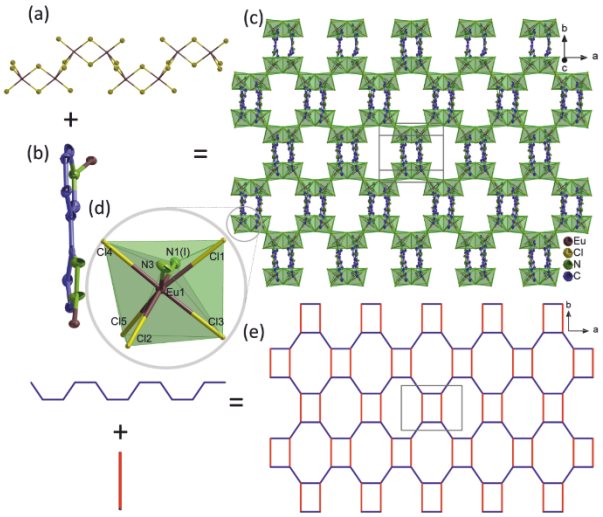

Fig. 2 (a) 1D wavelike inorganic chain as a SBU in $^{3}_{\infty}$[Eu(3-PyPzH)Cl_3] (**2**). (b) Pyridylpyrazole bridging between two adjacent Eu^{3+} ions. (c) Crystal structure of **2** with 3D sheets built up by a Ln–Cl chain connected *via* 3-PyPzH molecules. (d) A distorted pentagonal bipyramidal coordination sphere of the Eu^{3+} ion. (e) Topological representation of **2** as a uninodal 4-c net with **sra** topology.

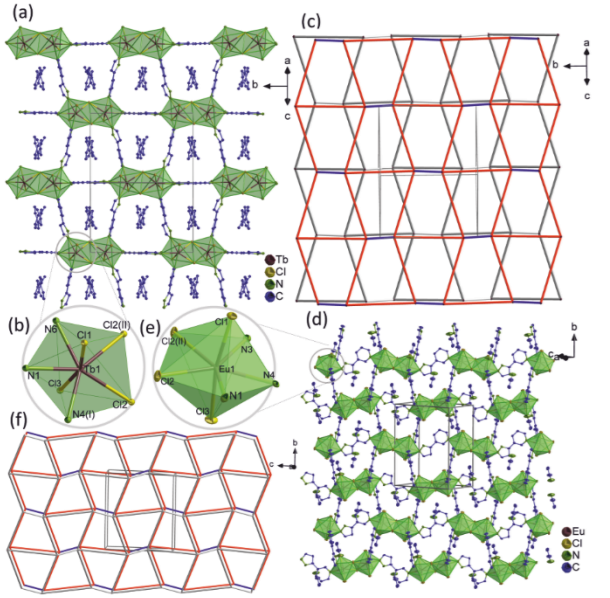

Fig. 3 (a) Crystal structure of $^{2}_{\infty}$[Tb_2(3-PyPzH)$_3Cl_6$]·2Tol (**4**) where the 2D-sheets are built up by Ln–Cl dimers which are connected *via* 3-PyPzH molecules. (b) A distorted pentagonal bipyramidal coordination sphere of the Tb^{3+} ion. (c) Topological representation of **4** as a uninodal 4-c net with sql topology and the blue lines represent "Cl-double-bridges". (d) Crystal structure of $^{2}_{\infty}$[Eu_2(3-PyPzH)$_3Cl_6$]·2MeCN (**5**) showing the formation of 2D sheets *via* connecting the Ln–Cl dimers with the 3-PyyPzH molecules. (e) A distorted pentagonal bipyramidal coordination sphere of the Eu^{3+} ion. (f) Topological representation of **4** as a uninodal 4-c net with sql topology. Symmetry operations: I $x - 1/2$, $-y + 1/2$, $z + 1/2$ II $-x + 1$, $-y + 1$, $-z + 1$.

$4^2{\cdot}6^3{\cdot}8$ is formed. Comparison and analysis of the lattice parameters of **2** and **3** (Table S7†) indicate that the unit cell volume and the Ln–N1 distances and the Ln–N3 distances show a decreasing trend for an increase in the charge density from europium to gadolinium. The Ln–N and Ln–Cl distances agree with the expected values for the halides and N-donor complexes of the trivalent lanthanides.[21] A comparison of the interatomic distances of **2** (Eu–N 251.7(6)–258.4(6) and Eu–Cl 261.4(2)–279.0(2) pm) and **3** (Gd–N 250.0(1)–256.0(1) and Gd–Cl 260.2(3)–278.1(2) pm) with related compounds known in the literature, such as [Ln_2(HTzDPTpy)$_2Cl_6$] (Ln = Eu and Gd, HTzDPTpy = 1,1′-biphenyl]-4-carbonitrile, 4′-[2,2′:6′,2″-terpyridin]-4′-yl),[25] shows good agreement between both distance types.

$^{2}_{\infty}$[Tb_2(3-PyPzH)$_3Cl_6$]·2Tol (**4**) and $^{2}_{\infty}$[Ln_2(3-PyPzH)$_3Cl_6$]·2MeCN, Ln = Eu^{3+} (**5**), Tb^{3+} (**6**), Dy^{3+} (**7**), Ho^{3+} (**8**), and Er^{3+} (**9**) crystallize in the monoclinic crystal system with the space group $P2_1/n$ (14). Each metal atom is hepta-coordinated by three nitrogen atoms from three ligand molecules and four chloride ions in a distorted pentagonal-bipyramidal geometry. All three neutral ligand molecules and the two equatorial chloride ions Cl2 and Cl2(II) act as a bridge between two neighboring trivalent lanthanide ions forming a 2D net (Fig. 3). **5**–**9** have a less distorted equatorial plane of the distorted pentagonal-bipyramidal coordination configuration than **4** (Fig. 3).

Considering the two-terminal axial Cl3 and Cl1 ions, the Cl3–Ln–Cl1 angle in **4** with a value of 163.55(2)° is far from 180° than that in **5**, **8** and **9** which gradually increases from 169.82(2)° in **5** to 170.91(4)° in **9** (Table S9†). The two-dimensional network of four-connected nodes in **4**–**9** adopts the **sql** topology[20b,26] with the Schlafli symbol $4^4{\cdot}6^2$. A comparison of the interatomic distances of **4** (Tb–N 249.0(1)–252.9(2) and Tb–$Cl_{terminal}$ 259.15(7), 261.75(7) pm) with a compound known from the literature, [$LnCl_3$(ptpy)(py)] (ptpy = 4′-phenyl-2,2′:6′,2″-terpyridine, py = pyridine)[27] shows good agreement between both distance types. Further comparison of **5** (Eu–N 253.3(2)–259.0(2) and Eu–Cl 260.68(7)–277.34(6) pm), **8** (Ho–N 248.2(7), 254.0(2) and Ho–$Cl_{terminal}$ 255.8(2), 262.6(2) pm) and **9** (Er–N 246.3(3)–254.0(2) and Er–Cl 254.4(1)–271.8(1) pm) with $^{2}_{\infty}$[Eu_2Cl_6(4,4′-bipy)$_3$]·2(4,4′-bipy), (4,4′-bipy = 4,4′-bipyridine),[28] [$HoCl_3$(dpe)(thz)$_2$]·thz (dpe = 1,2-di(4-pyridyl)ethylene, thz = 1,3-thiazole),[29] and [Er_2Cl_6(pym)$_2$(thz)$_4$] (pym = pyrimidine),[30] respectively, showed as well good agreement between both types of distances. As expected, the Tb–Cl_{bridge} of **4** and Ho–Cl_{bridge} of **8** show longer distances up to 273.21(7) in **4** and 272.6(2) pm in **8**.[21,31]

Additional compounds, which are anionic coordination polymers of the formula [(3-PyPzH$_2$)][Ln(3-PyPzH)$_2Cl_4$], Ln = Eu, Tb, Dy and Ho (**10**–**13**) form as byproducts and crystallize in the monoclinic crystal system with the space group $P2_1/n$ (14). Four-terminal chloride ions and two nitrogen atoms of two neutral ligands (Fig. 4) coordinate the metal ion. As a result of the coordination number of six and D_{4h} symmetry, a

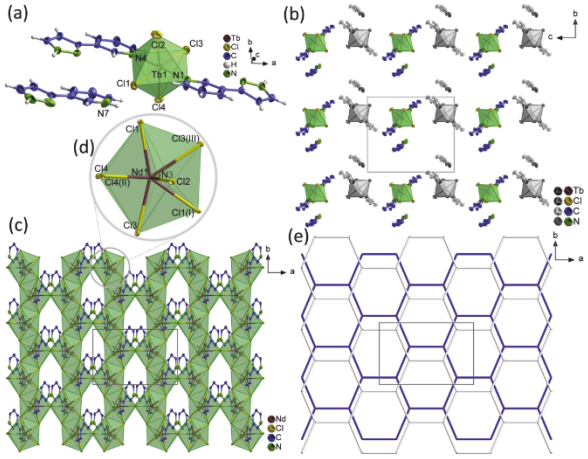

Fig. 4 (a) Extended coordination sphere of a Ln^{3+} ion in [(3-$PyPzH_2$)][Tb(3-$PyPzH)_2Cl_4$] (**11**). (b) Packing structure of **11** representing the series of isotypic compounds (**10–13**) with a view along [100]. (c) Crystal structure of $^2_\infty$[Nd(3-$PyPzH_2$)Cl_4] (**15**) with a view along [001]. (d) A distorted triangular dodecahedral coordination sphere of the Nd^{3+} ion. (e) Topological representation of **15** as a uninodal 3-c net with **hcb** topology. Symmetry operations: I $-x + 1/2, y-1/2, -z + 1/2$ II $-x + 1, y, -z + 1/2$ III $-x + 1/2, y + 1/2, -z + 1/2$.

distorted octahedron is observed for Ln^{3+}, Ln = Eu, Tb, Dy and Ho. In addition, a protonated ligand $(3\text{-}PyPzH_2)^+$ is intercalated and non-coordinated in the structure compensating for the negative charge of [Ln(3-$PyPzH)_2Cl_4$], Ln = Eu, Tb, Dy and Ho (**10–13**). As a consequence of the lanthanide contraction, a decreasing trend for the average Ln–N distance (from 250.8(3) in **10** to 245.0(2) pm in **13**) and for the volume of the unit cell for **10–13** is observed.

A comparison of the interatomic distances of **11** (Tb–N 247.6(2)–248.1(2) pm) and **12** (Dy–N 246.8(2) and Dy–Cl 260.3 (7) pm) with the closest examples found in the literature, [Tb(Tpm)Cl_3]·2MeCN (Tpm = tris(3,5-dimethylpyrazolyl) methane),[32] and the Dy^{3+} ion in the anionic part of the complex [$Dy(Tp^{Me2})_2$][$DyCl_3(Tp^{Me2})$]·CH_2Cl_2 (Tp^{Me2} = tris(3,5-dimethylpyrazolyl)borate)[33] also shows good agreement.

$^2_\infty$[Ln(3-$PyPzH_2$)Cl_4], Ln = La and Nd (**14**, **15**), crystallizes in the monoclinic crystal system with the space group *C*2/*c* (15). Each Ln^{3+} ion is coordinated by a protonated ligand $(3\text{-}PyPzH_2)^+$ and seven chlorine atoms, six of which act as a bridge between two neighboring trivalent lanthanide ions (Fig. 4). The coordination exhibits a distorted triangular dodecahedron geometry with C_{2v} symmetry. When the Nd^{3+} ion is treated as a 3-connected node and the chlorine bridge as a line, the structure of **15** can be simplified as a two-dimensional coordination polymer with **hcb** honeycomb[34] topology with the Schläfli symbol 6^3 and the vertex symbol 6·6·6. A comparison of the interatomic distances of **14** (La–N 272.0(2) and La–$Cl_{terminal}$ 280.9(5) pm) and **15** (Nd–N 264.2(6) and Nd–$Cl_{terminal}$ 275.2 pm) with structurally related compounds such as $^1_\infty$[$LnCl_3$(ptpy)] (Ln = La and Nd, ptpy = 4′-phenyl-2,2′:6′,2″-terpyridine)[27] shows good agreement. As expected, the Tb–Cl_{bridge} shows larger distances for **14** and **15** up to 288.1(2) pm.[31]

The obtained bulk materials of CP **1–9** were investigated by PXRD analysis; the resulting reflection patterns were in good agreement with the powder patterns simulated from single-crystal data (Fig. 5). The four salt-like complexes [(3-$PyPzH_2$)][Ln(3-$PyPzH)_2Cl_4$], Ln = Eu, Tb, Dy and Ho (**10–13**) were also obtained as byproducts (Fig. S9†). Their formation can be avoided by modifying the reaction conditions; more information about the synthesis and product formation can be found in the experimental part. For reactions with $LaCl_3$ and $NdCl_3$, the PXRD patterns of the bulk show additional crystalline phases, and $^2_\infty$[Ln(3-$PyPzH_2$)Cl_4], Ln = La^{3+} and Nd^{3+} (**14**, **15**) only as minor components (Fig. S10†).

Photophysical properties

UV-VIS-NIR absorption spectra. Electronic absorption spectra in the solid state were determined in addition to the excitation and emission spectra to provide detailed spectral interpretations for the free ligand (3-PyPzH), $^2_\infty$[Sm(3-PyPzH)Cl_3] (**1**), $^3_\infty$[Eu(3-PyPzH)Cl_3] (**2**), $^3_\infty$[Gd(3-PyPzH)Cl_3] (**3**), $^2_\infty$[Tb_2(3-$PyPzH)_3Cl_6$]·2Tol (**4**), $^2_\infty$[Eu_2(3-$PyPzH)_3Cl_6$]·2MeCN (**5**), $^2_\infty$[Dy_2(3-$PyPzH)_3Cl_6$]·2MeCN (**7**), $^2_\infty$[Ho_2(3-$PyPzH)_3Cl_6$]·2MeCN (**8**), and $^2_\infty$[Er_2(3-$PyPzH)_3Cl_6$]·2MeCN (**9**) from 200 to 800/1300 nm at room temperature (Fig. 6).

The reported absorption spectra localized on the ligand moieties of the Ln^{3+} based compounds were mostly investigated in solution,[35] while fewer examples were reported in the solid-state.[36] When examining Ln^{3+}-based absorption bands, the wavelength range is typically found to be limited in the literature, *e.g.*, it does not exceed 1000 nm for Ho^{3+} in [Ho(L)$(NO_3)_2$](PF_6)·H_2O (L = N^1,N^2-bis([2,2′-bipyridine]-6-ylmethylene)-1,2-ethanediamine),[37] 800 nm for Er^{3+} and Dy^{3+} and up to 650 nm for Sm^{3+} in $^2_\infty$[Ln(tfBDC)$(NO_3)$$(DMF)_2$]·DMF (Ln = Er^{3+}, Dy^{3+} and Sm^{3+}, H_2tfBDC = 2,3,5,6-tetrafluoroterephthalic acid).[38] In the absorption spectra of the free ligand, the absorption bands corresponding to the intra-ligand transitions π–π* and/or n → π*are in a range from below 200 to 270 nm and from 270 to 305 nm. Although the high absorption of the ligand in the visible region overlaps with most of the Laporte-forbidden 4f–4f transitions, the absorption spectra of **1**, **4**, **7**, **8**, and **9** show additional weak to medium bands that can be assigned to the respective 4f–4f transitions in both the VIS and NIR regions (Table 1).[38,39] For $^3_\infty$[Eu(3-PyPzH)Cl_3] (**2**), a broad shoulder in the region from 400 to 500 nm (Fig. 6b) is detected and attributed to the occurrence of a ligand-to-metal charge transfer (LMCT) N → Eu^{3+}.[40] This shoulder disappears for $^2_\infty$[Eu_2(3-$PyPzH)_3Cl_6$]·2MeCN (**5**), suggesting a reduced quenching effect. Comparably, low absorbance of these bands in **2**, **4**, and **5** is also observed in the literature for Eu-PDC and Tb-PDC, H_2PDC = pyridine-3,5-dicarboxylic acid.[36b]

Luminescence properties. The synthesized series of nine phase pure coordination polymers (**1–9**) shows photoluminescence properties for a wide range of lanthanides. Excitation and emission spectra were recorded in the solid state at room temperature (RT = 298 K) and 77 K for the free

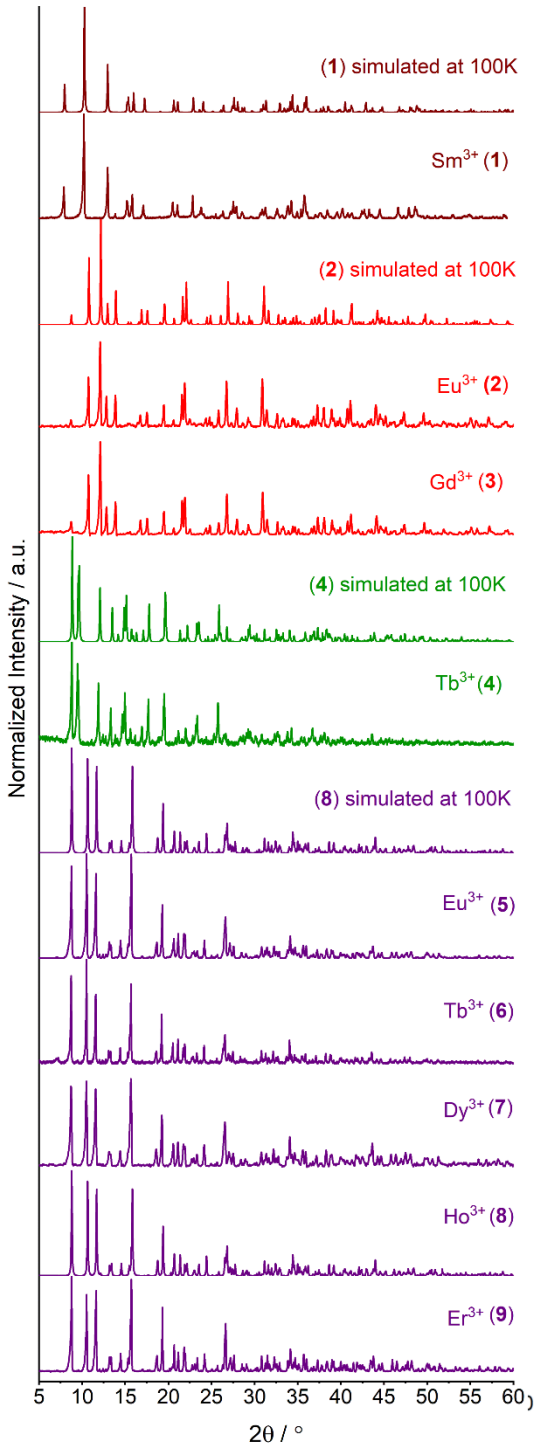

Fig. 5 Comparison of the experimental powder X-ray diffraction patterns of $^{2}_{\infty}$[Sm(3-PyPzH)Cl_3] (**1**), $^{3}_{\infty}$[Eu(3-PyPzH)Cl_3] (**2**), $^{3}_{\infty}$[Gd(3-PyPzH)Cl_3] (**3**), $^{2}_{\infty}$[Tb_2(3-PyPzH)$_3Cl_6$]·2Tol (**4**), $^{2}_{\infty}$[Eu_2(3-PyPzH)$_3Cl_6$]·2MeCN (**5**), $^{2}_{\infty}$[Tb_2(3-PyPzH)$_3Cl_6$]·2MeCN (**6**), $^{2}_{\infty}$[Dy_2(3-PyPzH)$_3Cl_6$]·2MeCN (**7**), $^{2}_{\infty}$[Ho_2(3-PyPzH)$_3Cl_6$]·2MeCN (**8**), and $^{2}_{\infty}$[Er_2(3-PyPzH)$_3Cl_6$]·2MeCN (**9**) at 298 K with the respective simulated patterns from single-crystal X-ray data.

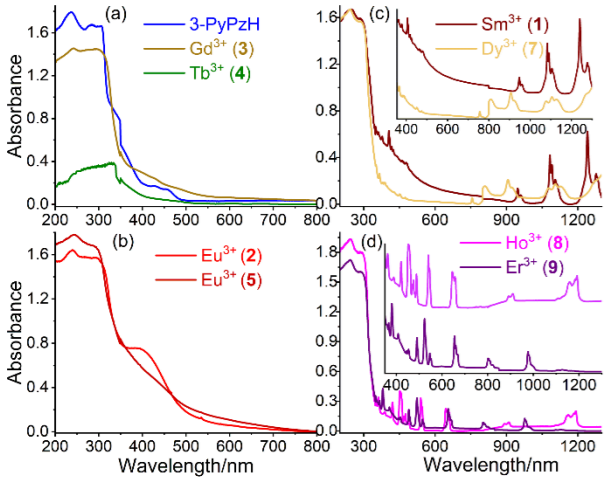

Fig. 6 Solid state absorption spectra measured at room temperature: (a) the free ligand (3-PyPzH), $^{3}_{\infty}$[Gd(3-PyPzH)Cl_3] (**3**), $^{2}_{\infty}$[Tb_2(3-PyPzH)$_3Cl_6$]·2Tol (**4**), (b) $^{3}_{\infty}$[Eu(3-PyPzH)Cl_3] (**2**), $^{2}_{\infty}$[Eu_2(3-PyPzH)$_3Cl_6$]·2MeCN (**5**), (c) $^{2}_{\infty}$[Sm(3-PyPzH)Cl_3] (**1**), $^{2}_{\infty}$[Dy_2(3-PyPzH)$_3Cl_6$]·2MeCN (**7**), (d) $^{2}_{\infty}$[Ho_2(3-PyPzH)$_3Cl_6$]·2MeCN (**8**), and $^{2}_{\infty}$[Er_2(3-PyPzH)$_3Cl_6$]·2MeCN (**9**).

ligand 3-PyPzH,[17,18,41] the 2D-coordination polymers **1** and **4–9** and the 3D-coordination polymers **2** and **3**. The investigated compounds (Fig. 7–9) show a broad excitation band of the coordinated ligand, which dominates in the UV region and is energetically blue-shifted upon coordination compared to the $S_1 \leftarrow S_0$ transition in free 3-PyPzH (at 330 nm). Furthermore, direct Eu^{3+} excitation in **2** and **5** and Tb^{3+} excitation in **4** are weakly observable indicated by a series of sharp low intensity lines assigned to the $^7F_0 \rightarrow {}^5D_{4-0}$ Eu^{3+} intra-4f^6 and $^7F_6 \rightarrow {}^5D_{3-0}$ Tb^{3+} intra-4f^8 transitions (Fig. 7). Thus, in all investigated compounds, the ligand is mainly responsible for the excitation. The synthesized compounds exhibit emission colors typical of the respective Ln^{3+} ions from green (Tb^{3+}), through yellow (Dy^{3+}) to red (Eu^{3+}), all being visible to the naked eye under a UV lamp. For $^{2}_{\infty}$[Sm(3-PyPzH)Cl_3] (**1**) and the NIR emitters $^{2}_{\infty}$[Ln_2(3-PyPzH)$_3Cl_6$]·2MeCN, Ln = Ho^{3+} and Er^{3+} (**8**, **9**), the photoluminescence could only be detected with a spectrometer.

An evaluation of the T_1 energy level of the ligand (λ_{onset} = 428 nm, ~23 364 cm^{-1}; Fig. 7) was possible in the emission spectrum of $^{3}_{\infty}$[Gd(3-PyPzH)Cl_3] (**3**). The heavy paramagnetic Gd^{3+} enhances an intersystem crossing from the singlet to the triplet state of 3-PyPzH[27,42] followed by a broad but structured emission occurring from the triplet T_1 energy level to the S_0 ground state which is already visible at room temperature and even better resolved at 77 K.

The emission maxima of the ligand 3-PyPzH are reportedly observed in the region of 400–410 nm.[17,18] This fluorescence band disappears completely after coordination with Tb^{3+} in both coordination polymers $^{2}_{\infty}$[Tb_2(3-PyPzH)$_3Cl_6$]·2Tol (**4**) and $^{2}_{\infty}$[Tb_2(3-PyPzH)$_3Cl_6$]·2MeCN (**6**) pointing out an excellent antenna effect. The highest intensity is found for the transition $^5D_4 \rightarrow {}^7F_5$ at 545 nm for **4** and **6**, as expected for Tb^{3+}.[43]

Table 1 Absorption wavelengths of transitions of $^{2}_{\infty}$[Sm(3-PyPzH)Cl_3] (**1**), $^{3}_{\infty}$[Eu(3-PyPzH)Cl_3] (**2**), $^{2}_{\infty}$[Tb_2(3-PyPzH)$_3Cl_6$]·2Tol (**4**), $^{2}_{\infty}$[Dy_2(3-PyPzH)$_3Cl_6$]·2MeCN (**7**), $^{2}_{\infty}$[Ho_2(3-PyPzH)$_3Cl_6$]·2MeCN (**8**), and $^{2}_{\infty}$[Er_2(3-PyPzH)$_3Cl_6$]·2MeCN (**9**) in the solid state

Intra-4f absorption transitions			
1	$^6H_{5/2}$ →	$^5D_{5/2}$, $^6P_{7/2}$, $^4K_{11/2}$, $^6P_{5/2}$ + $^4P_{5/2}$, $^4M_{19/2}$, $^4I_{13/2}$, $^4I_{11/2}$, $^4G_{7/2}$, $^4F_{3/2}$, $^4G_{5/2}$, $^6F_{11/2}$, $^6F_{9/2}$, $^6F_{7/2}$	363, 378, 406, 418, 425, 466, 478, 499, 528, 559, 947, 1083, 1240 nm
2	$^7F_0$ →	$^5D_2$, $^5D_1$, $^5D_0$	465, 526, 580 nm
4	$^7F_6$ →	$^5D_4$	488 nm
7	$^6H_{15/2}$ →	$^4I_{11/2}$, $^4M_{21/2}$ + $^4I_{13/2}$ + $^4K_{17/2}$ + $^4F_{7/2}$, $^4G_{11/2}$, $^4I_{15/2}$, $^4F_{9/2}$, $^6F_{3/2}$, $^6F_{5/2}$, $^6F_{7/2}$, $^6F_{9/2}$	366, 387, 427, 450, 474, 755, 809, 906, 1105 nm
8	$^5I_8$ →	$^5G_4$, $^5G_5$ + $^3G_5$, $^5G_6$, $^5F_2$, $^5F_3$, $^5F_4$ + $^5S_2$, $^5F_5$, $^5I_5$, $^5I_6$	362, 388, 421, 452, 475, 488, 540, 645, 910, 1192 nm
9	$^4I_{15/2}$ →	$^2H_{3/2}$, $^5G_6$ + $^5F_1$, $^4F_{7/2}$, $^4S_{3/2}$, $^4S_{8/2}$, $^4F_{9/2}$, $^4I_{9/2}$, $^4I_{11/2}$	367, 2P3/2, 408, 454, 490, 524, 546, 655, 804, 977 nm

The ratio between the intensities of the fluorescence S_1 → S_0 transition for the ligand and those of $^5D_0$ → ^7F_J, J = 0–4 is different in $^{3}_{\infty}$[Eu(3-PyPzH)Cl_3] (**2**) from that in $^{2}_{\infty}$[Eu_2(3-PyPzH)$_3Cl_6$]·2MeCN (**5**). For **2**, the main emission band is related to the ligand, with a maximum around 403 nm, while the emission spectrum of **5** is dominated by the hypersensitive $^5D_0$ → $^7F_2$ transition at 613 nm. Consequently, the two samples show different emission colors when placed under a UV lamp, as the contribution of the ligand causes a blue shift with respect to the typical red emission attributed to the Eu^{3+} ion.[44] Thus **4** seems to have better energy transfer from the ligand than **2**, which could stem from the LMCT quenching states observed in the absorption spectrum for **2**. An additional reason is their differentially extended networks, since the formation of a three-dimensional structure (**2**) may increase the probability of a Förster-based energy transfer.

The ligand-based emission is more dominant for $^{2}_{\infty}$[Sm(3-PyPzH)Cl_3] (**1**) and $^{2}_{\infty}$[Dy_2(3-PyPzH)$_3Cl_6$]·2MeCN (**7**) (Fig. 8) with maxima at 371 (for Sm^{3+}, overlapping with $^4G_{5/2}$ → $^6H_{J/2}$, J = 5, 7, 9, 11) and 377 nm (for Dy^{3+}, overlapping with $^4F_{9/2}$ → $^6H_{15/2}$, and $^6H_{13/2}$). NIR emission bands can also be observed for **1** at 905 and 948 nm corresponding to the $^4G_{5/2}$ → $^6F_{1/2}$, $^6F_{3/2}$, and $^6F_{5/2}$ transitions of Sm^{3+} ions and for **7** at 756, 852, 1022 and 1182 nm corresponding to the $^4F_{9/2}$ → $^6H_{9/2}$, $^6H_{7/2}$, and $^6F_{J/2}$, J = 7,5 transitions of Dy^{3+}, respectively.

For $^{2}_{\infty}$[Ho_2(3-PyPzH)$_3Cl_6$]·2MeCN (**8**), the ligand emission is almost exclusive, and only very low intensity of the 4f-based emission $^5F_5$ → $^5I_8$ could be detected (Fig. 7). The Ho^{3+}-based luminescence observed is weak, as it is effectively quenched by the high vibrational energy of the ligands and the electronic structure of Ho^{3+}.

For Er^{3+} in $^{2}_{\infty}$[Er_2(3-PyPzH)$_3Cl_6$]·2MeCN (**9**) (Fig. 9) an Er-specific 4f transition in the NIR region $^4I_{13/2}$ → $^4I_{15/2}$ (λ = 1540 nm) was observed in the emission spectrum.

In addition, for the compounds with suitable emission intensity, lifetime and quantum yield determinations were performed using overall process decay times (Table 2), taking into consideration that the QY of Gd^{3+} (**3**) was measured for solely ligand-centered luminescence, while for other Ln^{3+}, it was measured predominantly for metal-centered ones. Association of the intensity of S_1 ← S_0 with the 4f–4f excitation levels shows an excellent antenna effect for Tb^{3+} (**4**, **6**). A lower effectiveness of the antenna effect is detected for Eu^{3+} (**5**) followed by (**2**), Sm^{3+} in (**1**), and Dy^{3+} in (**7**). This results from the energy differences (ΔE) between the organic ligand triplet state (~23 364 cm^{-1}) and the energy positions of the various Ln^{3+} ions. Sm^{3+} ($^4G_{5/2}$ = 17 900 cm^{-1}), Eu^{3+} ($^5D_0$ = 20 100 cm^{-1}), Dy^{3+} ($^4F_{9/2}$ = 21 500 cm^{-1}) and Tb^{3+} ($^5D_4$ = 20 500 cm^{-1})[39a,c] show the respective emissive levels considering the Latva's rule resulting in ΔE = 5465, 3265, 1865, and 2865 cm^{-1} for Sm^{3+}, Eu^{3+}, Dy^{3+}, and Tb^{3+}, respectively. The ΔE value falls within the optimal range (2500–3000 cm^{-1}) for Tb^{3+}. Therefore, the Tb^{3+}-based compounds are expected to have the highest lifetime and quantum yield among the series.

This conclusion is supported by the observation of long lifetimes for the Tb^{3+} emissive state (>2 ms) compared to Eu^{3+} (220.1(4) for **2**, 170(4) μs for **5**), and Dy^{3+} (23(1) μs). In addition, the observed quantum yield (QY) is the highest for the Tb^{3+} coordination polymers **4** and **6** with QY = 73(1) and 76(1) %, respectively. It is followed by Gd^{3+} in $^{3}_{\infty}$[Gd(3-PyPzH)Cl_3] (**3**) with a value of 23(1) %. $^{2}_{\infty}$[Dy_2(3-PyPzH)$_3Cl_6$]·2MeCN (**7**) gives a QY of 2(1) % for both ligand and Dy^{3+}-based emissions.

The photophysical properties of the obtained products with Sm^{3+} (**1**), Eu^{3+} (**2**, **5**), Tb^{3+} (**4**, **6**), and Dy^{3+} (**7**) are comparable to those of other homoleptic frameworks based on 3-$PyPz^-$.

The relatively shorter lifetimes measured for **1**, **2**, and **5** compared to those reported for $^{3}_{\infty}$[Ln(3-PyPz)$_3$], Ln = Sm and Eu (15.89 and 576 μs, respectively)[18] can be explained by the ligand coordination to the lanthanide metal centers in its neutral form, thus maintaining the high-energy N–H bond vibration that could lead to a deactivation process without observation of emitted radiation. This behavior changes for Tb^{3+} (**4** and **6**) and Dy^{3+} (**7**), which have longer lifetimes than the deprotonated ligand in $^{3}_{\infty}$[Ln(3-PyPz)$_3$], Ln = Tb^{3+} (1.0874 ms) and Dy^{3+} (15 μs), which is attributed to increasing internal conversion processes for the latter. The QY of Tb^{3+} (**4** and **6**) is in the range of $^{3}_{\infty}$[Tb(3-PyPz)$_3$] (QY = 74.3%)[18] and not too far from that reported for [Tb_2Cl_6(μ-4,4′-bipy)(py)$_6$] (QY = 86%).[23]

Magnetic properties

Direct current (DC) magnetic susceptibility measurements were performed for $^{2}_{\infty}$[Dy_2(3-PyPzH)$_3Cl_6$]·2MeCN (**7**), $^{2}_{\infty}$[Ho_2(3-PyPzH)$_3Cl_6$]·2MeCN (**8**), and $^{2}_{\infty}$[Er_2(3-PyPzH)$_3Cl_6$]·2MeCN (**9**) in a temperature range of 3 to 300 K and under a magnetic field of 1 T. The data were fitted for $^{2}_{\infty}$[Dy_2(3-PyPzH)Cl_3]·2MeCN (**7**) (Fig. 10) in the given temperature range with a modified Curie–Weiss law $\chi = \chi_0 + C/(T - \theta)$[45] and an effective magnetic

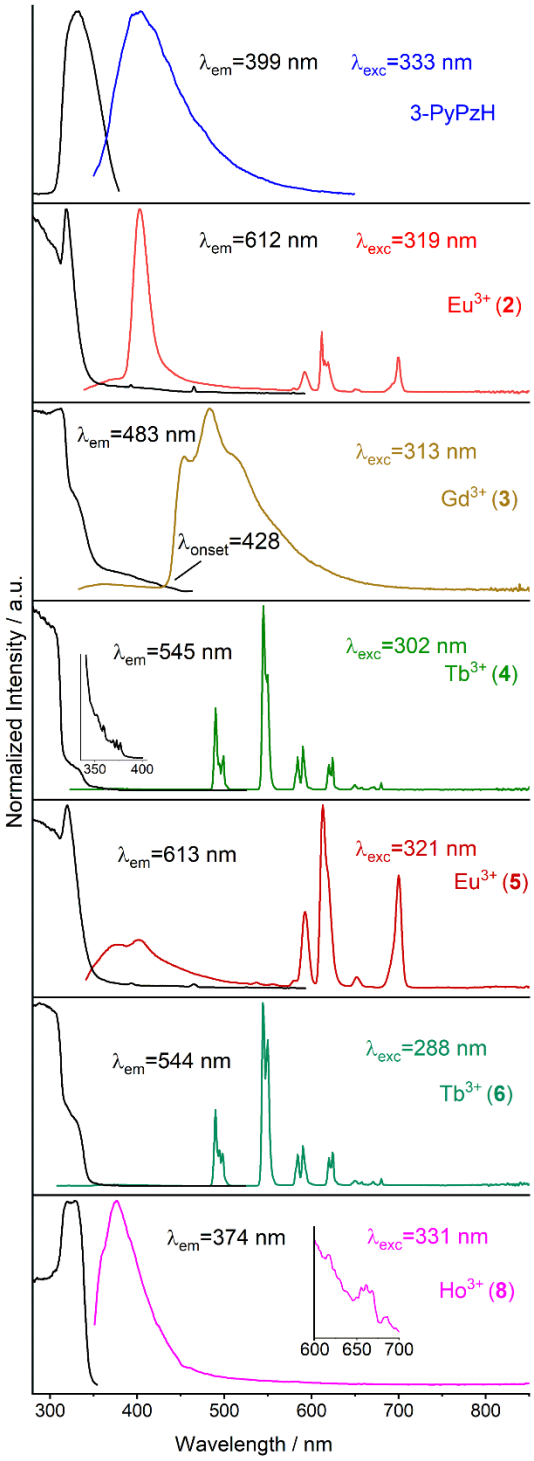

Fig. 7 Normalized solid state excitation (black) and emission spectra (colored) of $^{3}_{\infty}$[Eu(3-PyPzH)Cl_3] (**2**), $^{3}_{\infty}$[Gd(3-PyPzH)Cl_3] (**3**), $^{2}_{\infty}$[Tb_2(3-PyPzH)$_3Cl_6$]·2Tol (**4**), $^{2}_{\infty}$[Eu_2(3-PyPzH)$_3Cl_6$]·2MeCN (**5**), $^{2}_{\infty}$[Tb_2(3-PyPzH)$_3Cl_6$]·2MeCN (**6**), and $^{2}_{\infty}$[Ho_2(3-PyPzH)$_3Cl_6$]·2MeCN (**8**) at 77 K. Wavelengths for which the spectra were recorded are given in the legends.

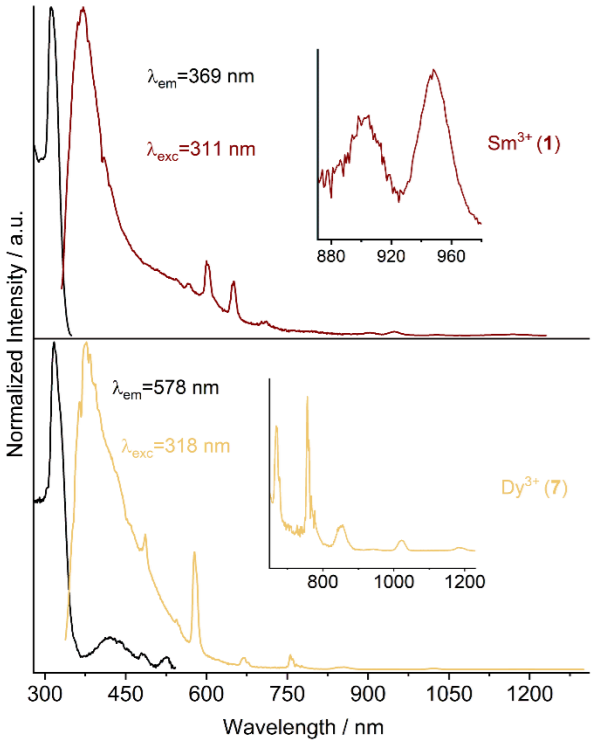

Fig. 8 Normalized solid-state excitation (black) and emission spectra (colored) of $^{2}_{\infty}$[Sm(3-PyPzH)Cl_3] (**1**) and $^{2}_{\infty}$[Dy_2(3-PyPzH)$_3Cl_6$]·2MeCN (**7**) at 77 K. Visible and NIR range emission spectra for **1** and **7** were brought to the same intensity at 711 and 756 nm, respectively. Wavelengths at which the spectra were recorded are shown in the legends.

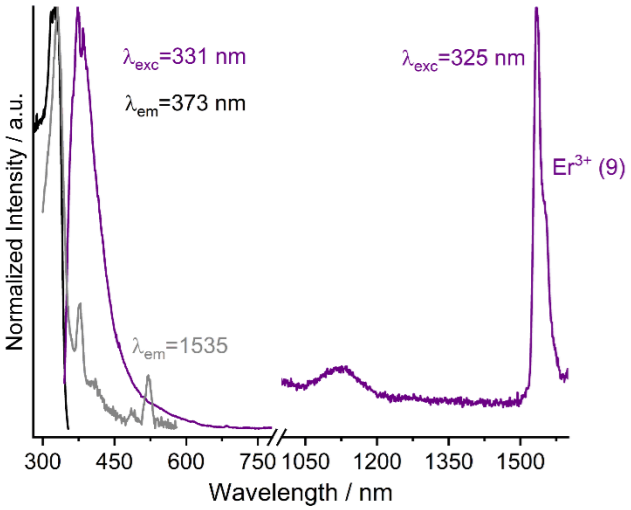

Fig. 9 Normalized solid state excitation (black for the measurement in the UV region and gray for the NIR region) and emission spectra (colored) of $^{2}_{\infty}$[Er_2(3-PyPzH)$_3Cl_6$]·2MeCN (**9**) at 77 K. Wavelengths at which the spectra were recorded are shown in the legends.

Table 2 Photoluminescence data of $^{2}_{\infty}$[Sm(3-PyPzH)Cl$_3$] (**1**), $^{3}_{\infty}$[Eu(3-PyPzH)Cl$_3$] (**2**), $^{3}_{\infty}$[Gd(3-PyPzH)Cl$_3$] (**3**), $^{2}_{\infty}$[Tb$_2$(3-PyPzH)$_3$Cl$_6$]·2Tol (**4**), $^{2}_{\infty}$[Eu$_2$(3-PyPzH)$_3$Cl$_6$]·2MeCN (**5**), $^{2}_{\infty}$[Tb$_2$(3-PyPzH)$_3$Cl$_6$]·2MeCN (**6**), $^{2}_{\infty}$[Dy$_2$(3-PyPzH)$_3$Cl$_6$]·2MeCN (**7**), $^{2}_{\infty}$[Ho$_2$(3-PyPzH)$_3$Cl$_6$]·2MeCN (**8**), and $^{2}_{\infty}$[Er$_2$(3-PyPzH)$_3$Cl$_6$]·2MeCN (**9**) in the solid state at 298 K

	τ^a	$\lambda_{ex}/\lambda_{em}{}^b$ [nm]	τ^c	$\lambda_{ex}/\lambda_{em}{}^d$ [nm]	Φ^e [%]	$\lambda_{ex}/\lambda_{em}{}^f$ [nm]
1	2.03(4) ns	368/598	2.7(1) ns	368/599	na	Na
2	0.2201(4) ms	324/612	0.233(2) ms	319/612	<0.5	320/360–715
3	0.151(2) ms	431/538	1.202(5) ms	313/483	22.7(1.5)	430/440–720
4	2.039(9) ms	306/545	2.22(2) ms	302/545	73.1(3)	310/475–690
5	0.170(4) ms	325/613	0.168(2) ms	321/613	na	na
6	2.294(9) ms	304/549	2.51(1) ms	308/544	76.0(1.4)	310/473–690
7	0.0230(1) ms	323/578	0.0235(2) ms	318/578	2.1(1)	320/330–630
8	0.98(2) ns	287/377	2.12(4) ns	287/374	na	na
9	1.31(5) ns	287/374	1.67(6) ns	287/374	na	na

^{a} Emission lifetimes determined at 298 K. ^{b} Excitation and emission wavelengths for emission lifetime at 298 K. ^{c} Emission lifetime determined at 77 K. ^{d} Excitation and emission wavelengths for emission lifetime at 77 K. ^{e} Quantum yield. ^{f} Excitation wavelength and emission wavelength ranges of QY measurements.

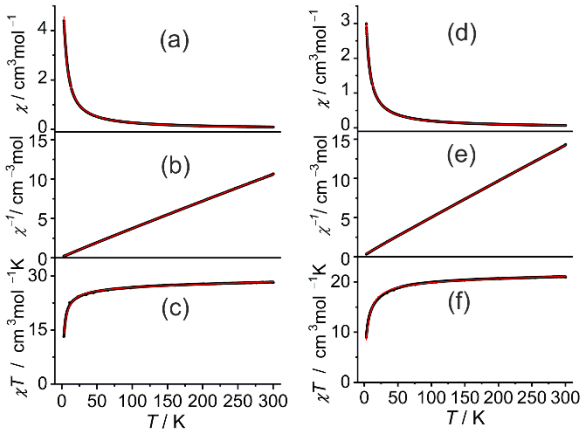

Fig. 10 Temperature dependence of the magnetic susceptibility of $^{2}_{\infty}$[Ln$_2$(3-PyPzH)$_3$Cl$_6$]·2MeCN, Ln = Dy (**7**) and Er (**9**) in a temperature range from 3 to 300 K and under a magnetic field of 1*T*: (a and d) χ *vs. T*, (b and e) χ^{-1} *vs. T*, and (c and f) χT *vs. T*. The solid red line represents the best fitting curve.

moment μ_{eff} of 10.389(1)μ_B, a Curie temperature θ of −2.781(7) K, and a temperature-independent paramagnetic susceptibility χ_0 of 5.41(4) × 10^{-3} cm^3 mol^{-1} were obtained. At room temperature, the $\chi_M T$ value is 28.21 cm^3 K mol^{-1}, which is close to the expected value (28.34 cm^3 K mol^{-1}) for two non-interacting Dy^{3+} ions ($^6H_{15/2}$, S = 5/2, L = 5, g = 4/3).[46] Upon cooling, a monotonic slow decrease of $\chi_M T$ takes place up to 13 K, where a significant decrease is observed, with $\chi_M T$ reaching 13.70 cm^3 K mol^{-1}.

For $^{2}_{\infty}$[Er$_2$(3-PyPzH)$_3$Cl$_6$]·2MeCN (**9**), a deviation from the paramagnetic Curie–Weiss behavior was observed in the χT *vs.* *T* plot, giving the values μ_{eff} of 9.013(2)μ_B, θ of −4.26(1) K, and χ_0 of 3.73(5) × 10^{-3} cm^3 mol^{-1} (Fig. 10). The $\chi_M T$ value at room temperature was determined to be 21.95 cm^3 K mol^{-1} which is close to but lower than the expected value (22.96 cm^3 K mol^{-1}) for two noninteracting Er^{3+} ions ($^4I_{15/2}$, S = 3/2, L = 6, g = 6/5).[46] An even lower value of 20.75 cm^3 K mol^{-1} was reported for {[Er$_2$(imidc)$_2$(H$_2$O)$_3$](H$_2$O)}$_n$, imidc = 4,5-imidazoledicarboxylic anion.[47] Upon cooling, a monotonic slow decrease of $\chi_M T$ takes place up to 4 K, at which a stronger decrease is observed, with $\chi_M T$ reaching 8.98 cm^3 K mol^{-1}. The small, negative Weiss constant θ for both Er^{3+} and Dy^{3+} is a result of spin–orbit coupling and the crystal field effect.[48]

The $\chi_M T$ value at room temperature for $^{2}_{\infty}$[Ho$_2$(3-PyPzH)$_3$Cl$_6$]·2MeCN (**8**) was determined to be 24.4 cm^3 K mol^{-1}. Upon cooling, $\chi_M T$ remained constant up to 127 K, and then $\chi_M T$ monotonically decreased to 9.7 cm^3 K mol^{-1}, indicating that the m_J levels of the $^5I_8$ ground-state multiplet of the Ho^{3+} ions become thermally depopulated.[49] The ferromagnetic interactions may be too weak to offset the sublevel depopulation, or there may be no ferromagnetic interactions.[50] Further confirmation was the absence of hysteresis in the field-dependent measurement (Fig. S32†). Therefore, the data were fitted with the modified Curie–Weiss law above the critical temperature (Fig. S31†) resulting in μ_{eff} of 9.16(7)μ_B, θ of 15(2) K, and χ_0 of 7.7(6) × 10^{-3} cm^3 mol^{-1}. The magnetic behavior of **8** is similar to that of the complex [Ho$_2$(DTE)$_3$(bipyridine)$_2$(H$_2$O)$_2$] (DTE = 1,2-bis(5-carboxyl-2-methyl-3-thienyl)perfluorocyclopentene)[49a] and both **8** and **9** have μ_{eff} values close to [Ho(C$_3$H$_2$O$_4$)(H$_2$O)$_4$]·NO$_3$ (9.95μ_B), [Er(C$_3$H$_2$O$_4$)(C$_3$H$_3$O$_4$)(H$_2$O)$_2$] (9.53μ_B) complexes ($C_3H_2O_4^{2-}$ = malonate dianion, $C_3H_3O_4^-$ = malonate anion).[51]

Thermal analysis

Simultaneous thermogravimetry/differential thermal analysis (TG/DTA) was carried out for $^{2}_{\infty}$[Sm(3-PyPzH)Cl$_3$] (**1**), $^{3}_{\infty}$[Eu(3-PyPzH)Cl$_3$] (**2**), and $^{2}_{\infty}$[Ho$_2$(3-PyPzH)$_3$Cl$_6$]·2MeCN (**8**), representing the isotypic compounds **5**–**9**, to inspect the thermal properties. Additionally, DTA/TG combined with mass spectrometry, DSC measurements, and high-temperature PXRD for $^{2}_{\infty}$[Tb$_2$(3-PyPzH)$_3$Cl$_6$]·2Tol (**4**) were performed to also identify the possible volatile components leaving the compounds and possible phase transition.

For $^{2}_{\infty}$[Sm(3-PyPzH)Cl$_3$] (**1**) (Fig. 11a), the equivalent 3-PyPzH is not fully released (about 84%) as indicated by the combined endothermic signals (1a, 1b, 1c) with an onset temperature of 320 °C and a mass loss of 30.2%. A further

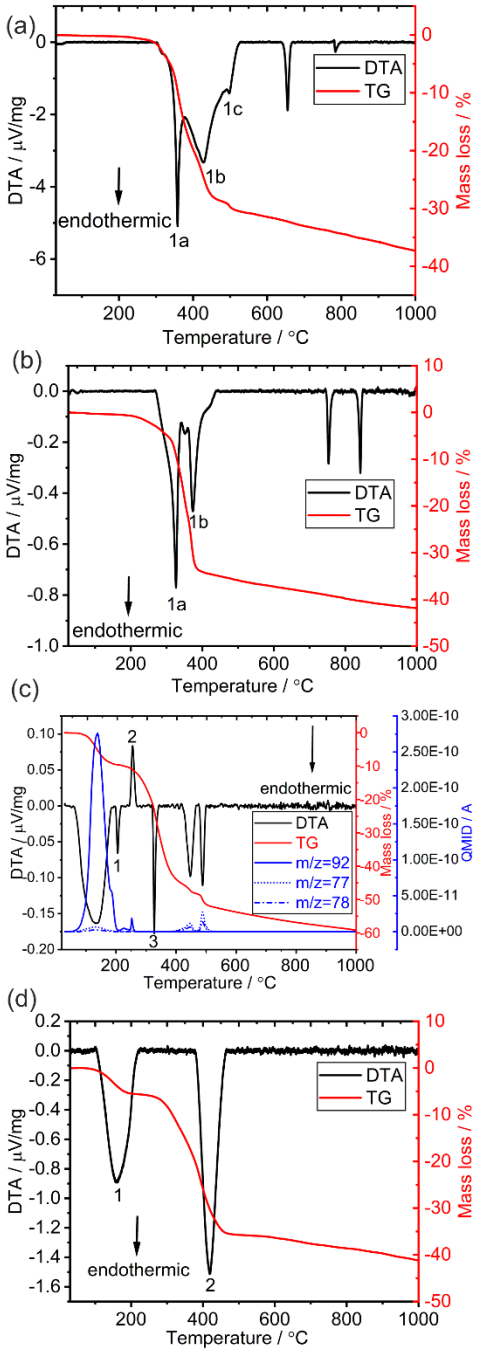

Fig. 11 (a, b and d) Simultaneous DTA-TG analysis for $^{2}_{\infty}$[Sm(3-PyPzH)Cl_3] (**1**), $^{3}_{\infty}$[Eu(3-PyPzH)Cl_3] (**2**), and $^{2}_{\infty}$[Ho_2(3-PyPzH)$_3Cl_6$]·2MeCN (**8**), respectively. (c) Simultaneous DTA-TG analysis combined with mass spectrometry for $^{2}_{\infty}$[Tb_2(3-PyPzH)$_3Cl_6$]·2Tol (**4**). The measurements were performed in a constant argon flow of 50 ml min^{-1} with a heating rate of 5 K min^{-1} from room temperature to 1000 °C. The DTA curve was baseline corrected after the measurement using the Origin™ software.

endothermic signal at the melting point of $SmCl_3$ (660 °C, theoretical mp of 677 °C)[52] is observable, followed by another endothermic signal at 785 °C indicating the formation of other phases, which agrees with the formation of $SmCl_3$ together with several unknown reflections in the powder diffraction pattern.

For $^{3}_{\infty}$[Eu(3-PyPzH)Cl_3] (**2**), about 95% release of 3-PyPzH was indicated by the combined endothermic signals 1a and 1b (Fig. 11b) with a mass loss of 34.3% in the TG curve with an onset temperature of 300 °C. The appearance of two endothermic signals at 750 and 840 °C far from the melting point of $EuCl_3$ (theoretical mp of 632 °C)[53] indicated the formation of other phases, which agrees with the lack of reflections of $EuCl_3$ and unknown reflections in the powder diffraction pattern.

The DTA/TG investigation together with simultaneous mass spectrometry for **4** (Fig. 11c) can further indicate the evolution of toluene molecules in the pore system ($C_7H_8^+$ *m*/*z* 92) with an initial mass loss in the TG curve of 9.8% at 130 °C. Further evolution of toluene takes place with the appearance of signals 2 and 3 with a mass loss of 5.9% to give a total mass loss of 15.7%, which correlates with two toluene molecules (a theoretical mass loss of 16%). The two endothermic (signal 2) and exothermic signals (signal 3) with onset temperatures of 190 °C and 230 °C, respectively may be attributed to the phase transitions. Temperature dependent PXRD measurements (HT-PXRD) (Fig. S37†) were performed from 70 to 310 °C. From 170 °C to 210 °C, new unknown reflections replaced those of $^{2}_{\infty}$[Tb_2(3-PyPzH)$_3Cl_6$]·2Tol which change again from 230 to 270 °C. DSC measurements (Fig. S38†) were also performed to confirm the irreversibility of the two transformation processes. The decomposition starts with an endothermic signal (signal 4) at about 310 °C, which matches also the HT-PXRD output. The fragments of the linker are released at about 400 °C ($C_5H_3N^+$ *m*/*z* 77, and $C_5H_4N^+$ *m*/*z* 78), while the mass loss of the three endothermic processes (4, 5, 6) correlates with three equivalents of 3-PyPzH (36.7%, theoretical mass loss 37.86%).

In $^{2}_{\infty}$[Ho_2(3-PyPzH)$_3Cl_6$]·2MeCN (**8**), the loss of the acetonitrile incorporated into the pore system is shown by an endothermic signal starting at 80 °C (Fig. 11d) and a mass loss of 6.8% corresponds to two equivalent MeCN molecules (theoretical mass loss of 7.6%). The endothermic signal 2 with an onset temperature of 365 °C and a mass loss of 28.7% coincides with two equivalents of 3-PyPzH (theoretical mass loss of 27.4%). The remaining equivalent of 3-PyPzH decomposes at a higher temperature, which correlates with a further mass loss after the observation of endothermic signal 2. Furthermore, black remnants could be observed after the measurement, indicating the partial carbonization of the ligand.

Experimental

Details on the analysis methods, instrumentation, crystallographic data, a comparison of the simulated and recorded

powder XRD patterns, large-scale photoluminescence spectra with labeled 4f–4f transitions, magnetic susceptibility measurements, and detailed IR bands from ATR-MIR investigations for the studied compounds are given in the ESI.†

General synthesis

All syntheses utilizing anhydrous lanthanide chlorides were performed under argon using vacuum lines, gloveboxes (MBraun Labmaster SP, Innovative Technology PureLab), Schlenk tubes, and Duran® glass ampules (outer ∅ 10 mm; wall thickness 1.5 mm). The solid reactants for the solvothermal reactions were mixed and sealed together with the solvent in an ampule under reduced pressure ($p = 1.0 \times 10^{-3}$ mbar). When needed, a stirring bar was added to the reaction mixture. The solvent was frozen using liquid nitrogen before vacuum was applied and the ampule was sealed. Subsequently, the prepared ampules were placed in heating furnaces (Büchi glass ovens or heating furnaces based on Al_2O_3 tubes with Kanthal wire resistance heating and NiCr/Ni temperature control elements), for which temperature programs and working steps according to the specific synthesis procedures were applied. After the solvents were removed, the solid raw products were dried at room temperature in a dynamic vacuum ($p = 1.0 \times 10^{-3}$ mbar) before further work steps. The bulk materials obtained were washed three times with 1 ml of dichloromethane (DCM) and finally dried at room temperature in a dynamic vacuum ($p = 1.0 \times 10^{-3}$ mbar).

Synthesis of $^{2}_{\infty}$[Sm(3-PyPzH)Cl$_3$] (1) was achieved by mixing 31.9 mg (124 μmol) of $SmCl_3$ with 55 mg (380 μmol) of 3-PyPzH in 0.3 ml acetonitrile (MeCN). In a heating furnace, the reaction mixture was heated to 120 °C at a rate of 10 °C h^{-1}. The temperature was maintained for 72 h. Afterwards, the reaction mixture was cooled to room temperature at a rate of 1 °C h^{-1}. Suitable colorless single-crystals were selected for a single-crystal X-ray diffraction (SCXRD) measurement. The colorless bulk material was washed with DCM to remove the excess ligand. Yield: 45 mg (90%). Elemental results calculated for $C_8H_7N_3Cl_3Sm$: C: 23.91%, H: 1.76%, N: 10.46%. Found: C: 23.59%, H: 1.84%, N: 10.51%. FTIR (ATR): $\tilde{\nu}$ = 3120 (w), 1612 (m), 1583 (w), 1459 (m), 1409 (w), 1289 (w), 1248 (w), 1189 (w), 1125 (w), 1095 (s), 1048 (m), 963 (s), 936 (s), 795 (m), 776 (s), 716 (w), 694 (s), 655 (m), 638 (m) cm^{-1}.

Synthesis of $^{3}_{\infty}$[Ln(3-PyPzH)Cl$_3$], Ln = Eu, Gd (2, 3) was achieved *via* mixing 25 mg (97 μmol) of $EuCl_3$ with 30 mg (207 μmol) of 3-PyPzH in 0.3 ml MeCN. The reaction mixture was placed in a furnace, where a three step-heating program was applied: the first step involved heating to 140 °C at a rate of 10 °C h^{-1}. In the second step, this temperature was maintained for 72 h until the oven was cooled to room temperature at a rate of 0.5 °C h^{-1}. Suitable yellow single-crystals were selected for an SCXRD measurement.

The yellow bulk material obtained was characterized by means of PXRD, IR-spectroscopy, and CHN-analysis. Yield: 37 mg (95%) for **2** and 36 mg (92%) for **3**. Elemental analysis calculated for $C_8H_7N_3Cl_3Eu$ (**2**): C: 23.81%, H: 1.75%, N: 10.41%. Found: C: 23.32%, H: 1.74%, N: 10.36% and for $C_8H_7N_3Cl_3Gd$ (**3**): C: 23.51%, H: 1.75%, N: 10.28%. Found: C: 23.73%, H: 1.72%, N: 10.82%. FTIR (ATR) for **2**: $\tilde{\nu}$ = 3119 (w), 1610(w), 1594 (w), 1487 (m), 1417 (s), 1198 (w), 1125 (w), 1098 (s), 1049 (m), 1033 (w), 964 (s), 940 (s), 825 (m), 804 (s), 767 (w), 696 (s), 655 (s), 639 (s), 545 (m), 475 (w) cm^{-1} and for **3**: $\tilde{\nu}$ = 3183 (s), 1613 (m), 1559 (m), 1524 (m), 1470 (m), 1368 (w), 1261 (w), 1184 (m), 1098 (w), 1056 (m), 957 (m), 771 (s), 698 (m), 671 (s), 439 (w) cm^{-1}.

Synthesis of $^{2}_{\infty}$[Tb$_2$(3-PyPzH)$_3$Cl$_6$]·2Tol (4) was achieved *via* a solvothermal reaction of 27.7 mg (104 μmol) of $TbCl_3$ with 30 mg (207 μmol) of 3-PyPzH in 0.3 ml of toluene. The phase pure bulk was only achievable with stirring using a Büchi oven. The furnace temperature was increased to 145 °C and maintained for 48 h followed by cooling to 25 °C. The excess ligand was washed three times with DCM and then dried *in vacuo* ($p = 1 \times 10^{-3}$ mbar). The colorless bulk material obtained was characterized *via* PXRD, IR-spectroscopy and CHN-analysis. Yield: 54 mg (90%). Elemental analysis calculated for $C_{38}H_{37}N_9Cl_6Tb_2$: C: 39.68%, H: 3.24%, N: 10.96%. Found: C: 38.82%, H: 2.96%, N: 10.14%. FTIR (ATR): $\tilde{\nu}$ = 3213 (s), 1632 (m), 1562 (m), 1526 (m), 1470 (w), 1422 (w), 1364 (w), 1253 (w), 1055 (m), 955 (m), 769 (m), 728 (m), 672 (m), 439 (w) cm^{-1}.

Single-crystals of $^{2}_{\infty}$[Tb$_2$(3-PyPzH)$_3$Cl$_6$]·2Tol (4) were acquired using the same amounts of reactants as those used for the previously described synthesis of **4**. The reaction mixture was placed in a tubular furnace, and the mixture was first heated to 130 °C within 48 h. This temperature was maintained for 72 h before the oven was cooled to room temperature within 48 h. This procedure resulted in colorless single-crystals which were selected for a single-crystal X-ray diffraction (SCXRD) measurement.

Synthesis of $^{2}_{\infty}$[Eu$_2$(3-PyPzH)$_3$Cl$_6$]·2MeCN (5) was achieved by a solvothermal reaction of 23.73 mg (92 μmol) of $EuCl_3$ with 20 mg (130 μmol) of 3-PyPzH in 0.3 ml of MeCN. In a heating furnace, the reaction mixture was heated to 100 °C at a rate of 10 °C h^{-1}, and then the temperature was maintained for 72 h until the temperature was lowered to 25 °C at a rate of 0.5 °C h^{-1}. Suitable light brown single-crystals were selected for the SCXRD measurement. The yellow bulk material was characterized *via* PXRD, IR-spectroscopy, and CHN-analyses. Yield: 42 mg (88%). Elemental results calculated for $C_{28}H_{27}N_{11}Cl_6Eu_2$: C: 32.52%, H: 2.63%, N: 14.90%. Found: C: 31.64%, H: 3.29%, N: 15.30%. FTIR (ATR): $\tilde{\nu}$ = 3218 (s), 1624 (m), 1561 (m), 1523 (w), 1370 (w), 1058 (s), 957 (m), 775 (m), 701 (w), 671 (m), 460 (m), 439 (m)cm^{-1}.

Synthesis of $^{2}_{\infty}$[Tb$_2$(3-PyPzH)$_3$Cl$_6$]·2MeCN (6) was accomplished *via* a mixture of 13.84 mg (52 μmol) of anhydrous $TbCl_3$ with 15 mg (103 μmol) of 3-PyPzH in 0.3 ml of MeCN. The reaction mixture was placed in a glass Büchi furnace where it was heated to 100 °C within 15 minutes. This temperature was maintained for 1 h until the temperature was increased again to 130 °C. After 24 h, the mixture was cooled to room temperature in 30 minutes. The obtained colorless bulk material was characterized *via* PXRD, IR-spectroscopy and CHN-analyses. Yield: 45 mg (83%). Elemental results calculated for $C_{28}H_{27}N_{11}Cl_6Tb_2$: C: 32.08%, H: 2.60%, N: 14.70%.

Found: C: 30.95%, H: 1.70%, N: 13.72%. FTIR (ATR): $\tilde{\nu}$ = 3184 (s), 1629 (m), 1561 (m), 1526 (m), 1468 (w), 1421 (w), 1365 (w), 1263 (w), 1055 (m), 955 (m), 770 (m), 702 (m), 673 (m), 435 (w) cm^{-1}.

Synthesis of $^{2}_{\infty}[Dy_2(3\text{-PyPzH})_3Cl_6]\cdot 2MeCN$ (7) was achieved *via* a reaction of 25.5 mg (94.7 μmol) of $DyCl_3$ with 20.6 mg (141.9 μmol) of 3-PyPzH in 0.3 ml MeCN. The reaction mixture was placed in a tubular furnace, where the mixture was heated first to 100 °C within 1 h, and then the temperature was increased to 120 °C within 10 h. This temperature was maintained for a further 10 h until the oven was cooled to room temperature within 3 h to give a colorless product. Yield: 45 mg (90%). Elemental results calculated for $C_{28}H_{27}N_{11}Cl_6Dy_2$: C: 31.87%, H: 2.58%, N: 14.60%. Found: C: 30.85%, H: 2.44%, N: 13.88%. FTIR (ATR): $\tilde{\nu}$ = 3185 (m), 1609 (m), 1558 (m), 1523 (m), 1461 (m), 1415 (w), 1367 (w), 1288 (m), 1096 (m), 1053 (m), 962 (m), 769 (s), 700 (m), 672 (m), 438 (w) cm^{-1}.

Synthesis of $^{2}_{\infty}[Ho_2(3\text{-PyPzH})_3Cl_6]\cdot 2MeCN$ (8) was achieved *via* a solvothermal reaction of 25.59 mg (94.3 μmol) of $HoCl_3$ with 20.5 mg (141.5 μmol) of 3-PyPzH in 0.3 ml of MeCN The reaction mixture was placed in a tubular furnace, where the mixture was first heated to 90 °C within 1 h. Afterwards, the temperature was increased to 120 °C in 10 h and maintained for 10 h until the oven was cooled to room temperature in 3 h to produce a light pink product. Yield: 46 mg (92%). Elemental results calculated for $C_{28}H_{27}N_{11}Cl_6Ho_2$: C: 31.72%, H: 2.57%, N: 14.53%. Found: C: 30.76%, H: 2.49%, N: 14.27%. FTIR (ATR): $\tilde{\nu}$ = 3184 (m), 1632 (m), 1561 (m), 1524 (m), 1461 (m), 1421 (w), 1367 (w), 1290 (w), 1096 (m), 1053 (m), 959 (m), 768 (s), 700 (s), 672 (m), 439 (w) cm^{-1}.

Synthesis of $^{2}_{\infty}[Er_2(3\text{-PyPzH})_3Cl_6]\cdot 2MeCN$ (9) was achieved *via* a solvothermal reaction of 25.69 mg (93.9 μmol) of $ErCl_3$ with 20.5 mg (141.5 μmol) of 3-PyPzH in 0.3 ml of MeCN. The reaction mixture was placed in a tubular furnace which was heated to 110 °C within 1 h. Then the temperature was increased again to 120 °C in 10 h. After an additional 10 h, the oven was cooled to room temperature within 3 h to produce a colorless product. Yield: 44 mg (88%). Elemental results calculated for $C_{28}H_{27}N_{11}Cl_6Er_2$: C: 31.58%, H: 2.56%, N: 14.47%. Found: C: 30.84%, H: 2.65%, N: 14.39%. FTIR (ATR): $\tilde{\nu}$ = 3218 (m), 1608 (m), 1557 (m), 1523 (m), 1468 (m), 1410 (m), 1364 (w), 1288 (w), 1097 (m), 1055 (s), 952 (m), 765 (s), 697 (m), 672 (s), 439 (w) cm^{-1}.

Single-crystals of $^{2}_{\infty}[Ln_2(3\text{-PyPzH})_3Cl_6]\cdot 2MeCN$, Ln = Ho, Er (8, 9) were obtained using the same amounts of reactants as those used for the previously described synthesis of **8** and **9**. The reaction mixture was placed in a tubular furnace, which was heated to 100 °C at a rate of 10 °C h^{-1}. This temperature was maintained for 72 h until the oven was cooled to room temperature at a rate of 0.5 °C h^{-1}. Suitable single-crystals were selected for an SCXRD measurement.

Single-crystals of $[(3\text{-PyPzH}_2)][Eu(3\text{-PyPzH})_2Cl_4]$ (10) were synthesized from a solvothermal reaction of 25.7 mg (99 μmol) of anhydrous $EuCl_3$ and 43 mg (296 μmol) of 3-PyPzH using 0.4 ml of toluene. The reaction mixture was placed in a tubular furnace; the temperature was increased to 140 °C in 48 h. This temperature was maintained for 96 h and then the reaction was cooled to RT in 72 h. Colorless single-crystals were taken out from the bulk and subjected to an SCXRD measurement.

Single-crystals of $[(3\text{-PyPzH}_2)][Tb(3\text{-PyPzH})_2Cl_4]$ (11) were obtained from a reaction of 26.5 mg (100 μmol) of anhydrous $TbCl_3$ and 43 mg (296 μmol) of 3-PyPzH in 0.6 ml of MeCN. The ampule was placed in a tubular furnace; the temperature was increased to 110 °C with a rate of 10 °C h^{-1}. This temperature was maintained for 72 h before being cooled to RT at a rate of 0.5 °C h^{-1}. Colorless single-crystals were taken out from the bulk and subjected to an SCXRD measurement.

Single-crystals of $[(3\text{-PyPzH}_2)][Dy(3\text{-PyPzH})_2Cl_4]$, and $[(3\text{-PyPzH}_2)][Ho(3\text{-PyPzH})_2Cl_4]$ (12, 13) were obtained by the same procedure as that used for **10** by addition of 26.72 mg (99 μmol) of $DyCl_3$ in **12** and 25.7 mg (96 μmol) of $HoCl_3$ in **13** using 0.3 ml of toluene. The temperature was increased to 150 °C in 48 h for **12**. For **13**, the temperature was increased to 130 °C in 96 h, and maintained for further 96 h. Then the temperature was reduced to RT in 96 h. In both cases, colorless single-crystals were selected for SCXRD measurements.

Single-crystals of $^{2}_{\infty}[La_2(3\text{-PyPzH}_2)Cl_4]$ (14) were synthesized by adding 11.3 mg (46 μmol) of $LaCl_3$ to 20 mg (138 μmol) of 3-PyPzH and 0.1 ml of MeCN in an ampule. The ampule was sealed under reduced pressure and then placed into a furnace. The temperature inside the furnace was increased to 120 °C in 12 h, and after 144 h the temperature was reduced back to RT in further 12 h. Very tiny crystals not suitable for the measurement were first obtained. The ampule was reinserted and the temperature was increased this time to 130 °C in 1 h, and after 216 h the temperature returned to RT in 1 h. Suitable sized colorless single-crystals were chosen for SCXRD.

Single-crystals of $^{2}_{\infty}[Nd_2(3\text{-PyPzH}_2)Cl_4]$ (15) were obtained by reacting 6.9 mg (28 μmol) of $NdCl_3$ with 20 mg (138 μmol) of 3-PyPzH in 0.3 ml of chlorobenzene or acetonitrile. The ampule was sealed under reduced pressure and placed into a furnace. The temperature of the ampule was increased to 230 °C in 46 h, and after 72 h the temperature reached RT at a rate of 0.5 °C h^{-1}. Colorless single-crystals attached to the wall of the ampule were selected for SCXRD.

Conclusions

Fifteen 3D- and 2D-coordination polymers and complexes of trivalent lanthanide chlorides together with 3-(3-pyridyl)pyrazole, varying in constitution and structures were synthesized by anhydrous solvothermal reactions in either acetonitrile, toluene or chlorobenzene in sealed ampules: $^{3}_{\infty}[Ln(3\text{-PyPzH})Cl_3]$, 3-PyPzH = 3-(3-pyridyl)pyrazole, Ln = Eu and Gd (**2**, **3**), $^{2}_{\infty}[Sm(3\text{-PyPzH})Cl_3]$ (**1**), $^{2}_{\infty}[Tb_2(3\text{-PyPzH})_3Cl_6]\cdot 2Tol$ (**4**), $^{2}_{\infty}[Ln_2(3\text{-PyPzH})_3Cl_6]\cdot 2MeCN$, Ln = Eu^{3+}, Tb^{3+}, Dy^{3+}, Ho^{3+} and Er^{3+} (**5**–**9**) and $^{2}_{\infty}[Ln(3\text{-PyPzH}_2)Cl_4]$, Ln = La and Nd (**14**, **15**), and $[(3\text{-PyPzH}_2)][Ln(3\text{-PyPzH})_2Cl_4]$, Ln = Eu, Tb, Dy and Ho (**10**–**13**). Altogether, two- and three-dimensional coordination polymers and salt-like complexes were obtained. A comparison of the

spectroscopic properties of the investigated coordination polymers using the three types of spectra, absorption, excitation, and emission, allows for a better understanding of the photophysical properties observed for the Ln series. UV-VIS-NIR spectrophotometry reveals detectable and distinguishable Laporte forbidden 4f–4f absorption transitions, especially for Sm^{3+}, Dy^{3+}, Ho^{3+}, and Er^{3+} beside the ligand-centered transitions. The triplet energy of the Gd^{3+} containing coordination polymer was elucidated as it shows strong phosphorescence of the ligand even at room temperature. For **1–9**, the intra-4f emission of the respective Ln^{3+} is activated by an antenna effect of the 3-PyPzH molecules of different effectivity, leading to Ln^{3+} sensitization with high QY = 73% and 76% for the Tb^{3+} compounds **4**, and **6**, respectively. DC magnetic investigations indicate that the Dy^{3+} (**7**) and Er^{3+} (**9**)-based coordination polymers exhibit the curie behavior without any interatomic interactions, while weak ferromagnetic coupling between the Ho–Ho centers was observed for **8**. The Ho^{3+} containing coordination polymer **8** shows the highest stability among the series up to 365 °C. Altogether, the anhydrous chloride containing coordination polymers of the lanthanide series together with 3-(3-pyridyl)pyrazole show versatile structures, and photophysical, thermal, and magnetic properties.

Conflicts of interest

There are no conflicts to declare.

Acknowledgements

The authors gratefully acknowledge the support of the Volkswagen Foundation within the project "Molecular materials – bridging magnetism and luminescence". H. Youssef gratefully acknowledges the Egyptian Ministry of Higher Education (MoHE) and the German Academic Exchange Service (DAAD) within the German Egyptian Research Long-term Scholarship (GERLS) Programme, 2017 (57311832) for a Ph.D. fellowship. I. V. Taydakov gratefully acknowledges the Russian Science Foundation (project no. 19-13-00272) for financial support.

References

1 (*a*) Y. Zhang, S. Yuan, G. Day, X. Wang, X. Yang and H.-C. Zhou, *Coord. Chem. Rev.*, 2018, **354**, 28–45; (*b*) P. R. Matthes, C. J. Höller, M. Mai, J. Heck, S. J. Sedlmaier, S. Schmiechen, C. Feldmann, W. Schnick and K. Müller-Buschbaum, *J. Mater. Chem.*, 2012, **22**, 10179–10187; (*c*) M. D. Allendorf, C. A. Bauer, R. K. Bhakta and R. J. T. Houk, *Chem. Soc. Rev.*, 2009, **38**, 1330–1352.

2 (*a*) J. Luzon and R. Sessoli, *Dalton Trans.*, 2012, **41**, 13556–13567; (*b*) G. Cucinotta, M. Perfetti, J. Luzon, M. Etienne, P. E. Car, A. Caneschi, G. Calvez, K. Bernot and R. Sessoli, *Angew. Chem., Int. Ed.*, 2012, **51**, 1606–1610.

3 S. V. Eliseeva and J.-C. G. Bünzli, *Chem. Soc. Rev.*, 2010, **39**, 189–227.

4 (*a*) J.-C. G. Bünzli and S. V. Eliseeva, *Basics of Lanthanide Photophysics, in Springer Series on Fluorescence: Lanthanide Luminescence: Photophysical, Analytical and Biological Aspects*, ed. O. S. Wolfbeis and M. Hof, Springer Verlag, Berlin, 2011, vol. 7, pp. 1–46; (*b*) T. J. Mooibroek, P. Gamez, A. Pevec, M. Kasunič, B. Kozlevčar, W.-T. Fu and J. Reedijk, *Dalton Trans.*, 2010, **39**, 6483–6487.

5 (*a*) R. J. Blagg, L. Ungur, F. Tuna, J. Speak, P. Comar, D. Collison, W. Wernsdorfer, E. J. L. McInnes, L. F. Chibotaru and R. E. P. Winpenny, *Nat. Chem.*, 2013, **5**, 673–678; (*b*) L. Sorace, C. Benelli and D. Gatteschi, *Chem. Soc. Rev.*, 2011, **40**, 3092–3104; (*c*) E. Coronado, C. Giménez-Saiz, A. Recuenco, A. Tarazón, F. M. Romero, A. Camón and F. Luis, *Inorg. Chem.*, 2011, **50**, 7370–7372; (*d*) J. Long, *Front. Chem.*, 2019, **7**, 63.

6 J. Long, Y. Guari, R. A. S. Ferreira, L. D. Carlos and J. Larionova, *Coord. Chem. Rev.*, 2018, **363**, 57–70.

7 (*a*) S. C. Manna, E. Zangrando, A. Bencini, C. Benelli and N. R. Chaudhuri, *Inorg. Chem.*, 2006, **45**, 9114–9122; (*b*) D. C. Izuogu, T. Yoshida, H. Zhang, G. Cosquer, K. Katoh, S. Ogata, M. Hasegawa, H. Nojiri, M. Damjanović, W. Wernsdorfer, T. Uruga, T. Ina, B. K. Breedlove and M. Yamashita, *Chem. – Eur. J.*, 2018, **24**, 9285–9294.

8 (*a*) L. Armelao, S. Quici, F. Barigelletti, G. Accorsi, G. Bottaro, M. Cavazzini and E. Tondello, *Coord. Chem. Rev.*, 2010, **254**, 487–505; (*b*) X. Zhu, W.-K. Wong, W.-Y. Wong and X. Yang, *Eur. J. Inorg. Chem.*, 2011, 4651–4674.

9 (*a*) M. Latva, H. Takalo, V.-M. Mukkala, C. Matachescu, J. C. Rodríguez-Ubis and J. Kankare, *J. Lumin.*, 1997, **75**, 149–169; (*b*) A. Bellusci, G. Barberio, A. Crispini, M. Ghedini, M. La Deda and D. Pucci, *Inorg. Chem.*, 2005, **44**, 1818–1825.

10 Q.-R. Wu, J.-J. Wang, H.-M. Hu, Y.-Q. Shangguan, F. Fu, M.-L. Yang, F.-X. Dong and G.-L. Xue, *Inorg. Chem. Commun.*, 2011, **14**, 484–488.

11 J. Fan, L. Liang, Y. Gu and X. Liu, *Opt. Mater.*, 2021, **12**, 100104.

12 M. Kasha, *Discuss. Faraday Soc.*, 1950, **9**, 14–19.

13 (*a*) O. Yushchenko, G. Licari, S. Mosquera-Vazquez, N. Sakai, S. Matile and E. Vauthey, *J. Phys. Chem. Lett.*, 2015, **6**, 2096–2100; (*b*) K. E. Henry, R. G. Balasingham, A. R. Vortherms, J. A. Platts, J. F. Valliant, M. P. Coogan, J. Zubieta and R. P. Doyle, *Chem. Sci.*, 2013, **4**, 2490–2495.

14 (*a*) H. Adams, S. R. Batten, G. M. Davies, M. B. Duriska, J. C. Jeffery, P. Jensen, J. Lu, G. R. Motson, S. J. Coles, M. B. Hursthouse and M. D. Ward, *Dalton Trans.*, 2005, 1910–1923; (*b*) J.-C. Li, H.-X. Li, H.-Y. Li, W.-J. Gong and J.-P. Lang, *Cryst. Growth Des.*, 2016, **16**, 1617–1625.

15 Y. Yu, W. Huang, Y. Chen, B. Gao, W. Wu and H. Jiang, *Green Chem.*, 2016, **18**, 6445–6449.

16 J. K. Yano, T. T. Denton, M. A. Cerny, X. Zhang, E. F. Johnson and J. R. Cashman, *J. Med. Chem.*, 2006, **49**, 6987–7001.

17 L.-R. Xing, Z. Lu, M. Li, J. Zheng and D. Li, *J. Phys. Chem. Lett.*, 2020, **11**, 2067–2073.

18 H. Youssef, A. E. Sedykh, J. Becker, T. Schäfer, I. V. Taydakov, H. R. Li and K. Müller-Buschbaum, *Chem. – Eur. J.*, 2021, **27**, 16634–16641.

19 (*a*) M. O'Keeffe, M. A. Peskov, S. J. Ramsden and O. M. Yaghi, *Acc. Chem. Res.*, 2008, **41**, 1782–1789; (*b*) A. F. Wells, *Three dimensional nets and polyhedra*, Wiley, New York, 1977.

20 (*a*) N. Kumar, S.-Q. Wang, S. Mukherjee, A. A. Bezrukov, E. Patyk-Kaźmierczak, D. O'Nolan, A. Kumar, M.-H. Yu, Z. Chang, X.-H. Bu and M. J. Zaworotko, *Chem. Sci.*, 2020, **11**, 6889–6895; (*b*) T. G. Mitina and V. A. Blatov, *Cryst. Growth Des.*, 2013, **13**, 1655–1664.

21 (*a*) R. D. Shannon, *Acta Crystallogr., Sect. A: Cryst. Phys., Diffr., Theor. Gen. Crystallogr.*, 1976, **32**, 751–767; (*b*) L. Eyring, in *Handbook on the physics and chemistry of rare earths*, ed. K. A. Gschneidner Jr. and L. Eyring, North-Holland, Amsterdam, 1979, vol. 3, pp. 337–399.

22 P. R. Matthes, F. Schönfeld, S. H. Zottnick and K. Müller-Buschbaum, *Molecules*, 2015, **20**, 12125–12153.

23 P. R. Matthes, J. Nitsch, A. Kuzmanoski, C. Feldmann, A. Steffen, T. B. Marder and K. Müller-Buschbaum, *Chem. – Eur. J.*, 2013, **19**, 17369–17378.

24 (*a*) X. Liu, X. Wang, T. Gao, Y. Xu, X. Shen and D. Zhu, *CrystEngComm*, 2014, **16**, 2779–2787; (*b*) X.-Z. Wang, D.-R. Zhu, Y. Xu, J. Yang, X. Shen, J. Zhou, N. Fei, X.-K. Ke and L.-M. Peng, *Cryst. Growth Des.*, 2010, **10**, 887–894.

25 Z. Wang, J.-T. Mo, P.-Y. Fu, C.-Y. Zhu, H.-J. Yu and M. Pan, *J. Lumin.*, 2020, **224**, 117299.

26 R. Sanii, C. Hua, E. Patyk-Kaźmierczak and M. J. Zaworotko, *Chem. Commun.*, 2019, **55**, 1454–1457.

27 A. E. Sedykh, D. G. Kurth and K. Müller-Buschbaum, *Eur. J. Inorg. Chem.*, 2019, **2019**, 4564–4571.

28 C. J. Höller, M. Mai, C. Feldmann and K. Müller-Buschbaum, *Dalton Trans.*, 2010, **39**, 461–468.

29 N. Dannenbauer, P. R. Matthes, T. P. Scheller, J. Nitsch, S. H. Zottnick, M. S. Gernert, A. Steffen, C. Lambert and K. Müller-Buschbaum, *Inorg. Chem.*, 2016, **55**, 7396–7406.

30 N. Dannenbauer, S. H. Zottnick and K. Müller-Buschbaum, *Z. Anorg. Allg. Chem.*, 2017, **643**, 1513–1518.

31 S. V. Klementyeva, M. Y. Afonin, A. S. Bogomyakov, M. T. Gamer, P. W. Roesky and S. N. Konchenko, *Eur. J. Inorg. Chem.*, 2016, **2016**, 3666–3672.

32 J. Long, D. M. Lyubov, T. V. Mahrova, A. V. Cherkasov, G. K. Fukin, Y. Guari, J. Larionova and A. A. Trifonov, *Dalton Trans.*, 2018, **47**, 5153–5156.

33 D. I. Alexandropoulos, K. R. Vignesh, H. Xie and K. R. Dunbar, *Dalton Trans.*, 2019, **48**, 10610–10618.

34 (*a*) T. Jiang and X.-M. Zhang, *Cryst. Growth Des.*, 2008, **8**, 3077–3083; (*b*) D. Sun, M.-Z. Xu, S.-S. Liu, S. Yuan, H.-F. Lu, S.-Y. Feng and D.-F. Sun, *Dalton Trans.*, 2013, **42**, 12324–12333.

35 (*a*) D. J. Lewis, F. Moretta, A. T. Holloway and Z. Pikramenou, *Dalton Trans.*, 2012, **41**, 13138–13146; (*b*) M. Mahato, P. P. Jana, K. Harms and H. P. Nayek, *RSC Adv.*, 2015, **5**, 62167–62172; (*c*) C. Y. Chow, S. V. Eliseeva, E. R. Trivedi, T. N. Nguyen, J. W. Kampf, S. Petoud and V. L. Pecoraro, *J. Am. Chem. Soc.*, 2016, **138**, 5100–5109.

36 (*a*) P. R. Satheesh Chandran, U. S. Soumya Mol, R. Drisya, M. R. Sudarsanakumar and M. R. Prathapachandra Kurup, *J. Mol. Struct.*, 2017, **1137**, 396–402; (*b*) X. Zhou, H. Wang, S. Jiang, G. Xiang, X. Tang, X. Luo, L. Li and X. Zhou, *Inorg. Chem.*, 2019, **58**, 3780–3788.

37 M. Hasegawa, H. Ohtsu, D. Kodama, T. Kasai, S. Sakurai, A. Ishii and K. Suzuki, *New J. Chem.*, 2014, **38**, 1225–1234.

38 C. Seidel, C. Lorbeer, J. Cybińska, A.-V. Mudring and U. Ruschewitz, *Inorg. Chem.*, 2012, **51**, 4679–4688.

39 (*a*) W. T. Carnall, P. R. Fields and K. Rajnak, *J. Chem. Phys.*, 1968, **49**, 4424–4442; (*b*) W. T. Carnall, P. R. Fields and K. Rajnak, *J. Chem. Phys.*, 1968, **49**, 4450–4455; (*c*) W. T. Carnall, P. R. Fields and K. Rajnak, *J. Chem. Phys.*, 1968, **49**, 4447–4449.

40 (*a*) Y. Kitagawa, P. P. Ferreira da Rosa and Y. Hasegawa, *Dalton Trans.*, 2021, **50**, 14978–14984; (*b*) A. Vogler and H. Kunkely, *Inorg. Chim. Acta*, 2006, **359**, 4130–4138.

41 W. J. Gee and S. R. Batten, *Chem. Commun.*, 2012, **48**, 4830–4832.

42 G. A. Crosby, R. E. Whan and R. M. Alire, *J. Chem. Phys.*, 1961, **34**, 743–748.

43 K. Binnemans, *Chem. Rev.*, 2009, **109**, 4283–4374.

44 K. Binnemans, *Coord. Chem. Rev.*, 2015, **295**, 1–45.

45 G. Amoretti and J. M. Fournier, *J. Magn. Magn. Mater.*, 1984, **43**, L217–L220.

46 O. Kahn, *Molecular magnetism*, Wiley-VCH, Weinheim, 1993.

47 T. K. Maji, G. Mostafa, H.-C. Chang and S. Kitagawa, *Chem. Commun.*, 2005, 2436–2438.

48 (*a*) C. Benelli and D. Gatteschi, *Chem. Rev.*, 2002, **102**, 2369–2388; (*b*) Y. H. Pham, V. A. Trush, A. N. Carneiro Neto, M. Korabik, J. Sokolnicki, M. Weselski, O. L. Malta, V. M. Amirkhanov and P. Gawryszewska, *J. Mater. Chem. C*, 2020, **8**, 9993–10009.

49 (*a*) G. Cosquer, M. Morimoto, M. Irie, A. Fetoh, B. K. Breedlove and M. Yamashita, *Dalton Trans.*, 2015, **44**, 5996–6002; (*b*) G. Cosquer, F. Pointillart, J. Jung, B. Le Guennic, S. Golhen, O. Cador, Y. Guyot, A. Brenier, O. Maury and L. Ouahab, *Eur. J. Inorg. Chem.*, 2014, 69–82.

50 (*a*) Y. Wang, X.-L. Li, T.-W. Wang, Y. Song and X.-Z. You, *Inorg. Chem.*, 2010, **49**, 969–976; (*b*) F. Luo, Z.-W. Liao, Y.-M. Song, H.-X. Huang, X.-Z. Tian, G.-M. Sun, Y. Zhu, Z.-Z. Yuan, M.-B. Luo, S.-J. Liu, W.-Y. Xu and X.-F. Feng, *Dalton Trans.*, 2011, **40**, 12651–12655.

51 S. Hussain, X. Chen, W. T. A. Harrison, S. Ahmad, M. R. J. Elsegood, I. U. Khan and S. Muhammad, *Front. Chem.*, 2019, **7**, 260.

52 W. Klemm and J. Rockstroh, *Z. Anorg. Allg. Chem.*, 1928, **176**, 181–199.

53 L. Rycerz and M. Gaune-Escard, *Z. Naturforsch., A: Phys. Sci.*, 2002, **57**, 215–220.

Table of Contents

Experimental

X-ray crystallography

SCXRD structure determinations of $^{2}_{\infty}$[Sm(3-PyPzH)Cl$_3$] (**1**) and $^{2}_{\infty}$[Tb$_2$(3-PyPzH)$_3$Cl$_6$]·2Tol (**5**) were performed on a BRUKER AXS Smart Apex 1 diffractometer with graphite monochromator (Mo-Kα radiation; λ = 71.073 pm) and a Bruker Cryoflex low-temperature system. The single-crystal X-ray determinations of $^{2}_{\infty}$[Sm(3-PyPzH)Cl$_3$] (**1**), $^{3}_{\infty}$[Ln(3-PyPzH)Cl$_3$], Ln = Eu, Gd (**2, 3**), $^{2}_{\infty}$[Tb$_2$(3-PyPzH)$_3$Cl$_6$]·2Tol (**4**), $^{2}_{\infty}$[Ln$_2$(3-PyPzH)$_3$Cl$_3$]·2MeCN, Ln = Eu, Ho, Er (**5**, **8, 9**), [(3-PyPzH$_2$)][Ln(3-PyPzH)$_2$Cl$_4$], Ln = Eu, Tb, Dy, Ho (**10**-**13**), and $^{2}_{\infty}$[Ln$_2$(3-PyPzH$_2$)Cl$_4$], Ln = La, Nd (**14**, **15**) were performed on a BRUKER AXS D8 Venture diffractometer equipped with dual IμS microfocus sources, a collimating Quazar multilayer mirror, a PHOTON100 detector, and an OXFORD CRYOSYSTEMS 700 low-temperature system. The data collections for the thirteen compounds **1**-**5** and **8**-**15** were performed at 100 K using Mo-K$_\alpha$ radiation. The structures were solved using direct methods, refined with the least-squares method implemented in ShelXL[1], and expanded by Fourier techniques. All non-hydrogen atoms were refined anisotropically. Hydrogen atoms were assigned to idealized geometric positions and included in structure factor calculations. It should further be noted that a ligand (3-PyPzH) in the asymmetric unit of **1, 4, 5, 8, 9** and of toluene as solvent in **5** were found to be fully disordered, and were refined with the help of restraints to achieve a proper structural model, SIMU (Atoms bonding to each other have similar size) and RIGU (Atoms bonding to each other have similar shape) restraints, were used over the full structural model to stabilize the refinement and prevent atoms from splitting or being refined as N.P.D (non-positive definite) to gain a better structure model. Altogether, 1, 5, 8, and 3 atoms become non-positive definite in **1**, **5**, **8**, and **9**, respectively, 3 atoms split in **4** when SIMU and RIGU restraints are omitted. Other restraints were introduced: equivalent bonds should have the same length: SADI; aromatic rings should be flat: FLAT, free hydrogen atom position refinement using X-ray data is not a valid approach in most cases: DFIX to ideal distance for **1**, and **4**; because effective occupancy of disordered atoms is about 25% of an atom in **1** and 50% of an atom in **4** and **9**, anisotropic displacement parameters of some, very similar atoms, were constrained to the same values: EADP; equivalent bonds should have the same length and create the same bond angles: SAME for **5**, **8**, and **9**. In **14**, hard SIMU and RIGU restraints as well as EADP (Atoms of the same type in similar positions can be described using the same anisotropic displacement parameters) constraints have been used to prevent most thermal parameters from being negatively defined. By omitting the restraints and constraints, 7 ligand atoms go to N.P.D which makes the refinement unstable. Depictions of the crystal structures were created using DIAMOND.[2] The ToposPro program package was used to determine the topology of the polymers.[3]

PXRD analyses of the investigated compounds **1-15** were carried out on a STOE STADI P diffractometer with a focusing Ge(111) monochromator and a Dectris MYTHEN 1K strip detector in Debye-Scherrer geometry. All powder samples were ground in a mortar and filled into Lindemann glass capillaries with 0.3 mm diameter under an inert gas atmosphere. All samples were measured in transmission geometry using Cu-K$_\alpha$ radiation (λ = 154.056 pm). Rietveld refinements were carried out for $^{2}_{\infty}$[Ln$_2$(3-PyPzH)$_3$Cl$_3$]·2MeCN, Ln = Tb, Dy (**6**, **7**) using the Topas-Academic V7 software suite.[4] High-temperature PXRD for **4** was carried out also on a STOE STADI P diffractometer but with a MYTHEN2 1K detector system-320 µm sensor thickness and the basic version of the capillary furnace attachment from RT to 1000 ◦C. The powder sample was ground in a mortar and filled into a quartz glass capillary with a 0.5 mm diameter. Both preparation of the capillary and measurement were carried out under an inert gas atmosphere.

Spectroscopic Investigations

Vibrational spectra were recorded from 2-5 milligrams of the compounds with an ALPHA FT-IR spectrometer from Bruker optics (ATR module) using OPUS software.

Absorption Spectra were measured on solid-state products using a standard Agilent Cary 5000 UV-VIS-NIR spectrophotometer with a Praying Mantis accessory, which had been mounted and aligned for use with the DRP-ASC ambient chamber. The source, detector, and grating changeovers were at the standard position of 350, 800, and 800 nm, respectively for all compounds under study except for $^{2}_{\infty}$[Er$_2$(3-PyPzH)$_3$Cl$_6$]·2MeCN (**9**). The detector and grating changeovers were set both at 850 nm for **9** because the break at 800 nm interfered with a significant absorption band. The reference spectrum was collected on PTFE, and the reference and the samples were packed in the ambient chamber inside the glovebox under inert conditions. Detailed absorption spectra are shown in the SI (Fig. S11-S19).

Photoluminescence spectra were recorded for ground solid samples after filling them in quartz glass tubes under argon. The measurements were performed at room temperature as well as 77 K (latter using the liquid nitrogen-filled assembly FL-1013 of HORIBA) with a HORIBA Jobin Yvon Spex Fluorolog 3 spectrometer equipped with a 450 W Xe short-arc lamp (USHIO), double-grated excitation, and emission monochromators, and a photomultiplier tube (R928P) using the FluoroEssence™ software. Excitation and emission spectra were corrected for the spectral response of the monochromators and the detector using spectral corrections provided by the constructor. Besides, a photodiode reference detector was used to correct the excitation spectra for the spectral distribution of the lamp intensity. A R5509-73 detector was used to collect the data in the NIR region. When required, the collection of data was performed using an edge filter (Newport 20CGA-345, 395, 495 for the visible region and Reichmann Optics RG 830 long pass for the NIR region). Emission spectra with gating were recorded using a xenon flashlamp with a pulse repetition rate of 41 ms.

Photoluminescence overall decay process times were determined using the above-mentioned HORIBA Jobin Yvon Spex Fluorolog 3 spectrometer equipped with a dual lamp housing (FL-1040A), a UV xenon flashlamp (Exelitas FX-1102), and a TCSPC (time-correlated single-photon counting) upgrade, or picosecond pulsed laser diode. Emission decays were recorded using DataStation software. Exponential tail fitting was used for the calculation of resulting intensity decay using Decay Analysis Software 6. The quality of the fit was confirmed by χ^2 values being below 1.2.

Photoluminescence quantum yields were determined with a second similar instrument HORIBA Jobin Yvon Spex Fluorolog 3 spectrometer equipped with a HORIBA Quanta-ϕ Integrating Sphere. For the measurements, solid samples were filled into Starna Micro Cell cuvettes 18-F/ST/C/Q/10 (fluorescence with

ST/C closed-cap, material UV quartz glass Spectrosil Q, pathlength 10 mm, matched). Magnesium oxide was used as reference material. Each sample was measured at least three times and the quantum yield values with standard deviation were evaluated afterward. The Quanta-ϕ Integrating Sphere was checked with a standard (sodium salicylate as a powder, λ_{ex} = 340 nm, λ_{em} = 365-600 nm, measured QY = 52 %, literature: 53 %).[5]

PPMS magnetic measurements

DC-magnetic data were collected with the aid of the VMS option of a physical property measurement system (ppms) of LOT-Quantum Design. Temperature-dependent magnetic data were recorded in the range from 1.8 to 300 K, with an applied field of 90 kOe. The collected data were corrected concerning the diamagnetic moment of the sample holder out of polypropylene. There is a hint on very low amounts of impurities in the Ho^{3+} sample, these impurities cannot be detected with the other analytical method applied. In order to avoid the interference of these impurities with our result, a fit from 230-300 K was taken.

Thermal analysis

Simultaneous DTA/TG (NETZSCH STA 409-PC) coupled with a mass-spectrometer (NETZSCH QMS 403 Aëolos) in a constant argon flow of 50 ml·min^{-1} with a heating rate of 5 K·min^{-1} from room temperature to 1000 °C was used to determine the thermal properties. Additionally, for compound **4** a cyclic DSC (NETZSCH DSC 404-C) was measured in a constant argon flow of 50 mL·min^{-1} with heating and cooling rates of 5 K·min^{-1}. For $^{2}_{\infty}$[Sm(3-PyPzH)Cl$_3$] (**1**), $^{3}_{\infty}$[Eu(3-PyPzH)Cl$_3$] (**2**), $^{2}_{\infty}$[Tb$_2$(3-PyPzH)$_3$Cl$_6$]·2Tol (**4**), and $^{2}_{\infty}$[Ho$_2$(3-PyPzH)$_3$Cl$_6$]·2MeCN (**8**), the DTA curve was baseline corrected after the measurement using the Origin™ software.

CHN analysis

A Thermo Scientific Flash EA – 1112 was used to perform the CHN analyses. The polymers were placed in a tin crucible with no less than one mass equivalent to V_2O_5. Specimens were made ready and stored under inert conditions till the time of the measurements.

Starting materials 3-(3-pyridyl)pyrazole / 3-(1H-pyrazol-3-yl)pyridine (3-PyPzH) was synthesized as reported in the literature and then purified by sublimation in a temperature gradient from 80 °C to room temperature under reduced pressure (p = 1.0 x 10^{-3} mbar) before reactions.[18, 51] LnCl$_3$, Ln = Sm, Tb, Dy, Ho, Er (anhydrous, 99.9 %, Sigma-Aldrich), EuCl$_3$ (anhydrous, 99.99 %, Sigma-Aldrich), and GdCl$_3$ (anhydrous, 99.9%, Strem Chemicals) were used as purchased. Acetonitrile (MeCN) (99.9 %, extra dry, Acros Organics), toluene (Tol) (99.85 %, extra dry, Acros Organics), chlorobenzene (99.8 %, extra dry, Acros Organics), and dichloromethane (DCM) (99.8 %, extra dry, Acros Organics) were degassed and stored over activated molecular sieves for 3 days before using.

1. a) G. M. Sheldrick, *Acta Crystallogr., Sect. A: Found. Crystallogr.*, 2015, **71**, 3-8; b) G. M. Sheldrick, *Acta Crystallogr., Sect. C: Struct. Chem.*, 2015, **71**, 3-8.
2. W. T. Pennington, *J. Appl. Crystallogr.*, 1999, **32**, 1028-1029.
3. V. A. Blatov, A. P. Shevchenko and D. M. Proserpio, *Cryst. Growth Des.*, 2014, **14**, 3576-3586.
4. A. A. Coelho, *J. Appl. Crystallogr.*, 2018, **51**, 210-218.
5. M. S. Wrighton, D. S. Ginley and D. L. Morse, *J. Phys. Chem.*, 1974, **78**, 2229-2233.

Crystallographic Data

The compounds were uploaded to the Cambridge Crystallographic DataBase with the following identifiers: CCDC 2159935 (**1**), 2159936 (**2**), 2159937 (**3**), 2159939 (**4**), 2159938 (**5**), 2159940 (**8**), 2159941 (**9**), 2159942 (**10**), 2159943 (**11**), 2159944 (**12**), 2159945 (**13**), 2159946 (**14**), and 2159947 (**15**) contain the supplementary crystallographic data. These data are provided free of charge by the Cambridge Crystallographic Data Centre.

Table S1. Crystallographic data of $^{2}_{\infty}$[Sm(3-PyPzH)Cl$_3$] (**1**), $^{3}_{\infty}$[Eu(3-PyPzH)Cl$_3$] (**2**), $^{3}_{\infty}$[Gd(3-PyPzH)Cl$_3$] (**3**).

Compound	$^{2}_{\infty}$[Sm(3-PyPzH)Cl$_3$]	$^{3}_{\infty}$[Eu(3-PyPzH)Cl$_3$]	$^{3}_{\infty}$[Gd(3-PyPzH)Cl$_3$]
CCDC number	2159935	2159936	2159937
Empirical formula	$C_8H_7N_3Cl_3Sm$	$C_8H_7N_3Cl_3Eu$	$C_8H_7N_3Cl_3Gd$
M_r / g·mol^{-1}	401.87	403.48	408.77
T / K	100(2)	100(2)	100(2)
λ / pm	71.073, Mo-K$_\alpha$	71.073, Mo-K$_\alpha$	71.073, Mo-K$_\alpha$
Crystal system	Orthorhombic	Orthorhombic	Orthorhombic
Space group	*Pbcm*	*Pcca*	*Pcca*
a / pm	1109.3(2)	1365.72(8)	1364.40(7)
b / pm	1365.1(2)	1008.85(6)	1007.61(5)
c / pm	776.3(1)	1639.0(1)	1638.58(8)
α, β, γ / °	90	90	90
V / 10^6 pm^3	1175.5(3)	2258.3(2)	2252.7(2)
Z	4	8	8
ρ_{calc} / g·cm^{-3}	2.271	2.373	2.411
μ / mm^{-1}	5.645	6.231	6.566
F(000)	756	1520	1528
Crystal size / mm^3	0.214 x 0.169 x 0.141	0.142 x 0.041 x 0.035	0.069 x 0.052 x 0.027
2θ_{min} / °	2.985	2.019	2.021
2θ_{max} / °	34.058	26.731	27.522
Reflections collected	39828	32732	37524
Independent reflections	2518	2411	2589
R(int)	0.0866	0.1786	0.0871
No. Of parameters	197	138	138
GOF	1.053	1.044	1.079
Final R indices [$I > 2\sigma(I)$]	R_1 = 0.0284, wR_2 = 0.0444	R_1 = 0.0411, wR_2 = 0.0819	R_1 = 0.0628, wR_2 = 0.1484
R indices (all data)	R_1 = 0.0440, wR_2 = 0.0480	R_1 = 0.0734, wR_2 = 0.0954	R_1 = 0.1004, wR_2 = 0.1816
$\Delta\rho_{max}$, $\Delta\rho_{min}$ / e·10^{-6}·pm^{-3}	1.457, -1.594	2.771, -1.159	5.209, -3.033

Table S2. Crystallographic data of $^{2}_{\infty}$[Tb$_2$(3-PyPzH)$_3$Cl$_6$]·2Tol (**4**), $^{2}_{\infty}$[Eu$_2$(3-PyPzH)$_3$Cl$_6$]·2MeCN (**5**), $^{2}_{\infty}$[Ho$_2$(3-PyPzH)$_3$Cl$_6$]·2MeCN (**8**), $^{2}_{\infty}$[Er$_2$(3-PyPzH)$_3$Cl$_6$]·2MeCN (**9**).

Compound	$^{2}_{\infty}$[Tb$_2$(3-PyPzH)$_3$Cl$_6$](Tol)$_2$	$^{2}_{\infty}$[Eu$_2$(3-PyPzH)$_3$Cl$_6$]·2MeCN	$^{2}_{\infty}$[Ho$_2$(3-PyPzH)$_3$Cl$_6$]·2MeCN	$^{2}_{\infty}$[Er$_2$(3-PyPzH)$_3$Cl$_6$]·2MeCN
CCDC number	2159939	2159938	2159940	2159941
Empirical formula	$C_{38}H_{37}N_9Cl_6Tb_2$	$C_{28}H_{27}N_{11}Cl_6Eu_2$	$C_{28}H_{27}N_{11}Cl_6Ho_2$	$C_{28}H_{27}N_{11}Cl_6Er_2$
M_r / g·mol^{-1}	1150.30	1034.22	1060.16	1064.82
T / K	100(2)	100(2)	100(2)	100(2)
λ / pm	71.073, Mo-K$_\alpha$	71.073 Mo-K$_\alpha$	71.073, Mo-K$_\alpha$	71.073 Mo-K$_\alpha$
Crystal system	Monoclinic	Monoclinic	Monoclinic	Monoclinic
Space group	*P*2$_1$/*n*	*P*2$_1$/*n*	*P*2$_1$/*n*	*P*2$_1$/*n*
a / pm	1226.5(2)	902.50(4)	903.26(9)	903.48(5)
b / pm	1466.9(2)	1522.38(6)	1513.7(2)	1511.15(8)
c / pm	1248.6(2)	1402.72(6)	1382.6(2)	1377.78(7)
α / °	90	90	90	90
β / °	107.408(3)	103.890(2)	103.912(3)	103.948(2)
γ / °	90	90	90	90
V / 10^6 pm^3	2143.6(4)	1870.9(2)	1835.0(3)	1825.6(2)
Z	2	2	2	2
ρ_{calc} / g·cm^{-3}	1.782	1.836	1.919	1.937
μ / mm^{-1}	3.686	3.787	4.755	5.042
F(000)	1120	1000	1016	1020
Crystal size / mm^3	0.145 x 0.102 x 0.064	0.086 x 0.069 x 0.065	0.070 x 0.025 x 0.022	0.050 x 0.049 x 0.022
2θ_{min} / °	2.042	2.444	2.028	2.034
2θ_{max} / °	32.125	27.536	26.019	26.022
Reflections collected	80347	215518	50698	75215
Independent reflections	7143	4305	3597	3590
R(int)	0.0854	0.1227	0.1663	0.1443
No. Of parameters	340	263	257	239
GOF	1.038	1.057	1.148	1.057
Final R indices [$I > 2\sigma(I)$]	R_1 = 0.0293, wR_2 = 0.0580	R_1 = 0.0202, wR_2 = 0.0406	R_1 = 0.0465, wR_2 = 0.1179	R_1 = 0.0255, wR_2 = 0.0471
R indices (all data)	R_1 = 0.0504, wR_2 = 0.0641	R_1 = 0.0281, wR_2 = 0.0429	R_1 = 0.0689, wR_2 = 0.1277	R_1 = 0.0423, wR_2 = 0.0518
$\Delta\rho_{max}$, $\Delta\rho_{min}$ / e·10^{-6}·pm^{-3}	1.052, -1.748	1.493, -0.647	2.605, -1.380	1.568, -0.693

Table S3. Crystallographic data of [(3-PyPzH$_2$)][Ln(3-PyPzH)$_2$Cl$_4$], Ln = Eu, Tb, Dy, Ho (**10-13**).

Compound	[(3-PyPzH$_2$)][Eu(3-PyPzH)$_2$Cl$_4$]	[(3-PyPzH$_2$)][Tb(3-PyPzH)$_2$Cl$_4$]	[(3-PyPzH$_2$)][Dy(3-PyPzH)$_2$Cl$_4$]	[(3-PyPzH$_2$)][Ho(3-PyPzH)$_2$Cl$_4$]
CCDC number	2159942	2159943	2159944	2159945
Empirical formula	$C_{24}H_{22}N_9Cl_4Eu$	$C_{24}H_{22}N_9Cl_4Tb$	$C_{24}H_{22}N_9Cl_4Dy$	$C_{24}H_{22}N_9Cl_4Ho$
M_r / g·mol^{-1}	730.26	737.22	740.80	743.23
T / K	100(2)	100(2)	100(2)	100(2)
λ / pm	71.073, Mo-K$_\alpha$	71.073, Mo-K$_\alpha$	71.073, Mo-K$_\alpha$	71.073, Mo-K$_\alpha$
Crystal system	Monoclinic	Monoclinic	Monoclinic	Monoclinic
Space group	*P*2$_1$/*c*	*P*2$_1$/*c*	*P*2$_1$/*c*	*P*2$_1$/*c*
a / pm	1252.62(4)	1248.21(6)	1248.02(4)	1245.97(4)
b / pm	1377.31(5)	1373.01(7)	1372.04(5)	1370.64(4)
c / pm	1597.69(6)	1596.94(8)	1596.95(6)	1596.14(4)
α / °	90	90	90	90
β / °	96.969(2)	97.093(2)	97.090(2)	97.2070(10)
γ / °	90	90	90	90
V / 10^6 pm^3	2736.0(2)	2715.9(2)	2713.6(2)	2704.3(2)
Z	4	4	4	4
ρ_{calc} / g·cm^{-3}	1.773	1.803	1.813	1.825
μ / mm^{-1}	2.716	3.031	3.181	3.354
F(000)	1440	1448	1452	1456
Crystal size / mm^3	0.109 x 0.066 x 0.058	0.154 x 0.101 x 0.095	0.072 x 0.050 x 0.028	0.322 x 0.152 x 0.15
2θ_{min} / °	1.638	1.644	2.215	1.647
2θ_{max} / °	30.651	27.547	27.538	27.482
Reflections collected	183851	71182	128032	78011
Independent reflections	8432	6274	6257	6199
R(int)	0.3313	0.0516	0.0747	0.1566
No. Of parameters	344	343	343	343
GOF	1.001	1.060	1.041	0.948
Final R indices [$I > 2\sigma(I)$]	R_1 = 0.0418, wR_2 = 0.0703	R_1 = 0.0262, wR_2 = 0.0529	R_1 = 0.0203, wR_2 = 0.0413	R_1 = 0.0231, wR_2 = 0.0405
R indices (all data)	R_1 = 0.0862, wR_2 = 0.0812	R_1 = 0.0357, wR_2 = 0.0563	R_1 = 0.0279, wR_2 = 0.0435	R_1 = 0.0384, wR_2 = 0.0430
$\Delta\rho_{max}$, $\Delta\rho_{min}$ / e·10^{-6}·pm^{-3}	3.020, -0.728	2.014, -0.840	1.863, -0.560	1.306, -0.507

Table S4. Crystallographic data of $^{2}_{\infty}$[Ln(3-PyPzH$_2$)Cl$_4$], Ln = La, Nd (**14**, **15**).

Compound	$^{2}_{\infty}$[La(3-PyPzH$_2$)Cl$_4$]	$^{2}_{\infty}$[Nd(3-PyPzH$_2$)Cl$_4$]
CCDC number	2159946	2159947
Empirical formula	$C_8H_8N_3Cl_4La$	$C_8H_8N_3Cl_4Nd$
M_r / g·mol^{-1}	426.88	432.21
T / K	100(2)	100(2)
λ / pm	71.073, Mo-K$_\alpha$	71.073, Mo-K$_\alpha$
Crystal system	Monoclinic	Monoclinic
Space group	*C*2/*c*	*C*2/*c*
a / pm	1348.0(3)	1336.7(1)
b / pm	883.1(2)	868.25(7)
c / pm	2108.6(5)	2092.9(2)
α / °	90	90
β / °	97.213(8)	97.014(2)
γ / °	90	90
V / 10^6 pm^3	2490.0(1)	2410.8(3)
Z	8	8
ρ_{calc} / g·cm^{-3}	2.277	2.382
μ / mm^{-1}	4.262	5.166
F(000)	1616	1640
Crystal size / mm^3	0.050 x 0.037 x 0.019	0.075 x 0.065 x 0.002
2θ_{min} / °	1.947	1.961
2θ_{max} / °	26.371	27.522
Reflections collected	2396	17823
Independent reflections	2396	2783
R(int)	-	0.0685
No. Of parameters	123	145
GOF	1.215	1.134
Final R indices [$I > 2\sigma(I)$]	R_1 = 0.0857, wR_2 = 0.1576	R_1 = 0.0461, wR_2 = 0.1021
R indices (all data)	R_1 = 0.1145, wR_2 = 0.1669	R_1 = 0.0647, wR_2 = 0.1092
$\Delta\rho_{max}$, $\Delta\rho_{min}$ / e·10^{-6}·pm^{-3}	1.397, -1.395	3.086, -2.352

Table S5. Rietveld refinement of Powder X-ray diffraction data (PXRD) of $^{2}_{\infty}$[Ln$_2$(3-PyPzH)$_3$Cl$_6$]·2MeCN, Ln = Tb, Dy (**6, 7**) based on X-ray single- crystal data (SCXRD) of $^{2}_{\infty}$[Ho$_2$(3-PyPzH)$_3$Cl$_6$]·2MeCN (**8**).

Compound	$^{2}_{\infty}$[Tb$_2$(3-PyPzH)$_3$Cl$_6$]·2MeCN	$^{2}_{\infty}$[Dy$_2$(3-PyPzH)$_3$Cl$_6$]·2MeCN
Empirical formula	$C_{28}H_{27}N_{11}Cl_6Tb_2$	$C_{28}H_{27}N_{11}Cl_6Dy_2$
M_r / g·mol^{-1}	1048.16	1048.16
Crystal system	Monoclinic	Monoclinic
Space group	*P*2$_1$/*n*	*P*2$_1$/*n*
a / pm	914.01(5)	913.71(6)
b / pm	1527.55(8)	1525.2(1)
c / pm	1395.10(9)	1391.3(1)
α / °	90	90

β / °	104.049(4)	104.095(4)
γ / °	90	90
V / 10^6 pm^3	1889.6(2)	1880.6(2)
Z	2	2
R_{wp}	4.845	5.493
R_{exp}	2.720	3.318
GOF	1.781	1.656

Crystal Structures, Interatomic Distances, and Angles

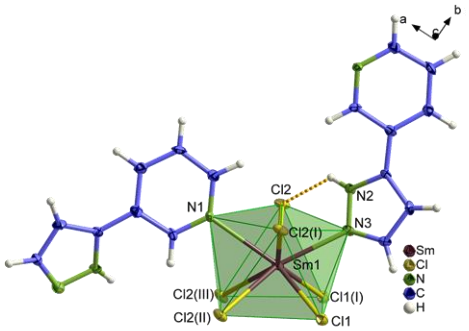

Fig. S1. Extended coordination sphere of Ln^{3+} in $^2_\infty$[Sm(3-PyPzH)Cl$_3$] (**1**). The coordination polyhedra around Ln^{3+} is indicated in green and the thermal ellipsoids describe a 50 % probability level of the atoms. The disordered components are omitted for clarity. Symmetry operations: : I x,y,-z+1/2 II x,-y+1/2,z-1/2 III x,-y+1/2,-z+1.

Table S6. Selected interatomic distances (pm) and angles (◦) of $^2_\infty$[Sm(3-PyPzH)Cl$_3$] (**1**). Symmetry operations: : I x,y,-z+1/2 II x,-y+1/2,z-1/2 III x,-y+1/2,-z+1.

Atoms	$^2_\infty$[Sm(3-PyPzH)Cl$_3$]
Sm1-Cl1, Cl1^{I}	282.21(7)
Sm1-Cl2, Cl2^{I}	275.05(6)
Sm1-Cl2^{II}, Cl2^{III}	282.80(6)
Sm1-N3	257.0(2)
Sm1-N1	264.0(3)
Cl1-Sm1-Cl1^{I}	86.90(3)
Cl1-Sm1-Cl2^{II}	72.22(2)
Cl1^{I}-Sm1-Cl2^{II}	119.63(2)
Cl2-Sm1-Cl1	146.36(2)
Cl2^{I}-Sm1-Cl1	73.37(2)

Cl2-Sm1-Cl2^{II}	141.29(2)	
Cl2^{I}-Sm1-Cl2^{II}	80.47(2)	
Cl2^{I}-Sm1-Cl2	108.85(3)	
Cl2^{I}-Sm1-Cl2^{III}	141.29(2)	
Cl2^{II}-Sm1-Cl2^{III}	71.11(3)	
N3-Sm1-Cl2^{I}	74.7(7)	
N3-Sm1-Cl2	71.0(7)	
N3-Sm1-Cl1	77.7(6)	
N3-Sm1-Cl1^{I}	74.6(6)	
N3-Sm1-Cl2^{II}	145.3(7)	
N3-Sm1-Cl2^{III}	141.1(7)	

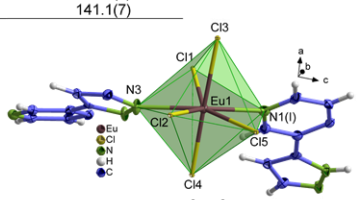

Fig. S2. Extended coordination sphere of Ln^{3+} in $^3_\infty$[Eu(3-PyPzH)Cl$_3$] (**2**) represents the isotypic two coordination polymers **2**, and **3**. The coordination polyhedra around Ln^{3+} is indicated in green and the thermal ellipsoids describe a 50 % probability level of the atoms. Symmetry operations: : I - x,-y+1,z-1/2.

Table S7. Selected interatomic distances (pm) and angles (◦) of $^3_\infty$[Ln(3-PyPzH)Cl$_3$], Ln=Eu and Gd (**2**, **3**). Symmetry operations: : I - x,-y+1,z-1/2.

Compound	$^3_\infty$[Eu(3-PyPzH)Cl$_3$]	$^3_\infty$[Gd(3-PyPzH)Cl$_3$]
Ln1-Cl1	279.0(2)	278.1(2)
Ln1-Cl2	274.7(2)	274.0(2)
Ln1-Cl3	276.2(2)	275.4(2)
Ln1-Cl4	261.4(2)	260.2(3)
Ln1-Cl5	274.9(2)	273.9(2)
Ln1-N1^{I}	258.4(6)	256.0(1)
Ln1-N3	251.7(6)	250.0(1)
Cl2- Ln1-Cl1	136.67(4)	137.07(7)
Cl2- Ln1-Cl3	85.08(3)	85.34(5)
Cl2- Ln1-Cl5	73.82(6)	73.47(9)
Cl3- Ln1-Cl1	76.27(6)	76.27(9)
Cl4- Ln1-Cl1	102.39(6)	102.5(1)
Cl4- Ln1-Cl2	96.91(5)	96.45(8)
Cl4- Ln1-Cl3	177.98(5)	178.20(9)
Cl4- Ln1-Cl5	91.02(5)	91.20(8)
Cl5- Ln1-Cl1	142.95(4)	142.91(7)
Cl5- Ln1-Cl3	89.22(4)	89.11(5)
N1^{I}- Ln1-Cl1	73.6(2)	73.5(2)
N1^{I}- Ln1-Cl2	146.3(2)	146.2(2)

N1^{I}- Ln1-Cl3	90.8(2)	91.2(3)
N1^{I}- Ln1-Cl4	87.4(2)	87.2(3)
N1^{I}- Ln1-Cl5	72.7(2)	72.9(2)
N3- Ln1-Cl1	72.1(2)	71.8(3)
N3- Ln1-Cl2	74.4(2)	74.7(3)
N3- Ln1-Cl3	102.3(2)	101.9(3)
N3- Ln1-Cl4	78.6(2)	78.8(3)
N3- Ln1-Cl5	144.1(2)	145.2(3)
N3- Ln1-N1^{I}	138.8(2)	138.5(3)

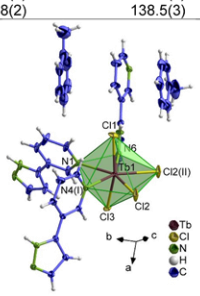

Fig. S3. Extended coordination sphere of Ln^{3+} in $^2_\infty$[Tb$_2$(3-PyPzH)$_3$Cl$_6$]·2Tol (**4**). The coordination polyhedra around Ln^{3+} is indicated in green and the thermal ellipsoids describe a 50 % probability level of the atoms. The disordered components are omitted for clarity. Symmetry operations: : I x-1/2,-y+1/2,z+1/2 II -x+1,-y+1,-z+1.

Table S8. Selected interatomic distances (pm) and angles (◦) of $^2_\infty$[Tb$_2$(3-PyPzH)$_3$Cl$_6$]·2Tol (**4**). Symmetry operations: : I x-1/2,-y+1/2,z+1/2 II -x+1,-y+1,-z+1.

Compound	$^2_\infty$[Tb$_2$(3-PyPzH)$_3$Cl$_6$]·2Tol
Tb1-Cl1	261.75(7)
Tb1-Cl2	270.17(7)
Tb1-Cl2^{II}	273.21(7)
Tb1-Cl3	259.15(7)
Tb1-N1	249.0(1)
Tb1-N4^{I}	252.9(2)
Tb1-N6	251.1(2)
Cl1-Tb1-Cl2	99.37(3)
Cl1-Tb1-Cl2^{II}	93.07(3)
Cl2-Tb1-Cl2^{II}	73.78(3)
Cl3-Tb1-Cl1	163.55(2)
Cl3-Tb1-Cl2	96.48(3)
Cl3-Tb1-Cl2^{II}	95.54(3)
N1-Tb1-Cl1	81.9(3)
N1-Tb1-Cl2	144.6(3)
N1-Tb1-Cl2^{II}	141.6(3)

N1-Tb1-Cl3	82.6(3)
N1-Tb1-N4^{I}	72.1(3)
N1-Tb1-N6	69.4(3)
N4^{I}-Tb1-Cl1	92.64(5)
N4^{I}-Tb1-Cl2	72.48(5)
N4^{I}-Tb1-Cl2^{II}	146.27(5)
N4^{I}-Tb1-Cl3	87.95(5)
N6-Tb1-Cl1	83.28(6)
N6-Tb1-Cl2	146.00(5)
N6-Tb1-Cl2^{II}	72.22(5)
N6-Tb1-Cl3	86.04(6)
N6-Tb1-N1	69.4(3)
N6-Tb1-N4^{I}	141.50(7)

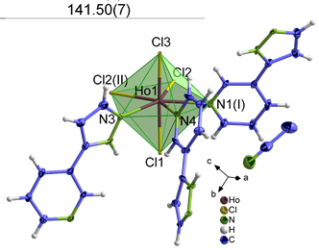

Fig. S4. Extended coordination sphere of Ln^{3+} in $^2_\infty$[Ho$_2$(3-PyPzH)$_3$Cl$_6$]·2MeCN (**8**) represents the series of isotypic coordination polymers **5-9**. The coordination polyhedra around Ln^{3+} is indicated in green and the thermal ellipsoids describe a 50 % probability level of the atoms. The disordered components are omitted for clarity. Symmetry operations: : I -x+1/2,y-1/2,-z+1/2 II -x,-y+1,-z.

Table S9. Selected interatomic distances (pm) and angles (◦) of $^2_\infty$[Ln$_2$(3-PyPzH)$_3$Cl$_6$]·2MeCN, Ln= Eu, Ho, Er (**5**, **8, and 9**). Symmetry operations: : I -x+1/2,y-1/2,-z+1/2 II -x,-y+1,-z.

Compound	$^3_\infty$[Eu$_2$(3-PyPzH)$_3$Cl$_6$]·2MeCN	$^2_\infty$[Ho$_2$(3-PyPzH)$_3$Cl$_6$]·2MeCN	$^2_\infty$[Er$_2$(3-PyPzH)$_3$Cl$_6$]·2MeCN
Ln1-Cl1	268.12(6)	262.6(2)	261.3(1)
Ln1-Cl2	274.28(6)	269.8(2)	268.4(1)
Ln1-Cl2^{II}	277.34(6)	272.6(2)	271.8(1)
Ln1-Cl3	260.68(7)	255.8(2)	254.4(1)
Ln1-N1^{I}	256.1(2)	250.3(7)	248.9(3)
Ln1-N3	253.3(2)	248.2(7)	246.3(3)
Ln1-N4	259.0(2)	254.0(2)	254.0(2)
Cl1- Ln1-Cl2	95.97(2)	95.32(7)	95.26(3)
Cl1- Ln1-Cl2^{II}	91.37(2)	91.32(7)	91.20(3)
Cl2- Ln1-Cl2^{II}	74.71(2)	74.26(7)	74.13(3)

Cl3- Ln1-Cl1	169.82(2)	170.67(7)	170.91(4)
Cl3- Ln1-Cl2	92.91(2)	93.12(7)	93.02(4)
Cl3- Ln1-Cl2^{II}	95.77(2)	94.80(7)	94.67(4)
N1^{I}- Ln1-Cl1	84.94(5)	85.6(2)	85.70(8)
N1^{I}- Ln1-Cl2	72.57(5)	72.7(2)	72.80(8)
N1^{I}- Ln1-Cl2^{II}	146.47(5)	146.4(2)	146.33(8)
N1^{I}- Ln1-Cl3	93.01(5)	93.2(2)	93.19(9)
N3- Ln1-Cl1	81.49(5)	82.1(2)	82.67(8)
N3- Ln1-Cl2	145.48(5)	145.2(2)	145.06(8)
N3- Ln1-Cl2^{II}	70.96(5)	71.1(2)	71.06(8)
N3- Ln1-Cl3	93.99(5)	93.2(2)	92.67(9)
N4- Ln1-Cl1	87.5(4)	88.2(7)	87.9(4)
N4- Ln1-Cl2	144.5(7)	144.0(2)	145.5(7)
N4- Ln1-Cl2^{II}	140.7(7)	141.0(1)	140.2(7)
N4- Ln1-Cl3	82.4(4)	82.7(7)	83.2(4)
N3- Ln1-N1^{I}	140.57(7)	140.9(2)	141.1(1)
N3- Ln1-N4	70.0(7)	70.0(2)	69.4(7)
N1^{I}- Ln1-N4	72.6(7)	72.0(2)	73.2(7)

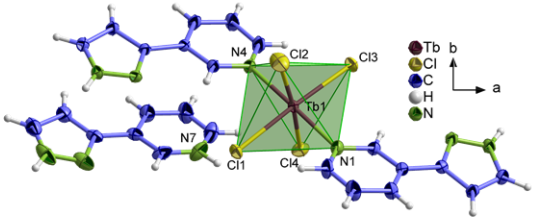

Fig. S5. Extended coordination sphere of Ln^{3+} in $[(3\text{-}PyPzH_2)][Tb(3\text{-}PyPzH)_2Cl_4]$ (**11**) represents the series of isotypic coordination polymers **10**-**13**. The coordination polyhedra around Ln^{3+} is indicated in green and the thermal ellipsoids describe a 50 % probability level of the atoms.

Table S10. Selected interatomic distances (pm) and angles (°) of $[(3\text{-}PyPzH_2)][Ln(3\text{-}PyPzH)_2Cl_4]$, Ln= Eu, Tb, Dy and Ho (**10**-**13**).

Compound	[(3-PyPzH$_2$)][Eu(3-PyPzH)$_2$Cl$_4$]	[(3-PyPzH$_2$)][Tb(3-PyPzH)$_2$Cl$_4$]	[(3-PyPzH$_2$)][Dy(3-PyPzH)$_2$Cl$_4$]	[(3-PyPzH$_2$)][Ho(3-PyPzH)$_2$Cl$_4$]
Ln1-Cl1	267.61(9)	264.91(7)	264.30(5)	263.05(7)
Ln1-Cl2	264.9(1)	262.21(7)	260.52(6)	259.78(7)
Ln1-Cl3	263.93(9)	261.36(7)	260.23(5)	258.98(7)
Ln1-Cl4	260.1(1)	257.95(8)	256.20(6)	255.60(7)
Ln1-N1	250.8(3)	247.6(2)	246.6 (2)	244.3(2)
Ln1-N4	251.4(3)	248.1(2)	247.0(2)	245.0(2)
Cl2- Ln1-Cl1	86.12(3)	86.42(2)	86.44(2)	86.53(2)
Cl3- Ln1-Cl1	176.61(3)	176.92(2)	176.91(2)	177.04(2)
Cl3- Ln1-Cl2	91.14(3)	91.01(2)	90.85(2)	90.89(2)

Cl4- Ln1-Cl1	91.23(3)	91.12(2)	91.04(2)	90.88(2)
Cl4- Ln1-Cl2	173.13(3)	173.98(3)	174.53(2)	174.52(2)
Cl4- Ln1-Cl3	91.71(3)	91.59(2)	91.78(2)	91.81(2)
N1- Ln1-Cl1	90.68(8)	90.97(6)	90.55(5)	90.77(5)
N1- Ln1-Cl2	86.68(8)	87.04(6)	87.35(5)	87.39(5)
N1- Ln1-Cl3	91.15(8)	90.61(6)	90.83(5)	90.55(5)
N1- Ln1-Cl4	87.01(8)	87.51(6)	87.82(5)	87.81(5)
N4- Ln1-Cl1	88.52(8)	88.52(6)	88.96(5)	88.81(5)
N4- Ln1-Cl2	91.62(8)	91.64(6)	91.58(5)	91.58(5)
N4- Ln1-Cl3	89.57(8)	89.84(6)	89.61(5)	89.82(5)
N4- Ln1-Cl4	94.65(8)	93.79(6)	93.23(5)	93.20(5)
N1- Ln1-N4	178.2(1)	178.61(8)	178.84(6)	178.91(7)

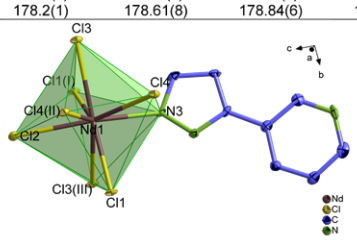

Fig. S6. Extended coordination sphere of Ln^{3+} in $^{2}_{\infty}[Nd(3\text{-}PyPzH_2)Cl_4]$ (**15**) represents the two isotypic coordination polymers **14** and **15**. The coordination polyhedra around Ln^{3+} is indicated in green and the thermal ellipsoids describe a 50 % probability level of the atoms. Symmetry operations: I -x+1/2,y-1/2,-z+1/2 II -x+1,y,-z+1/2 III -x+1/2,y+1/2,-z+1/2.

Table S11. Selected interatomic distances (pm) and angles (°) of $^{2}_{\infty}[Ln(3\text{-}PyPzH_2)Cl_4]$, Ln= La, Nd (**14, 15**). I -x+1/2,y-1/2,-z+1/2 II -x+1,y,-z+1/2 III -x+1/2,y+1/2,-z+1/2

Compound	$^{2}_{\infty}$[La(3-PyPzH$_2$)Cl$_4$]	$^{2}_{\infty}$[Nd(3-PyPzH$_2$)Cl$_4$]
Ln1-Cl1	281.4(5)	274.7(2)
Ln1-Cl2	280.9(5)	275.2(2)
Ln1-Cl3	284.9(5)	279.3(2)
Ln1-Cl4	294.1(5)	288.1(2)
Ln1-N3	272.0(2)	264.2(6)
Cl1- Ln1-Cl2	93.9(2)	93.55(6)
Cl1- Ln1-Cl3	156.0(1)	156.70(5)
Cl2- Ln1-Cl3	89.9(2)	89.73(6)
Cl1- Ln1-Cl4	82.3(2)	82.60(6)
Cl2- Ln1-Cl4	143.0(2)	142.14(6)
Cl3- Ln1-Cl4	80.5(2)	80.72(6)
N3- Ln1-Cl1	93.6(5)	94.3(2)
N3- Ln1-Cl2	148.8(4)	149.0(2)
N3- Ln1-Cl3	95.3(5)	94.7(2)
N3- Ln1-Cl4	68.1(4)	68.7(2)

Powder Diffraction

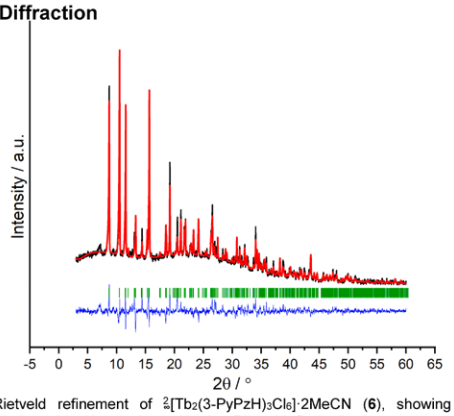

Fig. S7. Rietveld refinement of $^{2}_{\infty}[Tb_2(3\text{-}PyPzH)_3Cl_6]\cdot 2MeCN$ (**6**), showing the experimental data (black) together with the Rietveld fit (red), the corresponding difference plot (blue) as well as the hkl position markers (green).

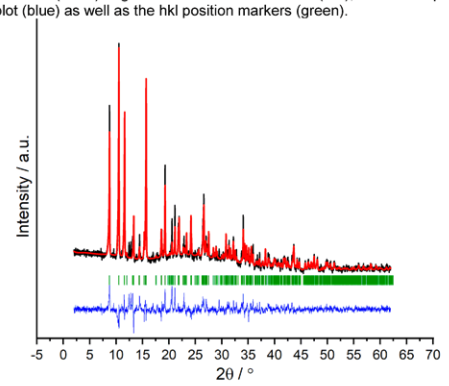

Fig. S8. Rietveld refinement of $^{2}_{\infty}[Dy_2(3\text{-}PyPzH)_3Cl_6]\cdot 2MeCN$ (**7**), showing the experimental data (black) together with the Rietveld fit (red), the corresponding difference plot (blue) as well as the hkl position markers (green).

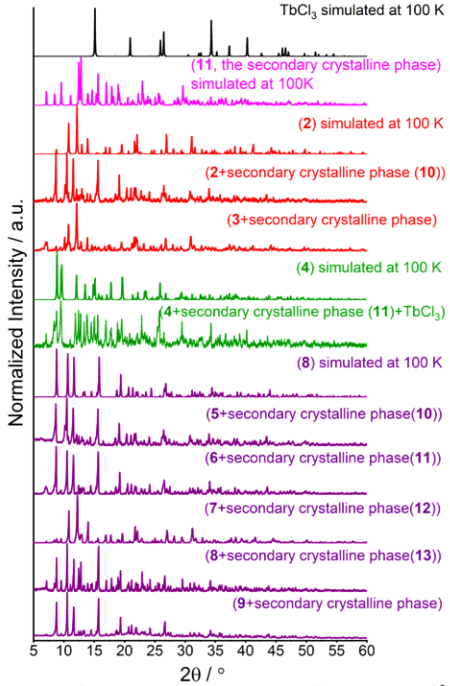

Fig. S9. Comparison of the experimental X-ray powder diffraction pattern of $^{3}_{\infty}[Eu(3\text{-}PyPzH)Cl_3]$ (**2**), $^{3}_{\infty}[Gd(3\text{-}PyPzH)Cl_3]$ (**3**), $^{2}_{\infty}[Tb_2(3\text{-}PyPzH)_3Cl_6]\cdot 2Tol$ (**4**), $^{2}_{\infty}[Eu_2(3\text{-}PyPzH)_3Cl_6]\cdot 2MeCN$ (**5**), $^{2}_{\infty}[Tb_2(3\text{-}PyPzH)_3Cl_6]\cdot 2MeCN$ (**6**), $^{2}_{\infty}[Dy_2(3\text{-}PyPzH)_3Cl_6]\cdot 2MeCN$ (**7**), $^{2}_{\infty}[Ho_2(3\text{-}PyPzH)_3Cl_6]\cdot 2MeCN$ (**8**), $^{2}_{\infty}[Er_2(3\text{-}PyPzH)_3Cl_6]\cdot 2MeCN$ (**9**) including secondary phases at 298 K with the respective simulated pattern from single-crystal X-ray data at 100 K for each individual case, the simulated pattern of $[(3\text{-}PyPzH_2)][Tb(3\text{-}PyPzH)_2Cl_4]$ (**11**) which represents the series of the secondary crystalline phase (**10-13**), as well as $TbCl_3$. The comparison shows the presence of the second crystalline phase together with the main product if the right reaction conditions (stated in the experimental part) were not followed.

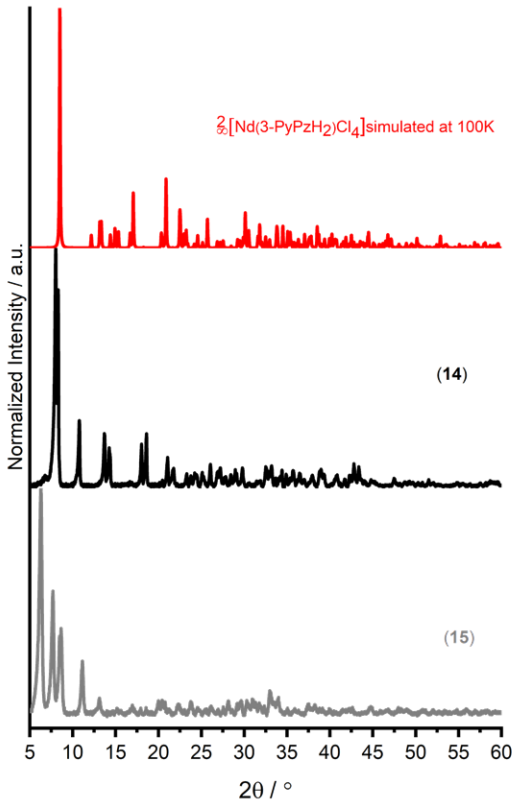

Fig. S10. Comparison of the experimental X-ray powder diffraction pattern at 298 K of ∞[La(3-PyPzH₂)Cl₄]·2MeCN (**14**), ∞[Nd(3-PyPzH₂)Cl₄]·2MeCN (**15**) with a simulated pattern from single-crystal X-ray data of ∞[Nd(3-PyPzH₂)Cl₄]·2MeCN (**15**).

Photophysical Properties

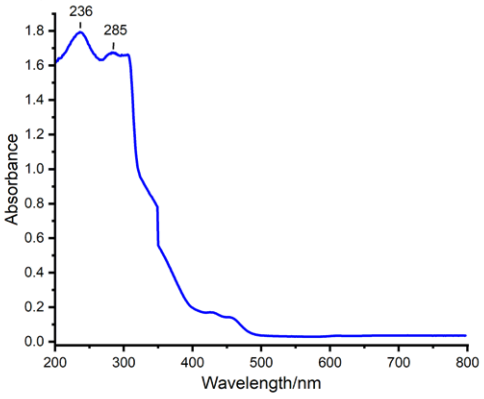

Fig. S11. Absorption spectra of 3-PyPzH in the solid state at room temperature.

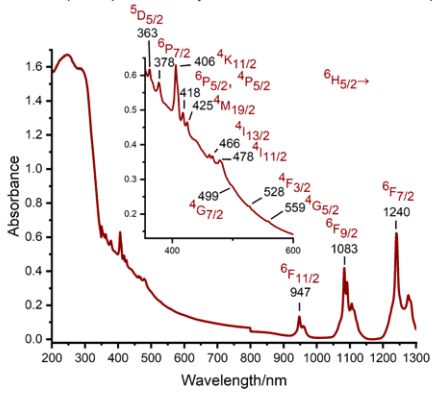

Fig. S12. Absorption spectra of ∞[Sm(3-PyPzH)Cl₃] (**1**) in the solid state at room temperature.

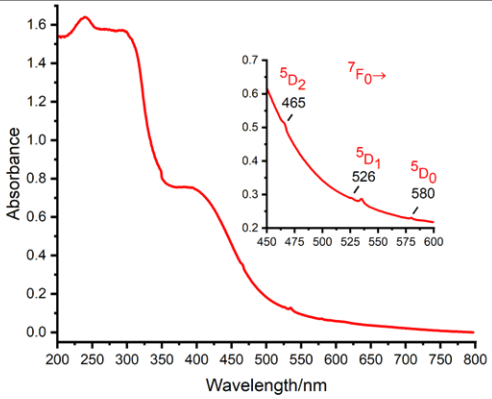

Fig. S13. Absorption spectra of ∞[Eu(3-PyPzH)Cl₃] (**2**) in the solid state at room temperature.

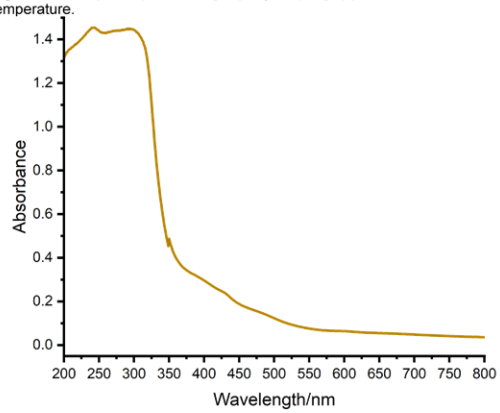

Fig. S14. Absorption spectra of ∞[Gd(3-PyPzH)Cl₃] (**3**) in the solid state at room temperature.

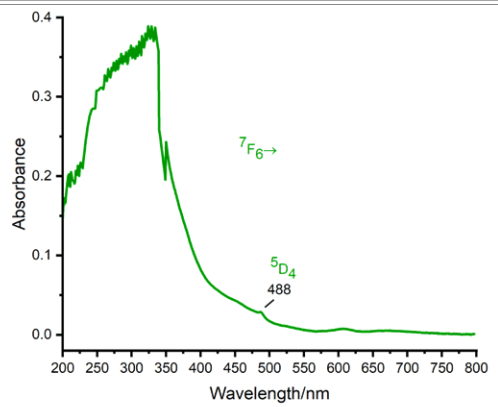

Fig. S15. Absorption spectra of ∞[Tb₂(3-PyPzH)₃Cl₆]·2Tol (**4**) in the solid state at room temperature.

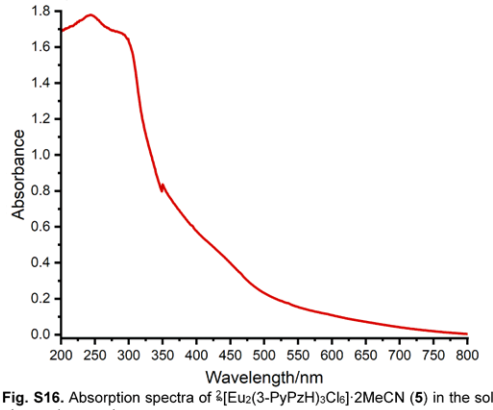

Fig. S16. Absorption spectra of ∞[Eu₂(3-PyPzH)₃Cl₆]·2MeCN (**5**) in the solid state at room temperature.

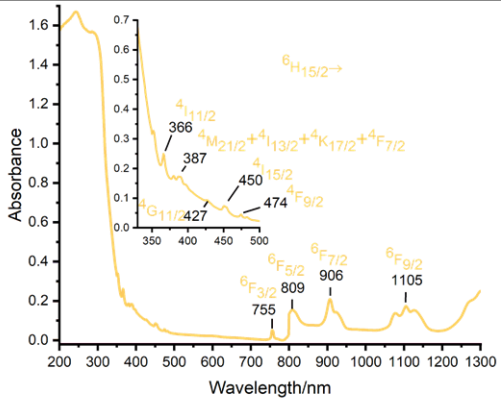

Fig. S17. Absorption spectra of [Dy2(3-PyPzH)3Cl6]·2MeCN (**7**) in the solid state at room temperature.

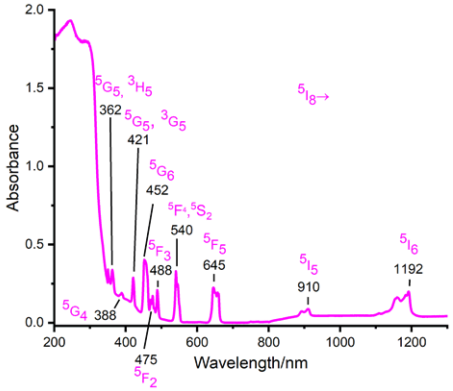

Fig. S18. Absorption spectra of [Ho2(3-PyPzH)3Cl6]·2MeCN (**8**) in the solid state at room temperature.

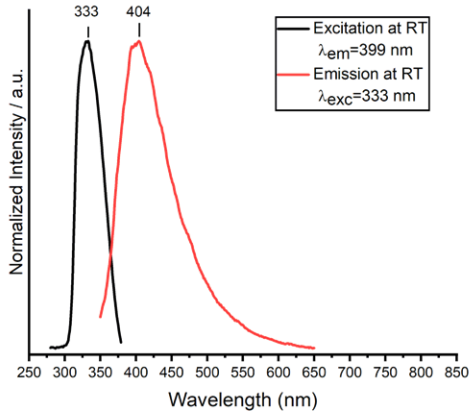

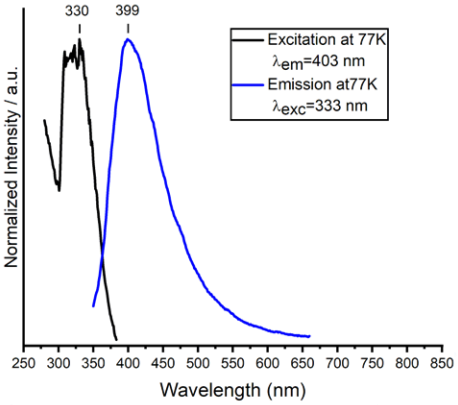

Fig. S21. Normalized excitation and emission spectra of 3-PyPzH at room temperature (top) and 77K (bottom). Wavelengths at which the spectra were recorded are reported in the legends.

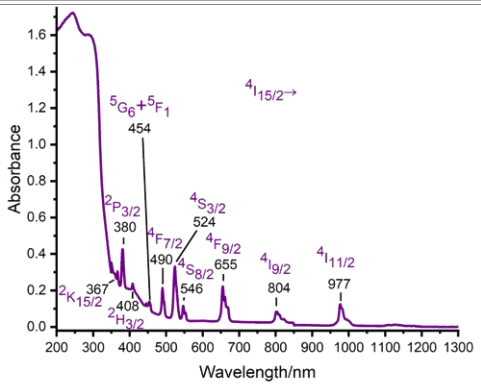

Fig. S19. Absorption spectra of [Er2(3-PyPzH)3Cl6]·2MeCN (**9**) in the solid state at room temperature.

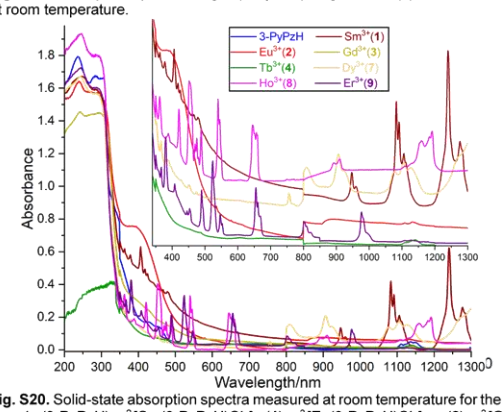

Fig. S20. Solid-state absorption spectra measured at room temperature for the free ligand (3-PyPzH), [Sm(3-PyPzH)Cl3] (**1**), [Eu(3-PyPzH)Cl3] (**2**), [Gd(3-PyPzH)Cl3] (**3**), [Tb2(3-PyPzH)3Cl6]·2Tol (**4**), [Eu2(3-PyPzH)3Cl6]·2MeCN (**5**), [Dy2(3-PyPzH)3Cl6]·2MeCN (**7**), [Ho2(3-PyPzH)3Cl6]·2MeCN (**8**), and [Er2(3-PyPzH)3Cl6]·2MeCN (**9**).

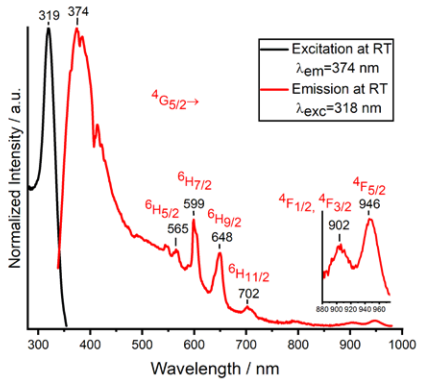

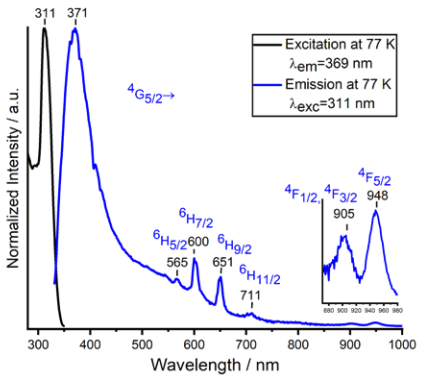

Fig. S22. Normalized excitation and emission spectra of [Sm(3-PyPzH)Cl3] (**1**) at room temperature (top) and 77K (bottom). Wavelengths at which the spectra were recorded are reported in the legends. Visible and NIR range emission spectra were brought to the same intensity at 702 (at RT) and 711 (at 77 K) nm.

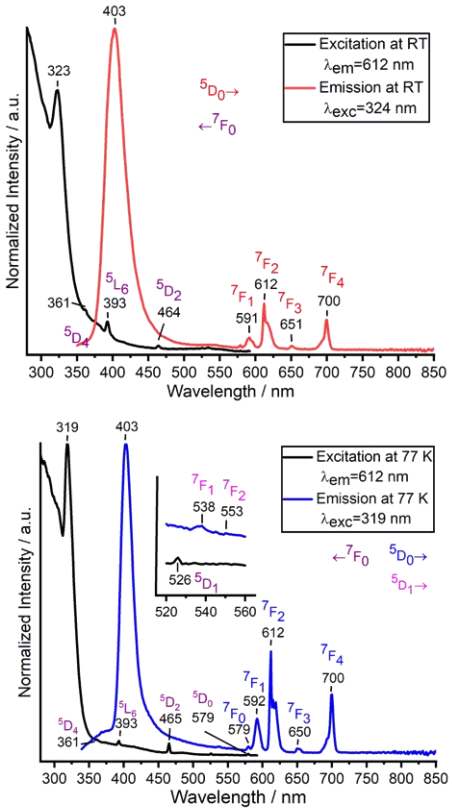

Fig. S23. Normalized excitation and emission spectra of $^{3}_{\infty}$[Eu(3-PyPzH)Cl$_3$] (**2**) at room temperature (top) and 77K (bottom). Wavelengths at which the spectra were recorded are reported in the legends.

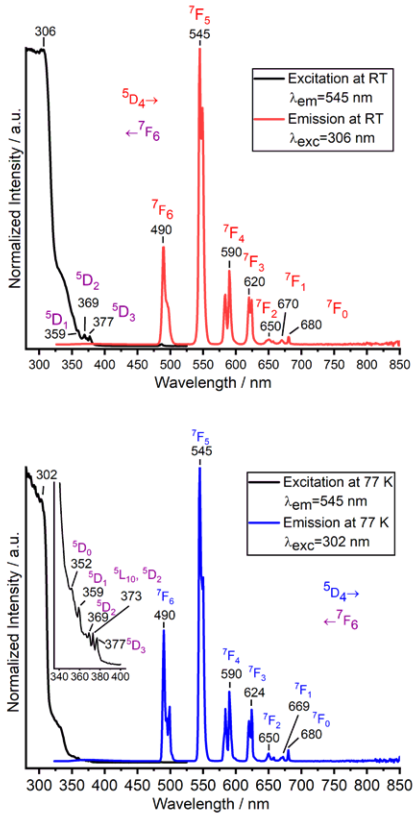

Fig. S25. Normalized excitation and emission spectra of $^{3}_{\infty}$[Tb$_2$(3-PyPzH)$_3$Cl$_6$]·2Tol (**4**) at room temperature (top) and 77K (bottom). Wavelengths at which the spectra were recorded are reported in the legends.

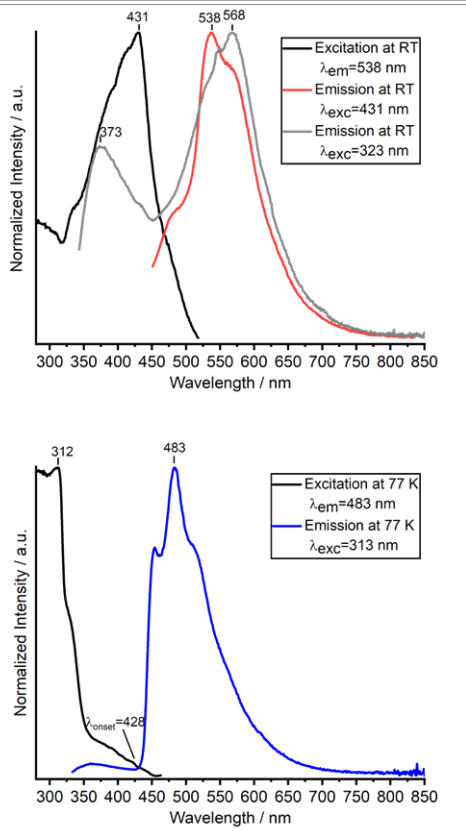

Fig. S24. Normalized excitation and emission spectra of $^{3}_{\infty}$[Gd(3-PyPzH)Cl$_3$] (**3**) at room temperature (top) and 77K (bottom). Wavelengths at which the spectra were recorded are reported in the legends.

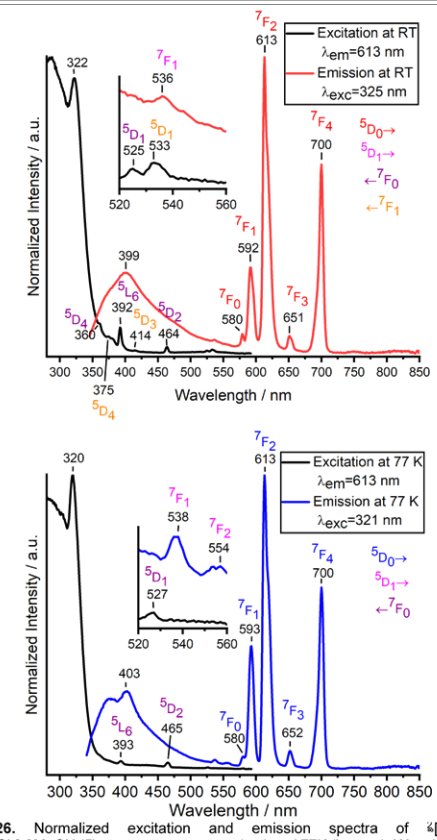

Fig. S26. Normalized excitation and emission spectra of $^{4}_{\infty}$[Eu$_2$(3-PyPzH)$_3$Cl$_6$]·2MeCN (**5**) at room temperature (top) and 77K (bottom). Wavelengths at which the spectra were recorded are reported in the legends.

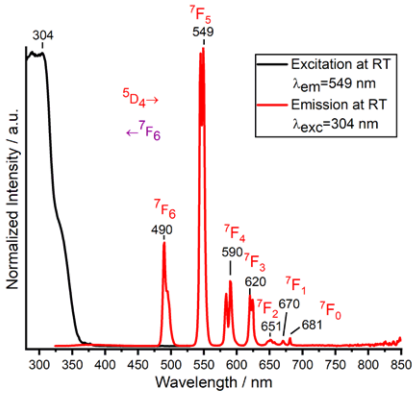

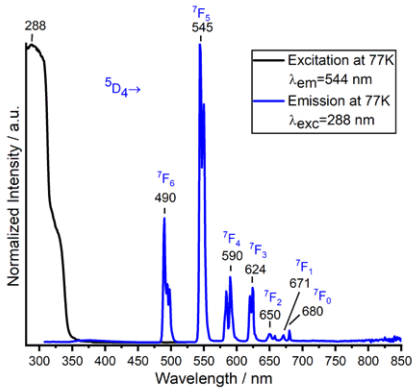

Fig. S27. Normalized excitation and emission spectra of $^{3}_{\infty}$[Tb$_2$(3-PyPzH)$_3$Cl$_8$]·2MeCN (**6**) at room temperature (top) and 77K (bottom). Wavelengths at which the spectra were recorded are reported in the legends.

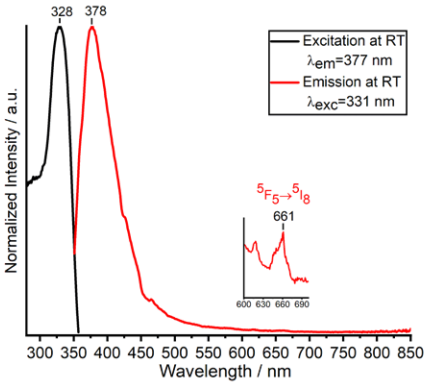

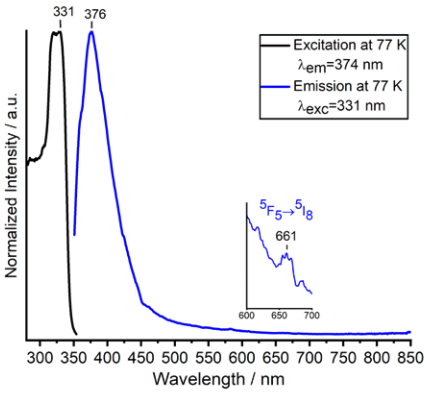

Fig. S29. Normalized excitation and emission spectra of $^{3}_{\infty}$[Ho$_2$(3-PyPzH)$_3$Cl$_8$]·2MeCN (**8**) at room temperature (top) and 77K (bottom). Wavelengths at which the spectra were recorded are reported in the legends.

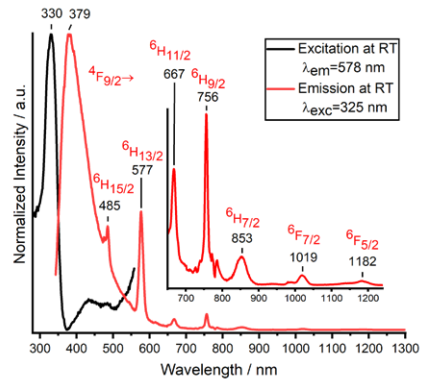

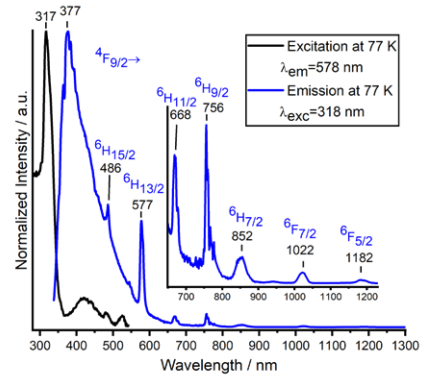

Fig. S28. Normalized excitation and emission spectra of $^{3}_{\infty}$[Dy$_2$(3-PyPzH)$_3$Cl$_8$]·2MeCN (**7**) at room temperature (top) and 77K (bottom). Wavelengths at which the spectra were recorded are reported in the legends. Visible and NIR range emission spectra were brought to the same intensity at 756 nm.

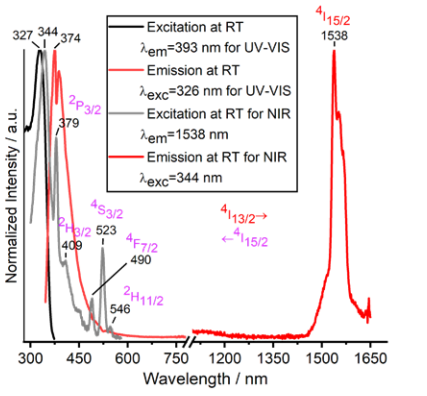

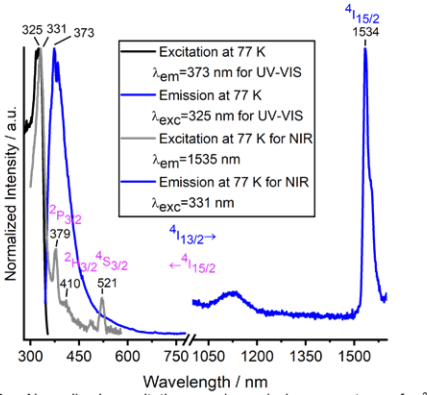

Fig. S30. Normalized excitation and emission spectra of $^{3}_{\infty}$[Er$_2$(3-PyPzH)$_3$Cl$_8$]·2MeCN (**9**) at room temperature (top) and 77K (bottom). Wavelengths at which the spectra were recorded are reported in the legends. Visible and NIR range emission spectra were normalized separately.

Magnetic Susceptibility

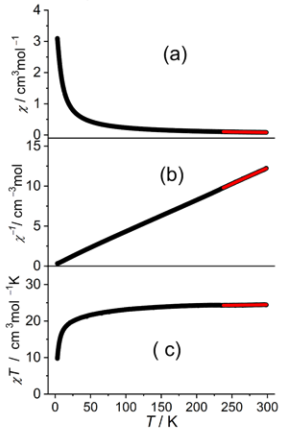

Fig. S31. a-c) Temperature dependency of the magnetic susceptibility of $^{2}_{\infty}$[Ho$_2$(3-PyPzH)$_3$Cl$_6$]·2MeCN (**8**) in a temperature range from 3 to 300 K and magnetic field 1T: a) χ vs T, b) χ^{-1} vs T , c) χT vs T. The solid red line represents the best fitting curve.

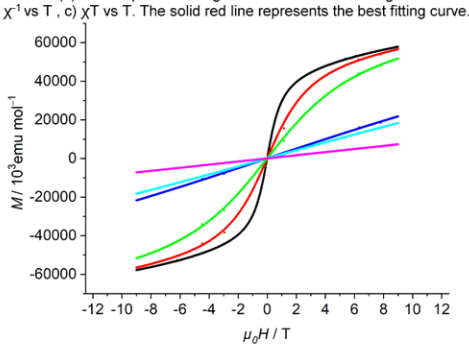

Fig. S32. Field-dependent measurement for $^{2}_{\infty}$[Ho$_2$(3-PyPzH)$_3$Cl$_6$]·2MeCN (**8**).

Thermal Analysis

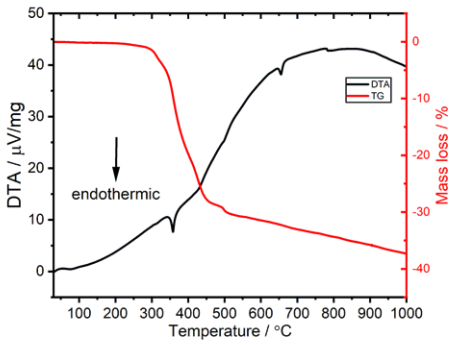

Fig. S33. Simultaneous DTA-TG analysis of $^{2}_{\infty}$[Sm(3-PyPzH)Cl$_3$] (**1**) representing the DTA curve without a baseline correction. The measurement was performed in a constant argon flow of 50 ml·min^{-1} with a heating rate of 5 K·min^{-1} from room temperature to 1000 °C.

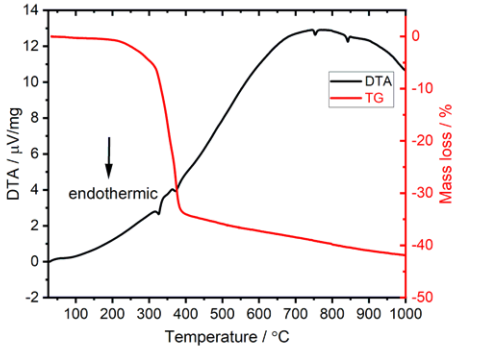

Fig. S34. Simultaneous DTA-TG analysis of $^{3}_{\infty}$[Eu(3-PyPzH)Cl$_3$] (**2**) representing the DTA curve without a baseline correction. The measurement was performed in a constant argon flow of 50 ml·min^{-1} with a heating rate of 5 K·min^{-1} from room temperature to 1000 °C.

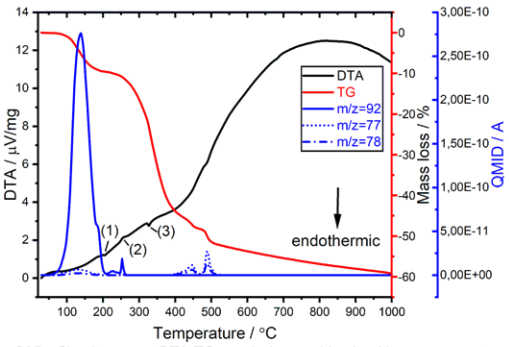

Fig. S35. Simultaneous DTA-TG analysis combined with mass spectrometry for $^{2}_{\infty}$[Tb$_2$(3-PyPzH)$_3$Cl$_6$]·2Tol (**4**) representing the DTA curve without a baseline correction. The measurement was performed in a constant argon flow of 50 ml·min^{-1} with a heating rate of 5 K·min^{-1} from room temperature to 1000 °C.

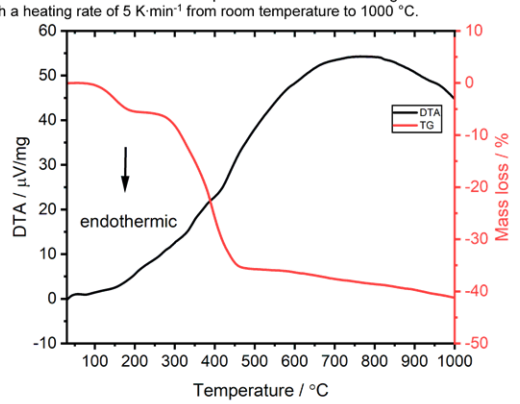

Fig. S36. Simultaneous DTA-TG analysis combined with mass spectrometry for $^{2}_{\infty}$[Ho$_2$(3-PyPzH)$_3$Cl$_6$]·2MeCN (**8**) representing the DTA curve without a baseline correction. The measurement was performed in a constant argon flow of 50 ml·min^{-1} with a heating rate of 5 K·min^{-1} from room temperature to 1000 °C.

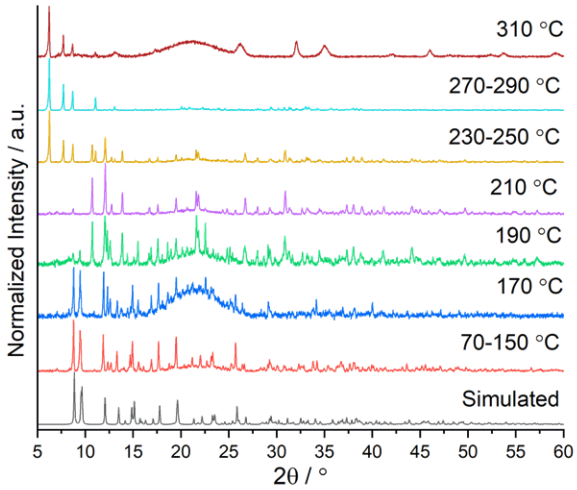

Fig. S37. Comparison of the experimental X-ray powder diffraction pattern at different temperatures from 70-310 °C of $^{2}_{\infty}$[Tb(3-PyPzH$_2$)Cl$_4$]·2Tol (**4**), with a simulated pattern from single-crystal X-ray data.

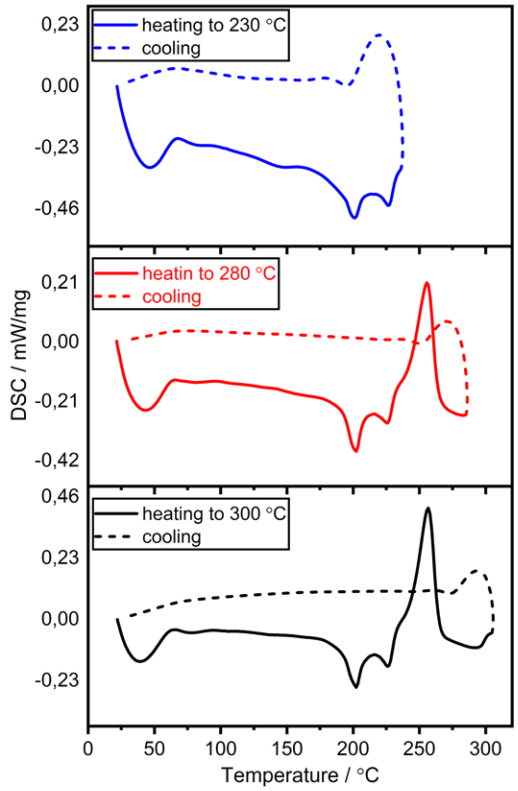

Fig. S38. Three DSC measurements of $^{2}_{\infty}$[Tb$_2$(3-PyPzH)$_3$Cl$_6$]·2Tol (**4**) with a heating and cooling rate of 5 K·min^{-1} in a temperature range from RT to 300 °C (bottom), 280 °C (middle) and 230 °C (top). The measurement was performed in a constant argon flow of 50 mL·min^{-1}.

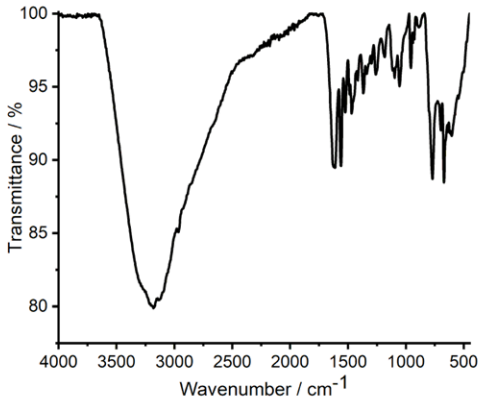

Fig. S41. The infrared spectrum (ATR) of coordination polymer $^{3}_{\infty}$[Gd(3-PyPzH)Cl$_3$] (**3**).

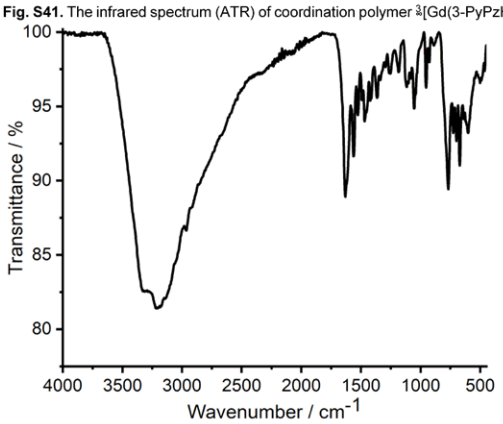

Fig. S42. The infrared spectrum (ATR) of coordination polymer $^{2}_{\infty}$[Tb$_2$(3-PyPzH)$_3$Cl$_6$]·2Tol (**4**).

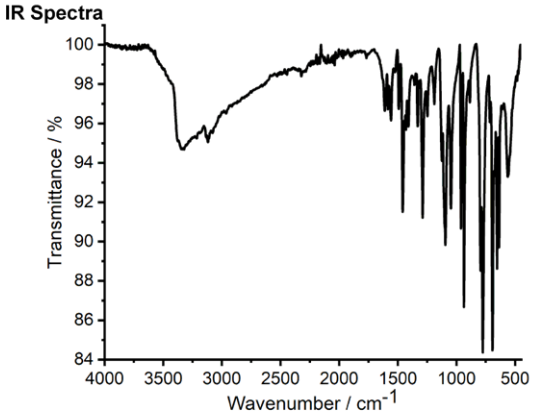

Fig. S39. The infrared spectrum (ATR) of coordination polymer $^{2}_{\infty}$[Sm(3-PyPzH)Cl$_3$] (**1**).

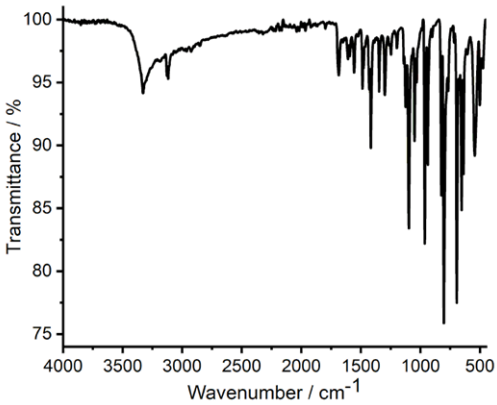

Fig. S40. The infrared spectrum (ATR) of coordination polymer $^{3}_{\infty}$[Eu(3-PyPzH)Cl$_3$] (**2**).

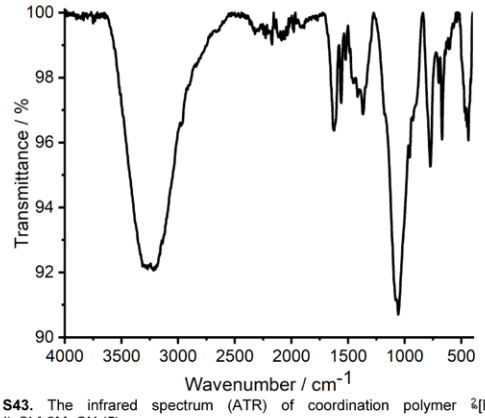

Fig. S43. The infrared spectrum (ATR) of coordination polymer $^{2}_{\infty}$[Eu$_2$(3-PyPzH)$_3$Cl$_6$]·2MeCN (**5**).

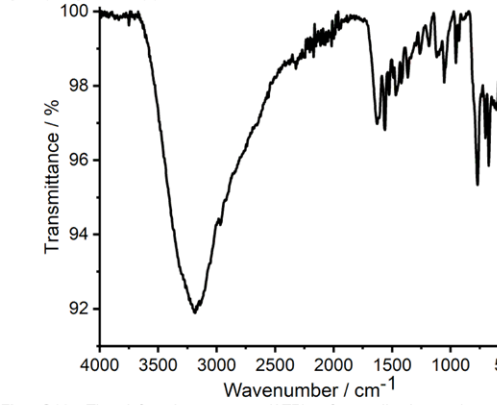

Fig. S44. The infrared spectrum (ATR) of coordination polymer $^{2}_{\infty}$[Tb$_2$(3-PyPzH)$_3$Cl$_6$]·2MeCN (**6**).

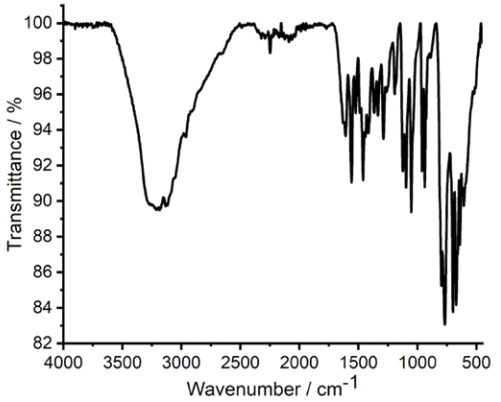

Fig. S45. The infrared spectrum (ATR) of coordination polymer $^{2}_{\infty}$[Dy_2(3-PyPzH)$_3Cl_6$]·2MeCN (**7**).

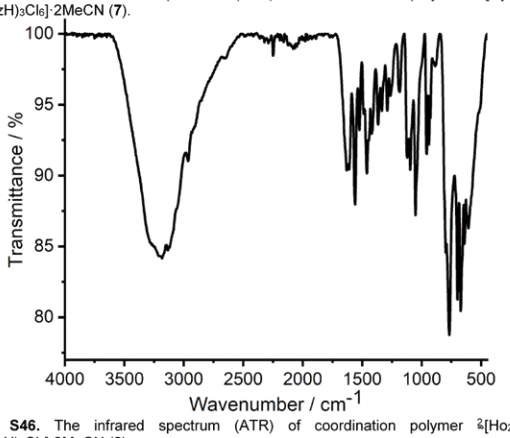

Fig. S46. The infrared spectrum (ATR) of coordination polymer $^{2}_{\infty}$[Ho_2(3-PyPzH)$_3Cl_6$]·2MeCN (**8**).

S41

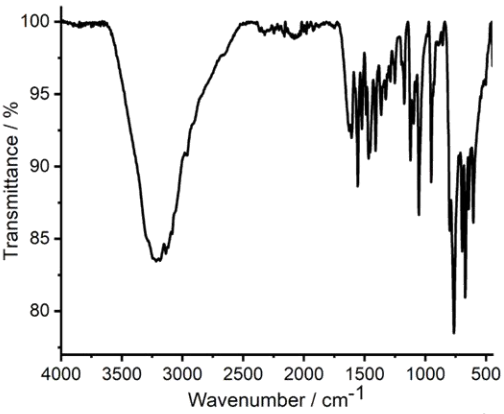

Fig. S47. The infrared spectrum (ATR) of coordination polymer $^{2}_{\infty}$[Er_2(3-PyPzH)$_3Cl_6$]·2MeCN (**9**).

S42

3.2.2. 3-(2-Pyridyl)pyrazole based luminescent 1D-coordination polymers and polymorphic complexes of various lanthanide chlorides including orange-emitting cerium(III)

This article has been published in the

Journal Inorganics

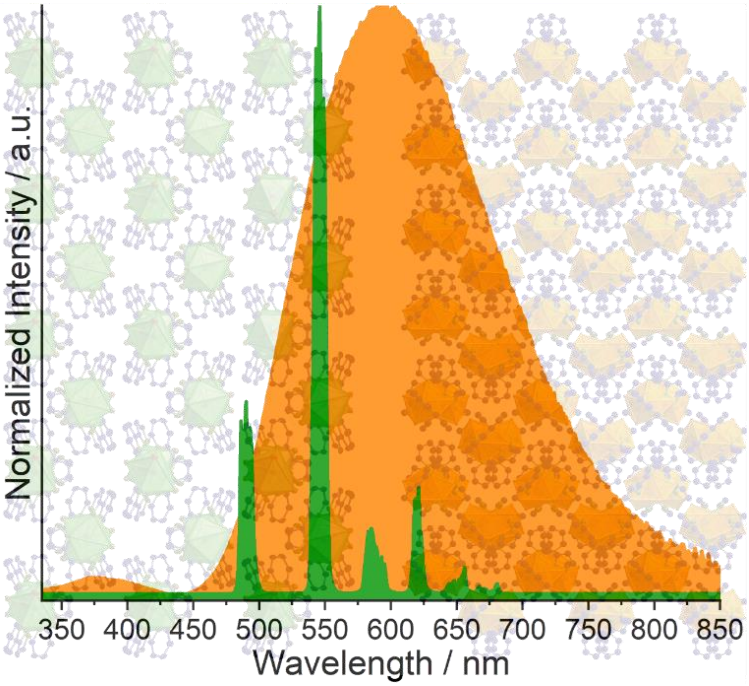

Heba Youssef, Alexander E. Sedykh, Jonathan Becker, Ilya V. Taydakov, and Klaus Müller-Buschbaum

Reprinted with permission from *Inorganics* **2022**, *10*, 254–275.

DOI 10.3390/inorganics10120254

inorganics

MDPI

Article

3–(2–Pyridyl)pyrazole Based Luminescent 1D-Coordination Polymers and Polymorphic Complexes of Various Lanthanide Chlorides Including Orange-Emitting Cerium(III)

Heba Youssef [1,2], Alexander E. Sedykh [1], Jonathan Becker [1], Ilya V. Taydakov [3] and Klaus Müller-Buschbaum [1,4,*]

[1] Institute of Inorganic and Analytical Chemistry, Justus–Liebig–University Giessen, Heinrich–Buff–Ring 17, 35392 Giessen, Germany
[2] Department of Chemistry, Faculty of Science, Mansoura University, El Gomhouria, Mansoura Qism 2, Dakahlia Governorate, Mansoura 11432, Egypt
[3] Lebedev Physical Institute of the Russian Academy of Sciences, Leninskiy pr–t, 53, 119991 Moscow, Russia
[4] Center of Materials Research (LAMA), Justus–Liebig–University Giessen, Heinrich–Buff–Ring 16, 35392 Giessen, Germany
* Correspondence: klaus.mueller-buschbaum@anorg.chemie.uni-giessen.de

Abstract: A series of 18 lanthanide-containing 1D-coordination polymers $^1{}_\infty[Ln_2(2–PyPzH)_4Cl_6]$, Ln = La, Nd, Sm, dinuclear polymorphic complexes α–, β–$[Ln_2(2–PyPzH)_4Cl_6]$, Ln = Sm, Eu, Gd, α–$[Tb_2(2–PyPzH)_4Cl_6]$, and $[Gd_2(2–PyPzH)_3(2–PyPz)Cl_5]$, mononuclear complexes $[Ce(2–PyPzH)_3Cl_3]$, $[Ln(2–PyPzH)_2Cl_3]$, Ln = Tb, Dy, Ho, and Er, and salt-like complexes $[Gd_3(2–PyPzH)_8Cl_8]Cl$ and $[PyH][Tb(2–PyPzH)_2Cl_4]$ were obtained from the reaction of the respective lanthanide chloride with the 3–(2–pyridyl)pyrazole (2–PyPzH) ligand at different temperatures. An antenna effect through ligand-to-metal energy transfer was observed for several products, leading to the highest luminescence efficiency displayed by a quantum yield of 92% in $[Tb(2–PyPzH)_2Cl_3]$. The Ce^{3+} ion in the complex $[Ce(2–PyPzH)_3Cl_3]$ exhibits a bright and orange 5d-based broadband emission with a maximum at around 600 nm, marking an example of a strong reduction of the 5d-excited states of Ce(III). The absorption spectroscopy shows ion-specific 4f–4f transitions, which can be assigned to Nd^{3+}, Sm^{3+}, Eu^{3+}, Dy^{3+}, Ho^{3+}, and Er^{3+} in a wide spectral range from UV–VIS to the NIR region.

Keywords: N-donor ligand; luminescence; polymorphism; cerium; lanthanides

Citation: Youssef, H.; Sedykh, A.E.; Becker, J.; Taydakov, I.V.; Müller-Buschbaum, K. 3–(2–Pyridyl)pyrazole Based Luminescent 1D-Coordination Polymers and Polymorphic Complexes of Various Lanthanide Chlorides Including Orange-Emitting Cerium(III). *Inorganics* **2022**, *10*, 254. https://doi.org/10.3390/inorganics10120254

Academic Editor: László Kótai

Received: 11 October 2022
Accepted: 8 December 2022
Published: 10 December 2022

1. Introduction

The coordination polymers (CPs) and complexes of lanthanides with N-donor ligands have been the focus of research efforts in recent decades [1–5]. Their hybrid nature results in distinctive photoluminescence (PL) properties [6–9] alongside a wide variety of other features and properties [10–13]. The PL of the lanthanide ions is mainly based on two types of transitions: 4f–4f or 5d–4f transitions [14]. In general, the emission intensity of 5d–4f transitions is often strong due to their allowed character, resulting in short excited-state lifetimes (<100 ns) [15–19]. The luminescence colors of these lanthanide ions, such as Eu^{2+}, Ce^{3+}, Sm^{2+}, etc., can vary upon the coordination environment due to the influence of the crystal field on the outermost 5d electron shell [20–23]. In contrast, spin-forbidden 4f–4f transitions (lifetimes up to the ms range) [24] with intrinsically low absorption coefficients have the 4f electron shell regularly shielded by the 5d electron shell, and the characteristic emission of these ions are therefore almost independent of the chemical surrounding, as observed in Tb^{3+}, Eu^{3+}, Dy^{3+}, Ho^{3+}, etc., [25]. A key factor is a proper ligand selection to sensitize the Ln^{3+} ion by ligand-to-metal energy transfer [26]. The organic ligand should also possess appropriate energy-donating states for efficient energy transfer [27].

Recently, the investigation and determination of the luminescence properties of Ce^{3+}-based CPs and complexes have increasingly become the focus of scientific interest after several reports in the literature of non-emissive Ce^{3+}-based compounds due to luminescence quenching by linkers and/or solvent molecules [28]. The reported Ce^{3+}-centered luminescence is mainly in the near UV and blue region [22,29,30]. Recently, the green/yellow [31–34] or even the unusual yellow emission [35] of some Ce^{3+}-based doped materials as well as the red emission of Ce/Pr systems and their application in solid-state LEDs have been reported [36–40].

Since 3–(3–pyridyl)pyrazole (3–PyPzH) and 3–(4–pyridyl)pyrazole (4–PyPzH) ligands have recently been used to obtain homoleptic and highly luminescent trivalent lanthanide 3D-CPs with the formula $^{3}_{\infty}$[Ln(3–PyPz)$_3$] and $^{3}_{\infty}$[Ln(4–PyPz)$_3$], Ln = Sm, Eu, Gd, Tb, Dy [7]. In addition, 3–PyPzH has been further used to obtain a variety of 3D-frameworks and 2D-networks as well as complexes of Ln-trichlorides differing in constitution and structure: $^{3}_{\infty}$[Ln(3–PyPzH)Cl$_3$], Ln = Eu, Gd, $^{2}_{\infty}$[Sm(3–PyPzH)Cl$_3$], $^{2}_{\infty}$[Tb$_2$(3–PyPzH)$_3$Cl$_6$]·2Tol, $^{2}_{\infty}$[Ln$_2$(3–PyPzH)$_3$Cl$_6$]·2MeCN, Ln = Eu^{3+}, Tb^{3+}, Dy^{3+}, Ho^{3+}, Er^{3+}, $^{2}_{\infty}$[Ln(3–PyPzH$_2$)Cl$_4$], Ln = La, Nd, and [(3–PyPzH$_2$)][Ln(3–PyPzH)$_2$Cl$_4$], Ln = Eu, Tb, Dy, Ho [2]. An antenna effect through ligand-to-metal energy transfer was observed for several products for both ligands, resulting in the highest luminescence efficiency for Tb^{3+}-based compounds, indicated by quantum yield reaching 76%. The reported results indicate the value of exploring new N-donor-based ligands and coordination compounds to achieve a wide variety of structures and PL for the lanthanides. Consequently, the objective of our work was the synthesis of new CPs and complexes along the lanthanide series with the tridentate ligand 3–(2–pyridyl)pyrazole (2–PyPzH) to develop a better understanding of the photophysical and thermal properties observed for the Ln series, as well as investigating the polymorphism, the ability of a pure compound to adopt more than one packing arrangement in the solid-state [41,42], of the studied compounds.

The highlight of this work is the strong bathochromic shift of the Ce^{3+}-based emission towards the red region of the visible spectrum and the high luminescence efficiency for the Tb^{3+} complex, reaching 92%.

2. Results and Discussion

2.1. Synthesis and Structural Analysis

Solvothermal syntheses of 3–(2–pyridyl)pyrazole (2–PyPzH) with anhydrous lanthanide trichlorides in either acetonitrile (MeCN), toluene (Tol), or pyridine (Py) were implemented to obtain a family of 18 CPs and complexes as shown in Scheme 1.

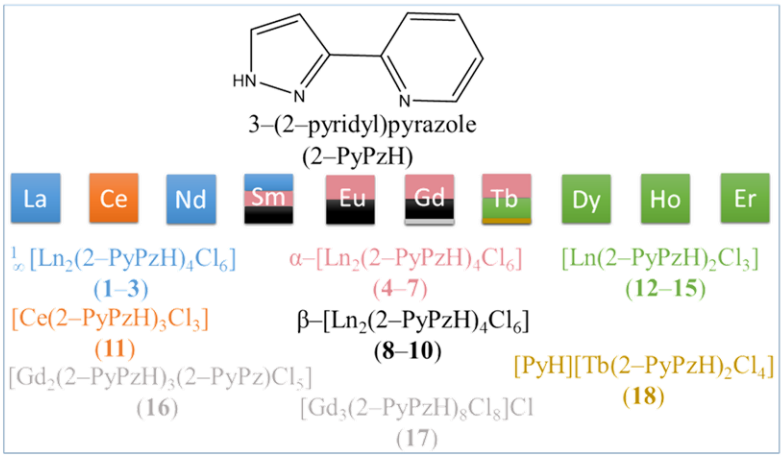

Scheme 1. Structural diversity and polymorphism of the products from the reactions of respective anhydrous $LnCl_3$ with 2–PyPzH. The color changes indicate a different crystal structure.

The structures of $^{1}_{\infty}[Ln_2(2–PyPzH)_4Cl_6]$, Ln = La (**1**), Nd (**2**), Sm (**3**), α–$[Ln_2(2–PyPzH)_4Cl_6]$, Ln = Eu (**5**), Gd (**6**), Tb (**7**), β–$[Ln_2(2–PyPzH)_4Cl_6]$, Ln = Sm (**8**), Eu (**9**), Gd (**10**), $[Ce(2–PyPzH)_3Cl_3]$ (**11**), $[Ln(2–PyPzH)_2Cl_3]$, Ln = Tb (**12**), Dy (**13**), Ho (**14**), Er (**15**), $[Gd_2(2–PyPzH)_3(2–PyPz)Cl_5]$ (**16**), $[Gd_3(2–PyPzH)_8Cl_8]Cl$ (**17**), and [PyH][Tb(2–PyPzH)$_2$Cl$_4$] (**18**) were determined by single crystal X-ray diffraction (SCXRD), whereas the structure of α–$[Sm_2(2–PyPzH)_4Cl_6]$ (**4**) was identified from microcrystalline product by powder X-ray diffraction (PXRD).

$^{1}_{\infty}[Ln_2(2–PyPzH)_4Cl_6]$, Ln = La (**1**), Nd (**2**), Sm (**3**), α–$[Ln_2(2–PyPzH)_4Cl_6]$, Ln = Sm (**4**), Eu (**5**), Gd (**6**), Tb (**7**), and $[Ln(2–PyPzH)_2Cl_3]$, Ln = Tb (**12**), Dy (**13**), Ho (**14**), Er (**15**) crystallize in the monoclinic crystal system with the space group $C2/c$ for **1–3** and $P2_1/c$ for **4–7** and **12–15**. $[Ce(2–PyPzH)_3Cl_3]$ (**11**) crystallizes in the orthorhombic crystal system of higher symmetry with the space group *Pbca*, while the β–$[Ln_2(2–PyPzH)_4Cl_6]$, Ln = Sm (**8**), Eu (**9**), and Gd (**10**) crystallizes in the triclinic crystal system with the space group $P\bar{1}$.

In $^{1}_{\infty}[Ln_2(2–PyPzH)_4Cl_6]$ (**1–3**), α–$[Ln_2(2–PyPzH)_4Cl_6]$ (**4–7**), and β–$[Ln_2(2–PyPzH)_4Cl_6]$ (**8–10**), each Ln^{3+} ion coordinates to four Cl^- ligands and four nitrogen atoms in a distorted triangular dodecahedral geometry. In **1–3**, a chlorine atom acts as a bridge between two adjacent Ln^{3+} ions to form a 1D-coordination polymer (Figure 1), while two chlorine atoms bridge the two Ln^{3+} ions in the dimeric complexes **4–10** (Figures 2 and S1). For the monomer complexes, the Ce^{3+} in $[Ce(2–PyPzH)_3Cl_3]$ (**11**) has a CN of nine coordinated by three chlorides and six nitrogen atoms of three 2–PyPzH ligands in a distorted tricapped trigonal prismatic geometry (Figure 3), while the Ln^{3+} in $[Ln(2–PyPzH)_2Cl_3]$ (**12–15**) has a CN of seven and is coordinated by three chloride ions and four nitrogen atoms of two 2–PyPzH ligands in a distorted capped trigonal prism (Figure 4). The differences in the orientation and position of the atoms between the polymorphs α–$[Ln_2(2–PyPzH)_4Cl_6]$ (**5**, **6**) and β–$[Ln_2(2–PyPzH)_4Cl_6]$ (**9, 10**) are minor when the two structures are overlaid (Figure S2). The α phase (higher crystallographic symmetry) is about 1.2% more densely packed than the β phase, resulting in a slightly shorter metal–metal distance (443.3(1) in **5** and 447.6(1) pm in **9**).

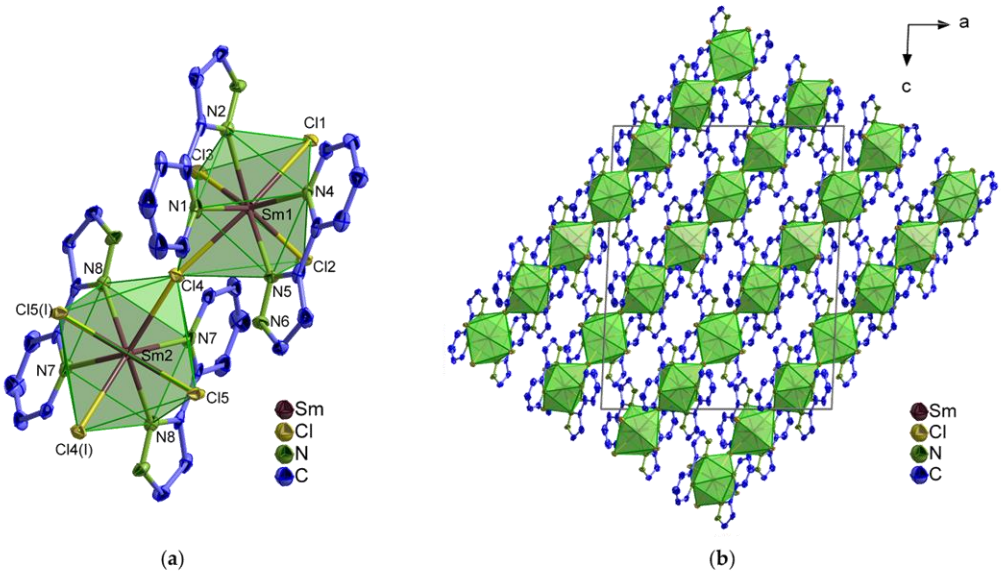

(**a**) (**b**)

Figure 1. (**a**) Extended coordination sphere of the Sm^{3+} ion in $^{1}_{\infty}[Sm_2(2–PyPzH)_4Cl_6]$ (**3**) representing the isotypic compounds **1–3**.; (**b**) crystal structure of **3** with a view along [010]. Symmetry operation: I −x+1,y,−z+1/2. In all figures, the hydrogen atoms are omitted for clarity and the coordination polyhedra around Ln^{3+} are shown in green, with thermal ellipsoids shown with a probability of 50%.

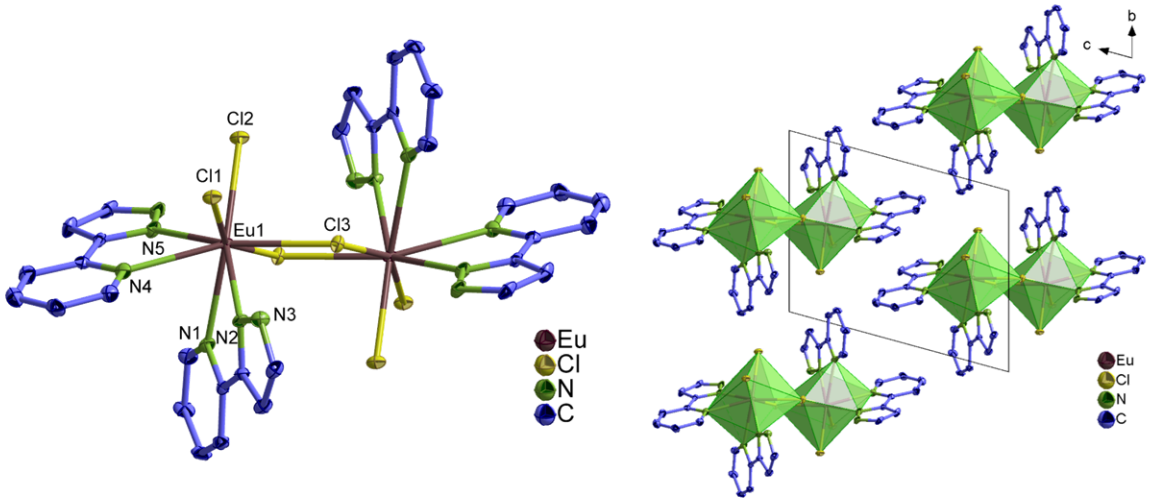

(**a**) (**b**)

Figure 2. (**a**) Extended coordination sphere of the Eu^{3+} ion in β–$[Eu_2(2–PyPzH)_4Cl_6]$ (**9**) representing the isotypic compounds **8**–**10**.; (**b**) crystal structure of **9** with a view along [100].

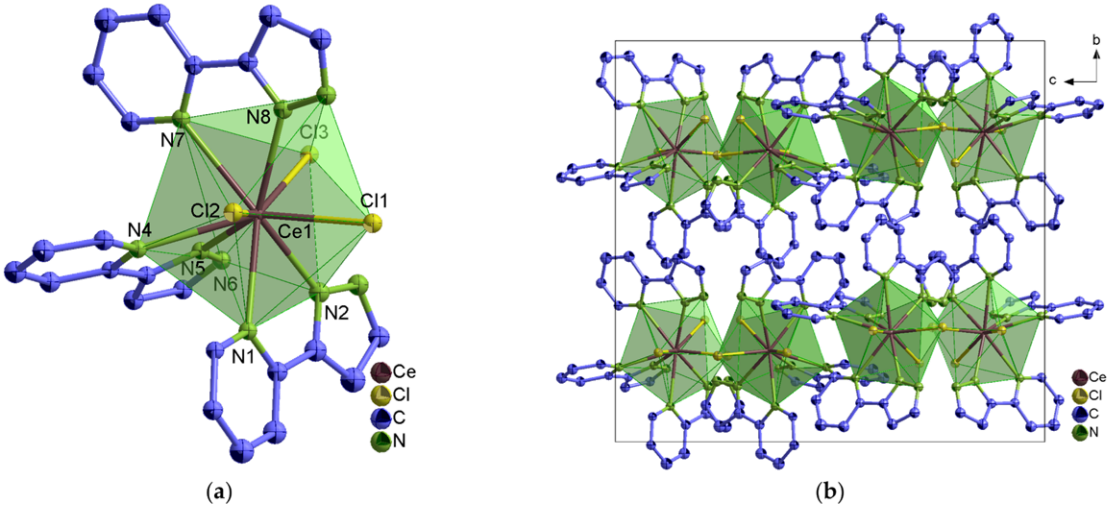

(**a**) (**b**)

Figure 3. (**a**) Extended coordination sphere of the Ce^{3+} ion in $[Ce(2–PyPzH)_3Cl_3]$ (**11**).; (**b**) crystal structure of **11** with a view along [100].

The Ln–N and Ln–Cl distances of the studied compounds agree with the expected range for the trivalent Ln ions in halides [43,44]. A comparison of the interatomic distances of β–$[Sm_2(2–PyPzH)_4Cl_6]$ (**9**) (average Sm–N 258.3 and Sm–Cl 269.2(1)–277.6(1) pm) with the structurally related complex $[Sm(\mu–Cl)_2Cl_4(phen)_4]\cdot 2CH_3OH$, (phen = 1,10–phenanthroline, average Sm–N 258.4 and Sm–Cl 269.1–281.8 pm) [45] resulted in a good agreement for both distances.

A further comparison of $[Ce(2–PyPzH)_3Cl_3]$ (**11**) (average Ce–N 270.2 and Ce–Cl 279.7(2)–283.2(1) pm) with the $[CeL]Cl_3\cdot 4H_2O$, (L = a chiral macrocyclic ligand derived from (1*R*,2*R*)–1,2–diphenylethylenediamine and 2,6–diformylpyridine, average Ce–N 273.42 and Ce–Cl 280.0–285.5 pm) [46] resulted in a good agreement for both distances. A further comparison of $[Tb(2–PyPzH)_2Cl_3]$ (**12**) (Tb–N(py) 255.9(4), 256.7(4), Tb–Cl 262.2(2) –267.3(2) pm) with the $[Ln_2Cl_6(\mu–4,4'–bipy)(py)_6]$, (bipy = 4,4′–bipyridine, py = pyridine, Tb–N 254.0–259.3, Tb–Cl 261.68–266.44 pm) [47] shows as well a good agreement for both distances.

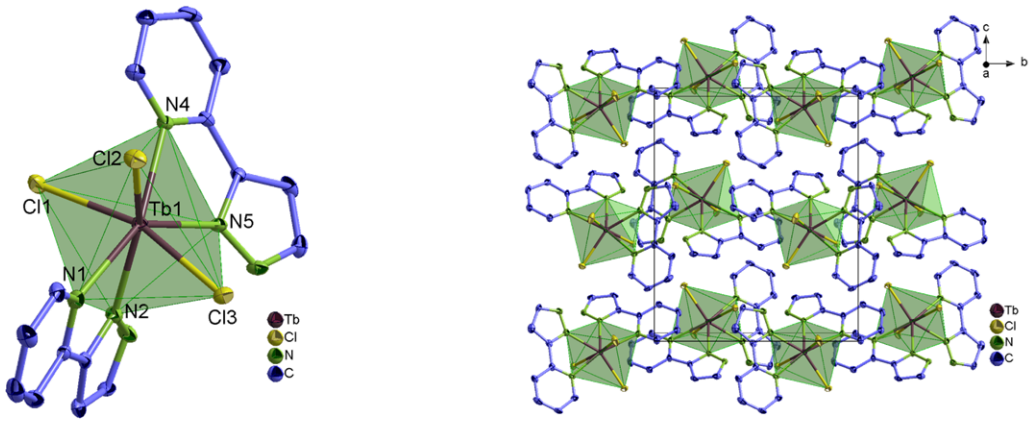

(**a**) (**b**)

Figure 4. (**a**) Extended coordination sphere of the Tb^{3+} ion in $[Tb(2–PyPzH)_2Cl_3]$ (**12**) representing the isotypic complexes **12**–**15**.; (**b**) packing structure of **12** with a view along [100].

Another three complexes of the formula, $[Gd_2(2–PyPzH)_3(2–PyPz)Cl_5]$ (**16**), $[Gd_3(2–PyPzH)_8Cl_8]Cl$ (**17**), and $[PyH][Tb(2–PyPzH)_2Cl_4]$ (**18**), are formed as byproducts and crystallize in the monoclinic, triclinic, and orthorhombic crystal systems with the space groups $P2_1/n$, $P\bar{1}$, and *Pbcn*, respectively. In $[Gd_2(2–PyPzH)_3(2–PyPz)Cl_5]$ (**16**) (Figure S3), both Gd^{3+} are octa-coordinated; one is coordinated to four chlorides and four nitrogen atoms of a 2–PyPzH and a deprotonated $2–PyPz^-$ in a distorted bicapped trigonal prism environment. Two chlorine atoms along with the $2–PyPz^-$ act as a bridge to the second Gd^{3+} ion, which coordinates to another four nitrogen atoms of two 2–PyPzH and a chloride ion in a distorted triangular dodecahedron. For the anionic complex $[Gd_3(2–PyPzH)_8Cl_8]Cl$ (**17**) (Figure S4), all three Gd^{3+} ions are octa-coordinated, forming distorted triangular dodecahedral polyhedra, with two Gd^{3+} ions coordinated to two Cl^- ligands and six nitrogen atoms of three 2–PyPzH. The third Gd^{3+} ion coordinates to four chloride ions and four nitrogen atoms of two 2–PyPzH. Electroneutrality is established by the existence of an uncoordinated chloride ion. For $[PyH][Tb(2–PyPzH)_2Cl_4]$ (**18**) (Figure S5), another distorted triangular dodecahedral polyhedron is formed due to the coordination of the Tb^{3+} ion to four Cl^- ligands and four nitrogen atoms of two 2–PyPzH. Electroneutrality is achieved through the formation of protonated pyridine.

The obtained bulk of the 1D-CPs (**1**–**3**) and the complexes (**4**–**6**, **8**, **9**, **11**–**15**) were investigated by PXRD. The experimental diffraction patterns of the studied compounds agree well with the corresponding diffraction patterns simulated from single crystal data in terms of reflection positions and intensities (Figures 5 and S6–S9). Additional Pawley refinements for **8** and **11** were carried out, confirming the phase purity of the investigated compounds (Figure S10). β–$[Gd_2(2–PyPzH)_4Cl_6]$ (**10**) is formed at higher temperatures in a mixture together with the α–Gd^{3+} phase (**6**) (Figure S11). Isolation of α–$[Tb_2(2–PyPzH)_4Cl_6]$ (**7**), $[Gd_2(2–PyPzH)_3(2–PyPz)Cl_5]$ (**16**), $[Gd_3(2–PyPzH)_8Cl_8]Cl$ (**17**), and $[PyH][Tb(2–PyPzH)_2Cl_4]$ (**18**) as single crystals was also possible. Tables with detailed crystallographic data and selected interatomic distances (pm) and angles (○) of the studied compounds are given in the Supplementary Materials (Tables S1–S13).

2.2. Photophysical Properties

2.2.1. UV–VIS–NIR Absorption Spectra

Electronic absorption spectra were recorded in the solid state at room temperature (RT) along with emission and excitation spectra to allow for detailed spectroscopic interpretations for $^1{}_\infty[Ln_2(2–PyPzH)_4Cl_6]$, Ln = La (**1**), Nd (**2**), Sm (**3**), α–$[Ln_2(2–PyPzH)_4Cl_6]$, Ln = Eu (**5**), Gd (**6**), β–$[Ln_2(2–PyPzH)_4Cl_6]$, Ln = Sm (**8**), Eu (**9**), $[Ce(2–PyPzH)_3Cl_3]$ (**11**), and $[Ln(2–PyPzH)_2Cl_3]$, Ln = Tb (**12**), Dy (**13**), Ho (**14**), Er (**15**). In the literature, the absorp-

tion spectra have mostly been measured in solution, examining the ligand-based absorption band [48–50], while fewer examples have examined the Ln-based absorption bands in the solid state [2,51–54].

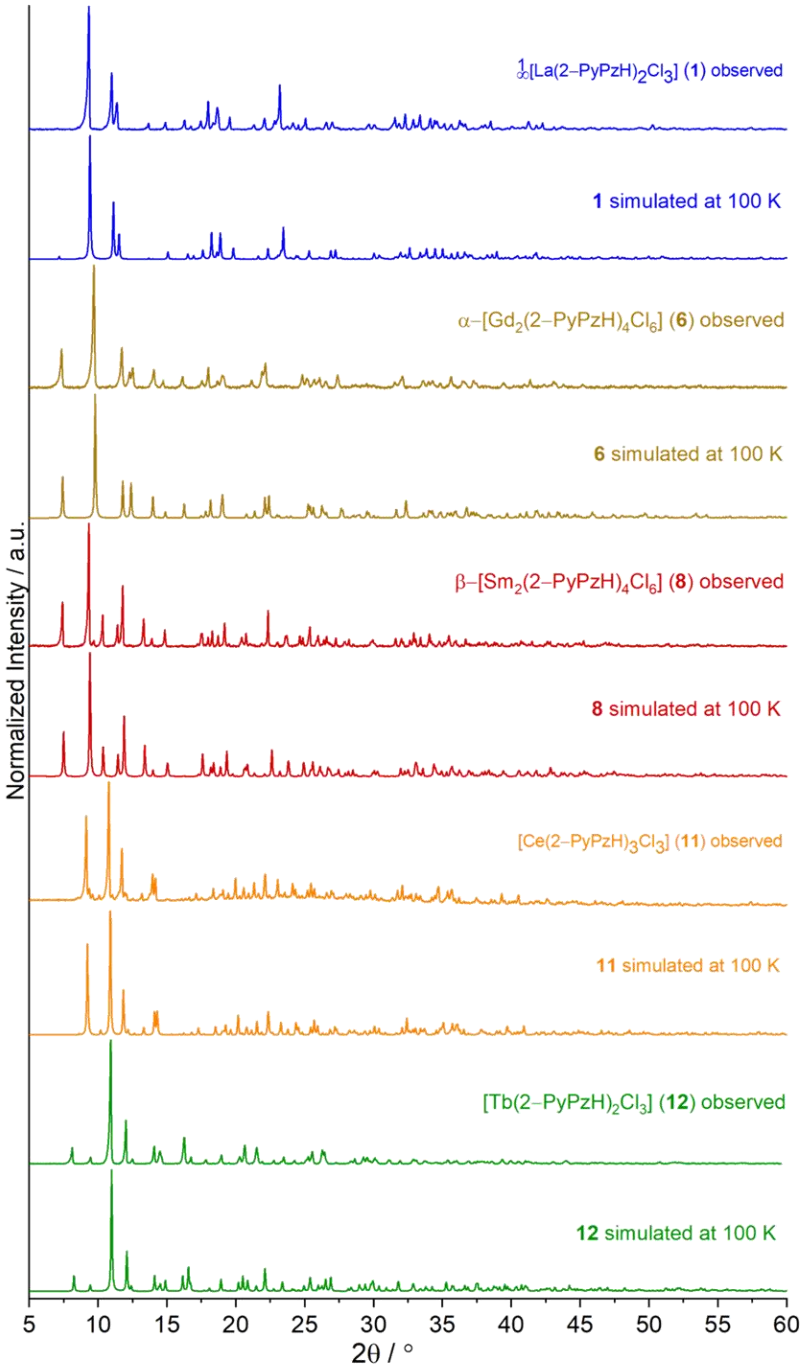

Figure 5. Comparison of exemplary experimental powder X-ray diffraction patterns of $^1_\infty$[La$_2$(2–PyPzH)$_4$Cl$_6$] (**1**), α–[Gd$_2$(2–PyPzH)$_4$Cl$_6$] (**6**), β–[Sm$_2$(2–PyPzH)$_4$Cl$_6$] (**8**), [Ce(2–PyPzH)$_3$Cl$_3$] (**11**), and [Tb(2–PyPzH)$_2$Cl$_3$] (**12**) as representatives of their isotypic 1D-CPs and complexes with the respective simulated pattern from single crystal X-ray data.

The absorption spectrum for 2–PyPzH (Figure S12) was as reported in the literature for the solid state and in acetonitrile solution (7.8×10^{-5} mol L^{-1}), with two characteristic K-band (*ca.* 210~265 nm) and B-band regions (285~350 nm) observed corresponding to the π–π* transitions [55,56]. An intense broad absorption band of the ligand in the UV range was detected for the compounds obtained (Figure 6). In addition, sharp and weak to medium bands originating from the respective f–f transitions (Table 1) in both the VIS and NIR regions for $^{1}_{\infty}$[Ln(2–PyPz)$_3$], Ln = Nd (**2**), Sm (**3**), α–[Eu$_2$(2–PyPzH)$_4$Cl$_6$] (**5**), β–[Ln$_2$(2–PyPzH)$_4$Cl$_6$], Ln = Sm (**8**), Eu (**9**), and [Ln(2–PyPzH)$_2$Cl$_3$], Ln = Dy (**13**), Ho (**14**), Er (**15**) ions [54,57–60] were observed. For [Ce(2–PyPzH)$_3$Cl$_3$] (**11**), the formation of a shoulder is observed at higher wavelengths due to the transition from 4f to 5d.

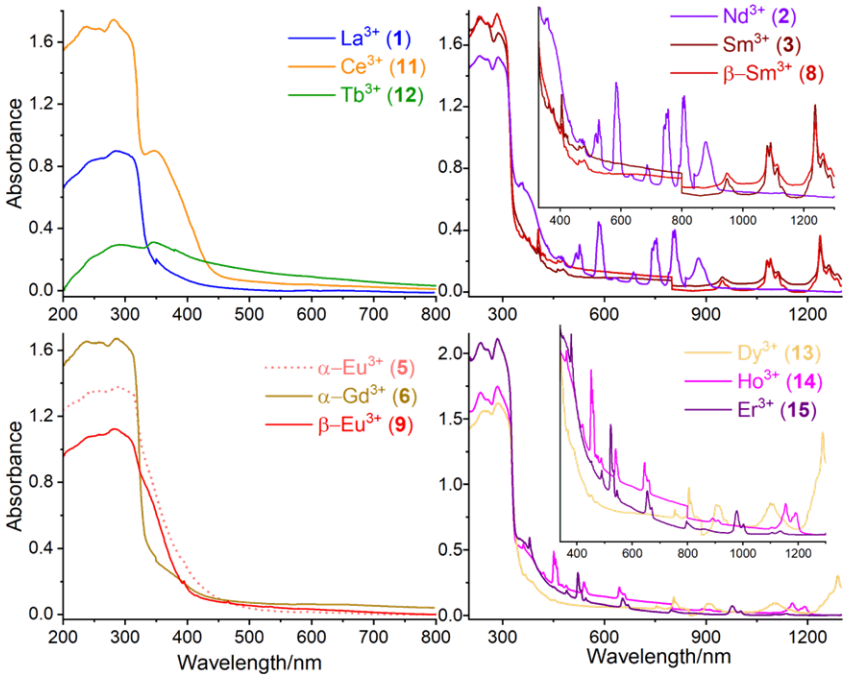

Figure 6. Solid-state absorption spectra of $^{1}_{\infty}$[Ln$_2$(2–PyPzH)$_4$Cl$_6$], Ln = La (**1**), Nd (**2**), Sm (**3**), α–[Ln$_2$(2–PyPzH)$_4$Cl$_6$], Ln = Eu (**5**), Gd (**6**), β–[Ln$_2$(2–PyPzH)$_4$Cl$_6$], Ln = Sm (**8**), Eu (**9**), [Ce(2–PyPzH)$_3$Cl$_3$] (**11**), and [Ln(2–PyPzH)$_2$Cl$_3$], Ln = Tb (**12**), Dy (**13**), Ho (**14**), Er (**15**) at room temperature.

2.2.2. Emission and Excitation Spectra

The photoluminescence properties were recorded for all bulk products, $^{1}_{\infty}$[Ln$_2$(2–PyPzH)$_4$Cl$_6$], Ln = La (**1**), Nd (**2**), Sm (**3**), α–[Ln$_2$(2–PyPzH)$_4$Cl$_6$], Ln = Sm (**4**), Eu (**5**), Gd (**6**), β–[Ln$_2$(2–PyPzH)$_4$Cl$_6$], Ln = Sm (**8**), Eu (**9**), [Ce(2–PyPzH)$_3$Cl$_3$] (**11**), and [Ln(2–PyPzH)$_2$Cl$_3$], Ln = Tb (**12**), Dy (**13**), Ho (**14**), Er (**15**) in the solid state at RT and 77 K. The complex [Ce(2–PyPzH)$_3$Cl$_3$] (**11**) shows remarkable photoluminescence properties with Ce^{3+}-centered light emission in the orange range of the visible spectrum, which can already be distinguishable by the eye under the UV lamp. The Ce^{3+} orange emitter is an exception within other Ce^{3+}-based emitters. Determinations via photoluminescence spectroscopy (Figure 7) revealed a broadband emission starting at 460 nm with a center at around 600 nm at 77 K and RT, indicating large crystal field splitting and a bathochromic shift for the emission wavelength. The excitation spectrum exhibits a shoulder at 370 nm, corresponding to the lowest energy levels of the crystal field splitting bands of the 5d-excited state of the Ce^{3+} ion. The maximum excitation band is at 315 nm, correlated with the coordinated 2–PyPzH ligand. To the best of our knowledge, an orange–red emitting undoped cerium compound (**11**) has hardly been reported, only for doped systems such

as $Gd_3Ga_5O_{12}$ doped with both Pr^{3+} and Ce^{3+} [40], $Y_3Al_5O_{12}$:Ce nanophosphor doped with Pr^{3+} [61], and the cerium-doped scandate [62,63]. The nanosecond scale luminescence lifetime (τ) of **11** (2.83 ns) (Table 2) results from the parity-allowed nature of the 5d–4f transition. In contrast, the longer lifetime for the parity-forbidden 4f–4f transitions in [Tb(2–PyPzH)$_2$Cl$_3$] (**12**) reaches 1.230(1) ms. By comparing both the lifetime and the quantum yield (QY) measured for Tb^{3+} (**12**) (τ = 1.230 (1) ms, QY = 91.8(1.6)%) with the reported $^3{}_\infty$[Tb(3–PyPz)$_3$], (3–PyPz$^-$ = 3–(3–pyridyl)pyrazolate, τ = 1.0874 ms, QY = 74%), $^3{}_\infty$[Tb(4–PyPz)$_3$] (4–PyPz$^-$ = 3–(4–pyridyl)pyrazolate, τ = 0.6273 ms, QY = 23.2%) [7], $^2{}_\infty$[Tb$_2$(3–PyPzH)$_3$Cl$_6$]·2Tol (3–PyPzH = 3–(3–pyridyl)pyrazole, τ = 2.039 ms, QY = 73.1), $^2{}_\infty$[Tb$_2$(3–PyPzH)$_3$Cl$_6$]·2MeCN, (τ = 2.294 ms, QY = 76%) [2], [Tb(bbpen)Cl] (bbpen^{2-} = N,N′–bis(2–oxidobenzyl)–N,N′–bis(pyridin–2–ylmethyl)–ethylenediamine, τ = 0.814 ms, QY = 90%), and [Ln(bbppn)Cl] (bbppn^{2-} = N,N′–bis(2–oxidobenzyl)–N,N′–bis–(pyridin–2–ylmethyl)–1,2–propanediamine, τ = 0.969 ms, QY = 92%) [64], the complex [Tb(2–PyPzH)$_2$Cl$_3$] (**12**) reaches the highest QYs reported among the related Tb-based compounds. The value of τ and QY for the Eu^{3+} containing α–[Eu$_2$(2–PyPzH)$_4$Cl$_6$] (**5**, τ = 1.15(1) ms, QY = 7.6(2)%), β–[Eu$_2$(2–PyPzH)$_4$Cl$_6$] (**9**, τ = 1.19(2) ms, QY = 12.8(6)%), and Dy^{3+} containing [Dy(2–PyPzH)$_2$Cl$_3$] (**13**, τ = 17.14(3) µs, QY = 3.3%) are also higher than for $^3{}_\infty$[Eu(3–PyPz)$_3$], (τ = 0.576 ms, QY = 0.33%), $^3{}_\infty$[Eu(4–PyPz)$_3$], (τ = 0.323 ms, QY = 0.11%), $^3{}_\infty$[Eu(3–PyPzH)Cl$_3$] (τ = 0.2201 ms, QY = <0.5%), $^2{}_\infty$[Eu$_2$(3–PyPzH)$_3$Cl$_6$]·2MeCN (τ = 0.170 ms, QY = na), $^3{}_\infty$[Dy(3–PyPz)$_3$] (τ = 15 µs, QY = 1.13%), and $^3{}_\infty$[Dy(4–PyPz)$_3$] (τ = 12.07 µs, QY = 1.15%). These values decrease significantly for Sm^{3+} (**3**), α–Sm^{3+} (**4**), and β–Sm^{3+} (**8**), reflecting an excellent antenna effect for Tb^{3+} (**12**), where the ligand is mainly responsible for the excitation and a good antenna effect for α–Eu^{3+} (**5**), β–Eu^{3+} (**9**), and Dy^{3+} (**13**), where additional weak direct 4f–4f excitation is present, indicated by a series of ion-specific sharp lines of low intensity and more distinguishable in Nd^{3+} (**2**), Sm^{3+} (**3**), α–Sm^{3+} (**4**), β–Sm^{3+} (**8**), and Er^{3+} (**15**) (Figures 7 and 8).

Table 1. Absorption wavelengths of the transitions of $^1{}_\infty$[Ln$_2$(2–PyPzH)$_4$Cl$_6$], Ln = Nd (**2**), Sm (**3**), α–[Eu$_2$(2–PyPzH)$_4$Cl$_6$] (**5**), β–[Ln$_2$(2–PyPzH)$_4$Cl$_6$], Ln = Sm (**8**), Eu (**9**), and [Ln(2–PyPzH)$_2$Cl$_3$], Ln = Dy (**13**), Ho (**14**), Er (**15**) in the solid state at room temperature.

	Intra–4f Absorption Transitions		λ_{max} (nm)
Nd^{3+} (**2**)	$^4I_{9/2}\rightarrow$	$^4D_{3/2}$, $^2P_{1/2}$, (^2D, ^2P)$_{3/2}$, $^4G_{7/2}$/$^2K_{13/2}$, $^4G_{5/2}$, $^2H_{11/2}$, $^4F_{9/2}$, $^4F_{7/2}$, $^4F_{5/2}$, $^4F_{3/2}$	359, 431, 473, 527, 583, 633, 686, 745, 807, 878 nm
Sm^{3+} (**3**)	$^6H_{5/2}\rightarrow$	$^4F_{7/2}$/$^6P_{3/2}$/$^4K_{11/2}$, (^6P,^4P)$_{5/2}$, $^4M_{19/2}$, $^4I_{13/2}$, $^4I_{11/2}$, $^4G_{7/2}$, $^4F_{3/2}$, $^4G_{5/2}$, $^6F_{11/2}$, $^6F_{9/2}$, $^6F_{7/2}$	405, 417, 425, 462, 479, 501, 529, 562, 948, 1090, 1237 nm
α–Eu^{3+} (**5**)	$^7F_0\rightarrow$	$^5L_6$, $^5D_2$, $^5D_1$, $^5D_0$	394, 465, 534, 579 nm
β–Sm^{3+} (**8**)	$^6H_{5/2}\rightarrow$	$^4H_{9/2}$/$^4D_{7/2}$, $^5D_{5/2}$, $^6P_{7/2}$, $^4F_{7/2}$/$^6P_{3/2}$/$^4K_{11/2}$, (^6P,^4P)$_{5/2}$, $^4M_{19/2}$, $^4I_{13/2}$, $^4I_{11/2}$, $^4G_{7/2}$, $^4F_{3/2}$, $^4G_{5/2}$, $^6F_{11/2}$, $^6F_{9/2}$, $^6F_{7/2}$	346, 363, 378, 405, 418, 424, 462, 478, 501, 529, 562, 947, 1083, 1240 nm
β–Eu^{3+} (**9**)	$^7F_0\rightarrow$	$^5L_6$, $^5D_3$, $^5D_2$, $^5D_1$, $^5D_0$	395, 415, 465, 534, 579 nm
Dy^{3+} (**13**)	$^6H_{15/2}\rightarrow$	$^5P_{5/2}$, $^4M_{21/2}$/$^4K_{17/2}$, $^4G_{11/2}$, $^4I_{15/2}$, $^4F_{9/2}$, $^6F_{3/2}$, $^6F_{5/2}$, $^6F_{7/2}$, $^6F_{9/2}$, $^6F_{11/2}$	366, 387, 427, 450, 474, 754, 805, 903, 1100, 1289 nm
Ho^{3+} (**14**)	$^7I_8\rightarrow$	(^5G,^3H)$_5$/$^3H_6$, (^5G,^3G)$_5$ $^5G_6$, $^5F_2$, $^5F_3$, $^5F_4$, $^5F_5$, $^5I_5$, $^5I_6$	362, 420, 451, 475, 488, 540, 645, 891, 1154 nm
Er^{3+} (**15**)	$^4I_{15/2}\rightarrow$	$^4G_{11/2}$, $^5F_{5/2}$, $^4F_{7/2}$, $^2H_{11/2}$, $^4S_{8/2}$, $^4F_{9/2}$, $^4I_{11/2}$	379, 452, 489, 522, 545, 654, 978 nm

A broad emission band was visible in the region from about 400–600 nm at 77 K in $^1{}_\infty$[La$_2$(2–PyPzH)$_4$Cl$_6$] (**1**) and α–[Gd$_2$(2–PyPzH)$_4$Cl$_6$] (**6**) and characterized to the triplet state of 2–PyPzH with λ_{onset} = 425 nm (23,529 cm^{-1}). The energy differences (ΔE) between the organic ligand triplet state and the energy position of Tb^{3+} ($^5D_4$ = 20,500 cm^{-1}) [57,59] considering the Latva's rule, ΔE = 3029 cm^{-1}, explain the long lifetime and the excellent quantum yield value of Tb^{3+}.

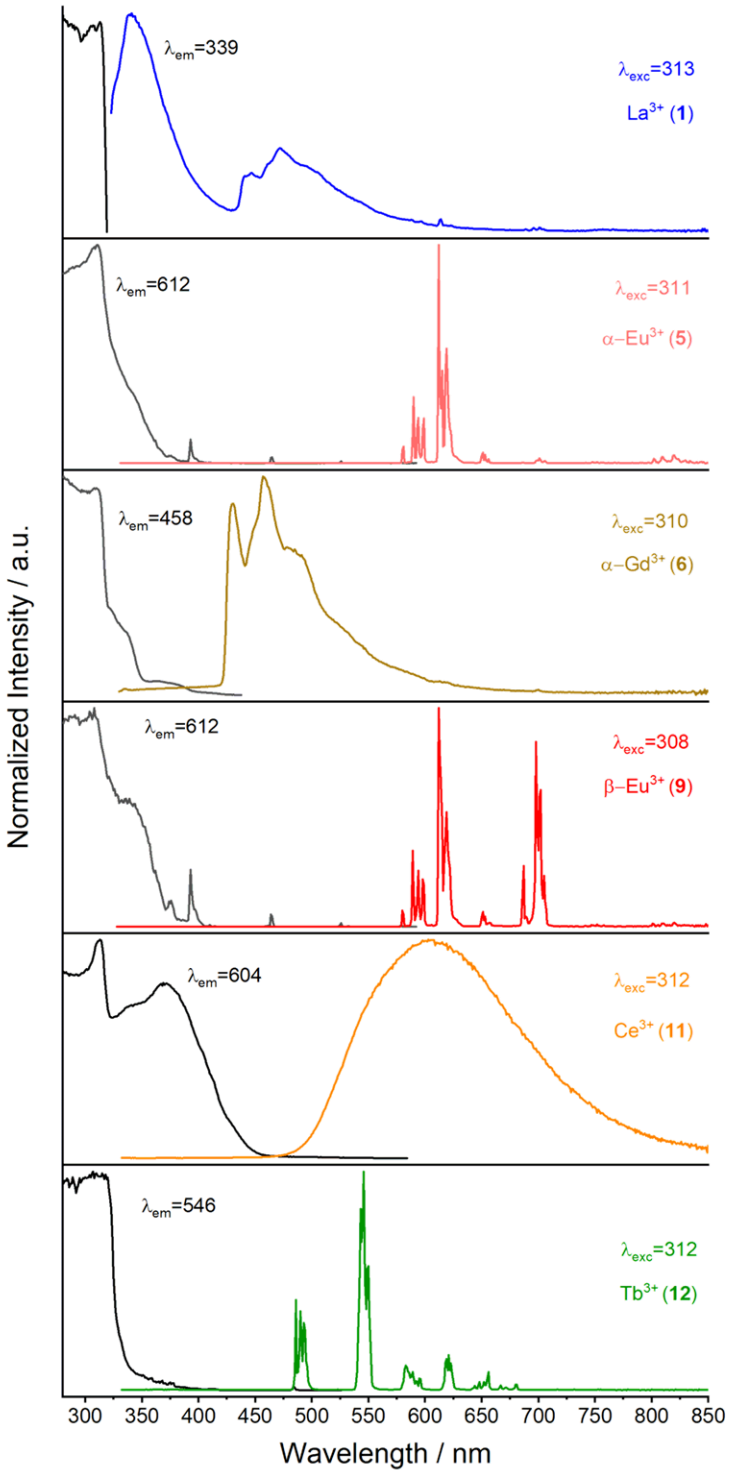

Figure 7. Normalized solid-state excitation (black) and emission spectra (colored) of $^{1}_{\infty}$[La_2(2–PyPzH)$_4Cl_6$] (**1**), α–[Ln_2(2–PyPzH)$_4Cl_6$], Ln = Eu (**5**), Gd (**6**), β–[Eu_2(2–PyPzH)$_4Cl_6$ (**9**), [Ce(2–PyPzH)$_3Cl_3$] (**11**), and [Tb(2–PyPzH)$_2Cl_3$] (**12**) at 77 K. Wavelengths for which the spectra were recorded are given in the legends.

Table 2. Photophysical data of $^{1}_{\infty}[Ln_2(2–PyPzH)_4Cl_6]$, Ln = La (**1**), Sm (**3**), α–$[Ln_2(2–PyPzH)_4Cl_6]$, Ln = Sm (**4**), Eu (**5**), Gd (**6**), β–$[Ln_2(2–PyPzH)_4Cl_6]$, Ln = Sm (**8**), Eu (**9**), $[Ce(2–PyPzH)_3Cl_3]$ (**11**), and $[Ln(2–PyPzH)_2Cl_3]$, Ln = Tb (**12**), Dy (**13**) in the solid state at RT and 77 K.

ID	$\tau_{(RT)}$ [1]	$\lambda_{ex}/\lambda_{em}$ [nm] [2]	$\tau_{(77\ K)}$ [3]	$\lambda_{ex}/\lambda_{em}$ [nm] [4]	Φ [%] [5]	$\lambda_{ex}/\lambda_{em}$ [nm] [6]
La^{3+} (**1**)	1.89(3) ns	287/364	1.41(1) ns	287/339	n/a	n/a
Sm^{3+} (**3**)	4.02(9) µs	321/598	1.23(3) ns	287/605	n/a	n/a
α–Sm^{3+} (**4**)	1.17(2) ns	287/599	1.09(2) ns	287/599	n/a	n/a
α–Eu^{3+} (**5**)	1.15(1) ms	305/612	1.435(3) ms	311/612	7.6(2)	310/570–720
α–Gd^{3+} (**6**)	0.117(2) ms	289/545	1.034(4) ms	310/458	n/a	n/a
β–Sm^{3+} (**8**)	2.7(1) µs	316/599	20.7(5) µs	316/599	n/a	n/a
β–Eu^{3+} (**9**)	1.19(2) ms	311/612	1.556(4) ms	308/612	12.8(6)	310/575–715
Ce^{3+} (**11**)	2.83(3) ns	368/595	5.6(1) ns	368/604	n/a	n/a
Tb^{3+} (**12**)	1.230(1) ms	321/546	1.287(1) ms	321/546	91.8(1.6)	318/473–692
Dy^{3+} (**13**)	17.14(3) µs	321/573	13.19(1) µs	321/574	3.3(1)	320/459–763

[1] Emission lifetimes determined at RT. [2] Excitation and emission wavelengths for the emission lifetime at RT. [3] Emission lifetime determined at 77 K. [4] Excitation and emission wavelengths for the emission lifetime at 77 K. [5] Quantum yield. [6] Excitation wavelength and emission range of QY determinations.

For $[Tb(2–PyPzH)_2Cl_3]$ (**12**), α–$[Eu_2(2–PyPzH)_4Cl_6]$ (**5**), and β–$[Eu_2(2–PyPzH)_4Cl_6]$ (**9**) (Figure 7), the highest intensity is found for the transitions $^5D_0 \rightarrow {}^7F_5$ at 545 nm and $^5D_4 \rightarrow {}^7F_2$ at 612 nm as expected for Tb^{3+} and Eu^{3+} ions [65,66], while multiple emission lines are Stark levels as a result of energy-level splitting due to the crystal field.

For α–Eu^{3+} (**5**), the hypersensitive transition $^5D_0 \rightarrow {}^7F_2$ shows a higher number of Stark components (612, 615, and 619 nm) than the triclinic β–Eu^{3+} (**9**) with two Stark components (612, 619 nm) and a higher intensity for the environmentally dependent transition $^5D_0 \rightarrow {}^7F_4$ at 77 K, confirming the different symmetry of the Eu^{3+} centers in **5** and **9**. For the transitions $^5D_0 \rightarrow {}^7F_J$, (J = 1, 3, 4) more Stark splitting is observed for α–Eu^{3+} (**5**) and β–Eu^{3+} (**9**) than the previously reported orthorhombic $^{3}_{\infty}[Eu(3–PyPzH)Cl_3]$, confirming the low symmetry for the former. For $^{1}_{\infty}[Sm(2–PyPzH)_4Cl_6]$ (**3**), α–$[Sm_2(2–PyPzH)_4Cl_6]$ (**4**), β–$[Sm_2(2–PyPzH)_4Cl_6]$ (**8**), $[Ln(2–PyPzH)_2Cl_3]$, Ln = Dy (**13**), and Ho (**14**) (Figure 8), the highest intensity is found at 600 nm (for Sm^{3+}, corresponds to $^4G_{5/2} \rightarrow {}^6H_{7/2}$), 574 nm (for Dy^{3+}, corresponds to $^4F_{9/2} \rightarrow {}^6H_{13/2}$), and 662 nm (for Ho^{3+}, corresponds to $^5F_5 \rightarrow {}^5I_8$). The f–f transitions are dominant in the 1D-CP of Sm^{3+} (**3**), while the ligand emission is more dominant in the β–Sm^{3+} (**8**) and further overlaps with the f–f transitions in the α–Sm^{3+} (**4**), which has its effect on the lifetime results; τ decreases from **3** (4.02(9) µs) through **8** (2.7(1) µs) to **4** (1.17(2) ns). This behavior reflects the quenching effect arising from the separation of the luminescent metal centers by the extended N-ligands [67], where a Cl^- ligand acts as a bridge between two neighboring Sm^{3+} ions in **3** and two Cl^- ligands act as bridges in **8** and **4**. NIR emission bands can also be observed for **3**, **4**, and **8** at about 790, 900, 945, 1030, and 1175 nm, corresponding to the transitions $^4G_{5/2} \rightarrow {}^6H_{13/2}$ and $^4G_{5/2} \rightarrow {}^6F_{J/2}$, J = 3, 5, 7, 9 of Sm^{3+}, as well as for **13** at 760, 850, 937, 1016, and 1178 nm corresponding to $^4F_{9/2} \rightarrow {}^6H_{J/2}$, (J = 9, 7, 5) and $^6F_{J/2}$, (J = 7, 5) of Dy^{3+} and for **14** at 991 and 1163 nm to $^5F_5 \rightarrow {}^5I_7$ and $^5I_6 \rightarrow {}^5I_8$, respectively.

For $^{1}_{\infty}[Nd(2–PyPzH)_4Cl_6]$ (**2**) and $[Er(2–PyPzH)_2Cl_3]$ (**15**), NIR emission bands at 887, 1066, and 1351 nm can also be observed, which correlate with the transitions $^4F_{3/2} \rightarrow {}^4I_{J/2}$, (J = 9, 11, 13) of Nd^{3+}, respectively, and for **15** at 1532 nm, correlated with the transition $^4I_{13/2} \rightarrow {}^4I_{15/2}$ of Er^{3+}. For $^{1}_{\infty}[La_2(2–PyPzH)_4Cl_6]$ (**1**), few peaks with very low intensity around 620 and 675 nm are attributed to impurities in the ppm range together with an efficient ligand-to-metal energy transfer. See the Supplementary Materials for half-page size absorption and photoluminescence spectra with designated 4f–4f transitions for the studied compounds (Figures S12–S38).

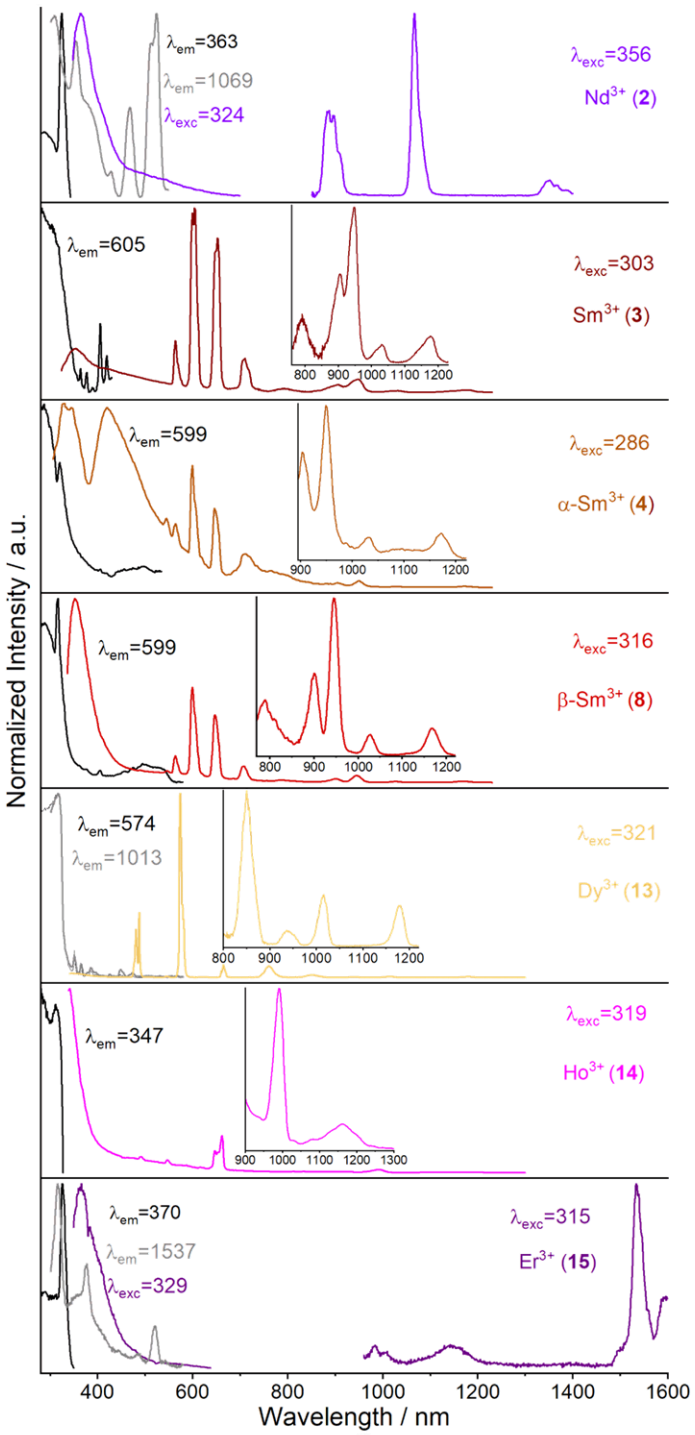

Figure 8. Normalized solid-state excitation (black) and emission spectra (colored) of $^{1}{}_{\infty}$[Ln_2(2–PyPzH)$_4Cl_6$], Ln = Nd (**2**), Sm (**3**), α–[Sm_2(2–PyPzH)$_4Cl_6$] (**4**), β–[Sm_2(2–PyPzH)$_4Cl_6$] (**8**), and [Ln(2–PyPzH)$_2Cl_3$], Ln = Dy (**13**), Ho (**14**), Er (**15**) at 77 K. Wavelengths for which the spectra were recorded are given in the legends.

2.3. Thermal Analysis

Simultaneous DTA and TG studies combined with mass spectrometry were performed for $^{1}_{\infty}[Sm_2(2–PyPzH)_4Cl_6]$ (**3**), α–$[Eu_2(2–PyPzH)_4Cl_6]$ (**5**), β–$[Eu_2(2–PyPzH)_4Cl_6]$ (**9**), and $[Tb(2–PyPzH)_2Cl_3]$ (**12**) (Figure 9). For $^{1}_{\infty}[Sm_2(2–PyPzH)_4Cl_6]$ (**3**) (Figure 9a), a release of one equivalent of 2–PyPzH (theoretical mass loss = 26.5%) is indicated by the first endothermic signal (signal 1) starting at 250 °C with a mass loss of 26.4%. The second equivalent of 2–PyPzH is not fully released within the following two endothermic signals (2, 3) with a mass loss of 18.1%. A further mass loss is observed at higher temperatures, coinciding with the decomposition of the remaining 2–PyPzH, with black residues observed after the measurement, indicating partial carbonization of the ligand.

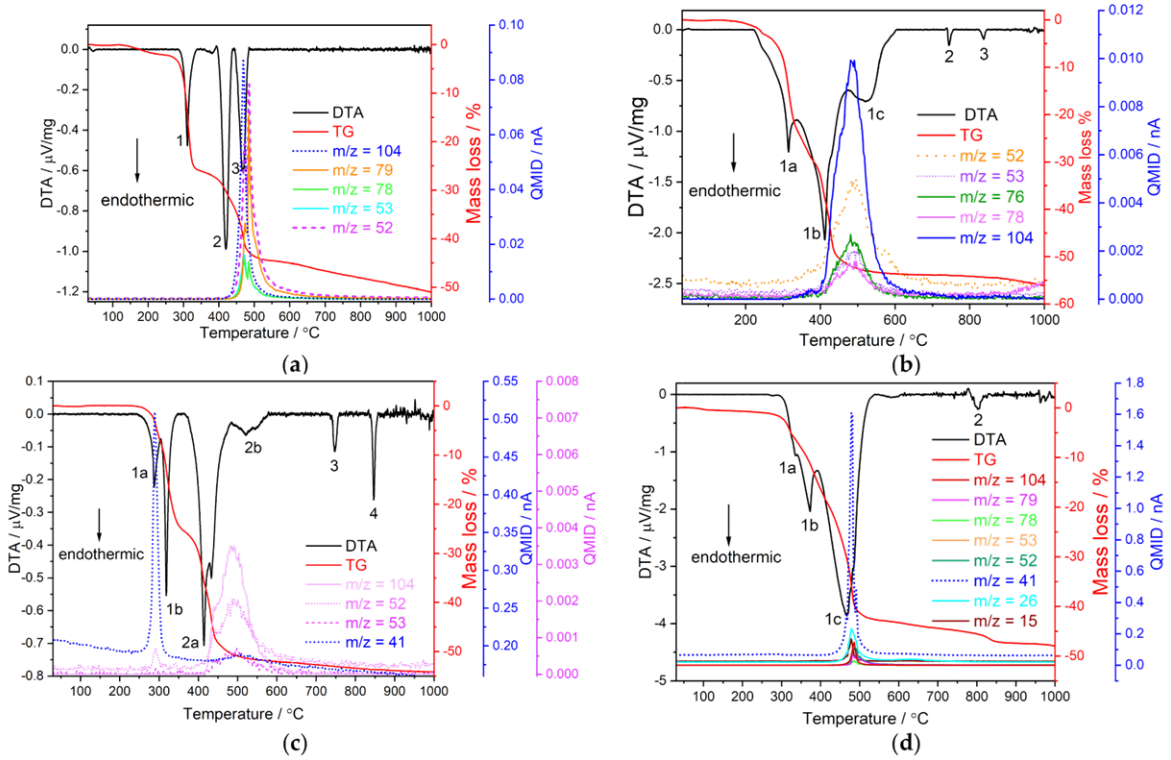

Figure 9. Simultaneous DTA/TG analysis together with mass spectrometry of (**a**) $^{1}_{\infty}[Sm_2(2–PyPzH)_4Cl_6]$ (**3**), (**b**) α–$[Eu_2(2–PyPzH)_4Cl_6]$ (**5**), (**c**) β–$[Eu_2(2–PyPzH)_4Cl_6]$ (**9**), and (**d**) $[Tb(2–PyPzH)_2Cl_3]$ (**12**). The investigation was performed in a constant argon flow of 50 mL·min^{-1} with a heating rate of 5 K·min^{-1} from RT to 1000 °C.

For α–$[Eu_2(2–PyPzH)_4Cl_6]$ (**5**) (Figure 9b), two equivalent 2–PyPzH (theoretical mass loss = 52.9%) are released during the combined endothermic signal (1a, 1b, 1c) with a mass loss of 53.7% in the TG and an onset temperature of 230 °C. For β–$[Eu_2(2–PyPzH)_4Cl_6]$ (**9**) (Figure 9c), one equivalent of 2–PyPzH (theoretical mass loss = 26.5%) is released, while the first combined endothermic signal starts at 230 °C (1a, 1b) with a mass loss of 25.8%. The loss of another equivalent 2–PyPzH is evidenced by a 25.6% mass loss during the second combined endothermic signal (2a, 2b). The appearance of two endothermic signals at 745, 835 °C (signals 2, 3) in α–Eu^{3+} (**5**) and at 745, 865 °C (signals 3, 4) in β–Eu^{3+} (**9**), far from the melting point of $EuCl_3$ (theoretical mp = 632 °C) [68], indicates the formation of other phases, confirmed by the lack of $EuCl_3$ reflections and the observation of unknown reflections in the PXRD pattern.

For $[Tb(2–PyPzH)_2Cl_3]$ (**12**) (Figure 9d), the two equivalent 2–PyPzH are not fully released within the combined endothermic signals (1a, 1b, 1c) with a mass loss of 42.9%

(theoretical mass loss = 52.3%) and an onset temperature of 250 °C. A further endothermic signal at 800 °C (signal 2) far from the melting point of $TbCl_3$ (581 °C) [69] is observed beside unknown reflections in the PXRD pattern, indicating the formation of other unknown phases, which cause further mass loss at higher temperatures.

In summary, the 1D-coordination polymer **3** and the monomer complex **12** show the highest stability among the series up to 250 °C, while **5** and **9** are stable up to 230 °C. Further confirmation of the decomposition processes in **3**, **5**, **9**, and **12** was the detection of a set of mass signals at the respective temperatures, which can be assigned to fragments of the ligand ($C_7H_6N^+$ m/z = 104, $C_5H_5N^+$ m/z = 79, $C_5H_2N^+$ m/z = 76, $C_5H_4N^+$ m/z = 78, $C_2HN_2^+$ m/z = 53, $C_2N_2^+$ m/z = 52, $C_2NH_3^+$ m/z = 41, $C_2H_3^+$ m/z = 27, $C_2H_2^+$ m/z = 26, CH_3^+ m/z = 15).

3. Materials and Methods

3.1. General Procedures

3–(2–pyridyl)pyrazole (2–PyPzH) was synthesized according to the previously reported procedure [70,71]. The method is described in detail in the Supplementary Materials. The lanthanide chlorides ($NdCl_3$, $SmCl_3$, $EuCl_3$, $TbCl_3$, $HoCl_3$: 99.9%, Sigma Aldrich, St Louis, MO, USA; $DyCl_3$, $GdCl_3$: 99.9%, Strem Chemicals, Newburyport, Massachusetts, United States; $LaCl_3$: 99.9%, Heraeus, Karlsruhe, Germany; $CeCl_3$: 99.9%, abcr, Karlsruhe, Germany) were purchased and used as received. All syntheses involving anhydrous lanthanide chlorides were performed under argon or using a vacuum line, gloveboxes (MBraun Labmaster SP, Innovative Technology PureLab, Garching, Germany), Schlenk tubes, and Duran® glass ampoules (outer ⌀ 10 mm, wall thickness 1.5 mm). Acetonitrile (MeCN), toluene, pyridine, and dichloromethane (DCM) were purified by distillation and dried using standard methods. The solid reactants for the solvothermal reactions were mixed and sealed together with the solvent in an ampoule under reduced pressure ($p = 1.0 \times 10^{-3}$ mbar). A stir bar was added to the reaction mixture when needed. Afterward, the prepared ampoules were placed in heating furnaces (Büchi glass ovens, Büchi Labortechnik, Flawil, Switzerland or heating furnaces based on Al_2O_3 tubes with Kanthal wire resistance heating and NiCr/Ni (Eurotherm 2416) temperature control elements), for which temperature programs and working steps according to the specific synthesis methods were applied. After removing the solvents, the solid raw products were dried at RT in a dynamic vacuum ($p = 1.0 \times 10^{-3}$ mbar) before further steps. The bulk materials were characterized by powder X-ray diffraction (PXRD) and CHN analysis. The infrared spectrum (ATR) of the studied compounds are given in the Supplementary Materials (Figures S39–S51).

3.2. X-ray Crystallography

SCXRD determinations were performed on a Bruker AXS D8 Venture diffractometer (Karlsruhe, Germany) equipped with dual IμS microfocus sources, a collimating Quazar multilayer mirror, a Photon 100 detector, and an Oxford Cryosystems 700 low-temperature system (Mo–K_α radiation; λ = 71.073 pm), except **11**, for which a Bruker AXS D8 Venture diffractometer (Germany) equipped with Photon III–C14 and an Oxford Cryosystems 800 low-temperature system (Mo–K_α radiation; λ = 71.073 pm) was used. For **2** and **18**, the data collections were performed at 200 K because of the cracking behavior of the single crystals upon cooling to 100 K. All other data were collected at 100 K. The structures were solved with direct methods and refined with the least squares method implemented in ShelX [72,73]. All non-hydrogen atoms were refined anisotropically. Hydrogen atoms were assigned to idealized geometric positions and included in structure factor calculations. Further, a ligand molecule (2–PyPzH) in the asymmetric unit of **1**, **2**, **3**, **5**, **6**, **17** and the pyridine solvent in **18** were found to be fully disordered and were refined with the help of restraints to achieve a proper structural model. The structures of **1–3, 5–18** have been deposited to the Cambridge Crystallographic Data Center (CCDC) as supplementary publication No. 2208098 (**1**), 2208099 (**2**), 2208100 (**3**), 2208101 (**5**), 2208102 (**6**), 2208103 (**7**),

2208104 (**8**), 2208105 (**9**), 2208106 (**10**), 2208107 (**11**), 2208108 (**12**), 2208109 (**13**), 2208110 (**14**), 2208111 (**15**), 2208112 (**16**), 2208113 (**17**), and 2208114 (**18**). Crystallographic data and selected interatomic distances are listed in Tables S1–S13 for the investigated compounds.

Depictions of the crystal structures were created with Diamond [74]. Structure overlays for polymorphs **5** and **9** were calculated with Mercury [75].

PXRD analyses of the investigated compounds were carried out on a Stoe Stadi P diffractometer (Darmstadt, Germany) with a focusing Ge(111) monochromator and a Dectris Mythen 1K strip detector in Debye–Scherrer geometry. All powder samples were ground in a mortar and filled into Lindemann glass capillaries with 0.3 mm diameter under an inert gas atmosphere. All samples were measured in transmission geometry with Cu–K_α radiation (λ = 154.056 pm). Data collection was done using the Stoe Powder Diffraction Software Package WinXPOW and Pawley fits on the data were performed using TOPAS Academic [76]. The data are listed in Figures 5 and S6–S11.

3.3. Synthesis

3.3.1. Synthesis of $^1{}_\infty[Ln_2(2\text{–}PyPzH)_4Cl_6]$, Ln = La (1), Nd (2), Sm (3)

A mixture of the respective $LnCl_3$ (76 µmol) and 2–PyPzH (158 µmol) in 0.3 mL MeCN was sealed in an evacuated Duran glass ampoule. The solvent was frozen using liquid nitrogen before a vacuum was applied to the ampoule and the ampoule was sealed. For **1** and **2**, the ampoule was heated in a tubular furnace to 160 °C within 24 h. The temperature was held for 24 h and then lowered to 25 °C within another 72 h. For **3**, the phase pure bulk was only achievable in a synthesis upon stirring using a Büchi oven. The furnace temperature was raised to 100 °C and held for 48 h until colorless crystals formed above the level of the solvent, followed by cooling to 25 °C. The obtained colorless crystalline bulk was washed with DCM before the characterization processes via SCXRD, PXRD, IR spectroscopy, and CHN analysis.

$^1{}_\infty[La_2(2\text{–}PyPzH)_4Cl_6]$: $C_{16}H_{14}N_6Cl_3La$ (535.59 g·mol^{-1}): C 36.81 (calcd. 35.88); H 3.33 (2.63); N 14.84 (15.69)%. Yield: 80%. FT-IR (ATR): $\tilde{\nu}$ = 3086 (w), 1604 (s), 1569 (w), 1531 (w), 1500 (m), 1456 (m), 1440 (w), 1426 (m), 1356 (m), 1289 (w), 1242 (w), 1181 (w), 1156 (m), 1136 (w), 1085 (s), 1058 (s), 1004 (m), 964 (m), 927 (w), 894 (w), 802 (w), 775 (s), 741 (w), 710 (m), 634 (m), 614 (w), 505 (w), 465 (w) cm^{-1}.

$^1{}_\infty[Nd_2(2\text{–}PyPzH)_4Cl_6]$: $C_{16}H_{14}N_6Cl_3Nd$ (540.92 g·mol^{-1}): C 34.87 (calcd. 35.53); H 2.52 (2.61); N 15.35 (15.54)%. Yield: 84%. FT-IR (ATR): $\tilde{\nu}$ = 3129 (w), 1605 (m), 1568 (w), 1531 (w), 1501 (m), 1456 (m), 1440 (m), 1426 (m), 1358 (m), 1290 (w), 1242 (w), 1181 (m), 1155 (m), 1138 (m), 1107 (w), 1085 (m), 1057 (m), 1005 (m), 964 (m), 927 (w), 892 (w), 801 (m), 773 (s), 742 (m), 710 (m), 634 (m), 614 (m), 506 (w), 467 (w) cm^{-1}.

$^1{}_\infty[Sm_2(2\text{–}PyPzH)_4Cl_6]$: $C_{16}H_{14}N_6Cl_3Sm$ (547.03 g·mol^{-1}): C 35.06 (calcd. 35.13); H 2.46 (2.58); N 15.85 (15.36)%. Yield: 86%. FT-IR (ATR): $\tilde{\nu}$ = 3123 (w), 1638 (w), 1607 (m), 1596 (w),1503 (w), 1457 (w), 1428 (m), 1361 (m), 1292 (w), 1247 (w), 1183 (w), 1157 (w), 1140 (w), 1087 (m), 1059 (m), 1006 (w), 966 (m), 928 (w), 774 (s), 743 (w), 710 (w), 635 (m), 615 (w), 507 (w), 468 (w) cm^{-1}.

3.3.2. Synthesis of α–$[Ln_2(2\text{–}PyPzH)_4Cl_6]$, Ln = Sm (4), Eu (5), Gd (6)

A mixture of the respective $LnCl_3$ (138 µmol) and 2–PyPzH (276 µmol) in 0.3 mL MeCN in **5** and **6** or toluene in **4** was prepared and sealed in an evacuated Duran glass ampoule. For **4**, the tubular furnace was heated to 120 °C within 24 h. The temperature was held for 72 h and then lowered to 25 °C within another 48 h. For **5** and **6**, phase pure bulk was achieved by stirring while using a Büchi oven. The furnace temperature was raised to 100 °C and held for 24 h until colorless crystals formed above the level of the solvent, followed by cooling to 25 °C. Colorless single crystals of the products (**6** and **7**) were selected for SCXRD measurements.

α–$[Sm_2(2\text{–}PyPzH)_4Cl_6]$: $C_{16}H_{14}N_6Cl_3Sm$ (547.03 g·mol^{-1}): C 34.71 (calcd. 35.13); H 2.55 (2.58); N 15.17 (15.36)%. Yield: 89%. FT-IR (ATR): $\tilde{\nu}$ = 3047 (w), 1602 (m), 1568 (w), 1532 (w), 1501 (m), 1459 (m), 1446 (w), 1427 (m), 1369 (w), 1295 (w), 1247 (w), 1190 (m),

1160 (w), 1141 (m), 1109 (w), 1087 (m), 1058 (m), 1004 (m), 966 (m), 929 (m), 898 (w), 812 (m), 784 (s), 768 (s), 705 (m), 676 (w), 632 (m), 611 (m), 510 (w), 471 (w) cm^{-1}.

α–[Eu_2(2–PyPzH)$_4Cl_6$]: $C_{16}H_{14}N_6Cl_3Eu$ (548.64 g·mol^{-1}): C 35.90 (calcd. 35.03); H 3.30 (2.57); N 14.42 (15.32)%. Yield: 87%. FT-IR (ATR): $\tilde{\nu}$ = 3115 (w), 1602 (m), 1568 (w), 1501 (w), 1460 (m), 1427 (w), 1369 (w), 1292 (w), 1247 (w), 1190 (m), 1161 (w), 1141 (w), 1087 (m), 1058 (m), 1005 (m), 966 (m), 930 (w), 812 (w), 784 (s), 768 (s), 705 (m), 675 (w), 632 (m), 611 (m), 510 (w), 470 (w) cm^{-1}.

α–[Gd_2(2–PyPzH)$_4Cl_6$]: $C_{16}H_{14}N_6Cl_3Gd$ (553.93 g·mol^{-1}): C 34.21 (calcd. 34.69); H 2.48 (2.55); N 14.47 (15.17)%. Yield: 82%. FT-IR (ATR): $\tilde{\nu}$ = 3123 (w), 1628 (w), 1602 (m), 1568 (w), 1502 (m), 1427 (m), 1361 (w), 1292 (w), 1246 (w), 1185 (w), 1161 (w), 1139 (w), 1087 (m), 1059 (m), 1005 (m), 966 (m), 928 (w), 897 (w), 767 (s), 710 (s), 632 (m), 610 (m), 469 (w) cm^{-1}.

3.3.3. Synthesis of β–[Ln_2(2–PyPzH)$_4Cl_6$], Ln = Sm (8), Eu (9)

A mixture of the respective $LnCl_3$ (138 μmol) and 2–PyPzH (276 μmol) in 0.3 mL MeCN was sealed in an evacuated glass ampoule after freezing the solvent. A Büchi oven with a stirrer was used to raise the temperature of the ampoule to 160 °C and held for three days until colorless crystals formed above the solvent level, followed by cooling to 25 °C. Appropriate colorless single crystals were then selected for SCXRD measurements. The bulk was characterized by PXRD, IR spectroscopy, and CHN analysis

β–[Sm_2(2–PyPzH)$_4Cl_6$]: $C_{16}H_{14}N_6Cl_3Sm$ (547.03 g·mol^{-1}): C 34.45 (calcd. 35.13); H 2.07 (2.58); N 14.99 (15.36)%. Yield: 85%. FT-IR (ATR): $\tilde{\nu}$ = 3056 (w), 1605 (m), 1568 (w), 1531 (w), 1499 (m), 1459 (m), 1444 (w), 1427 (m), 1366 (w),1294 (w), 1425 (w), 1188 (m), 1142 (m), 1109 (w), 1089 (s), 1059 (m), 1004 (w), 966 (m), 928 (w), 896 (w), 806 (w), 781 (s), 771 (s), 704 (s), 676 (m), 633 (m), 610 (s), 507 (w), 470 (w) cm^{-1}.

β–[Eu_2(2–PyPzH)$_4Cl_6$]: $C_{16}H_{14}N_6Cl_3Eu$ (548.64 g·mol^{-1}): C 34.22 (calcd. 35.03); H 1.71 (2.57); N 14.50 (15.32)%. Yield: 92%. FT-IR (ATR): $\tilde{\nu}$ = 3112 (w), 1681 (w), 1605 (m), 1568 (m), 1531 (w), 1499 (m), 1458 (m), 1440 (w), 1427 (m), 1362 (w), 1291 (w), 1244 (w), 1184 (m), 1153 (w), 1142 (m), 1109 (w), 1088 (s), 1059 (m), 1004 (m), 965 (m), 929 (w), 895 (w), 806 (w), 781 (s), 771 (s), 704 (s), 677 (m), 632 (m), 610 (m), 508 (w), 471 (w) cm^{-1}.

3.3.4. Synthesis of [Ce(2–PyPzH)$_3Cl_3$] (11)

A mixture of $CeCl_3$ (77 μmol) and 2–PyPzH (241 μmol) in 0.3 mL MeCN was sealed in an evacuated glass ampoule after freezing the solvent using liquid nitrogen. The ampoule was heated to 90 °C in 1 h and then 160 °C within 24 h. The temperature was held for 24 h and then lowered to 25 °C within 72 h. The obtained colorless crystalline bulk was washed with DCM before the characterization process using SCXRD, PXRD, IR spectroscopy, and CHN analysis. $C_{24}H_{21}N_9Cl_3Ce$ (681.97 g·mol^{-1}): C 43.15 (calcd. 42.27); H 3.90 (3.10); N 17.54 (18.48)%. Yield: 90%. FT-IR (ATR): $\tilde{\nu}$ = 3152 (w), 1633 (w), 1601 (m), 1567 (w), 1529 (w), 1500 (m), 1455 (m), 1440 (m), 1421 (m), 1358 (w), 1302 (w), 1283 (w), 1240 (w), 1189 (m), 1151 (w), 1138 (m), 1105 (w), 1086 (m), 1055 (m), 1002 (w), 959 (m), 928 (w), 909 (w), 762 (s), 713 (m), 686 (w), 629 (m), 615 (m), 595 (w), 515 (w), 466 (w) cm^{-1}.

3.3.5. Synthesis of [Ln(2–PyPzH)$_2Cl_3$], Ln = Tb (12), Dy (13), Ho (14), Er (15)

A mixture of the respective $LnCl_3$ (80 μmol) and 2–PyPzH (175 μmol) in 0.6 mL MeCN was sealed in an evacuated Duran glass ampoule after freezing the solvent. The ampoule was heated in a tubular furnace to 160 °C within 48 h. The temperature was held for 72 h and then lowered to 25 °C within another 96 h. The obtained colorless crystalline bulk was washed with DCM before the characterization process using SCXRD, PXRD, IR spectroscopy, and CHN analysis.

[Tb(2–PyPzH)$_2Cl_3$]: $C_{16}H_{14}N_6Cl_3Tb$ (555.60 g·mol^{-1}): C 33.95 (calcd. 34.59); H 2.37 (2.54); N 14.75 (15.13)%. Yield: 93%. FT-IR (ATR): $\tilde{\nu}$ = 3117 (w), 1601 (m), 1565 (w), 1536 (w), 1509 (m), 1469 (m), 1342 (m), 1368 (w), 1295 (w), 1244 (w), 1208 (m), 1159 (w),

1138 (w), 1111 (w), 1089 (m), 1055 (w), 1012 (m), 969 (m), 931 (w), 886 (w), 789 (m), 761 (s), 701 (m), 668 (m), 635 (m), 599 (m), 504 (w), 473 (w) cm^{-1}.

[Dy(2–PyPzH)$_2$Cl$_3$]: $C_{16}H_{14}N_6Cl_3Dy$ (559.18 g·mol^{-1}): C 34.96 (calcd. 34.37); H 2.41 (2.52); N 14.51 (15.03)%. Yield: 90%. FT-IR (ATR): $\tilde{\nu}$ = 3117 (w), 1602 (m), 1566 (w), 1536 (w), 1510 (m), 1469 (m), 1432 (m), 1369 (w), 1296 (w), 1244 (w), 1208 (m), 1159 (w), 1139 (m), 1112 (w), 1090 (m), 1056 (w), 1013 (m), 967 (m), 931 (w), 886 (w), 790 (m), 762 (s), 755 (s), 702 (m), 669 (m), 635 (m), 600 (m), 505 (w), 474 (w) cm^{-1}.

[Ho(2–PyPzH)$_2$Cl$_3$]: $C_{16}H_{14}N_6Cl_3Ho$ (561.61 g·mol^{-1}): C 33.60 (calcd. 34.22); H 2.33 (2.51); N 14.14 (14.96)%. Yield: 94%. FT-IR (ATR): $\tilde{\nu}$ = 3117 (w), 1602 (m), 1566 (w), 1536 (w), 1510 (m), 1468 (m), 1432 (m), 1369 (m), 1295 (m), 1244 (m), 1208 (m), 1159 (m), 1139 (m), 1112 (m), 1090 (m), 1056 (m), 1013 (m), 970 (m), 931 (w), 888 (w), 789 (m), 760 (s), 701 (m), 668 (m), 635 (m), 599 (m), 504 (w), 475 (w) cm^{-1}.

[Er(2–PyPzH)$_2$Cl$_3$]: $C_{16}H_{14}N_6Cl_3Er$ (563.94 g·mol^{-1}): C 33.53 (calcd. 34.08); H 2.08 (2.50); N 14.24 (14.90)%. Yield: 88%. FT-IR (ATR): $\tilde{\nu}$ = 3074 (w), 1604 (m), 1565 (m), 1537 (w), 1510 (m), 1469 (m), 1432 (m), 1370 (m), 1297 (m), 1245 (m), 1209 (m), 1159 (m), 1140 (m), 1089 (m), 1012 (m), 970 (m), 931 (m), 886 (w), 760 (s), 701 (m), 669 (m), 635 (m), 600 (m), 504 (w), 475 (w) cm^{-1}.

3.3.6. Single Crystals of α–[Tb$_2$(2–PyPzH)$_4$Cl$_6$] (7)

A mixture of $TbCl_3$ (19 μmol) and 2–PyPzH (59 μmol) in 0.3 mL MeCN was sealed in an evacuated glass ampoule after freezing the solvent. The ampoule was heated in a furnace to 160 °C within 48 h. The temperature was held for 72 h and then lowered to 25 °C within another 96 h. A colorless single crystal of the product was selected for SCXRD measurement.

3.3.7. Single Crystals of β–[Gd$_2$(2–PyPzH)$_4$Cl$_6$] (10)

A mixture of $GdCl_3$ (138 μmol) and 2–PyPzH (276 μmol) in 0.1 mL MeCN was sealed in an evacuated glass ampoule after freezing the solvent. The ampoule was heated in a Büchi oven to 160 °C by stirring until colorless crystals formed above the level of the solvent, followed by cooling to 25 °C. A colorless single crystal of the product was selected for SCXRD measurement.

3.3.8. Single Crystals of [Gd$_2$(2–PyPzH)$_3$(2–PyPz)Cl$_5$] (16) and [Gd$_3$(2–PyPzH)$_8$Cl$_8$]Cl (17)

A mixture of the respective $LnCl_3$ (138 μmol) and 2–PyPzH (276 μmol) in 0.3 mL MeCN was sealed in an evacuated glass ampoule after freezing the solvent. The ampoule was heated in a tubular furnace to 160 °C within 48 h. The temperature was held for 72 h and then lowered to 25 °C within another 24 h. A colorless single crystal of the product was selected for SCXRD measurement.

3.3.9. Single Crystals of [PyH][Tb(2–PyPzH)$_2$Cl$_4$] (18)

A mixture of $TbCl_3$ (19 μmol) and 2–PyPzH (59 μmol) in 0.1 mL pyridine was sealed in an evacuated glass ampoule after freezing the solvent. The ampoule was heated in a tubular furnace to 100 °C within 72 h. The temperature was held for 72 h and then lowered to 25 °C within another 96 h. A highly reflective colorless single crystal of the product was selected for the SCXRD measurement.

4. Conclusions

A novel Ce^{3+}-based orange-emitting material was synthesized from anhydrous $CeCl_3$ together with the ligand 3–(2–pyridyl)pyrazole (2–PyPzH). The obtained [Ce(2–PyPzH)$_3$Cl$_3$] represents the first undoped Ce^{3+} phosphor material to show intense orange emission based on 5d–4f transitions. This marks the presented compound an exception within other Ce^{3+}-based emitters. [Tb(2–PyPzH)$_2$Cl$_3$] exhibits high luminescence efficiency with a quantum yield of 92%, reflecting an excellent antenna effect through ligand-to-metal energy transfer. A great structural diversity has been observed along the lanthanide se-

ries, from 1D-coordination polymers through dimers to monomer complexes, all of which have been synthesized and characterized that are all luminescent. Two polymorphs are found for each Sm^{3+}, Eu^{3+}, and Gd^{3+} and the α-phase crystallizes at lower temperatures in the $P2_1/c$, while the β-phase crystallizes in the $P\bar{1}$ space group. The Ln^{3+} ions exhibit a change in coordination number from nine in Ce^{3+} to seven in Tb^{3+}, Dy^{3+}, Ho^{3+}, and Er^{3+} ions. The characterization of the new compounds was achieved by SC and PXRD, elemental analysis, IR, photoluminescence spectroscopy, and thermal analysis. Overall, this shows the high potential of coordination polymers and complexes with a pyridyl-pyrazole ligand as the N-donor for the design of materials with versatile structures as well as photophysical properties.

Supplementary Materials: The following supporting information can be downloaded at: https://www.mdpi.com/article/10.3390/inorganics10120254/s1, additional experimental details; Tables S1–S13: Crystallographic data and selected interatomic distances (pm) and angles (○) of $^1{}_\infty[Ln_2(2\text{–}PyPzH)_4Cl_6]$, Ln = La (**1**), Nd (**2**), Sm (**3**), α–$[Ln_2(2\text{–}PyPzH)_4Cl_6]$, Ln = Eu (**5**), Gd (**6**), Tb (**7**), β–$[Ln_2(2\text{–}PyPzH)_4Cl_6]$, Ln = Sm (**8**), Eu (**9**), Gd (**10**), $[Ce(2\text{–}PyPzH)_3Cl_3]$ (**11**), $[Ln(2\text{–}PyPzH)_2Cl_3]$, Ln = Tb (**12**), Dy (**13**), Ho (**14**), Eu (**15**), $[Gd_2(2\text{–}PyPzH)_3(2\text{–}PyPz)Cl_5]$ (**16**), $[Gd_3(2\text{–}PyPzH)_8Cl_8]Cl$ (**17**), and [PyH][Tb(2–$PyPzH)_2Cl_4$] (**18**); Figure S1: (**a**) Extended coordination sphere of Tb^{3+} ion in α–$[Tb_2(2\text{–}PyPzH)_4Cl_6]$ (**7**) representing the isotypic complexes **4**–**7**. (**b**) Packing structure of **7** with a view along [100]. In all figures, the hydrogen atoms are omitted for clarity and the coordination polyhedra around Ln^{3+} are indicated in green, with thermal ellipsoids shown with a probability of 50%; Figure S2: Overlay of the molecular structures of α–$[Eu_2(2\text{–}PyPzH)_4Cl_6]$ (red) (**5**) and β–$[Eu_2(2\text{–}PyPzH)_4Cl_6]$ (blue) (**9**); Figure S3: (**a**) Extended coordination sphere of Gd^{3+} ion in $[Gd_2(2\text{–}PyPzH)_3(2\text{–}PyPz)Cl_5]$ (**16**). (**b**) Packing structure of **16** with a view along [100]; Figure S4: (**a**) Extended coordination sphere of Gd^{3+} ion in $[Gd_3(2\text{–}PyPzH)_8Cl_8]Cl$ (**17**). (**b**) Packing structure of **17** with a view along [100]; Figure S5: (**a**) Extended coordination sphere of Tb^{3+} ion in [PyH][Tb(2–$PyPzH)_2Cl_4$] (**18**). (**b**) Packing structure of **18** with a view along [100], the protonated pyridine molecules were omitted for clarity. Symmetry operation: I -x+1,y,-z+3/2; Figures S6–S9 Comparison of the observed powder X-ray diffraction pattern (colored) of $^1{}_\infty[Ln_2(2\text{–}PyPzH)_4Cl_6]$, RE = La (**1**), Nd (**2**), Sm (**3**), α–$[Ln_2(2\text{–}PyPzH)_4Cl_6]$, Ln = Sm (**4**), Eu (**5**), Gd (**6**), β–$[Ln_2(2\text{–}PyPzH)_4Cl_6]$, Ln = Sm (**8**), Eu (**9**), and $[Ln(2\text{–}PyPzH)_2Cl_3]$, Ln = Tb (**12**), Dy (**13**), Ho (**14**), Er (**15**) with the corresponding simulated diffraction patterns from the single crystal X-ray data (black) for each case; Figure S10: Pawley refinement of (**a**) β–$[Sm_2(2\text{–}PyPzH)_4Cl_6]$ (**8**) with a GOF of 1.16, (**b**) $[Ce(2\text{–}PyPzH)_3Cl_3]$ (**11**) with a GOF of 1.87. The experimental data are shown in black, Pawley fit in red, the corresponding difference plot in blue, and the hkl position markers in green; Figure S11: Comparison of the observed powder X-ray diffraction pattern (colored) of a mixture of α–$[Gd_2(2\text{–}PyPzH)_4Cl_6]$ (**6**) and β–$[Gd_2(2\text{–}PyPzH)_4Cl_6]$ (**10**) with the simulated diffraction pattern from the single crystal X-ray data of **6** and **10** (black); Figures S12–S24: Absorption spectra of 2–PyPzH, $^1{}_\infty[Ln_2(2\text{–}PyPzH)_4Cl_6]$, Ln=La (**1**), Nd (**2**), Sm (**3**), α–$[Ln_2(2\text{–}PyPzH)_4Cl_6]$, Ln=Eu (**5**), Gd (**6**), β–$[Ln_2(2\text{–}PyPzH)_4Cl_6]$, Ln=Sm (**8**), Eu (**9**), $[Ce(2\text{–}PyPzH)_3Cl_3]$ (**11**), $[Ln(2\text{–}PyPzH)_2Cl_3]$, Ln=Tb (**12**), Dy (**13**), Ho (**14**), Er (**15**) in the solid state at room temperature; Figures S25–S38: Normalized excitation and emission spectra of 2–PyPzH, $^1{}_\infty[Ln_2(2\text{–}PyPzH)_4Cl_6]$, Ln=La (**1**), Nd (**2**), Sm (**3**), α–$[Ln_2(2\text{–}PyPzH)_4Cl_6]$, Ln=Sm (**4**), Eu (**5**), Gd (**6**), β–$[Ln_2(2\text{–}PyPzH)_4Cl_6]$, Ln=Sm (**8**), Eu (**9**), $[Ce(2\text{–}PyPzH)_3Cl_3]$ (**11**), and $[Ln(2\text{–}PyPzH)_2Cl_3]$, Ln=Tb (**12**), Dy (**13**), Ho (**14**), Er (**15**) at room temperature (top) and 77 K (bottom). Wavelengths at which the spectra were recorded are reported in the legends; Figures S39–S51: The infrared spectrum (ATR) of $^1{}_\infty[Ln_2(2\text{–}PyPzH)_4Cl_6]$, Ln=La (**1**), Nd (**2**), Sm(**3**), α–$[Ln_2(2\text{–}PyPzH)_4Cl_6]$, Ln=Sm (**4**), Eu (**5**), Gd (**6**), β–$[Ln_2(2\text{–}PyPzH)_4Cl_6]$, Ln=Sm (**8**), Eu (**9**), $[Ce(2\text{–}PyPzH)_3Cl_3]$ (**11**), and $[Ln(2\text{–}PyPzH)_2Cl_3]$, Ln=Tb (**12**), Dy (**13**), Ho (**14**), Er (**15**). Reference [77] is cited in the Supplementary Materials.

Author Contributions: Conceptualization, K.M.-B. and H.Y.; methodology, H.Y. and A.E.S.; software, H.Y. and J.B.; validation, H.Y.; formal analysis, H.Y., A.E.S. and J.B.; investigation, H.Y.; resources, I.V.T. and K.M.-B.; data curation, H.Y. and J.B.; writing—original draft preparation, H.Y.; writing—review and editing, H.Y., A.E.S., J.B., I.V.T. and K.M.-B.; visualization, H.Y.; supervision, K.M.-B.; project administration, K.M.-B.; All authors have read and agreed to the published version of the manuscript.

Funding: This research was funded by the Volkswagen Foundation within the project "Molecular materials—bridging magnetism and luminescence." Heba Youssef was awarded a PhD fellowship by the Egyptian Ministry of Higher Education (MoHE) and the German Academic Exchange Service (DAAD) within the German Egyptian Research Long-term Scholarship (GERLS) Program, 2017 (57311832), the funding agency is the German Academic Exchange Service Cairo. The synthesis of the studied ligand was funded by the Russian Science Foundation (project № 19–13–00272).

Data Availability Statement: CCDC 2208098 (**1**), 2208099 (**2**), 2208100 (**3**), 2208101 (**5**), 2208102 (**6**), 2208103 (**7**), 2208104 (**8**), 2208105 (**9**), 2208106 (**10**), 2208107 (**11**), 2208108 (**12**), 2208109 (**13**), 2208110 (**14**), 2208111 (**15**), 2208112 (**16**), 2208113 (**17**), 2208114 (**18**) contain the supplementary crystallographic data for this paper. These data can be obtained free of charge via http://www.ccdc.cam.ac.uk/conts/retrieving.html (or from the CCDC, 12 Union Road, Cambridge CB2 1EZ, UK; Fax: +44 1223 336033; email: deposit@ccdc.cam.ac.uk).

Conflicts of Interest: The authors declare no conflict of interest.

References

1. Forsberg, J.H. Complexes of lanthanide(III) ions with nitrogen donor ligands. *Coord. Chem. Rev.* **1973**, *10*, 195–226. [CrossRef]
2. Youssef, H.; Schäfer, T.C.; Becker, J.; Sedykh, A.E.; Basso, L.; Pietzonka, C.; Taydakov, I.V.; Kraus, F.; Müller-Buschbaum, K. 3D-Frameworks and 2D-networks of lanthanide coordination polymers with 3-pyridylpyrazole: Photophysical and magnetic properties. *Dalton Trans.* **2022**, *51*, 14673–14685. [CrossRef] [PubMed]
3. Drew, M.G.; Foreman, M.R.S.; Hudson, M.J.; Kennedy, K.F. Structural studies of lanthanide complexes with tetradentate nitrogen ligands. *Inorg. Chim. Acta* **2004**, *357*, 4102–4112. [CrossRef]
4. Miguirditchian, M.; Guillaneux, D.; François, N.; Airvault, S.; Ducros, S.; Thauvin, D.; Madic, C.; Illemassène, M.; Lagarde, G.; Krupa, J.C. Complexation of lanthanide(III) and actinide(III) cations with tridentate nitrogen-donor ligands: A luminescence and spectrophotometric study. *Nucl. Sci. Eng.* **2006**, *153*, 223–232. [CrossRef]
5. Sedykh, A.E.; Bissert, R.; Kurth, D.G.; Müller-Buschbaum, K. Structural diversity of salts of terpyridine derivatives with europium(III) located in both, cation and anion, in comparison to molecular complexes. *Z. Kristallogr. Cryst. Mater.* **2020**, *235*, 353–363. [CrossRef]
6. Höller, C.J.; Mai, M.; Feldmann, C.; Müller-Buschbaum, K. The interaction of rare earth chlorides with 4,4′-bipyridine for the reversible formation of template based luminescent Ln-N-MOFs. *Dalton Trans.* **2010**, *39*, 461–468. [CrossRef]
7. Youssef, H.; Sedykh, A.E.; Becker, J.; Schäfer, T.; Taydakov, I.V.; Li, H.R.; Müller-Buschbaum, K. Variable luminescence and chromaticity of homoleptic frameworks of the lanthanides together with pyridylpyrazolates. *Chem. Eur. J.* **2021**, *27*, 16634–16641. [CrossRef]
8. Sedykh, A.E.; Kurth, D.G.; Müller-Buschbaum, K. Two series of lanthanide coordination polymers and complexes with 4′-phenylterpyridine and their luminescence properties. *Eur. J. Inorg. Chem.* **2019**, *2019*, 4564–4571. [CrossRef]
9. Piguet, C.; Williams, A.F.; Bernardinelli, G.; Buenzli, J.C.G. Structural and photophysical properties of lanthanide complexes with planar aromatic tridentate nitrogen ligands as luminescent building blocks for triple-helical structures. *Inorg. Chem.* **1993**, *32*, 4139–4149. [CrossRef]
10. Ekberg, C.; Fermvik, A.; Retegan, T.; Skarnemark, G.; Foreman, M.; Hudson, M.; Englund, S.; Nilsson, M. An overview and historical look back at the solvent extraction using nitrogen donor ligands to extract and separate An(III) from Ln(III). *Radiochim. Acta* **2008**, *96*, 225–233. [CrossRef]
11. Matthes, P.R.; Schönfeld, F.; Zottnick, S.H.; Müller-Buschbaum, K. Post-synthetic shaping of porosity and crystal structure of Ln-Bipy-MOFs by thermal treatment. *Molecules* **2015**, *20*, 12125–12153. [CrossRef] [PubMed]
12. Meihaus, K.R.; Minasian, S.G.; Lukens, W.W., Jr.; Kozimor, S.A.; Shuh, D.K.; Tyliszczak, T.; Long, J.R. Influence of pyrazolate vs. N-heterocyclic carbene ligands on the slow magnetic relaxation of homoleptic trischelate lanthanide(III) and uranium(III) complexes. *J. Am. Chem. Soc.* **2014**, *136*, 6056–6068. [CrossRef]
13. Hassan, S.S.; Mohamed, E.F. Antimicrobial, antioxidant and antitumor activities of nano-structure Eu(III) and La(III) complexes with nitrogen donor tridentate ligands. *Appl. Organomet. Chem.* **2020**, *34*, e5258. [CrossRef]
14. Bünzli, J.-C.G.; Eliseeva, S.V. Basics of lanthanide photophysics. In *Springer Series on Fluorescence: Lanthanide Luminescence: Photophysical, Analytical and Biological Aspects*; Wolfbeis, O.S., Hof, M., Eds.; Springer: Berlin/Heidelberg, Germany, 2011; Volume 7, pp. 1–46.
15. Yin, H.; Carroll, P.J.; Anna, J.M.; Schelter, E.J. Luminescent Ce(III) complexes as stoichiometric and catalytic photoreductants for halogen atom abstraction reactions. *J. Am. Chem. Soc.* **2015**, *137*, 9234–9237. [CrossRef] [PubMed]
16. Qiao, Y.; Sergentu, D.-C.; Yin, H.; Zabula, A.V.; Cheisson, T.; McSkimming, A.; Manor, B.C.; Carroll, P.J.; Anna, J.M.; Autschbach, J.; et al. Understanding and controlling the emission brightness and color of molecular cerium luminophores. *J. Am. Chem. Soc.* **2018**, *140*, 4588–4595. [CrossRef] [PubMed]
17. Lindqvist-Reis, P.; Réal, F.; Janicki, R.; Vallet, V. Unraveling the ground state and excited state structures and dynamics of hydrated Ce^{3+} ions by experiment and theory. *Inorg. Chem.* **2018**, *57*, 10111–10121. [CrossRef]

18. Wang, L.; Zhao, Z.; Zhan, G.; Fang, H.; Yang, H.; Huang, T.; Zhang, Y.; Jiang, N.; Duan, L.; Liu, Z.; et al. Deep-blue organic light-emitting diodes based on a doublet *d–f* transition cerium(III) complex with 100% exciton utilization efficiency. *Light Sci. Appl.* **2020**, *9*, 157. [CrossRef]
19. Zhao, Z.; Wang, L.; Zhan, G.; Liu, Z.; Bian, Z.; Huang, C. Efficient rare earth cerium(III) complex with nanosecond $d-f$ emission for blue organic light-emitting diodes. *Natl. Sci. Rev.* **2021**, *8*, nwaa193. [CrossRef]
20. Qin, X.; Liu, X.; Huang, W.; Bettinelli, M.; Liu, X. Lanthanide-activated phosphors based on 4f-5d optical transitions: Theoretical and experimental aspects. *Chem. Rev.* **2017**, *117*, 4488–4527. [CrossRef]
21. Yin, H.; Carroll, P.J.; Manor, B.C.; Anna, J.M.; Schelter, E.J. Cerium photosensitizers: Structure–function relationships and applications in photocatalytic aryl coupling reactions. *J. Am. Chem. Soc.* **2016**, *138*, 5984–5993. [CrossRef]
22. Matthes, P.R.; Müller-Buschbaum, K. Synthesis and characterization of the cerium(III) UV-emitting 2D-coordination polymer $^{2\infty}[Ce_2Cl_6(4,4'\text{-bipyridine})_4]\cdot py$. *Z. Anorg. Allg. Chem.* **2014**, *640*, 2847–2851. [CrossRef]
23. Meyer, L.V.; Schönfeld, F.; Zurawski, A.; Mai, M.; Feldmann, C.; Müller-Buschbaum, K. A blue luminescent MOF as a rapid turn-off/turn-on detector for H_2O, O_2 and CH_2Cl_2, MeCN: $^3{}_\infty[Ce(Im)_3ImH]\cdot ImH$. *Dalton Trans.* **2015**, *44*, 4070–4079. [CrossRef] [PubMed]
24. Bünzli, J.-C.G. On the design of highly luminescent lanthanide complexes. *Coord. Chem. Rev.* **2015**, *293*, 19–47. [CrossRef]
25. Eliseeva, S.V.; Bünzli, J.-C.G. Lanthanide luminescence for functional materials and bio-sciences. *Chem. Soc. Rev.* **2010**, *39*, 189–227. [CrossRef] [PubMed]
26. Weissman, S. Intramolecular energy transfer the fluorescence of complexes of europium. *J. Chem. Phys.* **1942**, *10*, 214–217. [CrossRef]
27. Crosby, G.; Whan, R.; Alire, R. Intramolecular energy transfer in rare earth chelates. Role of the triplet state. *J. Chem. Phys.* **1961**, *34*, 743–748. [CrossRef]
28. Frey, S.T.; Horrocks, W.D., Jr. Complexation, luminescence, and energy transfer of Ce^{3+} with a series of multidentate amino phosphonic acids in aqueous solution. *Inorg. Chem.* **1991**, *30*, 1073–1079. [CrossRef]
29. Blasse, G.; Grabmaier, B.C. A general introduction to luminescent materials. In *Luminescent Materials*; Springer: Berlin/Heidelberg, Germany, 1994; pp. 1–9.
30. Fang, P.; Wang, L.; Zhan, G.; Yan, W.; Huo, P.; Ying, A.; Zhang, Y.; Zhao, Z.; Yu, G.; Huang, Y.; et al. Lanthanide cerium(III) tris(pyrazolyl)borate complexes: Efficient blue emitters for doublet organic light-emitting diodes. *ACS Appl. Mater. Interfaces* **2021**, *13*, 45686–45695. [CrossRef]
31. Kodama, N.; Tanii, Y.; Yamaga, M. Optical properties of long-lasting phosphorescent crystals Ce^{3+}-doped $Ca_2Al_2SiO_7$ and $CaYAl_3O_7$. *J. Lumin.* **2000**, *87*, 1076–1078. [CrossRef]
32. Kim, G.C.; Park, H.L.; Yun, S.I.; Moon, B.G. Solid solubility limit of cerium in CaS:Ce^{3+} phosphor. *J. Mater. Sci. Lett.* **1986**, *5*, 359–360. [CrossRef]
33. Van Krevel, J.W.H.; Hintzen, H.T.; Metselaar, R.; Meijerink, A. Long wavelength Ce^{3+} emission in Y–Si–O–N materials. *J. Alloys Compd.* **1998**, *268*, 272–277. [CrossRef]
34. Gauthier, G.; Jobic, S.; Evain, M.; Koo, H.-J.; Whangbo, M.-H.; Fouassier, C.; Brec, R. Syntheses, structures, and optical properties of yellow Ce_2SiS_5, $Ce_6Si_4S_{17}$, and $Ce_4Si_3S_{12}$ materials. *Chem. Mater.* **2003**, *15*, 828–837. [CrossRef]
35. Blasse, G.; Bril, A. A new phosphor for flying-spot cathode-ray tubes for color television: Yellow-emitting $Y_3Al_5O_{12}$–Ce^{3+}. *Appl. Phys. Lett.* **1967**, *11*, 53–55. [CrossRef]
36. Wu, D.; Hao, Z.; Zhang, X.; Pan, G.-H.; Luo, Y.; Zhang, L.; Zhao, H.; Zhang, J. Efficient energy back transfer from Ce^{3+} 5d state to Pr^{3+} $^1D_2$ level in $Lu_3Al_5O_{12}$ upon Pr^{3+} 4f5d excitation. *J. Lumin.* **2017**, *186*, 170–174. [CrossRef]
37. Peng, D.A.I.; Cheng, J.I.; Liming, S.H.E.N.; Qi, Q.I.A.N.; Guobiao, G.U.O.; Zhang, X.; Ningzhong, B.A.O. Photoluminescence properties of YAG: Ce^{3+},Pr^{3+} nano-sized phosphors synthesized by a modified co-precipitation method. *J. Rare Earths* **2017**, *35*, 341–346. [CrossRef]
38. Zeng, P.; Wei, X.; Zhou, S.; Yin, M.; Chen, Y. Evaluation of critical distances for energy transfer between Pr^{3+} and Ce^{3+} in yttrium aluminium garnet. *J. Appl. Phys.* **2016**, *120*, 093104. [CrossRef]
39. Ogiegło, J.M.; Zych, A.; Jüstel, T.; Meijerink, A.; Ronda, C.R. Luminescence and energy transfer in $Lu_3Al_5O_{12}$ scintillators co-doped with Ce^{3+} and Pr^{3+}. *Opt. Mater.* **2013**, *35*, 322–331. [CrossRef]
40. Kowalski, R.M.; Komar, J.; Solarz, P. On the combination of praseodymium and cerium, a new concept of improving orange-red luminescence. *J. Alloys Compd.* **2020**, *848*, 156228. [CrossRef]
41. Blagden, N.; Davey, R.J. Polymorph selection: Challenges for the future? *Cryst. Growth Des.* **2003**, *3*, 873–885. [CrossRef]
42. Meundaeng, N.; Rujiwatra, A.; Prior, T.J. Polymorphism in metal complexes of thiazole-4-carboxylic acid. *Transit. Met. Chem.* **2016**, *41*, 783–793. [CrossRef]
43. Shannon, R.D. Revised effective ionic radii and systematic studies of interatomic distances in halides and chalcogenides. *Acta Crystallogr. Sect. A* **1976**, *32*, 751–767. [CrossRef]
44. Eyring, L. The binary rare earth oxides. In *Handbook on the Physics and Chemistry of Rare Earths*; Gschneidner, K.A., Jr., Eyring, L., Eds.; Elsevier BV: Amsterdam, The Netherlands, 1979; Volume 3, pp. 337–399.
45. Kumar, R.; Singh, U.P. Molecular structure, photophysical and thermal properties of samarium(III) complexes. *J. Mol. Struct.* **2008**, *875*, 427–434. [CrossRef]

46. Mazurek, J.; Lisowski, J. Chiral macrocyclic lanthanide complexes derived from (1*R*, 2*R*)-1, 2-diphenylethylenediamine and 2,6-diformylpyridine. *Polyhedron* **2003**, *22*, 2877–2883. [CrossRef]
47. Matthes, P.R.; Nitsch, J.; Kuzmanoski, A.; Feldmann, C.; Steffen, A.; Marder, T.B.; Müller-Buschbaum, K. The series of rare earth complexes $[Ln_2Cl_6(\mu\text{-}4,4'\text{-bipy})(py)_6]$, Ln=Y, Pr, Nd, Sm-Yb: A molecular model system for luminescence properties in MOFs based on $LnCl_3$ and 4,4′-bipyridine. *Chem. Eur. J.* **2013**, *19*, 17369–17378. [CrossRef] [PubMed]
48. Lewis, D.J.; Moretta, F.; Holloway, A.T.; Pikramenou, Z. Evaluation of quinoline as a remote sensitiser for red and near-infrared emissive lanthanide(III) ions in solution and the solid state. *Dalton Trans.* **2012**, *41*, 13138–13146. [CrossRef] [PubMed]
49. Mahato, M.; Jana, P.P.; Harms, K.; Nayek, H.P. Lanthanide(III) morpholine 4-dithiocarbamate complexes: Pr(III) derivative shows first example of polymeric lanthanide(III) dithiocarbamate. *RSC Adv.* **2015**, *5*, 62167–62172. [CrossRef]
50. Chow, C.Y.; Eliseeva, S.V.; Trivedi, E.R.; Nguyen, T.N.; Kampf, J.W.; Petoud, S.; Pecoraro, V.L. Ga^{3+}/Ln^{3+} metallacrowns: A promising family of highly luminescent lanthanide complexes that covers visible and near-infrared domains. *J. Am. Chem. Soc.* **2016**, *138*, 5100–5109. [CrossRef]
51. Satheesh Chandran, P.R.; Soumya Mol, U.S.; Drisya, R.; Sudarsanakumar, M.R.; Prathapachandra Kurup, M.R. Structural studies of poly [(μ_2-acetato)(μ_3-5-aminoisophthalato) diaquacerium(III) monohydrate]: A new three dimensional fluorescent metal-organic framework constructed from dimers of CeO_9 polyhedra with hydrophilic 'S' shaped channels. *J. Mol. Struct.* **2017**, *1137*, 396–402. [CrossRef]
52. Zhou, X.; Wang, H.; Jiang, S.; Xiang, G.; Tang, X.; Luo, X.; Li, L.; Zhou, X. Multifunctional luminescent material Eu(III) and Tb(III) complexes with pyridine-3,5-dicarboxylic acid linker: Cystal structures, tunable emission, energy transfer, and temperature sensing. *Inorg. Chem.* **2019**, *58*, 3780–3788. [CrossRef]
53. Hasegawa, M.; Ohtsu, H.; Kodama, D.; Kasai, T.; Sakurai, S.; Ishii, A.; Suzuki, K. Luminescence behaviour in acetonitrile and in the solid state of a series of lanthanide complexes with a single helical ligand. *New J. Chem.* **2014**, *38*, 1225–1234. [CrossRef]
54. Seidel, C.; Lorbeer, C.; Cybińska, J.; Mudring, A.-V.; Ruschewitz, U. Lanthanide coordination polymers with tetrafluoroterephthalate as a bridging ligand: Thermal and optical properties. *Inorg. Chem.* **2012**, *51*, 4679–4688. [CrossRef]
55. Wang, J.-J.; Liu, C.-S.; Hu, T.-L.; Chang, Z.; Li, C.-Y.; Yan, L.-F.; Chen, P.-Q.; Bu, X.-H.; Wu, Q.; Zhao, L.-J.; et al. Zinc(II) coordination architectures with two bulky anthracene-based carboxylic ligands: Crystal structures and luminescent properties. *CrystEngComm* **2008**, *10*, 681–692. [CrossRef]
56. Liu, C.S.; Shi, X.S.; Li, J.R.; Wang, J.J.; Bu, X.H. Cd(II) coordination architectures with mixed ligands of 3-(2-pyridyl)pyrazole and pendant carboxylate ligands bearing different aromatic skeletons: Syntheses, crystal structures, and emission properties. *Cryst. Growth Des.* **2006**, *6*, 656–663. [CrossRef]
57. Carnall, W.T.; Fields, P.R.; Rajnak, K. Electronic energy levels in the trivalent lanthanide aquo Ions. I. Pr^{3+}, Nd^{3+}, Pm^{3+}, Sm^{3+}, Dy^{3+}, Ho^{3+}, Er^{3+}, and Tm^{3+}. *J. Chem. Phys.* **1968**, *49*, 4424–4442. [CrossRef]
58. Carnall, W.T.; Fields, P.R.; Rajnak, K. Electronic energy levels of the trivalent lanthanide aquo ions. IV. Eu^{3+}. *J. Chem. Phys.* **1968**, *49*, 4450–4455. [CrossRef]
59. Carnall, W.T.; Fields, P.R.; Rajnak, K. Electronic energy levels of the trivalent lanthanide aquo ions. III. Tb^{3+}. *J. Chem. Phys.* **1968**, *49*, 4447–4449. [CrossRef]
60. Huskowska, E.; Turowska-Tyrk, I.; Legendziewicz, J.; Riehl, J.P. The structure and spectroscopy of lanthanide(III) complexes with 2, 2′-bipyridine-1,1′-dioxide in solution and in the solid state: Effects of ionic size and solvent on photophysics, ligand structure and coordination. *New J. Chem.* **2002**, *26*, 1461–1467. [CrossRef]
61. Chawla, S.; Roy, T.; Majumder, K.; Yadav, A. Red enhanced YAG: Ce, Pr nanophosphor for white LEDs. *J. Exp. Nanosci.* **2014**, *9*, 776–784. [CrossRef]
62. Wang, Y.; Ding, J.; Zhao, Z.; Wang, Y. A cerium doped scandate broad orange-red emission phosphor and its energy transfer-dependent concentration and thermal quenching character. *Inorg. Chem.* **2018**, *57*, 14542–14553. [CrossRef]
63. Hasegawa, T.; Kim, S.W.; Ueda, T.; Ishigaki, T.; Uematsu, K.; Takaba, H.; Toda, K.; Sato, M. Unusual, broad red emission of novel Ce^{3+}-activated $Sr_3Sc_4O_9$ phosphors under visible-light excitation. *J. Mater. Chem. C* **2017**, *5*, 9472–9478. [CrossRef]
64. Aquino, L.E.D.N.; Barbosa, G.A.; Ramos, J.D.L.; Giese, S.O.K.; Santana, F.S.; Hughes, D.L.; Nunes, G.G.; Fu, L.; Fang, M.; Poneti, G.; et al. Seven-coordinate Tb^{3+} complexes with 90% quantum Yields: High-performance examples of combined singlet- and triplet-to-Tb^{3+} energy-transfer pathways. *Inorg. Chem.* **2021**, *60*, 892–907. [CrossRef] [PubMed]
65. Binnemans, K. Interpretation of europium(III) spectra. *Coord. Chem. Rev.* **2015**, *295*, 1–45. [CrossRef]
66. Binnemans, K. Lanthanide-based luminescent hybrid materials. *Chem. Rev.* **2009**, *109*, 4283–4374. [CrossRef]
67. Martin, A.; Narayanaswamy, R. Studies on quenching of fluorescence of reagents in aqueous solution leading to an optical chloride-ion sensor. *Sens. Actuators B Chem.* **1997**, *39*, 330–333. [CrossRef]
68. Rycerz, L.; Gaune-Escard, M. Thermodynamics of $EuCl_3$: Experimental enthalpy of fusion and heat capacity and estimation of thermodynamic functions up to 1300 K. *Z. Naturforschung A* **2002**, *57*, 215–220. [CrossRef]
69. Rycerz, L.; Gaune-Escard, M. Enthalpies of phase transitions and heat capacity of $TbCl_3$ and compounds formed in $TbCl_3$–MCl systems (M= K, Rb, Cs). *J. Therm. Anal. Calorim.* **2002**, *68*, 973–981. [CrossRef]
70. Amoroso, A.J.; Thompson, A.M.C.; Jeffery, J.C.; Jones, P.L.; McCleverty, J.A.; Ward, M.D. Synthesis of the new tripodal ligand tris-[3-(2′-pyridyl)pyrazol-1- yl]hydroborate, and the crystal structure of its europium(III) complex. *J. Chem. Soc. Chem. Commun.* **1994**, 2751–2752. [CrossRef]

71. Salinas Uber, J.; Vogels, Y.; van den Helder, D.; Mutikainen, I.; Turpeinen, U.; Fu, W.T.; Roubeau, O.; Gamez, P.; Reedijk, J. Pyrazole-based ligands for the [copper–TEMPO]-mediated oxidation of benzyl alcohol to benzaldehyde and structures of the Cu coordination compounds. *Eur. J. Inorg. Chem.* **2007**, *2007*, 4197–4206. [CrossRef]
72. Sheldrick, G.M. SHELXT—Integrated space-group and crystal-structure determination. *Acta Crystallogr. Sect. A Found. Adv.* **2015**, *71*, 3–8. [CrossRef]
73. Sheldrick, G.M. Crystal structure refinement with SHELXL. *Acta Crystallogr. Sect. C Struct. Chem.* **2015**, *71*, 3–8. [CrossRef]
74. Pennington, W.T. DIAMOND—Visual crystal structure information system. *J. Appl. Crystallogr.* **1999**, *32*, 1028–1029. [CrossRef]
75. Macrae, C.F.; Sovago, I.; Cottrell, S.J.; Galek, P.T.; McCabe, P.; Pidcock, E.; Platings, M.; Shields, G.P.; Stevens, J.S.; Towler, M. Mercury 4.0: From visualization to analysis, design and prediction. *J. Appl. Crystallogr.* **2020**, *53*, 226–235. [CrossRef] [PubMed]
76. Coelho, A.A. TOPAS and TOPAS-Academic: An optimization program integrating computer algebra and crystallographic objects written in C++: An. *J. Appl. Crystallogr.* **2018**, *51*, 210–218. [CrossRef]
77. Wrighton, M.S.; Ginley, D.S.; Morse, D.L. Technique for the determination of absolute emission quantum yields of powdered samples. *J. Phys. Chem.* **1974**, *78*, 2229–2233. [CrossRef]

Table of Contents

Experimental

Spectroscopic Investigations

Vibrational spectra were recorded from 2–5 milligrams of the compounds with an ALPHA FT–IR spectrometer from Bruker optics (ATR module) using OPUS software.

Absorption Spectra were measured on solid–state products using a standard Agilent Cary 5000 UV–VIS–NIR spectrophotometer with a Praying Mantis accessory, which had been mounted and aligned for use with the DRP–ASC ambient chamber. The source, detector, and grating changeovers were at the standard position of 350, 800, and 800 nm, respectively, for all studied compounds except $^1_\infty$[Nd(2–PyPzH)$_2$Cl$_3$] (**2**) and [Dy(2–PyPzH)$_2$Cl$_3$] (**13**), the detector and grating changeovers were set to 850 nm. For $^1_\infty$[Nd(2–PyPzH)$_2$Cl$_3$] (**2**), β–[Sm$_2$(2–PyPzH)$_4$Cl$_6$] (**8**), and [Ce(2–PyPzH)$_3$Cl$_3$] (**11**), the source has been set to 380, 330, and 320 nm, respectively. The reference spectrum was collected on PTFE and the reference and samples were packed in the ambient chamber within the glovebox under inert conditions. Water has absorption bands in the NIR region at around 1370 and 1850 nm, which interferes with the absorption of our Ln^{3+} ions. In order to avoid these interferences, we carried out the measurements up to 1300 nm.

Photoluminescence spectra were recorded for ground solid samples after filling them in quartz glass tubes under argon. Measurements were performed at room temperature as well as 77 K (the latter using the liquid nitrogen–filled assembly FL–1013 of HORIBA) with a HORIBA Jobin Yvon Spex Fluorolog 3 spectrometer equipped with a 450 W Xe short–arc lamp (USHIO), double–grated excitation, emission monochromators, and a photomultiplier tube (R928P) using the FluoroEssence™ software. Excitation and emission spectra were corrected for the spectral response of the monochromators and detector using spectral corrections provided by the constructor. In addition, a photodiode reference detector was used to correct the excitation spectra for the spectral distribution of the lamp intensity. An R5509–73 detector was used to collect the data in the NIR region. When needed, data collection was performed using an edge filter (Newport 20CGA–345, 395, 495 for the visible range and Reichmann Optics RG 830 longpass for the NIR range). Emission spectra with gating were recorded using a xenon flashlamp with a pulse repetition rate of 41 ms.

Photoluminescence overall decay process times were determined using the aforementioned HORIBA Jobin Yvon Spex Fluorolog 3 spectrometer equipped with a dual lamp housing (FL–1040A), a UV–xenon flashlamp (Exelitas FX–1102), and a TCSPC (time–correlated single–photon counting) upgrade, or pulsed picosecond laser diode. Emission decays were recorded using DataStation software. Exponential tail fitting was used to calculate the resulting intensity decay using Decay Analysis Software 6. The quality of the fit was confirmed by χ^2 values being below 1.2.

Photoluminescence quantum yields were determined using a second similar instrument HORIBA Jobin Yvon Spex Fluorolog 3 spectrometer equipped with a HORIBA Quanta–ϕ Integrating Sphere. For the measurements, solid samples were filled into Starna Micro Cell cuvettes 18–F/ST/C/Q/10 (fluorescence with ST/C closed–cap, material UV quartz glass Spectrosil Q, pathlength 10 mm, matched). Magnesium oxide was used as reference material. Each sample was measured at least three times and then the quantum yield values with standard deviation were evaluated. The Quanta–ϕ Integrating Sphere was checked with a standard (sodium salicylate as a powder, λ_{ex} = 340 nm, λ_{em} = 365–600 nm, measured QY = 52%, literature: 53%) [77].

Thermal analysis

Simultaneous DTA/TG (NETZSCH STA 409–PC) coupled to a mass spectrometer (NETZSCH QMS 403 Aëolos) in a constant argon flow of 50 mL·min^{-1} with a heating rate of 5 K·min^{-1} from room temperature to 1000 °C was used to determine the thermal properties. The DTA curve was baseline–corrected after the measurement using the Origin™ software.

CHN analysis

A Thermo Scientific Flash EA–1112 was used to perform the CHN analyses. The samples were placed in a tin crucible with at least one mass equivalent of V_2O_5. The samples were prepared and stored under inert conditions until the measurements.

Crystallographic Data

CCDC 2208098 (**1**), 2208099 (**2**), 2208100 (**3**), 2208101 (**5**), 2208102 (**6**), 2208103 (**7**), 2208104 (**8**), 2208105 (**9**), 2208106 (**10**), 2208107 (**11**), 2208108 (**12**), 2208109 (**13**), 2208110 (**14**), 2208111 (**15**), 2208112 (**16**), 2208113 (**17**), 2208114 (**18**) contain the supplementary crystallographic data. These data are provided free of charge by the Cambridge Crystallographic Data Centre.

Table S1. Crystallographic data of $^1_\infty$[Ln$_2$(2–PyPzH)$_4$Cl$_6$], Ln = La (**1**), Nd (**2**), and Sm (**3**).

Compound	**$^1_\infty$[La$_2$(2–PyPzH)$_4$Cl$_6$]**	**$^1_\infty$[Nd$_2$(2–PyPzH)$_4$Cl$_6$]**	**$^1_\infty$[Sm$_2$(2–PyPzH)$_4$Cl$_6$]**
CCDC number	2208098	2208099	2208100
Empirical formula	$C_{16}H_{14}N_6Cl_3La$	$C_{16}H_{14}N_6Cl_3Nd$	$C_{16}H_{14}N_6Cl_3Sm$
M_r / g·mol^{-1}	535.59	540.92	547.03
T / K	100(2)	200(2)	100(2)
λ / pm	71.073, Mo–K$_\alpha$	71.073, Mo–K$_\alpha$	71.073, Mo–K$_\alpha$
Crystal system	Monoclinic	Monoclinic	Monoclinic
Space group	*C*2/*c*	*C*2/*c*	*C*2/*c*
a / pm	2033.6(1)	2031.3(1)	1993.4(1)
b / pm	1190.2(1)	1186.3(1)	1192.3(1)
c / pm	2489.7(2)	2466.6(2)	2449.5(1)
α / °	90	90	90
β / °	92.802(2)	92.326(2)	92.519(2)
γ / °	90	90	90
V / 10^6 pm^3	6018.7(5)	5939.0(6)	5816.5(5)
Z	12	12	12
ρ_{calc} / g·cm^{-3}	1.773	1.815	1.874
μ / mm^{-1}	2.541	3.040	3.455
F(000)	3120	3156	3180
Crystal size / mm^3	0.059 x 0.035 x 0.031	0.172 x 0.114 x 0.077	0.604 x 0.108 x 0.082
θ_{min} / °	1.983	2.007	2.175
θ_{max} / °	27.589	30.582	26.731
Reflections collected	214731	62094	58706
Independent reflections	6998	9066	6173
R(int)	0.0613	0.1365	0.0756
No. Of parameters	454	430	442
GOF	1.119	0.990	1.166
Final *R* indices [*I* > 2σ(I)]	R_1 = 0.0319, wR_2 = 0.0752	R_1 = 0.0450, wR_2 = 0.0651	R_1 = 0.0445, wR_2 = 0.0789
R indices (all data)	R_1 = 0.0403, wR_2 = 0.0794	R_1 = 0.0938, wR_2 = 0.0753	R_1 = 0.0574, wR_2 = 0.0819
$\Delta\rho_{max}$, $\Delta\rho_{min}$ / e·10^{-6}·pm^{-3}	2.571, –1.170	1.115, –1.334	2.160, –2.454

Table S2. Crystallographic data of α–[Ln_2(2–PyPzH)$_4Cl_6$], Ln = Eu (**5**), Gd (**6**), and Tb (**7**).

Compound	α–[Eu_2(2–PyPzH)$_4Cl_6$]	α–[Gd_2(2–PyPzH)$_4Cl_6$]	α–[Tb_2(2–PyPzH)$_4Cl_6$]
CCDC number	2208101	2208102	2208103
Empirical formula	$C_{16}H_{14}N_6Cl_3Eu$	$C_{16}H_{14}N_6Cl_3Gd$	$C_{16}H_{14}N_6Cl_3Tb$
M_r / g·mol^{-1}	548.64	553.93	555.60
T / K	100(2)	100(2)	100(2)
λ / pm	71.073, Mo–K_α	71.073 Mo–K_α	71.073, Mo–K_α
Crystal system	Monoclinic	Monoclinic	Monoclinic
Space group	$P2_1/c$	$P2_1/c$	$P2_1/c$
a / pm	811.5(1)	809.1(1)	809.5(1)
b / pm	2380.2(2)	2376.4(2)	2368.7(1)
c / pm	1055.4(1)	1053.3(1)	1054.2(1)
α / °	90	90	90
β / °	112.34(1)	112.19(1)	112.437(1)
γ / °	90	90	90
V / 10^6 pm^3	1885.6(2)	1875.2(3)	1868.31(9)
Z	4	4	4
ρ_{calc} / g·cm^{-3}	1.933	1.962	1.975
μ / mm^{-1}	3.764	3.977	4.227
F(000)	1064	1068	1072
Crystal size / mm^3	0.035 x 0.033 x 0.032	0.067 x 0.038 x 0.023	0.423 x 0.376 x 0.152
θ_{min} / °	2.255	2.257	2.260
θ_{max} / °	26.020	27.136	37.032
Reflections collected	33885	46710	122560
Independent reflections	3695	4156	9509
R(int)	0.0781	0.0956	0.0573
No. Of parameters	299	329	235
GOF	1.048	1.054	1.112
Final R indices [$I > 2\sigma(I)$]	R_1 = 0.0326, wR_2 = 0.0638	R_1 = 0.0409, wR_2 = 0.0895	R_1 = 0.0241, wR_2 = 0.0500
R indices (all data)	R_1 = 0.0511, $wR2$ = 0.0724	R_1 = 0.0694, wR_2 = 0.1066	R_1 = 0.0331, wR_2 = 0.0524
$\Delta\rho_{max}$, $\Delta\rho_{min}$ / e·10^{-6}·pm^{-3}	2.119, –1.824	3.501, –2.013	1.961, –1.527

Table S3. Crystallographic data of β–[Ln_2(2–PyPzH)$_4Cl_6$], Ln = Sm (**8**), Eu (**9**), Gd (**10**) and [Ce(2–PyPzH)$_3Cl_3$] (**11**).

Compound	β–[Sm_2(2–PyPzH)$_4Cl_6$]	β–[Eu_2(2–PyPzH)$_4Cl_6$]	β–[Gd_2(2–PyPzH)$_4Cl_6$]	[Ce(2–PyPzH)$_3Cl_3$]
CCDC number	2208104	2208105	2208106	2208107
Empirical formula	$C_{16}H_{14}N_6Cl_3Sm$	$C_{16}H_{14}N_6Cl_3Eu$	$C_{16}H_{14}N_6Cl_3Gd$	$C_{24}H_{21}N_9Cl_3Ce$
M_r / g·mol^{-1}	547.03	548.64	553.93	681.97
T / K	100(2)	100(2)	100(2)	100(2)
λ / pm	71.073, Mo–K_α	71.073, Mo–K_α	71.073, Mo–K_α	71.073, Mo–K_α
Crystal system	Triclinic	Triclinic	Triclinic	Orthorhombic
Space group	$P\bar{1}$	$P\bar{1}$	$P\bar{1}$	$Pbca$
a / pm	832.3(1)	831.4(1)	830.1(2)	1329.8(1)
b / pm	1045.6(1)	1045.6(2)	1050.6(3)	1916.0(1)
c / pm	1226.0(1)	1224.2(2)	1229.9(3)	2051.1(1)
α / °	74.63(1)	74.60(1)	75.20(1)	90
β / °	86.96(1)	86.88(1)	86.95(1)	90
γ / °	68.71(1)	68.64(1)	68.34(1)	90
V / 10^6 pm^3	957.5(1)	954.5(2)	962.9(4)	5226.1(5)
Z	2	2	2	8
ρ_{calc} / g·cm^{-3}	1.897	1.909	1.910	1.734
μ / mm^{-1}	3.497	3.718	3.872	2.082
F(000)	530	532	534	2696
Crystal size / mm^3	0.027 x 0.026 x 0.015	0.050 x 0.036 x 0.019	0.061 x 0.047 x 0.014	0.021 x 0.032 x 0.074
θ_{min} / °	2.387	2.169	1.714	2.112
θ_{max} / °	27.253	27.170	27.308	27.132
Reflections collected	95185	33424	21316	94436
Independent reflections	4281	4211	4281	5784
R(int)	0.1488	0.0560	0.0624	0.1012
No. Of parameters	235	235	236	334
GOF	1.040	0.874	1.167	1.040
Final R indices [$I > 2\sigma(I)$]	R_1 = 0.0262, wR_2 = 0.0444	R_1 = 0.0274, wR_2 = 0.0956	R_1 = 0.0398, wR_2 = 0.0816	R_1 = 0.0309, wR_2 = 0.0645
R indices (all data)	R_1 = 0.0393, wR_2 = 0.0473	R_1 = 0.0332, wR_2 = 0.1021	R_1 = 0.0499, wR_2 = 0.0846	R_1 = 0.0412, wR_2 = 0.0709
$\Delta\rho_{max}$, $\Delta\rho_{min}$ / e·10^{-6}·pm^{-3}	1.683, –0.804	1.007, –1.368	1.235, –0.900	1.764, –0.595

Table S4. Crystallographic data of [Ln(2–PyPzH)$_2Cl_3$], Ln = Tb (**12**), Dy (**13**), Ho (**14**), and Eu (**15**).

Compound	[Tb(2–PyPzH)$_2Cl_3$]	[Dy(2–PyPzH)$_2Cl_3$]	[Ho(2–PyPzH)$_2Cl_3$]	[Er(2–PyPzH)$_2Cl_3$]
CCDC number	2208108	2208109	2208110	2208111
Empirical formula	$C_{16}H_{14}N_6Cl_3Tb$	$C_{16}H_{14}N_6Cl_3Dy$	$C_{16}H_{14}N_6Cl_3Ho$	$C_{16}H_{14}N_6Cl_3Er$
M_r / g·mol^{-1}	555.60	559.18	561.61	563.94
T / K	100(2)	100(2)	100(2)	100(2)
λ / pm	71.073, Mo–K_α	71.073, Mo–K_α	71.073, Mo–K_α	71.073, Mo–K_α
Crystal system	Monoclinic	Monoclinic	Monoclinic	Monoclinic
Space group	$P2_1/c$	$P2_1/c$	$P2_1/c$	$P2_1/c$
a / pm	1072.9(1)	1070.9(2)	1072.0(1)	1073.0(1)
b / pm	1221.8(1)	1222.1(2)	1220.1(1)	1218.5(1)
c / pm	1467.1(1)	1466.1(2)	1465.3(1)	1464.6(1)
α / °	90	90	90	90
β / °	92.66(1)	92.32(1)	91.989(3)	91.761
γ / °	90	90	90	90
V / 10^6 pm^3	1921.2(2)	1917.1(5)	1915.43(14)	1913.9(1)
Z	4	4	4	4
ρ_{calc} / g·cm^{-3}	1.921	1.937	1.948	1.957
μ / mm^{-1}	4.111	4.328	4.562	4.816
F(000)	1072	1076	1080	1084
Crystal size / mm^3	0.131 x 0.022 x 0.014	0.112 x 0.059 x 0.033	0.224 x 0.201 x 0.137	0.196 x 0.081 x 0.034
θ_{min} / °	1.900	1.903	2.530	2.175
θ_{max} / °	26.413	25.578	34.969	38.565
Reflections collected	32112	61699	75143	107396
Independent reflections	3944	3596	8419	10826
R(int)	0.0894	0.0759	0.1273	0.0845
No. Of parameters	235	235	235	235
GOF	1.038	1.068	1.065	1.026
Final R indices [$I > 2\sigma(I)$]	R_1 = 0.0360, wR_2 = 0.0639	R_1 = 0.0263, wR_2 = 0.0583	R_1 = 0.0600, wR_2 = 0.1190	R_1 = 0.0303, wR_2 = 0.0514
R indices (all data)	R_1 = 0.0556, wR_2 = 0.0705	R_1 = 0.0345, wR_2 = 0.0618	R_1 = 0.1137, wR_2 = 0.1377	R_1 = 0.0531, wR_2 = 0.0565
$\Delta\rho_{max}$, $\Delta\rho_{min}$ / e·10^{-6}·pm^{-3}	1.628, –0.890	1.631, –1.113	5.536, –2.807	2.231, –1.785

Table S5. Crystallographic data of [Gd_2(2–PyPzH)$_3$(2–PyPz)Cl_5] (**16**), [Gd_3(2–PyPzH)$_8Cl_8$]Cl (**17**), and [PyH][Tb(2–PyPzH)$_2Cl_4$] (**18**).

Compound	[Gd_2(2–PyPzH)$_3$(2–PyPz)Cl_5]	[Gd_3(2–PyPzH)$_8Cl_8$]Cl	[PyH][Tb(2–PyPzH)$_2Cl_4$]
CCDC number	2208112	2208113	2208114
Empirical formula	$C_{32}H_{27}N_{12}Cl_5Gd_2$	$C_{64}H_{56}N_{24}Cl_9Gd_3$	$C_{21}H_{20}N_7Cl_4Tb$
M_r / g·mol^{-1}	1071.40	1952.12	671.16
T / K	100(2)	100(2)	200(2)
λ / pm	71.073 Mo–K_α	71.073, Mo–K_α	71.073, Mo–K_α
Crystal system	Monoclinic	Triclinic	Orthorhombic
Space group	$P2_1/n$	$P\bar{1}$	$Pbcn$
a / pm	1047.5(1)	994.2(2)	1205.5(1)
b / pm	1982.9(1)	1963.5(3)	1230.6(1)
c / pm	1914.4(1)	2016.1(3)	1762.2(2)
α / °	90	69.87(1)	90
β / °	102.37(1)	88.81(1)	90
γ / °	90	78.39(1)	90
V / 10^6 pm^3	3883.8(4)	3614.6(8)	2614.1(2)
Z	4	2	4
ρ_{calc} / g·cm^{-3}	1.832	1.794	1.705
μ / mm^{-1}	3.771	3.112	3.137
F(000)	2064	1906	1312
Crystal size / mm^3	0.31 x 0.102 x 0.027	0.076 x 0.038 x 0.036	0.285 x 0.150 x 0.122
θ_{min} / °	2.054	2.056	2.633
θ_{max} / °	27.193	27.103	27.133
Reflections collected	76683	163558	32818
Independent reflections	8618	15930	2895
R(int)	0.1076	0.0890	0.0496
No. Of parameters	460	1001	177
GOF	1.074	1.100	1.069
Final R indices [$I > 2\sigma(I)$]	R_1 = 0.0454, wR_2 = 0.0968	R_1 = 0.0463, wR_2 = 0.0869	R_1 = 0.0197, wR_2 = 0.0365
R indices (all data)	R_1 = 0.0800, wR_2 = 0.1109	R_1 = 0.0678, wR_2 = 0.0935	R_1 = 0.0320, wR_2 = 0.0406
$\Delta\rho_{max}$, $\Delta\rho_{min}$ / e·10^{-6}·pm^{-3}	2.264, –1.227	1.537, –1.340	0.369, –0.488

Interatomic distances and Angles

Table S6. Selected interatomic distances (pm) and angles (°) of $^1_\infty$[Ln$_2$(2–PyPzH)$_4$Cl$_6$], Ln= La (**1**), Nd (**2**), and Sm (**3**). Symmetry operations: I -x+1,y,-z+1/2.

Compound	$^1_\infty$[La$_2$(2–PyPzH)$_4$Cl$_6$]	$^1_\infty$[Nd$_2$(2–PyPzH)$_4$Cl$_6$]	$^1_\infty$[Sm$_2$(2–PyPzH)$_4$Cl$_6$]
Ln1–Cl1	290.4(1)	287.7(1)	283.9(1)
Ln1–Cl2	281.6(1)	275.0(1)	272.0(2)
Ln1–Cl3	277.5(1)	272.4(1)	269.6(2)
Ln1–Cl4	292.4(1)	289.2(1)	285.6(2)
Ln2–Cl4	294.5(1)	292(1)	288.8(2)
Ln2–Cl5	280.3(1)	273.8(1)	270.6(2)
Ln1–N1	273.9(3)	268.6(3)	265.5(5)
Ln1–N2	262.2(3)	256.1(3)	253.2(5)
Ln1–N4	275.5(3)	270.3(4)	267.0(5)
Ln1–N5	263.3(3)	257.0(3)	254.2(5)
Ln2–N7	269(2)	267(1)	265(1)
Ln2–N8	266(2)	260(1)	255(1)
Cl1–Ln1–Cl2	78.6(1)	78.1(1)	78.0(1)
Cl1–Ln1–Cl3	78.1(1)	78.0(1)	78.0(1)
Cl3–Ln1–Cl2	92.2(1)	92.7(1)	94.2(1)
Cl1–Ln1–Cl4	151.4(1)	150.1(1)	149.0(1)
Cl2–Ln1–Cl4	75.7(1)	75.6(1)	75.9(1)
Cl3–Ln1–Cl4	90.8(1)	89.1(1)	87.7(1)
Cl4– Ln2–Cl4^I	132.9(1)	132.7(1)	133.3(1)
Cl5–Ln2–Cl4	79.9(1)	79.6(1)	79.0(1)
Cl5^I–Ln2–Cl4	76.6(1)	76.5(1)	76.5(1)
Cl5–Ln2–Cl5^I	118.8(1)	117.8(1)	115.2(1)
N1–Ln1–Cl1	75.8(1)	76.1(1)	76.0(1)
N1–Ln1–Cl2	150.5(1)	149.5(1)	147.5(2)
N1–Ln1–Cl3	96.4(1)	97.6(1)	98.9(1)
N1–Ln1–Cl4	132.1(1)	133.0(1)	133.9(2)
N2–Ln1–Cl1	125.1(1)	125.6(1)	125.5(1)
N2–Ln1–Cl2	148.2(1)	148.5(1)	149.7(1)
N2–Ln1–Cl3	75.1(1)	75.1(1)	75.2(1)
N2–Ln1–Cl4	75.6(1)	75.3(1)	75.4(1)
N4–Ln1–Cl1	128.1(1)	129.5(1)	131.2(1)
N4–Ln1–Cl2	112.6(1)	111.3(1)	109.6(1)
N4–Ln1–Cl3	145.9(1)	145.6(1)	144.8(1)
N4–Ln1–Cl4	74.2(1)	74.3(1)	74.1(2)
N5–Ln1–Cl1	70.6(1)	71.3(1)	72.0(2)
N5–Ln1–Cl2	84.7(1)	82.4(1)	80.8(1)
N5–Ln1–Cl3	148.5(1)	149.2(1)	150.0(1)
N5–Ln1–Cl4	118.5(1)	118.5(1)	119.1(1)
N7–Ln2–Cl4	81.8(2)	81.1(2)	80.8(2)
N7^I–Ln2–Cl4	136.0(2)	82.8(3)	137.5(2)
N7–Ln2–Cl5	145.0(3)	144.4(3)	143.8(3)
N7^I–Ln2–Cl5	85.2(4)	85.9(4)	88.4(3)
N8–Ln2–Cl4	135.8(3)	135.0(2)	134.5(3)

N8^I–Ln2–Cl4	75.1(2)	75(2)	74.7(2)
N8^I–Ln2–Cl5	76.8(4)	75.9(3)	76.0(3)
N8^I–Ln2–Cl5^I	144.3(3)	145.1(2)	146.2(3)
N2–Ln1–N1	61.1(1)	61.9(1)	62.7(2)
N2–Ln1–N4	71.6(1)	71.6(1)	71.3(2)
N4–Ln1–N1	73.8(1)	74.4(1)	74.9(2)
N5–Ln1–N1	73.4(1)	74.1(1)	73.1(2)
N5–Ln1–N2	121.2(1)	122.5(1)	122.2(2)
N5–Ln1–N4	60.9(1)	61.8(1)	62.4(2)
N7^I–Ln2–N7	87.6(8)	88.2(7)	86.6(6)
N8–Ln2–N7	61.2(2)	62.2(2)	62.9(2)
N8^I–Ln2–N7	69.7(5)	70.3(5)	69.8(5)
N8^I– Ln2–N8	110.0(6)	112.1(5)	113.3(5)

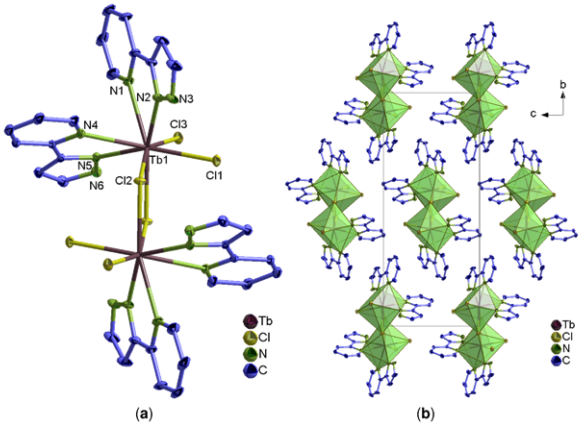

(**a**) (**b**)

Figure S1. (**a**) Extended coordination sphere of Tb^{3+} ion in α–[Tb$_2$(2–PyPzH)$_4$Cl$_6$] (**7**) representing the isotypic complexes **4**–**7**. (**b**) Packing structure of **7** with a view along [100]. In all figures, the hydrogen atoms are omitted for clarity and the coordination polyhedra around Ln^{3+} are shown in green, with thermal ellipsoids shown with a probability of 50%.

Table S7. Selected interatomic distances (pm) and angles (°) of α–[Ln$_2$(2–PyPzH)$_4$Cl$_6$], Ln=Eu (**6**), Gd (**7**), and Tb (**8**).

Compound	α–[Eu$_2$(2–PyPzH)$_4$Cl$_6$]	α–[Gd$_2$(2–PyPzH)$_4$Cl$_6$]	α–[Tb$_2$(2–PyPzH)$_4$Cl$_6$]
Ln1–Cl1	277.6(2)	266.5(2)	266.0(1)
Ln1–Cl2	270.8(2)	276.7(2)	275.8(1)
Ln1–Cl3	266.9(2)	269.9(2)	269.2(1)
Ln1–N1	265.1(4)	266.0(2)	262.5(2)
Ln1–N2	248.7(5)	249.0(2)	247.3(2)
Ln1–N4	262.0(2)	264.6(5)	262.7(2)
Ln1–N5	250.0(2)	247.4(6)	246.0(2)
Cl1–Ln1–Cl2	87.0(1)	83.7(1)	83.1(1)
Cl1–Ln1–Cl3	84.1(1)	80.7(1)	80.8(1)
Cl3–Ln1–Cl2	81.1(1)	87.0(1)	87.5(1)
N1–Ln1–Cl1	104.2(1)	116.2(4)	118.7(1)
N1–Ln1–Cl2	131.5(1)	151.0(3)	148.0(1)
N1–Ln1–Cl3	146.1(1)	76.5(4)	74.6(1)
N2–Ln1–Cl1	73.9(1)	76.8(5)	79.6(1)
N2–Ln1–Cl2	76.3(1)	146.7(3)	148.5(1)
N2–Ln1–Cl3	148.9(2)	115.7(5)	115.1(1)
N4–Ln1–Cl1	144.0(3)	146.1(2)	146.0(1)
N4–Ln1–Cl2	71.4(6)	104.5(2)	104.2(1)
N4–Ln1–Cl3	119.1(7)	131.8(2)	132.0(1)
N5–Ln1–Cl1	152.6(4)	148.8(2)	148.0(1)
N5–Ln1–Cl2	114.9(6)	74.0(2)	73.9(1)
N5–Ln1–Cl3	83.4(6)	76.7(2)	76.5(1)
N2–Ln1–N1	62.7(2)	62.1(4)	63.1(1)
N2–Ln1–N4	73.2(5)	79.2(6)	77.6(1)
N4–Ln1–N1	72.7(7)	71.4(5)	71.6(1)
N5–Ln1–N1	74.4(7)	79.1(4)	76.3(1)
N5–Ln1–N2	125.5(5)	132.7(4)	130.6(1)
N5–Ln1–N4	62.7(4)	62.8(2)	63.3(1)

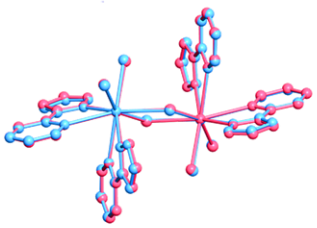

Figure S2. Overlay of the molecular structures of α–[Eu$_2$(2–PyPzH)$_4$Cl$_6$] (red) (**5**) and β–[Eu$_2$(2–PyPzH)$_4$Cl$_6$] (blue) (**9**).

Table S8. Selected interatomic distances (pm) and angles (°) of β–[Ln$_2$(2–PyPzH)$_4$Cl$_6$], Ln= Sm (**8**), Eu (**9**), and Gd (**10**).

Compound	β–[Sm$_2$(2–PyPzH)$_4$Cl$_6$]	β–[Eu$_2$(2–PyPzH)$_4$Cl$_6$]	β–[Gd$_2$(2–PyPzH)$_4$Cl$_6$]
Ln1–Cl1	272.8(1)	272(1)	271.1(2)
Ln1–Cl2	269.2(1)	268.5(1)	267.7(2)
Ln1–Cl3	277.6(1)	276.2(1)	276.0(2)
Ln1–N1	265.1(3)	264.6(4)	264.1(5)
Ln1–N2	251.1(3)	251.2(3)	249.0(5)
Ln1–N4	267.0(3)	266.0(4)	265.5(5)
Ln1–N5	250.0(3)	249.1(3)	247.6(5)
Cl1–Ln1–Cl2	82.1(1)	81.9(1)	81.4(1)
Cl1–Ln1–Cl3	86.7(1)	87.0(1)	86.6(1)
Cl3–Ln1–Cl2	86.1(1)	86.2(1)	86.5(1)
N1–Ln1–Cl1	130.5(1)	130.8(1)	130.9(1)
N1–Ln1–Cl2	145.9(1)	145.8(1)	145.9(1)
N1–Ln1–Cl3	103.2(1)	103.2(1)	103.9(1)
N2–Ln1–Cl1	74.5(1)	74.7(1)	75.1(1)
N2–Ln1–Cl2	150.4(1)	150.3(1)	150.5(1)
N2–Ln1–Cl3	74.7(1)	74.6(1)	74.9(1)
N4–Ln1–Cl1	77.0(1)	76.7(1)	76.8(1)
N4–Ln1–Cl2	114.9(1)	114.9(1)	114.1(2)
N4–Ln1–Cl3	150.7(1)	150.6(1)	150.7(2)
N5–Ln1–Cl1	119.1(1)	118.7(1)	119.1(2)
N5–Ln1–Cl2	77.3(1)	77.0(1)	77.0(2)
N5–Ln1–Cl3	146.4(1)	146.2(1)	146.2(1)
N2–Ln1–N1	62.3(1)	62.6(1)	62.5(2)
N2–Ln1–N4	77.6(1)	77.6(1)	77.6(2)
N4–Ln1–N1	71.3(1)	71.5(1)	71.3(2)
N5–Ln1–N1	77.3(1)	77.5(1)	76.8(2)
N5–Ln1–N2	130.2(1)	130.6(1)	130.2(2)
N5–Ln1–N4	62.0(1)	62.4(1)	62.4(2)

Table S9. Selected interatomic distances (pm) and angles (°) of [Ce(2–PyPzH)$_3$Cl$_3$] (**11**).

Atoms	[Ce(2–PyPzH)$_3$Cl$_3$]	Atoms	[Ce(2–PyPzH)$_3$Cl$_3$]
Ce1–Cl1	279.9(2)	N1–Ce1–Cl2	77.03(9)
Ce1–Cl2	279.7(2)	N2–Ce1–Cl1	70.0(1)
Ce1–Cl3	283.2(1)	N2–Ce1–Cl2	128.9(1)
Ce1–N1	271.5(4)	N5–Ce1–Cl1	137.2(1)
Ce1–N2	264.6(4)	N5–Ce1–Cl2	134.4(1)
Ce1–N4	282.6(4)	N8–Ce1–Cl1	74.3(1)
Ce1–N5	260.7(4)	N8–Ce1–Cl2	71.1(1)
Ce1–N7	280.4(4)	N1–Ce1–N4	68.7(1)
Ce1–N8	261.1(4)	N1–Ce1–N7	137.3(1)
Cl1–Ce1–Cl3	86.5(1)	N2–Ce1–N1	60.8(2)
Cl2–Ce1–Cl3	146.7(1)	N2–Ce1–N4	110.7(2)
N1–Ce1–Cl3	132.2(1)	N2–Ce1–N7	138.3(2)
N2–Ce1–Cl3	72.1(1)	N5–Ce1–N1	80.5(2)
N4–Ce1–Cl3	125.5(1)	N5–Ce1–N2	67.8(2)
N5–Ce1–Cl3	74.1(1)	N5–Ce1–N4	59.5(1)
N7–Ce1–Cl3	75.8(1)	N5–Ce1–N7	78.4(2)
N8–Ce1–Cl3	76.1(1)	N5–Ce1–N8	133.5(2)
Cl1–Ce1–N4	147.4(1)	N7–Ce1–N4	68.6(1)
Cl1–Ce1–N7	133.7(1)	N8–Ce1–N1	144.6(2)
Cl2–Ce1–N4	75.4(1)	N8–Ce1–N2	133.0(2)
Cl2–Ce1–N7	92.1(1)	N8–Ce1–N4	115.9(2)
N1–Ce1–Cl1	85.5(1)	N8–Ce1–N7	60.1(2)

Table S10. Selected interatomic distances (pm) and angles (°) of [Ln(2–PyPzH)$_2$Cl$_3$], Ln= Tb (**12**), Dy (**13**), Ho (**14**), and Er (**15**).

Compound	[Tb(2–PyPzH)$_2$Cl$_3$]	[Dy(2–PyPzH)$_2$Cl$_3$]	[Ho(2–PyPzH)$_2$Cl$_3$]	[Er(2–PyPzH)$_2$Cl$_3$]
Ln1–Cl1	263.1(2)	261.7(1)	261.1(2)	260.2(1)
Ln1–Cl2	262.2(2)	261.4(1)	260(2)	259.1(1)
Ln1–Cl3	267.3(2)	265.7(1)	265.4(2)	264.5(1)
Ln1–N1	256.7(4)	255.6(3)	253.7(5)	253.2(2)
Ln1–N2	244.2(4)	242.9(3)	242.2(5)	240.5(2)
Ln1–N4	255.9(4)	255.1(3)	253.6(5)	252.7(2)
Ln1–N5	245.4(4)	244.6(3)	243.7(5)	241.9(2)
Cl1–Ln1–Cl2	94.4(1)	95.1(1)	95.4(1)	95.5(1)
Cl1–Ln1–Cl3	161.9(1)	162.1(1)	162.1(1)	162.1(1)
Cl3–Ln1–Cl2	92.0(1)	91.1(1)	91.0(1)	90.5(1)
N1–Ln1–Cl1	85.5(1)	85.6(1)	85.4(1)	85.4(1)
N1–Ln1–Cl2	85.6(1)	85.7(1)	85.4(1)	85.5(1)
N1–Ln1–Cl3	78.1(1)	78.2(1)	78.5(1)	78.3(1)
N2–Ln1–Cl1	84.1(1)	83.8(1)	83.5(1)	83.5(1)
N2–Ln1–Cl2	150.7(1)	151.3(1)	151.3(2)	151.7(1)
N2–Ln1–Cl3	82.0(1)	82.8(1)	82.9(1)	83.3(1)
N4–Ln1–Cl1	75.4(1)	75.3(1)	75.4(1)	75.5(1)
N4–Ln1–Cl2	81.9(1)	81.6(1)	81.4(1)	81.1(1)
N4–Ln1–Cl3	122.3(1)	122.3(1)	122.1(1)	122.2(1)
N5–Ln–Cl1	112.3(1)	112.0(1)	111.7(1)	112.2(1)
N5–Ln1–Cl2	127.8(1)	127.3(1)	127.4(1)	127.1()
N5–Ln1–Cl3	76.3(1)	76.6(1)	76.8(1)	76.6(1)
N2–Ln1–N1	65.1(2)	65.6(1)	65.9(2)	66.3(1)
N2–Ln1–N4	125.4(2)	125.3(1)	125.5(2)	125.3(1)
N4–Ln–N1	156.2(2)	155.9(1)	155.5(2)	155.3(1)
N5–Ln1–N1	138.1(2)	138.2(1)	138.6(2)	138.4(1)
N5–Ln1–N2	78.8(2)	78.6(1)	78.5(2)	78.3(1)
N5–Ln1–N4	64.2(2)	64.4(1)	64.5(2)	64.9(1)

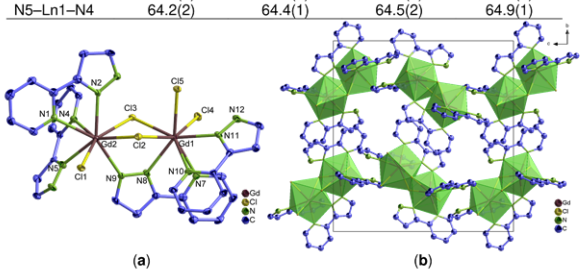

(**a**) (**b**)

Figure S3. (**a**) Extended coordination sphere of Gd^{3+} ion in [Gd$_2$(2–PyPzH)$_3$(2–PyPz)Cl$_5$] (**16**). (**b**) Packing structure of **16** with a view along [100].

Table S11. Selected interatomic distances (pm) and angles (°) of [Gd$_2$(2–PyPzH)$_3$(2–PyPz)Cl$_5$] (**16**).

Atoms	[Gd$_2$(2–PyPzH)$_3$(2–PyPz)Cl$_5$]	Atoms	[Gd$_2$(2–PyPzH)$_3$(2–PyPz)Cl$_5$]
Gd1–Cl1	268.3(2)	N5–Gd1–Cl3	77.1(1)
Gd1–Cl2	276.0(2)	N7–Gd2–Cl2	149.5(1)
Gd1–Cl3	281.0(2)	N7–Gd2–Cl3	76.5(1)
Gd2–Cl2	281.6(2)	N7–Gd2–Cl4	73.5(1)
Gd2–Cl3	276.1(2)	N7–Gd2–Cl5	114.9(1)
Gd2–Cl4	270.8(2)	N8–Gd2–Cl2	145.5(1)
Gd2–Cl5	278.3(2)	N8–Gd2–Cl3	85.4(2)
Gd1–N1	261.9(5)	N8–Gd2–Cl4	76.2(2)
Gd1–N2	250.3(5)	N8–Gd2–Cl5	76.9(2)
Gd1–N4	263.5(5)	N9–Gd2–Cl1	85.4(2)
Gd1–N5	249.0(5)	N9–Gd2–Cl2	76.2(2)
Gd2–N7	257.4(5)	N9–Gd2–Cl3	76.9(2)
Gd2–N8	243.3(5)	N10–Gd2–Cl2	73.4(1)
Gd2–N9	248.5(5)	N10–Gd2–Cl3	143.4(1)
Gd2–N10	263.3(5)	N10–Gd2–Cl4	132.3(1)
Gd2–N11	247.3(5)	N10–Gd2–Cl5	110.8(1)
Cl1–Gd1–Cl2	79.1(1)	N11–Gd2–Cl2	112.9(2)
Cl1–Gd1–Cl3	153.7(1)	N11–Gd2–Cl3	152.3(1)
Cl2–Gd1–Cl3	78.0(1)	N11–Gd2–Cl4	78.9(2)
Cl3–Gd2–Cl2	77.8(1)	N11–Gd2–Cl5	76.6(1)
Cl3–Gd2–Cl5	82.3(1)	N1–Gd1–N4	74.7(2)
Cl4–Gd2–Cl3	81.4(1)	N2–Gd1–N1	63.0(2)
Cl4–Gd2–Cl2	152.2(1)	N2–Gd1–N4	81.0(2)
Cl4–Gd2–Cl5	84.5(1)	N5–Gd1–N1	77.3(2)
Cl5–Gd2–Cl2	74.7(1)	N5–Gd1–N2	132.4(2)
N1–Gd1–Cl1	74.6(1)	N5–Gd1–N4	63.2(2)
N1–Gd1–Cl2	118.1(1)	N7–Gd2–N10	67.4(2)
N1–Gd1–Cl3	128.2(1)	N8–Gd2–N7	65.0(2)
N2–Gd1–Cl1	77.5(1)	N8–Gd2–N10	78.0(2)
N2–Gd1–Cl2	135.4(1)	N8–Gd2–N11	132.9(2)
N2–Gd1–Cl3	144.8(1)	N9–Gd2–N1	151.7(2)
N4–Gd1–Cl1	79.0(1)	N9–Gd2–N2	144.8(2)
N4–Gd1–Cl2	148.2(1)	N9–Gd2–N4	108.6(2)
N4–Gd1–Cl3	115.8(1)	N9–Gd2–N5	79.4(2)
N5–Gd1–Cl1	129.2(1)	N11–Gd2–N7	76.1(2)
N5–Gd1–Cl2	118.1(1)	N11–Gd2–N10	62.7(2)

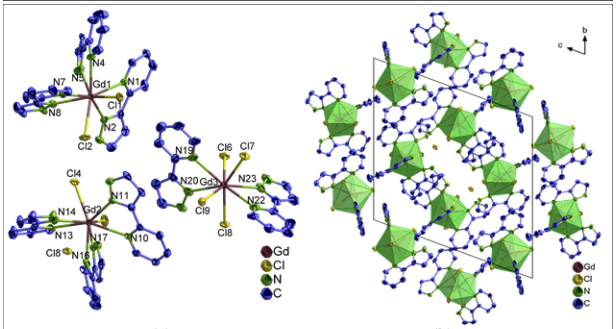

(**a**) (**b**)

Figure S4. (**a**) Extended coordination sphere of Gd^{3+} ion in [Gd$_3$(2–PyPzH)$_8$Cl$_8$]Cl (**17**). (**b**) Packing structure of **17** with a view along [100].

Table S12. Selected interatomic distances (pm) and angles (°) of [Gd$_3$(2–PyPzH)$_8$Cl$_8$]Cl (**17**).

Atoms	[Gd$_3$(2–PyPzH)$_8$Cl$_8$]Cl	Atoms	[Gd$_3$(2–PyPzH)$_8$Cl$_8$]Cl
Gd1–Cl1	265.5(2)	N14–Gd2–Cl5	147.5(3)
Gd1–Cl2	271.1(2)	N16–Gd2–Cl4	150.8(1)
Gd2–Cl4	271.1(2)	N16–Gd2–Cl5	83.6(1)
Gd2–Cl5	266.2(2)	N17–Gd2–Cl4	135.8(1)
Gd3–Cl6	271.5(2)	N17–Gd2–Cl5	135.5(1)
Gd3–Cl7	271.3(2)	N19–Gd3–Cl6	71.9(1)
Gd3–Cl8	276.2(2)	N19–Gd3–Cl7	78.9(2)
Gd3–Cl9	273.3(2)	N19–Gd3–Cl8	132.2(2)
Gd1–N1	268.4(5)	N19–Gd3–Cl9	75.1(1)
Gd1–N2	249.0(5)	N20–Gd3–Cl6	76.8(1)
Gd1–N4	259.7(5)	N20–Gd3–Cl7	141.0(2)
Gd1–N5	260.3(5)	N20–Gd3–Cl8	70.4(2)
Gd1–N7	259.8(5)	N20–Gd3–Cl9	81.3(1)
Gd1–N8	251.4(5)	N22–Gd3–Cl6	131.9(2)
Gd2–N10	263.3(5)	N22–Gd3–Cl7	76.5(1)
Gd2–N11	247.2(5)	N22–Gd3–Cl8	73.9(1)
Gd2–N13	259.0(2)	N22–Gd3–Cl9	80.8(2)
Gd2–N14	260.0(2)	N23–Gd3–Cl6	72.2(2)
Gd2–N16	257.9(5)	N23–Gd3–Cl7	83.4(1)
Gd2–N17	259.2(5)	N23–Gd3–Cl8	73.7(1)
Gd3–N19	266.5(5)	N23–Gd3–Cl9	141.6(2)
Gd3–N20	256.8(6)	N2–Gd1–N1	62.3(2)

Gd3–N22	264.1(6)	N2–Gd1–N5	86.5(2)
Gd3–N23	258.1(6)	N2–Gd1–N7	144.1(2)
N2–Gd1–N8	91.1(2)	N4–Gd1–N1	78.9(2)
N2–Gd1–N4	138.5(2)	N4–Gd1–N5	63.1(2)
N8–Gd1–N4	104.5(2)	N4–Gd1–N7	75.8(2)
Cl1–Gd1–Cl2	82.1(1)	N5–Gd1–N1	65.2(2)
Cl5–Gd2–Cl4	87.1(1)	N7–Gd1–N1	153.6(2)
Cl6–Gd3–Cl8	105.0(1)	N7–Gd1–N5	108.7(2)
Cl6–Gd3–Cl9	146.2(1)	N8–Gd1–N1	130.5(2)
Cl7–Gd3–Cl6	87.5(1)	N8–Gd1–N7	64.6(2)
Cl7–Gd3–Cl8	148.6(1)	N8–Gd1–N5	72.7(2)
Cl7–Gd3–Cl9	93.6(1)	N11–Gd2–N10	63.7(2)
Cl9–Gd3–Cl8	91.4(1)	N11–Gd2–N13	148.8(5)
N1–Gd1–Cl1	82.6(1)	N11–Gd2–N14	96.2(3)
N1–Gd1–Cl2	126.1(1)	N11–Gd2–N16	132.8(2)
N2–Gd1–Cl1	107.8(1)	N11–Gd2–N17	78.8(2)
N2–Gd1–Cl2	74.1(1)	N13–Gd2–N10	147.4(5)
N4–Gd1–Cl1	79.3(2)	N13–Gd2–N14	63.0(3)
N4–Gd1–Cl2	146.4(1)	N14–Gd2–N10	135.0(3)
N5–Gd1–Cl1	133.7(1)	N16–Gd2–N10	75.5(2)
N5–Gd1–Cl2	143.7(1)	N16–Gd2–N13	75.4(6)
N7–Gd1–Cl1	85.4(1)	N16–Gd2–N14	96.6(4)
N7–Gd1–Cl2	75.0(1)	N16–Gd2–N17	63.6(2)
N8–Gd1–Cl1	147(1)	N17–Gd2–N10	66.9(2)
N8–Gd1–Cl2	77.3(1)	N17–Gd2–N13	111.7(5)
N10–Gd2–Cl4	129(1)	N17–Gd2–N14	70.0(4)
N10–Gd2–Cl5	76.7(1)	N20–Gd3–N19	62.4(2)
N11–Gd2–Cl4	76.3(1)	N20–Gd3–N22	139.3(2)
N11–Gd2–Cl5	107.5(1)	N20–Gd3–N23	123.6(2)
N13–Gd2–Cl4	76.4(6)	N22–Gd3–N19	144.1(2)
N13–Gd2–Cl5	85.9(3)	N23–Gd3–N19	140.4(2)
N14–Gd2–Cl4	77.0(4)	N23–Gd3–N22	61.2(2)

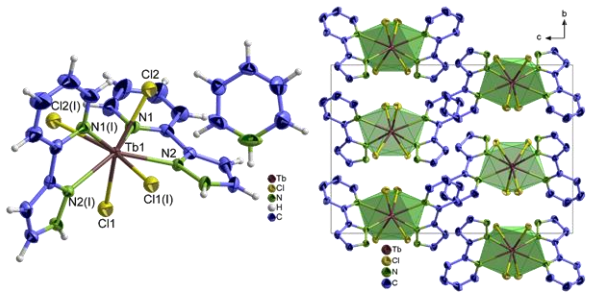

(**a**) (**b**)

Figure S5. (**a**) Extended coordination sphere of Tb^{3+} ion in [PyH][Tb(2–PyPzH)$_2$Cl$_4$] (**18**). (**b**) Packing structure of **18** with a view along [100], the protonated pyridine molecules were omitted for clarity. Symmetry operation: I -x+1,y,-z+3/2.

Table S13. Selected interatomic distances (pm) and angles (°) of [PyH][Tb(2–PyPzH)$_2$Cl$_4$] (**18**).

Atoms	[PyH][Tb(2–PyPzH)$_2$Cl$_4$]	Atoms	[PyH][Tb(2–PyPzH)$_2$Cl$_4$]
Tb1–Cl1	272.0(1)	N1–Tb1–Cl2	72.0(1)
Tb1–Cl2	269.8(1)	N1^{I}–Tb1–Cl2	78.7(1)
Tb1–N1	267.8(2)	N1^{I}–Tb1–N1	136.9(1)
Tb1–N2	252.2(2)	N2^{I}–Tb1–N2	132.9(1)
Cl1–Tb1–Cl1^{I}	100.7(1)	N2–Tb1–N1	62.6(1)
Cl2–Tb1–Cl1	145.0(1)	N2–Tb1–N1^{I}	138.9(1)
Cl2–Tb1–Cl1^{I}	93.4(1)	N2^{I}–Tb1–Cl2	141.3(1)
Cl2^{I}–Tb1–Cl1^{I}	145.0(1)	N2–Tb1–Cl2	76.7(1)
Cl2–Tb1–Cl2^{I}	92.9(1)		

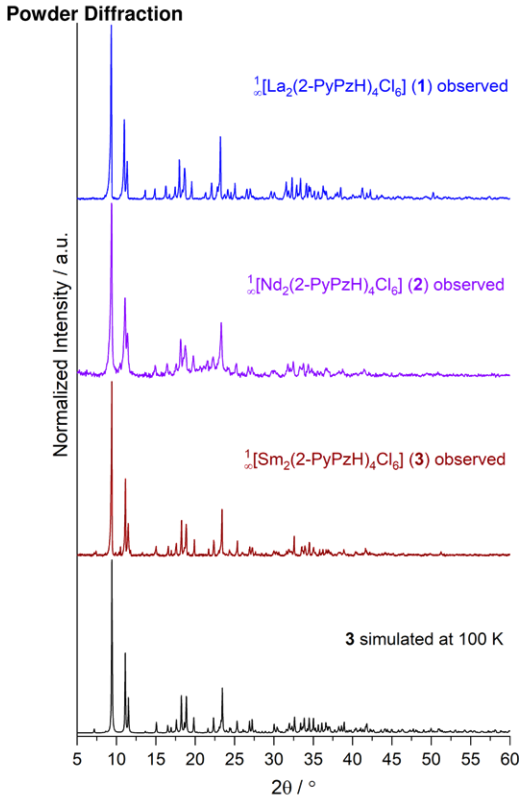

Figure S6. Comparison of the observed powder X–ray diffraction pattern (colored) of $^{1}_{\infty}$[Ln$_2$(2–PyPzH)$_4$Cl$_6$], RE = La (**1**), Nd (**2**), Sm (**3**) with the simulated diffraction pattern from the single crystal X–ray data of $^{1}_{\infty}$[Sm$_2$(2–PyPzH)$_4$Cl$_6$] (**3**) (black).

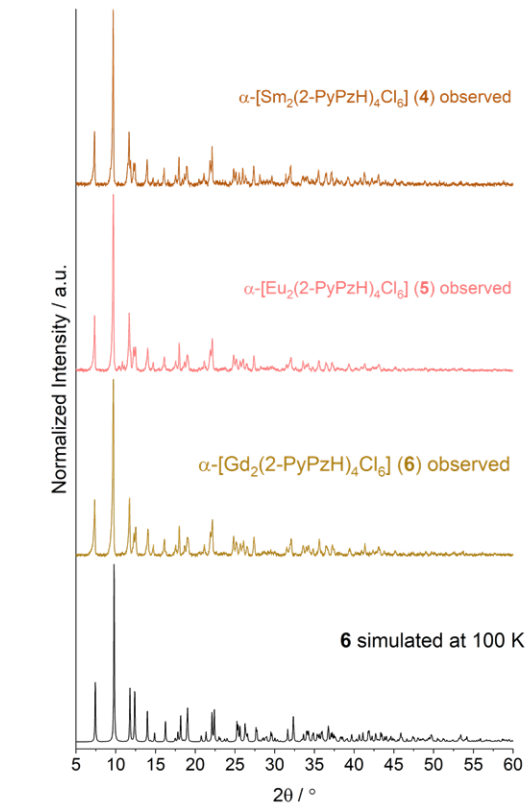

Figure S7. Comparison of the observed powder X–ray diffraction pattern (colored) of α–[Ln$_2$(2–PyPzH)$_4$Cl$_6$], Ln = Sm (**4**), Eu (**5**), Gd (**6**) with the simulated diffraction pattern from the single crystal X–ray data of α–[Gd$_2$(2–PyPzH)$_4$Cl$_6$] (**6**) (black).

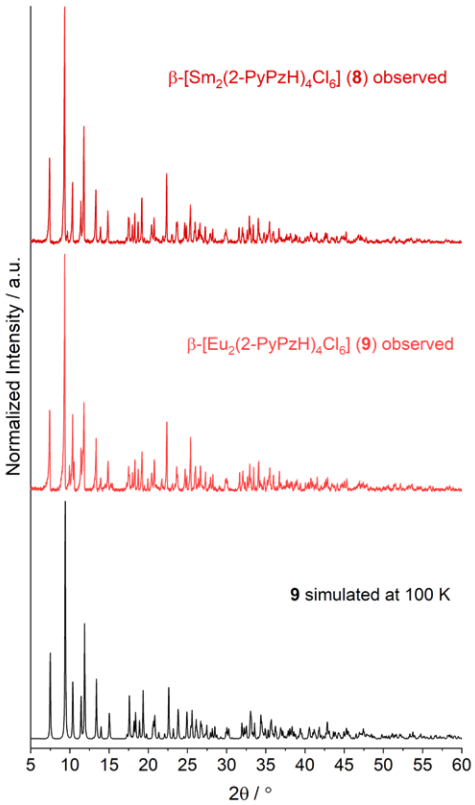

Figure S8. Comparison of the observed powder X–ray diffraction pattern (colored) of β–[Ln2(2–PyPzH)4Cl6], Ln = Sm (**8**), Eu (**9**) with the simulated diffraction pattern from the single crystal X–ray data of β–[Eu2(2–PyPzH)4Cl6] (**9**) (black).

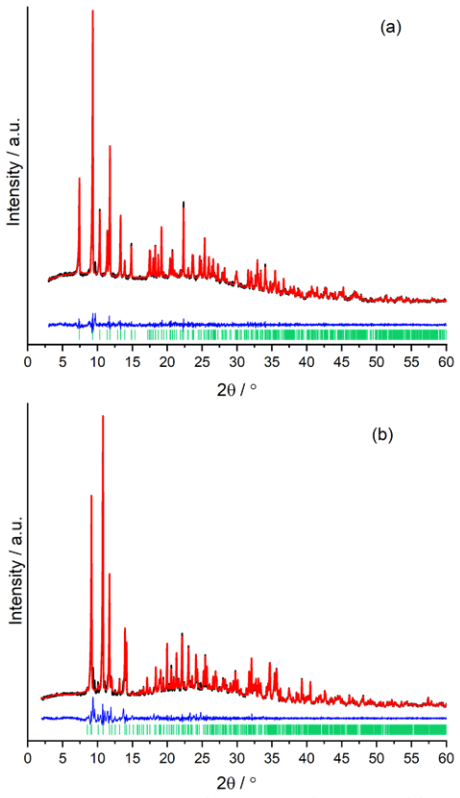

Figure S10. Pawley refinement of (**a**) β–[Sm2(2–PyPzH)4Cl6] (**8**) with a GOF of 1.16, (**b**) [Ce(2–PyPzH)3Cl3] (**11**) with a GOF of 1.87. The experimental data are shown in black, Pawley fit in red, the corresponding difference plot in blue, and the hkl position markers in green.

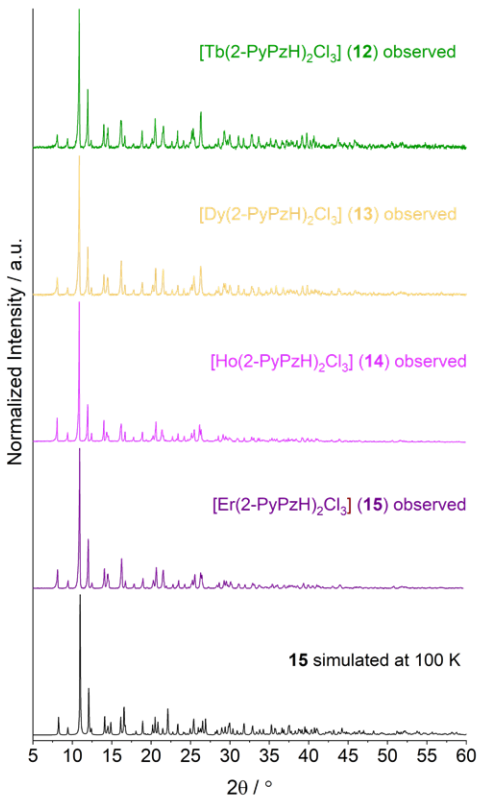

Figure S9. Comparison of the observed powder X–ray diffraction pattern (colored) of [Ln(2–PyPzH)2Cl3], Ln = Tb (**12**), Dy (**13**), Ho (**14**), and Er (**15**) with the simulated diffraction pattern from the single crystal X–ray data of [Er(2–PyPzH)2Cl3] (**15**) (black).

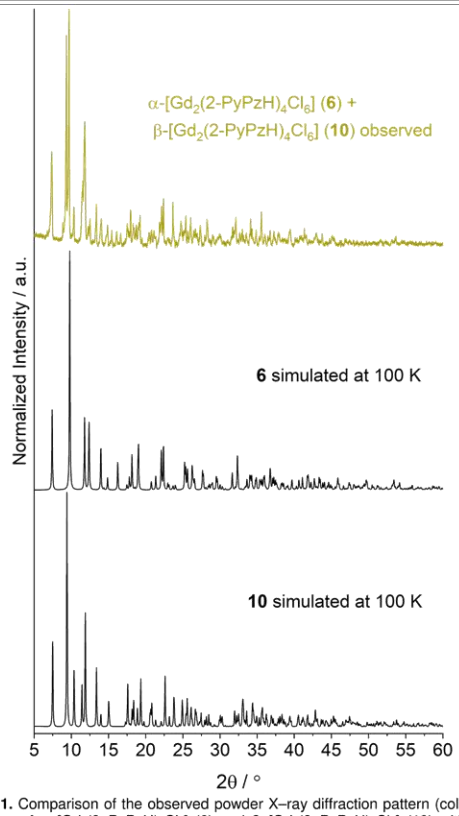

Figure S11. Comparison of the observed powder X–ray diffraction pattern (colored) of a mixture of α–[Gd2(2–PyPzH)4Cl6] (**6**) and β–[Gd2(2–PyPzH)4Cl6] (**10**) with the simulated diffraction pattern from the single crystal X–ray data at 100 K of α–[Gd2(2–PyPzH)4Cl6] (**6**) and β–[Gd2(2–PyPzH)4Cl6] (**10**) (black).

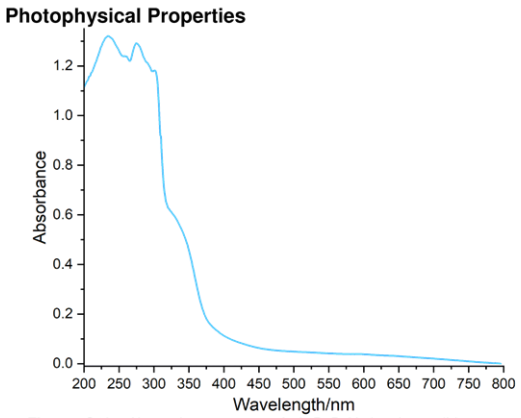

Figure S12. Absorption spectra of 2–PyPzH in the solid–state at room temperature.

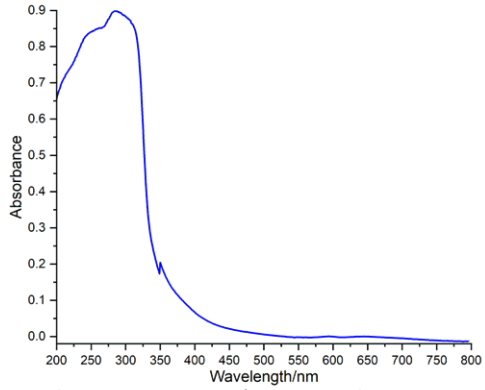

Figure S13. Absorption spectra of $^1_\infty$[La$_2$(2–PyPzH)$_4$Cl$_6$] (**1**) in the solid–state at room temperature.

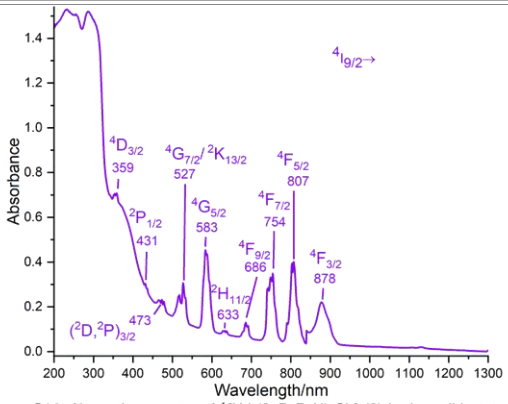

Figure S14. Absorption spectra of $^1_\infty$[Nd$_2$(2–PyPzH)$_4$Cl$_6$] (**2**) in the solid–state at room temperature.

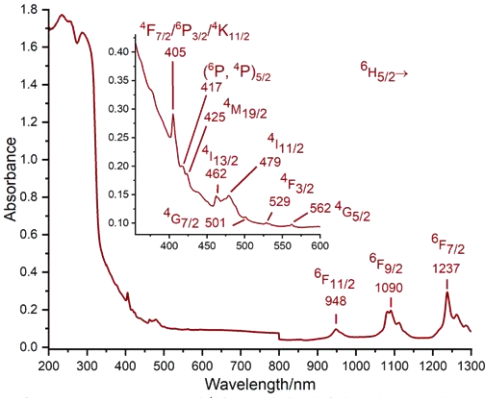

Figure S15. Absorption spectra of $^1_\infty$[Sm$_2$(2–PyPzH)$_4$Cl$_6$] (**3**) in the solid–state at room temperature.

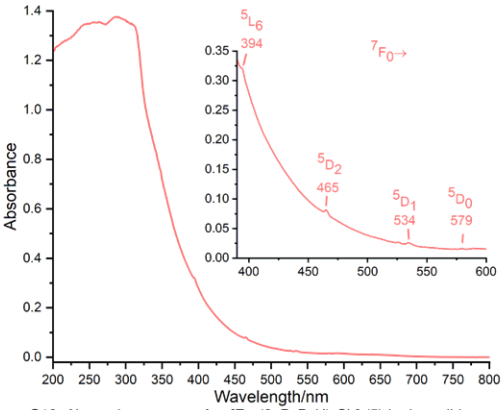

Figure S16. Absorption spectra of α–[Eu$_2$(2–PyPzH)$_4$Cl$_6$] (**5**) in the solid–state at room temperature.

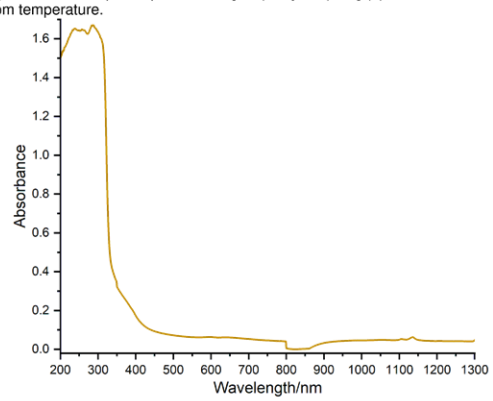

Figure S17. Absorption spectra of α–[Gd$_2$(2–PyPzH)$_4$Cl$_6$] (**6**) in the solid–state at room temperature.

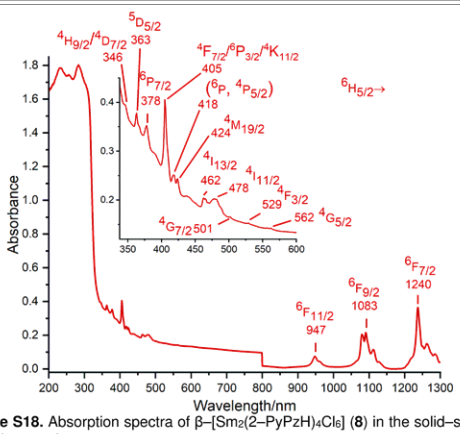

Figure S18. Absorption spectra of β–[Sm$_2$(2–PyPzH)$_4$Cl$_6$] (**8**) in the solid–state at room temperature.

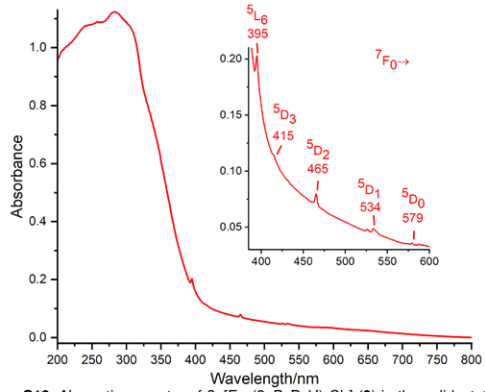

Figure S19. Absorption spectra of β–[Eu$_2$(2–PyPzH)$_4$Cl$_6$] (**9**) in the solid–state at room temperature.

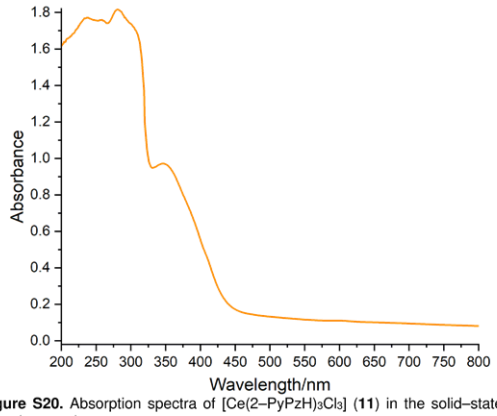

Figure S20. Absorption spectra of $[Ce(2–PyPzH)_3Cl_3]$ (**11**) in the solid–state at room temperature.

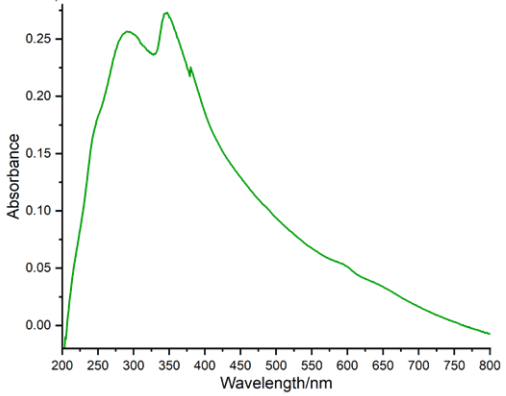

Figure S21. Absorption spectra of $[Tb(2–PyPzH)_2Cl_3]$ (**12**) in the solid–state at room temperature.

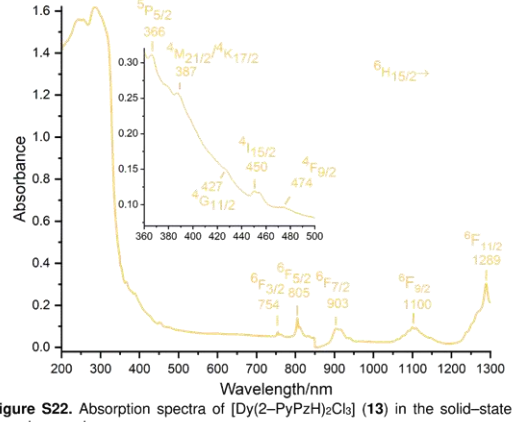

Figure S22. Absorption spectra of $[Dy(2–PyPzH)_2Cl_3]$ (**13**) in the solid–state at room temperature.

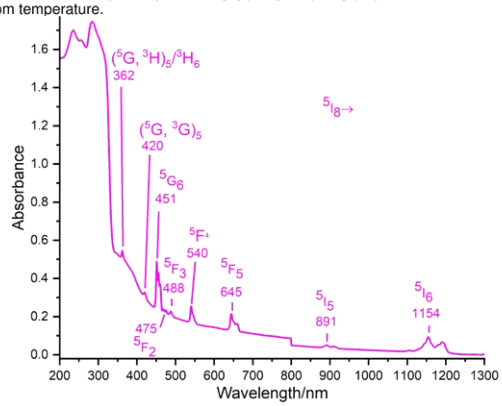

Figure S23. Absorption spectra of $[Ho(2–PyPzH)_2Cl_3]$ (**14**) in the solid–state at room temperature.

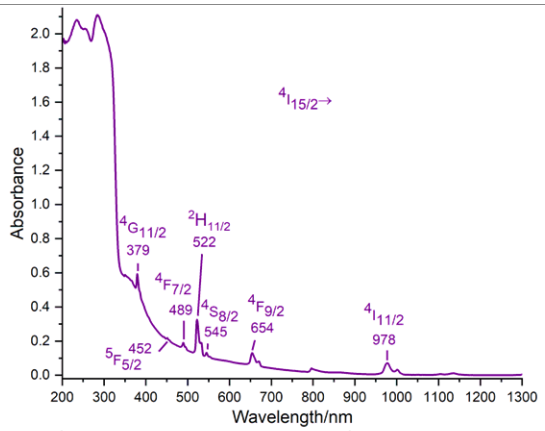

Figure S24. Absorption spectra of $[Er(2–PyPzH)_2Cl_3]$ (**15**) in the solid–state at room temperature.

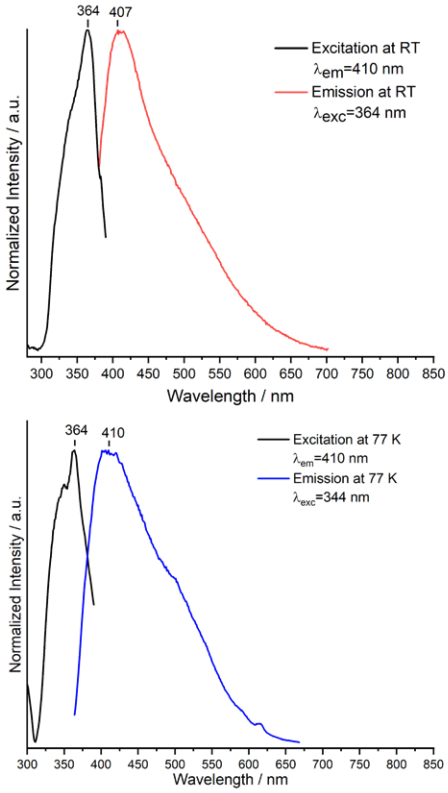

Figure S25. Normalized excitation and emission spectra of 2–PyPzH at room temperature (top) and 77 K (bottom). Wavelengths at which the spectra were recorded are reported in the legends.

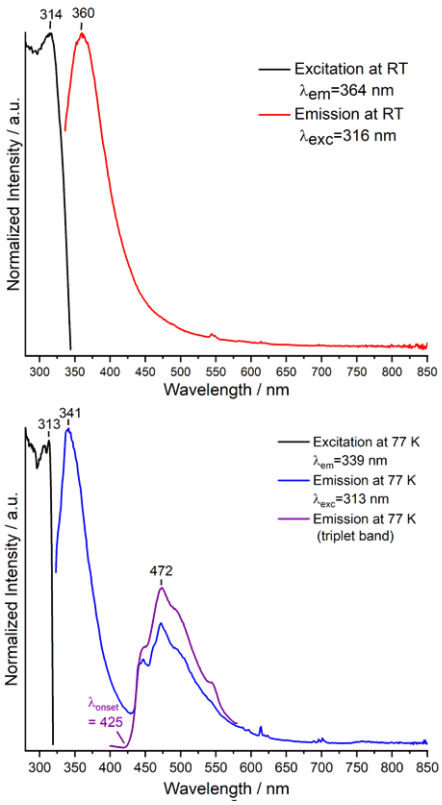

Figure S26. Normalized excitation and emission spectra of ¼[La$_2$(2–PyPzH)$_4$Cl$_6$] (**1**) at room temperature (top) and 77 K (bottom). Wavelengths at which the spectra were recorded are reported in the legends.

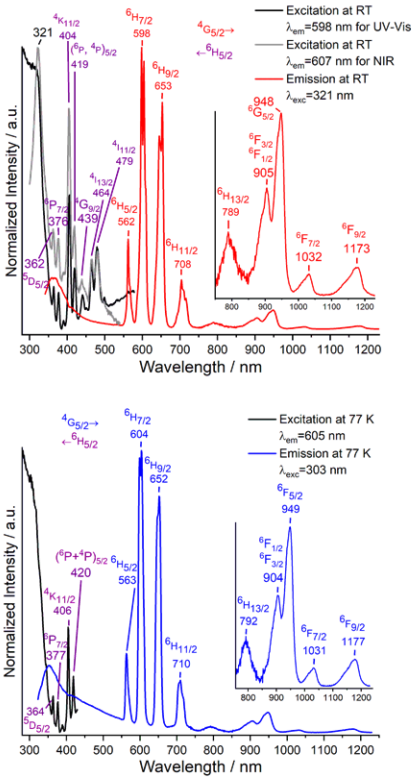

Figure S28. Normalized excitation and emission spectra of ¼[Sm$_2$(2–PyPzH)$_4$Cl$_6$] (**3**) at room temperature (top) and 77 K (bottom). Wavelengths at which the spectra were recorded are reported in the legends. Visible and NIR range emission spectra were brought to the same intensity at 708 (at RT) and 710 nm (at 77 K).

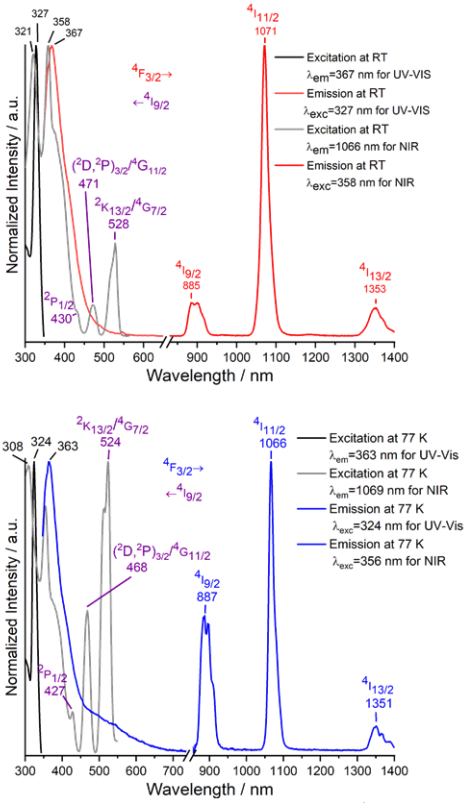

Figure S27. Normalized excitation and emission spectra of ¼[Nd$_2$(2–PyPzH)$_4$Cl$_6$] (**2**) at room temperature (top) and 77 K (bottom). Wavelengths at which the spectra were recorded are reported in the legends.

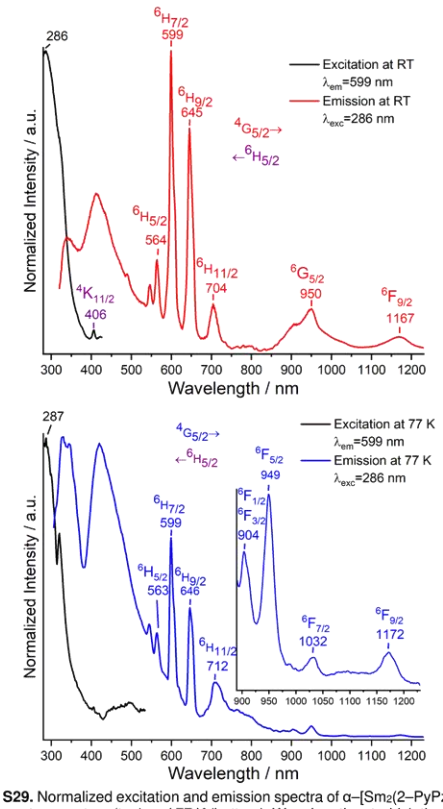

Figure S29. Normalized excitation and emission spectra of α–[Sm$_2$(2–PyPzH)$_4$Cl$_6$] (**4**) at room temperature (top) and 77 K (bottom). Wavelengths at which the spectra were recorded are reported in the legends. Visible and NIR range emission spectra were brought to the same intensity at 704 (at RT) and 712 nm (at 77 K).

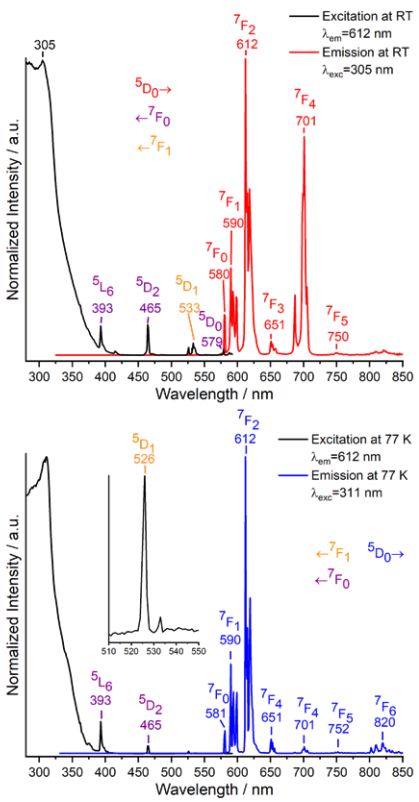

Figure S30. Normalized excitation and emission spectra of α–[Eu2(2–PyPzH)4Cl6] (**5**) at room temperature (top) and 77 K (bottom). Wavelengths at which the spectra were recorded are reported in the legends.

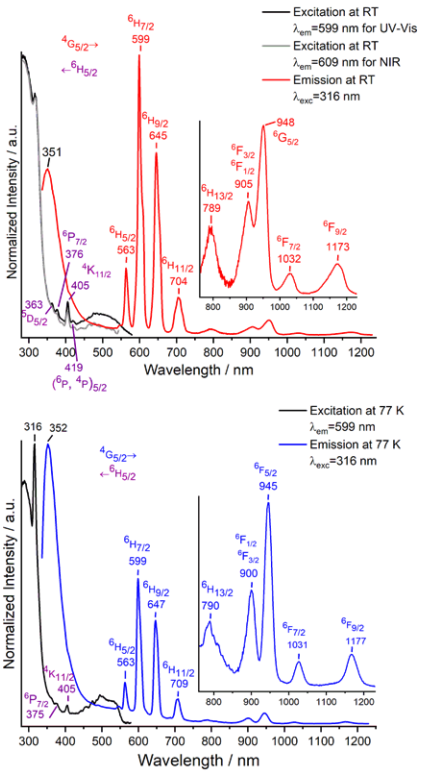

Figure S32. Normalized excitation and emission spectra of β–[Sm2(2–PyPzH)4Cl6] (**8**) at room temperature (top) and 77 K (bottom). Wavelengths at which the spectra were recorded are reported in the legends. Visible and NIR range emission spectra were brought to the same intensity at 704 (at RT) and 709 (at 77 K) nm.

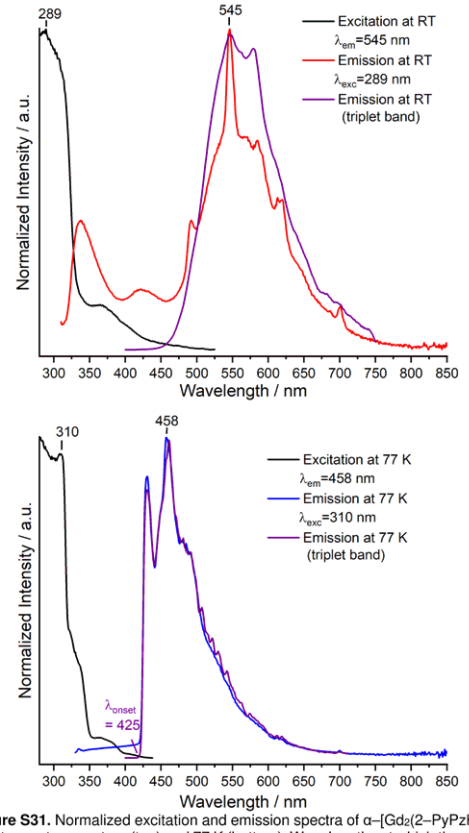

Figure S31. Normalized excitation and emission spectra of α–[Gd2(2–PyPzH)4Cl6] (**6**) at room temperature (top) and 77 K (bottom). Wavelengths at which the spectra were recorded are reported in the legends.

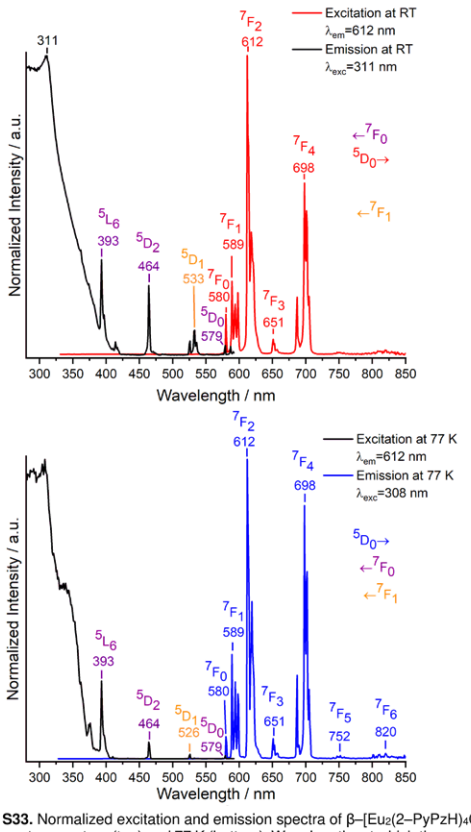

Figure S33. Normalized excitation and emission spectra of β–[Eu2(2–PyPzH)4Cl6] (**9**) at room temperature (top) and 77 K (bottom). Wavelengths at which the spectra were recorded are reported in the legends.

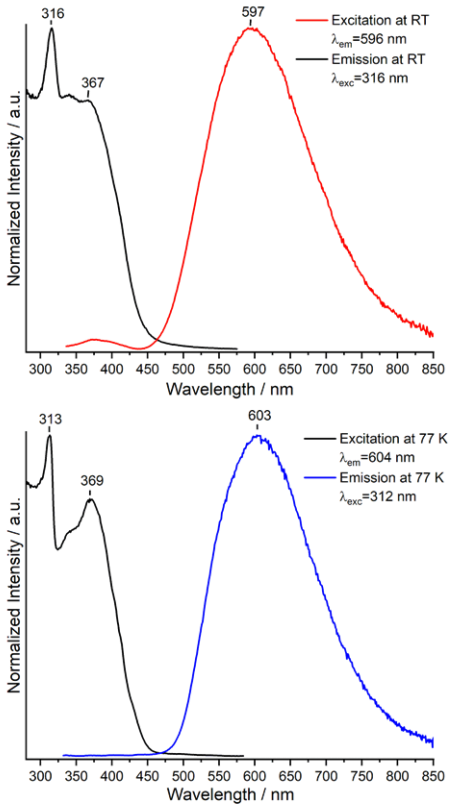

Figure S34. Normalized excitation and emission spectra of [Ce(2–PyPzH)$_3$Cl$_3$] (**11**) at room temperature (top) and 77 K (bottom). Wavelengths at which the spectra were recorded are reported in the legends.

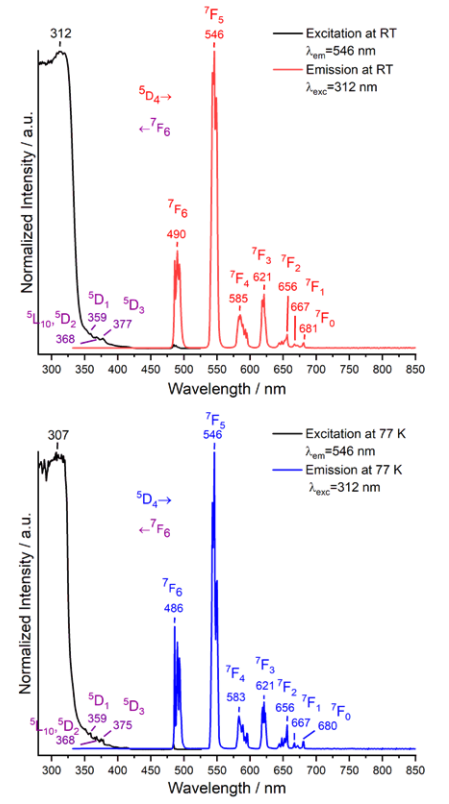

Figure S35. Normalized excitation and emission spectra of [Tb(2–PyPzH)$_2$Cl$_3$] (**12**) at room temperature (top) and 77 K (bottom). Wavelengths at which the spectra were recorded are reported in the legends.

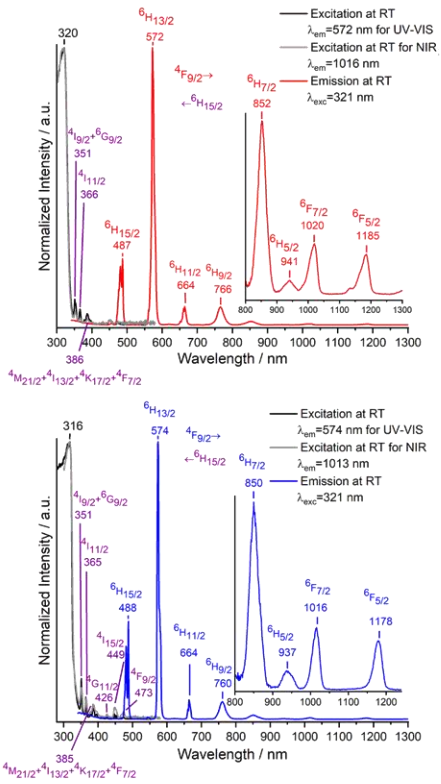

Figure S36. Normalized excitation and emission spectra of [Dy(2–PyPzH)$_2$Cl$_3$] (**13**) at room temperature (top) and 77 K (bottom). Wavelengths at which the spectra were recorded are reported in the legends. Visible and NIR range emission spectra were brought to the same intensity at 766 (at RT) and 760 (at 77 K) nm.

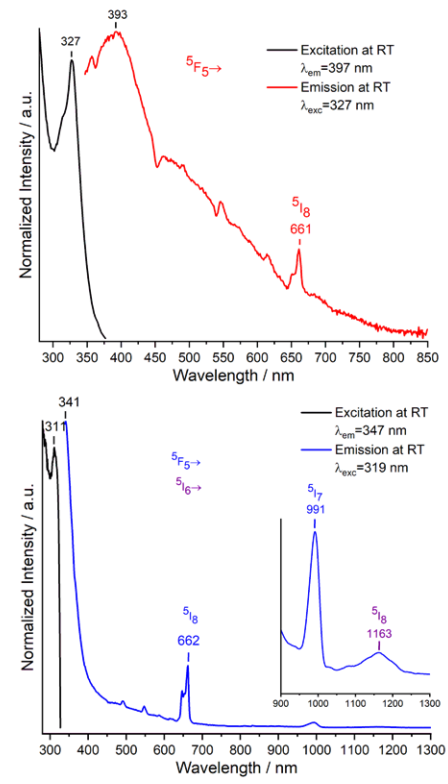

Figure S37. Normalized excitation and emission spectra of [Ho(2–PyPzH)$_2$Cl$_3$] (**14**) at room temperature (top) and 77 K (bottom). Wavelengths at which the spectra were recorded are reported in the legends. Visible and NIR range emission spectra were brought to the same intensity at 662 (at 77 K) nm.

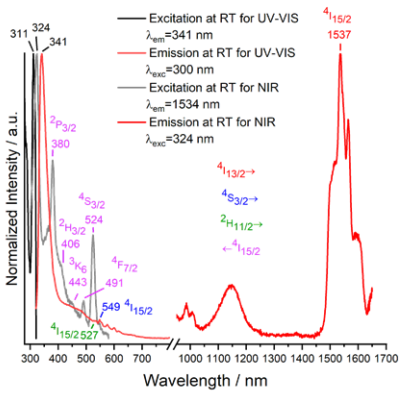

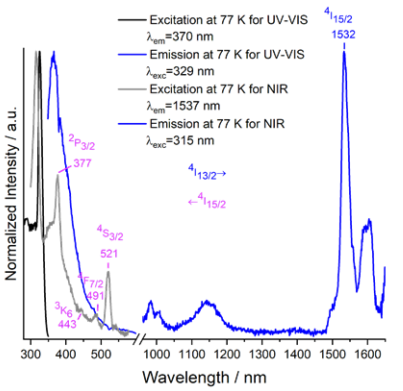

Figure S38. Normalized excitation and emission spectra of [Er(2–PyPzH)$_2$Cl$_3$] (**15**) at room temperature (top) and 77 K (bottom). Wavelengths at which the spectra were recorded are reported in the legends.

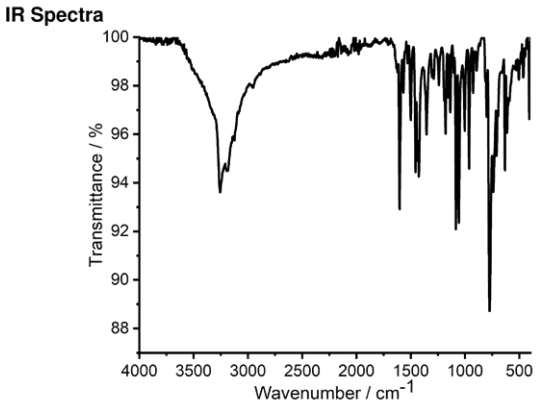

Figure S39. The infrared spectrum (ATR) of $^1_\infty$[La$_2$(2–PyPzH)$_4$Cl$_6$] (**1**).

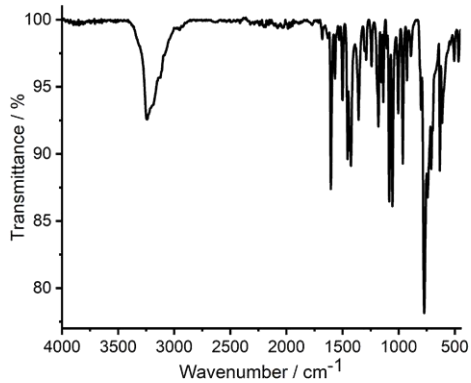

Figure S40. The infrared spectrum (ATR) of $^1_\infty$[Nd$_2$(2–PyPzH)$_4$Cl$_6$] (**2**).

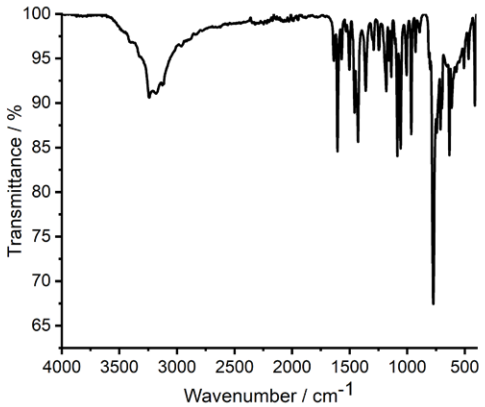

Figure S41. The infrared spectrum (ATR) of $^1_\infty$[Sm$_2$(2–PyPzH)$_4$Cl$_6$] (**3**).

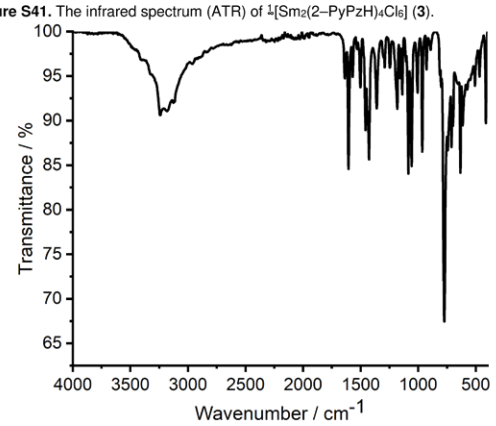

Figure S42. The infrared spectrum (ATR) of α–[Sm$_2$(2–PyPzH)$_4$Cl$_6$] (**4**).

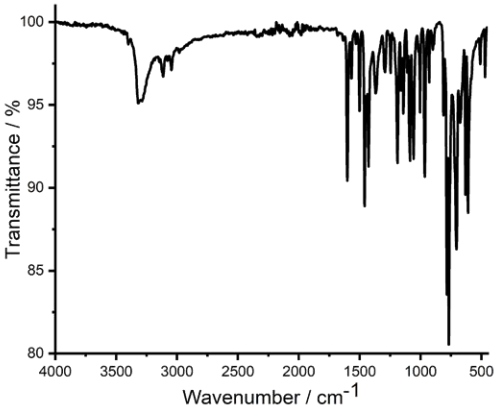

Figure S43. The infrared spectrum (ATR) of α–[Eu$_2$(2–PyPzH)$_4$Cl$_6$] (**5**).

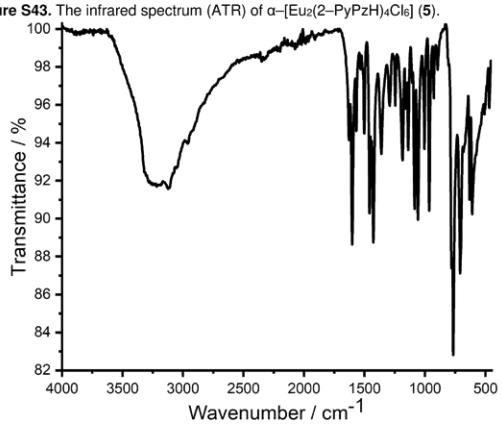

Figure S44. The infrared spectrum (ATR) of α–[Gd$_2$(2–PyPzH)$_4$Cl$_6$] (**6**).

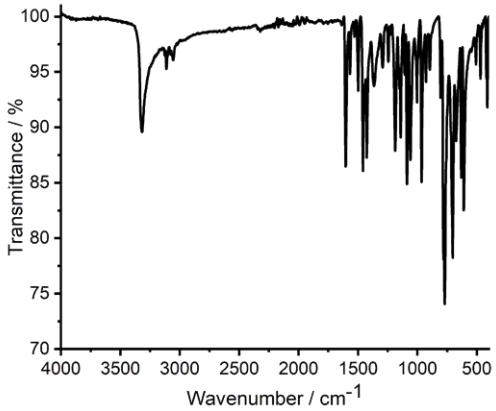

Figure S45. The infrared spectrum (ATR) of β–[Sm_2(2–PyPzH)$_4Cl_6$] (**8**).

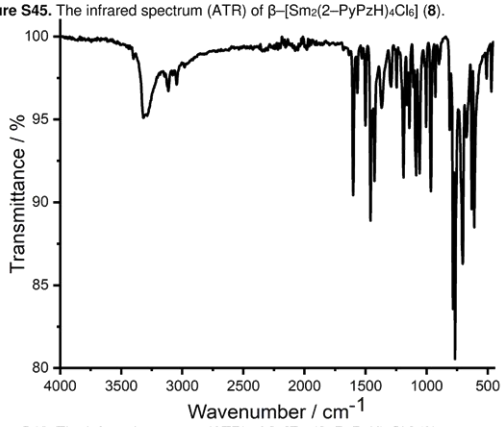

Figure S46. The infrared spectrum (ATR) of β–[Eu_2(2–PyPzH)$_4Cl_6$] (**9**).

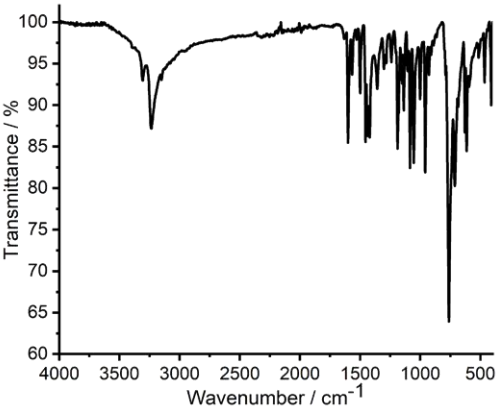

Figure S47. The infrared spectrum (ATR) of [Ce(2–PyPzH)$_3Cl_3$] (**11**).

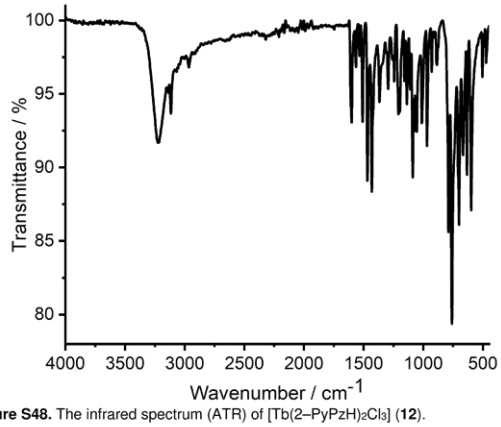

Figure S48. The infrared spectrum (ATR) of [Tb(2–PyPzH)$_2Cl_3$] (**12**).

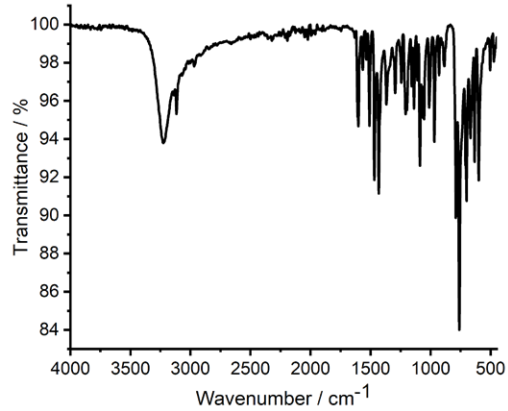

Figure S49. The infrared spectrum (ATR) of [Dy(2–PyPzH)$_2Cl_3$] (**13**).

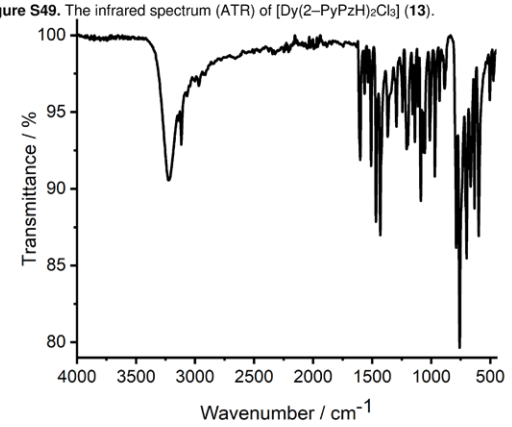

Figure S50. The infrared spectrum (ATR) of [Ho(2–PyPzH)$_2Cl_3$] (**14**).

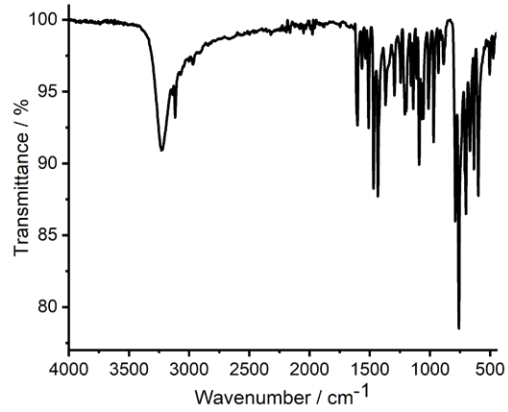

Figure S51. The infrared spectrum (ATR) of [Er(2–PyPzH)$_2Cl_3$] (**15**).

4. Results overview and summary

In attempts to achieve molecular magnetism, about eighty 3D-, 2D-, and 1D-coordination polymers (CPs) and complexes were synthesized from elemental lanthanides or anhydrous trivalent lanthanide chlorides together with one of three main ligands: 3-(2-pyridyl)pyrazole (2-PyPzH), 3-(3-pyridyl)pyrazole (3-PyPzH), and 3-(4-pyridyl)pyrazole (4-PyPzH). In counting, three heterobimetallic lanthanide/alkaline earth (Ln/AE) and two monometallic AE^{2+}-based complexes were synthesized. The crystal structures were mostly determined by single-crystal X-ray diffraction (SCXRD), while powder X-ray diffraction (PXRD) and subsequent Pawley refinements were utilized to characterize some structures, which confirmed being isotypic with the structures from SCXRD. All bulk products were characterized by PXRD. Topological analysis for the prepared 3D-frameworks and 2D-networks was performed to ensure a better understanding of the crystal structures. Simultaneous differential thermal analysis (DTA) and thermogravimetry (TG) combined with mass spectrometry were carried out to investigate the thermal behavior of the prepared compounds. A comparison of the spectroscopic properties of the studied coordination polymers and complexes through the three types of spectra—absorption, excitation, and emission—allows for a better understanding of the photophysical properties observed for the Ln series. In addition, lifetime determinations at RT and 77 K using overall process decay times and quantum yield (QY) determinations were performed for compounds with suitable emission intensities. Direct current (DC) magnetic susceptibility measurements were performed for selected Dy^{3+}-, Er^{3+}-, and Ho^{3+}-based CPs.

The distinct position of the pyridyl nitrogen atom in 2-PyPzH, 3-PyPzH, and 4-PyPzH (Scheme 4.1) resulted in three different homoleptic series of 1D and 3D coordination polymers upon anhydrous solvothermal reaction with elemental lanthanides in pyridine (Py), or additionally as a solvent-free synthesis, to obtain the 1D-CPs series. The isotypic series $^{3}_{\infty}[Ln(3\text{-}PyPz)_3]$, Ln = Ce−Nd, Sm−Tm crystallize in the cubic crystal system with the space group $Pa\bar{3}$, while the two isotypic series $^{1}_{\infty}[Ln(2\text{-}PyPz)_3]$, Ln = La−Nd, Sm−Ho and $^{3}_{\infty}[Ln(4\text{-}PyPz)_3]$, Ln = La−Nd, Sm−Tm, crystallize in the monoclinic crystal system with the space groups $P2_1$ and $P2_1/n$, respectively. In the three series, the Ln^{3+} ion coordinates to nine nitrogen atoms from three ligands, resulting in the identical general chemical formula of $C_{24}H_{18}N_9Ln$. The two nitrogen atoms of the pyrazolate ring act as a bridge between two neighboring trivalent lanthanide ions, forming 1D-CPs while coordinating to the same Ln^{3+} ion, with the ligand itself acting as

a bridge between two adjacent Ln^{3+} ions forming the two series of homoleptic 3D-CPs. It is notable that there is a lake in the Tm^{3+}-nitrogen-based complexes and coordination polymers in the literature, especially for the nine-coordinated Tm^{3+}, where only three examples were reported.[144-146] The topological presentation of the two isotypic series $^{3}_{\infty}[Ln(3\text{-}PyPz)_3]$, Ln = La–Nd, Sm–Tm and $^{3}_{\infty}[Ln(4\text{-}PyPz)_3]$, Ln = La–Nd, Sm–Tm, pass **pcu** topology with a Schläfli symbol of $4^{12}.6^3$ when assuming that the lanthanide centers act as nodes with threefold connectivity. The synthesized compounds of the three-homoleptic series show good thermal stability from 360 to 400 °C.

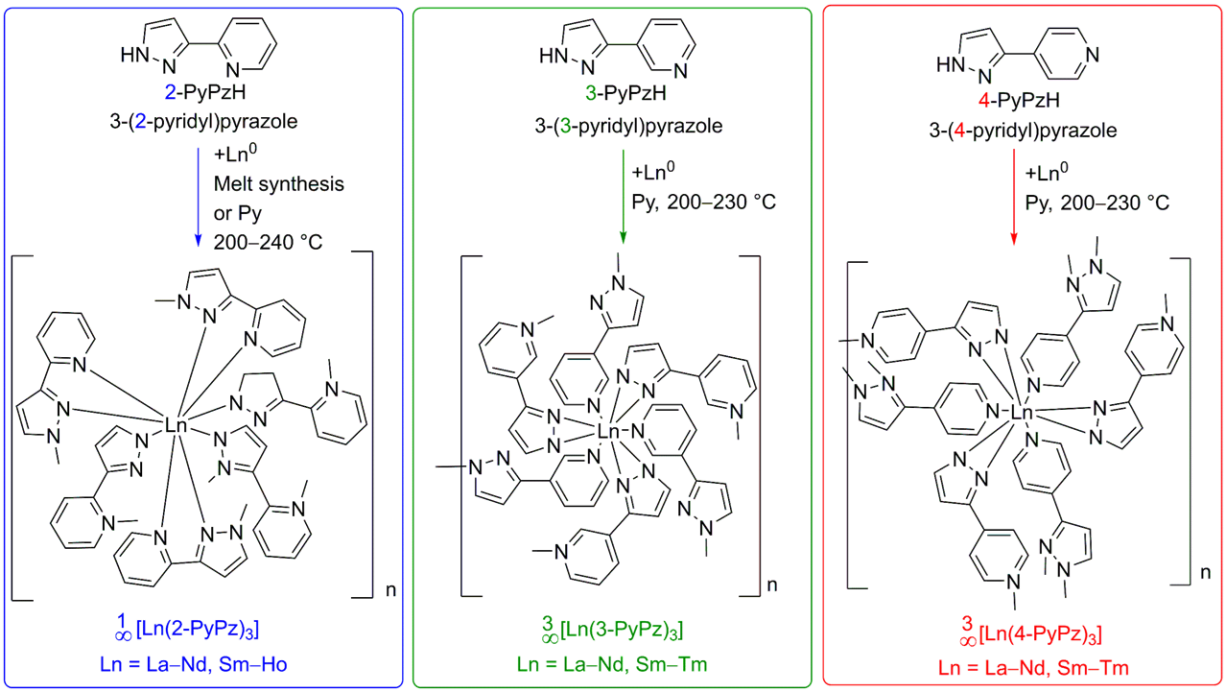

Scheme 4.1. Synthetic scheme for Ln^{3+}-based coordination polymers, comparing the different products from 1D to 3D coordination polymers.

Heteroleptic divalent europium $^{2}_{\infty}[Eu(4\text{-}PyPz)_2(Py)_2]$ (Scheme 4.2) as an example of other Ln oxidation states and additional 2D-networks with Ce^{3+} and Tm^{3+} of the formula $^{2}_{\infty}[Ln(4\text{-}PyPz)_3(Py)]$ were synthesized when the pyridine (Py), which was utilized as a solvent in the solvothermal reaction, served as a co-ligand. In addition, $^{2}_{\infty}[Ln_2(4\text{-}PyPz)_6]\cdot Py$ with Yb^{3+} and Lu^{3+}, including two lanthanide sites, were synthesized when different temperatures and molar ratios of the redox reactions were applied. All crystallize in the monoclinic crystal system with different space groups $P2_1$, *Cc*, and $P2_1/n$, respectively. The coordination number of nine continues for Ce^{3+}, Tm^{3+}, and one site in Yb^{3+} and Lu^{3+} 2D-networks, while the coordination number of eight appears for Eu^{2+} and the other site in Yb^{3+} and Lu^{3+} networks. The Tm^{3+}-based CPs $^{2}_{\infty}[Tm(4\text{-}PyPz)_3(Py)]$, $^{3}_{\infty}[Tm(4\text{-}PyPz)_3]$, and $^{3}_{\infty}[Tm(3\text{-}PyPz)_3]$ have a nitrogen coordination number

of nine, which is unusual in the lanthanide chemistry, as stated before.[144-146] The detected topology for the 2D-networks $^{2}_{\infty}$[Eu(4-PyPz)$_2$(Py)$_2$] and $^{2}_{\infty}$[Ln(4-PyPz)$_3$(Py)], Ln = Ce^{3+}, Tm^{3+} is **sql** topology with the Schläfli symbol $4^4 \cdot 6^2$ which differs from the previously stated **pcu** topology of the 3D-frameworks.

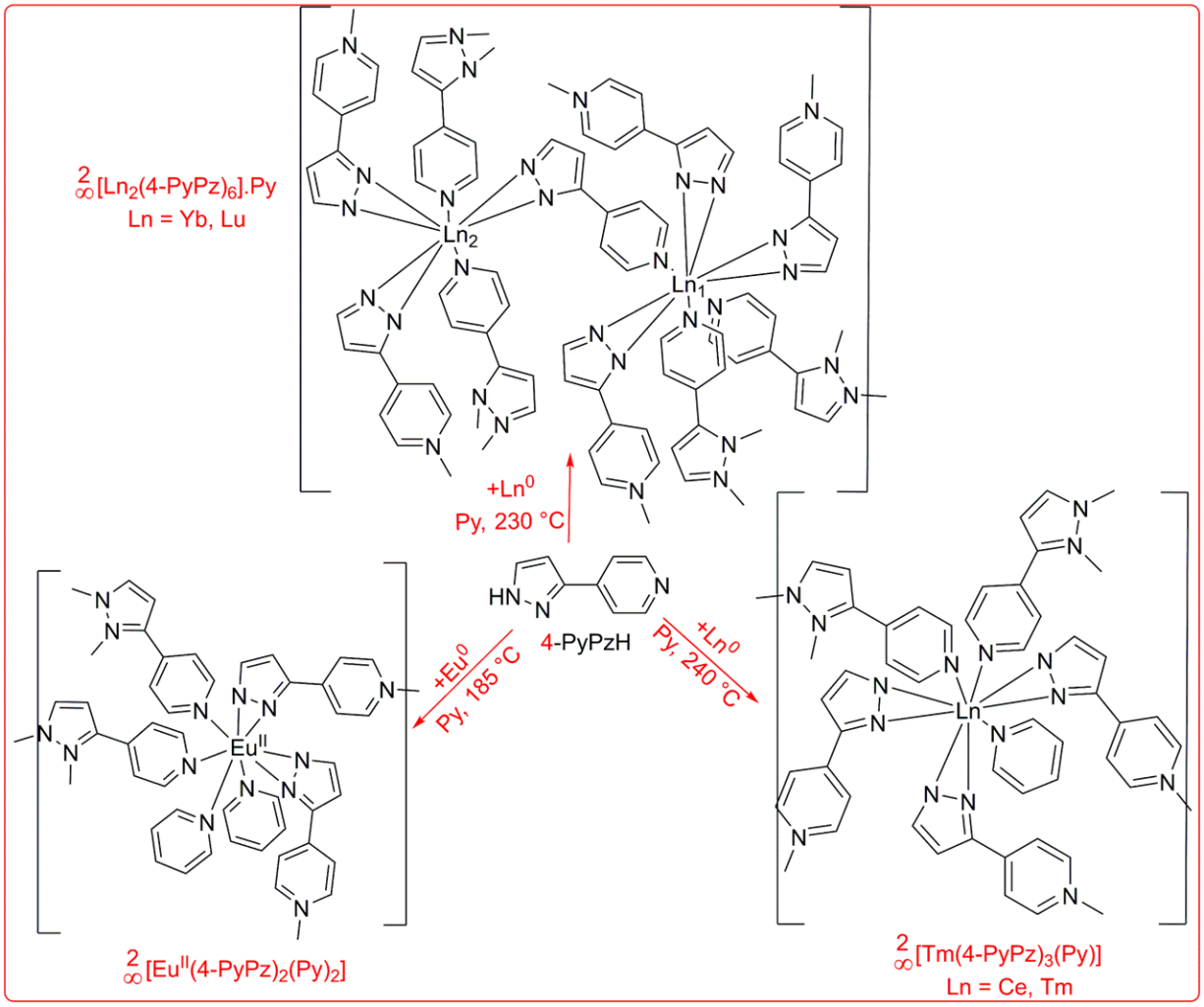

Scheme 4.2. Synthetic scheme showing the Ln-based 2D-networks based on the 4-PyPzH ligand.

Three heterobimetallic complexes [Tb$_2$AE(2-PyPz)$_8$], AE = Ca, Sr, Ba, were obtained by anhydrous solvothermal reactions of 2-PyPzH with a mixture of elemental Tb and the corresponding AE (Scheme 4.3), while two mononuclear complexes [AE(2-PyPz)$_2$(2-PyPzH)$_2$], AE = Ca, Sr, resulted from the reaction with elemental alkaline earth metals. All complexes crystallize in the monoclinic crystal system, [Tb$_2$AE(2-PyPz)$_8$], AE = Sr, Ba and [Sr(2-PyPz)$_2$(2-PyPzH)$_2$] in $P2_1/n$ and [Ca(2-PyPz)$_2$(2-PyPzH)$_2$] in $C2/c$, except for [Tb$_2$Ca(2-PyPz)$_8$], which crystallizes in the triclinic crystal system with space group $P\bar{1}$. The Ln^{3+} ions show a change in coordination number from nine in the 1D-CPs series to eight in the heterobimetallic products, and the AE^{2+} ions go from six to eight upon the change between monometallic and bimetallic products. For [Tb$_2$AE(2-PyPz)$_8$], the

higher tendency of Ln^{3+} to form high coordination numbers drives Tb^{3+} to allocate a position, in which it can coordinate with two nitrogen atoms of both the pyridyl ring and the pyrazolate ring of each tridentate ligand, so that each rare earth ion binds to three chelating bridging ligands and a terminal pyridylpyrazolate anion. These ligands bridge through the pyrazolate ring to the central hexacoordinated alkaline earth atom. For $[AE(2\text{-}PyPz)_2(2\text{-}PyPzH)_2]$, each ligand acts as a bidentate chelating Lewis base and the electroneutrality is settled by two protons bridging two pyrazolate moieties with two neutral ligands. The larger ionic radius of eight-coordinate AE^{2+} in the monometallic complexes leads to a general elongation of the Ca–N(pz) distance, with N(pz) being the pyrazolate nitrogen atom, compared to the heterobimetallic complexes, in which AE^{2+} is six-coordinate. The change in the ionic radius of AE^{2+} increases the AE–N distances from Ca^{2+} to Sr^{2+}. The DTA/TG investigation for $[Tb_2Ca(2\text{-}PyPz)_3]$ exhibits thermal stability up to 400 °C.

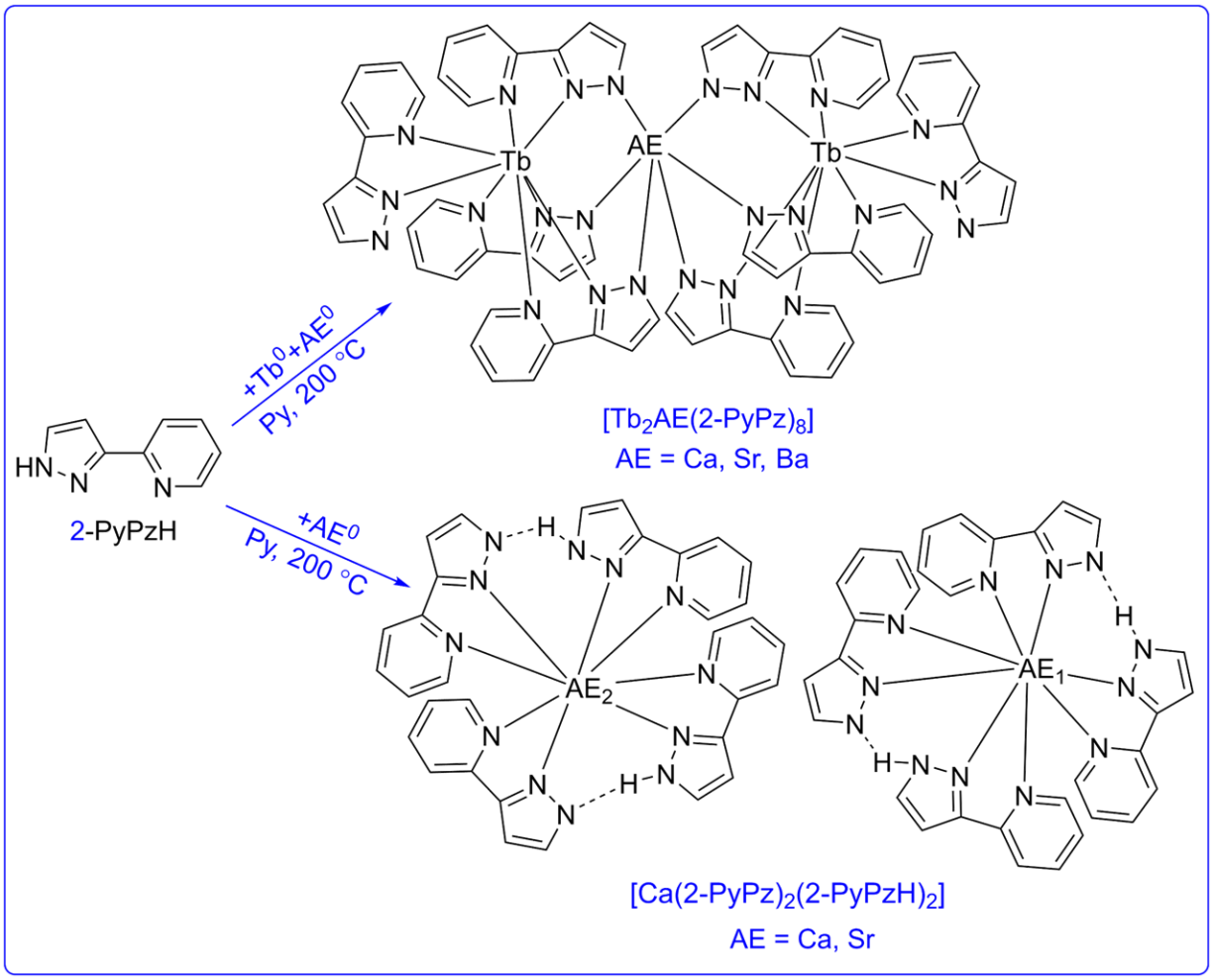

Scheme 4.3. Synthetic scheme for reactions with 2-PyPzH to obtain bimetallic complexes (top) and alkaline earth-based complexes and their schematic structure.

All bulk products of the previously mentioned Ln containing 3D-frameworks, 2D-networks, 1D-zigzag CPs, and complexes were examined for their photoluminescence properties through the three types of spectra: absorption, excitation, and emission.

An exception was detected for undoped Ce^{3+} phosphor materials that show 5d–4f transitions with Ce^{3+}-centered light emission in the red region that can already be seen with the naked eye under the UV lamp. The Ce^{3+} pink-to-red emitters are an exception among other Ce^{3+}-based emitters. Most reported Ce^{3+} compounds are non-emissive due to luminescence quenching by linkers and solvent molecules.[16] The emissive Ce^{3+} examples in the literature are mainly near ultraviolet (UV) and blue-green emitters.[17-18] The emission spectra of $^{2}_{\infty}$[Ce(4-PyPz)$_3$(Py)] (**4-$^{2}_{\infty}$Ce**), $^{3}_{\infty}$[Ce(4-PyPz)$_3$] (**4-Ce**), $^{3}_{\infty}$[Ce(3-PyPz)$_3$] (**3-Ce**), and $^{1}_{\infty}$[Ce(2-PyPz)$_3$] (**2-$^{1}_{\infty}$Ce**) show broad bands centered at 650, 650, 641, and 620 nm, respectively, at RT, indicating large crystal field splitting and a large redshift for the emission wavelength. The intensity of the ligand-based emission decreases in the aforementioned order, causing the emission color to shift from pink through orange pink to red, as shown in the CIE 1931 chromaticity coordinate diagram (Figure 4.1). Both the absorption spectra and the excitation spectra show shoulders at higher wavelengths, which correlate with the lowest energy levels of the crystal field splitting bands of the 5d excited state of the Ce^{3+} ions. A short lifetime (τ), on the scale of a few ns, is measured due to the parity-allowed nature of the 5d–4f transition.

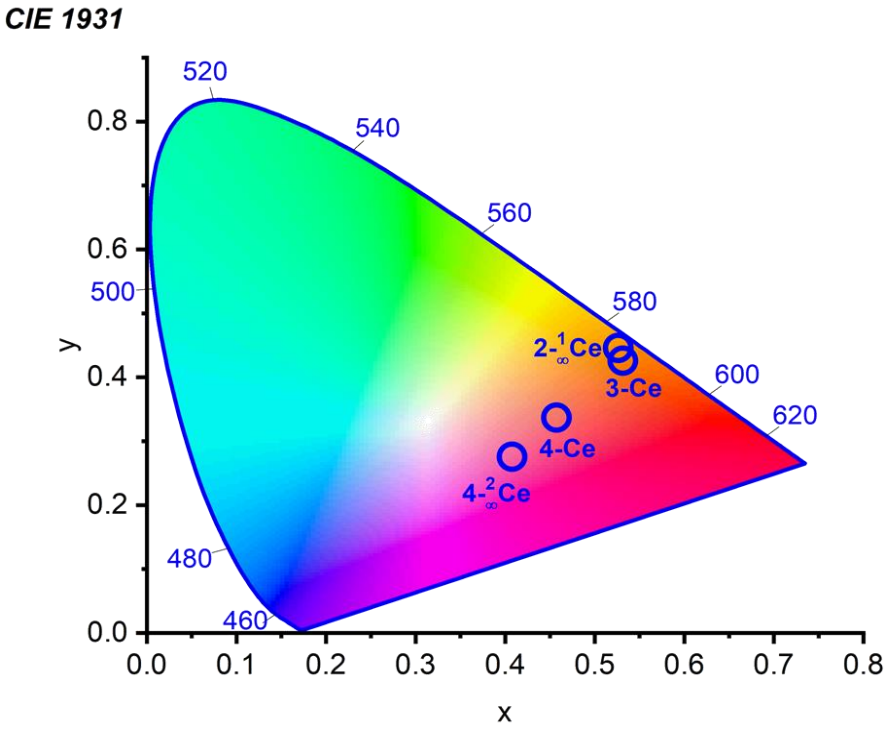

Figure 4.1. Chromaticity coordinate diagram (CIE 1931) of the emission colors of $^{2}_{\infty}$[Ce(4-PyPz)$_3$(Py)] (**4-$^{2}_{\infty}$Ce**), $^{3}_{\infty}$[Ce(4-PyPz)$_3$] (**4-Ce**), $^{3}_{\infty}$[Ce(3-PyPz)$_3$] (**3-Ce**), and $^{3}_{\infty}$[Ce(2-PyPz)$_3$] (**2-$^{1}_{\infty}$Ce**).

Recently, the generation of white light by mixing different monochromatic light sources has become an attractive feature of light-emitting materials.[32] One of the explored strategies to obtain white light is by combining red, green, and blue (RGB) sources to cover the visible region (400–700 nm) in the electromagnetic spectrum.[147] Therefore, the co-doping of the Gd-containing coordination polymers $^{1}_{\infty}$[Gd(2-PyPz)$_3$], $^{3}_{\infty}$[Gd(3-PyPz)$_3$], and $^{3}_{\infty}$[Gd(4-PyPz)$_3$] with Tb^{3+} (green emitter) and Eu^{3+} (red emitter) is established and used for chromaticity tuning. Mixing of the three emission colors results in a shift towards yellow, orange, and even towards the white point. The nearest point to the white light (for pure white x = 0.33, y = 0.33) was achieved by co-doping $^{3}_{\infty}$[Gd(3-PyPz)$_3$]:Eu^{3+},Tb^{3+} with 0.5 % Eu^{3+} to generate color coordinates of x = 0.30 and y = 0.37 at 77 K. This point is closer to the white light than others reported in the literature.[148] The possibility of tuning the luminescence chromaticity by co-doping of other homoleptic coordination polymers $^{1}_{\infty}$[Ln(2-PyPz)$_3$], $^{3}_{\infty}$[Ln(3-PyPz)$_3$], and $^{3}_{\infty}$[Ln(4-PyPz)$_3$] was also confirmed for the co-doping of the Tb- and Eu-containing frameworks with the respective counterions, where a downshift metal-to-metal energy transfer (MMET) from excited 4f states of Tb^{3+} to Eu^{3+} was observed. Altogether, this shows the high potential of the three series for co-doping to produce white light emission.

The CPs under study, with the exception of La^{3+}-, Ce^{3+}-, Eu^{2+}-, Gd^{3+}-, and Lu^{3+}-based coordination polymers, show photoluminescence with intra-4f emission of the Ln^{3+} ions activated by antenna effects of the pyridylpyrazolate ligands. A first indication for the excellent antenna effect is the complete disappearance of the ligand-based fluorescence band after coordination with Tb^{3+}, Eu^{3+}, Sm^{3+}, and Dy^{3+}. Good to high photoluminescence quantum yields (PLQY) of 23 % and 74 % are obtained for $^{3}_{\infty}$[Tb(4-PyPz)$_3$] and $^{3}_{\infty}$[Tb(3-PyPz)$_3$], making 4-$PyPz^-$ and 3-$PyPz^-$ perfect sensitizers for Tb^{3+} with relatively long lifetimes in the range of ms. The high PL quantum yields are likely facilitated by a good energy match between the donor (triplet ligand at ~23250 cm^{-1}) and acceptor ($^5D_4$ at ~20 500 cm^{-1}) states (ΔE ~2500–3000 cm^{-1}). By comparing the lifetime and the quantum yield measured for Tb^{3+} in $^{3}_{\infty}$[Tb(4-PyPz)$_3$] (τ = 0.6273 ms, QY = 23 %) and $^{3}_{\infty}$[Tb(3-PyPz)$_3$] (τ = 1.0874 ms, QY = 74 %) with previously reported compounds such as [TL$_3$](ClO_4)$_3$·H_2O·2MeCN, (L = 2,6-bis(1-methyl-imidazol-2-yl)pyridine), τ = 0.245 ms, QY = 17 %)[149] and [Tb(L^1)$_3$] (L^1H = 2-(1H-Pyrazol-1-yl)-6-(1H-tetrazol-5-yl)pyridine, τ = 1.23 ms, QY = 53 %)[150], the framework $^{3}_{\infty}$[Tb(3-PyPz)$_3$] reaches the high range of reported lifetimes and QYs among the related Tb^{3+}-based compounds and $^{3}_{\infty}$[Tb(4-PyPz)$_3$] reaches a moderate range. While 2-$PyPz^-$ is a

moderate sensitizer for both Tb^{3+} and Eu^{3+} ions in $^{1}_{\infty}[Ln(2\text{-}PyPz)_3]$ with a relatively shorter lifetime for Tb^{3+} (0.28 ms) but a longer lifetime for Eu^{3+} (0.87 ms) compared to $^{3}_{\infty}[Ln(3\text{-}PyPz)_3]$ and $^{3}_{\infty}[Ln(4\text{-}PyPz)_3]$, both have a PLQY limited to 6 %. The internal quantum yield (IQY) of the Eu^{3+}-centered emission was calculated using Wert's formula with a refractive index of 1.5.[37-38] The equation gives a moderate-high IQY of 37.2 %, which is in the middle of $^{3}_{\infty}[Eu(3\text{-}PyPz)_3]$ and $^{3}_{\infty}[Eu(4\text{-}PyPz)_3]$ 48 % and 33 %, respectively. The Sm^{3+} and Dy^{3+} show longer decay times with $3\text{-}PyPz^{-}$ and $4\text{-}PyPz^{-}$ as sensitizers than for $2\text{-}PyPz^{-}$, which could be related to the reduction of a back energy transfer. The PL of the studied CPs decays monoexponentially, thus indicating the presence of a single emissive species.

The emission spectra of $[Tb_2AE(2\text{-}PyPz)_8]$ display rather sharp lines, which can be identified with f–f transitions regarding Tb^{3+}. The ligand emission is also observable at RT for the bimetallic complexes, exhibiting a hypsochromic shift caused by a decrease in the π-electron density of the pyridylpyrazolate anions by the double linkage to two metal ions.

Although the excitation and emission spectra can provide a wealth of information, particularly about the coordination environment of the Ln^{3+} ions; it is uncommon to find the luminescence spectra for the Tm^{3+}-, Ho^{3+}-, and Pr^{3+}-based compounds. As mentioned, the nine-coordinated Tm^{3+} was only reported in three examples, and none of them investigated the photophysical properties, they mainly focused on the structural aspects.[144-146] In many other cases, poor ligand-to-metal sensitization or back energy transfer occurs to produce the ligand luminescence[151-153] where a significant ligand emission dominates the spectrum beside a single spectral band for the Tm^{3+}. Even non-efficient ligand-sensitization with only a ligand emission band in the emission spectra were shown.[154] In contrast, very good ligand-to-metal sensitization is observed for $^{3}_{\infty}[Tm(4\text{-}PyPz)_3]$ where the transitions $^1G_4 \rightarrow {}^3H_6$, $^3F_4$, $^3H_5$, and $^3H_4$ are readily observable. For $^{1}_{\infty}[Ln(2\text{-}PyPz)_3]$, $^{3}_{\infty}[Ln(3\text{-}PyPz)_3]$, and $^{3}_{\infty}[Ln(4\text{-}PyPz)_3]$, Ln = Ho and Pr the transitions in both visible (VIS) and near-infrared (NIR) regions are well observable indicating more efficient ligand sensitization than in many reported cases.[93, 154] NIR characteristic emission bands are also observable for Nd^{3+}, Sm^{3+}, Dy^{3+}, and Er^{3+}-based coordination polymers. For Nd^{3+}-based CPs, the emission at 1065 nm is the strongest, which is possibly useful for laser applications.[155-160] Nd^{3+}- and Er^{3+}-based materials attract much interest in the application of optical amplification because their emission bands, around 1.3 μm for Nd^{3+} and 1.5 μm for Er^{3+}, are in the desired region for the telecommunication

window.[156-157] In order to obtain a wide gain bandwidth for optical amplification, a broad emission band is desirable.[161] The full width at half maximum (FWHM) of the transition $^4I_{13/2} \rightarrow {}^4I_{15/2}$ of the Er^{3+}-based CPs, as an example, is 90 and 95 nm for $^3_\infty$[Er(4-PyPz)$_3$] and $^3_\infty$[Er(3-PyPz)$_3$], which may endow a wide gain bandwidth for optical amplification.[155, 162] Among the three emissions of Ho^{3+}-based CPs, the intensity of the emission band at 983 nm for $^3_\infty$[Ho(4-PyPz)$_3$] is the strongest, which is probably useful in biomedical applications.[155]

Detectable and distinguishable Laporte forbidden 4f−4f absorption transitions are also revealed in the UV-VIS-NIR spectrophotometry beside the ligand-centered transitions. The measured solid-state absorption spectra in a range of 200–1300 nm have enriched the literature, as the reported absorption spectra localized on the ligand moieties of the Ln^{3+}-based compounds were mostly investigated in solution,[163-165] while fewer examples are reported for the solid-state.[166-167] In addition, when examining Ln^{3+}-based absorption bands, the wavelength range is typically found to be limited in the literature, e.g., it does not exceed 1000 nm for Ho^{3+} in [Ho(L)(NO$_3$)$_2$](PF$_6$)·H$_2$O, (L = N^1,N^2-Bis([2,2′-bipyridine]-6-ylmethylene)-1,2-ethanediamine),[168] 800 nm for Er^{3+} and Dy^{3+}, and up to 650 nm for Sm^{3+} in $^2_\infty$[Ln(tfBDC)(NO$_3$)(DMF)$_2$]·DMF, (Ln = Er^{3+}, Dy^{3+}, and Sm^{3+}, H$_2$tfBDC = 2,3,5,6-tetrafluoroterephthalic acid).[169] Furthermore, the detection of a broad shoulder in the absorption spectra of $^2_\infty$[Eu(4-PyPz)$_2$(Py)$_2$], which is associated with a metal-to-ligand charge transfer (MLCT) transition from the Eu^{2+} 4f orbitals to the π* orbitals of the coordinated ligands, besides the shoulders detected in the absorption spectra of Ce^{3+}-based CPs which correlate with the lowest energy levels of the crystal field splitting bands of the 5d excited state of the Ce^{3+} ions, as stated before.

Altogether, this shows the high potential of the three series of coordination polymers together with pyridylpyrazolate ligands as N-donors for versatile photoluminescence properties.

A large structural diversity through fifteen 3D- and 2D- networks and complexes besides a series of eighteen lanthanide-containing 1D-coordination polymers, dinuclear polymorphic complexes, and mononuclear complexes were detected from anhydrous solvothermal reactions of trivalent lanthanide chlorides together with 3-PyPzH and 2-PyPzH, respectively in either acetonitrile (MeCN), toluene (Tol) or chlorobenzene (PhCl). A comparison between the different products of the two isomers is shown in Scheme 4.4. $^3_\infty$[Ln(3-PyPzH)Cl$_3$], Ln = Eu, Gd, $^2_\infty$[Sm(3-PyPzH)Cl$_3$], [Ce(2-PyPzH)$_3$Cl$_3$],

and [PyH][Tb(2-PyPzH)$_2$Cl$_4$] crystallize in the orthorhombic crystal system with the space group *Pcca, Pbcm*, *Pbca*, and *Pbcn*, respectively. $^2_\infty$[Ln$_2$(3-PyPzH)$_3$Cl$_6$]·2solv, Ln = Eu^{3+}, Tb^{3+}, Dy^{3+}, Ho^{3+}, Er^{3+}, solv = Tol and MeCN, [(3-PyPzH$_2$)][Ln(3-PyPzH)$_2$Cl$_4$], Ln = Eu, Tb, Dy, Ho, and [Gd$_2$(2-PyPzH)$_3$(2-PyPz)Cl$_5$] crystallize in the monoclinic crystal system with the space group *P*2$_1$/*n* while $^2_\infty$[Ln(3-PyPzH$_2$)Cl$_4$], Ln = La, Nd crystallize with the *C*2/*c* space group. Additional products with 2-PyPzH crystallize in the monoclinic crystal system, but with the space group *C*2/*c* in $^1_\infty$[Ln$_2$(2-PyPzH)$_4$Cl$_6$], Ln = La, Nd, Sm and with the space group *P*21/*c* in α-[Ln$_2$(2-PyPzH)$_4$Cl$_6$], Ln = Sm, Eu, Gd, Tb and [Ln(2-PyPzH)$_2$Cl$_3$], Ln = Tb, Dy, Ho, Er. The triclinic crystal system is only shown for the 2-PyPzH-based series in β-[Ln$_2$(2-PyPzH)$_4$Cl$_6$], Ln = Sm, Eu, Gd and [Gd$_3$(2-PyPzH)$_8$Cl$_8$]Cl, which crystallize in the space group $P\bar{1}$. It is notable that two polymorphs are found for each Sm^{3+}, Eu^{3+}, and Gd^{3+}, where the α-phase crystallizes at lower temperatures in higher symmetry.

As the ionic radius of the trivalent rare earth element decreases, the coordination number decreases through the 3-PyPzH-based series from eight for lanthanum, neodymium, and samarium to seven for europium through erbium to six for the salt-like complexes of europium, and terbium through holmium. For $^2_\infty$[Sm(3-PyPzH)Cl$_3$], the Sm^{3+} coordination sphere consists of two nitrogen atoms from two different 3-PyPzH ligands and six Cl$^-$ ligands. The 3-PyPzH molecule acts as a bridge between two adjacent Sm^{3+} ions to form a 1D zigzag building unit, while a secondary building unit (SBU) is formed by a 1D inorganic zigzag, in which three chloride ions act as a bridge between two adjacent Sm^{3+} ions to form a two-dimensional network with a **sql** topology and the Schläfli symbol 4^4.6^2. For the anionic CPs $^2_\infty$[Ln(3-PyPzH$_2$)Cl$_4$], Ln = La, Nd, each Ln^{3+} ion is coordinated by a protonated ligand (3-PyPzH$_2$)$^+$ and seven chlorine atoms, six of which act as a bridge between two neighboring trivalent lanthanide ions, forming a 2D-CP with a **hcb** honeycomb topology and the Schläfli symbol 6^3. For $^3_\infty$[Ln(3-PyPzH)Cl$_3$], Ln = Eu and Gd, each Ln^{3+} ion is hepta-coordinated to five chloride anions, one of which is terminal, and two N atoms from two ligands. The neighboring Ln^{3+} ions are linked by a chlorine bridge, forming a 1D inorganic wavelike [Ln(Cl)$_2$]$_n$ chain as a building unit. The 1D infinite chains are interconnected by pyridylpyrazole bridges, creating a 3D coordination polymer with a **sra** topology and the Schläfli symbol 4^2.6^3.8. For $^2_\infty$[Tb$_2$(3-PyPzH)$_3$Cl$_6$]·2Tol and $^2_\infty$[Ln$_2$(3-PyPzH)$_3$Cl$_6$]·2MeCN, Ln = Eu^{3+}, Tb^{3+}, Dy^{3+}, Ho^{3+}, and Er^{3+}, each Ln ion is hepta-coordinated by three nitrogen atoms from three ligand molecules and four chloride ions.

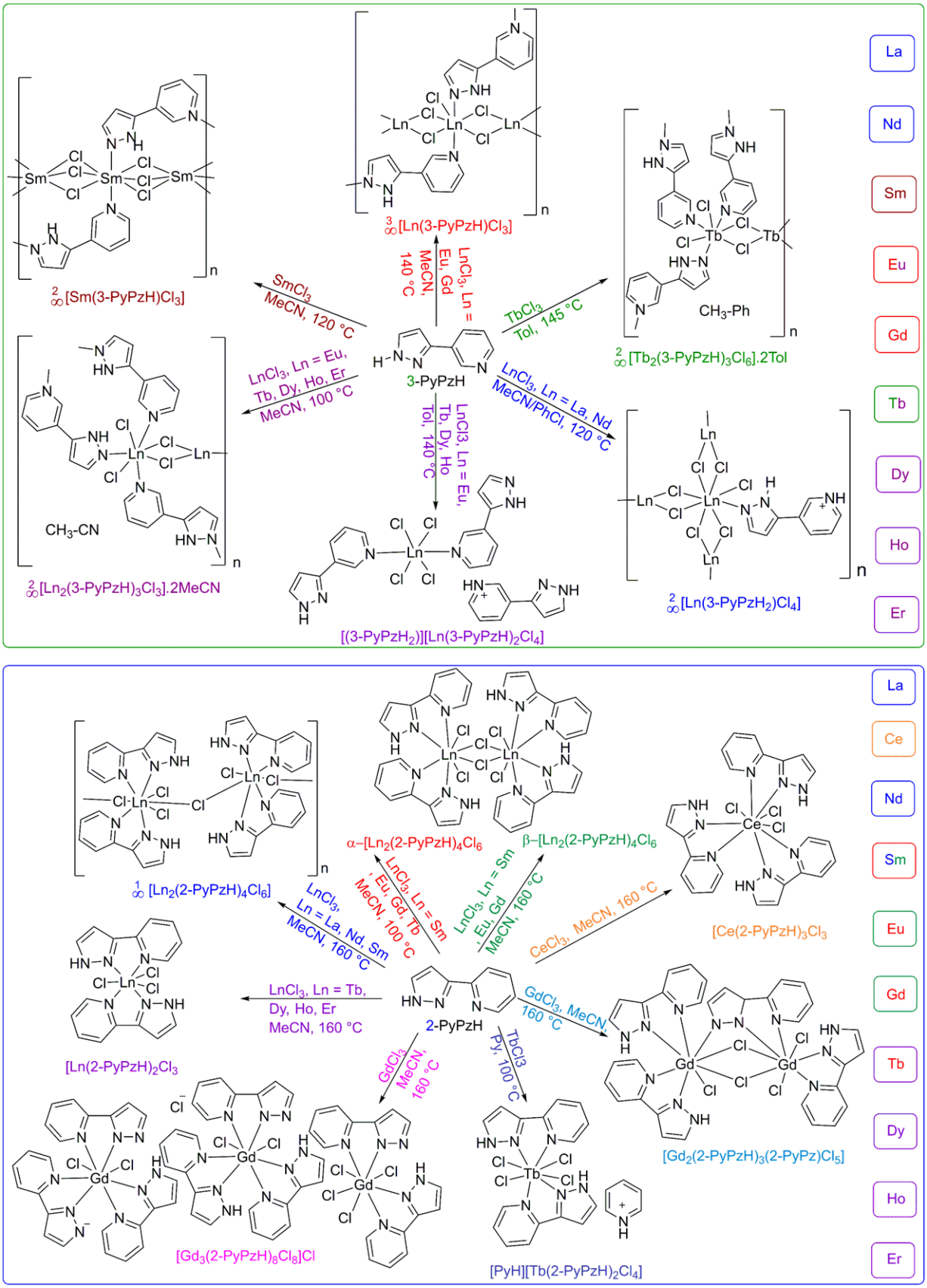

Scheme 4.4. Summarized synthetic scheme for $LnCl_3$-based coordination polymers, comparing the different products from complexes and salt like complexes through 1D and 2D to 3D coordination polymers.

All three neutral ligand molecules and the two equatorial chloride ions act as a bridge between two neighboring trivalent lanthanide ions, forming a 2D net that adopts the **sql** topology and the Schlafli symbol $4^4.6^2$. For the anionic complexes [(3-PyPzH$_2$)][Ln(3-PyPzH)$_2$Cl$_4$], Ln = Eu, Tb, Dy, Ho, the Ln ion coordinates four terminal chloride ions and two nitrogen atoms of two neutral ligands. In addition, a protonated ligand (3-PyPzH$_2$)$^+$ is intercalated and non-coordinated in the structure, compensating for the negative charge of the [Ln(3-PyPzH)$_2$Cl$_4$].

For the 2-PyPzH-based series, the CN decreases as well, from eight for lanthanum, neodymium, samarium, gadolinium, and terbium to seven in the monomeric complexes of terbium, dysprosium, holmium, and erbium. An exception is [Ce(2-PyPzH)$_3$Cl$_3$] with a CN of nine. For $^1_\infty$[Ln$_2$(2-PyPzH)$_4$Cl$_6$], Ln = La, Nd, Sm, α-[Ln$_2$(2-PyPzH)$_4$Cl$_6$], Ln = Sm, Eu, Gd, Tb, and β-[Ln$_2$(2-PyPzH)$_4$Cl$_6$], Ln = Sm, Eu, Gd, each Ln^{3+} ion coordinates to four Cl^- ligands and four nitrogen atoms. In $^1_\infty$[Ln$_2$(2-PyPzH)$_4$Cl$_6$], a chlorine atom acts as a bridge between two adjacent Ln^{3+} ions to form a 1D-coordination polymer, while two chlorine atoms bridge the two Ln^{3+} ions in the dimeric complexes α-[Ln$_2$(2-PyPzH)$_4$Cl$_6$] and β-[Ln$_2$(2-PyPzH)$_4$Cl$_6$]. For the monomer complexes, the Ce^{3+} in [Ce(2-PyPzH)$_3$Cl$_3$] is coordinated by three chlorides and six nitrogen atoms of three 2-PyPzH ligands, while the Ln^{3+} in [Ln(2-PyPzH)$_2$Cl$_3$], Ln = Tb, Dy, Ho, Er, is coordinated by three chloride ions and four nitrogen atoms of two ligands. The differences in the orientation and position of the atoms between the polymorphs α-[Ln$_2$(2-PyPzH)$_4$Cl$_6$] and β-[Ln$_2$(2-PyPzH)$_4$Cl$_6$] are minor when the two structures are overlaid. The α phase (higher crystallographic symmetry) is about 1.2 % more densely packed than the β phase, resulting in a slightly shorter metal–metal distance (443.3(1) in α-[Eu$_2$(2-PyPzH)$_4$Cl$_6$] and 447.6(1) pm in β-[Ln$_2$(2-PyPzH)$_4$Cl$_6$]). Overall, the case of lanthanide chloride-based CPs and complexes shows lower coordination numbers compared to the elemental lanthanide-based CPs.

The $^2_\infty$[Ho$_2$(3-PyPzH)$_3$Cl$_6$]·2MeCN shows the highest stability among the 3-PyPzH-based series up to 365 °C, while both the $^1_\infty$[Sm$_2$(2-PyPzH)$_4$Cl$_6$] and the [Tb(2-PyPzH)$_2$Cl$_3$] show less stability up to 250 °C. It is observable that the thermal product stabilities of the pyridylpyrazolate-based frameworks, networks, and complexes are higher than those of pyridylpyrazole-based compounds due to the strong bonds of the pyrazolate anions to the metal cations.

The unique photoluminescence properties with Ce^{3+}-centered light emission in the orange range of the visible spectrum continue also with the heteroleptic complex [Ce(2-

PyPzH)$_3$Cl$_3$], which can already be distinguished by the eye under the UV lamp. Determinations *via* photoluminescence spectroscopy revealed a broadband emission starting at 460 nm with a center at around 600 nm, indicating large crystal field splitting and a bathochromic shift for the emission wavelength generating a yellow-orange emission color as shown in the chromaticity coordinate diagram (CIE 1931) (Figure 4.2). The excitation spectrum exhibits a shoulder at 370 nm, corresponding to the lowest energy levels of the crystal field splitting bands of the 5d excited state of the Ce^{3+} ion, which coincides with the shoulder in the absorption spectra. The lifetime for the orange-phosphor (2.83(3) ns) is slightly longer than for the red-phosphor $^1_\infty$[Ce(2-PyPz)$_3$] (2.03(4) ns) and shorter than the pink and orange phosphors $^2_\infty$[Ce(4-PyPz)$_3$(Py)] (1.08(2) ns), $^3_\infty$[Ce(4-PyPz)$_3$] (1.16(2) ns), and $^3_\infty$[Ce(3-PyPz)$_3$] (1.26(2) ns).

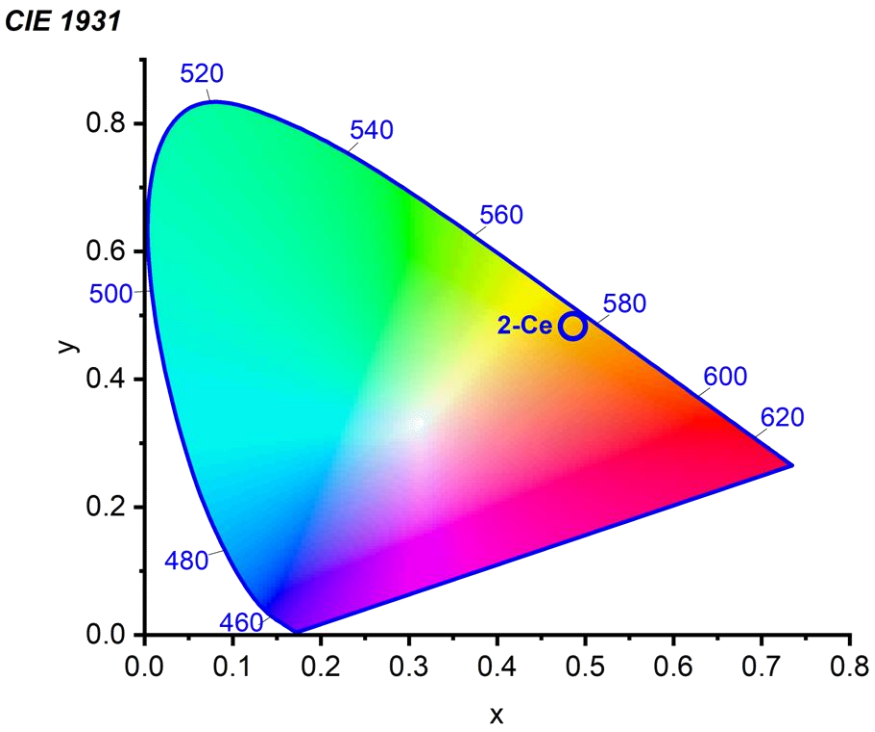

Figure 4.2. Chromaticity coordinate diagram (CIE 1931) of the emission colors of [Ce(2-PyPzH)$_3$Cl$_3$] (**2-Ce**).

For the phase-pure CPs and complexes, the intra-4f emission of the respective Ln^{3+} is activated by an antenna effect of the ligand molecules of different effectivity, leading to Ln^{3+} sensitization with high PLQY from 73 % and 76 % to 92 % for the Tb^{3+} compounds $^2_\infty$[Tb$_2$(3-PyPzH)$_3$Cl$_6$]·2Tol, $^2_\infty$[Tb$_2$(3-PyPzH)$_3$Cl$_6$]·2MeCN, and [Tb(2-PyPzH)$_2$Cl$_3$], respectively. A lower effectiveness of the antenna effect is detected for Eu^{3+} (8 % and 13 % for α-[Eu$_2$(2-PyPzH)$_4$Cl$_6$] and β-[Eu$_2$(2-PyPzH)$_4$Cl$_6$]) followed by the Dy^{3+} (2 % and 3 % for $^2_\infty$[Dy$_2$(3-PyPzH)$_3$Cl$_6$]·2MeCN and [Ln(2-PyPzH)$_2$Cl$_3$]) results in

longer lifetimes for the Tb^{3+} emissive state compared to Eu^{3+} and Dy^{3+}. When the photophysical properties of the obtained products were compared to the previously mentioned homoleptic frameworks based on 2-$PyPz^-$ and 3-$PyPz^-$, relatively shorter lifetimes was detected for Sm^{3+}-based products, $^3_\infty$[Eu(3-PyPzH)Cl_3], and $^2_\infty$[Eu_2(3-PyPzH)$_3Cl_6$]·2MeCN compared to those for the $^3_\infty$[Ln(3-PyPz)$_3$] and $^1_\infty$[Ln(2-PyPz)$_3$], Ln = Sm, Eu which can be explained by the ligand coordination to the lanthanide metal centers in its neutral form, thus maintaining the high-energy N–H bond vibration that could lead to a deactivation process without observation of emitted radiation. A further reason is the possible quenching effect of the Cl^- ligands. This behavior changes for both Tb^{3+}, Dy^{3+}, α-[Eu_2(2-PyPzH)$_4Cl_6$], and β-[Eu_2(2-PyPzH)$_4Cl_6$], which have longer lifetimes than with the deprotonated ligands in $^3_\infty$[Ln(3-PyPz)$_3$], $^1_\infty$[Ln(2-PyPz)$_3$], Ln = Tb^{3+}, Dy^{3+}, Eu^{3+} which is attributed to increasing internal conversion processes for the latter. When comparing the lifetime and quantum yield of the Tb^{3+}-containing compounds $^2_\infty$[Tb_2(3-PyPzH)$_3Cl_6$]·2Tol (τ = 2.039(9) ms, QY = 73 %), $^2_\infty$[Tb_2(3-PyPzH)$_3Cl_6$]·2MeCN (τ = 2.294(9) ms, QY = 76 %), and [Tb(2-PyPzH)$_2Cl_3$] (τ = 1.230 ms, QY = 92 %) with the highest reported lifetimes and quantum yield values in the literature, such as [Tb_2Cl_6(μ-4,4'-bipy)(py)$_6$] (τ = 3.598 ms, bipy = 4,4´-bipyridine, QY=86 %),[77] [Tb(bbpen)Cl] (bbpen^{2-} = N,N′-bis(2-oxidobenzyl)-N,N′-bis(pyridine-2-ylmethyl)-ethylenediamine, τ = 0.814 ms, QY = 90 %), and [Ln(bbppn)Cl] (bbppn^{2-} = N,N′-bis(2-oxidobenzyl)-N,N′-bis-(pyridine-2-ylmethyl)-1,2-propanediamine, τ = 0.969 ms, QY = 92 %),[170] the complex [Tb(2-PyPzH)$_2Cl_3$] reaches the highest QYs reported among the related Tb^{3+}-based compounds, and its lifetime lies in the long range. A broad shoulder in the VIS region of the absorption spectra is detected for $^3_\infty$[Eu(3-PyPzH)Cl_3] and attributed to the presence of a ligand-to-metal charge transfer (LMCT), which explains the higher intensity of the ligand emission in the emission spectra and the shorter lifetime observed compared to $^2_\infty$[Eu_2(3-PyPzH)$_3Cl_6$]·2MeCN.

NIR emission bands can be also observed for Nd^{3+}-, Sm^{3+}-, Dy^{3+}-, Ho^{3+}-, and Er^{3+}-based CPs and complexes. The Ho^{3+}-based luminescence observed is weak, as it is effectively quenched by the high vibrational energy of the ligands and the electronic structure of Ho^{3+}. The absorption spectroscopy shows ion-specific 4f–4f transitions that can be assigned for Nd^{3+}, Sm^{3+}, Eu^{3+}, Dy^{3+}, Ho^{3+}, and Er^{3+} in a wide range from UV-VIS to the NIR region. The full width at half maximum (FWHM) of the transition $^4I_{13/2}\rightarrow{}^4I_{15/2}$ is 80 nm for [Er(2-PyPzH)$_2Cl_3$], which may endow a wide gain bandwidth for optical amplification.[155, 162]

With the exception of $^{2}_{\infty}[Ho_2(3\text{-}PyPzH)_3Cl_6]\cdot 2MeCN$, which showed weak ferromagnetic coupling between Ho–Ho centers, direct current (DC) magnetic susceptibility measurements showed that Dy^{3+}, Ho^{3+}, and Er^{3+}-based coordination polymers obey the Curie behavior without detecting interatomic interactions. Due to the magnetic isolation of the lanthanide centers in the crystal lattice of the studied CPs shown in **Chapter 3** and **Appendix A**, the study of the interaction between the magnetic and photophysical properties was limited.

In summary, solvent free-high temperature and anhydrous solvothermal reactions of three pyridylpyrazoles with lanthanides led to the synthesis of 76 CPs and complexes that differ in constitution and structural extension. Redox-based reactions of elemental lanthanides have produced three series of 35 homoleptic 3D-, 2D-, and 1D-coordination polymers besides divalent europium and two other heteroleptic 2D-networks. Three heterobimetallic lanthanide/alkaline earth complexes and two alkaline earth complexes were also synthesized by melt-based synthesis of elemental lanthanide and/or alkaline earth metals (AE). Solvothermal synthesis using different solvents with lanthanide chlorides has produced 33 heteroleptic 3D- and 2D-coordination polymers and complexes, along with salt-like complexes. The CPs were characterized by SC and PXRD, elemental analysis, topological analysis, IR and photoluminescence spectroscopy, DC magnetic measurements, and thermal analysis. Unique pink through orange to red emissions based on 5d–4f transitions were detected for Ce^{3+}-based materials which offer a new perspective for solid-state lighting applications. The CPs show photoluminescence with intra-4f emission of the Ln^{3+} ions being activated by good to excellent antenna effects of the ligands leading to Ln^{3+} sensitization. The high quantum yield of Tb^{3+}, which reaches 92 %, and the uncommon NIR emission for Tm^{3+}, Ho^{3+}, and Pr^{3+} serve as evidence of the excellent efficacy of the N-donor ligands under study. These results suggest potential applications in solid state lighting, optical amplifications, and biomedicine. The tuning of the luminescence chromaticity towards white-light emission was proved to be possible for some frameworks, which is a desirable property for light-emitting materials. Direct current (DC) magnetic susceptibility measurements proved the magnetic isolation of the studied CPs, which limited the study of the interaction between the magnetic and photophysical properties. Overall, this shows the high potential of coordination polymers and complexes with a pyridyl-pyrazole ligand as the N-donor for the design of materials with versatile structures. These materials are able to exhibit very interesting photophysical properties.

5. References

[1] N. G. Connelly, T. Damhus, R. M. Hartshorn, A. T. Hutton, *Nomenclature of inorganic chemistry: IUPAC recommendations 2005*, RSC Publishing, Cambridge, **2005**.

[2] J.-C. G. Bünzli, in *Kirk-Othmer Encyclopedia of Chemical Technology*, John Wiley & Sons, Inc., New York, **2000**, pp. 1-43.

[3] J.-C. G. Bünzli, *J. Coord. Chem.* **2014**, *67*, 3706-3733.

[4] T. Gray, *Elements: A visual exploration of every known atom in the universe*, Hachette, United Kingdom, **2012**.

[5] R. Beatty, *The Lanthanides*, Marshall Cavendish, **2008**.

[6] S. Cotton, *Lanthanide and actinide chemistry*, John Wiley & Sons, **2013**.

[7] S. F. A. Kettle, in *Physical Inorganic Chemistry: a coordination chemistry approach*, Springer, Heidelberg, **1996**, pp. 238-268.

[8] A. de Bettencourt-Dias, in *Encyclopedia of Inorganic and Bioinorganic Chemistry*, John Wiley & Sons, **2012**.

[9] J.-C. G. Bünzli, S. V. Eliseeva, in *Springer Series on Fluorescence: Lanthanide Luminescence: Photophysical, Analytical and Biological Aspects, Vol. 7*, ed. O. S. Wolfbeis and M. Hof, Springer Verlag, Berlin, **2011**, pp. 1-46.

[10] O. Laporte, W. F. Meggers, *J. Opt. Soc. Am.* **1925**, *11*, 459-463.

[11] S. Comby, J.-C. G. Bünzli, in *Handbook on the physics and chemistry of rare earths, Vol. 37*, Elsevier, New York, **2007**, pp. 217-470.

[12] P. R. Matthes, K. Müller-Buschbaum, *Z. Anorg. Allg. Chem.* **2014**, *640*, 2847-2851.

[13] H. Yin, P. J. Carroll, B. C. Manor, J. M. Anna, E. J. Schelter, *J. Am. Chem. Soc.* **2016**, *138*, 5984-5993.

[14] X. Qin, X. Liu, W. Huang, M. Bettinelli, X. Liu, *Chem. Rev.* **2017**, *117*, 4488-4527.

[15] L. V. Meyer, F. Schönfeld, A. Zurawski, M. Mai, C. Feldmann, K. Müller-Buschbaum, *Dalton Trans.* **2015**, *44*, 4070-4079.

[16] S. T. Frey, W. D. Horrocks Jr., *Inorg. Chem.* **1991**, *30*, 1073-1079.

[17] G. Blasse, B. C. Grabmaier, in *Luminescent Materials*, Springer Berlin, **1994**, pp. 1-9.

[18] P. Fang, L. Wang, G. Zhan, W. Yan, P. Huo, A. Ying, Y. Zhang, Z. Zhao, G. Yu, Y. Huang, S. Gong, L. Duan, Z. Liu, Z. Bian, C. Huang, *ACS Appl. Mater. Interfaces* **2021**, *13*, 45686-45695.

[19] N. Kodama, Y. Tanii, M. Yamaga, *J. Lumin.* **2000**, *87*, 1076-1078.

[20] G. C. Kim, H. L. Park, S. I. Yun, B. G. Moon, *J. Mater. Sci. Lett.* **1986**, *5*, 359-360.

[21] J. W. H. Van Krevel, H. T. Hintzen, R. Metselaar, A. Meijerink, *J. Alloys Compd.* **1998**, *268*, 272-277.

[22] G. Gauthier, S. Jobic, M. Evain, H.-J. Koo, M.-H. Whangbo, C. Fouassier, R. Brec, *Chem. Mater.* **2003**, *15*, 828-837.

[23] G. Blasse, A. Bril, *Appl. Phys. Lett.* **1967**, *11*, 53-55.

[24] P. Zheng, S. Li, L. Wang, T.-L. Zhou, S. You, T. Takeda, N. Hirosaki, R.-J. Xie, *ACS Appl. Mater. Interfaces* **2018**, *10*, 14930-14940.

[25] W. Li, Y. Zhuang, P. Zheng, T.-L. Zhou, J. Xu, J. Ueda, S. Tanabe, L. Wang, R.-J. Xie, *ACS Appl. Mater. Interfaces* **2018**, *10*, 27150-27159.

[26] D. Zhang, W. Xiao, C. Liu, X. Liu, J. Ren, B. Xu, J. Qiu, *Nat. Commun.* **2020**, *11*, 2805.

[27] H. Wu, Z. Hao, G.-H. Pan, L. Zhang, H. Wu, X. Zhang, L. Zhang, J. Zhang, *J. Eur. Ceram. Soc.* **2020**, *40*, 2439-2444.

[28] D. Wu, Z. Hao, X. Zhang, G.-H. Pan, Y. Luo, L. Zhang, H. Zhao, J. Zhang, *J. Lumin.* **2017**, *186*, 170-174.
[29] J. M. Ogiegło, A. Zych, T. Jüstel, A. Meijerink, C. R. Ronda, *Opt. Mater.* **2013**, *35*, 322-331.
[30] D. A. I. Peng, J. I. Cheng, S. H. E. N. Liming, Q. I. A. N. Qi, G. U. O. Guobiao, X. Zhang, B. A. O. Ningzhong, *J. Rare Earths* **2017**, *35*, 341-346.
[31] P. Zeng, X. Wei, S. Zhou, M. Yin, Y. Chen, *J. Appl. Phys.* **2016**, *120*, 093104.
[32] R. M. Kowalski, J. Komar, P. Solarz, *J. Alloys Compd.* **2020**, *848*, 156228.
[33] S. Chawla, T. Roy, K. Majumder, A. Yadav, *J. Exp. Nanosci.* **2014**, *9*, 776-784.
[34] T. Hasegawa, S. W. Kim, T. Ueda, T. Ishigaki, K. Uematsu, H. Takaba, K. Toda, M. Sato, *J. Mater. Chem. C* **2017**, *5*, 9472-9478.
[35] Y. Wang, J. Ding, Z. Zhao, Y. Wang, *Inorg. Chem.* **2018**, *57*, 14542-14553.
[36] C.-H. Huang, *Rare earth coordination chemistry: fundamentals and applications*, John Wiley & Sons, Singapore, **2010**.
[37] A. Aebischer, F. Gumy, J.-C. G. Bünzli, *Phys. Chem. Chem. Phys.* **2009**, *11*, 1346-1353.
[38] M. H. V. Werts, R. T. F. Jukes, J. W. Verhoeven, *Phys. Chem. Chem. Phys.* **2002**, *4*, 1542-1548.
[39] S. V. Eliseeva, J.-C. G. Bünzli, *Chem. Soc. Rev.* **2010**, *39*, 189-227.
[40] D. C. Harris, M. D. Bertolucci, *Symmetry and Spectroscopy: An Introduction to Vibrational and Electronic Spectroscopy*, Courier Corporation, North Chelmsford, USA, **1989**.
[41] M. Latva, H. Takalo, V.-M. Mukkala, C. Matachescu, J. C. Rodríguez-Ubis, J. Kankare, *J. Lumin.* **1997**, *75*, 149-169.
[42] K. Müller-Buschbaum, F. Beuerle, C. Feldmann, *Microporous Mesoporous Mater.* **2015**, *216*, 171-199.
[43] N. Ishikawa, M. Sugita, T. Ishikawa, S.-y. Koshihara, Y. Kaizu, *J. Am. Chem. Soc.* **2003**, *125*, 8694-8695.
[44] N. Ishikawa, M. Sugita, T. Ishikawa, S.-y. Koshihara, Y. Kaizu, *J. Phys. Chem. B* **2004**, *108*, 11265-11271.
[45] L. Ungur, in *Lanthanide-Based Multifunctional Materials: From OLEDs to SIMs* (Eds.: P. Martín-Ramos, M. Ramos Silva), Elsevier, Amsterdam, **2018**, pp. 1-58.
[46] D. N. Woodruff, R. E. P. Winpenny, R. A. Layfield, *Chem. Rev.* **2013**, *113*, 5110-5148.
[47] S. Roy, A. Chakraborty, T. K. Maji, *Coord. Chem. Rev.* **2014**, *273-274*, 139-164.
[48] J. Jensen, A. R. Mackintosh, *Rare earth magnetism*, Clarendon Press, Oxford, United Kingdom, **1991**.
[49] K. Müller-Buschbaum, Y. Mokaddem, *Chem. Commun.* **2006**, 2060-2062.
[50] J. C. Rybak, I. Schellenberg, R. Pöttgen, K. Müller-Buschbaum, *Z. Anorg. Allg. Chem.* **2010**, *636*, 1720-1725.
[51] K. Müller-Buschbaum, *Z. Anorg. Allg. Chem.* **2005**, *631*, 811-828.
[52] A. Zurawski, J. C. Rybak, L. V. Meyer, K. Müller-Buschbaum, *Z. Anorg. Allg. Chem.* **2013**, *639*, 261-267.
[53] K. Müller-Buschbaum, *Zeitschrift für Naturforschung B* **2006**, *61*, 792-798.
[54] A. Zurawski, M. Mai, D. Baumann, C. Feldmann, K. Müller-Buschbaum, *Chem. Commun.* **2011**, *47*, 496-498.
[55] K. Müller-Buschbaum, Y. Mokaddem, *Eur. J. Inorg. Chem.* **2006**, *3*, 2000-2010.
[56] K. Müller-Buschbaum, Y. Mokaddem, *Z. Anorg. Allg. Chem.* **2008**, *634*, 2360-2366.
[57] K. Müller-Buschbaum, Y. Mokaddem, F. M. Schappacher, R. Pöttgen, *Angew. Chem., Int. Ed.* **2007**, *46*, 4385-4387.

[58] G. B. Deacon, C. M. Forsyth, *Inorganic Chemistry Highlights* **2002**, 139-153.
[59] K. Müller-Buschbaum, C. C. Quitmann, *Inorg. Chem.* **2003**, *42*, 2742-2750.
[60] C. C. Quitmann, K. Müller-Buschbaum, *Z. Anorg. Allg. Chem.* **2004**, *630*, 2422-2430.
[61] K. Müller-Buschbaum, C. C. Quitmann, *Zeitschrift für Kristallographie-Crystalline Materials* **2005**, *220*, 158-165.
[62] K. Müller-Buschbaum, C. C. Quitmann, *Z. Anorg. Allg. Chem.* **2003**, *629*, 1610-1616.
[63] K. Müller-Buschbaum, C. C. Quitmann, *Eur. J. Inorg. Chem.* **2004**, *2*, 4330-4337.
[64] C. C. Quitmann, V. Bezugly, F. R. Wagner, K. Müller-Buschbaum, *Z. Anorg. Allg. Chem.* **2006**, *632*, 1173-1186.
[65] C. C. Quitmann, K. Müller-Buschbaum, *Zeitschrift fur Naturforschung - Section B Journal of Chemical Sciences* **2004**, *59*, 562-566.
[66] C. C. Quitmann, K. Müller-Buschbaum, *Z. Anorg. Allg. Chem.* **2005**, *631*, 1191-1198.
[67] J. C. Rybak, L. V. Meyer, J. Wagenhöfer, G. Sextl, K. Müller-Buschbaum, *Inorg. Chem.* **2012**, *51*, 13204-13213.
[68] J. C. Rybak, M. Tegel, D. Johrendt, K. Mtiller-Buschbaum, *Zeitschrift fur Kristallographie* **2010**, *225*, 187-194.
[69] A. De Cian, M. Moussavi, J. Fischer, R. Weiss, *Inorg. Chem.* **1985**, *24*, 3162-3167.
[70] M. S. Haghighi, C. R. Teske, H. Honborg, *Z. Anorg. Allg. Chem.* **1992**, *608*, 73-80.
[71] G. B. Deacon, A. Gitlits, P. W. Roesky, M. R. Bürgstein, K. C. Lim, B. W. Skelton, A. H. White, *Chem. Eur. J.* **2001**, *7*, 127-138.
[72] G. B. Deacon, A. Gitlits, B. W. Skelton, A. H. White, *Chem. Commun.* **1999**, 1213-1214.
[73] L. Natrajan, J. Pécaut, M. Mazzanti, C. LeBrun, *Inorg. Chem.* **2005**, *44*, 4756-4765.
[74] J. Scott, D. J. Mindiola, *Dalton Trans.* **2009**, 8463-8472.
[75] N. Dannenbauer, S. H. Zottnick, K. Müller-Buschbaum, *Z. Anorg. Allg. Chem.* **2017**, *643*, 1513-1518.
[76] P. R. Matthes, F. Schönfeld, S. H. Zottnick, K. Müller-Buschbaum, *Molecules* **2015**, *20*, 12125-12153.
[77] P. R. Matthes, J. Nitsch, A. Kuzmanoski, C. Feldmann, A. Steffen, T. B. Marder, K. Müller-Buschbaum, *Chem. Eur. J.* **2013**, *19*, 17369-17378.
[78] P. R. Matthes, C. J. Höller, M. Mai, J. Heck, S. J. Sedlmaier, S. Schmiechen, C. Feldmann, W. Schnick, K. Müller-Buschbaum, *J. Mater. Chem.* **2012**, *22*, 10179-10187.
[79] P. R. Matthes, J. Eyley, J. H. Klein, A. Kuzmanoski, C. Lambert, C. Feldmann, K. Müller-Buschbaum, *Eur. J. Inorg. Chem.* **2015**, *2015*, 826-836.
[80] N. Dannenbauer, P. R. Matthes, **2016**, 6529-6540.
[81] J. G. Leipoldt, L. D. C. Bok, S. S. Basson, J. S. Van Vollenhoven, A. E. Laubscher, *J. Inorg. Nucl. Chem.* **1976**, *38*, 2241-2244.
[82] N. Dannenbauer, P. R. Matthes, T. P. Scheller, J. Nitsch, S. H. Zottnick, M. S. Gernert, A. Steffen, C. Lambert, K. Müller-Buschbaum, *Inorg. Chem.* **2016**, *55*, 7396-7406.
[83] J.-K. Sun, C. Chen, L.-X. Cai, C.-X. Ren, B. Tan, J. Zhang, *Chem. Commun.* **2014**, *50*, 15956-15959.
[84] L.-F. Wang, J.-Z. Qiu, J.-L. Liu, Y.-C. Chen, J.-H. Jia, J. Jover, E. Ruiz, M.-L. Tong, *Chem. Commun.* **2015**, *51*, 15358-15361.

[85] K. P. Carter, K. E. Thomas, S. J. A. Pope, R. J. Holmberg, R. J. Butcher, M. Murugesu, C. L. Cahill, *Inorg. Chem.* **2016**, *55*, 6902-6915.
[86] K. V. Vasudevan, N. A. Smith, B. L. Scott, E. A. McKigney, M. W. Blair, J. C. Gordon, R. E. Muenchausen, *Inorg. Chem.* **2011**, *50*, 4627-4631.
[87] J. Lhoste, N. Henry, T. Loiseau, F. Abraham, *Polyhedron* **2011**, *30*, 1289-1294.
[88] X. N. Fang, B. X. Tang, X. G. Yi, R. Y. Kuang, Y. P. Xu, *Russian Journal of Coordination Chemistry* **2018**, *44*, 169-172.
[89] L. L. Cai, Y. T. Hu, Y. Li, K. Wang, X. Q. Zhang, G. Muller, X. M. Li, G. X. Wang, *Inorg. Chim. Acta* **2019**, *489*, 85-92.
[90] R. T. Golkowski, N. S. Settineri, X. Zhao, D. R. McMillin, *The Journal of Physical Chemistry A* **2015**, *119*, 11650-11658.
[91] A. E. Sedykh, R. Bissert, D. G. Kurth, K. Müller-Buschbaum, *Z. Kristallogr. – Cryst. Mater.* **2020**, *235*, 353-363.
[92] A. E. Sedykh, M. Becker, M. T. Seuffert, D. Heuler, M. Maxeiner, D. G. Kurth, C. E. Housecroft, E. C. Constable, K. Müller-Buschbaum, *ChemPhotoChem* **2022**, e202200244.
[93] A. E. Sedykh, D. G. Kurth, K. Müller-Buschbaum, *Eur. J. Inorg. Chem.* **2019**, *2019*, 4564-4571.
[94] R.-f. Li, R.-h. Li, X.-f. Liu, X.-h. Chang, X. Feng, *RSC Adv.* **2020**, *10*, 6192-6199.
[95] A. A. Kitos, D. A. Gálico, N. Mavragani, R. Castañeda, J. O. Moilanen, J. L. Brusso, M. Murugesu, *Chem. Commun.* **2021**, *57*, 7818-7821.
[96] C. J. Höller, M. Mai, C. Feldmann, K. Müller-Buschbaum, *Dalton Trans.* **2010**, *39*, 461-468.
[97] A. E. Sedykh, J. J. Pflug, T. C. Schäfer, R. Bissert, D. G. Kurth, K. Müller-Buschbaum, *ACS Sustainable Chem. Eng.* **2022**, *10*, 5101-5109.
[98] T.-L. Hu, J.-J. Wang, J.-R. Li, X.-H. Bu, *J. Mol. Struct.* **2006**, *796*, 18-22.
[99] C. S. Liu, X. S. Shi, J. R. Li, J. J. Wang, X. H. Bu, *Cryst. Growth Des.* **2006**, *6*, 656-663.
[100] L. He, L. Duan, J. Qiao, D. Zhang, L. Wang, Y. Qiu, *Chem. Commun.* **2011**, *47*, 6467-6469.
[101] F. L. Liu, J. Tao, *Chem. Eur. J.* **2017**, *23*, 18252-18257.
[102] A. D. Burrows, D. J. Kelly, M. I. H. Mohideen, M. F. Mahon, V. M. Pop, C. Richardson, *CrystEngComm* **2011**, *13*, 1676-1682.
[103] L.-M. Zhang, F.-Z. Hua, C. Feng, K. Zou, Y.-M. Yang, G.-N. Zhang, Y.-C. Wang, H. Zhao, *J. Inorg. Organomet. Polym. Mater.* **2022**, *32*, 423-430.
[104] S.-Z. Zhan, M. Li, J. Zheng, Q.-J. Wang, S. W. Ng, D. Li, *Inorg. Chem.* **2017**, *56*, 13446-13455.
[105] A. J. Amoroso, A. M. C. Thompson, J. C. Jeffery, P. L. Jones, J. A. McCleverty, M. D. Ward, *J. Chem. Soc., Chem. Commun.* **1994**, *24*, 2751-2752.
[106] M. R. Del Giudice, C. Mustazza, A. Borioni, F. Gatta, K. Tayebati, F. Amenta, P. Tucci, S. Pieretti, *Arch. Pharm. Pharm. Med. Chem.* **2003**, *336*, 143-154.
[107] V. J. Bauer, H. P. Dalalian, W. J. Fanshawe, S. R. Safir, E. C. Tocus, C. R. Boshart, *J. Med. Chem.* **1968**, *11*, 981-984.
[108] D. Su, Y. Liu, S. Li, S. Ding, Y. Jin, Z. Wang, X. Hu, L. Zhang, *Eur. J. Inorg. Chem.* **2017**, *2017*, 651-658.
[109] J. Wang, D. Su, D. Wang, S. Ding, C. Huang, H. Huang, X. Hu, Z. Wang, S. Li, *Inorg. Chem.* **2015**, *54*, 10648-10655.
[110] A. Bremer, C. M. Ruff, D. Girnt, U. Müllich, J. Rothe, P. W. Roesky, P. J. Panak, A. Karpov, T. J. J. Müller, M. A. Denecke, A. Geist, *Inorg. Chem.* **2012**, *51*, 5199-5207.
[111] S. Trofimenko, *J. Am. Chem. Soc.* **1966**, *88*, 1842-1844.

[112] T. G. Hodgkins, D. R. Powell, *Inorg. Chem.* **1996**, *35*, 2140-2148.
[113] J. L. Koch, P. A. Shapley, *Organometallics* **1997**, *16*, 4071-4076.
[114] Y.-J. Sun, B. Zhao, P. Cheng, *Inorg. Chem. Commun.* **2007**, *10*, 583-585.
[115] S. Trofimenko, *Polyhedron* **2004**, *23*, 197-203.
[116] S. Trofimenko, *Chem. Rev.* **1993**, *93*, 943-980.
[117] P. L. Jones, A. J. Amoroso, J. C. Jeffery, J. A. McCleverty, E. Psillakis, L. H. Rees, M. D. Ward, *Inorg. Chem.* **1997**, *36*, 10-18.
[118] A. J. Amoroso, J. C. Jeffery, P. L. Jones, J. A. McCleverty, L. Rees, A. L. Rheingold, Y. Sun, J. Takats, S. Trofimenko, M. D. Ward, G. P. A. Vap, *J. Chem. Soc., Chem. Commun.* **1995**, 1881-1882.
[119] M. D. Ward, J. A. McCleverty, J. C. Jeffery, *Coord. Chem. Rev.* **2001**, *222*, 251-272.
[120] Z. R. Bell, G. R. Motson, J. C. Jeffery, J. A. McCleverty, M. D. Ward, *Polyhedron* **2001**, *20*, 2045-2053.
[121] N. C. Harden, J. C. Jeffery, J. A. McCleverty, L. H. Rees, M. D. Ward, *New J. Chem.* **1998**, *22*, 661-663.
[122] D. A. Bardwell, J. C. Jeffery, P. L. Jones, J. A. McCleverty, E. Psillakis, Z. Reeves, M. D. Ward, *J. Chem. Soc., Dalton Trans.* **1997**, 2079-2086.
[123] E. A. Mikhalyova, A. V. Yakovenko, M. Zeller, K. S. Gavrilenko, M. A. Kiskin, S. S. Smola, V. P. Dotsenko, I. L. Eremenko, A. W. Addison, V. V. Pavlishchuk, *Dalton Trans.* **2017**, *46*, 3457-3469.
[124] N. Armaroli, G. Accorsi, F. Barigelletti, S. M. Couchman, J. S. Fleming, N. C. Harden, J. C. Jeffery, K. L. V. Mann, J. A. McCleverty, L. H. Rees, S. R. Starling, M. D. Ward, *Inorg. Chem.* **1999**, *38*, 5769-5776.
[125] G. M. Davies, H. Adams, S. J. A. Pope, S. Faulkner, M. D. Ward, *Photochem. Photobiol. Sci.* **2005**, *4*, 829-834.
[126] E. A. Mikhalyova, A. V. Yakovenko, M. Zeller, M. A. Kiskin, Y. V. Kolomzarov, I. L. Eremenko, A. W. Addison, V. V. Pavlishchuk, *Inorg. Chem.* **2015**, *54*, 3125-3133.
[127] Z. R. Reeves, K. L. V. Mann, J. C. Jeffery, J. A. McCleverty, M. D. Ward, F. Barigelletti, N. Armaroli, *J. Chem. Soc., Dalton Trans.* **1999**, 349-355.
[128] A. Beeby, B. P. Burton-Pye, S. Faulkner, G. R. Motson, J. C. Jeffery, J. A. McCleverty, M. D. Ward, *J. Chem. Soc., Dalton Trans.* **2002**, *9*, 1923-1928.
[129] H. Adams, S. R. Batten, G. M. Davies, M. B. Duriska, J. C. Jeffery, P. Jensen, J. Lu, G. R. Motson, S. J. Coles, M. B. Hursthouse, M. D. Ward, *Dalton Trans.* **2005**, 1910-1923.
[130] K. Weis, H. Vahrenkamp, *Inorg. Chem.* **1997**, *36*, 5589-5591.
[131] Y.-W. Yip, H. Wen, W.-T. Wong, P. A. Tanner, K.-L. Wong, *Inorg. Chem.* **2012**, *51*, 7013-7015.
[132] I. A. Gass, B. Moubaraki, S. K. Langley, S. R. Batten, K. S. Murray, *Chem. Commun.* **2012**, *48*, 2089-2091.
[133] A. C. Coelho, A. C. Gomes, J. A. Fernandes, F. A. A. Paz, S. S. Braga, L. Rino, L. Pereira, M. Pillinger, I. S. Gonçalves, *Eur. J. Inorg. Chem.* **2014**, *2014*, 1284-1288.
[134] J. H. Zou, Q. Liu, J. F. Dong, M. J. Cao, Q. Q. Wu, Q. Y. Yue, Q. Y. Li, G. W. Yang, *Aust. J. Chem.* **2015**, *68*, 1152-1159.
[135] S. Bala, A. Goswami, S. Sengupta, S. Ganguly, S. Bhattacharya, S. Khanra, R. Mondal, *Cryst. Growth Des.* **2013**, *13*, 5068-5075.
[136] S. Bala, A. Adhikary, S. Bhattacharya, M. S. Bishwas, P. Poddar, R. Mondal, *ChemistrySelect* **2017**, *2*, 11341-11345.

[137] S. Bala, M. S. Bishwas, B. Pramanik, S. Khanra, K. M. Fromm, P. Poddar, R. Mondal, *Inorg. Chem.* **2015**, *54*, 8197-8206.
[138] S. Bhattacharya, S. Bala, R. Mondal, *CrystEngComm* **2019**, *21*, 5665-5672.
[139] R. J. Blagg, L. Ungur, F. Tuna, J. Speak, P. Comar, D. Collison, W. Wernsdorfer, E. J. L. McInnes, L. F. Chibotaru, R. E. P. Winpenny, *Nat. Chem.* **2013**, *5*, 673-678.
[140] L. Chen, J. Zhou, A. Yuan, Y. Song, *Dalton Trans.* **2017**, *46*, 15812-15818.
[141] I. D. Hughes, M. Däne, A. Ernst, W. Hergert, M. Lüders, J. Poulter, J. B. Staunton, A. Svane, Z. Szotek, W. M. Temmerman, *Nature* **2007**, *446*, 650-653.
[142] L.-R. Xing, Z. Lu, M. Li, J. Zheng, D. Li, *J. Phys. Chem. Lett.* **2020**, *11*, 2067-2073.
[143] K. Tuong Ly, R.-W. Chen-Cheng, H.-W. Lin, Y.-J. Shiau, S.-H. Liu, P.-T. Chou, C.-S. Tsao, Y.-C. Huang, Y. Chi, *Nat. Photonics* **2017**, *11*, 63-68.
[144] M. del C. Fernández-Fernández, R. Bastida, A. Macías, P. Pérez-Lourido, C. Platas-Iglesias, L. Valencia, *Inorg. Chem.* **2006**, *45*, 4484-4496.
[145] M. N. Bochkarev, G. V. Khoroshenkov, H. Schumann, S. Dechert, *J. Am. Chem. Soc.* **2003**, *125*, 2894-2895.
[146] M. G. B. Drew, D. Guillaneux, M. J. Hudson, P. B. Iveson, M. L. Russell, C. Madic, *Inorg. Chem. Commun.* **2001**, *4*, 12-15.
[147] S. SeethaLekshmi, A. Ramya, M. Reddy, S. Varughese, *Journal of Photochemistry and Photobiology C: Photochemistry Reviews* **2017**, *33*, 109-131.
[148] F. Zhang, P. Yan, H. Li, X. Zou, G. Hou, G. Li, *Dalton Trans.* **2014**, *43*, 12574-12581.
[149] D. M. Lyubov, A. N. Carneiro Neto, A. Fayoumi, K. A. Lyssenko, V. M. Korshunov, I. V. Taydakov, F. Salles, Y. Guari, J. Larionova, L. D. Carlos, J. Long, A. A. Trifonov, *J. Mater. Chem. C* **2022**, *10*, 7176-7188.
[150] K. Senthil Kumar, B. Schäfer, S. Lebedkin, L. Karmazin, M. M. Kappes, M. Ruben, *Dalton Trans.* **2015**, *44*, 15611-15619.
[151] J. A. Ridenour, K. P. Carter, R. J. Butcher, C. L. Cahill, *CrystEngComm* **2017**, *19*, 1172-1189.
[152] J. Feng, H.-J. Zhang, S.-Y. Song, Z.-F. Li, L.-N. Sun, Y. Xing, X.-M. Guo, *J. Lumin.* **2008**, *128*, 1957-1964.
[153] O. A. Serra, E. J. Nassar, P. S. Calefi, I. L. V. Rosa, *J. Alloys Compd.* **1998**, *275-277*, 838-840.
[154] R. J. Batrice, A. K. Adcock, P. M. Cantos, J. A. Bertke, K. E. Knope, *Cryst. Growth Des.* **2017**, *17*, 4603-4612.
[155] L.-N. Sun, J.-B. Yu, G.-L. Zheng, H.-J. Zhang, Q.-G. Meng, C.-Y. Peng, L.-S. Fu, F.-Y. Liu, Y.-N. Yu, *Eur. J. Inorg. Chem.* **2006**, *2006*, 3962-3973.
[156] W. P.-W. Lai, W.-T. Wong, *New J. Chem.* **2000**, *24*, 943-944.
[157] S. I. Klink, P. O. Alink, L. Grave, F. G. Peters, J. W. Hofstraat, F. Geurts, F. C. van Veggel, *Journal of the Chemical Society, Perkin Transactions 2* **2001**, 363-372.
[158] S. Lin, R. J. Feuerstein, A. R. Mickelson, *J. Appl. Phys.* **1996**, *79*, 2868-2874.
[159] J. Feng, S.-Y. Song, R.-P. Deng, W.-Q. Fan, H.-J. Zhang, *Langmuir* **2010**, *26*, 3596-3600.
[160] L. Sun, Y. Qiu, T. Liu, J. Z. Zhang, S. Dang, J. Feng, Z. Wang, H. Zhang, L. Shi, *ACS Appl. Mater. Interfaces* **2013**, *5*, 9585-9593.
[161] R. Van Deun, P. Nockemann, C. Görller-Walrand, K. Binnemans, *Chem. Phys. Lett.* **2004**, *397*, 447-450.

[162] O.-H. Park, S.-Y. Seo, J.-I. Jung, J. Y. Bae, B.-S. Bae, *J. Mater. Res.* **2003**, *18*, 1039-1042.
[163] D. J. Lewis, F. Moretta, A. T. Holloway, Z. Pikramenou, *Dalton Trans.* **2012**, *41*, 13138-13146.
[164] M. Mahato, P. P. Jana, K. Harms, H. P. Nayek, *RSC Adv.* **2015**, *5*, 62167-62172.
[165] C. Y. Chow, S. V. Eliseeva, E. R. Trivedi, T. N. Nguyen, J. W. Kampf, S. Petoud, V. L. Pecoraro, *J. Am. Chem. Soc.* **2016**, *138*, 5100-5109.
[166] P. R. Satheesh Chandran, U. S. Soumya Mol, R. Drisya, M. R. Sudarsanakumar, M. R. Prathapachandra Kurup, *J. Mol. Struct.* **2017**, *1137*, 396-402.
[167] X. Zhou, H. Wang, S. Jiang, G. Xiang, X. Tang, X. Luo, L. Li, X. Zhou, *Inorg. Chem.* **2019**, *58*, 3780-3788.
[168] M. Hasegawa, H. Ohtsu, D. Kodama, T. Kasai, S. Sakurai, A. Ishii, K. Suzuki, *New J. Chem.* **2014**, *38*, 1225-1234.
[169] C. Seidel, C. Lorbeer, J. Cybińska, A.-V. Mudring, U. Ruschewitz, *Inorg. Chem.* **2012**, *51*, 4679-4688.
[170] L. E. D. N. Aquino, G. A. Barbosa, J. D. L. Ramos, S. O. K. Giese, F. S. Santana, D. L. Hughes, G. G. Nunes, L. Fu, M. Fang, G. Poneti, A. N. Carneiro Neto, R. T. Moura, R. A. S. Ferreira, L. D. Carlos, A. G. MacEdo, J. F. Soares, *Inorg. Chem.* **2021**, *60*, 892-907.

Appendix A. Additional direct current (DC) magnetic measurements

Direct current (DC) magnetic susceptibility measurements were further performed for $^{3}_{\infty}$[Dy(4-PyPz)$_3$], $^{3}_{\infty}$[Dy(4-PyPz)$_3$] in a temperature range of 3 to 300 K and under a magnetic field of 1 T. The data were fitted in the given temperature range with a modified Curie–Weiss law.

A.1. DC magnetic susceptibility measurements for $^{3}_{\infty}$[Dy(4-PyPz)$_3$]

An effective magnetic moment μ_{eff} of 11.098(2) μB, a Weiss constant θ of −2.859(8) K, and a temperature-independent paramagnetic susceptibility χ_0 of 13.13(2) × 10^{-3} cm^3 mol^{-1} were obtained. At room temperature, the $\chi_M T$ value is 19.23 cm^3 K mol^{-1}, which is higher than the theoretical value for the corresponding noninteracting Dy^{3+} ions ($^6H_{15/2}$, S = 5/2, L = 5, g = 4/3, χT = 14.17 cm^3 K mol^{-1}). Upon cooling, a monotonic slow decrease of $\chi_M T$ takes place up to 45 K, where a significant decrease is observed, with $\chi_M T$ reaching 7.3 cm^3 K mol^{-1}. The small, negative Weiss constants θ are results of spin-orbit coupling as well as the crystal field effect.

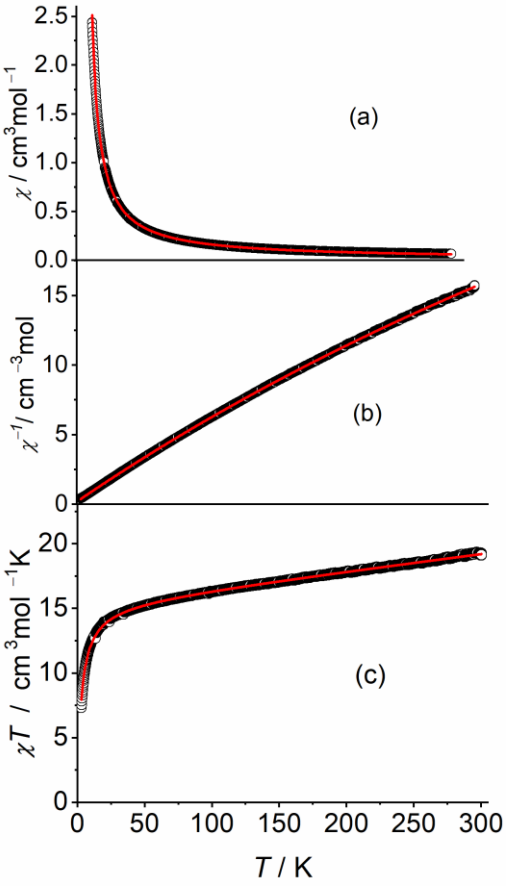

Figure A.1. Temperature dependency of the magnetic susceptibility of $^{3}_{\infty}$[Dy(4-PyPz)$_3$] in a temperature range from 3 to 300 K and magnetic field 1T: a) χ vs T, b) χ^{-1} vs T , c) χT vs T. The solid red line represents the best fitting curve.

A.2. DC magnetic susceptibility measurements for $^{3}_{\infty}$[Er(4-PyPz)$_3$]

An effective magnetic moment μ_{eff} of 8.805(8) μB, a Weiss constant θ of −6.84(6) K, and a temperature-independent paramagnetic susceptibility χ_0 of 17.65(7) × 10^{-3} cm^3 mol^{-1} were obtained. At room temperature, the $\chi_M T$ value is 14.51 cm^3 K mol^{-1}, which is higher than the theoretical value for the corresponding noninteracting Er^{3+} ions ($^4I_{15/2}$, S = 3/2, L = 6, g = 6/5, χT = 11.48 cm^3 K mol^{-1}). Upon cooling, a monotonic slow decrease of $\chi_M T$ takes place up to 75 K, where a significant decrease is observed, with $\chi_M T$ reaching 3.7 cm^3 K mol^{-1}. The small, negative Weiss constants θ are results of spin-orbit coupling as well as the crystal field effect.

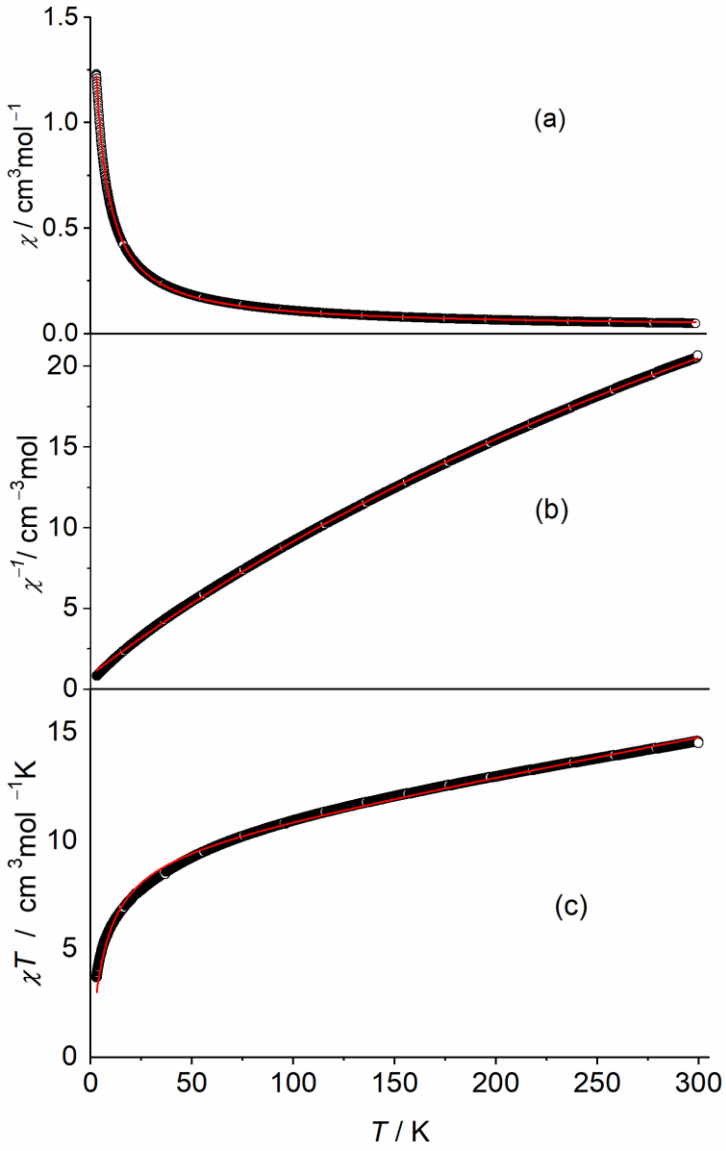

Figure A.2. Temperature dependency of the magnetic susceptibility of $^{3}_{\infty}$[Er(4-PyPz)$_3$] in a temperature range from 3 to 300 K and magnetic field 1T: a) χ vs T, b) χ^{-1} vs T , c) χT vs T. The solid red line represents the best fitting curve.

Appendix B. List of used ligands and abbreviations

2-PyPzH	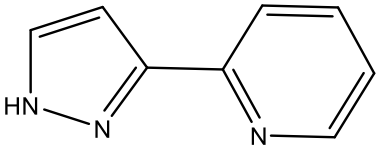 3-(2-pyridyl)pyrazole $C_8H_7N_3$ FW 145.165 g · mol^{-1}
3-PyPzH	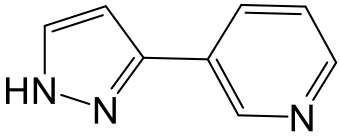 3-(3-pyridyl)pyrazole $C_8H_7N_3$ FW 145.165 g · mol^{-1}
4-PyPzH	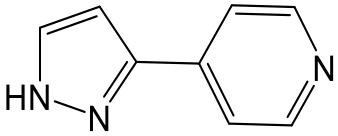 3-(4-pyridyl)pyrazole $C_8H_7N_3$ FW 145.165 g · mol^{-1}

AE	Alkaline earth element
CCDC	Cambridge Crystallographic Data Centre
CIE	Commission internationale de l'éclairage
CP	Coordination polymer
DC	Direct current
DTA	Differential thermal analysis
ED	Electric dipole
IC	Internal conversion
IED	Induced electric dipole
ILCT	Intra-ligand charge transfer
ISC	Intersystem crossing
IC	Internal conversion
LMCT	Ligand-to-metal charge transfer
Ln	Lanthanide
MD	Magnetic dipole
MeCN	Acetonitrile
MLCT	Metal-to-ligand charge transfer
MMET	Metal-to-metal energy transfer
NIR	Near-infrared
PhCl	Chlorobenzene
PLQY or Φ	Photoluminescence quantum yield
Py	pyridine
PXRD	Powder X-ray diffraction

RT	Room temperature
SC	Single crystal
SCXRD	Single-crystal X-ray diffraction
TG	Thermogravimetry
Tol	Toluene
UV	Ultraviolet
VIS	visible